BEILSTEIN JOURNAL OF NANOTECHNOLOGY

Biological and biomimetic materials and surfaces

Edited by Stanislav N. Gorb and Thomas Speck

Imprint

Beilstein Journal of Nanotechnology
www.bjnano.org
ISSN 2190-4286
Email: journals-support@beilstein-institut.de

The *Beilstein Journal of Nanotechnology* is published by the Beilstein-Institut zur Förderung der Chemischen Wissenschaften.

Beilstein-Institut zur Förderung der Chemischen Wissenschaften
Trakehner Straße 7–9
60487 Frankfurt am Main
Germany
www.beilstein-institut.de

BEILSTEIN JOURNAL OF NANOTECHNOLOGY

Biological and biomimetic materials and surfaces

Stanislav Gorb*[1] and Thomas Speck*[2,3]

Editorial

Open Access

Address:
[1]Department of Functional Morphology and Biomechanics, Zoological Institute of the University of Kiel, Am Botanischen Garten 9, 24118 Kiel, Germany, [2]Plant Biomechanics Group & Botanic Garden, Faculty of Biology, University of Freiburg, Schänzlestr. 1, 79104 Freiburg, Germany, and [3]Freiburg Institute for Interactive Materials & Bioinspired Technologies (FIT), 79104 Freiburg, Germany

Email:
Stanislav Gorb* - sgorb@zoologie.uni-kiel.de; Thomas Speck* - thomas.speck@biologie.uni-freiburg.de

* Corresponding author

Keywords:
adhesion; bio-inspired materials; biomimetics; interfaces; lotus effect; surfaces

Beilstein J. Nanotechnol. **2017,** *8,* 403–407.
doi:10.3762/bjnano.8.42

Received: 22 November 2016
Accepted: 23 December 2016
Published: 08 February 2017

This article is part of the Thematic Series "Biological and biomimetic materials and surfaces".

Editor-in-Chief: T. Schimmel

This Thematic Series is a tribute to Wilhem Barthlott, a famous German botanist, an observant naturalist, and a truly outstanding personality, on the occasion of his 70th birthday. One of his most important achievements was building a bridge between systematic studies of plant surfaces and the nano-/microtechnology of superhydrophobic, self-cleaning, and air-holding technical surfaces.

From everyday life experience, we all know that during watering or rainfall, water rolls off the leaves of many plants in the form of spherical droplets leaving the leaves themselves entirely dry. This effect can be seen in an especially impressive manner on the leaves of the sacred lotus (*Nelumbo nucifera*) and Tropaeolum (*Tropaeolum majus*). Interestingly, with the rolling off of water droplets, dirt particles as well as fungus spores and bacteria are also very efficiently removed from the leaf surfaces as they are more tightly attached to the water droplet than to the leaf surface. The reason for this physicochemical "self-cleaning behaviour" is the double-structured water-repellent surface of the plant leaves which is comprised of micro- and nanostructured wax on dome-shaped papillose epidermis cells. Dirt particles as well as microorganisms and fungus spores are attached only via a few contact points to the leaf surface which has a micro-/nanoscale roughness. The same holds for the water droplets which become spherical for energetic reasons and cannot wet the leaf surface [1-3].

The discovery of this phenomenon and its structural basis dates back to the 1970s when Wilhelm Barthlott studied the micro- and nanostructures on the surfaces of plant leaves, flowers, seeds and pollen during his Ph.D. thesis at the University of Heidelberg using one of the first scanning electron microscopes (SEMs) available for German botanists. His main interest in these years was plant systematics and he was interested if the fascinating nano- and microstructures he saw in the SEM are of importance for classifying the different plant taxa; this was proved true for many of these structures. Wilhelm Barthlott was especially interested in the tiny lipid structures, the so-called plant waxes, which later proved to be wax crystals that are formed by self-organisation processes and show specific shapes characteristic for different plant groups. To study these surface structures in the SEM, the leaves have to be prepared and

cleaned, and Wilhelm Barthlott soon realized that the leaves of some plant species were always clean whereas the surfaces of other species were always dirty. Surprisingly the smooth, wettable leaf surfaces were markedly dirty, whereas the water-repellent, hydrophobic leaf surfaces with microscale roughness were always clean. More than 40 years ago he verified this observation by performing simple experiments with Tropaeolum leaves and published the hypothesis that, in a specific manner, double-structured, hydrophobic surfaces are self-cleaning. He further hypothesized that this may be the main biological function of the micro-/nanostructured wax covering many plant leaves [4]. This first publication was largely ignored outside of the botanical community and the importance of this observation was, at that time, not realized by any surface science physicists or chemists. It took about 15 years before in the 1990s Wilhelm Barthlott, now serving as chair for Botany at the University of Bonn, started new studies based on his earlier work together with his then student Christoph Neinhuis, who now has a chair for botany at the Technical University of Dresden. Together they detailed and quantified the structural and functional basis of the self-cleaning effect with numerous more sophisticated experiments. They also proved that in order to establish comparable self-cleaning properties on technical surfaces, the micro- and nanostructures found on the plant leaves and the hydrophobicity of the plant waxes must be transferred [1,5,6]. This has successfully been done in some biomimetic products, for example, the facade paint Lotusan® produced by Sto SEA Pte. [7] or the product Tegotop® 210 from Evonik Industries AG. The products are sold under the brand name Lotus-Effect® which has become a near synonym for functional, water-repellent surfaces in general. Without exaggeration one can say that Lotus-Effect® surfaces, together with fasteners inspired by gecko attachment structures, can be considered as "flagships" of contemporary surface-related biomimetic research. Still today questions related to these effects are the topic of novel state-of-the-art studies in the fields of basic and applied research, as can be seen in some articles of this Thematic Series.

A second type of surface structure that has been observed is the so-called *Salvinia* effect that has been quantitatively characterized in collaboration with Thomas Schimmel from the Karlsruhe Institute of Technology (KIT) [8]. The biomimetic potential of this effect was first understood in the early 2000s by Wilhelm Barthlott. The swimming ferns of the genus *Salvinia*, but also other swimming and diving organisms (e.g., some spider and bug species as well as a few birds and mammals), typically possess double-structured, flexible, hairy structures on their outer surfaces which can trap an air layer under water for time spans of several minutes, days and even months. The biological importance of these air layers may be buoyancy, insulation, oxygen supply during diving and/or friction reduction during swimming and diving. The main interest in biomimetic products lies in the potential friction reduction and in antifouling properties. For example, this could be practically implemented by covering the underwater parts of ship hulls with *Salvinia* effect coatings. Ongoing projects with ship builders aim to realize this biomimetic application [9].

In addition to the fields of botanical–biomimetic research, Wilhelm Barthlott has significantly contributed to many other fields of botany, for example, systematics and functional morphology of carnivorous plants and epiphytic cacti, biogeography/biodiversity and pollination biology (UV signatures). Some of these topics have become objects of interest in biomimetic research and are partially covered in articles in this Thematic Series [10,11].

For his studies on self-cleaning surfaces, and especially for the successful transfer of this technology to bioinspired self-cleaning technical products, Wilhelm Barthlott has been awarded with several prestigious prizes, for example, the Philipp-Morris Forschungspreis, the Karl Heinz Beckurts-Preis and the Deutscher Umweltpreis, to name just a few.

This Thematic Series of the *Beilstein Journal of Nanotechnology* is a collection of papers ranging from studies on structure–property relationships of biological materials and surfaces to the development of technical systems inspired by biological studies. In other words, this issue aimed at isolating the different stages of the biomimetic process. On one hand, it reflects the research phases of Wilhelm Barthlott and his collaborators that crossed from biological observations to the development of technical products. On the other hand, it shows the variety of facets of biomimetic research in general. This Thematic Series also covers a wide range of biological and technical systems and can be interesting for biologists, physicists, chemists, as well as materials scientists and engineers fascinated by biomimetics. The first article addresses the general relationship between universities, society, industry, and discuss borders within universities, borders in thinking, and the great amount of energy loss due to these borders. In the second part of this paper, Neinhuis demonstrates the impact of the research conducted by Wilhelm Barthlott and highlights the fact that, throughout his scientific career, many of the above-mentioned borders were removed, shifted or became more penetrable [12].

Plant systems

Poppinga et al. conducted snap–trap closure experiments in air and under water and presented strong evidence that adult snaps of the Venus flytrap (*Dionaea muscipula*) are similarly fast in aerial and submersed states. The authors showed that minute

seedling traps are much slower and do not yet incorporate elastic instabilities responsible for the fast motion. These findings are discussed in biomechanical and biomimetic contexts [10].

The paper by Masselter et al. is devoted to the mechanically relevant structures and their mechanical behaviour in various arborescent and shrubby monocotyledons plants with an emphasis on the structure–function relationships in *Dracaena marginata* stems [11]. Based on the results of microscopy and mechanical testing, a model of mechanical interactions between tissues and vascular bundles in the *D. marginata* stem was generated, and the potential significance of the results for the development of branched and unbranched bio-inspired fibre-reinforced systems with enhanced properties is discussed.

The hydrated mucilage of the *Plantago lanceolata* seed causes specific adhesive and frictional properties, playing an important role in seed dispersal. Kreitschitz et al. studied these tribological properties of the seed envelope under different hydration conditions and revealed the presence of cellulose fibrils in the mucilage in a microscopy study, which are presumably responsible for the uniform distribution of the mucilaginous layer on the seed surface. They may additionally protect the mucilage against the mechanical and chemical impact of the animal digestion systems [13].

Animal systems

Resilin is a rubber-like protein derived from arthropod exoskeletons. It is composed of a stable network of randomly orientated peptide chains that are covalently cross-linked by dityrosine and trityrosine. Due to this molecular structure, resilin bears a high flexibility and resilience. The review by Michels et al. summarizes the presence of resilin and its functional significance in membrane and joint systems, jumping and catapulting systems, attachment and prey catching systems, reproductive, folding and feeding systems, as well as in traumatic reproductive systems [14].

The diets of marine zooplanktonic copepod crustaceans comprise a large proportion of the diatom taxa whose silicified shells exhibit extremely impressive mechanical stability. The ability of copepod species to efficiently break stable diatom structures is based on feeding tools with strongly specialized material architecture, chemical compositions and mechanical properties. The paper by Michels et al. [15] is the review of recent studies on copepod feeding tools. Their siliceous teeth consist of composite materials with silica-based cap-like structures situated on chitin-bearing cuticle sockets that are connected through flexible resilient areas containing resilin protein. This composite architecture contributes to the performance of the siliceous teeth in damaging diatomes and increases their resistance to mechanical damage.

The thin hind wings of diving beetles (Dytiscidae) are fragile and protected by their elytra (leathery forewings). In the resting beetle, the hind wings are folded over the abdomen; in flight, they are unfolded in order to provide aerodynamic forces. The paper by Sun et al. demonstrates that the unfolding process of the hind wing of *Cybister japonicus* is driven by the haemolymph motion in the wing veins. The hind wing extending process is simulated in a numerical model. This finding can assist the design of new, bioinspired, deployable systems [16].

The adhesive tongues of frogs are an efficient tool capable of capturing fast moving prey. It is plausible that the interaction between the tongue surface and the adhesive mucus coating is important for generating strong pull-off forces. The paper by Kleinteich and Gorb is a comparative study of tongue surfaces in nine frog species [17]. All examined species bear microscopical papillae, but different species have microstructure of different shape. The specific microstructure might presumably contribute to the particular adhesive performance of different frog species and may correlate with the prey spectra between the taxa studied. This study opens an interesting possibility of combining surface microstructures with adhesive fluids to enhance dynamical performance of the next generation of adhesives.

The majority of insects bear adhesive foot pads, which are used in locomotion on smooth vertical surfaces and ceilings. The functioning of the pads depends on various environmental factors. Heepe et al. showed that the attachment performance of the beetle *Coccinella septempunctata* depends on the relative humidity. The authors demonstrated that both low (15%) and high (99%) environmental humidity leads to a decrease of attachment forces generated by beetles [18]. The paper by England et al. systematically investigated beetle attachment ability on eight different surfaces having different structural and physico-chemical properties. The results show that chemical surface properties had no considerable effect on the beetle attachment. In contrast, the surface micro- and nanotopography strongly affected measured attachment forces [19].

Animal adhesive systems also perform well on the majority of rough surfaces, but not on all of them. Rough surfaces can change the real contact area and thereby diminish the effectiveness of the biological adhesive system. In the paper by Crawford et al. [20], the authors experimentally tested the effect of surface roughness on the adhesive ability of the tree frog *Litoria caerulea*. They demonstrated that at small scale roughness, frog pad adhesion may even surpass that measured on smooth substrates, whereas at large scale roughness, the adhesion was

reduced. Presumably, on the latter substrates, the pads secrete an insufficient amount of fluid to fill the gaps between the asperities [20].

Modelling and biomimetic systems

Antony et al. [21] present the sustainability assessment of the facade paint Lotusan®, which is a well-known biomimetic development based on the research of Wilhelm Barthlott. The authors used criteria from the Association of German Engineers (VDI) to verify whether the product can be defined as biomimetic. Using a systematic comparative product sustainability assessment (PROSA), the authors demonstrated that this cost-effective and resource-saving product is indeed biomimetic. It is also shown that Lotusan® has a low environmental impact [21].

The regular solution theory was applied by Akerboom et al. to study the advancing and receding contact angles of a liquid drop. The authors additionally applied a three-gradient model for a liquid/vapour system in contact with a complex surface geometry [22]. The authors concluded that the air entrapment is presumably not the main reason for the advancing contact angle variability. Since the contact line between fluid and uneven solid surface is pinned and curved, it induces curvature perpendicular to the plane, and the contact line does not move continuously but rather through a set of depinning transitions. Therefore, it is concluded that the full 3D structure of the surface, rather than any simplified parameter, determines the final observed contact angle.

Chemical analyses of insect tarsal fluid motivated Speidel et al. to prepare 12 biologically inspired, heterogeneous, synthetic emulsions. The microscopic structure was analysed and adhesive, frictional, and rheological properties were tested. The authors have clearly demonstrated that by varying their chemical composition, synthetic heterogeneous emulsions can be adjusted to have diverse consistencies and mimic certain rheological and tribological properties of natural tarsal insect adhesives [23].

In one of the articles of this Thematic Series, Egorov et al. proposed a relatively simple protocol for 3D printing of complex-shaped biocompatible structures based on sodium alginate and calcium phosphate for bone tissue engineering [24]. The analysis of 3D printed structures shows that they possess large interconnected porous systems and compressive strengths from 0.45 to 1.0 MPa, which demonstrates the rather strong potential of this approach for fabrication of biocompatible scaffolds.

In general, this Thematic Series discusses numerous experimental methods for the characterization of the mechanical properties of biological materials and surfaces at the micro- and nanoscale. The Thematic Series combines approaches from biology, physics, chemistry, materials science, and engineering and therefore represents an example of modern interdisciplinary science. Due to this latter reason, we hope that the contributions from this Thematic Series will be of interest to both engineers and physicists, who use inspirations from biology to design technical materials and systems, as well as to biologists, who apply physical and engineering approaches to understand how biological systems function.

The editors would like to thank all the authors for contributing their first-class work to this Thematic Series. We are also grateful to all referees for their constructive reports which facilitated the high quality of the manuscripts and also allowed us to publish in a timely manner. Finally, we thank the Editorial Team at the Beilstein-Institut for their continuous great support of biology- and biomimetics-related topics in this journal.

Stanislav Gorb and Thomas Speck

Kiel and Freiburg, December 2016

References

1. Barthlott, W.; Neinhuis, C. *Planta* **1997,** *202,* 1–8. doi:10.1007/s004250050096
2. Neinhuis, C. Sammlungen als Ausganspunkte für bahnbrechende Entdeckungen. In *Bionik - Faszinierende Lösungen der Natur für die Technik der Zukunft;* Speck, T.; Speck, O.; Neinhuis, C.; Bargel, H., Eds.; Lavori-Verlag: Freiburg, Germany, 2012; pp 18–21.
3. Speck, T.; Speck, O.; Neinhuis, C.; Bargel, H. *Bionik - Faszinierende Lösungen der Natur für die Technik der Zukunft;* Lavori-Verlag: Freiburg, Germany, 2012.
4. Barthlott, W.; Wollenweber, E. *Zur Feinstruktur, Chemie und taxonomischen Signifikanz epicuticularer Wachse und ähnlicher Sekrete;* Steiner Verlag: Stuttgart, Germany, 1981.
5. Barthlott, W. Selbstreinigende Oberflächen von Gegenständen sowie Verfahren zur Herstellung derselben. German Patent DE 595 04 640.1, Feb 4, 1999.
6. Neinhuis, C.; Barthlott, W. *Ann. Bot. (Oxford, U. K.)* **1997,** *79,* 667–677. doi:10.1006/anbo.1997.0400
7. Technical Bulletin Lotusan®: facade paint with Lotus effect® technology. http://www.sto.de (accessed July 15, 2015).
8. Barthlott, W.; Schimmel, T.; Wiersch, S.; Koch, K.; Brede, M.; Barczewski, M.; Walheim, S.; Weis, A.; Kaltenmaier, A.; Leder, A.; Bohn, H. F. *Adv. Mater.* **2010,** *22,* 2325–2328. doi:10.1002/adma.200904411
9. Barthlott, W. The Salvinia Effect: Stable air retention under water for drag reduction in ships. *International Society of Bionic Engineering;* ISBE Newsletter 2: Changchun, China, 2013.
10. Poppinga, S.; Kampowski, T.; Metzger, A.; Speck, O.; Speck, T. *Beilstein J. Nanotechnol.* **2016,** *7,* 664–674. doi:10.3762/bjnano.7.59
11. Masselter, T.; Haushahn, T.; Fink, S.; Speck, T. *Beilstein J. Nanotechnol.* **2016,** *7,* 1602–1619. doi:10.3762/bjnano.7.154
12. Neinhuis, C. *Beilstein J. Nanotechnol.* **2017,** *8,* 394–402. doi:10.3762/bjnano.8.41

13. Kreitschitz, A.; Kovalev, A.; Gorb, S. N. *Beilstein J. Nanotechnol.* **2016,** *7,* 1918–1927. doi:10.3762/bjnano.7.183
14. Michels, J.; Appel, E.; Gorb, S. N. *Beilstein J. Nanotechnol.* **2016,** *7,* 1241–1259. doi:10.3762/bjnano.7.115
15. Michels, J.; Gorb, S. N. *Beilstein J. Nanotechnol.* **2015,** *6,* 674–685. doi:10.3762/bjnano.6.68
16. Sun, J.; Wu, W.; Ling, M.; Bhushan, B.; Tong, J. *Beilstein J. Nanotechnol.* **2016,** *7,* 904–913. doi:10.3762/bjnano.7.82
17. Kleinteich, T.; Gorb, S. N. *Beilstein J. Nanotechnol.* **2016,** *7,* 893–903. doi:10.3762/bjnano.7.81
18. Heepe, L.; Wolff, J. O.; Gorb, S. N. *Beilstein J. Nanotechnol.* **2016,** *7,* 1322–1329. doi:10.3762/bjnano.7.123
19. England, M. W.; Sato, T.; Yagihashi, M.; Hozumi, A.; Gorb, S. N.; Gorb, E. V. *Beilstein J. Nanotechnol.* **2016,** *7,* 1471–1479. doi:10.3762/bjnano.7.139
20. Crawford, N.; Endlein, T.; Pham, J. T.; Riehle, M.; Barnes, W. J. P. *Beilstein J. Nanotechnol.* **2016,** *7,* 2116–2131. doi:10.3762/bjnano.7.201
21. Antony, F.; Grießhammer, R.; Speck, T.; Speck, O. *Beilstein J. Nanotechnol.* **2016,** *7,* 2100–2115. doi:10.3762/bjnano.7.200
22. Akerboom, S.; Kamperman, M.; Leermakers, F. A. M. *Beilstein J. Nanotechnol.* **2016,** *7,* 1377–1396. doi:10.3762/bjnano.7.129
23. Speidel, M. W.; Kleemeier, M.; Hartwig, A.; Rischka, K.; Ellermann, A.; Daniels, R.; Betz, O. *Beilstein J. Nanotechnol.* **2017,** *8,* 45–63. doi:10.3762/bjnano.8.6
24. Egorov, A. A.; Fedotov, A. Yu.; Mironov, A. V.; Komlev, V. S.; Popov, V. K.; Zobkov, Y. V. *Beilstein J. Nanotechnol.* **2016,** *7,* 1794–1799. doi:10.3762/bjnano.7.172

License and Terms

BEILSTEIN JOURNAL OF NANOTECHNOLOGY

Mandibular gnathobases of marine planktonic copepods – feeding tools with complex micro- and nanoscale composite architectures

Jan Michels[*1,2] and Stanislav N. Gorb[1]

Review

Open Access

Address:
[1]Department of Functional Morphology and Biomechanics, Institute of Zoology, Christian-Albrechts-Universität zu Kiel, Am Botanischen Garten 1–9, D-24118 Kiel, Germany and [2]Biological Oceanography, GEOMAR Helmholtz Centre for Ocean Research Kiel, Düsternbrooker Weg 20, D-24105 Kiel, Germany

Email:
Jan Michels[*] - jmichels@zoologie.uni-kiel.de

* Corresponding author

Keywords:
crystalline silica; diatom frustule; mandibular gnathobase; marine planktonic copepod; resilin

Beilstein J. Nanotechnol. **2015,** *6,* 674–685.
doi:10.3762/bjnano.6.68

Received: 16 June 2014
Accepted: 29 January 2015
Published: 06 March 2015

This article is part of the Thematic Series "Biological and biomimetic materials".

Associate Editor: K. Koch

Abstract

Copepods are dominant members of the marine zooplankton. Their diets often comprise large proportions of diatom taxa whose silicified frustules are mechanically stable and offer protection against grazers. Despite of this protection, many copepod species are able to efficiently break even the most stable frustule types. This ability requires specific feeding tools with mechanically adapted architectures, compositions and properties. When ingesting food, the copepods use the gnathobases of their mandibles to grab and, if necessary, crush and mince the food items. The morphology of these gnathobases is related to the diets of the copepods. Gnathobases of copepod species that mainly feed on phytoplankton feature compact and stable tooth-like structures, so-called teeth. In several copepod species these gnathobase teeth have been found to contain silica. Recent studies revealed that the siliceous teeth are complex microscale composites with silica-containing cap-like structures located on chitinous exoskeleton sockets that are connected with rubber-like bearings formed by structures with high proportions of the soft and elastic protein resilin. In addition, the silica-containing cap-like structures exhibit a nanoscale composite architecture. They contain some amorphous silica and large proportions of the crystalline silica type α-cristobalite and are pervaded by a fine chitinous fibre network that very likely serves as a scaffold during the silicification process. All these intricate composite structures are assumed to be the result of a coevolution between the copepod gnathobases and diatom frustules in an evolutionary arms race. The composites very likely increase both the performance of the siliceous teeth and their resistance to mechanical damage, and it is conceivable that their development has favoured the copepods' dominance of the marine zooplankton observed today.

Review

Significance of copepods in marine pelagic food webs

Crustaceans of the subclass Copepoda (Figure 1) inhabit an impressively large variety of aquatic habitats [1]. In all regions of the earth they can be found in almost any body of water including habitats with extreme conditions such as the deep sea, active hot hydrothermal vents and very cold brine channel systems of sea ice. Copepods are assumed to contribute the largest amount of individuals to the metazoans, even larger than those contributed by insects and nematodes [2,3]. In the marine pelagial the abundance of copepods is particularly pronounced. As a result of this, in all ocean areas worldwide copepods represent the most numerous zooplankton group contributing 55 to 95% of the total zooplankton individuals [4]. The diet of many copepod species contains large proportions of phytoplankton, and copepods are an important food source for various fish

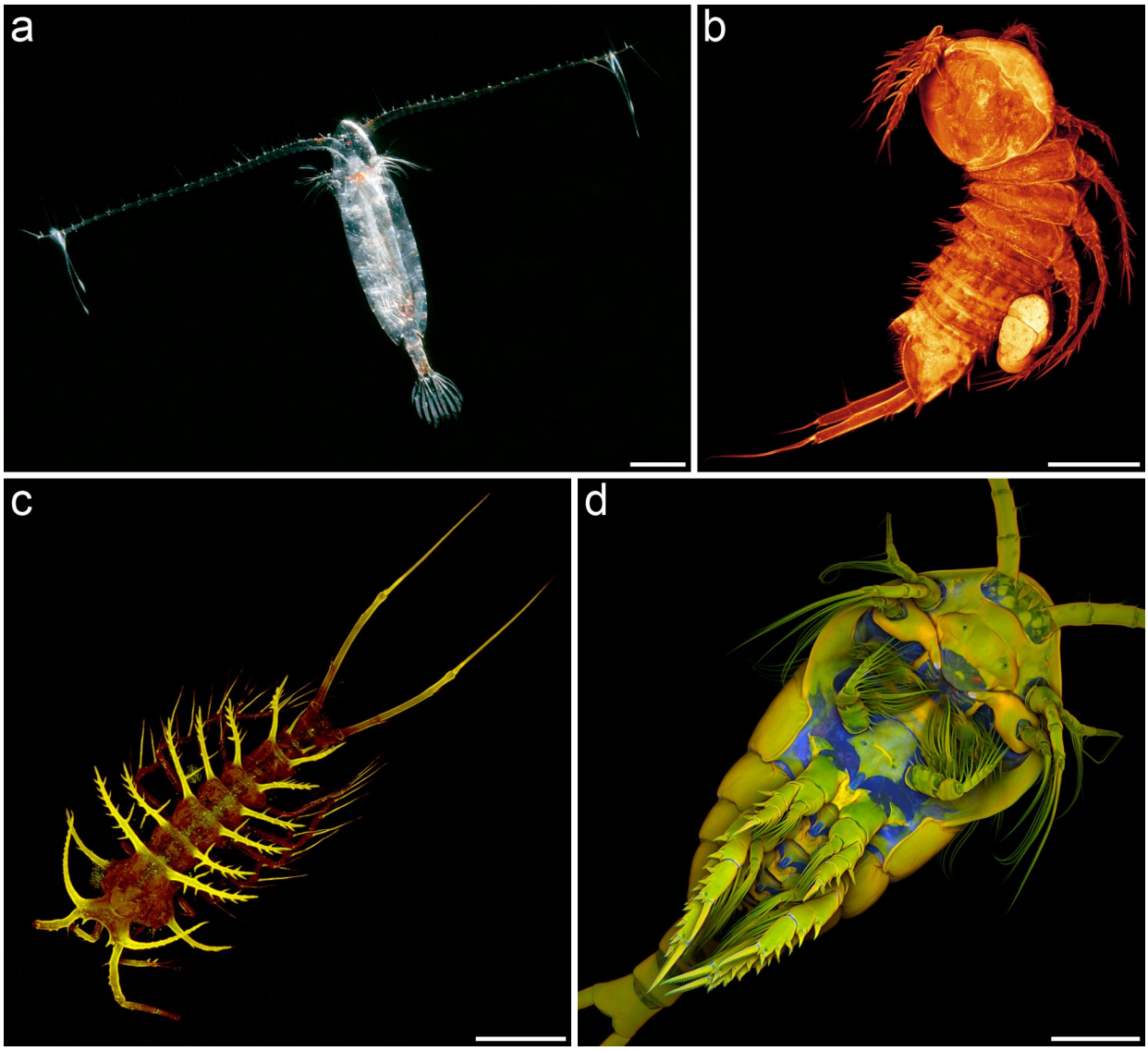

Figure 1: Exemplary copepod species. (a) Female of *Calanoides acutus*, one of the dominant calanoid copepod species within the zooplankton of the Southern Ocean (dorsal view). (b) Female of the harpacticoid copepod genus *Mesocletodes*, collected from deep-sea sediment in the Southern Ocean (lateral view). (c) Female of *Ceratonotus steiningeri*, a harpacticoid deep-sea copepod species, collected from sediment in the Angola Basin at a water depth of 5389 m (dorsal view). (d) Female of the planktonic calanoid copepod species *Temora longicornis*, collected in the North Sea (ventral view). Scale bars = 1 mm (a), 100 µm (b, c), 200 µm (d). (a) Photograph (courtesy of Ingo Arndt). (b–d) Confocal laser scanning micrographs (maximum intensity projections). (b–d) Adapted with permissions from [9-11].

species and a large number of other organisms feeding on zooplankton. Accordingly, due to their dominance within the zooplankton, copepods are the main primary consumers and significant links between the primary producers and organisms of higher trophic levels. As such, they represent important food web components and therefore key organisms for processes such as carbon cycling and nutrient regeneration in the marine pelagial [5,6]. In many ocean areas, diatoms account for a large proportion of the phytoplankton ([5,7,8] and citations therein). For this reason they often are an important food source for copepods, and the knowledge of feeding interactions between these two groups of organisms is essential for the understanding of processes related to the food web and energy and particle fluxes in the marine pelagial.

Mandibular gnathobases – specific feeding tools with morphologies adapted to the diets of the copepods

Copepods usually possess five pairs of mouthparts (Figure 2a), which are used to detect, collect and take up food organisms and particles [12-18]. The mouthparts create water streams, so-called feeding currents, at the ventral side of the copepods' bodies and scan these currents for food organisms and particles by means of mechanoreceptors and chemoreceptors. After detection, the organisms and particles are evaluated with the aid of these receptors, and the favoured ones are moved to the stoma of the copepods by additional movements of the mouthparts. Subsequently, the food items are grabbed and, if necessary, crushed and minced by the mandibular gnathobases, the basal parts of the mandibles, before being ingested. While, in general, the morphology of the mouthparts differs between species with different diets [19-22], the differences in the morphology of the mandibular gnathobases are particularly pronounced and clearly related to the diet of the respective copepod species [19-21,23,24]. The different gnathobase morphologies can be classified in three main groups: (1) gnathobases of copepods that are carnivorous and feed mainly on other zooplankton organisms have relatively long and sharp tooth-like structures (called 'teeth' in the following), and the number of teeth is smaller than those of the gnathobases of the other two groups (Figure 2b); (2) copepod species that mainly feed on phytoplankton possess robust gnathobases with compact and relatively short teeth at their distal ends (Figure 2c–e); (3) omnivorous copepods have gnathobases with a morphology representing an ecotonal form between the morphologies of the other two groups (Figure 2f). The gnathobases of the first group are often rather specialised. Prominent examples for such a specialisation are the gnathobases of the calanoid copepod genus *Heterorhabdus*. They possess only a small number of teeth, and their ventral tooth exhibits a complex morphology that is comparable to the architecture of hypodermic needles and is strongly adapted to catching, anaesthetising and killing prey organisms [25]. This tooth is hollow and features two openings, one at its base and another one at its tip. The lumen of such a tooth is filled with venom or anaesthetic secreted from glandular cells through specific labral pores, which are located close to the opening of the tooth base when the gnathobase is in its 'inoperative position' at the labrum. The ventral tooth of the left gnathobase is exceptionally long (Figure 2b), and it is easily conceivable that this tooth can be efficiently used by the carnivorous copepods to spear prey and inject the venom or anaesthetic into its body. In general, the gnathobases of the first group are suitable to pierce and tear apart the prey with their long, pointed and sharp teeth and the reduced number of teeth. By contrast, due to their short, compact and relatively numerous teeth, the gnathobases of the second group seem to be very capable of crushing stable food items such as diatoms. The teeth of these gnathobases have usually been called 'grinding teeth' [19]. However, a grinding function of these teeth to crush for example stable diatom frustules is not very conceivable. Many of the respective gnathobase teeth possess small cusps that would clearly decrease the efficiency of such a mechanism. It is much more likely that the copepods crush food items such as diatom frustules by exerting pressure with their gnathobase teeth and thereby concentrating the force on a clearly smaller area by means of the small teeth cusps. Especially in the case of the hollow diatom frustules the application of such a punctual pressure seems to be advantageous over a grinding mechanism and likely leads to a more effective disruption of the frustule structures.

Mandibular gnathobases with siliceous teeth

In many calanoid copepod species, some of the gnathobase teeth obviously have another material composition than the rest of the gnathobases. This different appearance can easily be shown in an ordinary way by bright-field microscopy, and it becomes clearly evident when the gnathobases are visualized with scanning electron microscopy (e.g., Figures 2c–e, 3a, 3c–e, 5a, 6a). Already several decades ago the application of simple preparation methods and microscopy techniques resulted in the assumption that such teeth are composed of silica [27]. However, it was not until many years later that the presence of gnathobase tooth structures with similar material properties was mentioned and described for additional copepod species [28-30], and not earlier than several additional years later the application of microprobe and electron diffraction analyses confirmed the presence of silica in such teeth [31]. The analyses indicated that the silica is present in the teeth in the form of opal, a hydrated amorphous type of silica. For this reason, the term 'opal teeth' was established. The application of both differential interference contrast microscopy and transmission electron microscopy revealed the morphogenesis of the

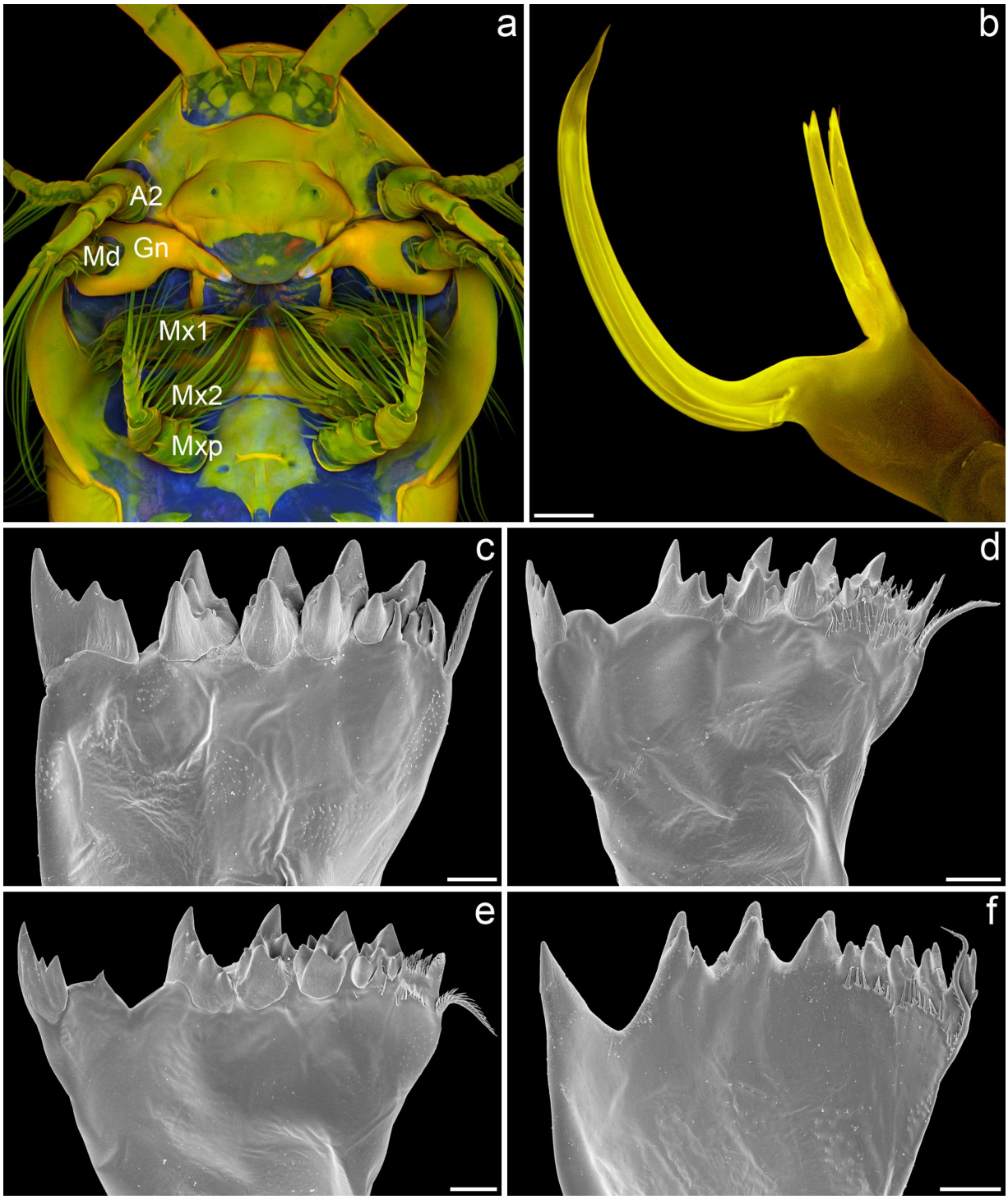

Figure 2: Mouthparts and different types of mandibular gnathobases of calanoid copepods. (a) Section of the micrograph shown in Figure 1d, indicating the location of the five pairs of mouthparts of *Temora longicornis*. A2 = second antenna, Md = mandible, Gn = mandibular gnathobase, Mx1 = first maxilla, Mx2 = second maxilla, Mxp = maxilliped. (Only one mouthpart of each pair is marked.) (b) Confocal laser scanning micrograph (maximum intensity projection) showing the left gnathobase of a male *Heterorhabdus* sp. from the Southern Ocean (cranial view). (c–f) Scanning electron micrographs showing the left gnathobases from females of different Antarctic copepod species (all cranial view). (c) *Rhincalanus gigas*. (d) *Calanoides acutus*. (e) *Calanus propinquus*. (f) *Metridia gerlachei*. Scale bars = 50 µm (b), 25 µm (c–e), 20 µm (f). (b) Adapted with permission from [26].

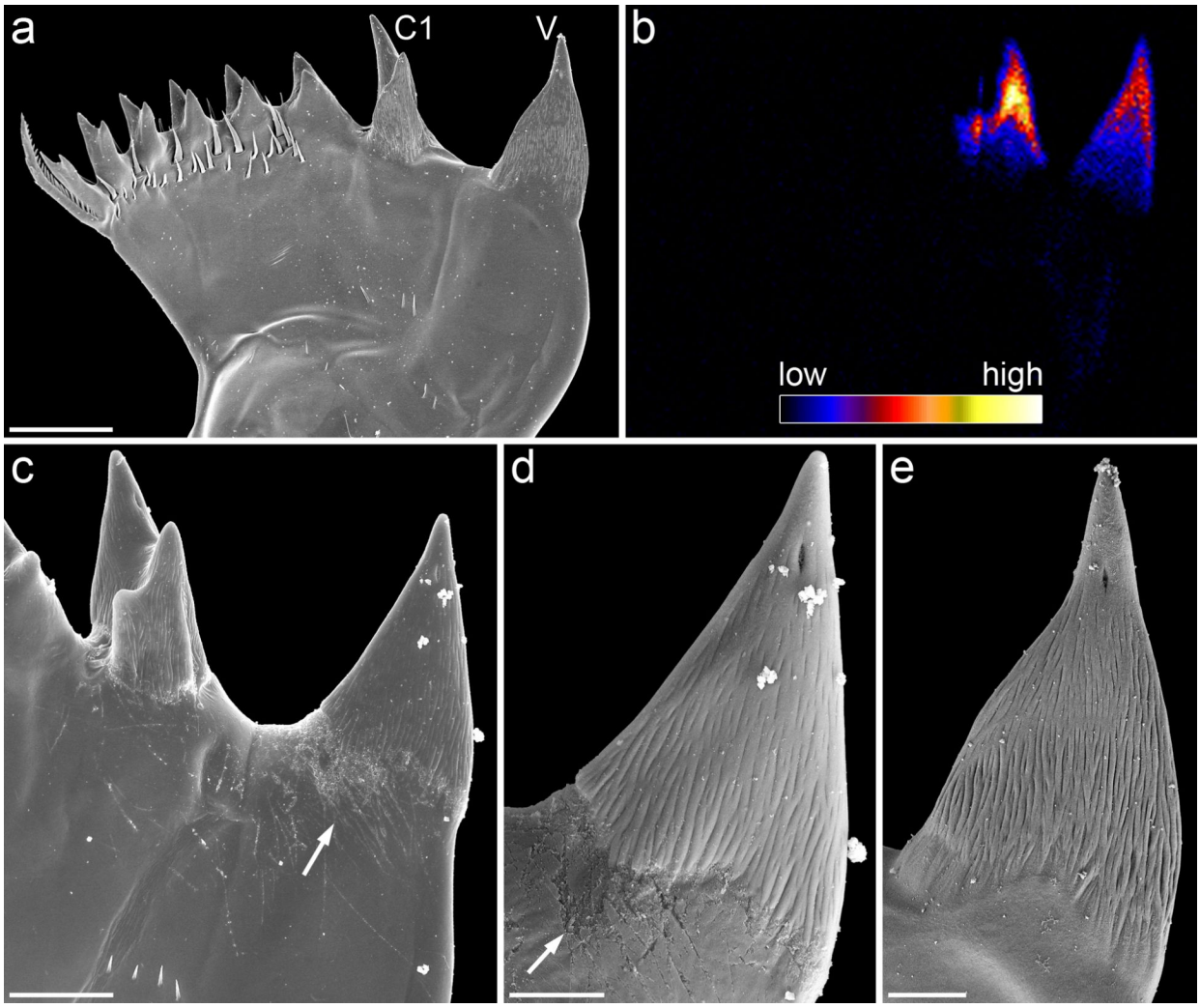

Figure 3: Mandibular gnathobases of female *Centropages hamatus*. (a, c–e) Scanning electron micrographs (all cranial view). (a) Overview of the distal part of a gnathobase. (c) Overview of the ventral part of the distal gnathobase structures. (d) Detailed view of the ventral tooth shown in (c). (e) Detailed view of the ventral tooth shown in (a). (b) Micro-particle-induced X-ray emission (μ-PIXE) mapping showing the distribution and concentration of silicon in the distal part of a gnathobase. The orientation of the gnathobase is similar to that of the gnathobase shown in (a). The results of the elemental analysis indicate that the ventral tooth (V) and the first central tooth (C1) contain silica. The arrows indicate areas with a large number of scratches. Scale bars = 20 μm (a), 10 μm (c), 5 μm (d, e). Figure reproduced with permission from [32].

siliceous teeth [31]. They develop early in the pre-moult phase of the moult cycle. After the formation of fibrous tooth moulds, these moulds are connected via ducts to glandular tissue located in the proximal part of the gnathobase. It is assumed that unpolymerised silicic acid is released by this gland tissue and transported inside the ducts to the moulds where the silicification takes place. The final siliceous crown-like or cap-like structures are located on a socket consisting of chitinous exoskeleton material (Figure 6b).

Recent studies revealed new insights into the architecture of the siliceous teeth. While the presence of silica in the gnathobase teeth was confirmed with modern high-resolution elemental analysis techniques and confocal laser scanning microscopy [32-34] (Figures 3b, 4c–e, 5b,d), the results of high-resolution transmission electron microscopy analyses clearly indicate that the silica in the gnathobase teeth is composed of only some amorphous silica and large proportions of crystalline silica [33]. Evidence for a crystalline structure of the siliceous teeth had already been mentioned earlier but unfortunately without showing and describing any results [30]. The recent analyses showed that the crystalline silica material present in the siliceous teeth is consistent with the mineral α-cristobalite [33].

In nature, silica biomineralisation typically takes place on organic matrices composed of compounds such as chitin and

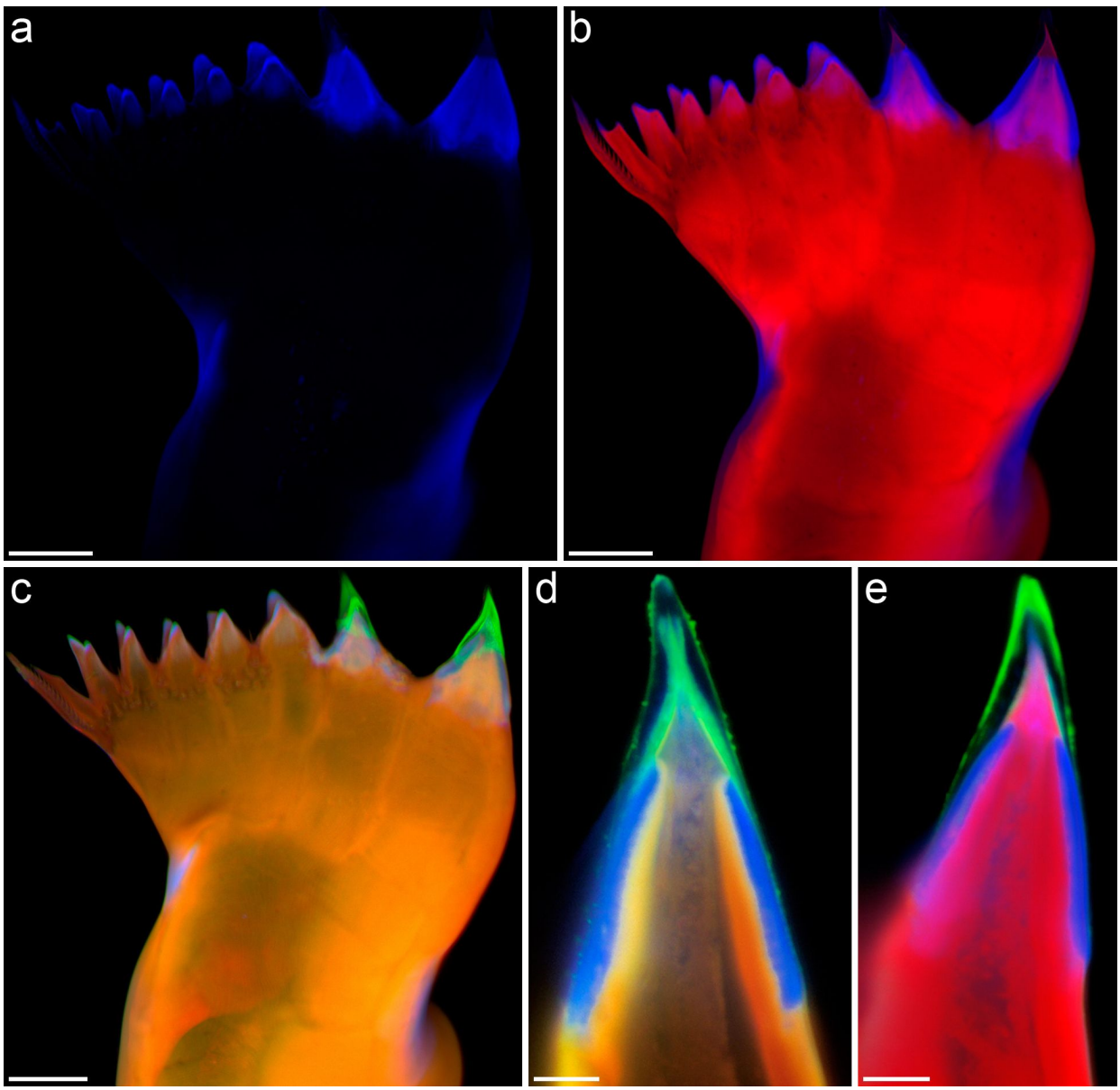

Figure 4: Mandibular gnathobases of female *Centropages hamatus*. (a–e) Confocal laser scanning micrographs (all cranial view) ([a–c] maximum intensity projections showing the whole gnathobase; [d, e] 1-µm-thick optical sections through the ventral tooth). (a) Distribution of resilin. (b) Chitinous exoskeleton (red) and resilin-dominated structures (blue). (c–e) Chitinous exoskeleton (orange, red), resilin-dominated structures (blue, light blue) and silica-containing structures (green). Scale bars = 20 µm (a, b, c), 5 µm (d, e). Figure adapted with permission from [32].

collagen that are preferential sites for nucleation and control the formation of the silica structures [35]. Siliceous diatom frustules, for example, contain an internal organic network of cross-linked chitin fibres that is assumed to be a scaffold for silica deposition [36]. After chemical removal of the silica from the gnathobases or fracturing the siliceous cap-like structures, fibre networks become visible in the siliceous gnathobase teeth [33] (Figure 6b,c). The fibres are similar in appearance to those present in the diatom frustules, and they were shown to also be chitinous [33]. It is very likely that the fibre networks serve as templates or scaffolds during the silicification process and are congruent with the fibrous tooth moulds mentioned above.

The silica-containing structures in the copepod gnathobases likely increase the mechanical strength and stability of the gnathobase teeth, and they are assumed to have coevolved with the siliceous diatom frustules [32,37]. For copepod species that mainly feed on phytoplankton this is certainly conceivable.

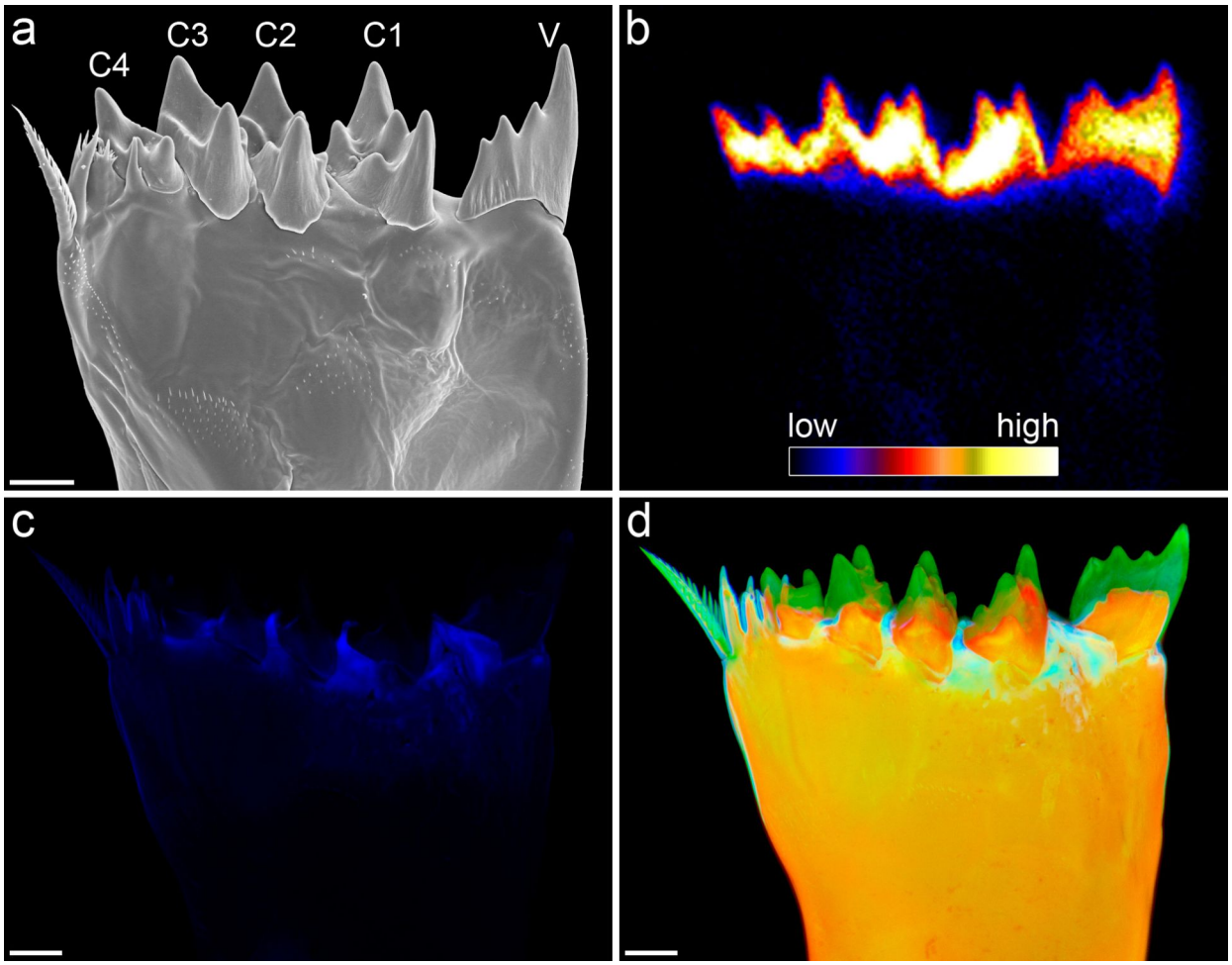

Figure 5: Mandibular gnathobases of female *Rhincalanus gigas*. (a) Scanning electron micrograph showing the distal part of a gnathobase (cranial view). (b) μ-PIXE mapping depicting the distribution and concentration of silicon in the distal part of a gnathobase. The orientation of the gnathobase is similar to that of the gnathobase shown in (a). (c, d) Confocal laser scanning micrographs (maximum intensity projections) showing the material composition of the distal part of a gnathobase (caudal view). (c) Distribution of resilin. (d) Chitinous exoskeleton (orange), resilin-dominated structures (blue, light blue, turquoise) and silica-containing structures (green). The results indicate that the ventral tooth (V) and all central teeth (C1–C4) feature a silica-containing cap-like structure located on top of a chitinous socket. Scale bars = 25 μm. Figure adapted with permission from [33]. Copyright 2015 Elsevier.

However, the presence of silica in gnathobase teeth of carnivorous copepods [25] suggests that siliceous teeth represent an adaptation to frequent mechanical loads in general. In this context, the degree of silicification seems to be related to the mechanical stability of the main food items and thereby to the intensity of the prevalent loads. In siliceous teeth such as the cannula-like ones of *Heterorhabdus* spp., which are likely exposed to relatively moderate forces only, the silica-containing structures are relatively small and not particularly pronounced [25]. By contrast, siliceous teeth regularly facing strong mechanical interactions with diatom frustules, which can be mechanically very stable [37] and therefore cause high forces affecting the teeth during feeding, typically have very pronounced silica-containing structures, which seem to be rather compact and stable [24] (Figures 2c–e, 5a, 6a). For this reason a coevolution between diatom frustules and gnathobases with very pronounced siliceous teeth is very likely.

The question regarding the origin of the silica in the gnathobase teeth arose already relatively long ago [28]. There are two potential sources. The copepods could either take up silicic acid from the seawater where it is present in all ocean areas [38,39], or they could utilise the silica that they ingest when they feed on diatoms or other copepods with siliceous teeth for the formation of their own siliceous teeth. Laboratory experiments showed that the copepods take up silicic acid from the seawater and are able to cover their silicon demand for the formation of siliceous teeth even at rather low silicic acid concentrations [30]. The results indicate that the lowest natural marine silicic acid concentrations, found in oligotrophic ocean areas, are still

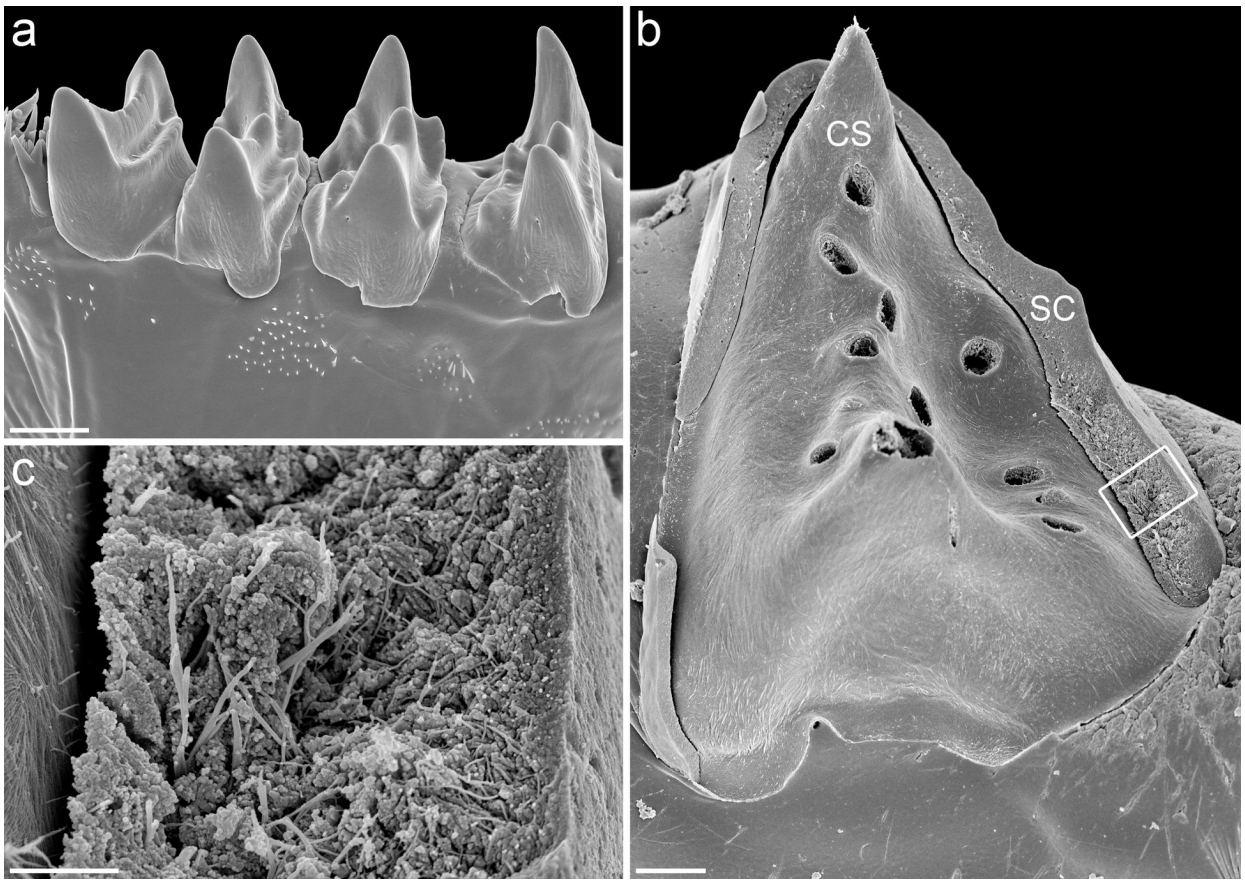

Figure 6: Mandibular gnathobases of female *Rhincalanus gigas*. Scanning electron micrographs (all caudal view). (a) The four central teeth. (b) Central tooth after the removal of large parts of the silica-containing cap-like structure. (c) Detailed view of the structures marked by the rectangular frame in (b). Scale bars = 20 µm (a), 5 µm (b), 1 µm (c). CS = chitinous socket, SC = silica-containing cap-like structure. Figure adapted with permission from [33]. Copyright 2015 Elsevier.

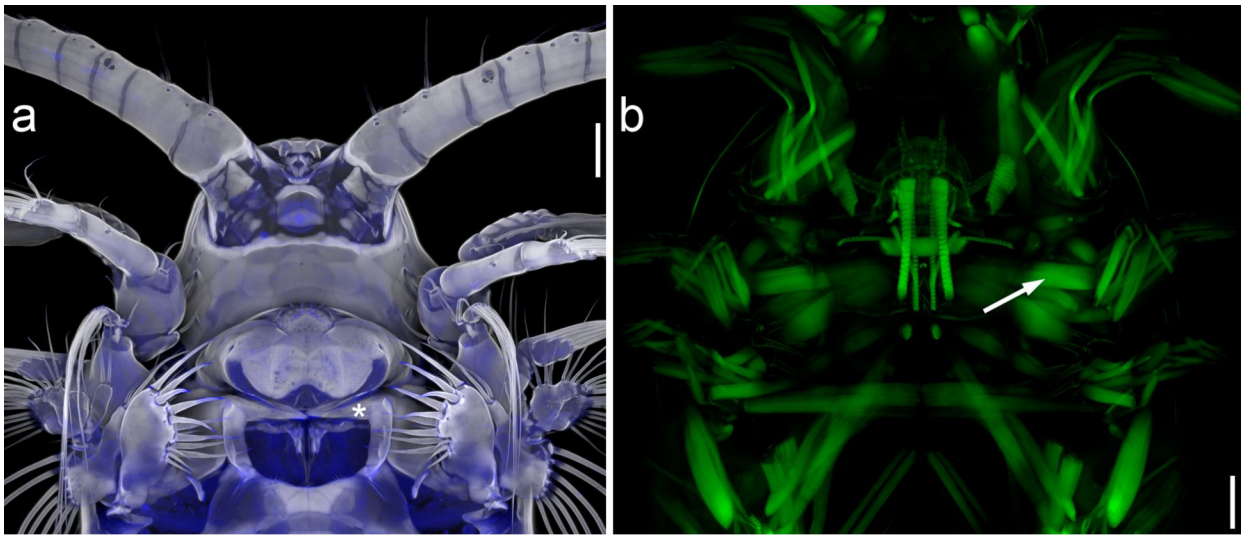

Figure 7: Muscular system of the anterior part of *Centropages hamatus*. Confocal laser scanning micrographs (maximum intensity projections) showing ventral views of the exoskeleton (a) and the muscles (b) of female *C. hamatus*. Please note that the two micrographs show different sections of two different copepod specimens. The asterisk and the arrow indicate the positions of the left gnathobase and the strong muscles of the left mandible, respectively. Scale bars = 50 µm. Figure reproduced with permission from [10]. Copyright 2014 Wiley-VCH Verlag GmbH & Co KGaA.

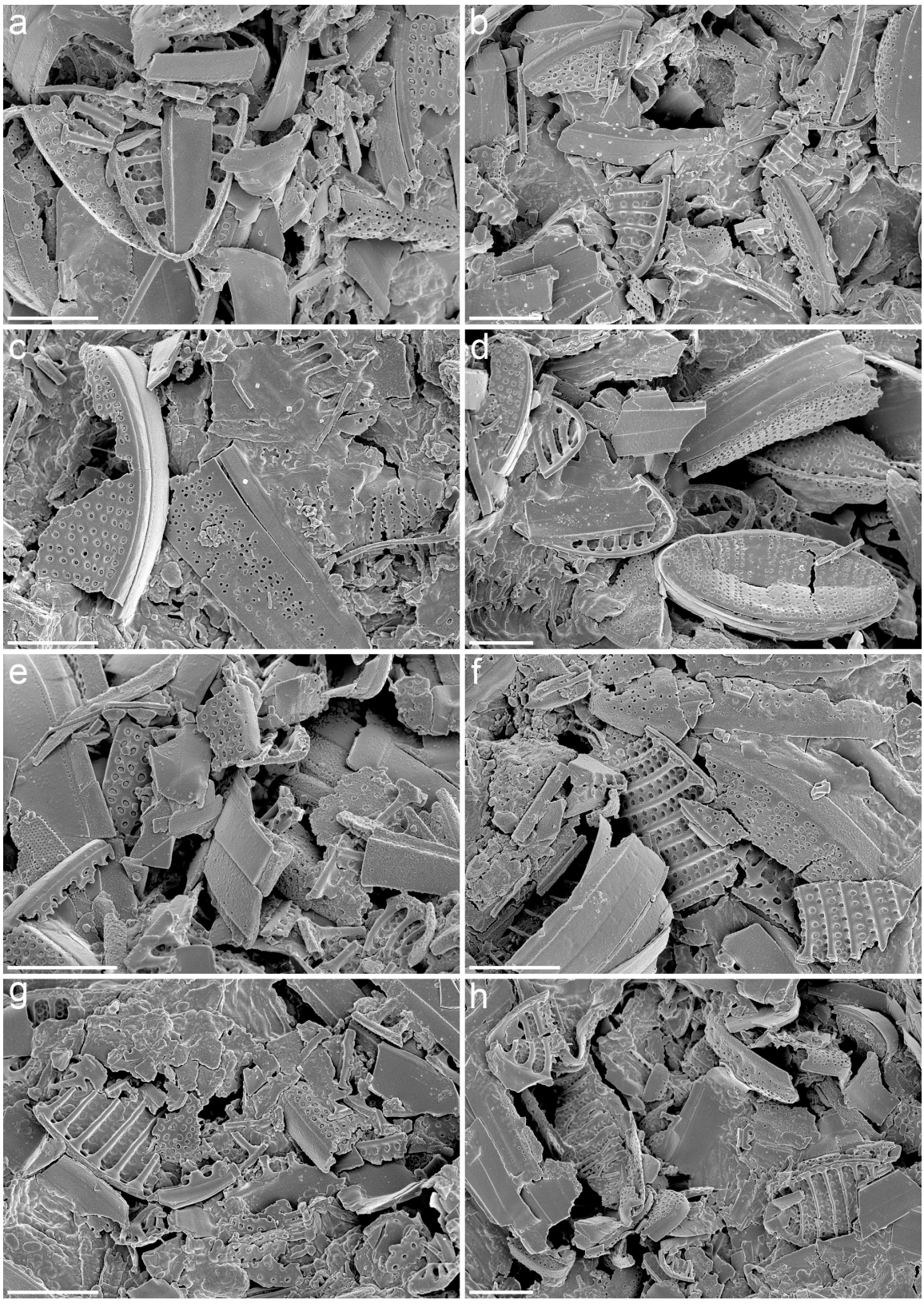

Figure 8: Faecal pellets from feeding experiments with the diatom species *Fragilariopsis kerguelensis* and juveniles (copepodite stage V) of the Antarctic copepod species *Calanus propinquus*. (a–h) Scanning electron micrographs showing pieces of *F. kerguelensis* frustules present in the faecal pellets. Scale bars = 5 µm.

high enough to sufficiently supply the copepods with silicon. Nevertheless, it is imaginable that the copepods use both potential sources and, besides taking up silicic acid from the seawater, also extract silicon from their diet where it is often present in high concentrations and therefore represents an efficient source. However, this hypothesis has never been investigated so far. In a respective experiment the frustules of living diatoms could be labeled with the radioisotope ^{32}Si, and the diatoms could be fed to copepodids (juvenile copepods) to test if ^{32}Si is included in the siliceous teeth of the copepods after moulting.

Up to now the mechanical stability of the silica-containing structures of gnathobase teeth has not been analysed. Such an analysis could potentially be performed using nanoindentation. However, because of the small dimensions of the structures it would be rather difficult to get reliable results. For insect mandibles, many of which are known to contain relatively high concentrations of zinc and manganese [40,41], it has been shown that the metal incorporations increase the hardness of the mandible material [42,43]. Copepod gnathobases often exhibit scratches caused by contact with hard food items. Interestingly, these scratches are typically only found on the surfaces of the chitinous material while the surfaces of the siliceous structures seem to be resistant to such abrasive damage (Figure 3c,d). This indicates that the presence of silica very likely increases the hardness and stiffness of the gnathobase teeth and therefore has a similar effect as zinc and manganese have in insect mandibles.

Mandibular gnathobases, diatom frustules and the evolutionary arms race

In addition to the presence of mechanically stable silica-containing structures, recent detailed analyses of the material composition of copepod gnathobases yielded further indication of a coevolution between diatom frustules and very pronounced siliceous teeth. The respective analyses had been inspired by the knowledge that structures consisting of hard materials easily break because of local stress concentrations under high mechanical loads when they are in contact with other hard structures [44]. To test the idea that the non-siliceous gnathobase parts might have evolved specific properties that reduce the risk of wear and damage of the siliceous teeth, the materials embedding and bearing these teeth were recently investigated in the two calanoid copepod species *Centropages hamatus* and *Rhincalanus gigas*, both of which have diets with significant proportions of diatoms [32,33]. Interestingly, in the gnathobases of both species exoskeleton structures with high proportions of the elastic protein resilin were discovered. The results show that the architecture and the composition of the composite structures in the gnathobase teeth are much more complex than previously assumed. In *C. hamatus*, the siliceous teeth feature a cap-like structure that contains high resilin proportions. This structure is located on top of a chitinous socket and covered by another cap-like structure containing silica (Figure 4). The siliceous teeth of *R. gigas* are characterised by a silica-containing cap-like structure that is situated on top of a chitinous socket (Figure 5d). At the bases of the sockets of the siliceous teeth, the gnathobase exoskeleton features high proportions of resilin (Figure 5c,d), while, by contrast, in the central and proximal parts of the gnathobase the exoskeleton is dominated by chitinous material.

Compared with chitinous exoskeleton material, resilin is very soft and elastic [45,46]. At first view it might be surprising that hard and stiff structures, which are supposed to be adapted to crushing stable diatom frustules, are combined with very soft structures. When the copepods feed on diatoms, local stress concentrations caused by mechanical loads on the tips of the siliceous teeth might exceed the breaking stress level and thereby increase the risk of crack formation in and breakage of the teeth. In comparable situations, when mechanical systems have to resist severe mechanical challenges, a subtle combination of materials with different mechanical properties (or a gradient in the material properties) can make these systems more resistant to damage and wear because such an architecture minimises the probability of local stress concentrations and, in the case of an initial damage, prevents further crack propagation [47,48]. It is conceivable that the soft and elastic resilin-dominated structures of the siliceous teeth function as flexible supports of the hard and stiff tooth structures. In case the breaking stress level is reached, these structures might be deformed by compression and thereby reduce stress concentrations in the tooth material. Such a mechanism likely improves the resistance of the siliceous teeth to mechanical damage. In *C. hamatus*, additional structures with high resilin proportions, located at the dorsal edge of the central part and at the ventral edge of the proximal part of the gnathobases (Figure 4a–c), might function as a cushioning system that makes the whole gnathobases resilient and thereby further reduces the risk that the siliceous teeth are mechanically damaged.

Diatoms, which often feature complex frustule architectures that very likely have evolved to increase the mechanical stability of the frustules and provide resistance to compression loads applied to the frustules from outside [37], represent the most stable food items found in copepod diets. Intact diatoms can survive the passage through the guts of zooplankton organisms [49]. For this reason being able to crush and mince the diatom frustules is important for the copepods to better digest the diatom cells. However, successful crushing and mincing of such mechanically protected frustules requires specifically adapted feeding tools. Accordingly, the presence of very complex

composite tooth structures containing diverse materials such as resilin and silica supports the assumption that the respective siliceous copepod teeth have specifically coevolved with the stable diatom frustules in an evolutionary arms race (for the explanation of the term 'arms race' see [50]) and enable the copepods to more efficiently feed on and utilise their main food organisms.

Protection against specific 'attack systems' of grazers and predators is assumed to be the main factor that controls plankton evolution having resulted in the existence of a large variety of morphologies and chemical and mechanical defence systems [51]. In this context, the copepod gnathobases featuring hard and stable biomineralised tooth structures with soft and elastic supports represent examples of highly-adapted 'attack systems'. A powerful operation of the gnathobases is likely ensured by pronounced mandibular muscles (Figure 7). This combination might be a prerequisite for the copepods' documented ability to crush and mince the diatom frustules into small pieces [52,53]. Large copepods such as the Antarctic species *Calanus propinquus* with pronounced siliceous teeth (Figure 2e) are capable of destroying even the frustules of the diatom *Fragilariopsis kerguelensis* (Figure 8) that are particularly stable [37]. The copepods' effective crushing and mincing of diatom frustules certainly not only depend on the morphology and the material composition of the gnathobases but are also related to the dimensions of the copepods and their diatom food. In feeding experiments, for example, the relatively small copepod *Acartia clausi* was observed to damage only frustules of the small size fraction of the diatoms offered, while the larger species *Centropages hamatus* and *Temora longicornis* were able to also damage the frustules of the large size fractions [53].

Besides their morphological adaptations, copepods exhibit specific feeding techniques and strategies enabling them to better utilise the available diatom food. Frustules of large diatoms such as *Coscinodiscus wailesii* are not always completely destroyed and ingested during feeding. *T. longicornis* was observed to break only small pieces out of the *C. wailesii* frustules, and subsequently it ingested the cell contents and dropped the frustules [54]. In other experiments, *C. hamatus* exhibited a similar feeding strategy. While smaller *C. wailesii* frustules were broken in pieces, the large frustules were only 'opened' by breaking a hole in the girdle band, which was shown to be the frustules' weakest part [53].

In general, the adapted gnathobase morphologies and material compositions combined with effective feeding techniques and strategies make copepods very powerful antagonists of diatoms in the evolutionary arms race. Copepod features such as the shape of the body, the antennae equipped with a high amount of sensors, powerful muscles enabling exceptional escape jumps, the capability to remotely detect and capture prey and efficient mate finding are assumed to be the basis for the success of the marine planktonic copepods [55]. Nevertheless, it is conceivable that the development of the complex composite gnathobase structures that are adapted to efficiently capturing (or grabbing), crushing and mincing food items also accounts considerably for the dominance of the copepods observed today within the marine zooplankton.

Acknowledgements

This project was financially supported by the virtual institute 'PlanktonTech' of the Helmholtz Association. Sigrid Schiel kindly provided copepod samples, and Ruth Alheit helped with the sorting of the samples. The provision of the photograph showing the live *Calanoides acutus* specimen by Ingo Arndt is gratefully acknowledged.

References

1. Huys, R.; Boxshall, G. A. *Copepod Evolution;* The Ray Society: London, United Kingdom, 1991.
2. Hardy, A. *The Open Sea. The World of Plankton;* Collins: London, United Kingdom, 1970.
3. Humes, A. G. *Hydrobiologia* **1994,** *292–293,* 1–7. doi:10.1007/BF00229916
4. Longhurst, A. R. *Prog. Oceanogr.* **1985,** *15,* 1–35. doi:10.1016/0079-6611(85)90036-9
5. Verity, P. G.; Smetacek, V. *Mar. Ecol. Prog. Ser.* **1996,** *130,* 277–293. doi:10.3354/meps130277
6. Turner, J. T. *Zool. Stud.* **2004,** *43,* 255–266.
7. Smetacek, V. *Protist* **1999,** *150,* 25–32. doi:10.1016/S1434-4610(99)70006-4
8. Armbrust, E. V. *Nature* **2009,** *459,* 185–192. doi:10.1038/nature08057
9. Michels, J.; Büntzow, M. *J. Microsc. (Oxford, U.K.)* **2010,** *238,* 95–101. doi:10.1111/j.1365-2818.2009.03360.x
10. Michels, J. Confocal Laser Scanning Microscopy – Detailed Three-dimensional Morphological Imaging of Marine Organisms. In *Imaging Marine Life: Macrophotography and Microscopy Approaches for Marine Biology;* Reynaud, E. G., Ed.; Wiley-VCH: Weinheim, Germany, 2013; pp 69–91. doi:10.1002/9783527675418.ch4
11. Michels, J.; Gorb, S. N. *J. Microsc. (Oxford, U.K.)* **2012,** *245,* 1–16. doi:10.1111/j.1365-2818.2011.03523.x
12. Koehl, M. A. R.; Strickler, J. R. *Limnol. Oceanogr.* **1981,** *26,* 1062–1073. doi:10.4319/lo.1981.26.6.1062
13. Paffenhöfer, G.-A.; Strickler, J. R.; Alcaraz, M. *Mar. Biol. (Heidelberg, Ger.)* **1982,** *67,* 193–199. doi:10.1007/BF00401285
14. Strickler, J. R. *Science* **1982,** *218,* 158–160. doi:10.1126/science.218.4568.158
15. Price, H. J.; Paffenhöfer, G.-A.; Strickler, J. R. *Limnol. Oceanogr.* **1983,** *28,* 116–123. doi:10.4319/lo.1983.28.1.0116
16. Bundy, M. H.; Vanderploeg, H. A. *J. Plankton Res.* **2002,** *24,* 215–223. doi:10.1093/plankt/24.3.215
17. Malkiel, E.; Sheng, J.; Katz, J.; Strickler, J. R. *J. Exp. Biol.* **2003,** *206,* 3657–3666. doi:10.1242/jeb.00586

18. Koehl, M. A. R. *J. Biomech.* **2004,** *37,* 789–795. doi:10.1016/j.jbiomech.2003.06.001
19. Anraku, M.; Omori, M. *Limnol. Oceanogr.* **1963,** *8,* 116–126. doi:10.4319/lo.1963.8.1.0116
20. Arashkevich, Ye. G. *Oceanology (Engl. Transl.)* **1969,** *9,* 695–709.
21. Schnack, S. B. Functional Morphology of Feeding Appendages in Calanoid Copepods. In *Functional Morphology of Feeding and Grooming in Crustacea;* Felgenhauer, B. E.; Watling, L.; Thistle, A. B., Eds.; Balkema: Rotterdam, Netherlands, 1989; pp 137–151.
22. Ohtsuka, S.; Onbé, T. *Mar. Biol. (Heidelberg, Ger.)* **1991,** *111,* 213–225. doi:10.1007/BF01319703
23. Itoh, K. *Bull. Plankton Soc. Jpn.* **1970,** *17,* 1–10.
24. Michels, J.; Schnack-Schiel, S. B. *Mar. Biol. (Heidelberg, Ger.)* **2005,** *146,* 483–495. doi:10.1007/s00227-004-1452-1
25. Nishida, S.; Ohtsuka, S. *Mar. Biol. (Heidelberg, Ger.)* **1996,** *126,* 619–632. doi:10.1007/BF00351329
26. Michels, J. *J. Microsc. (Oxford, U.K.)* **2007,** *227,* 1–7. doi:10.1111/j.1365-2818.2007.01787.x
27. Beklemishev, K. V. *Dokl. Akad. Nauk. SSSR* **1954,** *97,* 543–545.
28. Sullivan, B. K.; Miller, C. B.; Peterson, W. T.; Soeldner, A. H. *Mar. Biol. (Heidelberg, Ger.)* **1975,** *30,* 175–182. doi:10.1007/BF00391591
29. Vyshkvartseva, N. V. Structure of the Mandibles in the Genus *Calanus* s.l. in Relation to Latitudinal Zonality. In *Geographical and Seasonal Variability of Marine Plankton;* Zvereva, Z. A., Ed.; Israel Program for Scientific Translations: Jerusalem, Israel, 1975; pp 186–199.
30. Miller, C. B.; Nelson, D. M.; Guillard, R. R. L.; Woodward, B. L. *Biol. Bull. (Woods Hole, MA, U.S.A.)* **1980,** *159,* 349–363. doi:10.2307/1541099
31. Miller, C. B.; Nelson, D. M.; Weiss, C.; Soeldner, A. H. *Mar. Biol. (Heidelberg, Ger.)* **1990,** *106,* 91–101. doi:10.1007/BF02114678
32. Michels, J.; Vogt, J.; Gorb, S. N. *Sci. Rep.* **2012,** *2,* No. 465. doi:10.1038/srep00465
33. Michels, J.; Vogt, J.; Simon, P.; Gorb, S. N. *Zoology (Munich, Ger.)*, in press. doi:10.1016/j.zool.2014.11.001
34. Bechstein, K.; Michels, J.; Vogt, J.; Schwartze, G. C.; Vogt, C. *Anal. Bioanal. Chem.* **2011,** *399,* 501–508. doi:10.1007/s00216-010-4373-5
35. Ehrlich, H. *Int. Geol. Rev.* **2010,** *52,* 661–699. doi:10.1080/00206811003679521
36. Brunner, E.; Richthammer, P.; Ehrlich, H.; Paasch, S.; Simon, P.; Ueberlein, S.; van Pée, K.-H. *Angew. Chem., Int. Ed.* **2009,** *48,* 9724–9727. doi:10.1002/anie.200905028
37. Hamm, C. E.; Merkel, R.; Springer, O.; Jurkojc, P.; Maier, C.; Prechtel, K.; Smetacek, V. *Nature* **2003,** *421,* 841–843. doi:10.1038/nature01416
38. Tréguer, P.; Nelson, D. M.; Van Bennekom, A. J.; DeMaster, D. J.; Leynaert, A.; Quéguiner, B. *Science* **1995,** *268,* 375–379. doi:10.1126/science.268.5209.375
39. Pilson, M. E. Q. *An Introduction to the Chemistry of the Sea,* 2nd ed.; Cambridge University Press: New York, NY, U.S.A., 2012. doi:10.1017/CBO9781139047203
40. Hillerton, J. E.; Robertson, B.; Vincent, J. F. V. *J. Stored Prod. Res.* **1984,** *20,* 133–137. doi:10.1016/0022-474X(84)90020-1
41. Quicke, D. L. J.; Wyeth, P.; Fawke, J. D.; Basibuyuk, H. H.; Vincent, J. F. V. *Zool. J. Linn. Soc.* **1998,** *124,* 387–396. doi:10.1111/j.1096-3642.1998.tb00583.x
42. Schofield, R. M. S.; Nesson, M. H.; Richardson, K. A. *Naturwissenschaften* **2002,** *89,* 579–583. doi:10.1007/s00114-002-0381-4
43. Cribb, B. W.; Stewart, A.; Huang, H.; Truss, R.; Noller, B.; Rasch, R.; Zalucki, M. P. *Naturwissenschaften* **2008,** *95,* 17–23. doi:10.1007/s00114-007-0288-1
44. Bhushan, B. *Modern Tribology Handbook, Vol. 2;* CRC Press: Boca Raton, FL, U.S.A., 2000. doi:10.1201/9780849377877
45. Weis-Fogh, T. *J. Mol. Biol.* **1961,** *3,* 648–667. doi:10.1016/S0022-2836(61)80028-4
46. Andersen, S. O.; Weis-Fogh, T. *Adv. Insect Physiol.* **1964,** *2,* 1–65. doi:10.1016/S0065-2806(08)60071-5
47. Gibson, L. J.; Ashby, M. F. *Cellular Solids: Structure and Properties;* Pergamon Press: New York, NY, U.S.A., 1988.
48. Wang, R. Z.; Weiner, S. *J. Biomech.* **1997,** *31,* 135–141. doi:10.1016/S0021-9290(97)00131-0
49. Fowler, S. W.; Fisher, N. S. *Deep-Sea Res., Part A* **1983,** *30,* 963–969. doi:10.1016/0198-0149(83)90051-1
50. Dawkins, R.; Krebs, J. R. *Proc. R. Soc. London, Ser. B* **1979,** *205,* 489–511. doi:10.1098/rspb.1979.0081
51. Smetacek, V. *Nature* **2001,** *411,* 745. doi:10.1038/35081210
52. Turner, J. T. *Bull. Mar. Sci.* **1978,** *28,* 487–500.
53. Friedrichs, L.; Hörnig, M.; Schulze, L.; Bertram, A.; Jansen, S.; Hamm, C. *Mar. Ecol. Prog. Ser.* **2013,** *481,* 41–51. doi:10.3354/meps10227
54. Jansen, S. *Helgol. Mar. Res.* **2008,** *62,* 251–255. doi:10.1007/s10152-008-0113-z
55. Kiørboe, T. *J. Plankton Res.* **2011,** *33,* 677–685. doi:10.1093/plankt/fbq159

License and Terms

BEILSTEIN JOURNAL OF NANOTECHNOLOGY

Comparative kinematical analyses of Venus flytrap (*Dionaea muscipula*) snap traps

Simon Poppinga*[1,2], Tim Kampowski[1,2], Amélie Metzger[1], Olga Speck[1,3] and Thomas Speck[1,2,3]

Full Research Paper

Open Access

Address:
[1]Plant Biomechanics Group, Botanic Garden, University of Freiburg, Schänzlestraße 1, 79104 Freiburg, Germany, [2]Freiburg Materials Research Center (FMF), University of Freiburg, Stefan-Meier-Straße 21, 79104 Freiburg, Germany and [3]Freiburg Centre for Interactive Materials and Bio-Inspired Technologies (FIT), Georges-Köhler-Allee 105, 79110 Freiburg, Germany

Email:
Simon Poppinga* - simon.poppinga@biologie.uni-freiburg.de

* Corresponding author

Keywords:
biomechanics; carnivorous plant; Droseraceae; fast plant movement; functional morphology

Beilstein J. Nanotechnol. **2016,** *7,* 664–674.
doi:10.3762/bjnano.7.59

Received: 07 December 2015
Accepted: 11 April 2016
Published: 04 May 2016

This article is part of the Thematic Series "Biological and biomimetic materials and surfaces".

Guest Editor: S. N. Gorb

Abstract

Although the Venus flytrap (*Dionaea muscipula*) can be considered as one of the most extensively investigated carnivorous plants, knowledge is still scarce about diversity of the snap-trap motion, the functionality of snap traps under varying environmental conditions, and their opening motion. By conducting simple snap-trap closure experiments in air and under water, we present striking evidence that adult *Dionaea* snaps similarly fast in aerial and submersed states and, hence, is potentially able to gain nutrients from fast aquatic prey during seasonal inundation. We reveal three snapping modes of adult traps, all incorporating snap buckling, and show that millimeter-sized, much slower seedling traps do not yet incorporate such elastic instabilities. Moreover, opening kinematics of young and adult *Dionaea* snap traps reveal that reverse snap buckling is not performed, corroborating the assumption that growth takes place on certain trap lobe regions. Our findings are discussed in an evolutionary, biomechanical, functional–morphological and biomimetic context.

Introduction

The terrestrial Venus flytrap (*Dionaea muscipula*) is certainly the most iconic carnivorous plant [1-3], but the spectacular movement of its snap traps (Figure 1) is not yet fully understood. After reception of mechanical stimuli by prey on trigger hairs, the two trap lobes begin to move towards each other. This initial motion is mainly driven by active hydraulic actuation (i.e., turgor-induced cell deformation) [4,5], but a relaxation of mechanically pre-stressed mesophyll cells could also play a supporting role [6,7]. The concave lobes (as seen from the outside) store elastic energy during the initial motion, which is suddenly released when they flip to a convex curvature [8]. This second motion step, the snap-buckling process, greatly enhances the overall movement speed of the relatively large traps (ca. 2 cm in length), so that also fast prey can be caught [9]. After the relatively slow initial and rapid second motion step, the trap closes further but much slower owing to a poro-

elastically dampened motion of the hydrated lobes [8]. For digestion of prey, the trap forms a firmly sealed digestion chamber [2] that acts similar to an animal stomach.

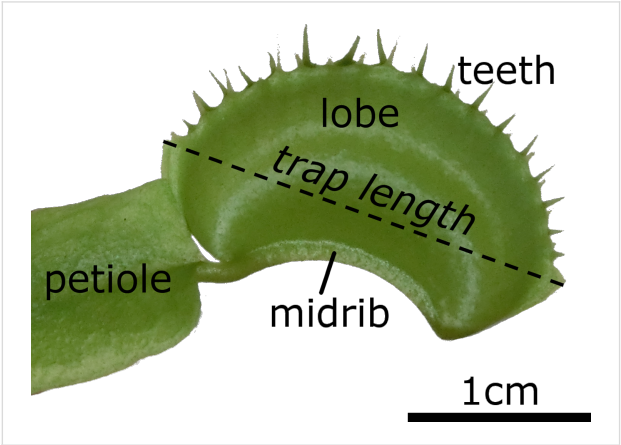

Figure 1: A closed *Dionaea muscipula* trap. Petiole and leaf blade serve the function of photosynthesis. In addition, the leaf blade is highly modified and contains a midrib which connects the two trap lobes. On the upper margins of the lobes, several "teeth" are located which interlock in the closed state of the trap. Trap lengths as presented in this article were measured as indicated.

Knowledge about the functionality of the traps under various, naturally occurring environmental conditions and in the different developmental stages of the plant is scarce at best. *Dionaea* grows in habitats that become seasonally inundated [10,11], can reportedly grow in a submersed state for months and is also capable of capturing aquatic animals, e.g., newts [12]. Detailed investigations regarding these potentially coincidental captures do not exist, and the question arises whether the traps function reliably under water. Conceivably, the denser surrounding medium (water) dampens the snapping motion, and water and prey potentially may become flushed out of the trap during snapping [13,14]. Moreover, *Dionaea* seedlings already possess a carnivorous habit [15], but nothing is known about trap closure kinematics in such an early stage of growth. What is more, although it is generally known that growth processes lead to trap opening [2], the lobe movement during this process and possible implications for the underlying opening mechanics has not yet been investigated.

For shedding some light on the above mentioned questions, we tested the snapping performance in terms of closure duration for submersed adult traps compared to traps snapping in air, and analyzed if trap closure leads to considerable water displacement out of the trap during closure. We additionally characterized different types of snapping modes which we observed during the above tests, investigated the snapping motions of seedlings and, furthermore, the opening kinematics of a young and an adult snap trap.

Results

Raw data, analytical procedures and detailed results are presented in Supporting Information File 1 (raw data), Supporting Information File 2 (statistical analyses for the comparative snapping experiment) and Supporting Information File 3 (statistical analyses for the seedling snapping experiments).

Snapping modes and trap performance under water

Testing of a set of general assumptions during the statistical analyses revealed that the underlying dataset of snapping events (air/water) (Supporting Information File 1) is independent, not normally distributed (Shapiro–Wilk test) and homoscedastic (Levene test, *car* package). Additionally, the descriptive statistics confirmed these characteristics. The trap lengths are not significantly different between the traps analyzed in the different surrounding media (Wilcoxon rank sum test, $W = 487.5$; $p > 0.05$) (Figure 2a). The median trap length is 2 cm (IQR: 0.73 cm; min: 1.2 cm; max: 3.1 cm) ($n = 60$). The snapping durations are not significantly different between the traps analyzed in the different surrounding media (Wilcoxon rank sum test, $W = 472$; $p > 0.05$) (Figure 2b) and do not correlate with the trap lengths (Spearman's $rho = -0.21$) (Figure 2c). The median snapping duration is 0.37 s (IQR: 0.23 s; min: 0.17 s; max: 3.1 s) ($n = 60$). Since neither trap lengths nor snapping durations differ significantly between the given surrounding media, we were able to pool the data.

We recognized the following snapping modes among the 60 traps tested in the comparative air/water analysis: Synchronously moving trap lobes (found in 39 traps) either perform a "normal" snapping, with a sudden snap buckling of the two lobes (in 38 traps) (Figure 3a, Supporting Information File 4), or a progressive snapping, with the closing motion and snap buckling beginning at the apical part of the trap and progressing towards the basal part (only in one trap) (Figure 3b, Supporting Information File 5). The lobes of the other 21 traps possessed strikingly asynchronously moving lobes (Figure 3c); either the triggered lobe moved first (12 traps) (Supporting Information File 6), or the non-triggered lobe (9 traps) (Supporting Information File 7). Snapping modes are independent from the surrounding medium (air/water) (Fisher's exact test, $p > 0.05$) (Supporting Information File 2).

Ink drops deposited into the nine submersed traps were not subject to considerable outflows during snapping, which would have indicated a theoretical flushing out of prey. The trap lobes perform a motion similar to a clasping movement around the water body and the ink drop inside the trap, which is apparently due to the three-dimensional bending deformation of the lobes. We observed asynchronous as well as "normal" snapping

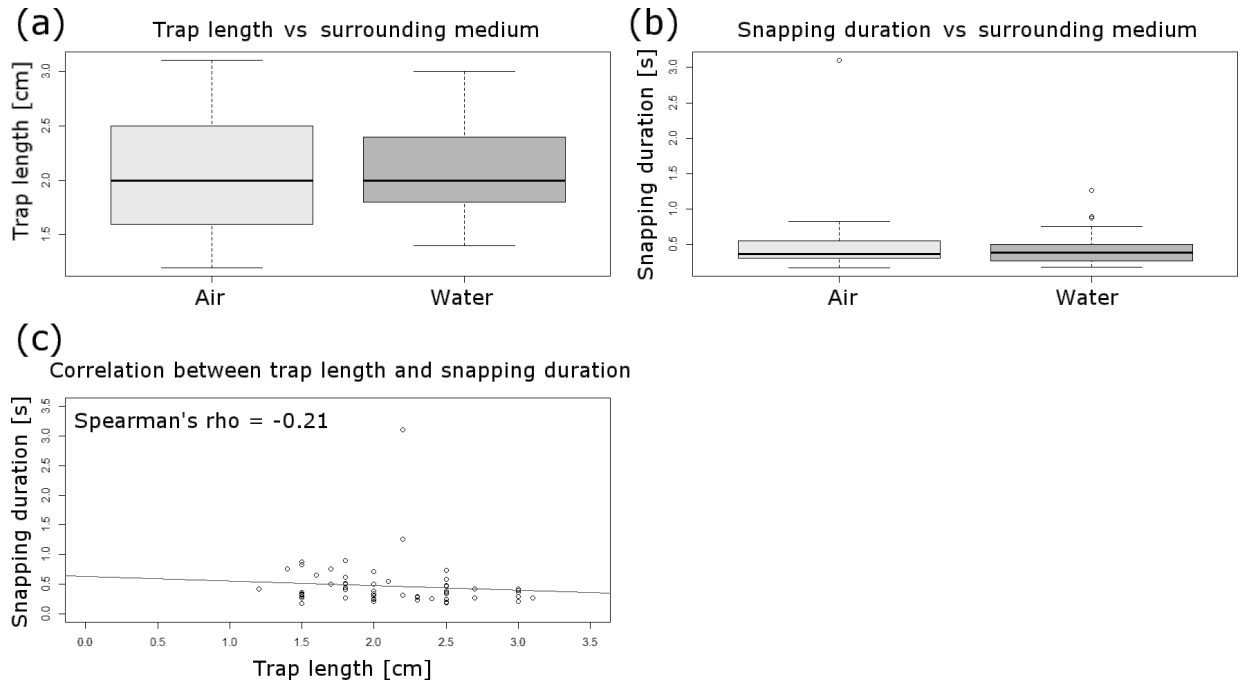

Figure 2: Statistical analyses of the comparative air/water snapping experiment. (a) Boxplot comparison of trap lengths in air and under water. The sample sizes for each surrounding medium is $n = 30$. The trap lengths are not significantly different between the different surrounding media (Wilcoxon rank sum test, $W = 487.5$; $p > 0.05$). (b) Boxplot comparison of snapping durations in air and under water. The sample sizes for each surrounding medium is $n = 30$. The snapping durations are not significantly different between the different surrounding media (Wilcoxon rank sum test, $W = 472$; $p > 0.05$). (c) Snapping durations do not correlate significantly with the trap lengths (Spearman's $rho = -0.21$). The regression line is indicated.

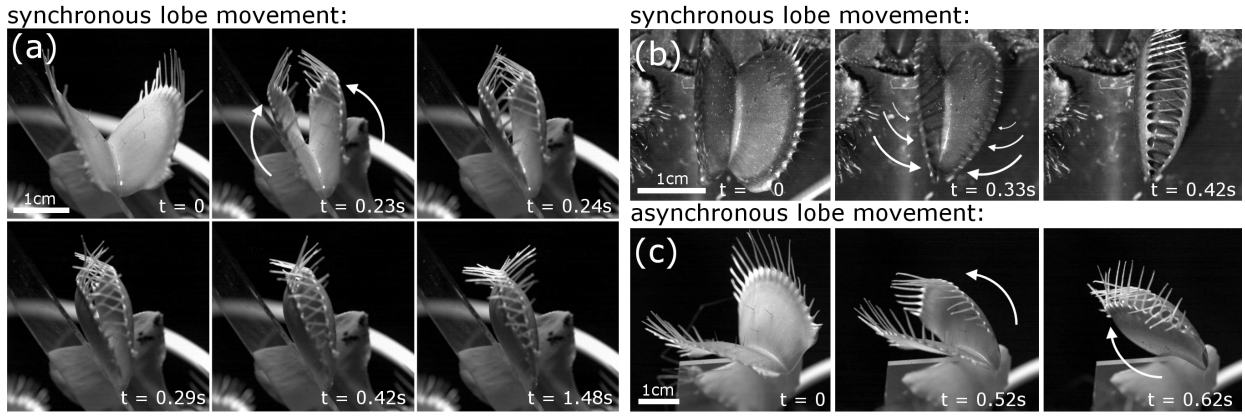

Figure 3: Snapping modes of Venus flytrap. (a) Synchronous lobe movements either lead to a sudden curvature inversion of both trap lobes ("normal" snapping), or (b) to a snap buckling beginning at the apical part of the trap and progressing towards the basal part. (c) In asynchronous trap lobes, one of the lobes moves first. Time scales are indicated, arrows depict lobe movement. At $t = 0.29$ s in (a), the trap is in the state defined as the closed state in this article (see Experimental section). Afterwards, the poroelastically dampened closure motion proceeds, but much slower (see timescales).

motions in the nine traps. In one video (Supporting Information File 8, Figure 4), a remaining ink thread extending from the syringe is clearly visible. This thread is not distorted during the closure motion until it becomes ruptured by a trap lobe. This indicates that the water body in the trap lumen indeed is rather undisturbed by the movement of the closing lobes. Even after trap closure, the ruptured thread is visible inside the trap and apparently undistorted. Nonetheless, an outflow of water and ink through narrow gaps at the apical and basal ends of the trap is visible.

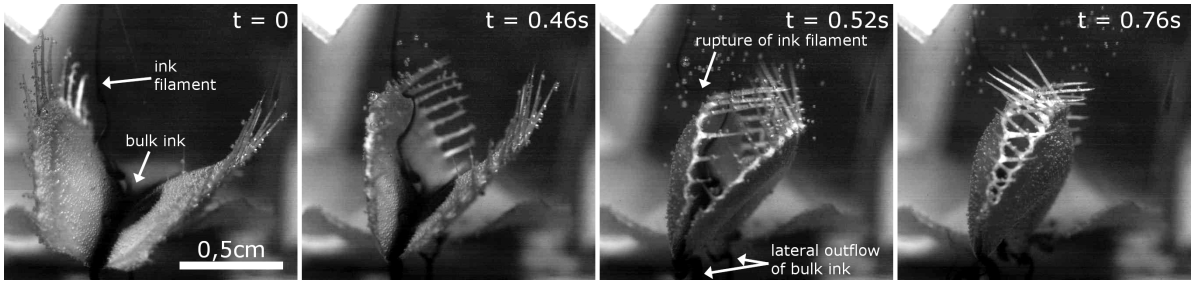

Figure 4: Snapping of a trap under water. Time scale is indicated. An ink filament reaching into the trap with the ink drop is visible. During snapping, no noticeable distortion of the filament, but an outflow of bulk ink out of small gaps at the lateral trap parts is visible. The trap lobes move asynchronously, whereby the triggered lobe (the left lobe in the images) moves first. Images are from Supporting Information File 8.

Comparative kinematics of seedling and adult traps

All traps of the analyzed seedlings showed synchronous lobe closure movements. Seedling traps either do not close completely, with the motion stopping when the marginal teeth are in contact with each other, or perform a "normal" closing motion as described above (Figure 5). The angle between the open seedling trap lobes is noticeably smaller as in adult traps. We measured ca. 48° in one seedling and ca. 82° in one adult trap (Figure 5a,b).

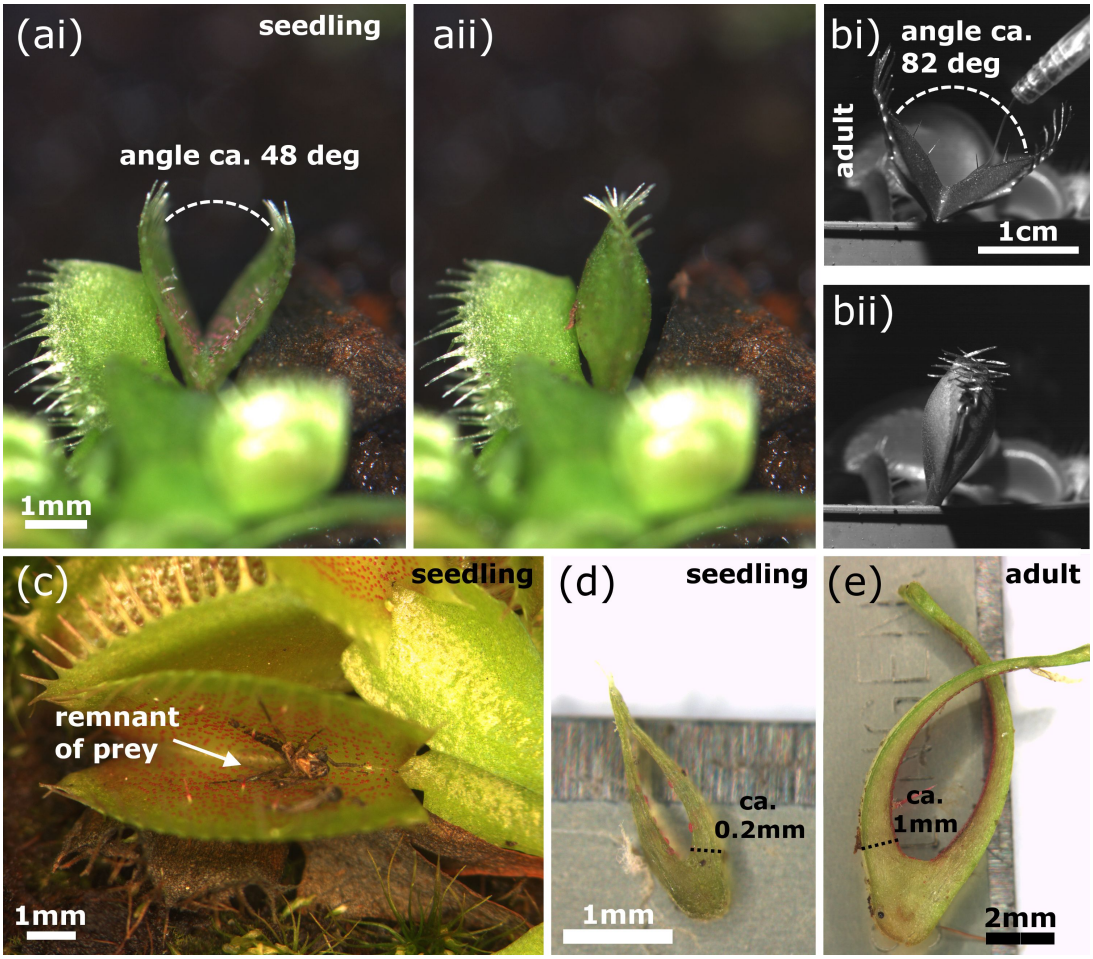

Figure 5: Seedling and adult traps. (a) A seedling trap in the open and closed state, the opening angle is indicated. (b) An adult trap in the open and closed state, the opening angle is indicated. (c) Seedlings cultivated in the Botanic Garden Freiburg often showed arthropod remnants inside the traps, indicating successful prey capture. (d) Section of a seedling trap. (e) Section of an adult trap. (d) and (e) were used for approximations of lobe thicknesses required for calculations in the discussion.

Testing of a set of general assumptions during the statistical analyses revealed that the underlying dataset (Supporting Information File 1) of seedling trap lengths is normally distributed, whereas snapping durations are not normally distributed, and both sets are heteroscedastic. The median length of seedling traps is 0.46 cm (IQR: 0.06 cm; min: 0.31 cm; max: 0.53 cm) (n = 12), which is – not surprisingly – highly significantly different from the trap lengths found for adult traps (Wilcoxon rank sum test, W = 252; p < 0.001) (Figure 6a). The median snapping duration of seedling traps is 7.63 s (IQR: 8.61 s; min: 4.96 s; max: 21.82 s) (n = 12), which is highly significantly longer than the closing durations found for adult traps (Wilcoxon rank sum test, W = 0; p < 0.001) (Figure 6b), and also showed no correlation with the trap lengths (Spearman's rho = −0.11) (Figure 6c).

The seedling trap motions are very continuous and not characterized by the otherwise typical movement steps differing in speed observed in adult traps (slow, fast, slow) (Figure 7). Additionally, no inversion of lobe curvature is visible (Supporting Information File 9). The adult trap analyzed in these experiments closed much faster within ca. 0.6 s (which is in general agreement with the snapping durations for adult snap traps described above) and shows a rapid intermediate lobe distance decrease, which can be attributed to the fast shape change caused by snap buckling. Trap opening took ca. 24 h in the seedling (Supporting Information File 10) and 16 h in the adult trap (Supporting Information File 11). In both traps, it represents a continuous process without any sudden acceleration of the lobes (Figure 7).

Discussion

Our analyses indicate that several snapping modes exist in adult *Dionaea* traps (Figure 3). As we did not perform repetitive experiments with the same traps, we cannot give an answer to the question if these phenomena are recurrent, i.e., if they are morphologically and/or physiologically predetermined for a given trap. In what way the modes influence (i.e., favor or hinder) prey capture can neither be concluded from this study, but we can assume (according to the short trap closure durations measured for all snapping modes) that *Dionaea* is theoretically capable of capturing prey with any mode. Also, it remains to be answered how these diverging post-stimulatory mechanical answers are evoked. Probably, differences in the processes of stimulus signal transduction, reception and processing [16-19], as well as differences in trap lobe anatomy, mechanical properties or the general vigor of the plant influence the process and the mode of snapping [2,20-23]. Our observations on the different modes of trap closing could be of potential interest for biomimetic approaches [24] where fast and large-scale deformation of thin shells as well as principles for generation, storage and release of elastic energy are important.

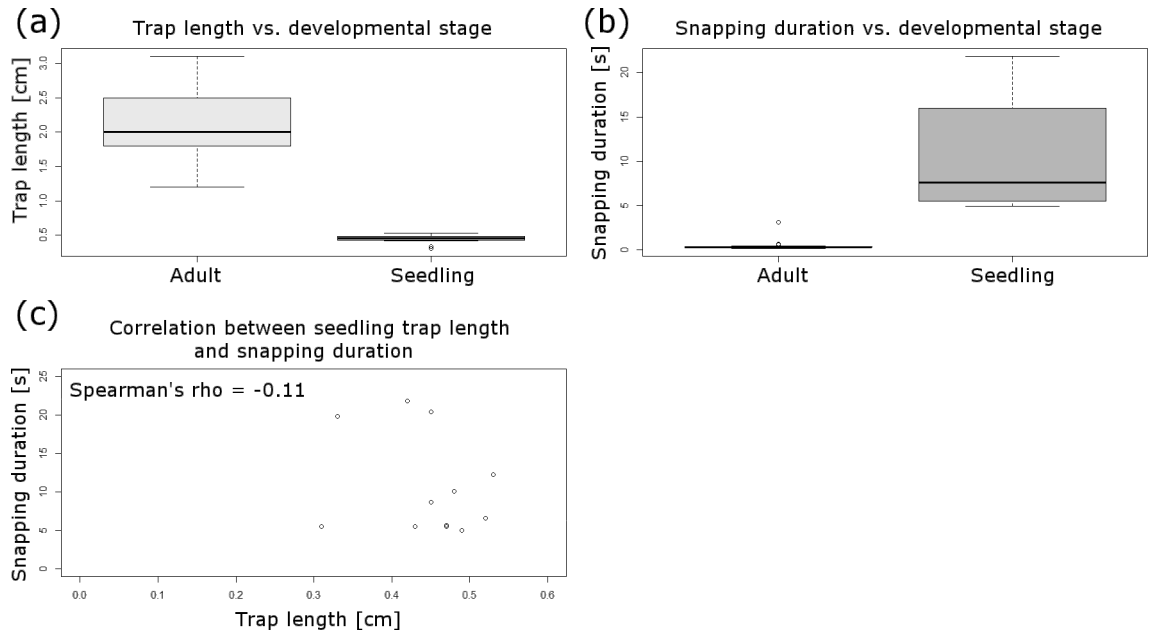

Figure 6: Statistical analyses of the comparative seedling trap/adult trap snapping experiment. (a) Boxplot comparison of trap lengths in different developmental stages of the Venus flytrap. The sample size for adult traps is n = 21 (see Experimental section), for seedlings n = 12. The trap lengths are highly significantly different between the two growth stages. (b) Boxplot comparison of snapping durations in different developmental stages of the Venus flytrap. The sample size for adult traps is n = 21 (see Experimental section), for seedlings n = 12. The snapping durations for adult traps are highly significantly shorter than for seedling traps. (c) Snapping durations do not correlate with the trap lengths in seedlings (Spearman's rho = −0.21).

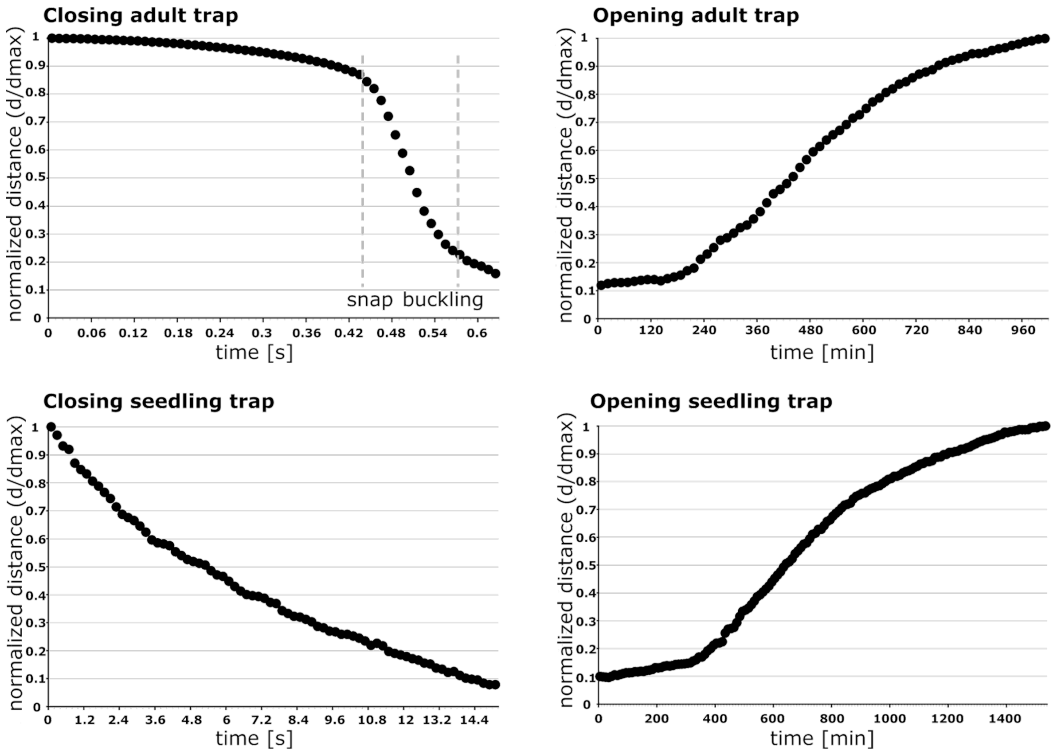

Figure 7: Comparative kinematics of closing and opening motions in adult and seedling traps. Note the different time scales indicated. The adult trap closes very rapidly and performs a sudden geometrical change (snap buckling, indicated by dashed grey lines), whereas the much slower closing of the seedling trap is a very continuous process without any noticeable acceleration. Opening traps also move very continuously, indicating that no reverse snap-buckling takes place either in the adult traps or in the seedling traps. The normalized distance d^* is calculated as ratio of d, the remaining distance between the lobes measured for various phases of closure, over d_{max}, the distance between the lobes in the fully open trap.

As adult traps close similarly fast under water as they do in air (Figure 2b), and because of the fact that no considerable water displacement out of the trap is visible during this process (Figure 4), the Venus flytrap is without doubt capable of capturing fast aquatic prey. We consider it as unlikely that prey could escape through the small lateral gaps of the closed trap which are visible in Figure 4 and in Supporting Information File 8. Detailed future analyses should take into account using tracer particles, several cameras and particle image velocimetry (PIV) methods for tracking the water displacement. The question if trapping events under water occur only occasionally and by coincidence is also a matter for possible future studies. The factor "prey attraction" should additionally be analyzed, i.e., to what extent it plays a role for the submersed plant. Moreover, future studies could also tackle the question if *Dionaea* is able to perform prey digestion under water, i.e., if the digestion chamber is sealed watertight.

The sister species to *D. muscipula* is the aquatic Waterwheel plant (*Aldrovanda vesiculosa*) [25,26]. *Aldrovanda* features snap traps under water that are similarly fast as the aerial traps of *Dionaea*, but which, in contrast, are small enough (ca. 4–5 mm in length) to move purely hydraulically. The much smaller *Aldrovanda* trap can be actuated hydraulically ca. 100 times more rapidly than the *Dionaea* trap [9]. Triggering by prey entails turgor changes in motor cells [27-31] leading to a bending of a midrib kinematically coupled to the trap lobes, which simultaneously close without performing curvature inversions [13,27,32]. Hence, the *Dionaea* trap consists of two independent, active kinematical elements (the lobes, each performing hydraulic motion and snap buckling), whereas the *Aldrovanda* trap consist of one kinematical element, the midrib, which actively bends and couples the undeformed lobes. We assume that the asynchronous *Dionaea* snapping as observed and described above is relevantly based on this division into two independent kinematical elements, and we consider it as unlikely that such a mode also occurs in *Aldrovanda* (which, however, remains to be investigated experimentally).

Due to a lack of fossilized intermediate forms, the question of how snap traps evolved is still a matter of debate. Gibson and Waller [33] argue that selection to catch and retain large prey favored evolution of snap traps in general, but after Hutchens and Luken [34], *Dionaea* prey capture is rather opportunistic than selective. Poppinga and Joyeux [13] have hypothesized

that the different snap-trap mechanics are adaptations to the respective life form (terrestrial vs aquatic). Hence, the *Aldrovanda* mechanism could be an optimized means to reliably capture prey under water, whereas the *Dionaea* trap snaps shut rapidly on land. From our comparative study (air/water) we can conclude that the *Dionaea* trap mechanism (hydraulics plus elastic relaxation of a comparably large thin shell) is presumably not an adaptation to the terrestrial lifeform in regard to mere trap functioning, because the same mechanism works also well under water. In return, it would be interesting to perform a study comparable to the present one in which the *Aldrovanda* trap snaps in air. Owing to the small size of the *Aldrovanda* trap and due to the lower density of the surrounding medium, we may speculate that snapping in air is presumably of comparable (or even higher) speed than under water. So why do *Aldrovanda* and *Dionaea* possess two different trap closure mechanics and does there exist a selective advantage for one of the snapping modes in air or under water? Probably, the selection to catch and retain large prey [33] in combination with the ability to catch a broad range of prey of different sizes [34] favored the evolution of the *Dionaea* trap, whereas *Aldrovanda* relies on capture of abundant and small zooplankton [35,36].

Dionaea seedlings capture their prey with millimeter-sized traps (Figure 5). The closure durations measured are much higher than in the similarly small *Aldrovanda* traps and in adult *Dionaea* traps (Figure 6b). This presumably indicates that much slower prey is being caught in nature. In traps of our cultivated seedlings we often observed remnants of arthropods (Figure 5c), indicating successful prey capture and digestion as investigated in detail by Hatcher and Hart [15]. The angle between the lobes of seedling traps is small (Figure 5a), which is probably a structural requirement to achieve "reasonable" trap closure durations with (relatively) slow movement speeds.

Based on the snapping durations measured and on our kinematical analyses (Figure 7) we can now assume that snap buckling as a motion speed boost is not (or, to a much lesser degree) implemented as a feature already in young traps. It remains to be investigated if this is morphologically manifested in a lesser lobe curvature and/or lesser lobe thickness. Both parameters are known to strongly influence the snap-buckling behavior [8]. For calculating the theoretical speed of hydraulic actuation according to Skotheim and Mahadevan [9], we measured the approximate lobe thicknesses from photographs of seedling and adult traps crosscut in their mid-planes (Figure 5d,e). The thicknesses were measured at the bottom parts of the trap lobes where Forterre et al. [8] indicate the strongest lobe surface extensions caused by the hydraulically actuated movement. By approximation of a seedling trap lobe thickness of $L_s \approx 200$ µm we see that the theoretical timescale for water displacement, the poroelastic time $\tau_{ps} \approx 0.064$ s, is well below the fastest snapping duration measured ($\tau_s = 4.96$ s). This allows us to speculate that traps of Venus flytrap seedlings are indeed actuated mainly or exclusively hydraulically and that the additional feature of snap buckling probably only appears when "size matters", i.e., in later developmental stages when the traps are too large to move fast and to become actuated mainly hydraulically. For lobes of adult traps with the typical thickness $L_{a1} \approx 500$ µm [9], respectively with the measured thickness $L_{a2} \approx 1$ mm, we have $\tau_{pa1} \approx 0.4$ s [9] and $\tau_{pa2} \approx 1.6$ s, which both are well above the measured fastest snapping duration ($\tau_a = 0.17$ s). Presumably, the *Aldrovanda* trap is much faster as a *Dionaea* seedling trap owing to the kinematic amplification mechanism, which enables large-scale deformation with a minute initial, hydraulically evoked deformation of the midrib [13,32].

The opening of the analyzed adult trap and seedling trap is a very slow process (adult: ca. 16 h; seedling: ca. 24 h). The motions are continuous and without any noticeable sudden acceleration (Figure 7). We speculate that growth [2] takes place on certain lobe region(s) and that the mechanically difficult and, hence, energetically costly (or even impossible?) inversion of lobe curvature by reverse snap buckling is avoided in adult traps. As the process of cell elongation during growth is naturally limited, the traps die once a critical length has been reached (after 3–12 snapping actions, [11]). Theoretically, traps of seedlings could reopen by simply reversing the processes involved in hydraulic snapping without a growth-based increase in size, which might be beneficial for repetitive prey capture and survival in such a young developmental stage.

Our results showing that the snapping duration in adult traps does not correlate with trap length (Figure 2c) seem to contradict the hypothesis formulated by Forterre et al. [8], who postulate that larger traps should have higher snapping speeds. This is based on the finding that the snap-buckling behavior depends on the dimensionless parameter $\alpha = W^4 \cdot \kappa^2 / h^2$, with W being the size of the leaf, κ the mean curvature of the trap lobes, and h the leaf thickness. As we did not measure W and κ in our study and because the traps investigated are more or less similar in size, our results have to be regarded with caution, and further comparative studies should take the mentioned parameters and a larger variety of trap sizes into consideration. Figure 2b shows that there are no conspicuous variations in terms of measured closure durations between the traps tested underwater (15 °C) and in air (20–25 °C), which indicates that movement speed is not or only to a little degree influenced by temperature. Nonetheless, because the duration of the overall trap motion is ultimately dictated by the flow of interstitial water through the lobes, future comparative snapping experiments should be per-

formed in temperature-constant chambers to exclude even small temperature-dependent physiological differences.

As a conclusion it can be said that the Venus flytrap has evolved a remarkable trapping system that functions as well in air as under water, and which can be considered as an optimized system for nutrient acquisition of a carnivorous plant growing in seasonally inundated habitats. Similar reports on carnivorous plants with traps functioning under different environmental conditions are, e.g., the resinous *Roridula* sticky traps [37] and the rainwater-dependent pitfall trapping systems in *Nepenthes* [38,39]. The *Dionaea* trap is not "only" a "simple" snap trap but possesses different snapping modes, movement mechanics and actuation principles, which greatly broadens our understanding of this (in)famous carnivore and opens up novel perspectives for future studies.

Experimental

Plant material

We analyzed healthy, well-watered and potted adult *D. muscipula* plants as well as half-year-old seedlings, all cultivated in a temperate greenhouse of the Botanic Garden Freiburg.

General cinematographic analyses

For filming fast closure motions, traps were stimulated with a nylon thread on the trigger hairs of one lobe and recorded with a high-speed camera (Motion Scope Y4, Redlake, USA, recording speed 100 fps) in combination with a macro objective lens (Zeiss Makro-Planar T*2/100 mm ZF), a cold light source (techno light 270, Karl Storz GmbH & Co.KG, Tuttlingen) and by using the software Motion Studio x64 2.12.12.00 (IDT, USA). For filming the slow opening motions, the closed traps were recorded with a ColorView II camera (recording speed: 1 frame per 10 or per 15 min) mounted on a horizontally adjusted SZX9 stereo microscope and by using the cell^D 2.6 software (Olympus Corp., Tokyo, Japan). Trap sizes were measured after closure at their largest lateral dimensions either directly on the plant or from photographs by using Fiji/ImageJ 1.48r [40] (Figure 1).

Comparison of snapping durations in air and under water and characterization of snapping modes

Traps were recorded in air (temperature in our lab ca. 20–25 °C, relative air humidity ca. 34.5–43.5%) and under water. For each trial we used 30 different traps from 30 different plants so that, in total, 60 traps from 60 plants were tested. For the experiments with submersed traps, the respective potted plants were consecutively placed in a 20 cm deep, small plastic tank filled with tap water (temperature ca. 15 °C). Warmer water (20–25 °C) was not used because it often led to undesired trap closure.

Video analyses were performed with Fiji/ImageJ as described above. Firstly, the snapping events were categorized whether the trap lobes close simultaneously or not. Traps with noticeably asynchronous lobes were subdivided into traps where the stimulated lobe moves first, and where the not-stimulated lobe moves first. From all snapping events the snapping durations were measured. For this purpose, we counted the number of video frames starting from the last frame where no motion is visible until the frame where the teeth of the lobe margins interlock in such a way that they extend to the other lobe's margin (see Figure 2). We chose this point in time as the "closed state" because 1) the important and fast snap-buckling process is already finished, 2) in this state the interlocking teeth presumably effectively deter escape of prey by forming a mechanically strong mesh, 3) because the subsequent, final closure movement step is poroelastically dampened and very variable in duration and is also often influenced by teeth blocking the counterpart lobe.

Only smooth and failure-free motions were analyzed. In the cases where the motion of the lobes was asynchronous, we counted the frames from the beginning of the motion of the first lobe until both lobes have moved to the above described closed state.

We used the software GNU R 3.1.1 [41] including the additional packages "*car*" [42] and "*psych*" [43] for statistical analyses (Supporting Information File 2). We analyzed trap lengths and snapping durations for significant differences for traps tested under aerial or submersed conditions using Wilcoxon rank sum tests. The relationship between trap length and snapping duration was examined calculating Spearman's rank correlation coefficient (*rho*), whereas the dependency between the snapping mode and the surrounding medium was studied using Fisher's exact test.

Qualitative analysis of water displacement during snapping under water

We carefully placed several ink drops (T10 blau, Lamy GmbH, Heidelberg-Wieblingen,) with a syringe onto the midribs of nine submerged traps, which were subsequently stimulated and recorded as described above. Video analyses were performed with Fiji/ImageJ.

Comparative kinematical analyses of seedling and adult traps

Movements of 12 traps from different seedlings were recorded by using the high-speed-equipment described above and

analyzed with Fiji/ImageJ. Trap closure durations in seedlings had to be calculated in another way as described for adult traps, because we found that the traps often do not close completely (see Results section). Therefore, we counted the frames from the beginning of the motion up to the frame were the motion stops completely.

For statistical analyses, we again used GNU R 3.1.1 including the same additional packages and procedures as described above (Supporting Information File 3). We used 21 adult traps with synchronously moving lobes from the above described comparative air/water analysis (see Results section) for comparison. We analyzed trap lengths and snapping durations of seedlings and the above mentioned adult traps for significant differences, and additionally analyzed the correlation between seedling trap length and snapping duration.

From the high-speed-videos of one additional seedling trap and from an additional adult trap we measured in each case the distance between the two lobes during snapping. Subsequently, we then calculated the normalized distance d^* according to the formula

$$d^* = d/d_{\max} ,$$

with d being the respective remaining distance measured and $d_{\max}$ the distance between the lobes in the fully open trap. One more additional seedling trap and one additional adult trap were recorded during opening as described above. From the resulting videos we also calculated the normalized distances d^*.

Supporting Information

Supporting Information File 1
MS Excel file with raw data.
[http://www.beilstein-journals.org/bjnano/content/supplementary/2190-4286-7-59-S1.xlsx]

Supporting Information File 2
Statistical analyses for the comparative air/under water snapping experiment.
[http://www.beilstein-journals.org/bjnano/content/supplementary/2190-4286-7-59-S2.pdf]

Supporting Information File 3
Statistical analysis: Venus flytrap seedlings.
[http://www.beilstein-journals.org/bjnano/content/supplementary/2190-4286-7-59-S3.pdf]

Supporting Information File 4
Movie file (.mov, MPEG-4 (Quick Time)) showing synchronous lobe movement (recording speed 100 fps, playback 20 fps).
[http://www.beilstein-journals.org/bjnano/content/supplementary/2190-4286-7-59-S4.mov]

Supporting Information File 5
Movie file (.mov, MPEG-4 (Quick Time)) showing progressive lobe movement (recording speed 100 fps, playback 20 fps).
[http://www.beilstein-journals.org/bjnano/content/supplementary/2190-4286-7-59-S5.mov]

Supporting Information File 6
Movie file (.mov, MPEG-4 (Quick Time)) showing asynchronous lobe movement (triggered lobe moves first) (recording speed 100 fps, playback 20 fps).
[http://www.beilstein-journals.org/bjnano/content/supplementary/2190-4286-7-59-S6.mov]

Supporting Information File 7
Movie file (.mov, MPEG-4 (Quick Time)) showing asynchronous lobe movement (non-triggered lobe moves first) (recording speed 100 fps, playback 20 fps).
[http://www.beilstein-journals.org/bjnano/content/supplementary/2190-4286-7-59-S7.mov]

Supporting Information File 8
Movie file (.mov, MPEG-4 (Quick Time)) showing trap closure under water. The ink drop inside the trap and the ink filament are visible (recording speed 100 fps, playback 20 fps).
[http://www.beilstein-journals.org/bjnano/content/supplementary/2190-4286-7-59-S8.mov]

Supporting Information File 9
Movie file (.mov, MPEG-4 (Quick Time)) showing closure of a seedling trap (recording speed 100 fps, playback 20 fps).
[http://www.beilstein-journals.org/bjnano/content/supplementary/2190-4286-7-59-S9.mov]

Supporting Information File 10
Movie file (.mov, MPEG-4 (Quick Time)) showing the opening of a seedling trap (recording speed 1 frame per 10 min, playback 20 fps).
[http://www.beilstein-journals.org/bjnano/content/supplementary/2190-4286-7-59-S10.mov]

Supporting Information File 11

Movie file (.mov, MPEG-4 (Quick Time)) showing the opening of an adult trap (recording speed 1 frame per 15 min, playback 20 fps).
[http://www.beilstein-journals.org/bjnano/content/supplementary/2190-4286-7-59-S11.mov]

Acknowledgements

We thank the German Federal Ministry of Education and Research (BMBF) (funding directive BIONA, 01RB0806) for long-lasting financial support. This work has been funded by the German Research Foundation (DFG) as part of the Transregional Collaborative Research Centre (SFB/Transregio) 141 'Biological Design and Integrative Structures'/project A04. The authors dedicate this work to Prof. Dr. Wilhelm Barthlott for his merits in carnivorous plants research.

References

1. Darwin, C. *Insectivorous plants;* Murray: London, United Kingdom, 1975. doi:10.5962/bhl.title.99933
2. Juniper, B. E.; Robins, R. J.; Joel, D. M. *The carnivorous plants;* Academic Press: London, United Kingdom, 1989.
3. Barthlott, W.; Porembski, S.; Seine, R.; Theisen, I. *The curious world of carnivorous plants: a comprehensive guide to their biology and cultivation;* Timber: Portland, U.S.A., 2007.
4. Hill, B. S.; Findlay, G. P. *Q. Rev. Biophys.* **1981,** *14,* 173–222. doi:10.1017/S0033583500002249
5. Williams, S. E.; Bennett, A. B. *Science* **1982,** *218,* 1120–1122. doi:10.1126/science.218.4577.1120
6. Hodick, D.; Sievers, A. *Planta* **1989,** *179,* 32–42. doi:10.1007/BF00395768
7. Colombani, M.; Forterre, Y. *Comput. Methods Biomech. Biomed. Eng.* **2011,** *14* (Suppl. 1), 115–117. doi:10.1080/10255842.2011.593757
8. Forterre, Y.; Skotheim, J. M.; Dumais, J.; Mahadevan, L. *Nature* **2005,** *433,* 421–542. doi:10.1038/nature03185
9. Skotheim, J. M.; Mahadevan, L. *Science* **2005,** *308,* 1308–1310. doi:10.1126/science.1107976
10. Schnell, D. E. *Carnivorous plants of the United States and Canada;* John F. Blair: Winston-Salem, U.S.A., 1976.
11. Bailey, T.; McPherson, S. *S. Dionaea. The Venus's Flytrap;* Redfern Natural History Productions: Poole, United Kingdom, 2012.
12. Roberts, P. R.; Oosting, H. J. *Ecol. Monogr.* **1958,** *28,* 193–218. doi:10.2307/1942208
13. Poppinga, S.; Joyeux, M. *Phys. Rev. E* **2011,** *84,* 041928. doi:10.1103/PhysRevE.84.041928
14. Poppinga, S.; Masselter, T.; Speck, T. *BioEssays* **2013,** *35,* 649–657. doi:10.1002/bies.201200175
15. Hatcher, C. R.; Hart, A. G. *Int. J. Ecol.* **2014,** 135207. doi:10.1155/2014/135207
16. DiPalma, J. R.; McMichael, R.; DiPalma, M. *Science* **1966,** *152,* 539–540. doi:10.1126/science.152.3721.539
17. Volkov, A. G.; Adesina, T.; Jovanov, E. *Plant Signaling Behav.* **2007,** *2,* 139–144. doi:10.4161/psb.2.3.4217
18. Volkov, A. G.; Adesina, T.; Markin, V. S.; Jovanov, E. *Plant Physiol.* **2008,** *146,* 694–702. doi:10.1104/pp.107.108241
19. Hedrich, R. *Physiol. Rev.* **2012,** *92,* 1777–1811. doi:10.1152/physrev.00038.2011
20. Volkov, A. G.; Pinnock, M.-R.; Lowe, D. C.; Gay, M. S.; Markin, V. S. *J. Plant Physiol.* **2011,** *168,* 109–120. doi:10.1016/j.jplph.2010.06.007
21. Volkov, A. G.; Murphy, V. A.; Clemmons, J. I.; Curley, M. J.; Markin, V. S. *J. Plant Physiol.* **2012,** *169,* 55–64. doi:10.1016/j.jplph.2011.08.003
22. Volkov, A. G.; Harris, S. L., II; Vilfranc, C. L.; Murphy, V. A.; Wooten, J. D.; Paulicin, H.; Volkova, M. I.; Markin, V. S. *J. Plant Physiol.* **2013,** *170,* 25–32. doi:10.1016/j.jplph.2012.08.009
23. Volkov, A. G.; Forde-Tuckett, V.; Volkova, M. I.; Markin, V. S. *Plant Signaling Behav.* **2014,** *9,* e27793. doi:10.4161/psb.27793
24. Guo, Q.; Dai, E.; Han, X.; Xie, S.; Chao, E.; Chen, Z. *J. R. Soc., Interface* **2015,** *12,* 20150598. doi:10.1098/rsif.2015.0598
25. Cameron, K. M.; Wurdack, K. J.; Jobson, R. W. *Am. J. Bot.* **2002,** *89,* 1503–1509. doi:10.3732/ajb.89.9.1503
26. Rivadavia, F.; Kondo, K.; Kato, M.; Hasebe, M. *Am. J. Bot.* **2003,** *90,* 123–130. doi:10.3732/ajb.90.1.123
27. Ashida, J. *Mem. Coll. Sci., Univ. Kyoto, Ser. B* **1934,** 141–244.
28. Iijima, T.; Sibaoka, T. *Plant Cell Physiol.* **1981,** *22,* 1595–1601.
29. Iijima, T.; Sibaoka, T. *Plant Cell Physiol.* **1982,** *23,* 679–688.
30. Iijima, T.; Sibaoka, T. *Plant Cell Physiol.* **1983,** *24,* 51–60.
31. Iijima, T.; Sibaoka, T. *Plant Cell Physiol.* **1985,** *26,* 1–13.
32. Joyeux, M. *Phys. Rev. E* **2013,** *88,* 034701. doi:10.1103/PhysRevE.88.034701
33. Gibson, T. C.; Waller, D. M. *New Phytol.* **2009,** *183,* 575–587. doi:10.1111/j.1469-8137.2009.02935.x
34. Hutchens, J. J.; Luken, J. O. *Botany* **2009,** *87,* 1007–1010. doi:10.1139/B09-064
35. Akeret, B. *Bot. Helv.* **1993,** *103,* 193–199.
36. Cross, A. *Aldrovanda. The Waterwheel Plant;* Redfern Natural History Productions: Poole, United Kingdom, 2012.
37. Voigt, D.; Konrad, W.; Gorb, S. *Interface Focus* **2015,** *5,* 20140053. doi:10.1098/rsfs.2014.0053
38. Bohn, H. F.; Federle, W. *Proc. Natl. Acad. Sci. U. S. A.* **2004,** *101,* 14138–14143. doi:10.1073/pnas.0405885101
39. Bauer, U.; Paulin, M.; Robert, D.; Sutton, G. P. *Proc. Natl. Acad. Sci. U. S. A.* **2015,** *112,* 13384–13389. doi:10.1073/pnas.1510060112
40. Schindelin, J.; Arganda-Carreras, I.; Frise, E.; Kaynig, V.; Longair, M.; Pietzsch, T.; Preibisch, S.; Rueden, C.; Saalfeld, S.; Schmid, B.; Tinevez, J.-Y.; White, D. J.; Hartenstein, V.; Eliceiri, K.; Tomancak, P.; Cardona, A. *Nat. Methods* **2012,** *9,* 676–682. doi:10.1038/nmeth.2019
41. *R: A language and environment for statistical computing;* R Foundation for Statistical Computing: Vienna, Austria, 2014, http://www.R-project.org/.
42. Fox, J.; Weisberg, S. *An R Companion to Applied Regression,* 2nd ed.; Sage: Thousand Oaks, U.S.A., 2011. http://socserv.socsci.mcmaster.ca/jfox/Books/Companion
43. Revelle, W. psych: Procedures for Personality and Psychological Research. Northwestern University: Evanston, IL, U.S.A., 2015; http://personality-project.org/r.

BEILSTEIN JOURNAL OF NANOTECHNOLOGY

Frog tongue surface microstructures: functional and evolutionary patterns

Thomas Kleinteich* and Stanislav N. Gorb

Full Research Paper

Open Access

Address:
Functional Morphology and Biomechanics, Zoology Department, Kiel University, 24118 Kiel, Germany

Email:
Thomas Kleinteich* - tkleinteich@zoologie.uni-kiel.de

* Corresponding author

Keywords:
adhesion; amphibians; biological materials; feeding; high-resolution micro-CT

Beilstein J. Nanotechnol. **2016,** *7,* 893–903.
doi:10.3762/bjnano.7.81

Received: 09 March 2016
Accepted: 06 June 2016
Published: 22 June 2016

This article is part of the Thematic Series "Biological and biomimetic materials and surfaces".

Associate Editor: K. Koch

Abstract

Frogs (Lissamphibia: Anura) use adhesive tongues to capture fast moving, elusive prey. For this, the tongues are moved quickly and adhere instantaneously to various prey surfaces. Recently, the functional morphology of frog tongues was discussed in context of their adhesive performance. It was suggested that the interaction between the tongue surface and the mucus coating is important for generating strong pull-off forces. However, despite the general notions about its importance for a successful contact with the prey, little is known about the surface structure of frog tongues. Previous studies focused almost exclusively on species within the Ranidae and Bufonidae, neglecting the wide diversity of frogs. Here we examined the tongue surface in nine different frog species, comprising eight different taxa, i.e., the Alytidae, Bombinatoridae, Megophryidae, Hylidae, Ceratophryidae, Ranidae, Bufonidae, and Dendrobatidae. In all species examined herein, we found fungiform and filiform papillae on the tongue surface. Further, we observed a high degree of variation among tongues in different frogs. These differences can be seen in the size and shape of the papillae, in the fine-structures on the papillae, as well as in the three-dimensional organization of subsurface tissues. Notably, the fine-structures on the filiform papillae in frogs comprise hair-like protrusions (Megophryidae and Ranidae), microridges (Bufonidae and Dendrobatidae), or can be irregularly shaped or absent as observed in the remaining taxa examined herein. Some of this variation might be related to different degrees of adhesive performance and may point to differences in the spectra of prey items between frog taxa.

Introduction

Frogs (Lissamphibia: Anura) are famous for their adhesive tongues, which allow them to catch elusive prey. While the movements of the tongue during feeding in different groups of frogs have received considerable attention in the past [1-6], little is known about the functional mechanisms for the adhesiveness of frog tongues. Obviously, adhesion is critical to

secure the prey item and to move it into the mouth. In a previous study we demonstrated for South American horned frogs (genus *Ceratophrys*) that the adhesive forces that frog tongues can produce and withstand are even higher than the body weight of the animals, at least if measured against a glass surface [7]. Further, we found that adhesive forces are higher if less mucus remained on our test surface and that the amount of the mucus coverage increases with increasing contact duration. These results suggested (1) that during the initial contact formation, only small amounts of mucus are present on the tongue and (2) that besides chemical and physical properties of the mucus, other mechanisms at the interface between a frog tongue and a target will have an important impact on tongue adhesiveness [7].

Frog tongues are known to have two types of papillae on their surface. So-called fungiform papillae (type 1) are surrounded by numerous, smaller filiform papillae (type 2) [8]. The fungiform papillae are suggested to act as chemoreceptors, while the filiform papillae are the places for mucus production [9-12]. Owing to the fact that the filiform papillae cover wide parts of the adhesive tongue surface in frogs, the interaction between the filiform papillae, the mucus layer, and the target surface of a prey item will be critical for a successful feeding event. Thus, besides mucus production, the filiform papillae as surface microstructures might actually mediate adhesive performance. More recently we discussed the contribution of the filiform papillae to the adhesive mechanism of the tongue in the frog *Ceratophrys ornata* [13]. We suggested that the papillae increase the adaptability of the tongue to uneven surfaces and may help to form and anchor fibrils of mucus that emerge before a frog tongue is about to loose the contact with a target surface.

While it has been shown before, that the anatomy of frog tongues can be very diverse in different anuran taxa [14], little is known about the diversity of tongue surface structures in frogs. Besides a study on the ornamentation of the tongue in the dicroglossid frog *Fejervarya cancrivora* [15] (the frog is referred to as *Rana cancrivora* in that study), only the tongue surfaces in a few species of the genera *Rana* [15-21] and *Bufo* [22-24] have been described in the literature. Further accounts on tongues in *Hyla arborea* [9] and *Calyptocephalella gayi* [25] focus on the fungiform papillae but neglect the filiform papillae despite their presumably important role in tongue adhesion. Iwasaki (2002) [8] highlights notable differences in the filiform papillae between *Rana* spp. and *Bufo japonicus*. In *Rana* spp., the filiform papillae appear as hair-like structures, while in *B. japonicus*, the filiform papillae rather take the form of ridges. In a more recent study, however, Elsheikh et al. [24] described hair-like filiform papillae for another species within the Bufonidae, i.e., *Sclerophrys regularis* (in [24] as *Bufo regularis*).

Besides the surface profile and mechanical properties of the tongue surface, the tissues underlying the surface represent another important factor for the adhesive performance of the tongue. The configuration of subsurface tissues will determine how well a tongue can adapt to a target surface and how well the tongue withstands the forces that act during protraction and retraction. Besides our recent description of the inner anatomy of the tongue in *Ceratophrys ornata* [13], nothing is known about the three-dimensional architecture of the tissues underneath the tongue surface in frogs. This kind of data might shed light on the presence of potential gradients of the material stiffness that were previously described for attachment structures in beetles [26,27], grasshopers [28], and geckos [29].

Here we combine scanning electron microscopy and high-resolution micro-computed tomography (micro-CT) to provide comparative accounts on the surface profiles and subsurface structures of the tongues in nine different frog species. The aims of this study are: (1) to evaluate patterns of the diversity of tongue surfaces in frogs, (2) to provide descriptions on the three-dimensional organization of the tissues underneath the frog tongue surface, and (3) to understand patterns of tongue variation in frogs within both evolutionary and biomechanical contexts.

Experimental

We studied the tongue anatomy of nine different species comprising eight of the currently 55 recognized taxa (families) within the Anura [30]. A list of specimens is provided in Table 1. The specimens were either made available by the Zoological Museum Hamburg (ZMH) or were derived from the uncatalogued stock of the Zoological Institute and Museum at Kiel University. In the latter case, we used our own specimen IDs (TK) herein. All specimens were stored in 70% ethanol. Two specimens actually belonged to the same genus but comprised two different species: *Litoria infrafrenata* and *L. caerulea*. As these two species appeared to be very similar in their tongue anatomy, they are referred to as *Litoria* spp. herein. The two specimens of *Ceratophrys ornata* have been examined in prior studies on feeding and tongue adhesion in frogs of the genus *Ceratophrys* [13,31]. The *Litoria caerulea* specimen studied herein was previously used for a study on toe-pad anatomy in tree frogs [32].

We examined the surface structures of frog tongues by using scanning electron microscopy (SEM). For SEM we prepared pieces from the central regions of the tongues. These pieces were first dehydrated in an ascending series of ethanol (70%,

Table 1: Specimens examined herein.

taxon (family)	species	collection ID	SVL [mm]	method	voxel size µCT [µm]
Alytidae	*Discoglossus pictus*	ZMH A11869	48	SEM	—
Alytidae	*Discoglossus pictus*	ZMH A11885	48	µCT	0.67
Bombinatoridae	*Bombina variegata*	ZMH A11872	38	SEM	—
Bombinatoridae	*Bombina variegata*	ZMH A11873	37	µCT	0.67
Bufonidae	*Bufo bufo*	TK Bufo01	N/A	µCT & SEM	0.73
Ceratophryidae	*Ceratophrys ornata*	ZMH A11916	59	SEM	—
Ceratophryidae	*Ceratophrys ornata*	ZMH A11917	70	µCT & SEM	0.87
Dendrobatidae	*Oophaga histrionica*	ZMH A11874	29	µCT	0.87
Dendrobatidae	*Oophaga histrionica*	ZMH A11875	32	SEM	—
Hylidae	*Litoria caerulea*	TK Litoria01	68	µCT & SEM	0.53
Hylidae	*Litoria infrafrenata*	ZMH A11870	75	µCT & SEM	0.87
Megophryidae	*Megophrys nasuta*	ZMH A11865	71	SEM	—
Megophryidae	*Megophrys nasuta*	ZMH A11866	103	µCT	0.87
Megophryidae	*Megophrys nasuta*	ZMH A11868	68	µCT	0.67
Ranidae	*Rana* (*Lithobates*) *pipiens*	TK Rana01	N/A	µCT	1.13
Ranidae	*Rana* (*Lithobates*) *pipiens*	TK Rana02	N/A	SEM	—

90%, 100%; each step was maintained for 24 h). For specimens that were also used for micro-computed tomography prior to SEM (see Table 1), two additional dehydration steps (30% and 50%) were necessary, as the micro-CT imaging was performed in distilled water. After dehydration, the tongue specimens were critical point dried with a Quorum E3000 critical point drying system (Lewes, UK). Then the tongue specimens were mounted with the dorsal side facing upwards onto aluminum stubs using carbon-containing double-sided adhesive tape. The specimens were then coated with a 10 nm gold–palladium layer by using a Leica SCD05 Sputter Coater (Leica Microsystems GmbH, Wetzlar, Germany). For scanning electron microscopy, we used a Hitachi S-4800 scanning electron microscope at an accelerating voltage of 3 kV (Hitachi High-Technologies Europe GmbH, Krefeld, Germany).

We used micro-computed tomography (micro-CT or µCT) to study the three-dimensional arrangement of tissues underneath the tongue surface. To visualize soft tissue structures, such as the epithelium and muscle fibers, we stained the frogs with 4% Lugol's iodine potassium iodide solution before we dissected the tongues. For this purpose, we followed the protocol by Metscher [33] but adjusted the staining duration to two weeks to allow the staining solution to diffuse deep into entire frog specimens. After staining, we dissected the tongues and cut out pieces that were approximately 1.5 mm × 1.5 mm × 2 mm (length × width × height) from the dorsal surface in central regions of the tongue. These pieces were then placed into the tips of pipettes that we filled with distilled water. To prevent leakage during the scan, we wrapped the pipette tips with laboratory film (Parafilm M®, Bemis Company Inc., Oshkosh, WI, USA). We then mounted the pipette tips with the tongue specimens into a Skyscan 1172 desktop micro-CT scanner (Bruker microCT, Kontich, Belgium). We operated the micro-CT scanner with a source voltage of 40 kV and a current of 250 µA. The small size of the specimens allowed us to fit the pieces of tongue tissue into a very narrow field of view (<2 mm) during the scan, which corresponds to the maximal magnification of the Skyscan 1172 and resulted in voxel sizes of less than 1 µm (Table 1). From the X-ray images, captured during micro-CT scanning, we reconstructed image stacks of virtual cross-sections through the entire specimen with the software NRecon (Bruker microCT, Kontich, Belgium). These image stacks were then exported as 16 bit TIFF files, which we analyzed and visualized with the 3D visualization software package Amira 6.0 (FEI SAS, Mérignac Cedex, France). The micro-CT data of the *Ceratophrys ornata* specimen was already used in a previous study [13] and is accessible at http://dx.doi.org/10.5061/dryad.066mr.

Results

Tongue surface structures: Two types of papillae cover the dorsal surface of frog tongues: numerous filiform papillae build a matrix in that the larger fungiform papillae are embedded (Figure 1). We observed notable interspecific differences in the size and shape of these papillae. The fungiform papillae have roughly the same diameter of 70 to 90 µm in the *Bombina variegata*, *Discoglossus pictus, Ceratophrys ornata, Litoria* spp. (Figure 1A–D), and *Bufo bufo* (Figure 1G) specimens examined (Table 2). However, in *Megophrys nasuta* (Figure 1E)

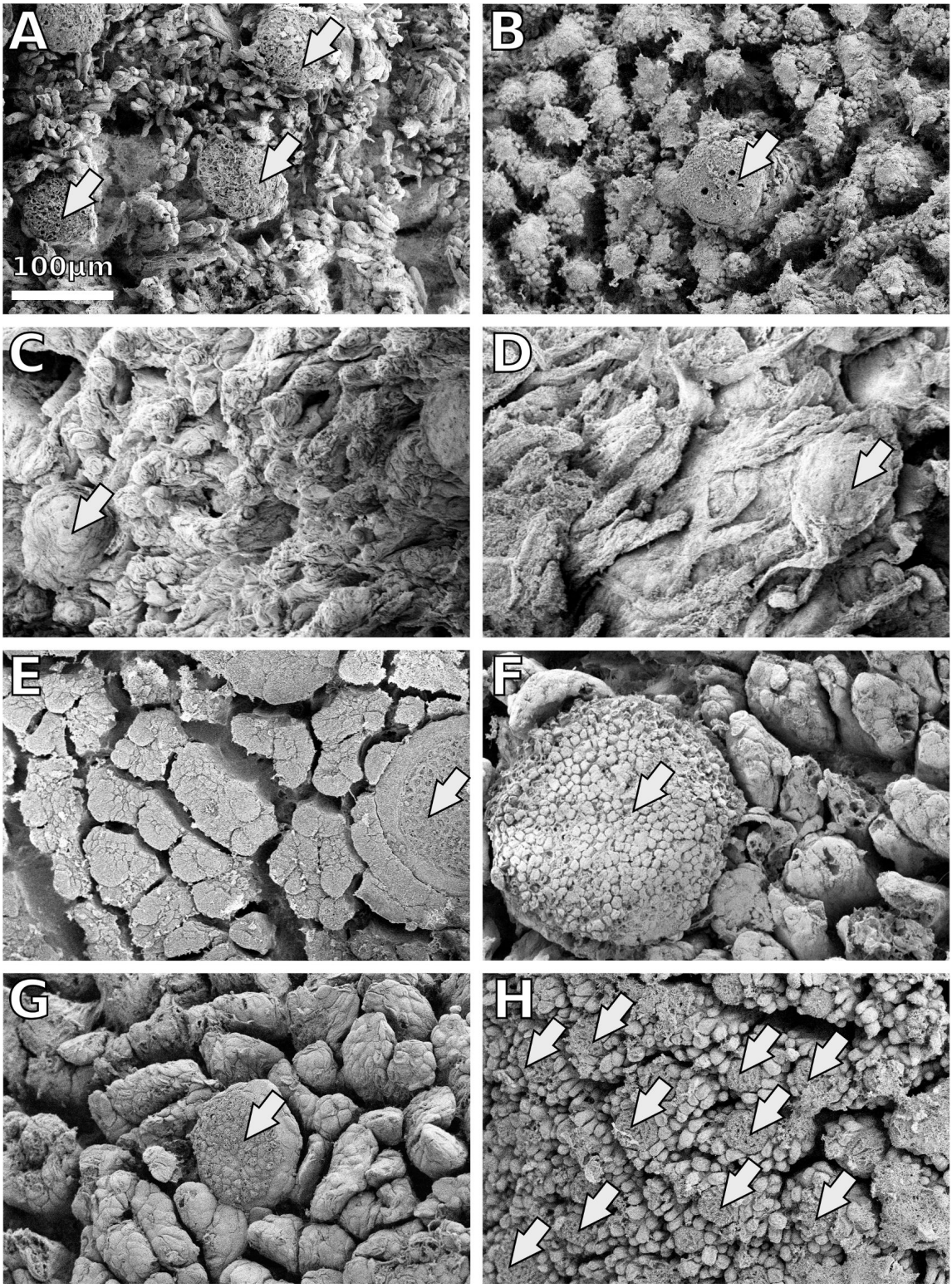

Figure 1: Scanning electron microscopy of frog tongue surfaces. All images are at the same scale. A – *Bombina variegata*, B – *Discoglossus pictus*, C – *Ceratophrys ornata,* D – *Litoria infrafrenata*, E – *Megophrys nasuta,* F – *Rana (Lithobates) pipiens*, G – *Bufo bufo*, H – *Oophaga histrionica*. Frog tongue surfaces are covered by fungiform papillae (arrows), which are embedded in a matrix of smaller filiform papillae. The examined species differ notably in the size and the shape of the papillary surface structures.

Table 2: Measurements of tongue papillae in micrometers based on Figure 1.

	Bombina variegata	*Discoglossus pictus*	*Ceratophrys ornata*	*Litoria infrafrenata*	*Megophrys nasuta*	*Rana (Lithobates) pipiens*	*Bufo bufo*	*Oophaga histrionica*
fungiform papillae	62.87	79.72	78.24	85.27	125.00	216.15	87.69	30.29
	69.98	—	78.19	81.73	—	—	—	29.34
	67.73	—	—	—	—	—	—	27.55
average	66.86	79.72	78.22	83.50	125.00	216.15	87.69	29.06
filiform papillae	8.46	5.47	21.39	16.47	19.86	52.19	32.56	8.99
	6.02	6.02	19.19	17.46	21.08	51.77	34.04	9.64
	7.00	8.77	23.93	19.28	25.41	51.47	34.88	8.19
	7.09	7.14	19.88	13.58	18.27	43.50	35.03	8.25
	6.60	6.34	14.89	12.71	20.91	53.93	32.00	8.01
	5.94	7.21	22.33	11.38	20.86	38.35	31.07	7.96
average	6.85	6.83	20.27	15.15	21.07	48.54	33.26	8.51

and *Rana (Lithobates) pipiens* (Figure 1F), the fungiform papillae appear larger than in the remainder species. In *Oophaga histrionica,* the fungiform papillae are smaller (Figure 1H; Table 2).

The filiform papillae appear as rod-like protrusions with a diameter of approximately 7 µm in *Bombina variegata*, *Discoglossus pictus*, and *Oophaga histrionica*. In *Ceratophrys ornata*, the filiform papillae also appear rod-like, but with a thicker diameter of 20 µm and a lower aspect ratio (Figure 1C). In *Megophrys nasuta*, *Rana (Lithobates) pipiens*, and *Bufo bufo*, the filiform papillae are thicker than in the remainder species, and clutches of filiform papillae form ridge-like structures (Figure 1E–G). In *Litoria* spp., unlike any other species studied herein, the filiform papillae were found to be elongated and hair-like (Figure 1D). The terminal parts of the filiform papillae in frog tongues have a rounded shape except for *M. nasuta*, in which the filiform papillae have flat tips (Figure 1E).

Further we found interspecific variation in the surface patterns of the filiform papillae (Figure 2). In *Megophrys nasuta*, the tips of the filiform papillae are covered by hair-like protrusions, which were approximately 80 nm in diameter (Figure 2E). In *Rana* (*Lithobates*) *pipiens*, hair-like protrusions are also present on the filiform papillae. However, these structures in *R. pipiens* are much larger compared to *M. nasuta* and appear only in patches (Figure 2F). The filiform papillae in *Bufo bufo* and *Oophaga histrionica* differ from the remainding species examined by being covered with nanoscale surface ridges (Figure 2G,H). In *Bombina variegata*, *Discoglossus pictus*, *Ceratophrys ornata*, and *Litoria* spp., no notable surface structures could be observed. The surfaces of the filiform papillae in these species appear irregularly shaped (Figure 2A–D).

Three-dimensional organization of the tongue tissue: Contrast enhanced high-resolution micro-CT imaging allowed us to visualize the three-dimensional organization of subsurface soft tissue structures in frog tongues (Figure 3 and Figure 4). The resulting voxel sizes for the micro-CT datasets ranged from 0.53 to 1.13 µm (Table 1). With this spatial resolution, we were able to identify structures in the micrometer scale, such as the filiform and fungiform papillae (Figure 3). In *Oophaga histrionica*, however, the spatial resolution of the micro-CT dataset was not sufficient to discriminate between the two types of surface papillae (Figure 3H).

Underneath the surface papillae, we found a layer of lacunar structures that in the micro-CT data appear to be almost hollow inside (Figure 4; Supplementary movies). In *Bombina variegata, Discoglossus pictus, Litoria* spp., and *Rana (Lithobates) pipiens*, these lacunae are elongated and of cylindrical shape. Muscle fibers of the tongue musculature emerge between these cylinders towards the tongue surface (Figure 4; movies in Supporting Information File 1). In *Megophrys nasuta* and *Bufo bufo*, the lacunar structures appear to be more spherical than in *B. variegata, D. pictus, Litoria* spp., and *R. pipiens*. Further, in *M. nasuta*, the lacunae are stacked in two, in *B. bufo* even in up to four layers (movies 5 and 7 in Supporting Information File 1). In the *Ceratophrys ornata* specimen, the layer underneath the surface papillae was only poorly stained in the micro-CT scan and lacunae are not visible. However, in a deeper layer,

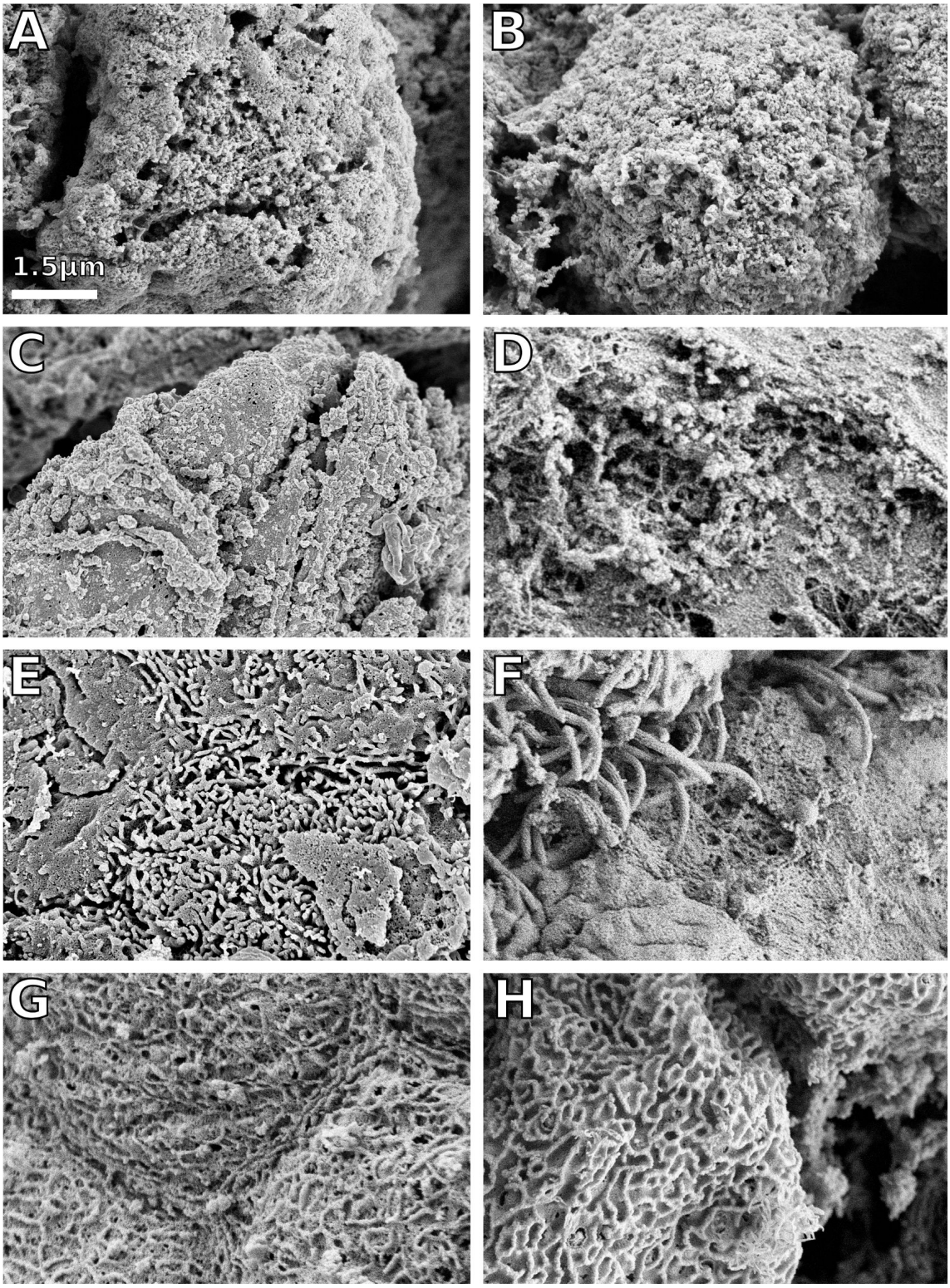

Figure 2: Scanning electron microscopy of the filiform papillae on frog tongues. All images are at the same scale. A – *Bombina variegata*, B – *Discoglossus pictus*, C – *Ceratophrys ornata*, D – *Litoria infrafrenata*, E – *Megophrys nasuta*, F – *Rana* (*Lithobates) pipiens*, G – *Bufo bufo*, H – *Oophaga histrionica*. The filiform papillae show a remarkable degree of interspecific variation. In *M. nasuta* (E) and *R. pipiens* (F), we found hair-like outgrowths on the filiform papillae; in *B. bufo* (G) and *O. histrionica* (F), the filiform papillae are covered by micro-ridges.

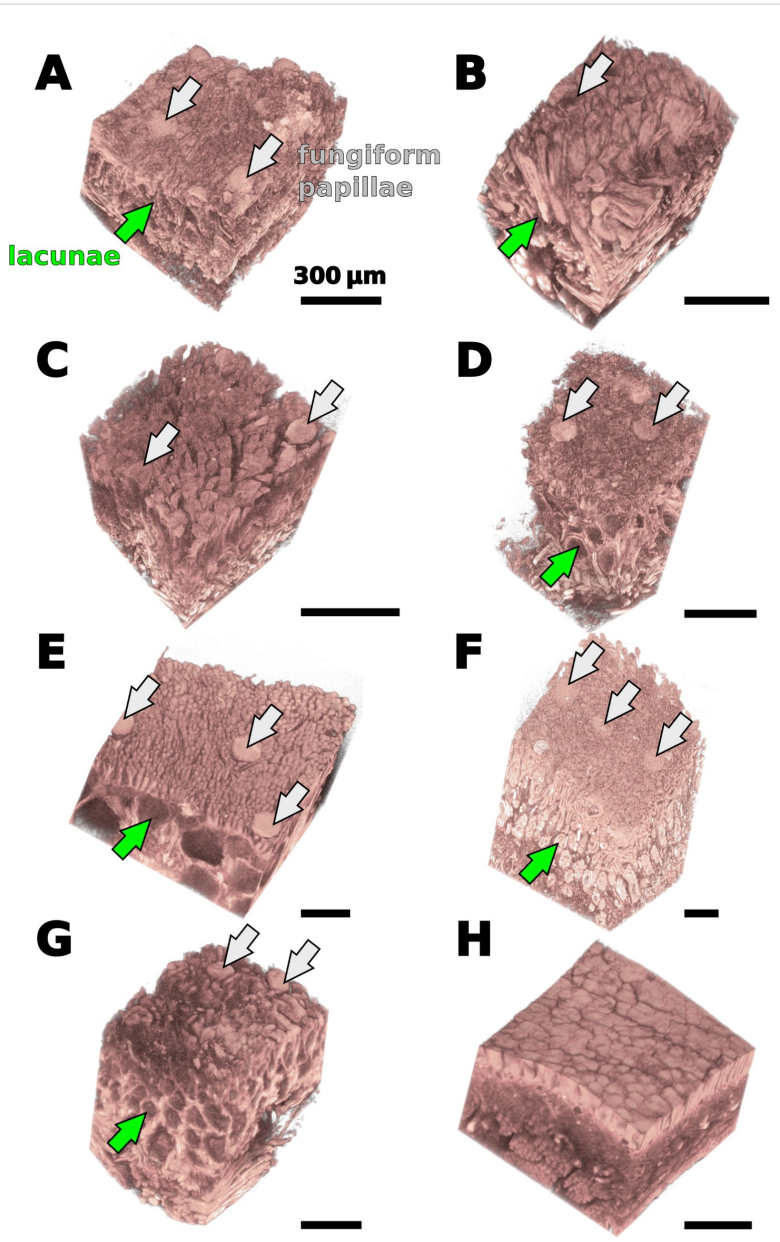

Figure 3: Micro-CT images of tissue fragments that were derived from the surfaces of frog tongues. A – *Bombina variegata*, B – *Discoglossus pictus*, C – *Ceratophrys ornata*, D – *Litoria caerulea*, E – *Megophrys nasuta*, F – *Rana* (*Lithobates*) *pipiens*, G – *Bufo bufo*, H – *Oophaga histrionica*. Except for *C. ornata* (C) and *O. histrionica* (H), the fungiform papillae (grey arrows) can easily be identified in the micro-CT data. Underneath the papillary surface structures lies a layer with lacunar structures that appear hollow in the micro-CT scan (green arrows). Both size and shape of these lacunae strongly vary among different species.

spherical structures can be seen that differ from the hollow lacunae in the remainder species and show a strong X-ray absorption contrast (Figure 4C). Muscle fibers run in-between these spherical structures towards the dorsal surface of the tongue in *C. ornata*. In *Oophaga histrionica*, we were not able to identify lacunae underneath the surface papillae by using micro-CT imaging. Underneath the layer consisting of lacunar, respectively spherical structures in the case of *Ceratophrys ornata*, bundles of tongue muscle fibers are arranged parallel and perpendicular to the tongue surface (movie 3 in Supporting Information File 1). In *Oophaga histrionica*, the fibers of the tongue musculature appear to run directly underneath the surface papillae of the tongue (Figure 4H, movie 8 in Supporting Information File 1).

Discussion

Here we demonstrate a high degree of interspecific variation in the surface anatomy of frog tongues. Differences can be seen in

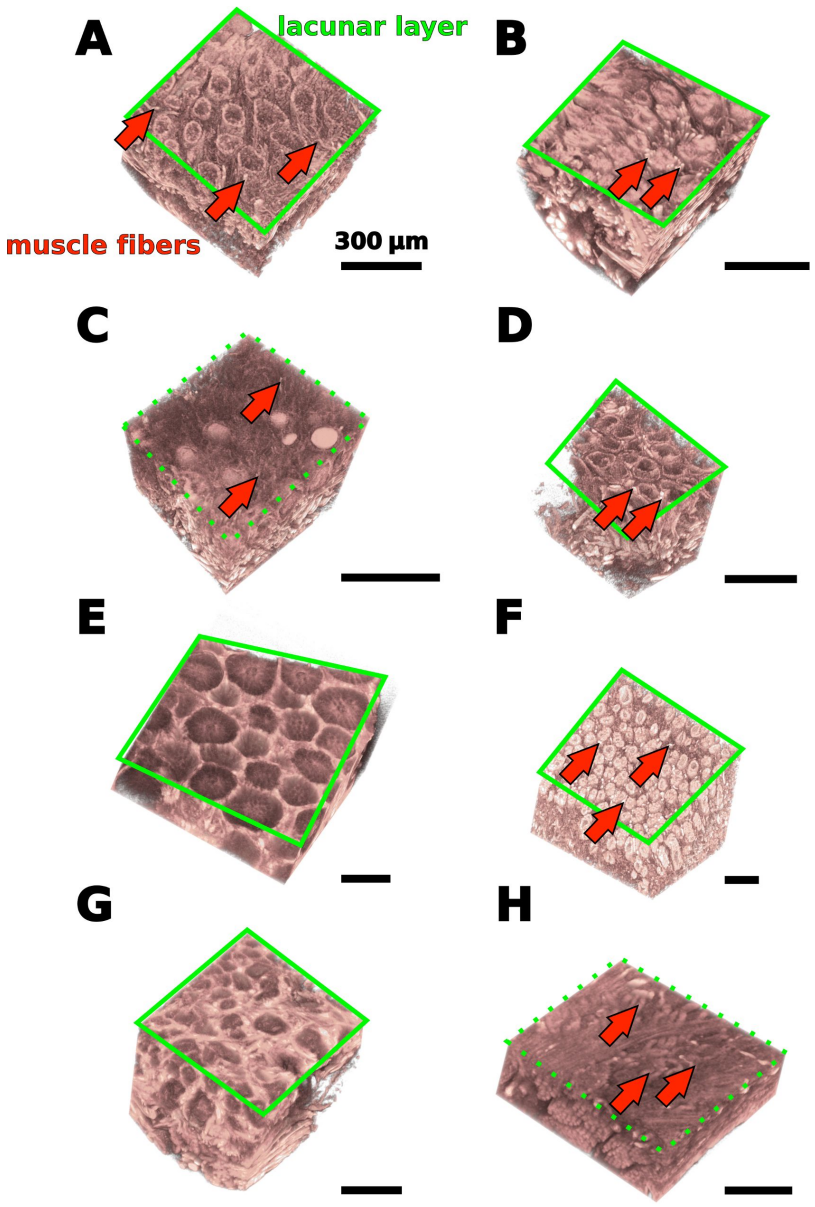

Figure 4: Virtual section through the micro-CT data of tongue tissue fragments at the level of the lacunar layer. A – *Bombina variegata*, B – *Discoglossus pictus*, C – *Ceratophrys ornata*, D – *Litoria caerulea*, E – *Megophrys nasuta*, F – *Rana* (*Lithobates*) *pipiens*, G – *Bufo bufo*, H – *Oophaga histrionica*. In *B. variegata* (A), *D. pictus* (B), and *L. infrafrenata* (D), the lacunae seem to be more similar than in the remainder species. In *C. ornata* (C) and *O. histrionica* (H), we were not able to find lacunae by using micro-CT imaging. Full slice movies of the micro-CT data are available in Supporting Information File 1. Muscle fibers (red arrows) emerge between the lacunae and face towards the tongue surface.

the arrangement of tissue layers close to the tongue surface and in the density, shape, and surface profiles of the filiform papillae. Although we lack experimental data on tongue performance for most of the species discussed herein, we hypothesize that these differences are likely to have effects on the adhesive and frictional properties of the tongues in frogs.

Especially the numerous filiform papillae may play a key-role in tongue adhesion besides their function in mucus production. The papillae themselves deform under compression and thus help to make the tongue adaptable to surface asperities of the prey item. In *Megophrys nasuta* and *Rana (Lithobates) pipiens*, where we found hair-like structures on top of the filiform papillae. This second level of hierarchical organization is hypothesized to increase the adaptability of the tongue under load. The micro-ridges on the filiform papillae in *Bufo bufo* and *Oophaga histrionica* and the irregular surface structures in *Bombina variegata, Discoglossus pictus, Ceratophrys ornata*,

and *Litoria* spp. probably will not deform as much under compression as the hair-like structures in *M. nasuta* and *R. pipiens*. Thus, in *B. variegata, D. pictus, C. ornata*, and *Litoria* spp., the adaptability of the tongue to surface asperities of the prey will only depend on the filiform papillae themselves.

It seems reasonable to assume that species that form and maintain a better contact with the prey surface are more likely to generate high adhesive forces during tongue feeding. Other than for *Ceratophrys* sp. [7], we have no force data on tongue adhesion available at this time. However, another measure for tongue adhesive performance might be the sizes of typical prey items as these are captured with the tongues. *Bufo bufo* and *Oophaga histrionica* are known to feed on relatively small prey, such as ants [34-37], while *M. nasuta* and *R. pipiens* are considered to be generalist feeders capturing a wide variety of prey items of different sizes and even preying upon small vertebrates [36]. This picture, however, becomes much more complicated if one also considers the other species examined herein. Especially frogs within the genus *Ceratophrys* are known to be voracious generalist feeders [31,38-40] and their tongues can produce notable adhesive forces [7]. However, the *C. ornata* examined in the work described herein lacks hair-like outgrowths on its filiform papillae and, therefore, its tongue might be less adaptable to the prey surface than those of *M. nasuta* or *R. pipiens*.

We previously argued that the filiform papillae also interact with the mucus covering the tongues in live frogs [13] (see also Sperry and Wassersug [41]). Frog tongues might thus be considered as composite structures of mucus plus papillae. The size, aspect ratio, and distribution of the papillae will have an impact on how this composite is stabilized. Denser arrays of surface papillae are likely to improve the cohesion within the mucus-papillae composite, and thus prevent failure of the mucus layer during tongue retraction. It is plausible to assume that different species have different physical (rheological) properties of the mucus, and that these properties are correlated with a particular microstructure of the tongue or vice versa. The viscosity of the mucus is critical for attachment especially given the short time frames between tongue impact and retraction, which happens within milliseconds [5-7,42]. The rapidness with which mucus can wet a target surface will decrease with increasing viscosity. Denser arrays of filiform papillae might allow for less viscose mucus that is still stable enough to withstand the tongue pulling forces. Based on the size of the filiform papillae (Figure 1), we would therefore expect for our specimen sample that *Oophaga histrionica* has the least viscous mucus, while *Bufo bufo*, *Rana* (*Lithobates*) *pipiens*, and *Megophrys nasuta* are predicted to have the most viscous mucus. This hypothesis, however, remains to be tested in future studies.

Besides the profile of the surface, also the composition of the underlying tissues will have an impact on the adhesive performance of the tongue. Such a role of deeper tissue layers, which influence the compliance of the adhesive structure, has recently been shown for the feet of grasshoppers [28] and geckos [29]. Although we did not measure the material attributes herein, the architecture of the subsurface layers might suggest the presence of a material gradient in frog tongues as well. It seems reasonable to assume that the mucus coverage on the tongue surface is more compliant than the filiform papillae themselves, which are in turn more flexible than the lacunar sub-surface layer. The muscle fibers underneath the lacunar layer supposedly have even higher stiffness than the lacunar layer. Such material gradients can be beneficial for adhesion as they will allow for a high adaptability to a target surface profile, while maintaining mechanical stability [26,27] and integrity of layered tissues.

The lacunar sub-surface layer that we describe herein for frog tongues is very similar in the three species that use mechanical pulling for feeding (as defined by Nishikawa [6]), i.e., *Bombina variegata, Discoglossus pictus,* and *Litoria* spp. but very diverse in the remainder species that use tongue projection. During mechanical pulling, the tongue deforms by action of the tongue musculature and is slightly protracted over the tip of the lower jaw [6,42]. However, other than during tongue projection, the tongue is not passively elongated by inertia. A more complete taxon sampling and evaluation of the physical properties of the lacunar layer in different frog tongues are needed to test if there is a mechanical benefit of cylindrical lacunae for mechanical pulling.

Further, it is important to keep in mind the limitations of micro-CT imaging here. The voxel sizes of the tongue surface scans were less than one micrometer. However, to visualize structures, several connected voxels are needed. Thus the spatial resolution of our approach is more likely in the range of three to four micrometers. Structures that are in the sub-micrometer range, such as the hair-like extrusions on top of the filiform papillae in *Megophrys nasuta*, therefore cannot be detected with the micro-CT. The absence of lacunae in *Ceratophrys ornata* and *Oophaga histrionica*, might be an artifact that is caused by a limited spatial resolution of our micro-CT setup. Further, although the lacunae generally appear hollow in the micro-CT scans, they might be filled with structures that could either be too thin to be detected with the micro-CT, that are X-ray transparent, or that cannot be stained by LUGOL's solution. For *Pelophylax porosus*, a close relative to *Rana* (*Lithobates*) *pipiens*, Iwasaki et al. [12] prepared histological sections of the

tongue and according to Figure 1 in their publication, the small lacunar structures in *L. pipiens* we describe herein relate to alveolar salivary glands. For *C. ornata,* we prepared fractured pieces of a critical point dried tongue and examined them with the SEM and also did not find lacunar spaces [13]. Future studies on the comparative histology of frog tongues will shed more light into this variation of the tongue at the microscopic level. The benefit of micro-CT imaging, however, is the immediate availability of the three-dimensional architecture of the investigated structures, which cannot be provided with other methods.

Despite the adhesive and frictional properties, also evolutionary relationships between the species examined might provide explanations for the interspecific variation we found herein. The tongues in *Discoglossus pictus* and *Bombina variegata* are rather similar, if compared to the remainder species examined herein. The two taxa, to which *D. pictus* and *B. variegata* belong to, i.e., the Alytidae and Bombinatoridae are widely considered as sister groups within anuran phylogeny [43-45]. Furthermore, *Bufo bufo* (Bufonidae) and *Oophaga histrionica* (Dendrobatidae) are closely related as the Bufonidae were either found to be the sister taxon to the Dendrobatidae [44,45] or to the Dendrobatidae plus species within the genus *Thoropa* [43]. The micro-ridges on the surface of the filiform papillae in *B. bufo* and *O. histrionica* are thus likely to be homologous and might represent a synapomorphy of the Bufonidae and Dendrobatidae. Similar ridges were previously described for a second species within the Bufonidae, i.e., *Bufo japonicus* [22].

However, besides the presence of micro-ridges on the surface of the filiform papillae, the tongues in *Bufo bufo* and *Oophaga histrionica* differ notably in their arrangement of the surface papillae and their three-dimensional organization. While the presence of micro-ridges in these two species might be explained by a close phylogenetic relationship of the Bufonidae and Dendrobatidae, the variation found in the shape and arrangement of the surface papillae and tongue tissue layers in these two species seems to be manifested at a smaller taxonomic scale. Further, the tongues of *Megophrys nasuta, Rana (Lithobates) pipiens, Litoria* spp., and *Ceratophrys ornata* all have unique characters, such as the hair-like protrusions on the flat tips of the filiform papillae in *M. nasuta*, the patches of hairs on the filiform papillae in *R. pipiens*, the shape of the filiform papillae in *Litoria* spp. and the presence of X-ray dense spherical subsurface structures in *C. ornata*. Our taxon sampling herein proves insufficient to trace these unique tongue characteristics through anuran phylogeny. Many questions regarding the evolutionary and functional implications of this structural diversity remain and certainly inspire future research endeavors.

Supporting Information

Supporting Information features a ZIP file containing eight slice movies through the micro-CT datasets, one for each of the following species: *Bombina orientalis* (Supplementary_Movie_01_Bombina.mov), *Discoglossus pictus* (Supplementary_Movie_02_Discoglossus.mov), *Ceratophrys ornata* (Supplementary_Movie_03_Ceratophrys.mov), *Litoria caerulea* (Supplementary_Movie_04_Litoria.mov), *Megophrys nasuta* (Supplementary_Movie_05_Megophrys.mov), *Rana* (*Lithobates*) *pipiens* (Supplementary_Movie_06_Rana.mov), *Bufo bufo* (Supplementary_Movie_07_Bufo.mov) and *Oophaga histrionica* (Supplementary_Movie_08_Oophaga.mov).

Supporting Information File 1

Slice movies through the micro-CT datasets of eight different frog species.
[http://www.beilstein-journals.org/bjnano/content/supplementary/2190-4286-7-81-S1.zip]

Acknowledgements

We wish to thank the members of the Functional Morphology and Biomechanics group at Kiel University for numerous insightful discussions on adhesion in biological systems. The help of Esther Appel and Joachim Oesert in preparing the specimens for scanning electron microscopy is much appreciated. We are grateful for the support by Alexander Haas and Jakob Hallermann from the Centre of Natural History and Zoological Museum in Hamburg who provided specimens and granted permission to dissect the tongues from the museums specimens examined herein. TK was supported by the German Research Foundation (DFG grant KL2707/2-1).

References

1. Emerson, S. B. *Am. J. Anat.* **1977,** *149,* 115–120. doi:10.1002/aja.1001490109
2. Gans, C.; Gorniak, G. C. *Am. J. Anat.* **1982,** *163,* 195–222. doi:10.1002/aja.1001630302
3. Gans, C.; Gorniak, G. C. *Science* **1982,** *216,* 1335–1337. doi:10.1126/science.216.4552.1335
4. Ritter, D.; Nishikawa, K. C. *J. Exp. Biol.* **1995,** *198,* 2025–2040.
5. Nishikawa, K. C.; Gans, C. *J. Exp. Biol.* **1996,** *199,* 2511–2529.
6. Nishikawa, K. C. In *Feeding: Form, function, and evolution in tetrapod vertebrates;* Schwenk, K., Ed.; Academic Press: Cambridge, MA, U.S.A., 2000; pp 117–147. doi:10.1016/B978-012632590-4/50006-X
7. Kleinteich, T.; Gorb, S. N. *Sci. Rep.* **2014,** *4,* 5225. doi:10.1038/srep05225
8. Iwasaki, S.-i. *J. Anat.* **2002,** *201,* 1–13. doi:10.1046/j.1469-7580.2002.00073.x

9. Jaeger, C. B.; Hillman, D. E. Morphology of Gustatory Organs. In *Frog Neurobiology;* Llinás, R.; Precht, W., Eds.; Springer: Berlin, Germany, 1976; pp 588–606. doi:10.1007/978-3-642-66316-1_19
10. Osculati, F.; Sbarbati, A. *Prog. Neurobiol.* **1995,** *46,* 351–399. doi:10.1016/0301-0082(95)00006-H
11. Iwasaki, S.; Iwabuchi, Y.; Asami, T. *Tissue Cell* **1997,** *29,* 323–338. doi:10.1016/S0040-8166(97)80008-0
12. Iwasaki, S.; Iwabuchi, Y.; Okumura, Y. *Arch. Oral Biol.* **1998,** *43,* 463–471. doi:10.1016/S0003-9969(98)00023-5
13. Kleinteich, T.; Gorb, S. N. *R. Soc. Open Sci.* **2015,** *2,* 150333. doi:10.1098/rsos.150333
14. Regal, P. J.; Gans, C. *Evolution* **1976,** *30,* 718–734. doi:10.2307/2407812
15. Iwasaki, S.-i.; Wanichanon, C. *J. Morphol.* **1993,** *215,* 89–100. doi:10.1002/jmor.1052150106
16. Helff, O. M.; Mellicker, M. C. *Am. J. Anat.* **1941,** *68,* 339–369. doi:10.1002/aja.1000680303
17. Helff, O. M.; Mellicker, M. C. *Am. J. Anat.* **1941,** *68,* 371–395. doi:10.1002/aja.1000680304
18. Iwasaki, S.; Wanichanon, C. *Tissue Cell* **1991,** *23,* 385–391. doi:10.1016/0040-8166(91)90056-Y
19. Ojima, K.; Takeda, M.; Saiki, C.; Takahashi, T.; Matsumoto, S. *Ann. Anat.* **1997,** *179,* 393–397. doi:10.1016/S0940-9602(97)80027-1
20. Eşrefoğlu, M.; Temelli, A.; Eşrefoğlu, M. *J. Inonu Univ. Med. Fac.* **2000,** *7,* 67–72.
21. Guiraldelli, M. F.; Lopes, R. A.; Sala, M. A.; Lopes, T. R. V. P. *Int. J. Morphol.* **2011,** *29,* 226–233. doi:10.4067/S0717-95022011000100038
22. Iwasaki, S.-i.; Kobayashi, K. *Zool. Sci.* **1988,** *5,* 331–336.
23. Iwasaki, S.-i.; Miyata, K.; Kobayashi, K. *Zool. Sci.* **1989,** *6,* 681–689.
24. Elsheikh, E. H.; Atta, K. E.; Al-Zahaby, S. A. *J. Basic Appl. Zool.* **2013,** *66,* 131–138. doi:10.1016/j.jobaz.2013.07.004
25. Stensaas, L. J. *Am. J. Anat.* **1971,** *131,* 443–461. doi:10.1002/aja.1001310405
26. Peisker, H.; Michels, J.; Gorb, S. N. *Nat. Commun.* **2013,** *4,* 1661. doi:10.1038/ncomms2576
27. Gorb, S. N.; Filippov, A. E. *Beilstein J. Nanotechnol.* **2014,** *5,* 837–845. doi:10.3762/bjnano.5.95
28. Perez Goodwyn, P.; Peressadko, A.; Schwarz, H.; Kastner, V.; Gorb, S. *J. Comp. Physiol., A* **2006,** *192,* 1233–1243. doi:10.1007/s00359-006-0156-z
29. Gilman, C. A.; Imburgia, M. J.; Bartlett, M. D.; King, D. R.; Crosby, A. J.; Irschick, D. J. *PLoS One* **2015,** *10,* e0134604. doi:10.1371/journal.pone.0134604
30. AmphibiaWeb. http://www.amphibiaweb.org (accessed March 2, 2016).
31. Kleinteich, T. *Salamandra* **2015,** *51,* 209–211.
32. Barnes, W. J. P.; Baum, M.; Peisker, H.; Gorb, S. N. *J. Morphol.* **2013,** *274,* 1384–1396. doi:10.1002/jmor.20186
33. Metscher, B. D. *BMC Physiol.* **2009,** *9,* 11. doi:10.1186/1472-6793-9-11
34. Emerson, S. B. *Herpetologica* **1985,** *41,* 177–188.
35. Santana, A. S.; Juncá, F. A. *Braz. J. Biol.* **2007,** *67,* 125–131. doi:10.1590/S1519-69842007000100017
36. Wells, K. D. *The Ecology and Behavior of Amphibians;* University of Chicago Press: Chicago, IL, U.S.A., 2010.
37. Crnobrnja-Isailović, J.; Ćurčić, S.; Stojadinović, D.; Tomašević-Kolarov, N.; Aleksić, I.; Tomanović, Ž. *J. Herpetol.* **2012,** *46,* 562–567. doi:10.1670/10-264
38. Parsons, C. W. *Nature* **1932,** *130,* 279. doi:10.1038/130279b0
39. Duellman, W. E.; Lizana, M. *Herpetologica* **1994,** *50,* 51–64.
40. Silva, N. R.; Souza, P. R.; Gonçalves, M. F.; Demétrio, M. F.; Prado, C. P. A. *Herpetology Notes* **2014,** *7,* 93–95.
41. Sperry, D. G.; Wassersug, R. J. *Anat. Rec.* **1976,** *185,* 253–257. doi:10.1002/ar.1091850212
42. Deban, S. M.; Nishikawa, K. C. *J. Exp. Biol.* **1992,** *170,* 235–256.
43. Frost, D. R.; Grant, T.; Faivovich, J.; Bain, R. H.; Haas, A.; Haddad, C. F. B.; de Sá, R. O.; Channing, A.; Wilkinson, M.; Donnellan, S. C.; Raxworthy, C. J.; Campbell, J. A.; Blotto, B. L.; Moler, P.; Drewes, R. C.; Nussbaum, R. A.; Lynch, J. D.; Green, D. M.; Wheeler, W. C. *Bull. Am. Mus. Nat. Hist.* **2006,** *297,* 1–291. doi:10.1206/0003-0090(2006)297[0001:TATOL]2.0.CO;2
44. Roelants, K.; Gower, D. J.; Wilkinson, M.; Loader, S. P.; Biju, S. D.; Guillaume, K.; Moriau, L.; Bossuyt, F. *Proc. Natl. Acad. Sci. U. S. A.* **2007,** *104,* 887–892. doi:10.1073/pnas.0608378104
45. Pyron, R. A.; Wiens, J. J. *Mol. Phylogenet. Evol.* **2011,** *61,* 543–583. doi:10.1016/j.ympev.2011.06.012

License and Terms

BEILSTEIN JOURNAL OF NANOTECHNOLOGY

The hydraulic mechanism in the hind wing veins of *Cybister japonicus* Sharp (order: Coleoptera)

Jiyu Sun[*1,2], Wei Wu[1], Mingze Ling[3], Bharat Bhushan[*2] and Jin Tong[1]

Full Research Paper

Open Access

Address:
[1]Key Laboratory of Bionic Engineering (Ministry of Education), Jilin University, Changchun, 130025, P. R. China, [2]Nanoprobe Laboratory for Bio- & Nanotechnology and Biomimetics (NLB2); The Ohio State University, 201 W. 19th Avenue, Columbus, OH 43210-1142, USA and [3]State Key Laboratory of Automotive Dynamic Simulation, Jilin University, Changchun 130022, China

Email:
Jiyu Sun[*] - sjy@jlu.edu.cn; Bharat Bhushan[*] - bharat.bhushan@bjnano.org

* Corresponding author

Keywords:
bioinspiration; diving beetles; hydraulic mechanism; wings; micro air vehicles (MAVs)

Beilstein J. Nanotechnol. **2016,** *7,* 904–913.
doi:10.3762/bjnano.7.82

Received: 18 December 2015
Accepted: 16 June 2016
Published: 23 June 2016

This article is part of the Thematic Series "Biological and biomimetic materials and surfaces".

Guest Editor: S. N. Gorb

Abstract

The diving beetles (Dytiscidae, Coleoptera) are families of water beetles. When they see light, they fly to the light source directly from the water. Their hind wings are thin and fragile under the protection of their elytra (forewings). When the beetle is at rest the hind wings are folded over the abdomen of the beetle and when in flight they unfold to provide the necessary aerodynamic forces. In this paper, the unfolding process of the hind wing of *Cybister japonicus* Sharp (order: Coleoptera) was investigated. The motion characteristics of the blood in the veins of the structure system show that the veins have microfluidic control over the hydraulic mechanism of the unfolding process. A model is established, and the hind wing extending process is simulated. The blood flow and pressure changes are discussed. The driving mechanism for hydraulic control of the folding and unfolding actions of beetle hind wings is put forward. This can assist the design of new deployable micro air vehicles and bioinspired deployable systems.

Introduction

The concept of a micro air vehicle (MAV) was first introduced in the early 1990s. It was extensively researched because of its advantages over traditional aircraft, such as its small size, light weight, good concealment, flexibility, low cost, and portability. There are three main flight modes: fixed wing, rotor, and flapping. Insects possess a remarkable ability to fly, far superior to what humans achieved in the production of MAVs with a low Reynolds number.

In general, the hind wings of a beetle are larger than its forewings (elytra) to maintain the ability of the beetle to fly. One exception are the hind wings in perfectly flying jewel beetles, which are not folded at all and are smaller than its elytra. The hind wings of a beetle are membranous and folded under the elytra while at rest [1]. In order to be completely covered by the elytra, the hind wings have to be folded under them, even insofar as to be folded four times. The folding lines

found covering the hind wings allow them to be folded in a particular direction. The folding line intersection points and the angle between the folding lines determine the folding pattern [2]. The folding of the hind wings provides the following functionality: (1) flapping wings can change shape, giving them better aerodynamic characteristics [3]; (2) pleated wings are more rigid in flexion than planar ones; (3) when insects are not flying, the folding structure allows the hind wing to be folded as a small package, tucked under the elytra [4]; (4) by a complex folding pattern, the hind wing can be folded to even one-tenth the unfolded size [5]. Aside from muscle tissue, which can control several veins near the wing base, there are no supporting elements, such as bones or muscles, in the hind wing itself, and the folded region is at the tip of the wing. How, then, does a beetle realize the folding/unfolding of its hind wings? It was generally believed that this was achieved by the combined effect of external forces (wing base, thoracic muscle) and vein characteristics (such as vein discontinuities, venation change, and vein membrane elasticity) [1]. Additionally, the hemolymph runs within the veins, assisting in the folding and unfolding movements of the wings [5].

The folding/unfolding behavior of beetle hind wings has been extensively researched. Its mechanism has been under continuous investigation [3]. Forbes [6] first investigated the folding process of the hind wings of a beetle (*Pachnoda marginata*). When beetles are at rest, their wings will be folded and tucked under the elytra, and the folding process includes the lateral and longitudinal folding of the membranous hind wings. Folding is carried out along a folding line [7]. It may involve longitudinal folding of the wing membrane and sometimes transverse folding [1,8,9]. The beetle hind wing folds in a four-panel mechanism, meaning that the hind wing has four hinged plates as the basic structure, which are mutually folded when combined [10-12]. The system has a single degree of freedom of motion, which is composed of four folding lines connecting the four plates. The folding and unfolding is achieved by decreasing and increasing the angle between the two plates. In fact, integration of some basic mechanisms produces the various folding patterns [11]. Moreover, the hind wing diamond area type can play a central role as a spring [11,13]. The ribs are arranged in a certain way.

Another possibility is that the folding and unfolding actions are controlled by two different mechanisms [14]. Folding requires the synergistic action of abdominal and thoracic muscle forces [15,16]; resilin in some mobile joints, together with data on wing unfolding and flight kinematics that may result in elastic energy storage in the wing [17]; or leveraging the rigid wing membrane involved in the folding action [18]. The unfolding action comes from the contraction of muscles [1,8].

An insect wing consists of a thin membrane and a system of veins. There are cavities within major veins that contain nerves and trachea, and because they are connected with the hemocoel, hemolymph can flow into the wings (http://medlibrary.org/medwiki/Insect_wing). Hemolymph can transfer mechanical pressure caused by muscle contraction, and facilitate fluid-feeding, prey capture, pupation, and the ecdysis and eclosion processes [19]. However, this has not been confirmed or rejected by experiments regarding unfolding or folding actions [2].

In a previous work [20], we investigated the various hydraulic forces for the unfolding process of the hind wings in *Dorcus titanus platymelus* (Lucanidae, Coleoptera), which is a xylosaprophagous beetle, and its hind wings are folded down to 55% of their full length. In this paper, the hydraulic mechanism in the veins of hind wings of diving beetles (*C. japonicus*) was investigated, and the unfolding process, including blood flow and pressure changes, was simulated. The study of the hydraulic mechanism in the folding and unfolding process will be provide insights for the design of micro air vehicles with morphing wings, and give inspiration for the development of bioinspired deployable systems.

Experimental

Beetles

The diving beetle (*C. japonicus*) is an aggressive predator: larvae and imagines devour small fish and invertebrates (Figure 1A and Figure 1B). They live in fresh water and can swim actively. They have a pronounced flight capability when leaving the water, and they fly to migrate from one body of water to another. Wings are folded and the elytra are closed during the imaginal life activities of the beetle (swimming, hunting, reproduction), not only during rest. Their hind wings are folded under the elytra when at rest. Figure 1C shows an excised hind wing in the folded state, in which it is 30% shorter than in the deployed state (Figure 1D). The venation is shown in Figure 1D, where C is costa, ScA is subcosta anterio, RA is radius anterior, R is radius, MP is media posterior, CuA is cubitus anterior, AAP is anal anterior posterior, and AP_4 is anal posterior. Figure 1E–G shows the simulation model of a folded vein of *C. japonicus*. For observation and experimentation, beetles were captured in the wild in Guangdong City, Guangdong Province, China. Their body length was 35–40 mm.

Microstructure testing

Microstructure testing was conducted in a manner similar to that described in [20]. The microstructures of the cross sections of hind wing veins were captured using an inverted fluorescence microscope (OLYMPUS, LX71).

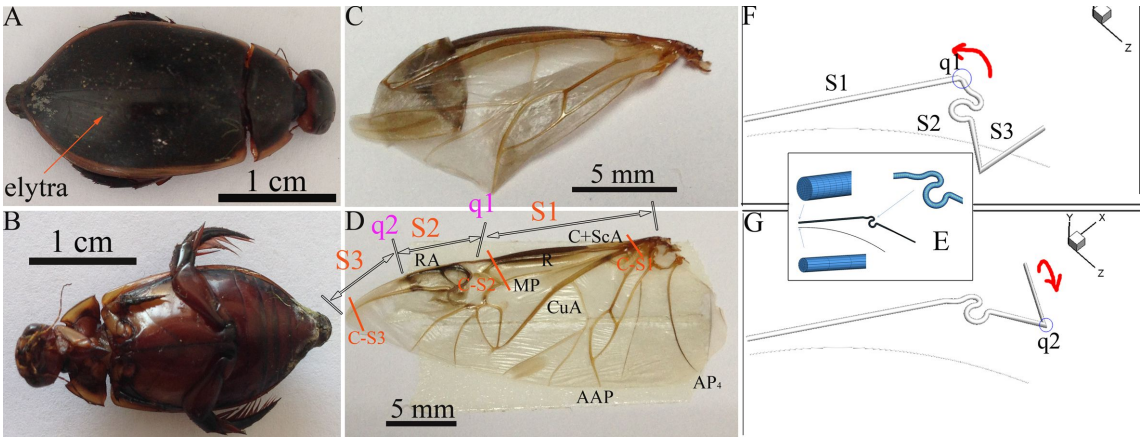

Figure 1: (A) and (B) *C. japonicus*, excised hind wings in folded state (C) and unfolded state (D), where C is costa, ScA is subcosta anterior, RA is radius anterior, R is radius, MP is media posterior, CuA is cubitus anterior, AAP is anal anterior posterior, and AP_4 is anal posterior. (E–G) The local mesh figure and the vein movement diagram. The costa vein was set as three segments: S1 is fixed, S2 is connected to S1 and can rotate, and S3 is connected to S2 and can rotate. S1 simulates C+ScA, while S2 and S3 simulate RA, which is the folded vein. q1 and q2 are rotating points. C-S1 to C-S3 are the cutting positions of the cross sections of the wing base, the posterior part of the wing, and the folded zone in C for Figure 3.

All beetles were anesthetized with ether. Their hind wings were cut out with a scalpel, and a 1 mm^2 area was sliced from the wing base, folded zone, and the posterior part of the wings. These were then quickly dipped in a 20% epoxy resin 812 solution. After cooling in ambient environment, they were put into an embedding box. Dehydration was reached with a gradient concentration of ethanol and acetone to replace the water in the wing tissues (using 70%, 80%, and 95% ethanol one time each for 10 min; 95% ethanol and 95% acetone (1:1) for 10 min; 100% concentration acetone twice for 20 min; and 100% concentration propylene oxide once for 20 min). After that, ultrathin sections of 50–100 nm thickness were cut out by an ultrathin slicing machine. In order to easily view the sample structure, dye (hematoxylin eosin) was used to stain the specimens.

To confirm which veins of the hind wings were involved in the hydraulic mechanism during unfolding, a retinal camera (Topcon, TRC-50DX-Type IA) was used. Retinal camera testing was performed with a fluorescent agent to color the walls of the veins. One milliliter of green fluorescent indicator (FITC) was injected into the beetle abdomen at time zero. The measurement was taken with an excitation wavelength of 488 nm in the retinal camera.

The unfolding hind wings process of the hind wings of a flying beetle was photographed with a high-speed camera (OLYMPUS, *i*-SPEED 3, camera speed of 400 frames/s). The beetle was suspended in front of the camera.

A biological pressure sensor and dynamic signal acquisition and analysis (DSA) were designed as a control system to investigate the variation of fluid pressure in the veins of the hind wings [20].

Definition of FLUENT software parameters

The speed and pressure changes during the unfolding process were numerically simulated via computational fluid dynamics (CFD) solver. To simulate the insect wing veins within the fluid flow during the unfolding process, the CFD solver, FLUENT 6.3.26, was used to solve the momentum conservation equations (Navier–Stokes equation, NS equation) based on the pressure method. The motion of an unfolding wing was modeled by using the dynamic mesh technique.

Assuming that the flow is laminar, the fluid medium is blood, and the inlet effect is not considered, the control equation of fluid flow in the beetle hind wing is the 3-D incompressible NS equation:

$$\frac{\partial \rho}{\partial t}+\left[\frac{\partial(\rho u)}{\partial x}+\frac{\partial(\rho \upsilon)}{\partial y}+\frac{\partial(\rho \omega)}{\partial z}\right]=0\,, \qquad (1)$$

where u, v, w are the velocity components (m/s) for the x, y, z-directions, respectively, and ρ is the density of the fluid. Momentum equations are given as,

$$\rho\frac{du}{dt}=-\frac{\partial p}{\partial x}+\frac{\partial \tau_{xx}}{\partial x}+\frac{\partial \tau_{yx}}{\partial y}+\frac{\partial \tau_{zx}}{\partial z}+\rho f_x\,, \qquad (2)$$

$$\rho\frac{d\upsilon}{dt}=-\frac{\partial p}{\partial y}+\frac{\partial\tau_{xy}}{\partial x}+\frac{\partial\tau_{yy}}{\partial y}+\frac{\partial\tau_{zy}}{\partial z}+\rho f_y\ , \quad (3)$$

$$\rho\frac{d\omega}{dt}=-\frac{\partial p}{\partial z}+\frac{\partial\tau_{xz}}{\partial x}+\frac{\partial\tau_{yz}}{\partial y}+\frac{\partial\tau_{zz}}{\partial z}+\rho f_z\ , \quad (4)$$

where f_x, f_y and f_z are the generalized source terms for the momentum equation, only for inertia force, the external forces on the volume element in the x, y and z-directions $F_x = F_y = F_z = 0$.

The purpose of simulation in this is the analysis of the motion of veins, mainly focusing on the vein expansion process, and the variation of the flow field and coordination. Thus, when defining the parameters for the simulation study, the model was set to a rigid body. If we are only concerned about the whole movement of the object and the internal deformation does not affect the whole movement, then the object can be simplified as a rigid body with no penetration of the wall [21].

Results and Discussion

Experimental

The deployment process of the hind wings of *C. japonicus* was recorded using a high-speed camera, as shown in Figure 2. At 0.036 s, the opening of the elytra appears; at 0.054 s, the hind wings slip from the elytra that are gradually rotating and ascending to a certain height; at 0.651 s, the hind wings start flapping but are still folded; until 0.741 s, the elytra keep rotating outward and lifting, creating sufficient space for the hind wings to flap. It is obvious that the hind wings are still folded at this time (0.741 s), and the double wings flap down with almost no time difference. Live beetles can control the state of wing folding by coordinated, sometimes asymmetrical or repeated movements of the hind wings, elytra, prothorax, and abdomen [22]. In particular, when longitudinal muscles contract, the tergum rises upwards with respect to the pleura (the fulcra of the wings) and thus move both wing plates down by the lever principle [23]. For air dynamics, the hind wings flapping at the same time helps to obtain aerodynamic force, resulting in a successful take-off [15,16,24,25]. At 0.759 s, the hind wing movement is at its lowest point, and the hind wings are completely expanded.

Figure 3A–C demonstrates the cross sections of the wing base, the posterior part of the wing, and the folded zone in C, respectively, of the hind wings of *C. japonicus*, with cutting positons as shown in Figure 1D. The exocuticle, endocuticle, and epidermis layers appear brown and light pink (the thin basement membrane), respectively, in a manner similar to that found in [20]. It was shown that vein cavities are irregularly shaped, and their cross-section cavities get smaller and smaller. Figure 3A shows that the C+ScA cavity is thicker towards the

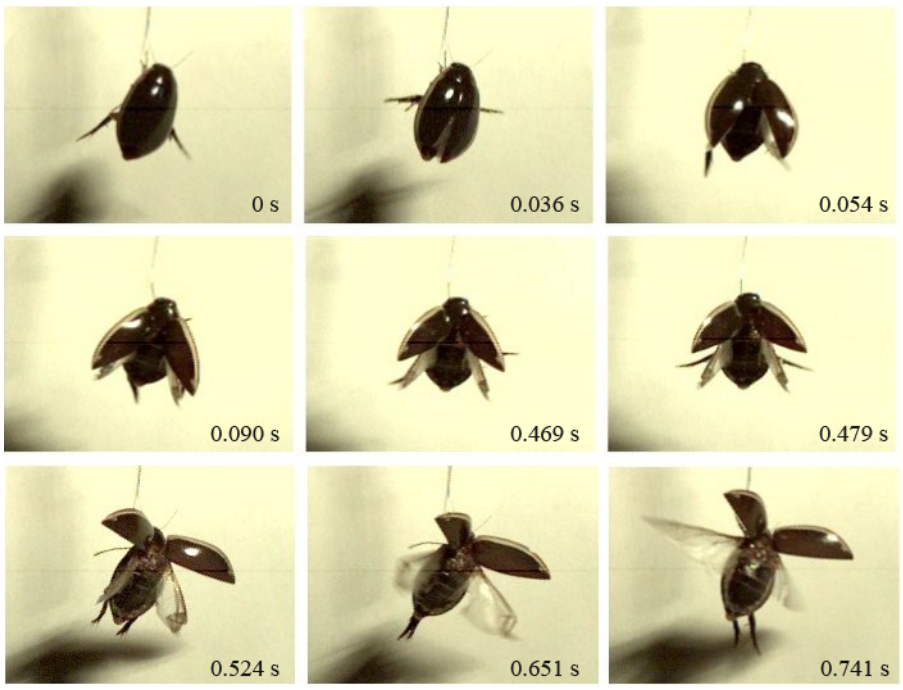

Figure 2: The unfolding process of the hind wings of *C. japonicus* captured by a high-speed camera.

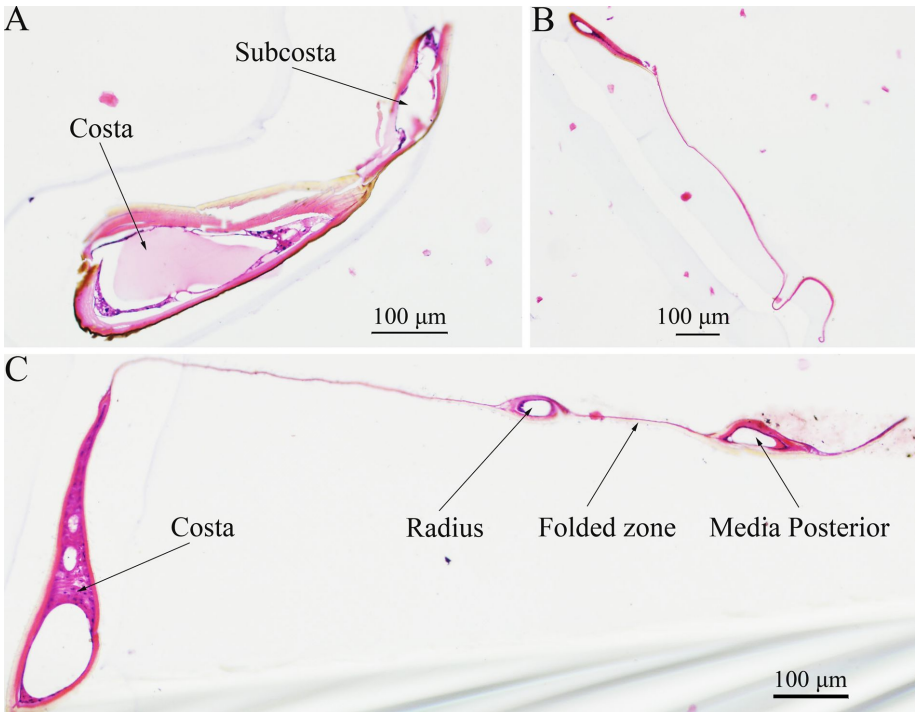

Figure 3: The cross sections of (A) the wing base (C-S1), (B) the posterior part of the wing (C-S2) and (C) the folded zone of the costa (C-S3) of *C. japonicus* (10 ×), obtained using an inverted fluorescence microscope. The vein cavity is irregular.

dorsal than at the ventral part of the wing [20]. The area of the vein cavity in the posterior part of the wing is the smallest (Figure 3B), shown as a narrow strip. The end with wire-like objects is the wing membrane. The left cavity in Figure 3C is the C+ScA cavity, the middle is the R cavity and folded zone, and the right cavity is MP vein cavity. Due to the wing membrane being thin and having a certain toughness, slicing the veins will produce a certain extension, resulting in the observed length of the vein section being longer than the actual one. The cross section of the folded zone between R and MP only shows a thin wing membrane connection, which is related to the folding pattern and cutting position.

A retinal camera was used to confirm which veins were involved in the hydraulic mechanism of the unfolding of the hind wings. A fluorescent agent was injected into the abdomen of a live beetle. At 0.05 s, fluorescence was found in CuA, and at 0.09 s it nearly flowed through AAP; 1.21 s later, C, CuA, AAP, and AP_4 were observed to be nearly full of fluorescence (Figure 4). After that, there was only a slow flow in C, and after 3.31 s, the fluorescence flowed through RA and stopped over 2 mm. This is different from what we observed in *Dorcus titanus platymelus*, in which the flow of body fluids is limited to the movement within the main veins – the costa and media posterior – and stops at the folding region [20]. This phenomenon is related to different profiles of C+ScA in the region of folding. Bending of the vein in *C. japonicus* is smooth in the folded wing, whereas in *Dorcus titanus platymelus* the turn is drastic. There, it is a sort of a hinge with a determinate axis of rotation, evident structure, and heterogenous structure: the anterior face of the bend is corrugated (a short bellows joint of 2–4 rings), the posterior face is a thin membrane, and the top and bottom faces are sclerotized plates. Pass [26] put forth the hypothesis that the hemolymph in some Coleoptera wings' veins circulates in relation to periodic heartbeat reversal and intermittent pulse activity of the wing-hearts. Wasserthal [27] showed that injection of dye into the wings of *Pieris rapae* demonstrated that the movement of hemolymph into the wings along the veins was a unidirectional flow. In adult Lepidoptera, Coleoptera and Diptera, and perhaps in some other insects, the blood is shunted backwards and forwards between the thorax and abdomen, rather than circulated [1].

During the deployment of the hind wings, the blood pressure in the veins of the wings changes continuously (Figure 5): the pressure starts from zero, gradually and quickly increases to the peak, fluctuates over some time before decreasing to a minimum, and finally returning to zero when the actions of the beetle stop. This is different from the results described in [20]. The first peak pressure and time for the four beetles were (0.238 s, 0.8 Pa), (0.539 s, 0.9 Pa), (0.287 s, 0.9 Pa) and (0.322 s, 0.8 Pa). For beetle 4, at 0.742 s, there was a maximum

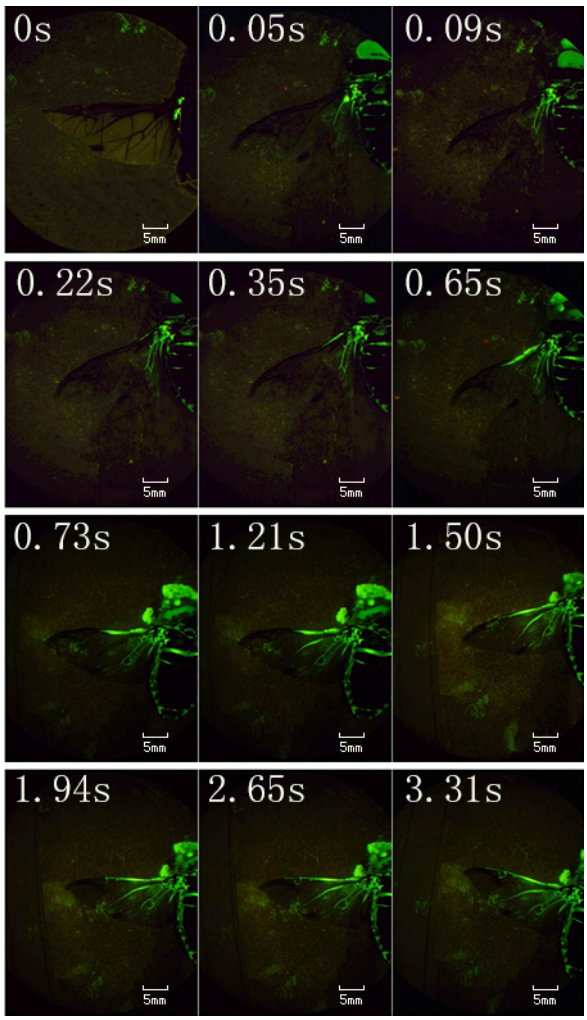

Figure 4: Fluorescence flow sequence in an unfolding hind wing of *C. japonicus*, captured using a retinal camera.

peak pressure of 1.4 Pa, which made the hind wing fully expand after some time of fluctuation (alternating high and low pressures, 1.4 Pa, −1.08 Pa, −1.3 Pa, −0.96 Pa, −1.16 Pa, −0.9 Pa, −1.2 Pa), at 2.562 s, the pressure reached 1.2 Pa. Then, the pressure began to gradually decrease until, at 3.164 s, the pressure was 0 Pa with the hind wing completely extended. After this, when the hind wings were flapping, the pressure values indicated that there was a certain degree of flexibility due to the hydraulic energy in the presence of the hind wing, which helped stabilize the flight motion. Small pressure peaks of the blood and the hind wing being open appeared to overcome the remaining consistent folding. The expansion required a total time of 3.012 s to 3.670 s. This is due to the size of the pressure and the length and weight of the hind wings being proportional, as shown in Figure 6. It is possible that the wing was locked in the open position mechanically [9]. When the wing extensor or flexor muscles relax or contract, levers simultaneously open or close the wing, and surely the muscles and the blood pressure must operate synergistically. The negative pressures in Figure 5 could be the result of the abrupt muscular unfolding of the wing tip applying "suction" to the system. Another possible reason for the negative pressures could be that, before opening of the elytra, the prothorax is depressed relative to the pterothorax, thus unlocking the elytra. With the abdomen depressed synchronously with the opening of the elytra and wing flapping, the beetle elevated [23]. This elevation of the abdomen increased internal pressure in the body without influencing the unfolding.

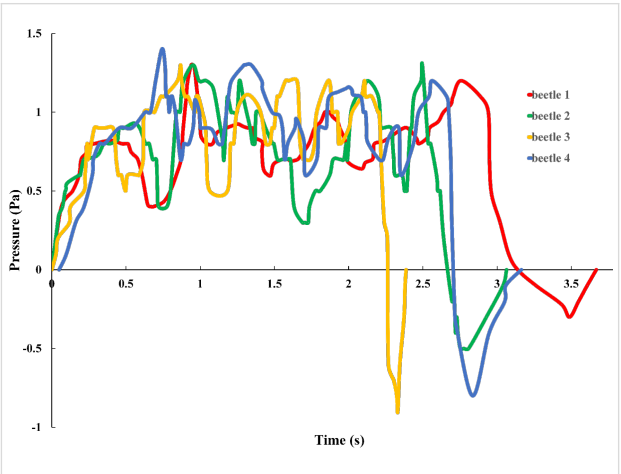

Figure 5: The change in blood pressure in the veins of the hind wings as a function of time.

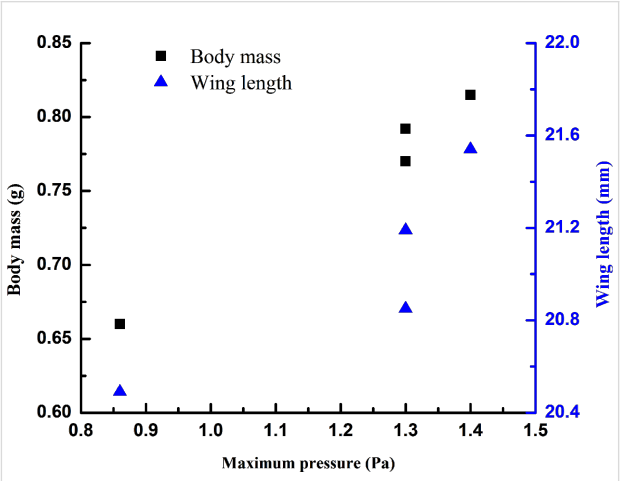

Figure 6: The blood pressure is proportional to the length of the wings and the body mass.

This expansion time is a little quicker than that measured in Figure 4 (3.31 s). It is supposed that in that test (Figure 4), the beetle was fully expanded and fixed, while in this test (Figure 5), the beetle was able to move freely, which accelerated blood flow in a manner similar to that described in [20].

Moreover, this expansion time is slower than that measured in Figure 2 (approx. 0.741 s). One possible explanation is that the hind wing in that test is a record of a natural state and without any restraint; by contrast, the beetle in the pressure measurement (Figure 5) was connected to the sensor and had missing elytra.

Simulation

The hexahedral mesh is orthogonal and gridded [28]. Thus, it will speed up convergence and improve the calculation accuracy. In Figure 1E, the total grid number shown in the graph is 135,000. At the same time, for the realization of the hind wing exercise, torsion was created in the folded position so that the fixed part and moving part of the costa veins were not in a plane (RA vein). Figure 1F and Figure 1G show the vein movement diagram. By using a high-speed camera to observe the folding/unfolding process of the beetle hind wings, it can be seen that the beetle costa vein root to the fold points is fixed (S1), and from the fold point to the end of the vein, where around their folds, inward folding occurred (S2 + S3). Accordingly, the costa was fixed to the first half; the rear section of the rotation movement around the respective rotation point, and specifically defined costa and RA vein of the center of rotation are the fold points. Unstructured meshes were used in the simulation; the computational domain was the internal domain. Inlet pressure was located in the root of the veins and exported to the wall for the single-phase flow model of computational physics. The open interface FLUENT allows users to customize the boundary conditions and other function variables. Thus, the pressure of the inlet was applied by the pressure boundary in this simulation, and a user-defined function (UDF) was used to apply the changing pressure implemented by the user program.

The blood circulation of insects is pumped by the heart in the abdomen, with arteries flowing to the head [1]. Because the front of the blood pressure is higher, it forces blood flow to the back of the blood chamber so that blood circulates in the entire blood chamber. The back side of the blood pressure in the accessory palsatory organ occurs through blood transmission to the outer epidermis of the vein because the liquid can transfer pressure in any direction, resulting in an axis of rotation of the torque and veins caused by rotation.

There are two stages: in the first stage, S1 is fixed and S2 rotates around the point q1; in the second stage, S1 and S2 are fixed, and S3 rotates around the point q2. As shown in Figure 7A–F, due to the relatively large geometric angle of the turning point, the blood will have a direct impact on the vein wall. Thus, in the formation of high pressure, especially in the first stage of the movement, the pressure is very obvious. In the first stage, at 0.9 s, the pressure in the blood vessel is more than 1 Pa because of the difference in pressure between the inside and outside of the walls of blood vessels, thus forming a rotating point and rotating torque. After 2.1 s, the first stage stops, and the middle part of the vein does not move. The pressure difference concentrates on the rotating point of the posterior segment, and there is the second moment of rotation. When S2 is completely extended around q1, the pressure in S1 is reduced, and high pressure concentrates in the rotated point q2 (2.1 s, Figure 7G). By this pressure, S3 is rotated by a little angle (2.4 s, Figure 7H). Then, the pressure continues to increase (2.7 s, Figure 7I), and at 3.0 s, the pressure in the veins undergoes a sharp decline until the end of the movement (Figure 7J–L). The pressure is greater than the end of the blood vessel vascular segment, which is mainly due to export to the wall; the flow will be stagnant here, and thus a high pressure zone will form. The high pressure area produces a torque around the rotation point. In the second stage, due to S1 and S2 being kept fixed, the differential pressure between the folding point and the entrance is obviously reduced. At the same time, to rotate S3, the differential pressure between the rotating point and export is larger. Between 3.3 and 3.6 s, the pressure differential of the venation front and end gradually decrease due to the venation almost having motion toward the limit position and the pressure transmission occurring more smoothly, thus producing reduced torque and slower speed.

The flow changes in the vasculature were also simulated (Figure 8). Figure 8A shows the change of flow as a function of the time (minus denotes outflow) in the wing base of the C vein (entrance point). Because the density is constant, the flow change directly responds to the variation in the flow velocity. At the beginning (0.1 s), because the entrance pressure is high, the hind wing venation just begins to unfold, with a great deal of blood flow from the wing base to the veins. With the movement gradually accelerated and the extending angle gradually increased, the veins produce a negative effect on the blood in the extending process of the wing, leading to outflow from the entrance. There is a slight fluctuation until the veins are fully expanded, and the entrance flow tends to 0; Figure 8B and Figure 8C show the pressure change with time at q1 and q2, similar to Figure 5 (the actual test curve).

Via FLUENT post-processing, we set up monitoring points at q1 and q2. In Table 1, before 2 s, the pressure loss of q1 is larger, which is due to the larger relative movement that exists in the left side and right side of q1 in stage 1. Thus, the relative flow and pressure loss are higher. After 2 s, the pressure loss of q1 is rapidly reduced to 0, which is due to q1 being in a static state in the second movement stage. Thus, there is no pressure loss. Similarly, for q2, the pressure loss always exists because it keeps moving.

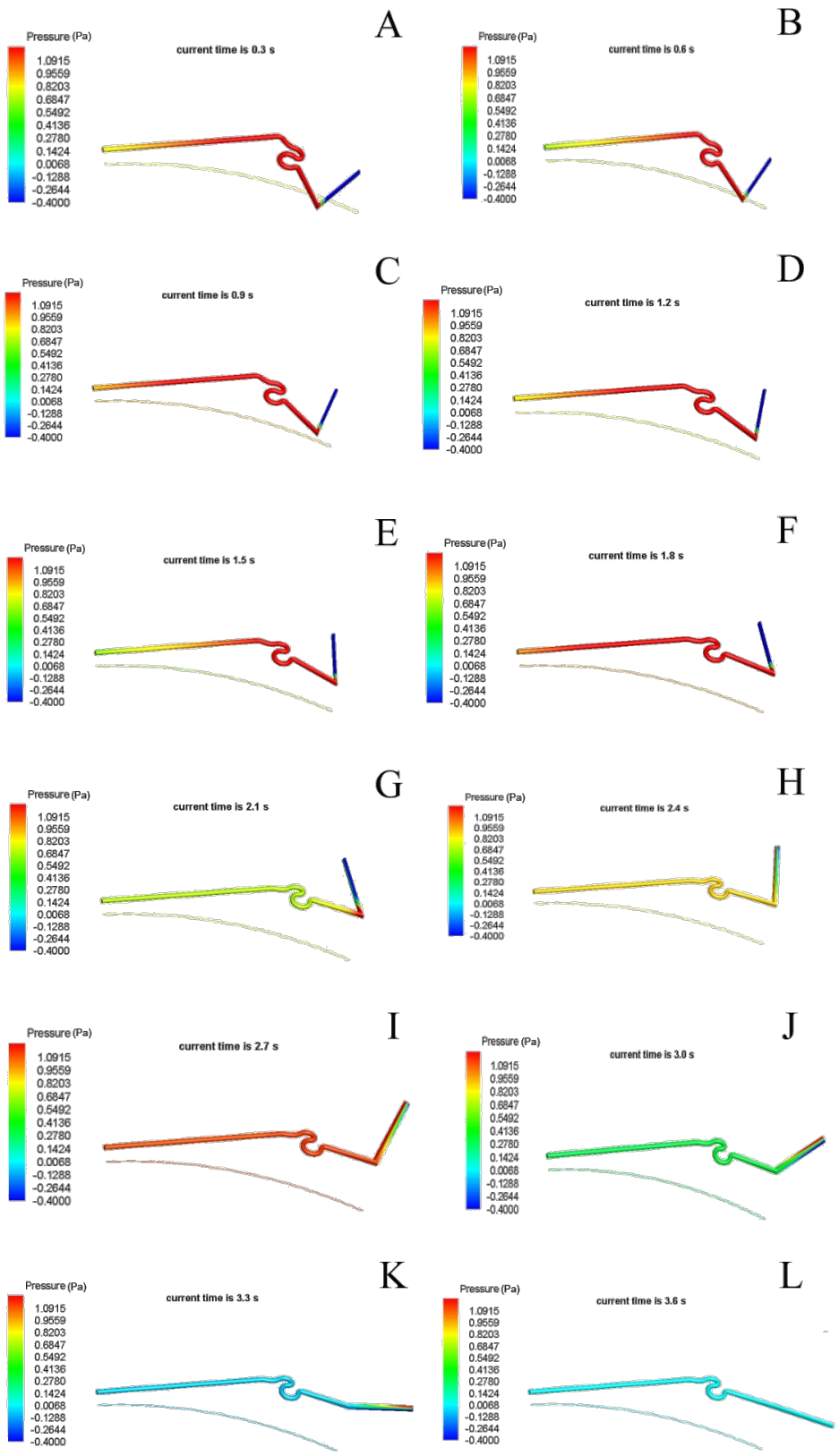

Figure 7: The simulation results of static pressure in a vein of a hind wing.

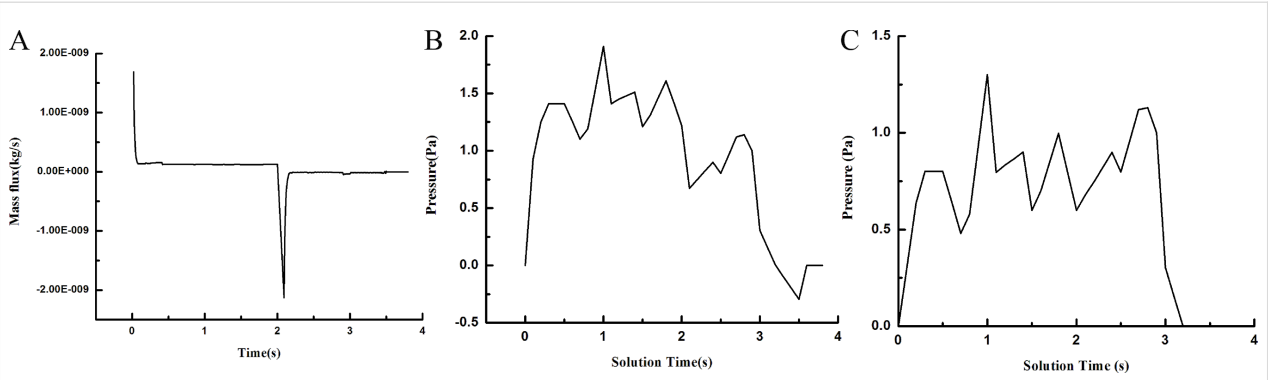

Figure 8: Blood flow changes in the venation of a hind wing of *C. japonicus* at the entrance (A); pressure change as a function of the time at rotation points q1 (B) and q2 (C).

Table 1: Pressure loss of flow during unfolding of the hind wing.

time (s)	pressure loss in q1 (Pa)	pressure loss in q2 (Pa)
0.6	0.608	0.610
1.2	0.606	0.607
1.8	0.904	0.905
2.4	0.001	0.028
3.0	0.0	0.005
3.6	0	0

Conclusion

The unfolding of the hind wings of *C. japonicus* and its hydraulic mechanism were investigated. To confirm which veins were involved in the hydraulic mechanism of the unfolding of the hind wings, the cross sections of the veins were captured using an inverted fluorescence microscope and flow of blood was examined by means of a retinal camera. After 3.31 s, C, CuA, AAP, and AP_4 were observed to be nearly full of fluorescence, and the fluorescence stopped at over RA 2 mm. To determine the unfolding action of the hind wings and corresponding time required for each action during the unfolding process, high speed camera sequences were used (400 frames/s). It was found that the beetle can start to flap its hind wings while they are still folded (0.651 s), and until 0.741 s, the hind wings were completely extended. Then, the pressure of the vein of the hind wings of four beetles during the unfolding process was tested. The results showed that with the unfolding action of the hind wings, the pressure kept changing. The wing veins unfolded within the flow field successive dynamic simulation deployment process of the hind wing during the entire time of travel in FLUENT. This is mainly from the two aspects of pressure and the velocity vector of the corresponding numerical study on the movement characteristics, which provide a bionic foundation to design and develop flying micro-robots.

Acknowledgements

This work was supported by the National Natural Science Foundation of China (31172144), by the National Science & Technology Pillar Program of China in the Twelfth Five-year Plan Period (2014BAD06B03), and by “Project 985” of Jilin University.

References

1. Chapman, R. F. *The Insects: Structure and Function,* 4th ed.; Cambridge University Press: Cambridge, United Kingdom, 1998. doi:10.1017/CBO9780511818202
2. Haas, F. Geometry and Mechanics of Hind-wing Folding in Dermaptera and Coleoptera. Master Thesis, University of Exeter, U.K., 1994.
3. Wootton, R. J. *J. Zool. (1965-1984)* **1981,** *193,* 447–468.
4. Fedorenko, D. N. *Evolution of the Beetle Hind wing, with Special Reference to Folding (Insecta, Coleoptera);* Pensoft Publishers: Sofia, Bulgaria, 2009.
5. Fenci, G. E.; Currie, N. Biomimetic Approach for the Creation of Deployable Canopies Based on the Unfolding of a Beetle Wing and the Blooming of a Flower. In *Biomimetic and Biohybrid Systems;* Wilson, S. P.; Verschure, P. F. M. J.; Mura, A.; Prescott, T. J., Eds.; Lecture Notes in Computer Science, Vol. 9222; Springer: Berlin, Germany, 2015; pp 101–112. doi:10.1007/978-3-319-22979-9_11
6. Forbes, W. T. M. *Psyche* **1924,** *31,* 254–258. doi:10.1155/1924/68247
7. Hammond, P. M. *Biol. J. Linn. Soc.* **1985,** *24,* 15–33. doi:10.1111/j.1095-8312.1985.tb00157.x
8. Brackenbury, J. H. Wing Folding in Beetles. In *IUTAM-IASS Symposium on Deployable Structures: Theory and Applications;* Pellegrino, S.; Guest, S. D., Eds.; Solid Mechanics and Its Applications, Vol. 80; Springer: Berlin, Germany, 2000; pp 37–44. doi:10.1007/978-94-015-9514-8_5
9. Haas, F.; Beutel, R. G. *Zoology (Munich, Ger.)* **2001,** *104,* 123–141. doi:10.1078/0944-2006-00017
10. Haas, F.; Wootton, R. J. *Proc. R. Soc. London, Ser. B* **1996,** *263,* 1651–1658. doi:10.1098/rspb.1996.0241
11. Haas, F. Wing Folding in Insects: A Natural, Deployable Structure. In *IUTAM-IASS Symposium on Deployable Structures: Theory and Applications;* Pellegrino, S.; Guest, S. D., Eds.; Solid Mechanics and Its Applications, Vol. 80; Springer: Berlin, Germany, 2000; pp 137–142. doi:10.1007/978-94-015-9514-8_15

12. Muhammad, A.; Nguyen, Q. V.; Park, H. C.; Hwang, D. Y.; Byun, D.; Goo, N. S. *J. Bionic Eng.* **2010,** *7,* 134–141. doi:10.1016/S1672-6529(09)60185-2
13. Haas, F.; Gorb, S.; Blickhan, R. *Proc. R. Soc. London, Ser. B* **2000,** *267,* 1375–1381. doi:10.1098/rspb.2000.1153
14. Forbes, W. T. M. *J. New York Entomol. Soc.* **1926,** *34,* 42–68.
15. Hammond, P. M. Wing-folding Mechanisms of Beetles, with Special Reference to Investigations of *Adephagan phylogeny* (Coleoptera). In *Carabid Beetles;* Erwin, T. L.; Ball, G. E.; Whitehead, D. R.; Halpern, A. L., Eds.; Springer: Berlin, Germany, 1979; pp 113–180. doi:10.1007/978-94-009-9628-1_7
16. Danforth, B. N.; Michener, C. D. *Ann. Entomol. Soc. Am.* **1988,** *81,* 342–349. doi:10.1093/aesa/81.2.342
17. Haas, F.; Gorb, S.; Wootton, R. J. *Arthropod Struct. Dev.* **2000,** *29,* 137–146. doi:10.1016/S1467-8039(00)00025-6
18. Wootton, R. J.; Herbert, R. C.; Young, P. G.; Evans, K. E. *Philos. Trans. R. Soc. London, Ser. B: Biol. Sci.* **2003,** *358,* 1577–1587. doi:10.1098/rstb.2003.1351
19. Kishimoto, N.; Natori, M. C.; Higuchi, K.; Ukegawa, K. New deployable membrane structure models inspired by morphological changes in nature. In *47th AIAA/ASME/ASCE/AHS/ASC Structures, Structural Dynamics, and Materials Conference,* Newport, Rhode Island, May 1–4, 2006; 2006; AIAA-2006-1898. doi:10.2514/6.2006-1898
20. Sun, J.; Ling, M.; Wu, W.; Bhushan, B.; Tong, J. *Int. J. Mol. Sci.* **2014,** *15,* 6009–6018. doi:10.3390/ijms15046009
21. Li, J. K.-J. *Dynamics of the vascular system;* Series on Bioengineering and Biomedical Engineering, Vol. 1; World Scientific Publishing Co Pte Ltd: Singapore, 2004; p 19.
22. Frantsevich, L. *Zoology (Munich, Ger.)* **2012,** *115,* 12–21. doi:10.1016/j.zool.2011.07.005
23. Frantsevich, L. *J. Insect Physiol.* **2012,** *58,* 1650–1662. doi:10.1016/j.jinsphys.2012.10.006
24. Luo, G.; Sun, M. *Acta Mech. Sin.* **2005,** *21,* 531–541. doi:10.1007/s10409-005-0072-4
25. Sun, J.; Bhushan, B. *RSC Adv.* **2012,** *2,* 12606–12623. doi:10.1039/c2ra21276e
26. Pass, G. *Annu. Rev. Entomol.* **2000,** *45,* 495–518. doi:10.1146/annurev.ento.45.1.495
27. Wasserthal, L. T. *Zoomorphology* **1983,** *103,* 177–192. doi:10.1007/BF00310476
28. Peyret, R. *Handbook of Computational Fluid Mechanics;* Academic Press: San Diego, CA, U.S.A., 1996.

License and Terms

BEILSTEIN JOURNAL OF NANOTECHNOLOGY

Functional diversity of resilin in Arthropoda

Jan Michels*, Esther Appel and Stanislav N. Gorb

Review

Open Access

Address:
Department of Functional Morphology and Biomechanics, Institute of Zoology, Christian-Albrechts-Universität zu Kiel, Am Botanischen Garten 1–9, D-24118 Kiel, Germany

Email:
Jan Michels* - jmichels@zoologie.uni-kiel.de

* Corresponding author

Keywords:
biological materials; biomechanics; composites; elastomeric proteins; functional morphology

Beilstein J. Nanotechnol. **2016,** *7,* 1241–1259.
doi:10.3762/bjnano.7.115

Received: 18 April 2016
Accepted: 15 July 2016
Published: 01 September 2016

This article is part of the Thematic Series "Biological and biomimetic materials and surfaces".

Associate Editor: K. Koch

Abstract

Resilin is an elastomeric protein typically occurring in exoskeletons of arthropods. It is composed of randomly orientated coiled polypeptide chains that are covalently cross-linked together at regular intervals by the two unusual amino acids dityrosine and trityrosine forming a stable network with a high degree of flexibility and mobility. As a result of its molecular prerequisites, resilin features exceptional rubber-like properties including a relatively low stiffness, a rather pronounced long-range deformability and a nearly perfect elastic recovery. Within the exoskeleton structures, resilin commonly forms composites together with other proteins and/or chitin fibres. In the last decades, numerous exoskeleton structures with large proportions of resilin and various resilin functions have been described. Today, resilin is known to be responsible for the generation of deformability and flexibility in membrane and joint systems, the storage of elastic energy in jumping and catapulting systems, the enhancement of adaptability to uneven surfaces in attachment and prey catching systems, the reduction of fatigue and damage in reproductive, folding and feeding systems and the sealing of wounds in a traumatic reproductive system. In addition, resilin is present in many compound eye lenses and is suggested to be a very suitable material for optical elements because of its transparency and amorphousness. The evolution of this remarkable functional diversity can be assumed to have only been possible because resilin exhibits a unique combination of different outstanding properties.

Review

Resilin – the pliant protein

Elastomeric proteins occur in a large range of organisms and biological structures, and the spectrum of their biological functions is very broad [1]. They feature a great diversity including well-known examples such as elastin, titin and fibrillin present in vertebrate muscles and connective tissues, byssus and abductin of bivalve molluscs and gluten of wheat [1]. Besides spider silk proteins, resilin is certainly the best-known among the elastomeric proteins existing in arthropods. The first description of resilin, which has often been called rubber-like protein, was based on analyses of three different insect exoskel-

eton elements: the wing hinge and the prealar arm of the desert locust (*Schistocerca gregaria*) (also described for the migratory locust (*Locusta migratoria*), Figure 1A,B) and the so-called elastic tendon of the pleuro-subalar muscles in dragonflies of the genus *Aeshna* [2]. Additional insights into the characteristics of resilin that had been gained shortly after this description [3,4] resulted in a comprehensive compilation of the then existing knowledge of resilin properties [5]. Resilin consists of a network of randomly orientated coiled polypeptide chains that have a high degree of flexibility and mobility and are linked together at regular intervals by stable covalent cross-links. Only the fully cross-linked protein is called resilin, whereas the not yet cross-linked or not fully cross-linked protein is called proresilin [6]. Within hydrolysates of resilin, glycine constitutes the largest proportion (30–40%) of the total residues [7,8]. Such hydrolysates also feature the two unusual amino acids dityrosine and trityrosine, which were identified to form the cross-links between the polypeptide chains [9].

The mechanical properties of resilin strongly depend on the degree of hydration because resilin is plasticised by water [5]. When resilin is completely hydrated, it behaves close to a

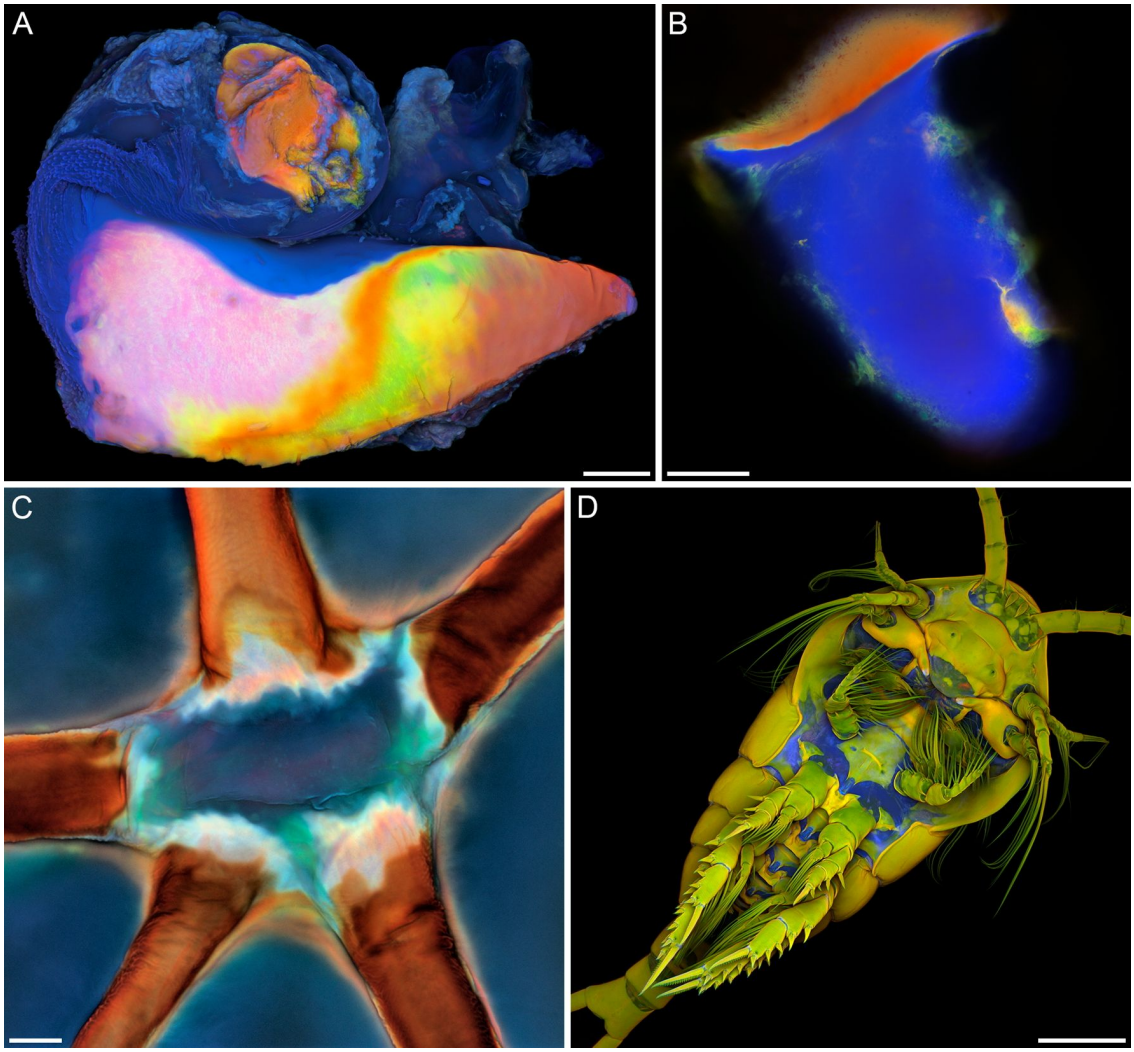

Figure 1: Occurrence of resilin in insects and crustaceans. Confocal laser scanning micrographs showing a wing hinge (A) and a prealar arm (B) of the migratory locust (*Locusta migratoria*), a wing vein joint of the common darter (*Sympetrum striolatum*) (C) and the ventral side of a female copepod of the species *Temora longicornis* (D). (A–C) Overlays of four different autofluorescences exhibited by the exoskeleton. Blue colours indicate large proportions of resilin, while green structures consist mainly of non- or weakly-sclerotised chitinous material, and red structures are composed of relatively strongly sclerotised chitinous structures. (D) Blue = autofluorescence of resilin, red = Congo red fluorescence of stained chitinous exoskeleton parts, green = mixture of autofluorescence and Congo red fluorescence of stained chitinous exoskeleton parts. (A, C, D) Maximum intensity projections. (B) Optical section. Scale bars = 100 µm (A, B), 20 µm (C), 200 µm (D). (A–D) Adapted with permission from [10], copyright 2011 John Wiley and Sons.

perfect rubber [3,4,11]. Due to its molecular prerequisites, resilin then exhibits a near-perfect resilience of up to 92–97% and a fatigue limit of over 300 million cycles [12]. With respect to resilience, resilin is unmatched by any other elastomeric protein and the best synthetic rubbers such as unfilled polybutadiene [13,14]. Fully hydrated resilin has a rather low stiffness. In the elastic tendons of dragonflies and locust ligaments mentioned above, it was found to have a Young's modulus of 0.6–0.7 MPa and 0.9 MPa, respectively [11]. In addition, fully hydrated resilin can be stretched to more than three times its original length and compressed to one third of its original length, and when the tensile and compressive forces are released, resilin goes back to its initial state without having any residual deformations [3,4,13].

Until today, resilin has been found to exist mainly in insect exoskeleton structures where this protein has a number of different functions, which include (1) the storage of elastic energy in jumping systems [15-20], (2) the reduction of fatigue in folding wings of beetles and dermapterans [21,22], (3) the enhancement of the adaptability of attachment pads to uneven surfaces [23] and (4) the generation of flexibility of wing vein joints in dragonflies and damselflies [24-26]. Resilin has also been reported to be present in the exoskeletons of other arthropod taxa such as crustaceans [10,27-30] (Figure 1D), scorpions [31] and centipedes [32]. In addition, resilin-like proteins that contain dityrosine and trityrosine are known to exist in several non-arthropod taxa including monogeneans [33,34], nematodes [35], mussels [36] and sea urchins [37] indicating that resilin likely originated much earlier in the evolution of invertebrates than previously assumed.

The properties of resilin-containing exoskeletons can strongly differ between structures and organisms. The reason is that in biological structures resilin seems to be rarely present in pure or nearly pure form but is known to commonly exist together with other proteins and/or chitin fibres in resilin-containing composites, which exhibit a mixture of the properties of the single components. In such composites, the resilin properties can even be 'overlain' by the properties of the other components making an identification of the presence of resilin in the respective structures with the criteria of Andersen and Weis-Fogh [5] very difficult. In addition, certain exoskeleton structures feature only some of the typical characteristics of resilin-containing material but lack the others. It is then often not possible to determine whether these structures contain resilin or other proteins resembling resilin. In such cases, it is conceivable that the respective exoskeleton material consists either of a protein with properties that are similar to those of resilin or of a mixture of resilin and other proteins. For exoskeleton structures with such properties, the term 'transitional cuticle' was established [5].

In order to allow a classification of exoskeleton structures as resilin-containing exoskeleton according to the definition of Andersen and Weis-Fogh [5], these structures must conform to the wing hinge, the prealar arm and the elastic tendon mentioned above with respect to their properties, which can be tested with a number of methods [5]. Resilin is colourless, transparent and amorphous. Accordingly, structures with very large resilin proportions can be easily distinguished from structures with relatively large proportions of chitin that are typically pigmented and only slightly transparent or sometimes, when the sclerotisation is very pronounced, not transparent at all. When immersed in aqueous media and in many anhydrous hydrophilic liquids, resilin exhibits an isotropic swelling, which is reversible and depends on the pH. (It is least pronounced at pH values of about 4.) In its hydrated state, resilin is swollen and features its typical rubbery nature, long-range deformability and complete elastic recovery. Furthermore, if hydrated resilin is tensioned, it will become birefringent, and the birefringence will be positive in the direction of the extension. When resilin is completely dried, it loses its rubber-like characteristics and becomes relatively hard and brittle. Proteolytic enzymes such as pepsin or trypsin can be applied to test for the presence and distribution of resilin, because resilin is known to be digested by such enzymes. Resilin has been shown to be stained by single conventional dyes. Chemical reactions with the Masson and Mallory dyes were mentioned to stain resilin red. Staining of resilin with aqueous solutions of methylene blue and toluidine blue is a common method and can provide good information about the presence and distribution of resilin. When resilin is stained with one of these two dyes, it does not show metachromasia. Among the amino acids that form resilin, dityrosine and trityrosine exhibit a relatively pronounced autofluorescence. This autofluorescence is present in natural resilin-containing structures and in isolated resilin (both before and after boiling in water) and in resilin hydrolysates. In neutral and alkaline solutions, its excitation and emission maxima are at about 320 nm and 415 nm, respectively [38,39]. The excitation spectrum of the resilin autofluorescence differs with changing pH conditions. In acid solutions, the excitation maximum is shifted considerably to about 285 nm, and the upper edge of the excitation peak is at about 330–340 nm [38,39]. The pH-induced changes of the excitation properties are reversible and take place rapidly [40].

The described resilin identification and visualization methods are not absolutely specific. Therefore, it is strongly advisable to apply not only one single method but a combination of several different ones to increase the reliability of the identification and detection of resilin. In recent years, an antibody to a recombinant *Drosophila melanogaster* pro-resilin (rec1-resilin) was developed and has been shown to be cross-reactive and to label

resilin in different insects [12,13,41,42]. Until today, this immunohistochemical method has been tested for only a small number of insects and only within the studies mentioned above. If it proves efficient in tests with a larger number of arthropod species, it will represent the first reliable method that specifically identifies resilin.

The development and improvement of methods applying techniques such as micromechanical testing, atomic force microscopy and confocal laser scanning microscopy (CLSM) have facilitated detailed studies of the distribution, composition and mechanical properties of resilin-containing exoskeleton structures in diverse organisms and at different levels of their organisation. One of these methods utilises a combination of different autofluorescences. In addition to resilin, other arthropod exoskeleton materials also exhibit autofluorescences, which can be efficiently visualized with fluorescence microscopy. This allows the production of overlays consisting of different micrographs that show different autofluorescences. Such overlays nicely exhibit differences in the autofluorescence composition, which are good indications for differences in the material composition and clearly reveal structures with relatively large resilin proportions within the analysed specimens [21,23,43]. However, when analysing arthropod exoskeleton structures for the presence of the autofluorescence of resilin, one has to bear in mind that some other compounds present in organisms exhibit autofluorescences whose properties are similar to those of the resilin autofluorescence, with excitation maxima in the UV range and emission maxima in the violet and blue ranges of the light spectrum [44-47].

If the autofluorescences are visualized by means of CLSM, the results will be very detailed and precise [10]. With a recently described method, four different autofluorescences are excited and detected separately, and certain colours are allocated to each of the four visualized fluorescence signals. On the resulting overlays, exoskeleton structures with large proportions of resilin are blue, while green structures consist mainly of non- or weakly-sclerotised chitinous material, and red structures are composed of relatively strongly sclerotised chitinous structures (for details see [10]; Figure 1A–C). Many of the confocal laser scanning micrographs shown in this review were created using this method.

Very often, gradients of the material composition with a considerably changing proportion of resilin are present in arthropod exoskeleton structures. Such resilin proportion gradients must also be reflected by gradients of the mechanical properties of the respective resilin-containing composites. The material composition of adhesive tarsal setae of beetles (Figure 2B) represents a good example for such gradients. Recently, the Young's modulus of such setae was measured along the longitudinal axis of the setae (Figure 2C). The measurements revealed that the Young's modulus of the material in the most distal section of each seta is relatively low (1.2 ± 0.3 MPa), whereas it is considerably higher at the setal base (6.8 ± 1.2 GPa). The differences in the Young's modulus between different regions correlate with the resilin proportion observed in the seta material [48]. When the setae are dehydrated, the Young's modulus of the setal tip material strongly increases from 1.2 to 7.2 GPa, and it exhibits no statistically significant differences along the complete setae [48], which is in accordance with the relationship between the material properties and the hydration status of resilin mentioned above. Besides the differences in the Young's modulus, the mechanical behaviour of the respective materials shows the pronounced differences in the material composition between the tips and the bases of fresh adhesive tarsal setae. While the material of the tip features only elastic deformation, both elastic and, to some extent, plastic deformation are observed in the material of the base [48]. This means that the purely elastic response of the tip is due to the presence of resilin, whereas the partially plastic deformation at the base is mainly due to the presence of stiffer tanned exoskeleton. It is very likely that effects similar to those observed in beetle adhesive tarsal setae exist in other exoskeleton structures with comparable gradients of the resilin proportion.

Occurrence and functions of resilin in different arthropod exoskeleton systems

Resilin is known from numerous arthropod exoskeletons where it is present in diverse structures and allows manifold functions, which in most cases are based on its very pronounced elasticity and its ability to completely recover after deformation. For example, resilin plays an important role in flight systems of insects, in particular in insects that use a wing beat with a low frequency (10–50 Hz) (see below). Resilin-containing exoskeleton structures have been described for various mechanical systems including leg joints [40,50], vein joints and membranous areas of insect wings [21,22,24], the food-pump of reduviid bugs [51], tymbal sound production organs of cicadas [52,53] and moths [54], abdominal cuticle of honey ant workers [55] and termite queens [56], the fulcral arms of the poison apparatus of ants [57] and the tendons of dragonfly flight muscles and basal wing joints of locusts (as already mentioned above) [5]. In the following, some selected representative structures and systems with large proportions of resilin are highlighted, and their functions are described.

Arthrodial membranes

Arthrodial membranes are cuticle areas that are typically thin, non-sclerotised and very flexible. Such membranes often are multifunctional units. The soft cuticles of caterpillars, for exam-

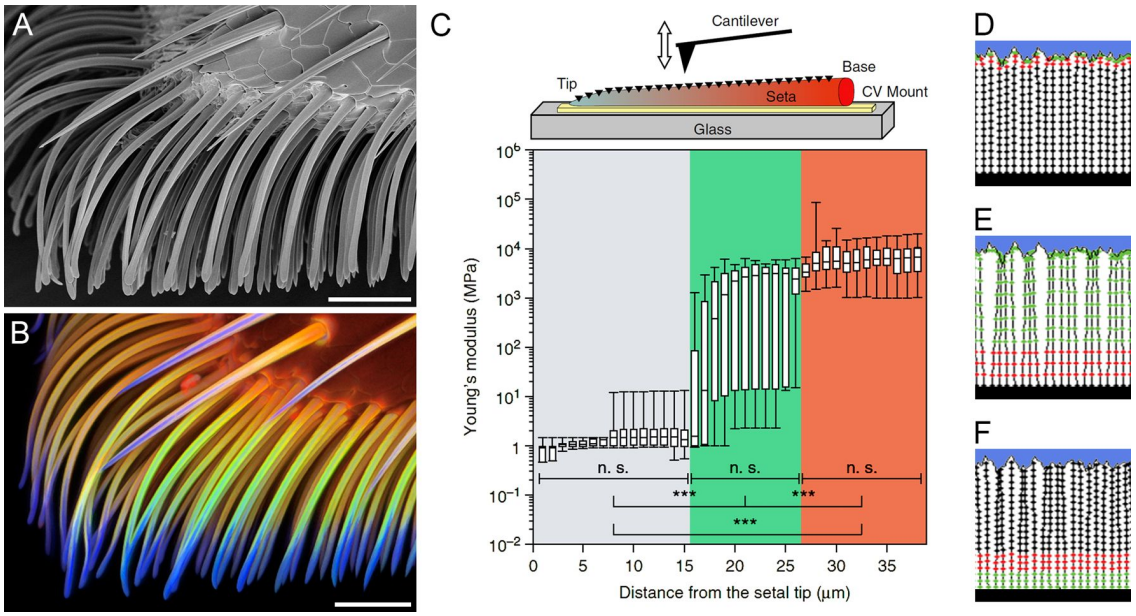

Figure 2: Distribution, mechanical properties and functional significance of resilin in adhesive tarsal setae. (A, B) Ventral part of the second adhesive pad of a female seven-spot ladybird (*Coccinella septempunctata*), lateral view. (A) Scanning electron micrograph. (B) Confocal laser scanning micrograph (maximum intensity projection) showing an overlay of four different autofluorescences exhibited by the exoskeleton. Blue colour indicates the presence of large proportions of resilin. (C) Box-and-Whisker plots showing the median Young's modulus of fresh adhesive tarsal setae obtained by atomic force microscopy nanoindentations (see the inset above the graph) along each seta. The borders of the boxes define the 25th and 75th percentiles, the median is indicated by a horizontal line, and the error bars define the 10th and 90th percentiles (n. s. = not significant, *** = highly significant). The background colours indicate the different seta sections. (D–F) Numerical model showing typical configurations of a filamentary structure (setal array) attached to a stiff support (black rectangle) in adhesive contact with a random fractal surface (blue region). Three types of fibres were tested: (D) stiff fibres with short elastic ends, (E) long elastic fibres connected to the base by short stiff roots and (F) stiff fibres with soft elastic segments near the base. The different stiffnesses of the segments are conditionally shown by circles with different colours. Stiff, medium and soft segments are marked by black, red and green circles, respectively. Scale bars = 25 µm (A, B). (A–C) Adapted with permission from [48], copyright 2013 Nature Publishing Group. (D–F) Adapted with permission from [49].

ple, have a combination of both a protective and a locomotory role, which is reflected in their ultrastructural architecture [58]. The main functions of arthrodial membranes are to connect sclerotised exoskeleton elements and allow relative movement of these elements and to extend whenever an increase in volume of the body is necessary [59,60]. In addition, some membranes are armoured with miniature protuberances on their surfaces and have a defence function [61,62]. For insects, two different types of membranes have previously been reported. The first type is a highly extensible membrane found in the locust abdomen that can extend up to ten times its original length [63-65]. This cuticle is highly specialised in its protein composition [66]. The second type is a folding laminated membrane that is less stretchable and has been found, for example, in the abdomen of the tsetse fly *Glossina morsitans* [66] and in the bug genus *Rhodnius* [67,68].

Membranous cuticle often contains large proportions of resilin (Figure 3). Examples are membrane structures connecting claws and pulvilli to the terminal tarsomere [43,50]. In the pretarsus of the drone fly (*Eristalis tenax*) (Insecta, Diptera, Syrphidae), for example, membranous cuticle with large proportions of resilin forms a spring-like (or joint-like) element (Figure 3A–C) that makes the pulvilli movable and thereby enables them to efficiently adapt to the substrate. In general, joints in legs typically feature membranes, which often contain large proportions of resilin and allow the relative movement of the joint elements (Figure 3D).

The neck membrane of dragonflies is another example. This flexible cuticle connects the neck sclerites and enables an extensive mobility of the head [69]. A recent study clearly revealed that the neck membrane material of the broad-bodied chaser (*Libellula depressa*) contains relatively large proportions of resilin, while the neighbouring sclerites are mainly composed of sclerotised chitinous material [10] (Figure 3E). Transmission electron microscopy showed that dragonfly neck membrane cuticle is rather homogenous and electron-lucent [69]. Membranous areas of insect cuticle nearly always exhibit a relatively intensive autofluorescence similar to that of resilin. This suggests that arthrodial membranes generally contain relatively large proportions of resilin. However, even very soft and flexible membranes such as the dragonfly neck membrane do not consist of pure resilin but rather represent resilin–chitin com-

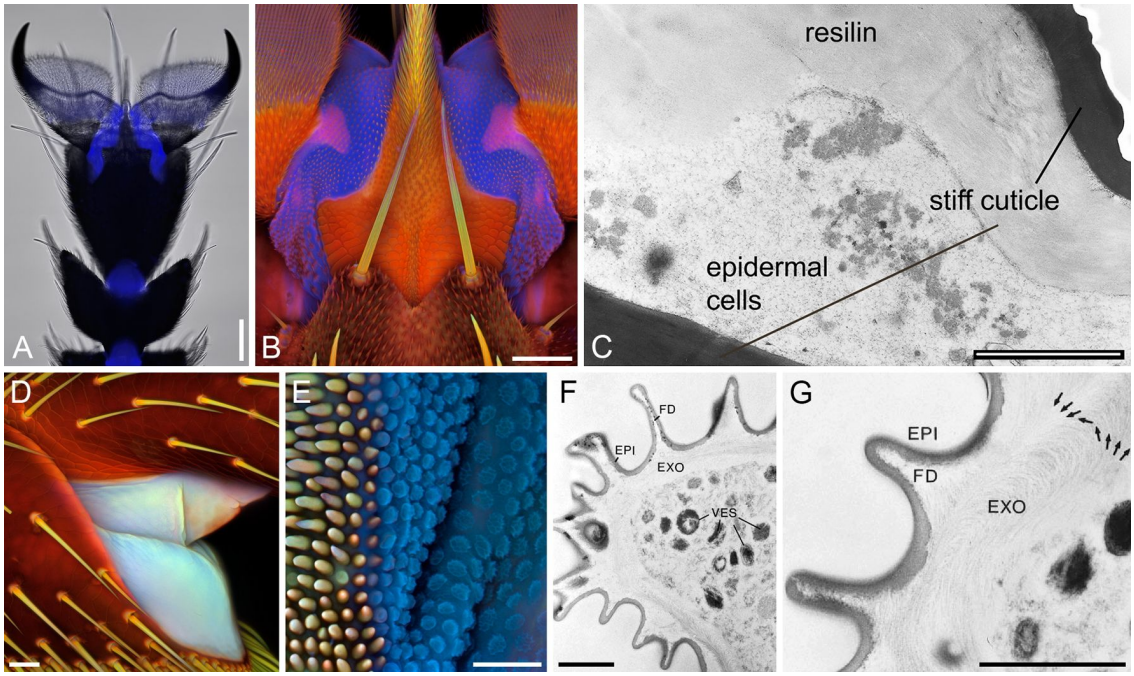

Figure 3: Resilin in arthrodial membranes of insects. (A, B) Pretarsus of the drone fly (*Eristalis tenax*), ventral view. (A) Overlay of a bright-field micrograph and a wide-field fluorescence micrograph showing the presence and distribution of resilin autofluorescence (blue). (B) Confocal laser scanning micrograph (maximum intensity projection) revealing large proportions of resilin (shown in blue) in the membranous structures between rigid sclerites of the pretarsus. (C) Pretarsus of the urban bluebottle blowfly (*Calliphora vicina*). Transmission electron micrograph showing an ultra-thin section through structures comparable to those shown in blue in B. (D) Lateral view of the joint between the tarsomeres 1 and 2 in the third leg of the seven-spot ladybird (*Coccinella septempunctata*). (E) Border between the neck membrane (right side) and a postcervical sclerite (left side) of the broad-bodied chaser (*Libellula depressa*). (F, G) Membranous cuticle in the neck area of the blue-tailed damselfly (*Ischnura elegans*). Transmission electron micrographs showing ultra-thin sections. EPI, epicuticle; EXO, exocuticle; FD, folds; VES, vesicles. Arrows: preferential orientation of chitin fibres. Scale bars = 100 µm (A), 50 µm (B), 2 µm (C), 20 µm (D, E), 1 µm (F, G). (A, B, D, E) Adapted with permission from [10], copyright 2011 John Wiley and Sons. (F, G) Adapted with permission from [69], copyright 2000 The Zoological Society of London.

posites in which some reinforcement by chitin-bearing microfibrils is clearly visible (Figure 3F,G).

Legged locomotion

Mechanisms of fast leg movements with an acceleration that can surpass the limitations of muscle contraction have been found in different insect groups including fleas [15,70], locusts [71], beetles [72,73] and true bugs [16-18,74]. The respective catapult-like devices have often evolved to enhance the acceleration in relatively short legs [75]. They usually contain specific types of joints that are typically supplemented with active power or latch muscles producing tractive force and trigger muscles that are responsible for releasing elastic energy from specific energy storage devices (see below).

In Auchenorrhyncha and Sternorrhyncha, the jumps are performed by metathoracic muscles that are directly connected to the trochanter of the hind leg and responsible for the movements of both trochanter and coxa [16,74] (Figure 4F). In the jumping cicada called black-and-red froghopper (*Cercopis vulnerata*) (Cercopidae), the complete extension of the hind leg takes less than one millisecond [16] (Figure 4E). This suggests that, in addition to the muscle system, an elastic spring system powers the jump. The application of fluorescence microscopy and histological staining revealed structures with large proportions of resilin in the pleural area of the metathorax (Figure 4A–D). These structures stretch dorso-ventrally across the entire pleural area (Figure 4F) and are much larger than comparable structures present in fleas (see below). Their dorsal and ventral parts are located close to the origin of the lateral portion of the power muscle and closely connected to the lateral part of the coxa, respectively. The resilin-containing structures very likely participate in the extension of both coxa and trochanter by the release of energy that is stored by deflection or twisting of their bar-like shape.

Fleas possess two pads with large proportions of resilin in their thorax [15]. These pads are located at the hindlegs and associated with the trochanteral depressor muscles that actuate the jumps. Before each jump, the pads are compressed, and then

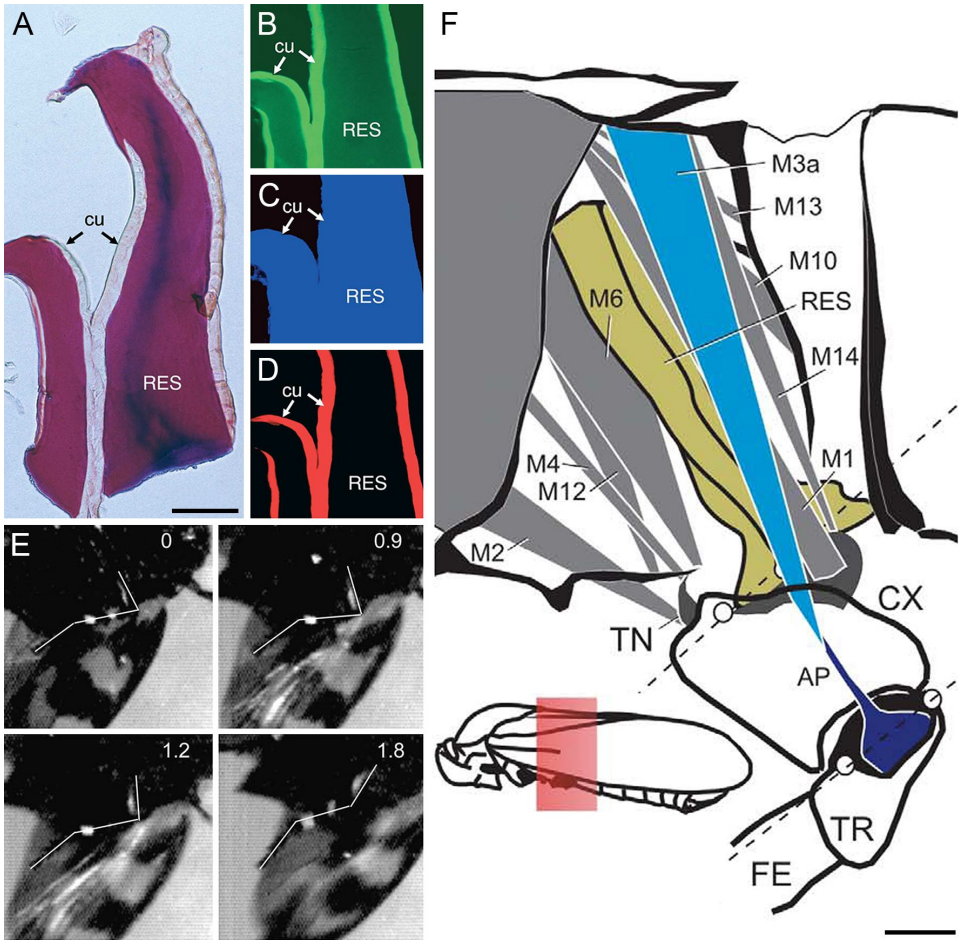

Figure 4: Resilin in the jumping system of the black-and-red froghopper (*Cercopis vulnerata*). (A–D) Cuticle supplemented with resilin in the pleural area of the metathorax. Horizontal sections through the pleural seam. (A) Paraffin-embedded cuticle stained after Cason. Bright-field micrograph. (B–D) Frozen sections of the structures shown in A. Wide-field fluorescence micrographs showing different autofluorescences exhibited by the exoskeleton. (B) Excitation: 512–546 nm; emission: 600–640 nm. (C) Excitation: 340–380 nm; emission: 420 nm. (D) Excitation: 710–775 nm; emission: 810–890 nm. cu, tanned cuticle; RES, structures containing resilin. (E) Sequence of single frames of a high-speed video recording of the cicada jump (ventral aspect). The numbers indicate the time scale in milliseconds. The approximate positions of femur, tibia and tarsus are indicated by white lines according to white marker dots on the leg. (F) Skeleton-muscle organisation of the cicada metathorax (medial aspect, right side). AP, apodeme of the trochanter extensor muscle M3; CX, coxa; FE, femur; M1, M2, M4, M6, M14, subcoxal muscles; M7, M9, M10, M11, M12, M13, M14, metathoracic muscles; M5, trigger muscle; M8a, M8b, trochanter flexor muscle; RES, resilin; TN, trochantine; TR, trochanter; white circles, condyli of the coxa and trochanter. The inset shows the position of the structures in the entire insect body. (A–F) Adapted with permission from [16], copyright 2004 Elsevier.

their elastic recoils provide energy for the rapid trochanter movements powering the jump. While fleas perform their jumps just with the hindlegs, snow fleas (Mecoptera, Boreidae) use their hind and middle leg pairs for jumping. They feature four resilin-containing pads, one at each of the legs involved in jumping, and these pads are similar to those of fleas with respect to their locations at the legs and their function [19].

For the jumping mechanism of fleas it was proposed that the whole energy required is stored in the resilin-containing pads [15]. However, the results of recent estimations indicate that resilin alone often can provide only a rather small proportion of the energy that is necessary to fulfil the large power demands of fast leg movements involved in actions such as jumping [17]. Energy storage devices used for jumping in froghoppers (Hemiptera, Cercopidae) and planthoppers (Hemiptera, Issidae) and for jumping and kicking in locusts were shown to be composites of relatively hard and stiff chitinous structures and structures with large proportions of resilin [17,18,20]. It was suggested that a large proportion of the energy needed for jumping is stored within the hard and stiff chitinous structures, which (because of the stiffness of the material) likely requires only small amounts of bending and, therefore, only short muscle contractions [17,18,20]. The flexibility and elasticity of resilin

are assumed to facilitate this mechanism by reducing the risk of fractures occurring within the stiffer material and by contributing to a rapid and complete return of the distorted energy storage devices to their original shapes [17,18,20]. It is conceivable that a large proportion of the energy storage devices existing in insects with fast leg movements, including those of fleas, feature composite architectures comparable to those described above.

The ability of resilin to store energy within jumping systems was shown to be also involved in an energy absorption function of a specific structure, called buckling region, that is present in each tibia of locust hind legs [76]. The buckling region is located in an area where the bending moment during jumping and kicking is high. When a hindleg slips during jumping or misses a target during kicking, this structure can buckle and thereby act as a shock absorber by dissipating energy that would otherwise have to be absorbed by other suctures such as the leg joints. The buckling region exhibits parts with large proportions of resilin that are assumed to contribute to the energy absorption and to the restoration of the original shape of the leg after buckling [76].

Flight systems: folds, tendons and microjoints

Resilin has already been found in various elements of insect flight apparatus, including tendons connecting muscles to pleural sclerites, wing hinge ligaments connecting the wings to the thoracic wall, prealar arms connecting pleural sclerites to the mesotergum, wing vein micro-joints connecting cross veins to longitudinal veins, regions of the wing membrane establishing a connection to the wing veins or defined patches within membrane cells, and cuticular layers within wing veins [2,5,21,22,77-79]. In these structures, resilin occurs either in the form of pure or nearly pure resilin (e.g., tendons) or mixed with varying amounts of chitin fibres (e.g., prealar arm), which tend to follow distinct directions or patterns and thereby influence the mechanical properties of the material [5,28]. All of these structures benefit to a more or less pronounced extent from the presence of resilin due to its low stiffness, high resilience, large and reversible extensibility, long fatigue time and ability of elastic energy storage and damping.

One of these flight system elements is a sausage-like swollen thoracic dragonfly tendon, which consists of virtually pure resilin and connects the pleuro-subalar muscle (which spans between the lower part of the pleuron and the subalar sclerite) to the subalar sclerite, which in turn connects to the axillary sclerites of the wing base [2] (Figure 5A,B). Together with the coxoalar muscle, it is assumed to control wing twisting (i.e., supination) during the upstroke by taking up wing movements and oscillating in length, while the attached pleuro-subalar muscle contracts slowly and tonically and keeps the tendon at a certain length and tension [5,80,81]. This is especially important for hovering and other refined flight manoeuvres [9]. It might also play a role in controlling excess wing motions during turbulent flows [81]. In the tendon, large reversible extensibility (e.g., over 250% in the forewing of the widow skimmer (*Libellula luctuosa*)) and a long fatigue time are of key importance for the functioning of this structure.

The wing hinge ligament of the forewing of locusts is located between the (meso-)pleural wing process and the second axil-

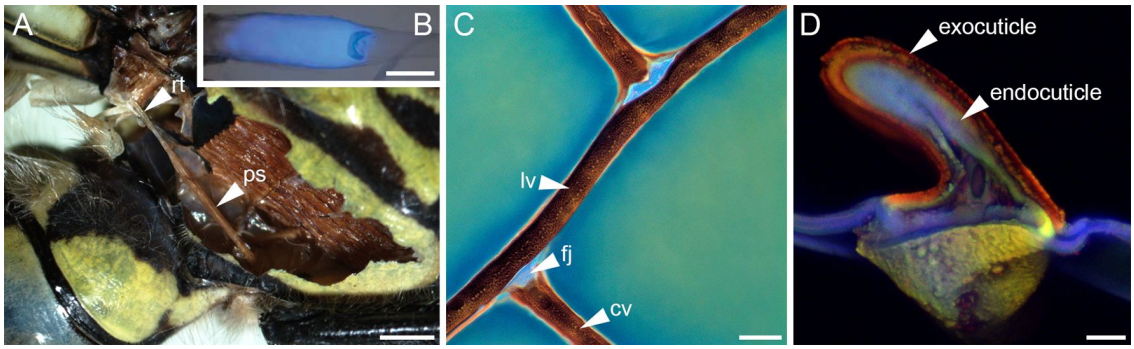

Figure 5: Resilin in flight systems of dragonflies. (A) Stereomicrograph depicting a resilin-bearing tendon (rt) of a pleuro-subalar muscle (ps) of the southern hawker (*Aeshna cyanea*). (B) Overlay of a bright-field micrograph and a wide-field fluorescence micrograph showing autofluorescence (blue) exhibited by resilin in a tendon of the genus *Zyxomma*. (C) Flexible wing vein joints (fj) joining cross veins (cv) to a longitudinal vein (lv) in a wing of the vagrant darter (*Sympetrum vulgatum*). (D) Cross section through a wing vein of *S. vulgatum*, revealing sclerotised exocuticle and resilin-bearing endocuticle. (C, D) Confocal laser scanning micrographs (maximum intensity projections) showing overlays of different autofluorescences exhibited by the exoskeletons. Structures with large proportions of resilin are shown in blue. Scale bars = 1 mm (A), 100 µm (B), 40 µm (C), 10 µm (D). (B) Adapted with permission from [13], copyright 2005 Nature Publishing Group. (D) Adapted with permission from [79], copyright 2015 John Wiley and Sons.

lary wing sclerite [5]. In Odonata, Dictyoptera and Orthoptera, wing hinge ligaments exist in the form of thick, rubber-like pads (Figure 1A) and, as reported for locust structures, consist of a rather tough, mainly chitinous ventral part and a soft dorsal part, which can be divided in a region of pure resilin and a region containing both chitin lamellae and resilin [5]. The results of several studies suggest that wing hinge ligaments take up compressive as well as tensile forces and can contribute to (1) the storage of kinetic energy at maximum wing deflection, for example during the upstroke when the wing hinge ligament is stretched, and (2) wing acceleration during the downstroke by elastic recoil [5,28,82]. In other insects, such as Lepidoptera, some Coleoptera and some Hymenoptera, these ligaments are tough and inextensible, and elastic energy storage is likely provided by the rigid thoracic cuticle and the flight muscle itself [5,28]. Due to the fact that resilin has mainly been found in the flight apparatus of insects flying with synchronous flight muscles at low wing beat frequencies of less than 50 Hz and with inertial forces being larger than aerodynamic forces, it is assumed that its resilience might be too small at high frequencies [5,11,28,83]. However, there is still some controversy about the frequency-dependent behaviour of resilin and chitin–resilin composites and its function in the wing hinge ligaments of insects with high wing beat frequencies [5]. For example, some small wing hinge ligaments have been found between different sclerites in the genera *Calliphora*, *Bombus*, *Apis* and *Oryctes* [5,84]. So far, only a few studies have investigated the decrease in resilience with increasing frequencies in the dragonfly tendon, locust prealar arm and cockroach tibia-tarsal joint resilin [5,11,81,83,85]. Whether the partly pronounced differences in the decrease rate of resilience between different frequency ranges are due to different measurement techniques or are actually due to differences in the material composition, still needs to be elucidated.

The prealar arm is located at the front edge of the mesotergum and establishes a connection to the first basalar sclerite of the pleural thoracic wall via a tough, flexible ligament [5]. The basalar sclerite in turn is connected to the humeral angle of the anterior part of the wing base. The prealar arm consists of around 23% chitin and 77% resilin and is structured by alternating layers of resilin and chitin fibrils, with the fibrils continuing into the dark, sclerotised cuticle at its base [5] (Figure 1B). Due to the directional arrangement of chitin fibrils, the mechanical behaviour of the prealar arm is assumed to be dominated by the mechanical properties of the chitin fibrils during stretching and by the properties of resilin during bending and compression [5,11]. In contrast to the subalar muscle, which is involved in wing supination, the contraction of the basalar muscle causes wing pronation through the connection to the humeral angle via the basalar sclerite. During muscle contraction, the prealar arm is deformed and can be assumed to play a role in elastic energy storage.

Cross veins in wings of dragonflies and damselflies were shown to form either stiff, inflexibly fused joints or flexible, resilin-bearing joints to the adjacent longitudinal veins [24-26,78,86] (Figure 5C). The distribution pattern of different wing vein joint types on the dorsal and ventral wing sides in various species is quite diverse, but was found to follow phylogenetic trends probably related to wing morphology and flight behaviour [26,78]. In general, flexible wing vein joints, together with the overall corrugated design of odonate wings, are assumed to feature a larger angular displacement than fused vein joints and, as a result, to provide the wing with increased chord-wise flexibility, which promotes passive wing deformations such as camber-formation during the downstroke, and, thereby, to improve the aerodynamic and mechanical performance of the wing [24,26,78,86,87]. Moreover, resilin is important for reducing stress concentrations in vein joints [87]. Resilin is not only present in wing vein joints but also in the wing membrane directly abutting on wing veins and internal cuticle layers of wing veins (i.e., the endocuticle) [78,79] (Figure 5D). A flexible suspension of the wing membrane is suggested to allow larger strain and thereby to help preventing its tear-off from the wing veins [79]. Furthermore, the stiffness gradient in wing veins, generated by a stiff, sclerotised outer layer (exocuticle) and a soft, compliant, resilin-bearing inner layer (endocuticle) is assumed to reduce the overall vein stiffness and to improve the damping properties of the vein as well as to delay Brazier ovalisation and to enhance the load-bearing capacity under large deformations [79,88].

By artificially stiffening single flexible, resilin-bearing vein joints in bumblebee wings through the application of microsplints (extra-fine polyester glitter glued with cyanoacrylate), it was experimentally shown that even a single resilin-bearing joint plays an important role in overall wing flexibility and vertical aerodynamic force production [89]. Ma et al. [90] found comparable resilin joints (e.g., the 1 m-cu joint) in wings of western honey bees (*Apis mellifera*) and assumed that they might play an analogous role in increasing the chordwise wing flexibility. Based on the distribution of resilin patches, wing veins, the occurrence of a flexible hook-mediated forewing–hindwing connection and observed wing deformations, they further suggested the existence of five flexion lines in one forewing–hindwing entity and assumed that these probably increase the cordwise flexibility and support camber formation. In addition, Mountcastle and Combes [91] demonstrated that a resilin-bearing joint at the leading edge (the costal break) in the wings of wasps plays a major role in mitigating wing wear by flexion along this joint when the wings hit an obstacle.

This mechanism is especially important for wings with wing veins extending all the way to the tip because such a design endows a wing with more spanwise rigidity than, for example, bumblebee wings that lack veins at the wing tip [91].

The occurrence of resilin in several broadened vein patches as well as in membranous folding lines was described for fan-like dermapteran hind wings [22,92]. These structures help folding the wing into a wing package being ten times smaller than the unfolded wing. This package can then be hidden under the short sclerotised forewings. The four-fold wing folding can be achieved without musculature activity and is assumed to be driven by elastic recoil of the anisotropically distributed resilin on either the ventral or the dorsal sides of broadened vein patches in intercalary and radiating veins, supported by the resilin-bearing radiating folds that influence the folding direction [22]. Unfolding of the hind wings is achieved either by wiping movements of the cerci (e.g., in the European earwig (*Forficula auricularia*) and the lesser earwig (*Labia minor*)) or by wing flapping (e.g., in the earwigs *Timomenus lugens*, which has very long cerci, and *Auchenomus* sp.) [22,93]. Both unfolding mechanisms are supported by several wing stiffening mechanisms such as the mid-wing mechanism and the claval flexion line, which keep the wing unfolded in all species examined [22,93]. These mechanisms were found to play an important role both in the static unfolded state of the wing and during flapping flight, in which they help to inhibit an unfavorable folding of the wing [92]. Furthermore, the flexible resilin-bearing folding lines were found to not only serve wing folding but also act as flexion lines at which the wing flexes during flight, thereby supporting the generation of an aerodynamically favourable cambered wing profile [92,94].

In beetle wings, resilin was found to occur at the marginal joint, between veins that separate during folding, and along flexion lines in membranous areas, leading to the hypothesis that elastic energy storage by resilin can support wing unfolding also in beetle wings [21]. However, this can, if at all, only be a supportive role because wing unfolding in beetles was stated to be mainly achieved by scissor-like movements of the RA and MP1+2 veins via contraction of the Musculus pleura alaris and the basalar muscles, which is possibly supported by hydraulic hemolymph pressure [95,96]. Like in dermapteran wings, in beetle wings resilin most probably delays material fatigue in highly stressed wing regions and might further play a role in wing deformation during flight [22].

In wings of the urban bluebottle blowfly (*Calliphora vicina*), resilin is mainly present in the proximal part of the wing, predominantly in the form of resilin-bearing patches between veins [77]. The occurence of resilin coincides with the proximal distribution of the maximum spanwise bending stress at the beginning of each stroke cycle and suggests that the resilin patches reduce the risk of breaking near the wing hinge due to a decrease in peak stress in the rigid wing parts [77].

Attachment systems

The contact formation of insect adhesive pads on substrates depends on the ability of the pads to adapt to the surface topography. In this context, specific micro- and nanostructures can enhance the quality of the contact [97-101]. In the case of attachment on rough substrates, multiple contacts, being formed by some adhesive systems, provide great advantages [102]. The formation of multiple contacts, which contribute to an increase of the overall length of the total peeling line, is facilitated by a hierarchical organisation of the attachment structures [103]. It was shown that the combination of thin tape-like contact tips of hairs (setae) and applied shear force lead to the formation of a maximal real contact area without slippage within the contact [104]. This indicates that material flexibility is very important for the contact formation of adhesive pads. With a minimal normal load, flexible materials can create a large contact area between the attachment structures and the substrate. However, elongated structures that are too flexible have a low mechanical stability [105]. For example, if insect setae are too soft, they can buckle and collapse, and so-called clusterisation (or condensation) can take place [106,107]. As a result of this, the functional advantages achieved through multiple adhesive contacts can be strongly reduced [103]. Accordingly, the composition and the properties of the material of insect adhesive setae represent an optimisation problem. There is evidence that during the evolution gradients of the thickness and the mechanical properties of the setae have developed as a solution of this problem. The presence of thickness gradients, revealed by scanning electron microscopy, is well-known for various insect adhesive setae [97]. Recently, a gradient of the material composition, present on the level of each single adhesive tarsal seta, was shown to exist in the seven-spot ladybird (*Coccinella septempunctata*) [48] (Figure 2A–C). The material of the setal tip contains large proportions of resilin, while the base of the seta consists mainly of sclerotised chitinous material. Between the tip and the base, a pronounced material composition gradient was revealed by CLSM. This gradient is reflected by a pronounced gradient of the material properties: the setal tip is rather soft, whereas the setal base is relatively stiff. Both gradients were hypothesised to represent an evolutionary optimisation that increases the attachment performance of the adhesive pads when they attach to rough surfaces due to an efficient adaptation of the soft and flexible setal tips to the substrate and a simultaneous prevention of setal clusterisation by means of the stiffer setal bases [48]. Since this hypothesis is difficult to test experimentally using biological specimens, it was tested

using numerical simulations [49] (Figure 2D–F). The results indicate that setae with long soft tips and rigid bases exhibit a strong adhesion but also a pronounced clusterisation (Figure 2E). Setae with rigid tips and soft bases have a low adhesion and a pronounced clusterisation (Figure 2F). Only setae with short soft tips and rigid bases feature optimal adhesion properties and simultaneously a minimum of clusterisation (Figure 2D), which confirms the hypothesis. Tarsal liquids produced by beetles are assumed to contribute to the adhesion efficiency of adhesive pads in the form of capillary interactions and cleaning effects. With regard to the resilin-dominated setal tips, an additional function is conceivable. As described above, resilin is only soft and flexible when it is hydrated. Accordingly, to keep the contribution of the large resilin proportions in the setal tips to the attachment performance of the adhesive pads on a high level, the hydration of the resilin must be maintained. It is imaginable that this is achieved by slowly evaporating tarsal liquids covering the setae and thereby keeping the resilin in the setal tips hydrated [48].

The presence of material gradients has also been demonstrated for smooth attachment devices of insects [23]. Interestingly, the gradients revealed in smooth adhesive pads of locusts and bush crickets differ from those existing in the adhesive tarsal setae described above. The smooth pads contain a relatively soft core, which is covered by a stiffer layer. Accordingly, the direction of the material gradient is opposite to that in the adhesive tarsal setae, which can be well explained by the different pad architecture. Smooth pads feature branching fibres (rods) that form foam-like structures. The spaces between the solid structures are filled with fluid. Due to this construction principle, the pads are kept in shape. The fibres are terminated by a relatively stiff superficial layer that keeps the positions of the relatively long and thin fibres (and thereby the distance between the fibre tips) constant [23,108]. This pad architecture was studied in detail in two orthopteran species, the great green bush-cricket (*Tettigonia viridissima*) (Ensifera) and the migratory locust (*Locusta migratoria*) (Caelifera), whose adhesive pads generally have a similar structural organisation [23] (Figure 6A–D). Both pads possess a flexible resilin-containing exocuticle with fibrils that are fused into relatively large rods oriented in an angle to the surface. However, slight differences in the pad architecture exist. Adhesive pads of *L. migratoria* feature a clearly thicker superficial layer as well as a higher density of rods than those of

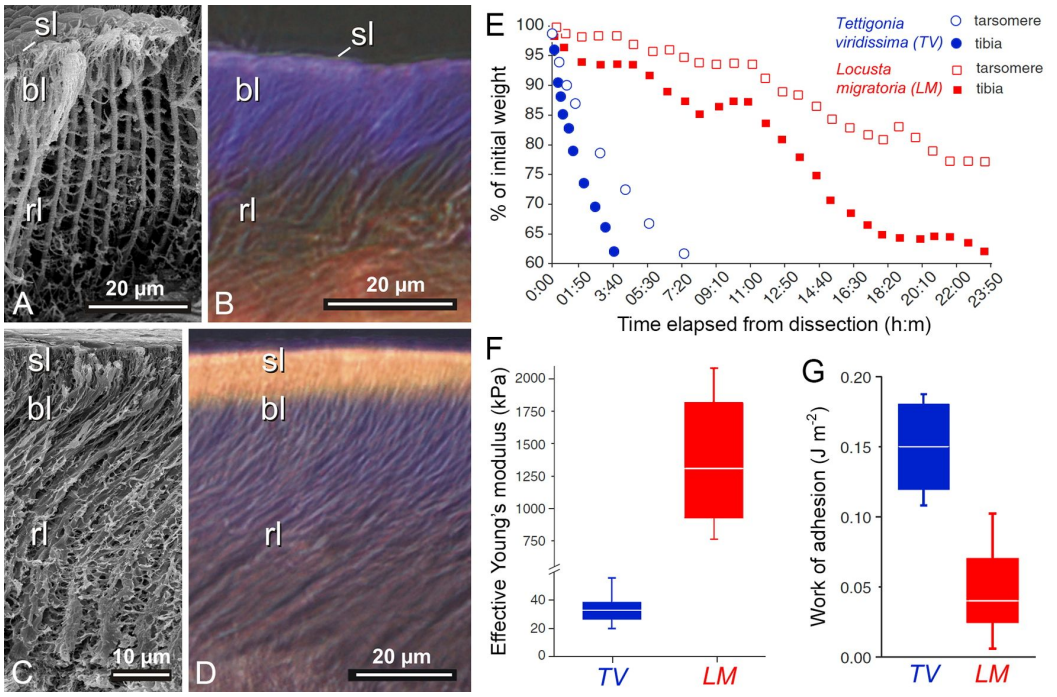

Figure 6: Material structure and properties of orthopteran adhesive pads (euplantulae). (A, B) Great green bush-cricket (*Tettigonia viridissima*). (C, D) Migratory locust (*Locusta migratoria*). (A, C) Scanning electron micrographs showing frozen, fractured, substituted, dehydrated and critical point dried pads. (B, D) Wide-field fluorescence micrographs showing frozen-cut pads. Structures with large proportions of resilin are violet/blue. sl, superficial layer; bl, layer of branching rods; rl, layer of primary rods. (E) Desiccation dynamics of tarsi and pieces of tibiae cut off the body in both species. (F) Effective Young's modulus of attachment pads of both species determined by means of indentation with a spherical tip radius of 250 µm. (G) Work of adhesion of attachment pads of both species measured by means of indentation with a sphere with a radius of 32 µm. In F and G, the ends of the boxes define the 25th and 75th percentiles, the lines indicate the medians, and the error bars define the 10th and 90th percentiles. (A–G) Adapted with permission from [23], copyright 2006 Springer.

T. viridissima (Figure 6A–D). In addition, indentation experiments revealed a higher effective Young's modulus and a lower work of adhesion for *L. migratoria* pads (Figure 6F,G). The lower adhesive properties of *L. migratoria* pads can be explained by the larger thickness of the relatively stiff superficial layer, which likely reduces the adaptability of the pad to the substrate much more than the relatively thin superficial layer of the *T. viridissima* adhesive pad. The superficial layer is assumed to also protect the pad from desiccation as indicated by experiments showing that cut-off adhesive pads of *T. viridissima* (with the relatively thin superficial layer) lose water much faster than those of *L. migratoria* (Figure 6E). Consequently, the material gradient provides a combination of conformability to the surface roughness of the substrate (The compliant material of the pad contributes to the efficient contact formation with the substrate.) and resistance to the dry environment. Such pad architectures likely depend on the preferred environment of each species and are the result of trade-offs between different factors such as evaporation rate, stiffness, stability and adhesion.

Mouthparts

The first mouthpart-related structures containing resilin were already mentioned shortly after the description of resilin. In the respective studies, resilin was found in the salivary and feeding pumps of assassin bugs [109] (cited in [110]), [111]. Later, the findings were confirmed and complemented by additional information about the resilin distribution [51]. In these pumps, which enable the bugs to suck relatively large amounts of blood in a short time period and to inject proteolytic enzymes into prey or assaulters or to spit on the latter, the resilin-containing structures function as elastic spring antagonists to muscles. A similar function was described for resilin-containing structures present in the maxillipeds of decapod crustaceans [112]. The movements of the flagella of these mouthparts influence the water flow through the gills as well as over chemoreceptors located on the head, and thereby they importantly contribute to active chemoreception and to signalling by distributing urine odours. Each of the flagella is abducted by the contraction of a single muscle. Due to this abduction, a structure that contains relatively large resilin proportions and is located in the joint between the flagellum und the exopodite of the maxilliped is bent. After relaxation of the muscle, this elastic structure recovers its original shape and moves the flagellum back to its resting position.

In general, due to its very pronounced elasticity and fatigue resistance, resilin appears to be a very suitable material for exoskeleton structures that are typically intensively deformed for a rather large number of times during the lifetime of the organisms. A butterfly proboscis, for example, is tightly and spirally coiled when it is in its resting position [113]. For the uptake of food, hemolymph is pumped into the proboscis resulting in the generation of hydrostatic pressure that completely uncoils the proboscis [113-115] and strongly changes the shape of certain proboscis elements. During this process, dorsal parts of the proboscis are compressed. These parts contain relatively large proportions of resilin and act as springs that cause the recoiling of the proboscis when the hydrostatic pressure is removed [115].

A remarkable resilin-containing adhesive prey-capture device, which is formed by the elongated labium, exists in rove beetles of the genus *Stenus* (Staphylinidae). This prey-capture apparatus can be protruded towards a prey within a few milliseconds. When sticky pads (modified paraglossae), which are located at the distal end of the prementum, adhere to the prey, the labium is withdrawn immediately, and thereby the prey is transported to the mouth region of the beetle where it can be seized with the mandibles [116-118]. The sticky pads feature a surface that is subdivided into numerous terminally branched outgrowths. During the prey capture, these surface structures are completely covered by an adhesive secretion that is produced in special glands located in the head capsule and makes the sticky pads a hairy, hierarchically structured and wet adhesive system. Similar to the insect tarsal adhesive pads mentioned above, softness and compliance of the pad cuticle contribute to the generation of strong adhesive forces by the pads. The cuticle material of certain parts of the sticky pads contains large proportions of resilin providing flexibility and elasticity and enabling the pads to efficiently adapt to the surface of the prey items [118].

Copepods are tiny crustaceans that inhabit nearly all aquatic habitats worldwide and are particularly abundant in the marine water column where they contribute large proportions of the zooplankton [119,120]. The diet of many of the marine planktonic species comprises relatively large fractions of diatoms (i.e., unicellular algae with silica-containing shells called frustules). Copepods use the gnathobases of their mandibles to grab and mince food particles. To be able to efficiently digest the diatom cells, the copepods must crack the frustules before the ingestion of the cells. The gnathobases possess tooth-like structures (called teeth in the following) at their distal ends [121]. In copepod species feeding on large amounts of diatoms, these teeth are rather compact and consist of complex composites that combine diverse structures and materials with a wide range of properties. Recently, the morphology and material composition of the gnathobases of two copepod species have been analysed and described in great detail [29,30]. The gnathobases of the calanoid copepod *Centropages hamatus* feature two larger and relatively compact teeth (Figure 7A–E). Each of these teeth possesses a chitinous socket, which is covered by a cap-like struc-

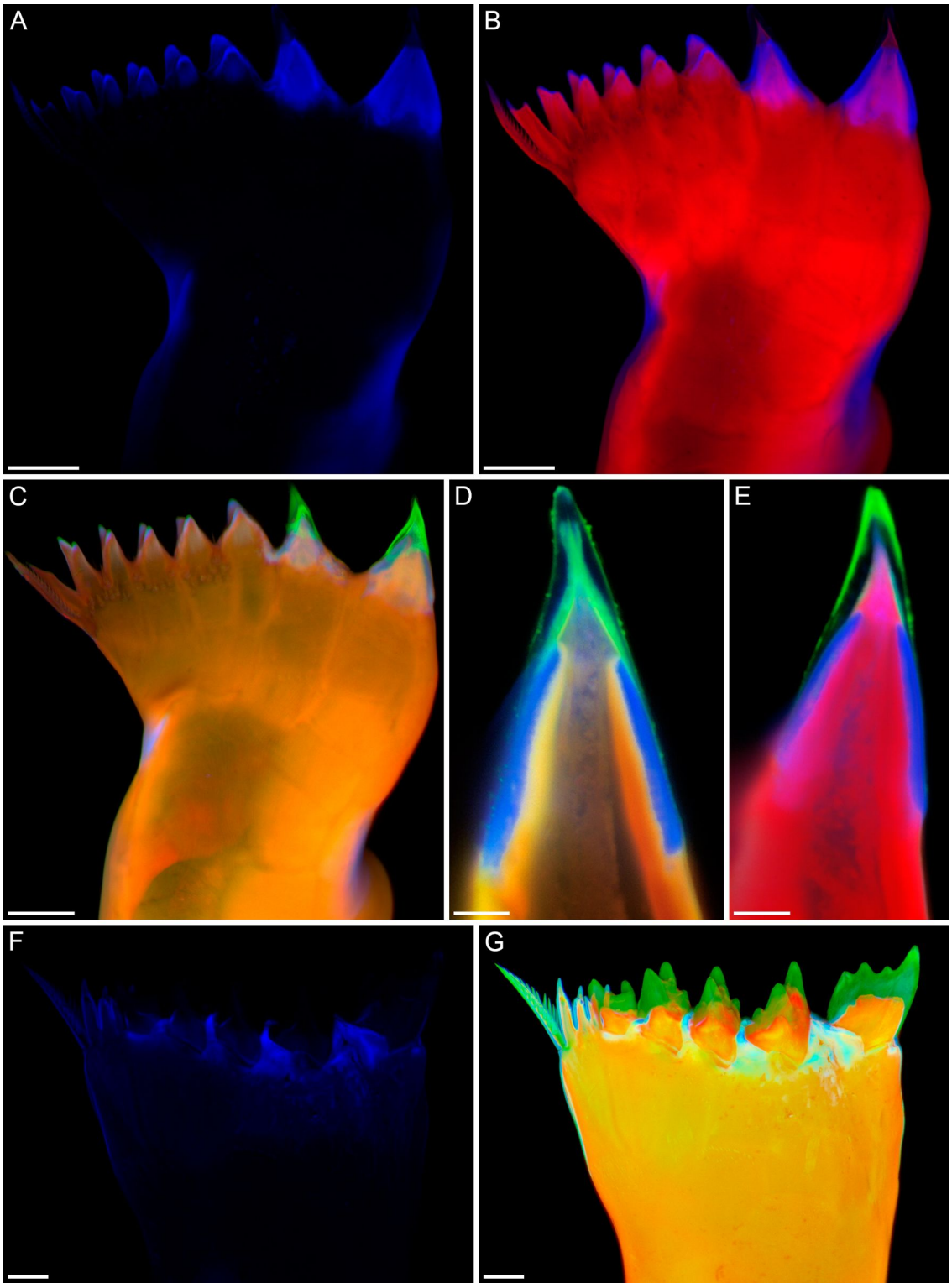

Figure 7: Morphology and material composition of mandibular gnathobases of copepods. Confocal laser scanning micrographs showing gnathobase structures of (A–E) a female of the copepod species *Centropages hamatus* and (F, G) a female of the copepod species *Rhincalanus gigas*. (A–C, F, G) Maximum intensity projections. (D, E) 1 µm thick optical sections through the largest tooth of the gnathobase. (A, F) Distribution of resilin. (B) Chitinous exoskeleton (red) and resilin-dominated structures (blue). (C–E, G) Chitinous exoskeleton (red, orange), resilin-dominated structures (blue, light blue, turquoise) and silica-containing structures (green). Scale bars = 20 µm (A, B, C), 5 µm (D, E), 25 µm (F, G). (A–E) Adapted with permission from [29]. (F, G) Adapted with permission from [30], copyright 2015 Elsevier.

ture with a large resilin proportion. On top, another cap-like structure that is composed of silica is located. All other gnathobase teeth are smaller, contain no silica, are mainly chitinous and have tips with large resilin proportions. *C. hamatus* is omnivorous and feeds on, among other organisms, diatoms and protists. It is assumed that the large silica-containing teeth are used for feeding on diatoms. The silica makes these teeth stiffer and more mechanically stable and thereby more efficient in cracking the diatom frustules. In case the diatom frustules are too stable and the pressure acting on the tips of the siliceous teeth exceeds the breaking stress level causing an increased risk of crack formation in and breakage of the teeth, the soft and elastic resilin-containing structures are supposed to function as flexible bearings that can be compressed and thereby reduce stress concentrations in the tooth material and increase the resistance of the teeth to mechanical damages. Additional structures with large resilin proportions, located in the central and proximal parts of the gnathobases, are assumed to have a damping function that makes the whole gnathobases resilient and further reduces the risk of mechanical damage of the teeth. The smaller gnathobase teeth of *C. hamatus* are likely used to grab protists. In this context, the grip of the tooth tips is suggested to be increased by

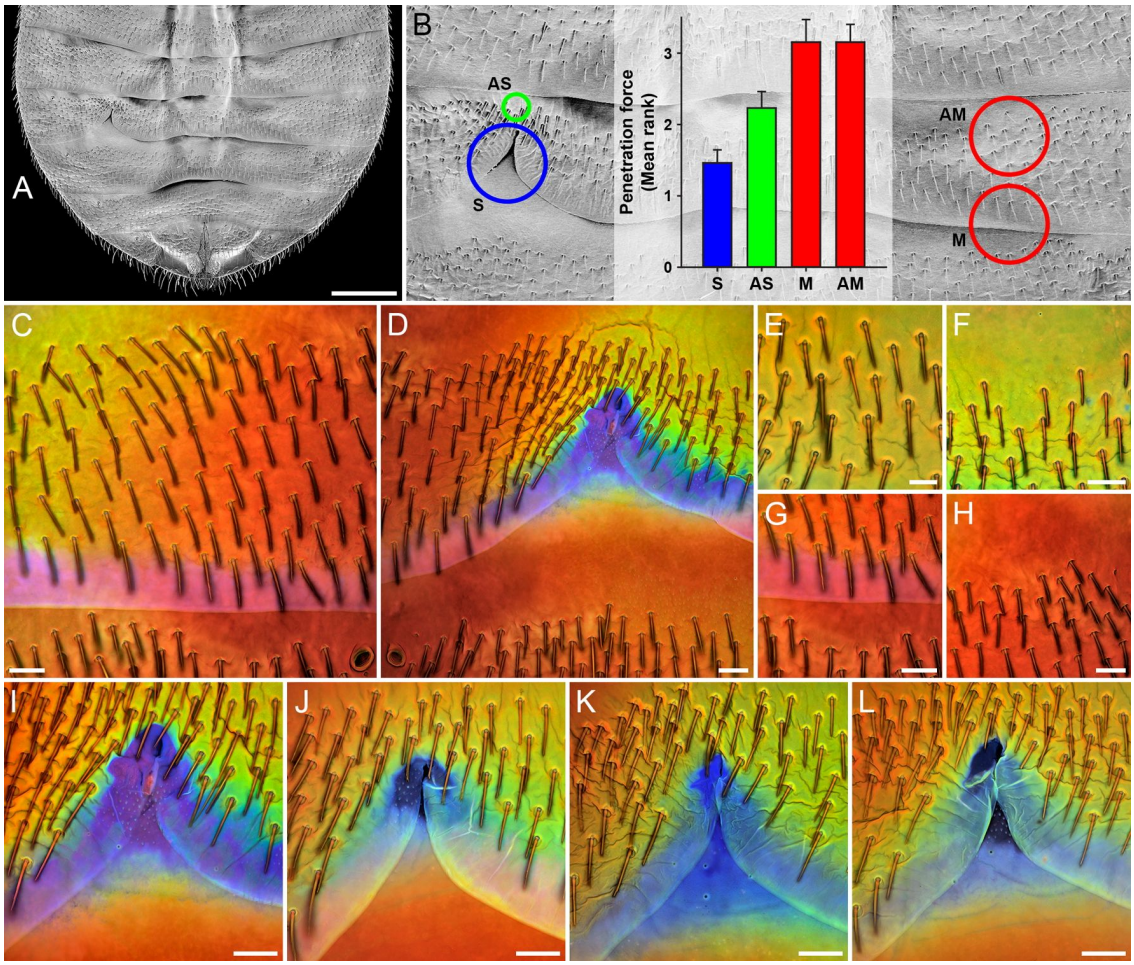

Figure 8: Material composition and properties of the ventral abdominal cuticle of females of the common bed bug (*Cimex lectularius*). (A) Abdomen overview (scanning electron micrograph). (B) Section of A indicating the locations of the spermalege (S) and three other cuticle areas called AS, M and AM, and penetration forces (mean ranks and standard errors) determined for these four cuticle sites. (C–L) Confocal laser scanning micrographs (maximum intensity projections) showing overlays of different autofluorescences exhibited by the exoskeletons. Blue colours indicate large proportions of resilin. (C, D) Autofluorescence composition of the cuticle in the left (C) and right (D) abdomen parts. The dominance of violet/blue autofluorescence (shown in blue) is restricted to the spermalege, clearly indicating that only at this site the cuticle contains large proportions of resilin. (E–H) Autofluorescence composition of the cuticle at the sites AS (E, F), M (G) and AM (H). The cuticle at M and AM consists mainly of sclerotised chitinous material, indicated by the dominance of autofluorescence shown in red, while the presence of large proportions of autofluorescence shown in green in the cuticle at AS indicates that the respective material consists mainly of weakly or non-sclerotised chitinous material. (I–L) Autofluorescence composition of the cuticle at the spermalegeS of different one-week-old females, indicating variation of the extent of the resilin-dominated spermalege structures between females. Scale bars = 500 µm (A), 50 µm (C, D, F–L), 25 µm (E). Figure reproduced with permission from [126].

the soft and elastic resilin making the grabbing process more efficient.

The gnathobases of the calanoid copepod *Rhincalanus gigas*, a species whose diet mainly consists of diatoms, are characterised by five relatively large and compact teeth that possess a combination of different materials comparable to that of the silica-containing teeth of *C. hamatus* (Figure 7F,G). Each of these teeth has a silica-containing cap-like structure, which is located on a chitinous socket. At the base of the socket, the gnathobase exoskeleton features large proportions of resilin. Like in the silica-containing teeth of *C. hamatus*, these resilin-containing structures very likely function as compressible supports reducing the risk of mechanical damages of the teeth during feeding on diatoms with stable frustules. In general, the complex composite systems in the gnathobase teeth are assumed to have co-evolved within an evolutionary arms race together with the diatom frustules [122].

Reproductive organs, mechanoreceptors and compound eyes

The mating of bed bugs represents a famous example of sexual conflict. During every successful mating event, the cuticle of the ventral side of the abdomen of the female is penetrated by the male with a cannula-like intromittent organ, and the male injects sperm and accessory gland fluids directly into the abdomen where the sperm migrate to the ovaries [123,124]. This traumatic insemination imposes survival costs on the females [124] but the females cannot avoid mating [125]. As a result of this sexual conflict, a female organ, the so-called spermalege, has evolved. In common bed bugs (*Cimex lectularius*), this organ is located on the right side of the ventral abdomen part where it is visible as a notch-like modification of the posterior edge of the fifth segment that exposes the subjacent intersegmental membrane and cuticle of the sixth segment (Figure 8A,B). A recent study revealed that the spermalege cuticle, by contrast to other cuticle sites analysed on the ventral

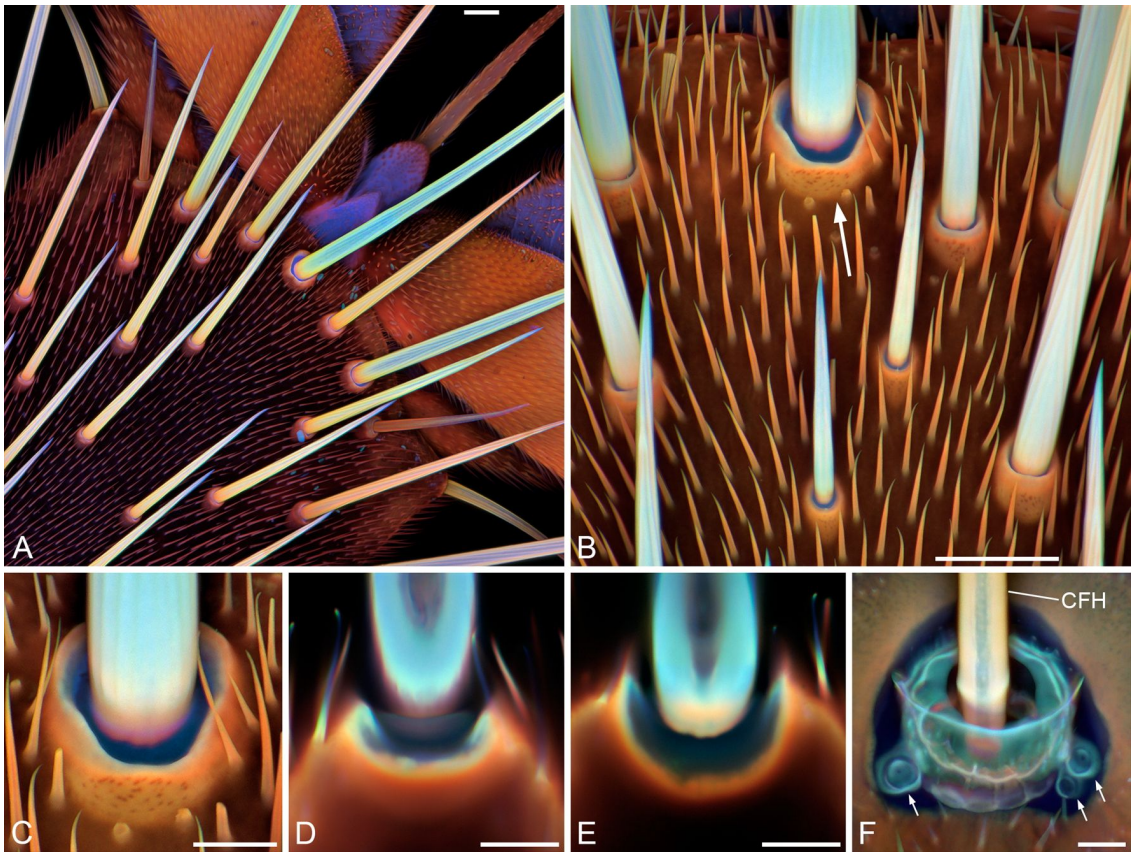

Figure 9: Resilin in mechanoreceptors. (A–F) Confocal laser scanning micrographs showing overlays of different autofluorescences exhibited by the exoskeletons. Blue colours indicate large proportions of resilin. (A) Dorsal view of the pretarsus of a third leg of a female drone fly (*Eristalis tenax*). (B) Dorsal view of a section of a second leg's pretarsus of a male *E. tenax*. The arrow highlights a hair plate sensillum. (C) Larger view of the hair plate sensillum highlighted in B. (D, E) Confocal laser scanning micrographs showing 1 µm thick optical sections through the hair plate sensillum shown in C. (F) Cercal filiform hair (CFH) and associated campaniform sensilla (highlighted by small arrows) on a cercus of a female house cricket (*Acheta domesticus*). (A–C, F) Maximum intensity projections. Scale bars = 25 µm (A, B), 10 µm (C–F). Figure reproduced with permission from [10], copyright 2011 John Wiley and Sons.

side of the female abdomen, contains large proportions of resilin [126] (Figure 8C–L). In microindentation tests, the penetration force necessary to pierce the resilin-rich spermalege cuticle was significantly lower than that necessary to pierce the other cuticle sites [126] (Figure 8B). In addition, evidence for a significantly reduced tissue damage and hemolymph loss was obtained for piercings of the spermalege cuticle compared with piercings of the other cuticle sites [126]. The results suggest that the material composition of the spermalege cuticle has evolved as a tolerance trait that reduces the mating costs of both the female and the male: due to the softness of resilin the penetration is easier for the male and causes less wounding of the female, and after the withdrawal of the intromittent organ the elasticity of resilin causes a sealing of the puncture reducing the hemolymph loss and the risk of bacterial infection.

Hair plate sensilla and campaniform sensilla are typical mechanoreceptors that are common in insect exoskeletons [127-129]. These receptors possess so-called joint membranes and cap membranes that are composed of large proportions of resilin [10,127,129]. On the dorsal side of the pretarsus of the drone fly (*Eristalis tenax*), for example, hair plate sensilla with rather long and relatively thick hairs are present (Figure 9A–E). The base of each hair is surrounded by a joint membrane that, due to its resilin-dominated material composition, is soft and flexible and allows movement and bending of the hair shaft resulting in a stimulation of the receptor. Because the long hairs project beyond and below the pulvilli of the pretarsus, they touch the substrate shortly before the pulvilli and likely have the function to indicate the upcoming contact between the pulvilli and the substrate. The cerci of crickets feature cercal filiform hairs associated with campaniform sensilla [128,130]. The latter and the bases and sockets of the filiform hairs are embedded in material that contains relatively large proportions of resilin [10] (Figure 9F) and, as mentioned above, very likely allow movement and bending of the shafts of the filiform hairs and the campaniform sensilla, which are very sensitive strain receptors (also called flex or displacement receptors), and thereby stimulate the respective dendrite of the sensory cell.

The presence of large proportions of resilin (in part also described as ‘resilin-like protein’) in compound eye lenses has been described for different arthropods [10,131-134] (Figure 10). While other exoskeleton components are typically micro- and nano-structured, coloured and pigmented and, there-

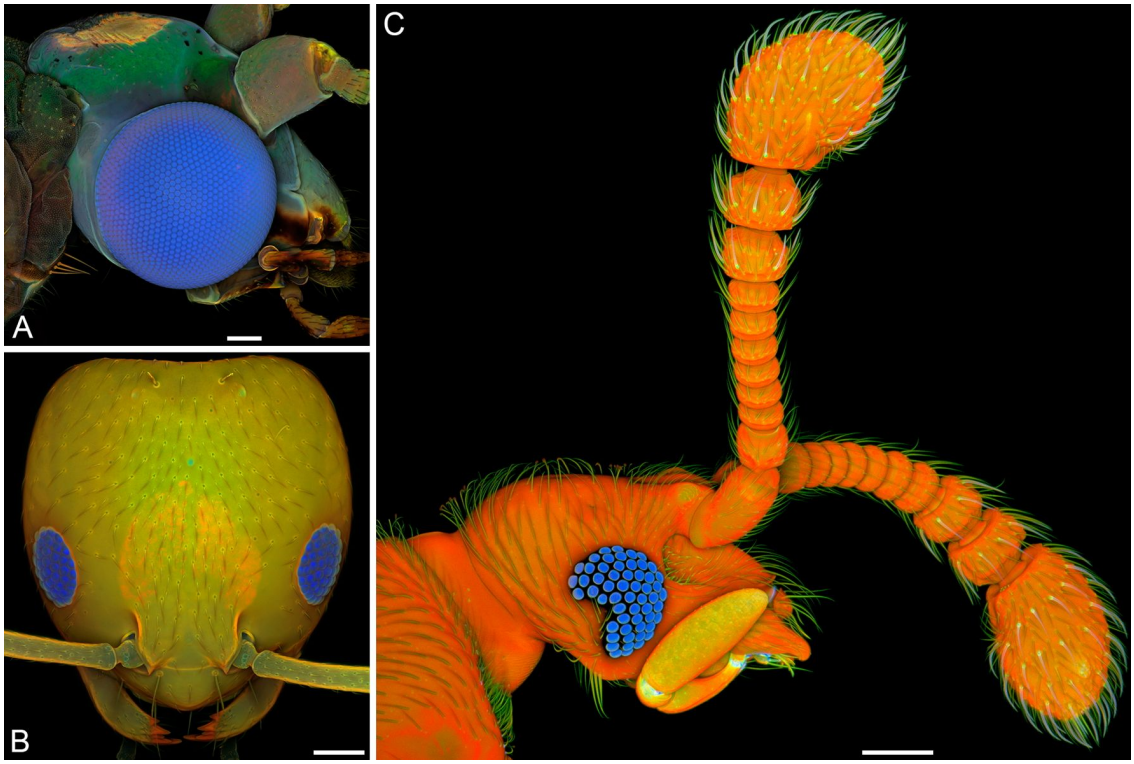

Figure 10: Resilin in compound eyes. Confocal laser scanning micrographs (maximum intensity projections) depicting overlays of different autofluorescences exhibited by the exoskeleton. Blue structures contain large proportions of resilin. (A) Lateral view of the head of a male green lacewing (*Chrysoperla carnea*). (B) Frontal view of the head of a pharaoh ant (*Monomorium pharaonis*) worker. (C) Lateral view of the head of a beetle of the genus *Circocerus*. Scale bars = 100 µm (A, C), 50 µm (B). (A, B) Adapted with permission from [10], copyright 2011 John Wiley and Sons.

fore, not suitable as material for optical elements, the pronounced transparency, the colourlessness and the amorphousness make resilin a perfect material for the construction of optical systems.

Conclusion

Exoskeleton structures with large proportions of resilin are common among arthropods. This review demonstrates the broad range of resilin functions in various exoskeleton structures. Resilin facilitates flexibility and compliance, elastic energy storage, elastic recovery, fatigue and damage reduction, sealing and transparency and thereby makes the respective exoskeleton systems rather effective. Due to its remarkable combination of different properties, resilin is a highly efficient multi-functional protein. In addition, together with other compounds and materials, it often forms complex and powerful composites that combine the properties and benefits of the single components and are capable of performing rather specific and challenging functions. These characteristics have very likely been the reason for the evolution of the large functional diversity of resilin-containing exoskeleton structures in arthropods.

Acknowledgements

Joseph Parker (Columbia University and American Museum of Natural History, New York, NY, U.S.A.) provided the specimen shown in the Figure 10C. Peter Attermeyer, Dario Furlani and Ingo Bartholomäus (Carl Zeiss Microscopy GmbH, Jena, Germany) permitted the use of a ZEISS LSM 800 and thereby enabled the production of the Figure 10C.

References

1. Shewry, P. R.; Tatham, A. S.; Bailey, A. J. *Elastomeric Proteins: Structures, Biomechanical Properties, and Biological Roles;* Cambridge University Press: Cambridge, United Kingdom, 2004.
2. Weis-Fogh, T. *J. Exp. Biol.* **1960,** *37,* 889–907.
3. Weis-Fogh, T. *J. Mol. Biol.* **1961,** *3,* 648–667. doi:10.1016/S0022-2836(61)80028-4
4. Weis-Fogh, T. *J. Mol. Biol.* **1961,** *3,* 520–531. doi:10.1016/S0022-2836(61)80018-1
5. Andersen, S. O.; Weis-Fogh, T. *Adv. Insect Physiol.* **1964,** *2,* 1–65. doi:10.1016/S0065-2806(08)60071-5
6. Andersen, S. O. *Insect Biochem. Mol. Biol.* **2010,** *40,* 541–551. doi:10.1016/j.ibmb.2010.05.002
7. Bailey, K.; Weis-Fogh, T. *Biochim. Biophys. Acta* **1961,** *48,* 452–459. doi:10.1016/0006-3002(61)90043-9
8. Andersen, S. O. Resilin. In *Comprehensive Biochemistry;* Florkin, M.; Stotz, E. H., Eds.; Elsevier: Amsterdam, Netherlands, 1971; Vol. 26C (Extracellular and Supporting Structures), pp 633–657.
9. Schultz, R. L. *Biochim. Biophys. Acta* **1964,** *93,* 211–213. doi:10.1016/0304-4165(64)90288-0
10. Michels, J.; Gorb, S. N. *J. Microsc.* **2012,** *245,* 1–16. doi:10.1111/j.1365-2818.2011.03523.x
11. Jensen, M.; Weis-Fogh, T. *Philos. Trans. R. Soc. London, Ser. B* **1962,** *245,* 137–169. doi:10.1098/rstb.1962.0008
12. Lyons, R. E.; Wong, D. C. C.; Kim, M.; Lekieffre, N.; Huson, M. G.; Vuocolo, T.; Merritt, D. J.; Nairn, K. M.; Dudek, D. M.; Colgrave, M. L.; Elvin, C. M. *Insect Biochem. Mol. Biol.* **2011,** *41,* 881–890. doi:10.1016/j.ibmb.2011.08.002
13. Elvin, C. M.; Carr, A. G.; Huson, M. G.; Maxwell, J. M.; Pearson, R. D.; Vuocolo, T.; Liyou, N. E.; Wong, D. C. C.; Merritt, D. J.; Dixon, N. E. *Nature* **2005,** *437,* 999–1002. doi:10.1038/nature04085
14. Rauscher, S.; Pomès, R. Structural Disorder and Protein Elasticity. In *Fuzziness;* Fuxreiter, M.; Tompa, P., Eds.; Advances in Experimental Medicine and Biology, Vol. 725; Springer: Berlin, Germany, 2012; pp 159–183. doi:10.1007/978-1-4614-0659-4_10
15. Bennet-Clark, H. C.; Lucey, E. C. A. *J. Exp. Biol.* **1967,** *47,* 59–76.
16. Gorb, S. N. *Arthropod Struct. Dev.* **2004,** *33,* 201–220. doi:10.1016/j.asd.2004.05.008
17. Burrows, M.; Shaw, S. R.; Sutton, G. P. *BMC Biol.* **2008,** *6,* 41. doi:10.1186/1741-7007-6-41
18. Burrows, M. *J. Exp. Biol.* **2010,** *213,* 469–478. doi:10.1242/jeb.037861
19. Burrows, M. *J. Exp. Biol.* **2011,** *214,* 2362–2374. doi:10.1242/jeb.056689
20. Burrows, M.; Sutton, G. P. *J. Exp. Biol.* **2012,** *215,* 3501–3512. doi:10.1242/jeb.071993
21. Haas, F.; Gorb, S.; Blickhan, R. *Proc. R. Soc. London, Ser. B* **2000,** *267,* 1375–1381. doi:10.1098/rspb.2000.1153
22. Haas, F.; Gorb, S.; Wootton, R. J. *Arthropod Struct. Dev.* **2000,** *29,* 137–146. doi:10.1016/S1467-8039(00)00025-6
23. Perez Goodwyn, P.; Peressadko, A.; Schwarz, H.; Kastner, V.; Gorb, S. *J. Comp. Physiol., A* **2006,** *192,* 1233–1243. doi:10.1007/s00359-006-0156-z
24. Gorb, S. N. *Naturwissenschaften* **1999,** *86,* 552–555. doi:10.1007/s001140050674
25. Appel, E.; Gorb, S. N. *Bioinspiration Biomimetics* **2011,** *6,* 046006. doi:10.1088/1748-3182/6/4/046006
26. Donoughe, S.; Crall, J. D.; Merz, R. A.; Combes, S. A. *J. Morphol.* **2011,** *272,* 1409–1421. doi:10.1002/jmor.10992
27. Kannupandi, T. *Acta Histochem.* **1976,** *56,* 73–79. doi:10.1016/S0065-1281(76)80028-1
28. Andersen, S. O. Structure and Function of Resilin. In *Elastomeric Proteins: Structures, Biomechanical Properties, and Biological Roles;* Shewry, P. R.; Tatham, A. S.; Bailey, A. J., Eds.; Cambridge University Press: Cambridge, United Kingdom, 2003; pp 259–278. doi:10.1017/CBO9780511546327.015
29. Michels, J.; Vogt, J.; Gorb, S. N. *Sci. Rep.* **2012,** *2,* 465. doi:10.1038/srep00465
30. Michels, J.; Vogt, J.; Simon, P.; Gorb, S. N. *Zoology (Munich, Ger.)* **2015,** *118,* 141–146.
31. Govindarajan, S.; Rajulu, G. S. *Experientia* **1974,** *30,* 908–909. doi:10.1007/BF01938354
32. Sundara Rajulu, G. *Indian J. Exp. Biol.* **1971,** *9,* 122–123.
33. Ramalingam, K. *Parasitology* **1973,** *66,* 1–7. doi:10.1017/S0031182000044383
34. Wong, W. L.; Michels, J.; Gorb, S. N. *Parasitology* **2013,** *140,* 95–98. doi:10.1017/S0031182012001370
35. Lopez-Llorca, L. V.; Fry, S. C. *Nematologica* **1989,** *35,* 165–179. doi:10.1163/002825989X00304
36. DeVore, D. P.; Gruebel, R. J. *Biochem. Biophys. Res. Commun.* **1978,** *80,* 993–999. doi:10.1016/0006-291X(78)91343-8
37. Foerder, C. A.; Shapiro, B. M. *Proc. Natl. Acad. Sci. U. S. A.* **1977,** *74,* 4214–4218. doi:10.1073/pnas.74.10.4214

38. Andersen, S. O. *Biochim. Biophys. Acta* **1963,** *69,* 249–262. doi:10.1016/0006-3002(63)91258-7
39. Andersen, S. O. *Acta Physiol. Scand.* **1965,** *66* (Suppl. 263), 1–81.
40. Neff, D.; Frazier, S. F.; Quimby, L.; Wang, R.-T.; Zill, S. *Arthropod Struct. Dev.* **2000,** *29,* 75–83. doi:10.1016/S1467-8039(00)00014-1
41. Burrows, M.; Borycz, J. A.; Shaw, S. R.; Elvin, C. M.; Meinertzhagen, I. A. *PLoS One* **2011,** *6,* e28456. doi:10.1371/journal.pone.0028456
42. Wong, D. C. C.; Pearson, R. D.; Elvin, C. M.; Merritt, D. J. *Dev. Dyn.* **2012,** *241,* 333–339. doi:10.1002/dvdy.23724
43. Niederegger, S.; Gorb, S. *J. Insect Physiol.* **2003,** *49,* 611–620. doi:10.1016/S0022-1910(03)00048-9
44. Fujimori, E. *Biochim. Biophys. Acta* **1978,** *534,* 82–88. doi:10.1016/0005-2795(78)90478-6
45. Garcia-Castineiras, S.; Dillon, J.; Spector, A. *Exp. Eye Res.* **1978,** *26,* 461–476. doi:10.1016/0014-4835(78)90132-X
46. Gast, R.; Lee, J. *Proc. Natl. Acad. Sci. U. S. A.* **1978,** *75,* 833–837. doi:10.1073/pnas.75.2.833
47. Giurginca, A.; Šustr, V.; Tajovský, K.; Giurginca, M.; Matei, I. *ZooKeys* **2015,** *515,* 111–125. doi:10.3897/zookeys.515.9395
48. Peisker, H.; Michels, J.; Gorb, S. N. *Nat. Commun.* **2013,** *4,* 1661. doi:10.1038/ncomms2576
49. Gorb, S. N.; Filippov, A. E. *Beilstein J. Nanotechnol.* **2014,** *5,* 837–846. doi:10.3762/bjnano.5.95
50. Gorb, S. N. *J. Morphol.* **1996,** *230,* 219–230. doi:10.1002/(SICI)1097-4687(199611)230:2<219::AID-JMOR8>3.0.CO;2-B
51. Edwards, H. A. *J. Exp. Biol.* **1983,** *105,* 407–409.
52. Young, D.; Bennet-Clark, H. C. *J. Exp. Biol.* **1995,** *198,* 1001–1019.
53. Bennet-Clark, H. C. *J. Exp. Biol.* **1997,** *200,* 1681–1694.
54. Skals, N.; Surlykke, A. *J. Exp. Biol.* **1999,** *202,* 2937–2949.
55. Raghu Varman, A. *J. Ga. Entomol. Soc.* **1981,** *16,* 11–13.
56. Raghu Varman, A. *Experientia* **1980,** *36,* 564. doi:10.1007/BF01965802
57. Raghu Varman, A.; Hermann, H. R., Jr. *J. Anim. Morphol. Physiol.* **1982,** *29,* 284–285.
58. Hepburn, H. R.; Levy, P. *J. Entomol. Soc. South. Afr.* **1975,** *38,* 131–141.
59. Vincent, J. F. V. Design for Living: The Elastic-sided Locust. In *The Insect Integument;* Hepburn, H. R., Ed.; Elsevier: Amsterdam, Netherlands, 1976; pp 401–419.
60. Hackman, R. H.; Goldberg, M. *Int. J. Parasitol.* **1985,** *15,* 249–254. doi:10.1016/0020-7519(85)90061-X
61. Richards, A. G.; Richards, P. A. *Int. J. Insect Morphol. Embryol.* **1979,** *8,* 143–157. doi:10.1016/0020-7322(79)90013-8
62. Hepburn, H. R. Structure of the Integument. In *Comprehensive Insect Physiology, Biochemistry and Pharmacology;* Kerkut, G. A.; Gilbert, L. I., Eds.; Pergamon Press: Oxford, United Kingdom, 1985; Vol. 3 (Integument, Respiration and Circulation), pp 1–58. doi:10.1016/b978-0-08-030804-3.50007-8
63. Vincent, J. F. V.; Wood, S. D. E. *Nature* **1972,** *235,* 167–168. doi:10.1038/235167a0
64. Vincent, J. F. V. *Proc. R. Soc. London, Ser. B* **1975,** *188,* 189–201. doi:10.1098/rspb.1975.0012
65. Vincent, J. F. V. *Tissue Cell* **1981,** *13,* 831–853. doi:10.1016/S0040-8166(81)80017-1
66. Hackman, R. H.; Goldberg, M. *J. Insect Physiol.* **1987,** *33,* 39–50. doi:10.1016/0022-1910(87)90102-8
67. Hackman, R. H. *J. Insect Physiol.* **1975,** *21,* 1613–1623. doi:10.1016/0022-1910(75)90199-7
68. Reynolds, S. E. *J. Exp. Biol.* **1975,** *62,* 69–80.
69. Gorb, S. N. *J. Zool.* **2000,** *250,* 479–494. doi:10.1111/j.1469-7998.2000.tb00791.x
70. Rothshild, M.; Schlein, Y.; Parker, K.; Neville, C.; Sternberg, S. *Philos. Trans. R. Soc. London, Ser. B* **1975,** *271,* 499–515.
71. Bennet-Clark, H. C. *J. Exp. Biol.* **1975,** *63,* 53–83.
72. Evans, M. E. G. *J. Zool. (1965-1984)* **1973,** *169,* 181–194.
73. Furth, D. G.; Traub, W.; Harpaz, I. *J. Exp. Zool.* **1983,** *227,* 43–47. doi:10.1002/jez.1402270107
74. Burrows, M. *J. Exp. Biol.* **2012,** *215,* 3612–3621. doi:10.1242/jeb.074682
75. Gronenberg, W. *J. Comp. Physiol., A* **1996,** *178,* 727–734. doi:10.1007/BF00225821
76. Bayley, T. G.; Sutton, G. P.; Burrows, M. *J. Exp. Biol.* **2012,** *215,* 1151–1161. doi:10.1242/jeb.068080
77. Lehmann, F. O.; Gorb, S.; Nasir, N.; Schützner, P. *J. Exp. Biol.* **2011,** *214,* 2949–2961. doi:10.1242/jeb.045351
78. Appel, E.; Gorb, S. N. *Zoologica* **2014,** *159,* 1–159.
79. Appel, E.; Heepe, L.; Lin, C.-P.; Gorb, S. N. *J. Anat.* **2015,** *227,* 561–582. doi:10.1111/joa.12362
80. Neville, A. C. *J. Exp. Biol.* **1960,** *37,* 631–656.
81. King, R. Dynamic Mechanical Properties of Resilin. Master's Thesis, Virginia Polytechnic Institute and State University, Blacksburg, VA, U.S.A., 2010.
82. Weis-Fogh, T. *J. Exp. Biol.* **1973,** *59,* 169–230.
83. Gosline, J.; Lillie, M.; Carrington, E.; Guerette, P.; Ortlepp, C.; Savage, K. *Philos. Trans. R. Soc. London, Ser. B* **2002,** *357,* 121–132. doi:10.1098/rstb.2001.1022
84. Nachtigall, W.; Wisser, A.; Eisinger, D. *J. Comp. Physiol., B* **1998,** *168,* 323–344. doi:10.1007/s003600050152
85. Choudhury, U. Dynamic Mechanical Properties of Cockroach (*Periplanata americana*) Resilin. Master's Thesis, Virginia Polytechnic Institute and State University, Blacksburg, VA, U.S.A., 2012.
86. Newman, D. J. S. *The Functional Wing Morphology of Some Odonata;* University of Exeter: Exeter, United Kingdom, 1982.
87. Rajabi, H.; Ghoroubi, N.; Darvizeh, A.; Dirks, J.-H.; Appel, E.; Gorb, S. N. *Bioinspiration Biomimetics* **2015,** *10,* 056003. doi:10.1088/1748-3190/10/5/056003
88. Rajabi, H.; Shafiei, A.; Darvizeh, A.; Dirks, J.-H.; Appel, E.; Gorb, S. N. *R. Soc. Open Sci.* **2016,** *3,* 160006. doi:10.1098/rsos.160006
89. Mountcastle, A. M.; Combes, S. A. *Proc. R. Soc. London, Ser. B* **2013,** *280,* 20130531. doi:10.1098/rspb.2013.0531
90. Ma, Y.; Ning, J. G.; Ren, H. L.; Zhang, P. F.; Zhao, H. Y. *J. Exp. Biol.* **2015,** *218,* 2136–2142. doi:10.1242/jeb.117325
91. Mountcastle, A. M.; Combes, S. A. *J. Exp. Biol.* **2014,** *217,* 1108–1115. doi:10.1242/jeb.092916
92. Deiters, J.; Kowalczyk, W.; Seidl, T. *Biol. Open* **2016,** *5,* 638–644. doi:10.1242/bio.016527
93. Haas, F.; Hwen, J. T. C.; Tang, H. B. *Arthropod Syst. Phylog.* **2012,** *70,* 95–105.
94. Wootton, R. J. *Annu. Rev. Entomol.* **1992,** *37,* 113–140. doi:10.1146/annurev.en.37.010192.000553
95. Haas, F.; Beutel, R. G. *Zoology (Munich, Ger.)* **2001,** *104,* 123–141.
96. Sun, J.; Ling, M.; Wu, W.; Bhushan, B.; Tong, J. *Int. J. Mol. Sci.* **2014,** *15,* 6009–6018. doi:10.3390/ijms15046009
97. Gorb, S. N. *Attachment Devices of Insect Cuticle;* Kluwer Academic Publishers: Dordrecht, Netherlands, 2001.

98. Gorb, S.; Beutel, R. *Naturwissenschaften* **2001,** *88,* 530–534. doi:10.1007/s00114-001-0274-y
99. Gorb, S. N.; Beutel, R. G.; Gorb, E. V.; Jiao, Y.; Kastner, V.; Niederegger, S.; Popov, V. L.; Scherge, M.; Schwarz, U.; Vötsch, W. *Integr. Comp. Biol.* **2002,** *42,* 1127–1139. doi:10.1093/icb/42.6.1127
100. Creton, C.; Gorb, S. *MRS Bull.* **2007,** *32,* 466–472. doi:10.1557/mrs2007.79
101. Voigt, D.; Schuppert, J. M.; Dattinger, S.; Gorb, S. N. *J. Insect Physiol.* **2008,** *54,* 765–776. doi:10.1016/j.jinsphys.2008.02.006
102. Hui, C.-Y.; Glassmaker, N. J.; Tang, T.; Jagota, A. *J. R. Soc., Interface* **2004,** *1,* 35–48. doi:10.1098/rsif.2004.0005
103. Varenberg, M.; Pugno, N. M.; Gorb, S. N. *Soft Matter* **2010,** *6,* 3269–3272. doi:10.1039/c003207g
104. Filippov, A.; Popov, V. L.; Gorb, S. N. *J. Theor. Biol.* **2011,** *276,* 126–131. doi:10.1016/j.jtbi.2011.01.049
105. Borodich, F. M.; Gorb, E. V.; Gorb, S. N. *Appl. Phys. A* **2010,** *100,* 63–71. doi:10.1007/s00339-010-5794-x
106. Jagota, A.; Bennison, S. J. *Integr. Comp. Biol.* **2002,** *42,* 1140–1145. doi:10.1093/icb/42.6.1140
107. Spolenak, R.; Gorb, S.; Arzt, E. *Acta Biomater.* **2005,** *1,* 5–13. doi:10.1016/j.actbio.2004.08.004
108. Gorb, S. N. Smooth Attachment Devices in Insects. In *Advances in Insect Physiology: Insect Mechanics and Control;* Casas, J.; Simpson, S. J., Eds.; Elsevier: London, United Kingdom, 2008; pp 81–116.
109. Edwards, J. S. Predation and Digestion in Assassin Bugs (Heteroptera, Reduviidae). Ph.D. Thesis, University of Cambridge, Cambridge, United Kingdom, 1960.
110. Bennet-Clark, H. *J. Exp. Biol.* **2007,** *210,* 3879–3881. doi:10.1242/jeb.001339
111. Bennet-Clark, H. C. *J. Exp. Biol.* **1963,** *40,* 223–229.
112. Burrows, M. *BMC Biol.* **2009,** *7,* 27. doi:10.1186/1741-7007-7-27
113. Krenn, H. W. *Zoomorphology* **1990,** *110,* 105–114. doi:10.1007/BF01632816
114. Eastham, L. E. S.; Eassa, Y. E. E. *Philos. Trans. R. Soc. London, Ser. B* **1955,** *239,* 1–43. doi:10.1098/rstb.1955.0005
115. Hepburn, H. R. *J. Insect Physiol.* **1971,** *17,* 637–656. doi:10.1016/0022-1910(71)90114-4
116. Betz, O.; Koerner, L.; Gorb, S. N. *Adhes. Adhes. Sealants* **2009,** *6,* 32–35.
117. Koerner, L.; Gorb, S. N.; Betz, O. *J. Insect Physiol.* **2012,** *58,* 155–163. doi:10.1016/j.jinsphys.2011.11.001
118. Koerner, L.; Gorb, S. N.; Betz, O. *Zoology (Munich, Ger.)* **2012,** *115,* 117–127.
119. Longhurst, A. R. *Prog. Oceanogr.* **1985,** *15,* 1–35. doi:10.1016/0079-6611(85)90036-9
120. Huys, R.; Boxshall, G. A. *Copepod Evolution;* The Ray Society: London, United Kingdom, 1991.
121. Michels, J.; Schnack-Schiel, S. B. *Mar. Biol. (Heidelberg, Ger.)* **2005,** *146,* 483–495.
122. Michels, J.; Gorb, S. N. *Beilstein J. Nanotechnol.* **2015,** *6,* 674–685. doi:10.3762/bjnano.6.68
123. Carayon, J. Traumatic Insemination and the Paragenital System. In *Monograph of Cimicidae (Hemiptera-Heteroptera);* Usinger, R. L., Ed.; Entomological Society of America: Lanham, MD, U.S.A., 1966; pp 81–166.
124. Stutt, A. D.; Siva-Jothy, M. T. *Proc. Natl. Acad. Sci. U. S. A.* **2001,** *98,* 5683–5687. doi:10.1073/pnas.101440698
125. Reinhardt, K.; Naylor, R.; Siva-Jothy, M. T. *Evolution* **2009,** *63,* 29–39. doi:10.1111/j.1558-5646.2008.00502.x
126. Michels, J.; Gorb, S. N.; Reinhardt, K. *J. R. Soc., Interface* **2015,** *12,* 20141107. doi:10.1098/rsif.2014.1107
127. Thurm, U. *Science* **1964,** *145,* 1063–1065. doi:10.1126/science.145.3636.1063
128. Heusslein, R.; Gnatzy, W. *Cell Tissue Res.* **1987,** *247,* 591–598. doi:10.1007/BF00215753
129. Keil, T. A. *Microsc. Res. Tech.* **1997,** *39,* 506–531. doi:10.1002/(SICI)1097-0029(19971215)39:6<506::AID-JEMT5>3.0.CO;2-B
130. Heußlein, R.; Gras, H.; Gnatzy, W. Functional Coupling of Cercal Filiform Hairs and Campaniform Sensilla in Crickets. In *Functional Surfaces in Biology;* Gorb, S. N., Ed.; Springer: Dordrecht, Netherlands, 2009; Vol. 1 (Little Structures with Big Effects), pp 203–233. doi:10.1007/978-1-4020-6697-9_12
131. Sannasi, A. *Experientia* **1970,** *26,* 154. doi:10.1007/BF01895549
132. Jaganathan, R.; Sundara Rajulu, G. *Indian Zool.* **1979,** *3,* 133–134.
133. Dey, S.; Raghuvarman, A. *Indian Zool.* **1983,** *7,* 31–34.
134. Viswanathan, S.; Varadaraj, G. *Odonatologica* **1985,** *14,* 155–157.

License and Terms

BEILSTEIN JOURNAL OF NANOTECHNOLOGY

Influence of ambient humidity on the attachment ability of ladybird beetles (*Coccinella septempunctata*)

Lars Heepe[‡1,2], Jonas O. Wolff[‡1,3] and Stanislav N. Gorb[*1]

Full Research Paper

Open Access

Address:
[1]Department of Functional Morphology and Biomechanics, Kiel University, Am Botanischen Garten 1–9, D-24118 Kiel, Germany, [2]Mads Clausen Institute, University of Southern Denmark, NanoSYD Alsion 2, 6400 Sønderborg, Denmark and [3]Department of Biological Sciences, Macquarie University, Sydney, NSW 2109, Australia

Email:
Stanislav N. Gorb[*] - sgorb@zoologie.uni-kiel.de

* Corresponding author ‡ Equal contributors

Keywords:
adhesion; beetle; biomechanics; force measurement; friction; insect; locomotion; surface

Beilstein J. Nanotechnol. **2016,** *7,* 1322–1329.
doi:10.3762/bjnano.7.123

Received: 14 June 2016
Accepted: 09 September 2016
Published: 22 September 2016

This article is part of the Thematic Series "Biological and biomimetic materials".

Associate Editor: K. Koch

Abstract

Many insects possess adhesive foot pads, which enable them to scale smooth vertical surfaces. The function of these organs may be highly affected by environmental conditions. Ladybird beetles (Coccinellidae) possess dense tarsal soles of tenent setae, supplemented with an adhesive fluid. We studied the attachment ability of the seven-spotted ladybird beetle (*Coccinella septempunctata*) at different humidities by horizontal traction experiments. We found that both low (15%) and high (99%) relative humidities lead to a decrease of attachment ability. The significantly highest attachment forces were revealed at 60% humidity. This relationship was found both in female and male beetles, despite of a deviating structure of adhesive setae and a significant difference in forces between sexes. These findings demonstrate that not only dry adhesive setae are affected by ambient humidity, but also setae that stick due to the capillarity of an oily secretion.

Introduction

Substrate attachment plays an important role in the niche occupation of plant-dwelling insects, since it is substantial for resting and locomotion in a complex environment. Consequently, a high diversity of friction and adhesion enhancing structures has evolved among insects [1,2]. Several studies showed that not only the intrinsic structure of an attachment organ determines its function, but also environmental parameters, such as the surface roughness or/and chemistry of the substrate [1,3-9]. Also the ambient temperature and humidity may affect the attachment ability of adhesive organs, as it was shown in the dry adhesive pads of geckoes [10-13] and spiders [14]. For small arthropods these conditions may highly vary microspatially, especially in the boundary layer of plant leaves [15]. Furthermore, on most surfaces there is an adsorbed film of

water molecules, with a thickness and mechanical properties highly influenced by ambient humidity [16,17]. Due to its polarity it can work as a bonding agent between two surfaces, and therefore have a substantial effect on adhesion [18-21]. In insects the terminal contact elements of tenent setae are not dry, but rather wetted by a fluid secretion that is usually a microemulsion of water and oil, with varying fractions of substances [22-31]. The mixture of both polar and non-polar substances presumably helps to wet both hydrophobic and hydrophilic surfaces building a fluid meniscus between the seta and the substrate to yield high capillary forces (wet adhesion). The fluid can increase the contact area by filling minute cavities of micro- and nano-rough surfaces, where setae otherwise cannot adapt to, and prevents slipping of the foot due to its specific rheological properties [31-35]. It was demonstrated that the presence of these secretions is crucial for the function of insect adhesive organs [6,36]. Adhesion is affected, if the water content of the secretion is manipulated by a water adsorbing substrate [28]. However, it is not clear, how the thickness and composition of the secretion fluid film are affected by ambient humidity.

In the present study, force measurements with tethered seven-spotted ladybirds (*Coccinella septempunctata*) were carried out in an environmental chamber at various controlled humidities. Experiments were carried out with female and male beetles, which differ in the structure of their adhesive pads [6]. Males possess tenent setae with discoidal tips that are assumed to be an adaptation to securely attach to the smooth elytrae of the female during both copulation and mate guarding [6,37]. Two main questions were asked. (1) Does ambient humidity influence the attachment ability of the wet adhesive system of *C. septempunctata*? (2) Is the attachment ability in both sexes likewise affected by ambient humidity?

Experimental

Animals

For this study, the seven-spotted ladybird beetle *Coccinella septempunctata* LINNAEUS 1758 (Coleoptera, Coccinellidae) was chosen (Figure 1A). This beetle species is a generalist, living on diverse plant surfaces [38,39]. In their natural environment, beetles are exposed to various humidities, hence, their adhesive system must be well adapted to changing environmental conditions. Beetles were collected from bracken (*Pteridium aquilinum*) in the New Botanical Garden at Kiel University, Schleswig-Holstein, Germany. They were kept individually in plastic tubes at a temperature of 22–24 °C and relative humidity of 40–50%. These conditions were consistent with those at which the beetles were captured. The beetles were fed with honey. Figure 1 shows the hairy attachment devices of *C. septempunctata*. The tarsus is composed of three tarsomeres

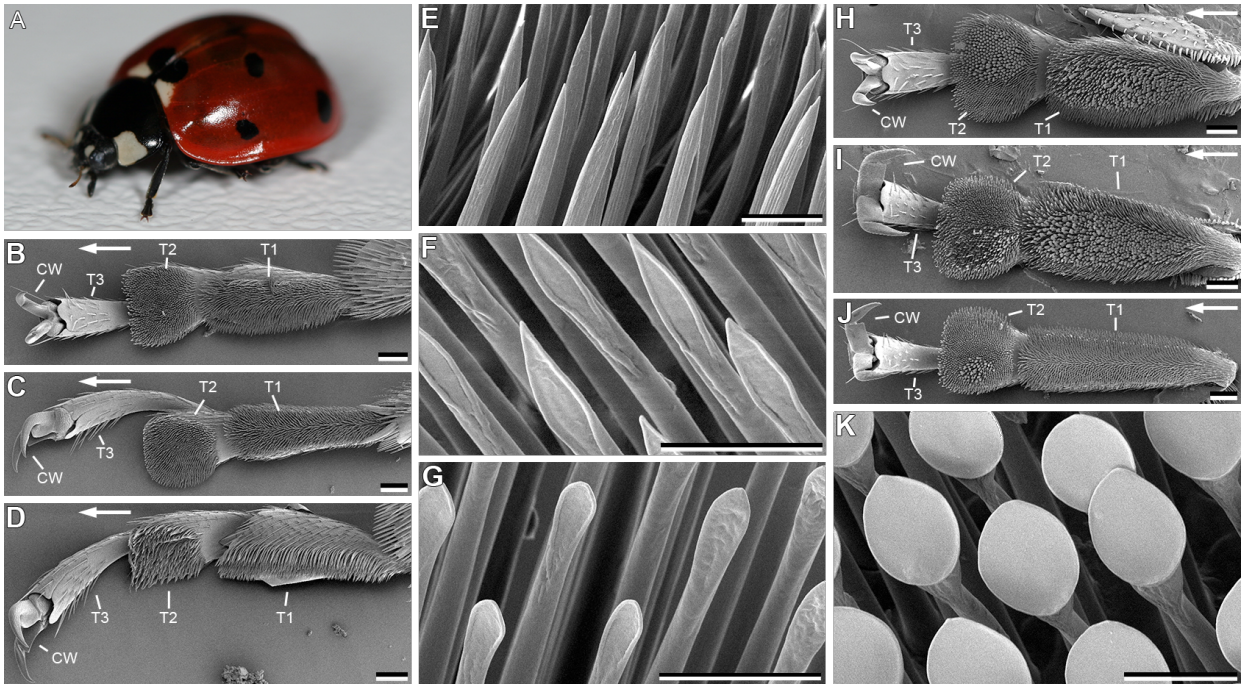

Figure 1: Attachment devices of *Coccinella septempuctata* (A) attachment devices. Tarsi of forelegs (B), midlegs (C), and hindlegs (D) in females are ventrally covered by different types of tenent setae (E–G). Tarsi of forelegs (H), midlegs (I), and hindlegs (J) in males. Tarsi of males were also ventrally covered by tenet setae types shown in (E, F), but have an additional type, which is terminated with discoidal terminal elements (K). CW, claws; T1, first proximal tarsomer; T2, second proximal tarsomer; T3, third proximal tarsomer. The arrows in (B–D) and (H–J) indicate distal direction. Scale bars in (B–D, H–J), 100 µm. Scale bars in (E–G, K), 10 µm.

and two ventrally curved claws (Figure 1B–D,H–J). Only the first two tarsomeres (T1 and T2 in Figure 1) are ventrally covered by tenent setae. Different types of tarsal adhesive setae were distinguished: (1) setae with a pointed, filamentous tips (Figure 1E), (2) setae with lanceolate tips (Figure 1F), (3) setae with a flattened and rounded, spatula-shaped tips (Figure 1G), and (4) setae terminated with discoidal terminal elements (Figure 1K). All four types of tarsal adhesive setae were found in males. Females show the first three types only. Setae terminated with discoidal terminal elements were found in the centre of the first two tarsomeres (T1 and T2 in Figure 1) for all legs in males (Figure 1H–J), except for the first tarsomer (T1) of the hindleg (Figure 1J).

Force measurements in a controlled atmosphere

Traction force experiments were performed in a polymethylmethacrylate (PMMA) chamber (30 × 14 × 14 cm) in which relative humidity could be manipulated by the controlled mixture of dry and wetted air (Figure 2, for details see [14]).

For this experiment, three levels of relative humidity (RH) were used: 15%, 60% and 99%. The RH was monitored with a P330 digital hygrometer (Dostmann electronic GmbH, Wertheim-Reicholzheim, Germany). To generate humid conditions, air was passed through a water bottle, so that the vapour concentration in the air increased. To reach 99% of relative humidity, slight heating was used to increase the amount of water vapour. This did not affect the temperature within the experimentation chamber. To generate a dry environment, dry air from a pressurized air pipe was pumped into the experimentation box. To stabilize ambient humidity and the thickness of adsorbed water films, the procedure was started about one hour before the experiments.

A strain-gauge force transducer (10 g capacity; World Precision Instruments, Inc., FL, USA) connected to a Biopac MP100 amplifier (Biopac System Inc., Goleta, CA, USA) was used to measure forces generated by the beetles. Force data were recorded with the AcqKnowledge 3.7.0 software (Biopac Systems Inc.). A half Plexiglas tube was installed inside the chamber, in order to guide beetle locomotion perpendicular to the force sensor and prevent it from climbing onto the lateral walls.

Prior to experiments the beetles were anesthetized with carbon dioxide and the elytra were glued together with a droplet of molten wax, to prevent them from flying (for details see [40]). Individual beetles were connected to the force transducer by a human hair (10–15 cm long) fixed to the elytra and to the force sensor with a droplet of molten wax. Beetles were placed on the Plexiglas bottom of the experimentation chamber and released such that they walk perpendicularly away from the force sensor. When the beetles were hold back by the strengthened hair they tried to pull forward, which led to transmission of traction forces to the force sensor. The traction force is dependent on the attachment ability of the pulling animal. This method has been used in previous studies [7,14,40]. We let the beetle pull for one minute and then repeated the experiment in a second run, to make sure that the performance of individual animals was stable. In total, 10 runs for each individual beetle for one minute at each of three humidity conditions were recorded.

The experiment was carried out in two different runs. The first run was done with 15 beetles (4 females and 11 males). All beetles were tested with one single level of humidity per day, further called Experiment 1. To exclude an influence of physiological conditions of individual animals on different experimental days, a second run was executed. In this run, 9 beetles

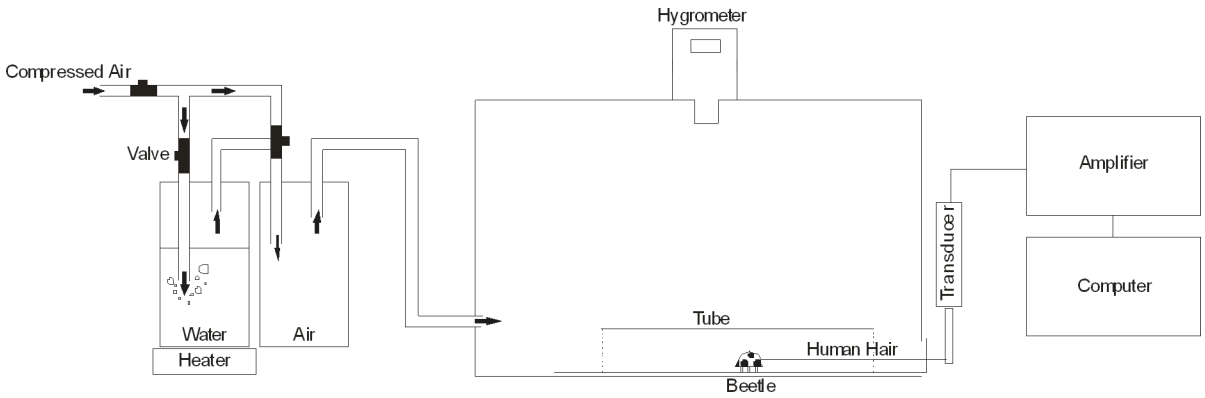

Figure 2: Schematic of the experimental setup used for traction force experiments under controlled ambient humidities. Tethered beetles were connected to a force sensor by a 15–20 cm long human hair. Humidity was controlled by mixing dry compressed air (approx. 15% relative humidity) and wet air. Wet air was produced by heating water in a glass bottle, in order to increase the amount of water vapour. Temperature was continuously monitored in the chamber to ensure that the use of the heater did not lead to temperature increase within the chamber. For details, see [14].

(3 females and 6 males) were tested. Individual beetles were tested on one day at all three levels of relative humidity in a randomized fashion, further called Experiment 2. To evaluate the effect of the relative humidity on attachment force in both sexes of *C. septempunctata*, a Kruskal–Wallis One Way ANOVA on Ranks followed by an all pairwise multiple comparison procedure (Tukey Test, SigmaPlot 11.0, Systat Software Inc, San José, CA, USA) has been performed. In order to evaluate the effect of sex on the attachment force, a Mann–Whitney Rank Sum Test has been applied to the pooled data. Therefore, the data of the different relative humidity has been pooled individually for both experiments and sexes.

Observations of the beetle behaviour at different relative humidities

A Plexiglas sheet was fixed with double side adhesive tape at three different positions: horizontal (0°), vertical (90°) and upside-down (180°) inside the experimentation chamber. We observed the locomotion behaviour of individual beetles on these surfaces. Additionally, to the three previously used humidity adjustments (RH of 15%, 60% and 99%), we made some observations at RH higher than 99%, when water began to condense on the substrate.

Results

Observational experiments

We observed that the beetle's attachment is affected, as the water begins to condense on the substrate, when the relative humidity exceeds 99%. In this case, beetles were not able to hold on the vertical Plexiglas slide and slid along its surface.

Experiment 1: One level of relative humidity per day

The attachment ability of beetles was highest at an RH of 60% and lower for RH of 15% and 99% (Figure 3). Here and later data will be shown as median [minimum, maximum]. At an RH of 15%, females reached the median force of 6.9 mN [2.7 mN, 12.4 mN]. At an RH of 60%, the median force was 11.2 mN [1.9 mN, 18.6 mN]. At an RH of 99%, the median force was 5.5 mN [2.0 mN, 17.5 mN]. The forces measured at different RH differed significantly (Kruskal–Wallis One Way ANOVA on Ranks: $N = 40$; $H = 30.035$; $df = 2$; $P \leq 0.001$). An all pairwise comparison (Tukey Test, see Table 1) revealed significant differences in measured traction forces between 15% RH and 60% RH as well as between 60% RH and 99% RH, but not between 15% RH and 99% RH.

At an RH of 15%, males reached the median force of 16.7 mN [8.1 mN, 23.4 mN]. At an RH of 60%, the median force was 22.4 mN [11.7 mN, 31.4 mN]. At an RH of 99%, the median force was 17.7 mN [8.2 mN, 27.0 mN]. The forces measured at different RH differed significantly (Kruskal–Wallis One Way ANOVA on Ranks: $N = 110$; $H = 133.1$; $df = 2$; $P \leq 0.001$). An all pairwise comparison (Tukey Test, see Table 1) revealed significant differences in measured traction forces for all levels of RH.

Experiment 2: Three levels of relative humidity per day

Similar to the first experiment, highest median attachment forces were observed at 60% RH (Figure 4). At an RH of 15%, females reached the median force of 7.1 mN [5.5 mN, 9.9 mN].

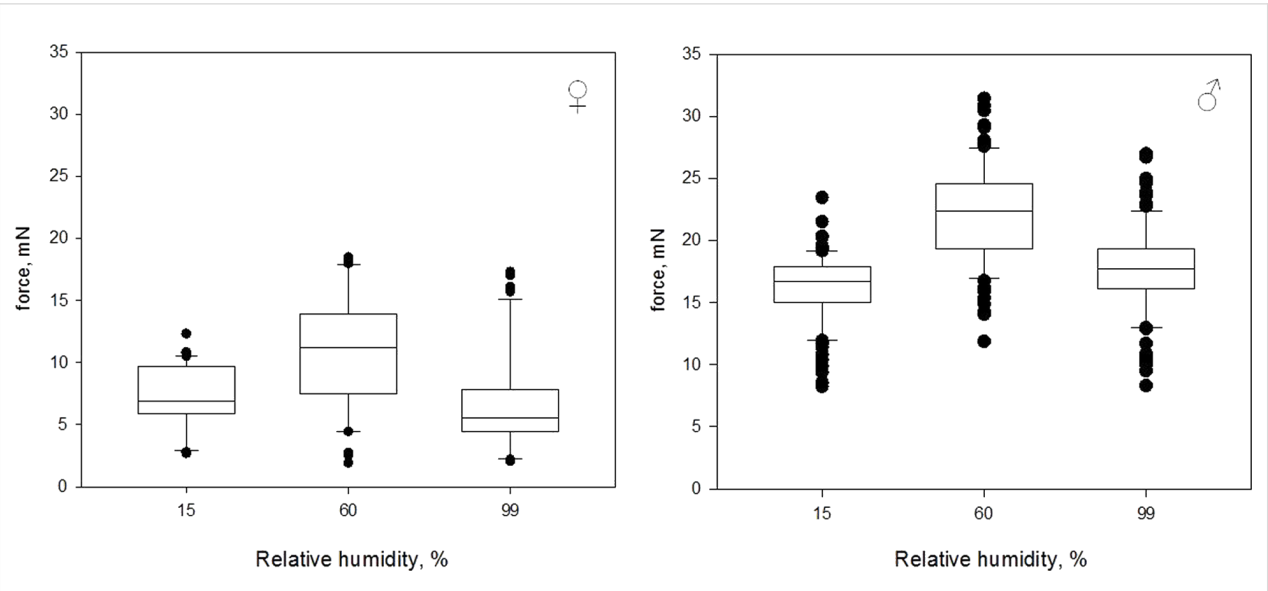

Figure 3: Box-and-whiskers plots, based on the results of the first experiment, with one RH level tested per day. The ends of the boxes define the 25th and 75th percentiles, with a line at the median and error bars defining the 10th and 90th percentiles, black dots represent the outliers.

Table 1: Statistics of the traction force measurements.

sex	humidity	Experiment	q-value	significance
female[a]	15% versus 60%	1	5.200	yes
female[a]	15% versus 99%	1	2.377	no
female[a]	60% versus 99%	1	7.577	yes
male[b]	15% versus 60%	1	15.634	yes
male[b]	15% versus 99%	1	3.776	yes
male[b]	60% versus 99%	1	11.858	yes
female[c]	15% versus 60%	2	6.003	yes
female[c]	15% versus 99%	2	3.473	yes
female[c]	60% versus 99%	2	2.530	no
male[d]	15% versus 60%	2	4.311	yes
male[d]	15% versus 99%	2	3.806	yes
male[d]	60% versus 99%	2	8.117	yes
female versus male[e]	pooled	1	$P < 0.001$	yes
female versus male[f]	pooled	2	$P < 0.001$	yes

[a–d]Kruskal–Wallis One Way ANOVA on Ranks with an all pairwise multiple comparison (Tukey Test). [e,f]Mann–Whitney Rank Sum Test.

At an RH of 60%, the median force was 8.8 mN [5.3 mN, 11.0 mN]. At an RH of 99%, the median force was 8.5 mN [1.6 mN, 11.3 mN]. The forces measured at different RH differed significantly (Kruskal–Wallis One Way ANOVA on Ranks: $N = 30$, $H = 18.167$, $df = 2$, $P \leq 0.001$). An all pairwise comparison (Tukey Test, see Table 1) revealed significant differences in measured traction forces between 15% RH and 60% RH as well as between 15% RH and 99% RH, but not between 60% RH and 99% RH.

At an RH of 15%, males reached the median force of 16.2 mN [13.2 mN, 20.4 mN]. At an RH of 60%, the median force was 17.2 mN [13.1 mN, 20.4 mN]. At an RH of 99%, the median force was 15.2 mN [11.6 mN, 19.1 mN]. The forces measured at different RH differed significantly (Kruskal–Wallis One Way ANOVA on Ranks: $N = 60$, $H = 32.984$, $df = 2$, $P \leq 0.001$). An all pairwise comparison (Tukey Test, see Table 1) revealed significant differences in measured traction forces for all levels of RH.

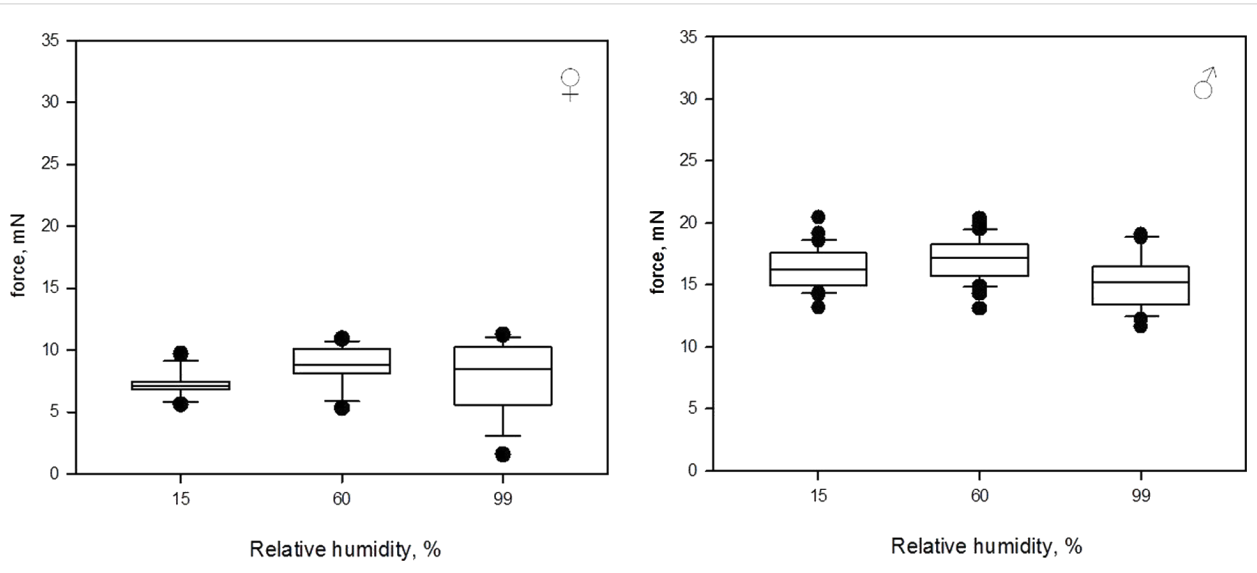

Figure 4: Box-and-whiskers diagrams based on the results of the second experiment with all three levels of RH tested at the same day. The ends of the boxes define the 25th and 75th percentiles, with a line at the median and error bars defining the 10th and 90th percentiles, black dots represent the outliers.

Effect of sex

A significant difference was detected between sexes ($P < 0.001$, Mann–Whitney Rank Sum Test, see Table 1), where males achieved two times higher forces than females at all three levels of RH. Thereby, the attachment ability of both males and females was likewise affected by ambient humidity.

Discussion

The present study demonstrates, for the first time, that the performance of a wet (fluid supplemented) adhesive pad is influenced by ambient humidity. Our results indicate an optimal range of relative humidity with maximal traction forces in ladybird beetles. Similar observations have been made in dry adhesive pads of spiders, using a similar setup and method as in the present study [14], and geckos, revealed in measurements with living animals [11] and with isolated setae [10]. This is particularly interesting since both types of adhesive systems (wet and dry) are supposed to be based on different physical interactions (capillarity versus van der Waals forces).

For the dry adhesive pads of spiders and geckos the humidity-related effects on adhesion can be explained by three different mechanisms: (1) capillary forces due to the formation of liquid bridges; (2) changes in the effective short-range interactions due to adsorbed monolayers of water on the substrate [11,14]; (3) humidity-dependent material properties of insect cuticle and β-keratin (main constituent of gecko setae) [41-44]. In geckos, the effect of a RH on viscoelastic properties of the setal shaft was shown [13]. It was argued that with an increasing humidity the viscoelastic bulk energy dissipation increases within setae while being pulled off the substrate, leading to higher resistance of the adhesive contact [12,45].

For *C. septempunctata* it was recently shown that the setal tips contain high amounts of the soft rubber-like protein resilin [46], which is a hygroscopic protein capable of binding high amounts of water [47]. Peisker et al. [46] showed a 6000-fold increase in the Young's modulus of the setal tips after drying. Consequently, the degree of hydration should also significantly affect the mechanical properties of the setae of the beetles in the present study and may also explain our results on ladybird beetles, at least the increase in traction forces from 15% RH to 60% RH.

Two other observations may further support the hypothesis that a change in material properties with increasing humidity is responsible for at least the increase in traction forces from 15% RH to 60% RH. Voigt et al. [48] observed significantly higher forces generated by beetles (*Leptinotarsa decemlineata*) on a dry surface, which were kept prior the experiment under humid conditions if compared to beetles kept prior the experiment under dry conditions. In the present study we observed a distinct difference between both types of experiments (Experiment 1 and 2). The differences between the measured traction forces, although significant, are smaller in case of all humidity levels measured on one day (Experiment 2), than in the case of one humidity level measured per day (Experiment 1). Since in Experiment 2 the humidity levels were randomized for individual runs, there were some beetles that were measured first at higher humidity and then at lower humidity. In combination with relatively short durations between individual runs, those individuals, according to the idea of changing material properties, should then show a better performance also at the lower humidity level if compared to Experiment 1, thus, reducing the observable differences between different humidity levels.

Although the hypothesis of changing material properties seems to be quite plausible, there are also several aspects speaking against it. The tarsal secretions in hairy attachment pads of beetles were found to be mainly lipid-based [22,26,27,49,50], with only a small volatile fraction (likely water) [30]. Peisker et al. [46] speculated that these secretions may have an additional function, apart from forming capillary bridges, which is to cover setal tips and thereby preventing the desiccation of setal tips, thus, keeping them in a soft rubber-like state. In this light, it seems unlikely that the setal tips absorb water from ambient humidity. However, this hypothesis has not been confirmed so far and little is known about where tarsal liquids are actually secreted and delivered in hairy attachment pads of beetles. Moreover, assuming capillarity to be responsible for the generated traction forces, it is not clear how the proposed increase in the viscoelastic bulk energy dissipation with increasing humidity should affect the attachment ability in this case, since the contact is mediated by the tarsal secretion and not by a solid–solid contact.

Coming back to the abovementioned mechanisms of capillary forces and/or changes in the effective short-range van der Waals interaction, which might influence the humidity dependent adhesion in geckos [10], it needs to be mentioned that both mechanisms require water to be present at the contact interface. It can be either absorbed water on the substrate, whose actual amount depends on the relative humidity and on the surface chemistry [19,51] or capillary condensation [52]. Due to the high content of lipids in the tarsal secretions of the beetles, a direct effect of water capillary bridges can be neglected. Though, it cannot totally be excluded that the composition and properties of the tarsal secretion are altered by ambient humidity. Thus, for example, different contributions from viscous forces could be expected [31,53]. For *C. septempunctata*, viscosity of the tarsal secretion was found to be of order 20 mPa·s [31] and droplets of volumes around 1 fL of the tarsal

secretion made contact angles smaller than 10° with freshly cleaved mica surfaces (calculation based on droplet geometries reported in [30]). Moreover, it is known that micro-emulsions may have complex structures depending on the particular water-to-oil ratio [54], which might also have significant effects on beetle adhesion. Indeed, it has been shown that the adhesive pad fluids of insects contain minute droplets of water that are crucial for the function of the adhesive system [28].

The reduction in traction forces observed in the present study at 99% RH (without visible water condensation) may be explained by a sufficient amount of adsorbed water on the substrate. It has been shown that the friction behaviour between two solids crucially depends on the water layer thickness between them [55]. At critical thickness of adsorbed monolayers water becomes liquid-like, which may render the onset of an "aquaplaning effect". Accordingly, in adhesion experiments of setal pads, adhesion rapidly dropped as soon as water condensation became visible on the substrate or moistening of substrate and/or pad surface ([14,56] and this study).

In nature, animals are constantly exposed to certain humidity. Most of insects live on plants containing a humid boundary layer in the vicinity of the plant surface. The humidity close to leaf surfaces ranges between 30% and 75% [57]. It is probable that the insects' adhesive pad is adapted to work most efficient under these conditions.

Finally, comparing absolute values in the attachment forces of *C. septempunctata* beetles, we found evidence for a sexual dimorphism. Male beetles generated higher adhesion than females, which was previously reported and explained by the presence of specialized setae with discoidal tips that can generate higher adhesion on smooth substrates due to their advantageous, geometry-induced homogenous stress distribution [58-60]. Similar results were previously obtained for chysomelid beetles [5,61]. The dimorphism is explained by the need of males to stay attached to the smooth elytrae of females during copulation and mate guarding. However, the attachment ability of males and females is similarly affected by humidity and, thus, underlying mechanisms of humidity dependent adhesion seem to be similar in both sexes.

Conclusion

The present study demonstrates, for the first time, the effect of ambient humidity on a wet adhesive pad that is supplemented by a lipid-based secretion. This shows that humidity similarly affects the function of both dry and wet adhesive pads. However, the underlying mechanisms leading to this effect remain unclear. To be able to distinguish between different mechanisms (changing material properties, water layer thickness, changing tarsal secretion properties), experiments with substrates of different surface free energy should be performed in the future.

Acknowledgements

The authors like to thank J. Oesert, L. Reichel and H. Peisker for help with the experimental setup. V. Kastner (Max Planck Institute for Metals Research, Stuttgart, Germany) and U. Köhler are acknowledged for improvement of language of an early version of the manuscript.

References

1. Gorb, S. N. *Attachment devices of insect cuticle;* Kluwer Academic Publishers: Dordrecht, Boston, London, 2001.
2. Gorb, S. N.; Beutel, R. G. *Naturwissenschaften* **2001,** *88,* 530–534. doi:10.1007/s00114-001-0274-y
3. Gorb, S. N.; Beutel, R. G.; Gorb, E. V.; Jiao, Y.; Kastner, V.; Niederegger, S.; Popov, V. L.; Scherge, M.; Schwarz, U.; Vötsch, W. *Integr. Comp. Biol.* **2002,** *42,* 1127–1139. doi:10.1093/icb/42.6.1127
4. Federle, W. *J. Exp. Biol.* **2006,** *209,* 2611–2621. doi:10.1242/jeb.02323
5. Voigt, D.; Schuppert, J. M.; Dattinger, S.; Gorb, S. N. *J. Insect Physiol.* **2008,** *54,* 765–776. doi:10.1016/j.jinsphys.2008.02.006
6. Gorb, E. V.; Hosoda, N.; Miksch, C.; Gorb, S. N. *J. R. Soc., Interface* **2010,** *7,* 1571–1579. doi:10.1098/rsif.2010.0081
7. Wolff, J. O.; Gorb, S. N. *J. Exp. Biol.* **2012,** *215,* 179–184. doi:10.1242/jeb.061507
8. Prüm, B.; Bohn, H. F.; Seidel, R.; Rubach, S.; Speck, T. *Acta Biomater.* **2013,** *9,* 6360–6368. doi:10.1016/j.actbio.2013.01.030
9. Grohmann, C.; Blankenstein, A.; Koops, S.; Gorb, S. N. *J. Exp. Biol.* **2014,** *217,* 4213–4220. doi:10.1242/jeb.108902
10. Huber, G.; Mantz, H.; Spolenak, R.; Mecke, K.; Jacobs, K.; Gorb, S. N.; Arzt, E. *Proc. Natl. Acad. Sci. U. S. A.* **2005,** *102,* 16293–16296. doi:10.1073/pnas.0506328102
11. Niewiarowski, P. H.; Lopez, S.; Ge, L.; Hagan, E.; Dhinojwala, A. *PLoS One* **2008,** *3,* e2192. doi:10.1371/journal.pone.0002192
12. Puthoff, J. B.; Prowse, M. S.; Wilkinson, M.; Autumn, K. *J. Exp. Biol.* **2010,** *213,* 3699–3704. doi:10.1242/jeb.047654
13. Prowse, M. S.; Wilkinson, M.; Puthoff, J. B.; Mayer, G.; Autumn, K. *Acta Biomater.* **2011,** *7,* 733–738. doi:10.1016/j.actbio.2010.09.036
14. Wolff, J. O.; Gorb, S. N. *Proc. R. Soc. London, Ser. B* **2011,** *279,* 139–143. doi:10.1098/rspb.2011.0505
15. Ferro, D. N.; Southwick, E. E. *Environ. Entomol.* **1984,** *13,* 926–929. doi:10.1093/ee/13.4.926
16. Miranda, P. B.; Xu, L.; Shen, Y. R.; Salmeron, M. *Phys. Rev. Lett.* **1998,** *81,* 5876. doi:10.1103/PhysRevLett.81.5876
17. Asay, D. B.; Kim, S. H. *J. Phys. Chem. B* **2005,** *109,* 16760–16763. doi:10.1021/jp053042o
18. Binggeli, M.; Mate, C. M. *Appl. Phys. Lett.* **1994,** *65,* 415. doi:10.1063/1.113020
19. Xiao, X.; Qian, L. *Langmuir* **2000,** *16,* 8153–8158. doi:10.1021/la000770o
20. Jang, J.; Schatz, G. C.; Ratner, M. A. *J. Chem. Phys.* **2004,** *120,* 1157. doi:10.1063/1.1640332
21. Asay, D. B.; Kim, S. H. *J. Chem. Phys.* **2006,** *124,* 174712. doi:10.1063/1.2192510
22. Ishii, S. *Appl. Entomol. Zool.* **1987,** *22,* 222–228.
23. Eisner, T.; Anesnansley, D. J. *Proc. Natl. Acad. Sci. U. S. A.* **2000,** *97,* 6568–6573. doi:10.1073/pnas.97.12.6568

24. Vötsch, W.; Nicholson, G.; Müller, R.; Stierhof, Y.-D.; Gorb, S. N.; Schwarz, U. *Insect Biochem. Mol. Biol.* **2002,** *32,* 1605–1613. doi:10.1016/S0965-1748(02)00098-X
25. Langer, M. G.; Ruppersberg, J. P.; Gorb, S. N. *Proc. R. Soc. London, Ser. B* **2004,** *271,* 2209–2215. doi:10.1098/rspb.2004.2850
26. Geiselhardt, S. F.; Geiselhardt, S.; Peschke, K. *Chemoecology* **2009,** *19,* 185–193. doi:10.1007/s00049-009-0021-y
27. Geiselhardt, S. F.; Federle, W.; Prüm, B.; Geiselhardt, S.; Lamm, S.; Peschke, K. *J. Insect Physiol.* **2010,** *56,* 398–404. doi:10.1016/j.jinsphys.2009.11.016
28. Dirks, J.-H.; Clemente, C. J.; Federle, W. *J. R. Soc., Interface* **2010,** *7,* 587–593. doi:10.1098/rsif.2009.0308
29. Betz, O. Adhesive exocrine glands in insects: morphology, ultrastructure, and adhesive secretion. In *Biological adhesive systems. From nature to technical and medical application;* Byern, J.; Grunwald, I., Eds.; Springer: Vienna, Austria, 2010; pp 111–152. doi:10.1007/978-3-7091-0286-2_8
30. Peisker, H.; Gorb, S. N. *J. Exp. Biol.* **2012,** *215,* 1266–1271. doi:10.1242/jeb.065722
31. Peisker, H.; Heepe, L.; Kovalev, A. E.; Gorb, S. N. *J. R. Soc., Interface* **2014,** *11,* 20140752. doi:10.1098/rsif.2014.0752
32. Abou, B.; Gay, C.; Laurent, B.; Cardoso, O.; Voigt, D.; Peisker, H.; Gorb, S. N. *J. R. Soc., Interface* **2010,** *7,* 1745–1752. doi:10.1098/rsif.2010.0075
33. Dirks, J.-H.; Federle, W. *Soft Matter* **2011,** *7,* 11047–11053. doi:10.1039/c1sm06269g
34. Kovalev, A. E.; Varenberg, M.; Gorb, S. N. *Soft Matter* **2012,** *8,* 7560–7566. doi:10.1039/c2sm25431j
35. Kovalev, A. E.; Filippov, A. E.; Gorb, S. N. *J. R. Soc., Interface* **2013,** *11,* 20130988. doi:10.1098/rsif.2013.0988
36. Drechsler, P.; Federle, W. *J. Comp. Physiol., A* **2006,** *192,* 1213–1222. doi:10.1007/s00359-006-0150-5
37. Stork, N. E. *J. Nat. Hist.* **1983,** *17,* 583–597. doi:10.1080/00222938300770481
38. Majerus, M. E. N. *Ladybirds;* Harper Collins: London, 1994.
39. Hodek, I.; Michaud, J. P. *Eur. J. Entomol.* **2008,** *105,* 1–12. doi:10.14411/eje.2008.001
40. Gorb, E. V.; Haas, K.; Henrich, A.; Enders, S.; Barbakadze, N.; Gorb, S. *J. Exp. Biol.* **2005,** *208,* 4651–4662. doi:10.1242/jeb.01939
41. Kitchner, A.; Vincent, J. F. V. *J. Mater. Sci.* **1987,** *22,* 1385–1389. doi:10.1007/BF01233138
42. Collins, S. N.; Cope, B. C.; Hopegood, L.; Latham, R. J.; Linford, R. G.; Reilly, J. D. *J. Mater. Sci.* **1998,** *33,* 5185–5191. doi:10.1023/A:1004479803611
43. Taylor, A. M.; Bonser, R. H. C.; Farrent, J. W. *J. Mater. Sci.* **2004,** *39,* 939–942. doi:10.1023/B:JMSC.0000012925.92504.08
44. Barbakadze, N.; Enders, S.; Gorb, S.; Arzt, E. *J. Exp. Biol.* **2006,** *209,* 722–730. doi:10.1242/jeb.02065
45. Chen, B.; Gao, H. *Int. J. Appl. Mechanics* **2010,** *2,* 1. doi:10.1142/S1758825110000433
46. Peisker, H.; Michels, J.; Gorb, S. N. *Nat. Commun.* **2013,** *4,* 1661. doi:10.1038/ncomms2576
47. Weis-Fogh, T. *J. Exp. Biol.* **1960,** *37,* 889–907.
48. Voigt, D.; Schuppert, J. M.; Dattinger, S.; Gorb, S. N. *J. Zool.* **2010,** *281,* 227–231. doi:10.1111/j.1469-7998.2010.00704.x
49. Kosaki, A.; Yamaoka, R. *Jpn. J. Appl. Entomol. Zool.* **1996,** *40,* 47–53. doi:10.1303/jjaez.40.47
50. Betz, O. *J. Morphol.* **2003,** *255,* 24–43. doi:10.1002/jmor.10044
51. Bhushan, B. *Handbook of Micro/Nano Tribology,* 2nd ed.; CRC Press: New York, 1998. doi:10.1201/9781420050493
52. Scherge, M.; Gorb, S. N. *Biological micro- and nanotribology – Nature's solutions;* Springer: Berlin, 2001. doi:10.1007/978-3-662-04431-5
53. Stefan, J. *Ann. Phys. (Berlin, Ger.)* **1875,** *230,* 316–318. doi:10.1002/andp.18752300213
54. De Gennes, P. G.; Taupin, C. *J. Phys. Chem.* **1982,** *86,* 2294–2304. doi:10.1021/j100210a011
55. Scherge, M.; Li, X.; Schaefer, J. A. *Tribol. Lett.* **1999,** *6,* 215–220. doi:10.1023/A:1019119925494
56. Stark, A. Y.; Sullivan, T. W.; Niewiarowski, P. H. *J. Exp. Biol.* **2012,** *215,* 3080–3086. doi:10.1242/jeb.070912
57. Boulard, T.; Mermier, M.; Fargues, J.; Smits, N.; Rougier, J.; Roy, J. C. *Agric. For. Meteorol.* **2002,** *110,* 159–176. doi:10.1016/S0168-1923(01)00292-1
58. Carbone, G.; Pierro, E.; Gorb, S. N. *Soft Matter* **2011,** *7,* 5545–5552. doi:10.1039/c0sm01482f
59. Heepe, L.; Kovalev, A. E.; Filippov, A. E.; Gorb, S. N. *Phys. Rev. Lett.* **2013,** *111,* 104301. doi:10.1103/PhysRevLett.111.104301
60. Heepe, L.; Carbone, G.; Pierro, E.; Kovalev, A. E.; Gorb, S. N. *Appl. Phys. Lett.* **2014,** *104,* 011906. doi:10.1063/1.4860991
61. Pelletier, Y.; Smilowitz, Z. *Can. Entomol.* **1987,** *119,* 1139–1142. doi:10.4039/Ent1191139-12

License and Terms

BEILSTEIN JOURNAL OF NANOTECHNOLOGY

Three-gradient regular solution model for simple liquids wetting complex surface topologies

Sabine Akerboom, Marleen Kamperman and Frans A. M. Leermakers*

Full Research Paper

Open Access

Address:
Physical Chemistry and Soft Matter, Wageningen University, Stippeneng 4, 6708 WE Wageningen, Netherlands

Email:
Frans A. M. Leermakers* - frans.leermakers@wur.nl

* Corresponding author

Keywords:
inverse opal; regular solution model; self-consistent field theory; surface topology; wetting

Beilstein J. Nanotechnol. **2016,** *7,* 1377–1396.
doi:10.3762/bjnano.7.129

Received: 25 April 2016
Accepted: 25 August 2016
Published: 04 October 2016

This article is part of the Thematic Series "Biological and biomimetic materials and surfaces".

Guest Editor: S. N. Gorb

Abstract

We use regular solution theory and implement a three-gradient model for a liquid/vapour system in contact with a complex surface topology to study the shape of a liquid drop in advancing and receding wetting scenarios. More specifically, we study droplets on an inverse opal: spherical cavities in a hexagonal pattern. In line with experimental data, we find that the surface may switch from hydrophilic (contact angle on a smooth surface $\theta_Y < 90°$) to hydrophobic (effective advancing contact angle $\theta > 90°$). Both the Wenzel wetting state, that is cavities under the liquid are filled, as well as the Cassie–Baxter wetting state, that is air entrapment in the cavities under the liquid, were observed using our approach, without a discontinuity in the water front shape or in the water advancing contact angle θ. Therefore, air entrapment cannot be the main reason why the contact angle θ for an advancing water front varies. Rather, the contact line is pinned and curved due to the surface structures, inducing curvature perpendicular to the plane in which the contact angle θ is observed, and the contact line does not move in a continuous way, but via depinning transitions. The pinning is not limited to kinks in the surface with angles θ_{kink} smaller than the angle θ_Y. Even for $\theta_{kink} > \theta_Y$, contact line pinning is found. Therefore, the full 3D-structure of the inverse opal, rather than a simple parameter such as the wetting state or θ_{kink}, determines the final observed contact angle.

Introduction

Wetting of surfaces is a key feature for many applications. The wetting properties of a surface depend on both the material and the surface topography. A famous example is the surface of a lotus leaf: Although the material of the leaf is hydrophilic (contact angle on a smooth substrate $\theta_Y < 90°$), the structured surface is hydrophobic (apparent contact angle $\theta > 90°$) [1]. Recently, different surface structures have been designed and fabricated from hydrophilic materials that show hydrophobic contact angles [2-10]. An example is an inverse opal as schematically shown in Figure 1. Our group recently reported

an increase of θ from ca. 80° to ca. 110° for an inverse opal of polypyrrole [10].

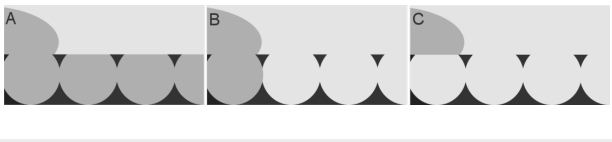

Figure 1: Schematic representation of the three wetting states on an inverse opal, A) impregnated state, B) Wenzel state, C) Cassie–Baxter state.

Our study is targeted to obtain (close to) molecular level insight in the wetting features of such surfaces using a simplistic modelling toolbox based on regular solution theory. To understand the increase in θ, which is observed at macroscopic length scales, details about the microscopic scale should be considered. For the simplest case in which a water droplet wets the structured surface on a microscopic level with its preferred angle θ_Y (see Figure 1B), the apparent contact angle, θ_W is given by [11]

$$\cos\theta_W = r\cos\theta_Y \quad (1)$$

with *r* the roughness of the surface (true contact area/projected area). This is called the Wenzel state, and it always magnifies the underlying wetting properties: θ decreases for hydrophilic materials and increases for hydrophobic materials. As the structured surfaces of interest, which are composed of a hydrophilic material, show an increase in θ, this implies that the droplet in these systems cannot be in the Wenzel state, or that the assumption of this model, namely that the parameter *r* captures all features of a surface topography relevant for the final droplet shape, is too simplistic.

A possible explanation of the increase in θ on structured surfaces, is air entrapment [12,13]. Air acts as hydrophobic patch (θ_Y for the water/air interface is 180°), and these patches lower the average surface energy of the surface (see Figure 1C) [14,15]. The resulting apparent contact angle for this so-called Cassie–Baxter state is then given by [16]

$$\cos\theta_{CB} = \Phi_s\cos\theta_Y - (1-\Phi_s) \quad (2)$$

with Φ_s the fraction under the droplet that is in contact with the solid and $(1-\Phi_s)$ the fraction under the droplet in contact with air. This approach thus defines the solid as a new material with a different effective surface energy on a macroscopic scale, and does not entail details about the droplet shape close to the surface structures on a microscopic level.

Another explanation of the difference in θ for a structured and unstructured surface of the same material is contact line pinning [17-20]. The three-phase contact line is hereby immobilized. Apart from chemical heterogeneities (which will not be discussed here), pinning occurs for a simple 1D system when the contact line encounters a kink in the surface, indicated with angle θ_{kink} in Figure 2. If $\theta_Y < \theta_{kink}$, the angle of the droplet with respect to the surface should exceed θ_Y in order to wet the surface after the kink (dotted area in Figure 2), and the droplet is thus pinned.

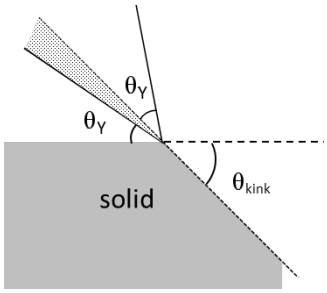

Figure 2: Surface structure induced contact line pinning in 1D: pinning occurs when $\theta_Y < \theta_{kink}$ (dotted area). The two θ_Y indicate the contact angle on the surface before and after the droplet has reached the kink.

However, pinning cannot result in any arbitrary shape. The mean curvature *J* of the liquid/vapour (L/V) interface of a droplet, is related to the pressure difference across the L/V interface, Δ*P,* and the interfacial tension γ according to the Young–Laplace equation [17]:

$$\Delta P = 2J\gamma\,. \quad (3)$$

Δ*P* and γ can be considered constant for a droplet (neglecting small curvature corrections, the deformation due to gravity and the near surface contributions expressed in the disjoining pressure), thus *J* should also be constant [13]. This implies that if the surface structure induces a curvature in one direction due to pinning, this should be compensated by the opposite curvature in the perpendicular direction. Hence, if structuring of a surface induces a noticeable curvature of the droplet parallel to the surface, this should lead to deformations of the droplet perpendicular to the surface. As the latter curvature is coupled to the apparent contact angle, which is commonly measured perpendicular to the surface, we notice contact angle variations.

The feature of hydrophilic surfaces showing hydrophobic contact angles is, for reasons mentioned above, often linked to re-entrant angles of the surface structures [21,22]. An additional argument besides pinning, is that the liquid/air interfacial area

should increase upon penetration of the liquid, creating more liquid/vapour interface [13]. This may imply that air entrapment occurs, even for hydrophilic materials [12,23].

Since it is difficult to observe local curvatures in the three phase contact line experimentally [18,24,25], in this study we turn to 'experiments in silico'. The present study is targeted to obtain insight in the wetting features of surfaces of hydrophilic materials that show hydrophobic contact angles and to differentiate between air entrapment and contact line pinning using a modelling approach.

Macroscopic approaches such as solving the Young–Laplace equation [26,27], minimizing the availability [28], or using geometry and energy [12] to find the droplet shape, do not take molecular details into account, and often require the contact angle as input parameter. Furthermore, air entrapment and coalescence [29] cannot be obtained by solving the Young–Laplace equation, and surfaces with re-entrant curvatures give impossible solutions [29]. Phase field methods [29], molecular dynamics (MD) [23,30-32], and mesoscopic lattice-Boltzmann (LB) models [33-37] are a viable option for this problem, but are challenging because wetting on complex structures involves multiple length scales [38] and the time needed to converge to a solution can be long [31,38].

In this paper we focus on the very well known regular solution theory, which is frequently used throughout the field of physical chemistry, but not so often applied for studying wetting on complex surface topologies in three dimensions. Our models can be solved using a surprisingly simple algorithm (e.g., a Pikar iteration) on a desktop PC in a few minutes CPU time. However, similar to some of the theoretical approaches mentioned above, there are limitations with respect to the size of the systems that realistically can be considered. Albeit these limitations can easily be lifted by a factor of ten when the equations are solved using modern supercomputer facilities (which we here did not do). Here we focus on equilibrium and metastable states, which allows us to consider both advancing as well as receding contact angles. Even though the regular solution model is very well known, we will start by giving some backgrounds and highlights of the regular solution model. This gives us an opportunity to fix some of our parameters in the system. We then present the model and study the wetting of inverse opal structures.

Results and Discussion

Regular solution theory

The start is a lattice model wherein the sites with linear length b are arranged in a cubic lattice geometry, that is, each cell has $Z = 6$ neighbours. Let there be M sites in the system and thus the volume is given by $V = Mb^3$. Sites are either filled by a solvent molecule, or the site is empty. The latter sites are said to be vacant and the number of vacant sites is N_V. The remaining sites are filled by solvent and hence there are $N = M - N_V$ sites filled. It is assumed that the solvent molecules only interact with each other when they occupy neighbouring sites and in this setting it is common to introduce the dimensionless Flory–Huggins interaction parameter, which is an Archimedean-like parameter needed for unlike contacts:

$$\chi = \frac{Z}{2k_BT}\left(2U_{LV} - U_{LL} - U_{VV}\right). \tag{4}$$

A positive value means that LL contacts and VV 'contacts' are favoured over LV ones and this implies a tendency towards demixing. When we assume random mixing (mean-field approximation) we can evaluate the mixing interaction energy in the system by $U_{mix} = N\chi\varphi_V$, where we ignored boundary effects and $\varphi_V = N_V/M$ is the volume fraction of vacancies. The entropy of mixing can be evaluated when we assume once more that the sites are randomly filled by solvent. The total number of ways to arrange the fluid and the vacancies is given by $\Omega = \binom{M}{N}$ and the mixing entropy is found by $S_{mix} = -k_B\cdot\ln\Omega = -k_B(N\cdot\ln\varphi + N_V\cdot\ln\varphi_V)$ with $\varphi = N/M$ and k_B the Boltzmann constant. The free energy of mixing is given by $F_{mix} = U_{mix} - T\cdot S_{mix}$. Introducing the dimensionless free energy density $f = F_{mix}/(Mb^3k_BT)$ wherein the thermal energy k_BT and the volume V are used to reduce the free energy, we obtain the well-known regular solution free energy density:

$$f = \varphi\ln\varphi + \varphi_V\ln\varphi_V + \chi\varphi\varphi_V \tag{5}$$

with $\varphi + \varphi_V = 1$. The first two terms are negative and promote the mixing of the solvent and vapour. The last term drives the demixing. The critical conditions are found by setting the second and third derivatives of the free energy density (Equation 5) with respect to the volume fraction of liquid to zero. From such analysis it is found that there is a solubility gap as soon as $\chi > \chi^{cr} = 2$. By symmetry the critical density $\varphi^{cr} = 1/2$.

Liquid/vapour interface

Very famous is the extension of the regular solution theory to the description of the L/V interface. In the footsteps of van der Waals [39] we like to find the density profile across a L/V interface $\varphi(z)$. Here z is a (lattice) coordinate running perpendicular to the interface. We set $z = 0$ at the interface and consider a lattice model with layer numbers $z = -M, -(M-1),\ldots,-1, 0, 1,\ldots, M-1, M$. The boundary layers $-M$ and M are taken large

enough so that the interface is not perturbed. We generalise Equation 5 and define a dimensionless free energy F as follows

$$F = \sum_{-M}^{M} \varphi(z)\ln\varphi(z) + \varphi_V(z)\ln\varphi_V(z) + \chi\varphi(z)\langle\varphi_V(z)\rangle, \quad (6)$$

where it is understood that the mean-field approximation is now applied along lattice layers. The angular brackets in the last term indicate that in the interaction term "curvature" information is included, which is needed to evaluate the number of liquid–vacancy contacts in the presence of density gradients. In continuous language, we need to introduce

$$\langle\varphi\rangle = \varphi + \frac{1}{6}\Delta\varphi \quad (7)$$

in the interaction term, which on a lattice and in a one-gradient functional of Equation 6, translates to a local averaging operation:

$$\langle\varphi(z)\rangle = \frac{1}{6}\left(\varphi(z-1) + 4\varphi(z) + \varphi(z+1)\right). \quad (8)$$

The target is to find the best volume fraction profiles that optimise the free energy F. Results are summarised in Figure 3.

Two volume fraction profiles are presented in Figure 3A, which were found numerically by minimizing Equation 6, for two values of χ, not far from but above $\chi^{cr} = 2$. We have set the liquid phase at negative values of z, whereas the vapour is at positive z. The position of the interface is set at $z = 0$ found by searching for $\varphi = 0.5$ (in three-gradient results we will find the interface by the same criterion). The profiles follow very accurately the tanh dependence (see Figure 3A for numerical results). We note that for $\chi = 2.2$ used below, these results deviate from the analytical predictions. Far from the interface the volume fraction profile levels off to the binodal values. The difference in volume fractions between the binodal values, here defined by $\Delta\varphi = \varphi(-M) - \varphi(M)$, is indicated in Figure 3A. The width W of the interface is numerically found by intersection of the tangent line at $z = 0$ with the binodal value. We can evaluate the surface tension γ, which is given in units k_BT/b^2, numerically, as discussed in section S1 of Supporting Information File 1.

In Figure 3B we prove that near the critical point (i) the surface tension, (ii) the width of the interface and (iii) $\Delta\varphi$ as found by our numerical solution accurately obey scaling relations with respect to the difference to the critical point $\Delta\chi = \chi - 2$.

Interestingly, near the critical point there is an analytical route to optimise the free energy F [40]. In short, near the critical point the density of the liquid (and thus also for the vacancies) is never far from the critical value. Introducing an order parameter $\varphi = \varphi - 0.5$, we can write F as a function of the order parameter and then Taylor series expand the logarithms up to the fourth order in the order parameter. As a result we obtain a Landau free energy in terms of the order parameter. An Euler–Lagrange optimisation then leads to the famous tanh-profile already known by van der Waals. We do not go into these details and mention that fully in line with the numerical results presented in Figure 3B the scaling exponents as found by this analytical route are in line with the numerical results: For the surface tension the (mean field) value is −3/2, it is 1/2 for the width of the interface, while the difference in densities of the two phases vanishes with an exponent −1/2 [40].

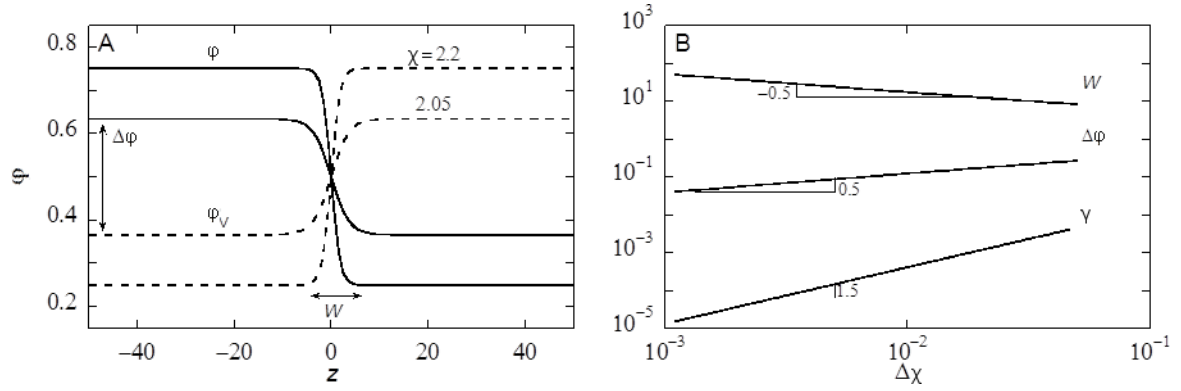

Figure 3: A) Examples of volume fraction profiles across a liquid/vapour interface found numerically by exact minimisation of Equation 6, with the interaction parameter $\chi = 2.05$ and $\chi = 2.2$ as indicated. B) Width of the interface (W), density difference between the two phases ($\Delta\varphi$) and dimensionless surface tension (γ) as function of $\Delta\chi = \chi - 2$ in double logarithmic coordinates.

Our aim is to present results that are relevant for the water/vapour system. Of course a symmetric lattice model falls short in this respect, because it assumes that as much water will be in the vapour phase as free volume will be in the water phase. The symmetry can only be broken in a more elaborate model wherein water is more realistically represented. We mention that such an approach is (at least in principle) possible, but here we choose not to go into such complications. We know that at ambient temperatures the water/vapour system is not near critical. Indeed it is very far from critical. Hence it is necessary to choose a sufficiently high χ value. In a lattice model it is advised to keep the width of the interface larger than the size of a lattice site (i.e., $W > b$). In the other limit one experiences many so-called lattice artefacts, which may frustrate the analysis of the shape of a droplet on top of a structurally complex surface. For this reason we choose here $\chi = 2.2$ for the liquid/vapour interactions, unless stated otherwise. For this value the width of the interface W is approximately 8 in units b. As the width of an air-with-water interface is just a few angstroms [41], we may infer that when the water/vapour system is the target of our calculations, the corresponding value of b is a value less than an angstrom. Again we accept deviations from the air/water system and advice to consider the value of b to be in the order of a few angstroms (say 0.2 nm). The fraction of liquid in the liquid-rich phase for $\chi = 2.2$ is about 0.7515, and the fraction of liquid in the vapour-rich bulk phase has the binodal value $\varphi^{\#} = 0.2485$. Again these values differ dramatically from our experimental system of water in air at 100% relative humidity. Finally, the interfacial tension in this system is given by $\gamma = 0.03326$ in units k_BT/b^2, which translates with $b = 0.2$ nm to 3.422 mN/m. This value is smaller than the known value for water. All these differences with respect to our experimental system are accepted as we search only for scenarios. For ease of reference we may call the liquid-rich phase "water" and the vacancy-rich phase "vapour".

Droplet on an unstructured solid

Still using the one-gradient approach, it is possible to study wetting phenomena using the regular solution model. We need remarkably few modifications in the system. The only issue is that we need to introduce a substrate. To do so, we first specify the lattice coordinates $z = 0, 1, 2,\ldots, M$, and introduce a surface component S as a boundary condition, that is, we choose $\varphi_S(0) = 1$ and $\varphi_S(z) = 0$ for all $z > 0$. The liquid and the vapour are allowed to be in the half-space $z > 0$. We have in principle two new interaction parameters χ_{LS} and χ_{VS} by introducing a "third" component.

Without losing generality we can set $\chi_{VS} = 0$, and keep $\chi_S = \chi_{LS}$ to specify the preferential adsorption of the liquid component on the surface. A negative value means that the solvent has a preference to sit next to the surface over the vapour. At $\chi_S = 0$ we expect a contact angle of 90°. Hydrophobic surfaces are modelled when $\chi_S > 0$. We will mostly restrict ourselves to hydrophilic surfaces, thus to $\chi_S < 0$.

In the case of a L/V system next to a surface the regular solution free energy assumes the form

$$F = \sum_{z=1}^{M} \varphi(z)\ln\varphi(z) + \varphi_V(z)\ln\varphi_V(z) + \chi\varphi(z)\langle\varphi_V(z)\rangle + \chi_S\varphi(z)\langle\varphi_S(z)\rangle, \tag{9}$$

where it is understood that the last term is only non-zero when $z = 1$, where it assumes the value $\chi_S\varphi(1)\langle\varphi_S(1)\rangle = \chi_S\varphi(1)/6$.

There are several routes to study wetting. Our preference goes to study so-called adsorption isotherms. Of course we need a solubility gap and thus $\chi > 2$ (we use a value of 2.2 throughout). Next, we consider a specific value of $\chi_S < 0$ and specify a given amount of solvent $\Gamma = N = \sum_{z=1}^{M}\varphi(z)$ in the system. We solve the self-consistent field equations and obtain the optimised density profile $\varphi(z)$. Far from the surface, the density profile converges to the bulk value φ^b. The adsorbed amount (surface excess) of liquid is found by:

$$\Gamma^{\sigma} = \sum_{z=1}^{M}\left(\varphi(z) - \varphi^b\right). \tag{10}$$

We focus on how the adsorption isotherms, $\Gamma^{\sigma}(\varphi^b)$, behave near the bulk binodal $\varphi^{\#}$. When upon the approach of the bulk binodal the adsorbed amount simply increases and diverges at the binodal value, we have a complete wetting situation and the contact angle is zero. Alternatively, the isotherm crosses the binodal at a finite value of the adsorbed amount, that is, for an amount $\Gamma^{\#} = \Gamma^{\sigma}(\varphi^b) < \infty$. We refer to this first crossing as the "microscopically thin film" adsorbed at the surface S. By means of a van der Waals loop the isotherm then returns to the binodal and approaches the infinite adsorbed amount upon the final approach towards the bulk binodal. We refer to this adsorbed amount as the "macroscopically thick film" on the surface. Such situation is typical for partial wetting states, where the macroscopically thick film represents the situation under a drop, and the thin film is found far away from the drop where a gas-like film resides on the substrate. As for each solution along the isotherm we have the surface tension accurately available from the self-consistent field (SCF) solution, we can find the contact angle from Young's law:

$$\cos\theta_Y - 1 = \frac{\gamma_{SV} - (\gamma_{SL} + \gamma_{LV})}{\gamma_{LV}} = \frac{\gamma_{thin} - \gamma_{thick}}{\gamma_{LV}}, \quad (11)$$

where all interfacial tensions are computed for systems in which the chemical potential is that corresponding to the bulk binodal. The value of γ_{thin} is found from the first crossing of the binodal, and γ_{thick} is the surface free energy in the system when there is a very thick adsorbed layer at the surface. Hence, we can obtain contact angle information without explicitly generating droplets. In passing we mention that for not too small droplets the contact angle as obtained by a three-gradient analysis (as used below) gives identical contact angles as the ones that follow from Equation 11, which used information from one-gradient regular solution models.

The contact angle of a liquid droplet θ_Y is calculated for various adsorption strengths χ_S and for different strengths of interaction between liquid and vapour χ (Figure 4). The more negative χ_S, the more favourable the interaction between S and L, and the more the droplet spreads, resulting in smaller θ_Y. Eventually, the liquid prefers to wet the solid completely, i.e., $\theta_Y = 0°$. At χ near the critical value of 2, the droplet enters the complete wetting regime ($\theta_Y = 0°$) already for very low values of the surface affinity χ_S. For strong segregations the interfacial energies increase and we need larger adsorption energies to enforce wetting.

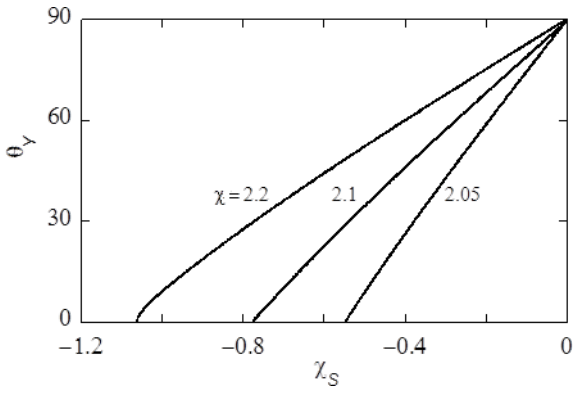

Figure 4: Contact angle of liquid on flat solid, θ_Y as function of the interaction parameter of the liquid with the solid, χ_S, for three different values of the interaction parameter of the liquid with the vapour, χ.

In this paper we aim to mimic a polypyrrole surface for which the water contact angle of a smooth surface is about $\theta_Y = 80°$. As we already selected $\chi = 2.2$, we will be in the correct contact angle regime when we set the adsorption energies around $\chi_S = -0.2$. Below we will always mention the strength of adsorption.

Liquid condensation in parallel slit

The surface structure of an inverse opal consists of close to spherical cavities. In such structures we should anticipate the occurrence of capillary condensation or, alternatively, capillary drying. For this reason we use the regular solution model to study classical capillary condensation. To this end we consider a system that contains two surfaces. One at $z = 0$ and another one at $z = D + 1$. Hence $\varphi_S(z) = 0$ for $z = 1, 2, \ldots, D$ and unity elsewhere. Now our regular solution free energy is given by

$$F = \sum_{z=1}^{D} \varphi(z)\ln\varphi(z) + \varphi_V(z)\ln\varphi_V(z) + \chi\varphi(z)\langle\varphi_V(z)\rangle + \chi_S\varphi(z)\langle\varphi_S(z)\rangle. \quad (12)$$

In this case the last term automatically accounts for the interactions with the surfaces, as it is non-zero for $z = 1$ and $z = D$. More specifically, F has two surface contributions $\chi_S\varphi(1)/6 + \chi_S\varphi(D)/6$.

As there are two interfaces, we anticipate the adsorption of the liquid onto both surfaces simultaneously. We want to record the adsorbed amount in the slit as a function of the (dimensionless) chemical potential ($\mu = \ln\varphi^b$) of the liquid component. One complication arises because in layers $z = 1, \ldots, D$, the bulk volume fraction may not be reached and we cannot simply "pick up" this value from the profiles. As explained in section S1 of Supporting Information File 1, the SCF protocol gives (as output) the volume fraction of a reference system that is in equilibrium with the molecules in the slit. This reference value is used to compute the isotherms. In Figure 5A we present an example for a slit distance $D = 10$ (in lattice units) and our default interaction parameters $\chi = 2.2$ and $\chi_S = -0.3$. Recall that under these conditions the surfaces are preferentially solvated by the liquid, and θ_Y is 68°. In such situations there is a large van der Waals loop in the adsorption isotherm (cf. Figure 5A). The Maxwell construction can be used to find where, in equilibrium, the step in the isotherm should take place. In line with the hydrophilic character of the surfaces we find the step in the subsaturated region. In Figure 5A the grey vertical line represents the bulk binodal value. The step takes place at a lower chemical potential (local binodal) than that corresponding to the bulk binodal. We define $\Delta\mu$ as the difference in $\ln\varphi^b$ between the local and bulk binodals as indicated in Figure 5A.

It is important to consider the isotherm in slightly more detail. After the jump in the isotherm the adsorbed amount only marginally increases further: the isotherm continues into the supersaturated region and as the system increases the bulk volume fraction, in the limit of very high concentrations the

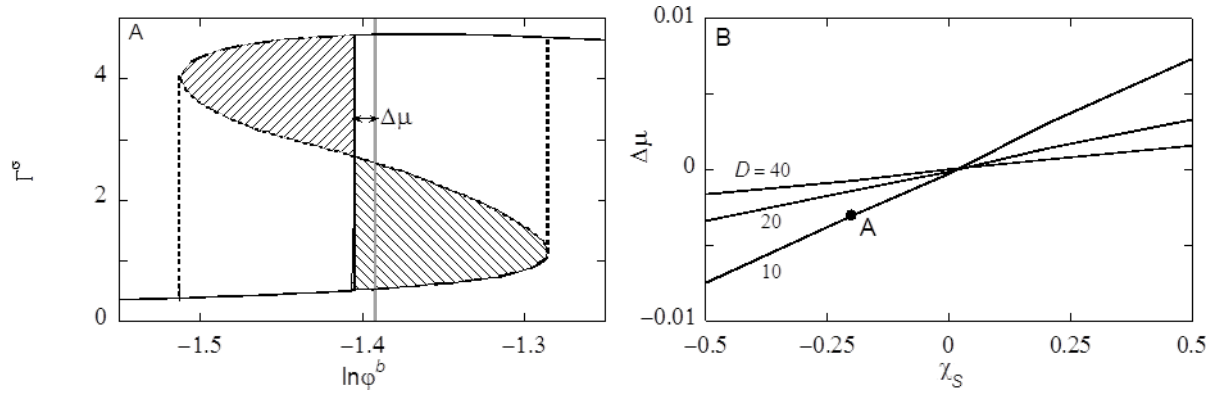

Figure 5: A) Adsorption amount Γ^{σ} of the liquid component as a function of the volume fraction of liquid in the vapour φ^{b} in lin–ln coordinates (*x*-axis is chemical potential), in a slit with surfaces that are a distance D = 10 apart and have an adsorption energy χ_S = −0.2. The metastable branches are dashed. The unstable part is dotted. The chemical potential $\mu^{\#}$ is indicated as the grey vertical line. The solid vertical line is placed at the chemical potential where a step in the isotherm takes place (local binodal). This step is found by the Maxwell construction, that is by the equal area argument (the two shaded regions have the same area). The difference in chemical potential Δμ between the place of the step and the binodal is indicated. The vertical dotted lines are placed at chemical potentials corresponding to the spinodal points. B) The chemical potential where the step in the isotherm (compared to value of the bulk binodal) Δμ takes place (at equilibrium) as function of χ_S for slit distances D =10, 20 and 40 as indicated. The solvent–vacancy interaction is set to χ = 2.2. The label A on the curve for D = 10 corresponds to the condition used in panel A.

excess should go down again to become zero in the limit of φ^{b} to 1.

The most interesting feature of the isotherm is the presence of a loop. Associated to the loop there are two spinodal points. These spinodal points are located at the turning points of the isotherm. There are two regions of metastability, namely between the local binodal and the first turning point. This spinodal point is found in the region of supersaturation. The other metastable region is found between the turning point in the subsaturated region and the local binodal in the top region of the isotherm. In the isotherm the metastable branches are indicated by dashed line parts. When in the absence of strong fluctuations the bulk volume fraction is increased, the slit may not necessarily change its contents at the local binodal, but instead remains dry up to – in the extreme case – the spinodal point is reached, and the slit is filled with liquid following the dashed line. Inversely, when the slit is wet, and the bulk concentration is reduced, the drying does not necessarily take place at the local binodal, but enter the other metastable branch. Again the drying must take place before or at the lower spinodal point (following the other dashed line). Hence in dynamical situations a hysteresis loop may be followed where the steps at the spinodal are indicated by the vertical dotted lines. The spinodal points have important roles in the advancing or receding contact line calculations (see below). Even though the van der Waals loop in the isotherm is due to the mean-field approximation, it is found that in real life experiments the system also may be trapped in metastable states very much alike those found in the mean-field model.

In Figure 5B we report that the difference between the local and the bulk binodal in confined spaces is a function of the affinity of the solvent for the substrate. When χ_S is more negative the Δμ increases to more negative values. Indeed when $\chi_S > 0$, that is for hydrophobic surfaces, the local binodal occurs at supersaturated solutions. With increasing D the local binodal shifts towards the bulk binodal.

Curved L/V interfaces: Kelvin and Laplace

Macroscopic droplets (with negligible curvature) cannot be generated using our method. As the system size is limited, our drops have L/V interfaces that are typically strongly curved. The thermodynamics of curved interfaces is well understood, but there are several complications. One of the issues is that the location of the interface is somewhat arbitrary. On top of this the interfacial tension in curved interfaces cannot uniquely be computed. It depends on the notion of the position of the interface. There exists a choice of the position of the interface, the so-called surface of tension, for which a small notional change of the radius does not influence the value of the surface tension. For this special case the Laplace equation simplifies to Equation 3, and the value of the interfacial tension does not deviate much from the planar value.

From the Laplace equation we know that in droplets with curved L/V interfaces there is a Laplace pressure. As a consequence the chemical potential of the liquid in a drop is at a higher chemical potential compared to systems with planar interfaces. The increased chemical potential is reflected in the oversaturation of water in the vapour phase; a phenomenon

named after Kelvin. With oversaturation of the system, which necessarily occurs in our calculations due to the finite size of our droplets, one will invariably get closer to the spinodal point of the capillary condensation process. Hence, oversaturation may trigger the filling of confined regions by the liquid. Small droplets cause a stronger oversaturation than larger droplets and the presence of small droplets may result in a spontaneous filling of the voids by capillary condensation when this may not yet occur for larger drops.

The radius specified by the surface of tension R_{SOT} coincides with the visual inspection of where the interface is for many systems. Below we therefore do not exactly determine the exact R_{SOT} and use the Ansatz that the interface position is where the solvent volume fraction hits the value $\varphi = 0.5$.

Three-gradient regular solution model

Let us next extend the regular solution theory to model liquid drops at a complex surface topology. We consider a three-gradient coordinate system $\mathbf{r} = (x, y, z)$ with $x = 1, 2,\ldots, M_x$, $y = 1, 2,\ldots, M_y$ and $z = 1, 2, \ldots, M_z$. In contrast to the one-gradient systems where the surfaces were treated through the boundary conditions, in three gradient models it is more natural that the surface component S will occupy lattice sites within the specified volume. Hence, we will specify all the lattice sites within the system: the volume fraction of S is unity and the remainder of the lattice sites are filled by the liquid and vapour components in the usual way. The regular solution free energy is straightforwardly generalised and both interactions between L and V as well as with the surface component S are accounted for:

$$F = \sum_{x=1}^{M_x}\sum_{y=1}^{M_y}\sum_{z=1}^{M_z}\varphi(\mathbf{r})\ln\varphi(\mathbf{r}) + \varphi_V(\mathbf{r})\ln\varphi_V(\mathbf{r}) + \chi\varphi(\mathbf{r})\langle\varphi_V(\mathbf{r})\rangle + \chi_S\varphi(\mathbf{r})\langle\varphi_S(\mathbf{r})\rangle, \quad (13)$$

wherein the angular brackets indicate that the free energy accounts for the "curvature" information in three directions. The lattice implementation is simply:

$$\begin{aligned}\langle\varphi(\mathbf{r})\rangle &= \langle\varphi(x,y,z)\rangle \\ &= \frac{1}{6}\big(\varphi(x-1,y,z)+\varphi(x+1,y,z) \\ &\quad +\varphi(x,y-1,z)+\varphi(x,y+1,z) \\ &\quad +\varphi(x,y,z-1)+\varphi(x,y,z+1)\big).\end{aligned} \quad (14)$$

Mirror-like, no-gradient boundary conditions are implemented in boundary layers in the system. This is implemented by setting $\varphi(0, y, z) = \varphi(1, y, z)$, $\varphi(M_x + 1, y, z) = \varphi(M_x, y, z)$, and similarly for the other boundaries in y- and z-directions. Using these boundary conditions it is possible to consider a representative part of the surface, while keeping the computation times and system volumes to a minimum.

In the calculations there are no assumptions regarding the effects of the line tension. The model fully accounts for these effects, but the line tension contributions in our systems were not explicitly extracted. The most important reason why we did not do so is that the line tension cannot be uniquely extracted from the overall grand potential, because a choice for the position of the three-phase contact line is required.

Specifying the inverse opal

The regular solution free energy of Equation 13 still requires detailed information on the distribution of the solid material S in the inverse opal. The idea is to consider a representative piece of a substrate that contains spherical cavities in a specified arrangement (i.e., crystalline ordering with close to hexagonal or square packing symmetries). The cut-off height controls the opening of the cavities as shown in the example of Figure 6. The parameters that control the surface topology are listed in Table 1. Below we will use the parameter $c = h/d$, which is a fraction at which the cavities were cut and Φ_S is the fraction of the "top" of the surface that is solid.

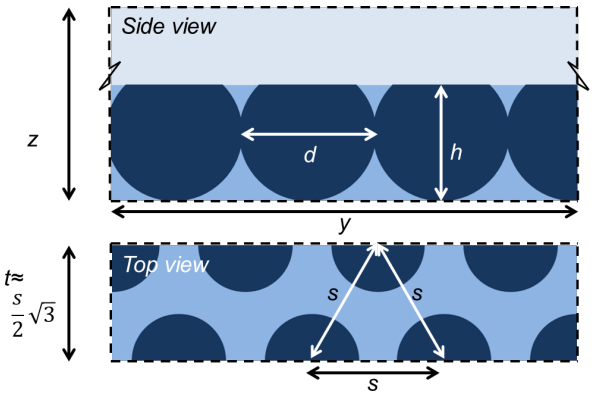

Figure 6: Schematic side view (z,y)-plane and top view (x,y)-plane of an inverse opal with two rows of $n = 3.5$ cavities in a staggered packing (3.5 cavity volumes are in the system, four cavity positions are required). The distance between two ($m = 2$) rows is t. For a hexagonal packing the two rows are displaced with respect to each other by a value $t \approx (s/2)\sqrt{3}$, where s is the distance between the cavities. On a lattice t must be an integer. Reflecting boundaries are applied in all directions.

The parameters of Table 1 completely specify how many cavities are present in the computation volume. Let the cavities be

Table 1: Parameters that determine the structure of the inverse opal. Even and odd rows of cavities are displaced by half the distance between the cavities in a row, that is, by *s*/2. All quantities are given in lattice units, that is in values of *b*. Below also the cut-off ratio $c = h/d$ (to specify which part of the cavity is cut-off) and Φ_S (the fraction of the top of the surface that is solid) is used.

symbol	parameter
D	diameter of a cavity (integer > 0)
S	spacing between two cavities in a row (integer of order *d*)
T	distance between the two rows (integer of order *d*)
N	'number' of cavities in a row (> 0) may also be non-integer
m	number of rows (integer > 1)
h	cut-off height of the solid phase (integer > 0)

numbered by $i = 1, 2, 3, \ldots, N_c$. In the example of Figure 6 there are two rows of 3.5 cavities and thus we need $i = 1, \ldots, 8$ cavity positions. The input parameters thus specify the coordinates of the cavities $\{\mathbf{r}_1, \mathbf{r}_2, \ldots, \mathbf{r}_i, \ldots, \mathbf{r}_{Nc}\}$. The cavities in the inverse opal are placed in rows along the *y*-direction, the direction perpendicular to the rows is the *x*-direction and the cavities are positioned at the lowest *z*-values possible, that is for all cavities *i*, $r_{iz} = d/2$ (cavity radius).

The solid phase extends up to a height $z = h$ where *h* is the cut-off height. The solution above the inverse opal starts at a height $z > h$. The first and last row in the *y*-direction have their centres on the boundary that is at $y = 1/2$ and $y = M_y + 1/2$, respectively. This implies that the system size in the *y*-direction is $M_y = (\mathrm{m} - 1)t$, where *t* is the distance between two rows and *m* is the number of rows. The system size in the *x*-direction is given by $M_x = ns$, with *n* the number of cavities in a row (when half the cavity is in the system the cavity counts by 0.5), and *s* the distance between cavities in a row. In the example of Figure 6, $M_x = 3.5s$. The system size in the *z*-direction should exceed *h* sufficiently so that a sessile drop can be on the substrate. In the first row the first cavity is by default with its centre at $x = 1/2$, that is, at the lower boundary. The first cavity in the second row is positioned at $x = (s + 1)/2$, et cetera.

All non-zero surface densities can now be computed. When for a coordinate $\mathbf{r}'$ the distance to all of the coordinates $\{\mathbf{r}_1, \mathbf{r}_2, \ldots, \mathbf{r}_i, \ldots, \mathbf{r}_{Nc}\}$ is larger than the radius of a cavity, i.e., $d/2$ and when the *z*-value is less or equal to *h*, we set $\varphi_S(\mathbf{r}') = 1$ and $\varphi_S(\mathbf{r}') = 0$, otherwise:

$$\varphi_S(\boldsymbol{r}') = \begin{cases} 1 & \mathbf{r}_z \le h \quad \text{and} \quad |\mathbf{r}_i - \mathbf{r}'| > \dfrac{d}{2} \quad \forall i \\ 0 & \text{otherwise} \end{cases}. \tag{15}$$

This solid distribution is fixed during the free energy optimisation. Of course only the coordinates that are not taken up by S can be filled with L or V. On the "top" of the solid phase it is of interest to know the fraction of sites occupied by S. These are easily evaluated by

$$\Phi_S = \frac{1}{M_x M_y} \sum_{x=1}^{M_x} \sum_{y=1}^{M_y} \varphi_S(x, y, h). \tag{16}$$

Analytical estimates of Equation 16 are given in section S2 of Supporting Information File 1. The cut-off height *h* normalised by the particle diameter *d* will be referred to by *c*:

$$c = \frac{h}{d}. \tag{17}$$

Below we will be interested in hexagonally ordered cavities. For an optimal hexagonal packing, the distance *s* between the particles along a row and the distance *t* between the rows, should obey $t = (s/2)\sqrt{3}$. However, on the lattice only integer values are allowed. Rounding to closest integer values must be implemented. For some values of the particle distances *s* there is a reasonable value of *t*, for other distances the error is relatively large. Only values of *s* which require rounding errors below 0.15 for the corresponding *t* value are used.

The parameters in Table 1 can be used to generate a large variety of inverse opal structures. As long as $s > d$, we have the situation that the cavities are isolated. However, the cavities may become interconnected when $s < d$. In experimental situations such overlap of cavities may occur, and then there are usually small openings connecting the cavities. This is why this particular parameter setting is allowed.

Example 1: liquid condensation in a weakly hydrophilic face centred square inverse opal

We first consider a simple inverse opal structure that has cavities with a diameter $d = 31$. The distance *s* between the cavities is set to 88, and the distance between the rows $t = 44$. This implies a face-centred square arrangement of the cavities. The number of cavities in a row is $n = 1$, whereas the number of rows is set to 3. As can be seen from Figure 7, this setting generates an equal box size in *x*- and *y*-directions. As the distance between the cavities exceeds the cavity diameter, we have isolated pockets. The surface interaction is set to a slightly hydrophilic value $\chi_S = -0.3$.

To compute the adsorption isotherm we start with a low amount of liquid in the system and then increase this amount step by

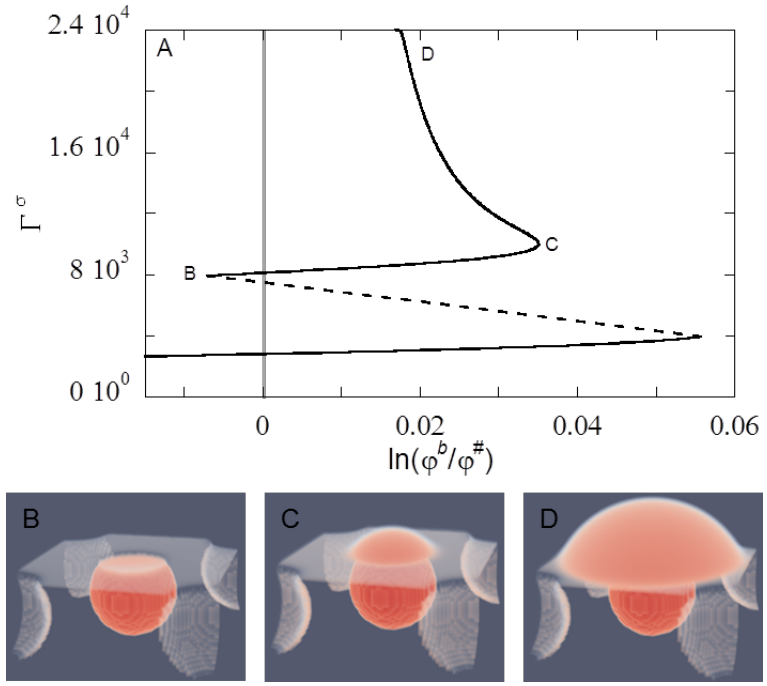

Figure 7: Liquid condensation in hydrophilic inverse opal (d = 31, s = 88, t = 44, m = 3, n = 1, h = 25 (c = 0.8)). A) Excess adsorbed amount of the liquid component in the system as a function of the volume fraction of the liquid normalised by the binodal value in lin–ln coordinates. The dashed part represents not the true part of the isotherm but rather connects two states, before the condensation of a pocket and after the condensation. The dotted, vertical line is at the bulk binodal $\varphi^{\#}$. The labels along the isotherm refer to the snapshot colour-coded density distributions given in panels B, C, D. Red is the high-density liquid phase, white is the low-density (gas) phase.

step. In the calculations the outcome of a given calculation serves as an initial guess for the subsequent calculation. This is why a system can be trapped in metastable states, similar to the experimental counterparts.

In Figure 7A we present the adsorbed amount of the liquid component $\Gamma^{\sigma} = \Gamma - V'\varphi^{b}$, where V' is the volume available for the L and V components, which is $V' = M_x M_y M_z - \Sigma_{\mathbf{r}}\varphi_S(\mathbf{r})$, as a function of the volume fraction of the liquid component in the bulk. Here we did not normalise with respect to the available surface area and thus this amount is proportional to the surface area. The bulk volume fraction is normalised by the bulk binodal value. The curve is plotted in lin–ln coordinates. Upon an increase in the amount of liquid component in the system Γ, first the vapour phase is gradually saturated with liquid and the adsorbed excess remains modest: At the surface a gaseous adsorption layer develops. Then, upon further increase of the amount, the binodal value is crossed and the system enters the super-saturation regime. The liquid film remains homogeneous along the surface, until $\Gamma^{\sigma} \approx 4000$, then a first-order jump in the isotherm takes place (cf. Figure 7A, dotted line). As can be seen in Figure 7B, at this stage a droplet formed in the confined space of the cavity and the curvature on the L/V interface in the opening is concave, resulting in a negative Laplace pressure inside the droplet. Since the chemical potential of the liquid molecules should be the same everywhere, this means that the vapour phase is under-saturated (see Figure 7A).

The volume fraction of liquid in the bulk φ^{b} increases as more liquid is added and passes the binodal value $\varphi^{\#}$ again. At this binodal point there is no under- or oversaturation, hence no curvature of the L/V interface at the opening (not shown). Additional liquid that is added to the droplet induces a convex curvature on top of the droplet, and the bulk oversaturates up to C in Figure 7A. The value of Γ^{σ} at this point is approximately 10000, and consists of a thin film ($\Gamma^{\sigma} \approx 4000$) and the macroscopic droplet ($\Gamma^{\sigma} \approx 6000$). The volume of a sphere with d = 31 is about 15600. Given that the density difference between the liquid-rich and vapour-rich phase is about 0.5, and that part of the thin liquid film becomes part of the macroscopic droplet, the valur of Γ^{σ} found at point C is in agreement with what is expected for a cavity with diameter d = 31.

Additional liquid is subsequently used not to fill the other cavities, but to increase the volume of the existing droplet (Figure 7D) and the droplet starts to spread on the substrate. Below we will follow this process in a slightly different geometry. The oversaturation needed for capillary condensation to occur for the other cavities is in this case not reached. This means that for this inverse opal, with d = 31, once condensation

has taken place, a droplet grows on top of the filled cavity and the remaining cavities are not filled via capillary condensation, but typically rather fill once the central droplet spreads over and on top of the other cavities (not shown).

Most inverse opals in experiments, which are fabricated using sacrificial particles, have cavities of hundreds of nanometres or more [3,10,42-44]. These sizes are much larger than the cavities considered in the current calculations. Smaller cavities can fill more easily via capillary condensation (cf. Figure 5B). Since the impregnating wetting state is not observed even for such small cavity sizes as used in Figure 7, we conclude that the impregnating wetting state due to capillary condensation is not likely to develop for practical inverse opals which are marginally hydrophilic.

In this surface structure, the cavities are not connected, whereas for some experimentally fabricated inverse opals all cavities may be interconnected via a small opening. Since the curvature of the droplet should be constant, the curvature of the liquid–vapour interface at the small opening is the same as for the rest of the macroscopic droplet [13], and hence the high curvature needed for the next cavity to be wetted via this opening, is not reached. Therefore, a cavity that is filled with liquid will wet the next cavity via the larger opening at the top, rather than through this small hole (not shown).

Droplets on top of the hexagonally ordered inverse opal

In the remainder of this paper we will focus on close-to-hexagonally packed cavities. In principle one can force a water-front to move along such a surface in an arbitrary direction. Here we focus on just one of the possible directions.

We consider solvent fronts along the x-direction, which spread by increasing the volume of the droplet, in the y-direction. Recalling that mirror-like boundary conditions are implemented in x-, y- and z-directions, in this scenario it suffices to have just two rows of cavities, that is $m = 2$. The system is much larger in the y-direction and we consider n cavities with a spacing s. For a hexagonal packing of cavities the distance s and the spacing t between rows are interconnected and we will mention just one of these parameters. The number of cavities that are considered in the y-direction is taken sufficiently large so that there are no boundary effects. The surface is thus sufficiently specified by mentioning the cavity diameter d, the distance between the cavities s and the cut-off height h, or equivalently $c = h/d$. Typically, we will initiate the calculation by means of some initial guess of the SCF. protocol such that a droplet develops with its symmetry plane along the $y = 1/2$ boundary.

Example 2: Advancing and receding drop fronts on a slightly hydrophilic hexagonally packed inverse opal

In Figure 8 we give representative examples of planar solvent droplets with their solvent front (on average) along the x-direction. The drops sit with their symmetry plane at $y = 1/2$. The inverse opal is characterised by the cavity diameter $d = 31$, the spacing between the cavities in the y-direction $s = 30$, the cut-off fraction $c = 0.80$, and the number of cavities in the y-direction, $n = 3.5$. The surface is slightly hydrophilic ($\chi_S = -0.3$).

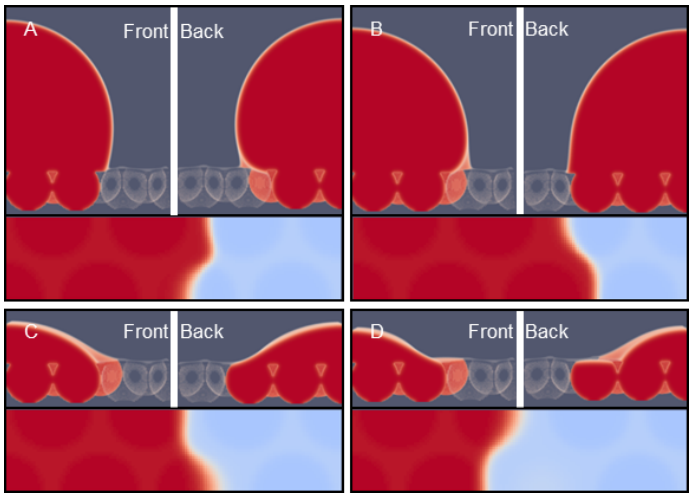

Figure 8: Four examples of droplets on an inverse opal with $d = 31$, $s = 30$, $c = 0.80$, $n = 3.5$, and $\chi_S = -0.3$. A,B) Two advancing water fronts with relatively high contact angles; C,D) two receding water fronts with low contact angles. For each panel the left (z, $+y$), right (z, $-y$) and bottom images (x, y) are for different view-points, that is, the left image is taken from the front, the right image is taken from the back, the bottom image is the top-view. Colour coding: Red is high-density liquid. Blue is low-density gas. White is intermediate density. The snapshots are taken from the calculations of Figure 9.

The cavities directly under the macroscopic water front are filled with liquid, while the other cavities remain empty. The water front is thus in the Wenzel wetting state (Figure 1). Notice that an additional cavity is filled going from A to B. Such an event gives discontinuities as discussed below. In B there is slightly more liquid in the system than in A, but the height of the drop in A is more than that in B. The liquid in the cavity is noticed as a volume reduction in the drop. The panels A and B are taken as examples of the droplet shape in a series of calculations for which the droplet volume was increased (see also below in Figure 9).We refer to these as advancing front lines. The other two panels (C and D) are taken for the situation that the drop volume was decreased and we refer to this situation as receding front lines. Three different view positions of the same drop are given in this figure to illustrate the features that present themselves in advancing and receding cases. From the top-view perspective, we see that the solvent front is not straight. It curves along the cavity openings and the exact shape of the front strongly "fluctuates" depending on the exact value of the droplet volume.

In one of the cases the front is at lower y-values at low x-values and in the other case it is inversed, the lowest y-value is at a high x-values. In the four cases shown in Figure 8 we see that the absolute value of differences in the y-position does not depend much on the advancing or receding modes.

As the three-phase contact line is curved, necessarily the contact angle must vary as well. The contact angles are best viewed from the side. The top graphs in Figure 8 are images taken from a "front" or "back" view point. We present both of these to illustrate that the shape in the (z,y)-plane depends slightly on the x-coordinate. Clearly, there is a huge difference in the contact angle between the advancing fronts (very high angles) and the receding fronts (very low angles). Furthermore, as can be seen in panel D, the receding droplet remains pinned on top of the liquid-filled cavity, resulting in a longer contact line as compared to advancing droplets.

For a given snapshot we can evaluate the contact angle $\theta(x,z)$ in the (z,y)-plane by estimating by interpolation the position y' of the interface, where the $\varphi(x, y', z) = 0.5$. In other words, the y'-position of the liquid/vapour interface depends both on x and z: $y' = y'(x, z)$. Then the local contact angle of the solvent front is a function of both x and z:

$$\theta\left(x,z\right)=\arctan\left(y'\left(x,z\right)-y'(x,z-1)\right), \tag{18}$$

which implies that the contact angle can only be computed for $z > 2$. The average angle at a height z is found by averaging along the x-direction:

$$\theta\left(z\right)=\frac{1}{M_x}\sum_{x=1}^{M_x}\theta\left(x,z\right), \tag{19}$$

while the standard deviation $\Delta\theta(z)$ measured in the x-direction is given by

$$\Delta\theta\left(z\right)=\sqrt{\frac{1}{M_x}\sum_{x=1}^{M_x}\left(\theta\left(x,z\right)-\theta\left(z\right)\right)^2}\,. \tag{20}$$

Similarly, the position of the interface $y'(x,z)$, the average position of the interface $y'(z)$ and the standard deviation $\Delta y'(z)$ are straightforwardly recorded.

In Figure 9A we plot the standard deviations $\Delta y'(z)$ as a function of $z - h$ (height above the substrate), and in Figure 9B $\theta(z)$

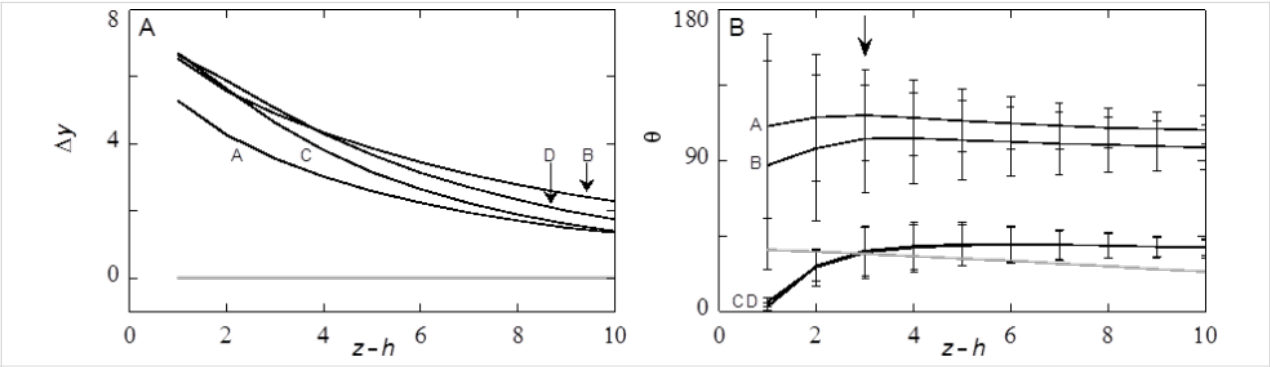

Figure 9: Examples of drop characteristics. A) The standard deviation (measured in x-direction) of the position of the interface $\Delta y'$ as a function of the height above the substrate $z - h$. The horizontal grey line represents the result on a smooth surface. B) The angle of the liquid/vapour front in the (z,y)-plane, $\theta(z)$ together with the standard deviation of the angle measured in the x-direction plotted as "error" bars. The grey curve is the contact angle of a similarly sized droplet on a smooth surface. The labels A–D correspond to the snapshots A–D in Figure 8: A,B advancing contact liquid front; C,D are receding liquid fronts.

together with the fluctuation in the angle $\Delta\theta(z)$ as "error" bars as a function of $z - h$ for the four droplets already shown in Figure 8 is plotted.

It is natural to expect that when the drop characteristics are considered further away from the surface that the influence of the surface is gradually reduced. This is why the $\Delta y'(z)$ is a decreasing function of z. Again, as noticed already from the snapshots, the value of $\Delta y'(z)$ does not depend much on the advancing or receding modes of wetting. That is why the four curves in Figure 9A are nearly the same. We refrain from trying to provide further comments about the differences. Similarly, far from the surface the angles become independent on x. That is why in Figure 9B the "error" bars diminish in size when $z - h$ is increased. Indeed very close to the substrate $z - h < 4$ the fluctuations are very large, that is about 50% of the value of θ.

We already noticed that the advancing contact angles are much larger than the receding ones. Figure 9B gives the numerical values more accurately: The advancing angles are on average larger than 90°, whereas the receding angles are about 45°, very close to the angles found for the unstructured surface (grey line). Interestingly, the average contact angle in the advancing mode can go through a small local maximum at a height $z - h = 3$. Such an effect hints to the presence of a foot on the droplets. However, at this height the fluctuations are large and we are hesitant not to over-interpret the results.

It is clear that, if we want to compare droplets and see trends, we need to reduce the outcome of the computations. That is why from hereon we will focus on the properties of the droplets on a height of $z - h = 3$ (as indicated by the arrow in Figure 9). At this height above the substrate the "foot" is not disturbing too much, while the structure of the surface is still well noticeable. We thus define (if not mentioned otherwise) the fluctuations of the liquid front measured as the standard deviation along the x-direction as $\Delta y = \Delta y'(h + 3)$, and the average contact angle of the drop $\theta = \theta(h + 3)$, as well as the fluctuations $\Delta\theta = \Delta\theta(h + 3)$.

The calculations of Figure 8 and Figure 9 were started with an initial amount of liquid $\Gamma = 3{\cdot}10^6$. More liquid is added to the system and these molecules are consumed by the drop. Hence the drop volume increased. Typically we performed ten liquid addition steps and for each of these new profiles are calculated to obtain an advancing angle. The amount of the liquid is subsequently stepwise decreased to check for hysteresis and to obtain a receding angle. The structural properties of the drops are recorded during this cycle and the results were collected in Figure 10.

The starting point of the calculations is not extremely well defined in terms of advancing or receding states. The initial guess takes the system in this case close to an advancing situation: the contact angle θ is rather high. Typically this initial drop is disregarded from our averaging (see below). Upon stepwise increase of the drop volume (closed spheres) Δy decreases from 5.5 to 4.0 while the contact angle θ increases gradually until point A is reached. The contact line did not move upon adding the liquid: The contact line is arrested as the contact line cannot be placed on top of a (water filled) cavity [45]. Then with a small increase the system jumps from A to B. Above we saw that in this event one extra cavity is filled with liquid. At this event the contact line de-pins jump-like in an event that may be referred to as a de-pinning transition [19]. In Figure 8A,B we see that the three-phase contact line has the opposite curvature in the x-direction. At this de-pinning event the average contact angle jumps downward to $\theta \approx 90°$ (cf.

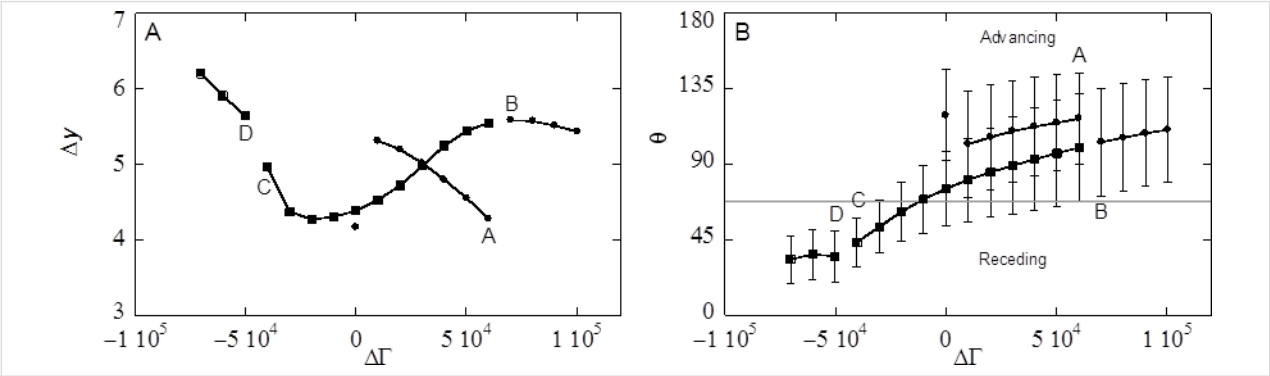

Figure 10: Examples of structural features of advancing and receding drop fronts. A) The fluctuations of the position of the liquid front along the x-direction at a height $z = h + 3$ as a function of the $\Delta\Gamma$ of the droplet component with an initial amount $\Gamma = 3{\cdot}10^6$. B) The corresponding average contact angle θ (measured at a height $z = h + 3$) and the standard deviation (plotted as error bars). The advancing liquid front is given by the solid sphere data points, the receding ones in solid square data points. The lines are to guide the eye. A discontinuity in the line represents a jump-wise change of the drops on the substrate. The labels A–D correspond to the snapshots of Figure 8 and the structural data of Figure 9. A and B are along the advancing branch, whereas C and D are taken from the receding drop fronts. Parameters are similar as in Figure 8 and Figure 9.

Figure 10B) and Δy jump-like increases from 4.0 to 5.5 (cf. Figure 10A). The contact angle close to the surface and directly in front of the cavity that fills up, switches thereby from $\theta > 90°$ to $\theta \approx 90°$ (cf. Figure 8A,B). These increased contact angles with respect to θ_Y (68° for $\chi_S = -0.3$) are hereby found for a hydrophilic surface without air entrapment. The system may experience more of such events when more and more liquid is added. After another four additions of volume we were close to the initial condition and the advancing contact line calculations were stopped.

For receding water fronts (Figure 8C,D), computed by taking liquid out of the system (the squares in Figure 10), we first retrace a part of the advancing curve, that is, the four latest volume additions were undone and the same results were recovered. However, as soon as the volume of the drop is decreased compared to point B we follow a different route. We do not jump to point A, but rather follow the trend downward for the average contact angle θ (cf. Figure 10B) while also the fluctuations Δy decrease. Close to the initial volume the contact angle is found to be close to the value on the smooth surface $\theta = \theta_Y$. At this point the curvature of the dependence $\Delta y(\Delta\Gamma)$ changes. Further reduction of the volume of the drop leads to a local minimum of Δy, while the contact angle drops significantly below the value of θ_Y. Then point C is reached (cf. Figure 8C). Now the receding front is pinned on top of a liquid filled cavity. The low contact angle on top of the cavity, clearly visible for the right-hand site of droplet Figure 8C, is explained by the fact that the liquid wets a surface of the same material (namely the liquid in the cavity). During receding, the water front is thus pinned at the liquid/liquid surface with a local θ of 0°. The cavity remains filled after the droplet has retracted from the cavity (see cavity on the right-hand site of droplet D) which occurs once again step-wise. During this de-pinning step the three-phase contact line rearranges its curvature again (cf. Figure 8C,D). At this de-pinning transition the value of Δy increases jump-like, while the average contact angle decreases somewhat. Upon further reduction of the drop volume the Δy increases further while the contact angles remain low.

The traces of Figure 10A,B imply a hysteresis: The curves for adding and reducing volume only overlap when no de-pinning transition has occurred in between the addition or removal steps. The contact line of the advancing droplet experiences a surface consisting of solid and vapour, whereas the contact line of the receding angle experiences a surface consisting of solid and liquid. The true receding angle is only visible for values of $\Delta\Gamma$ between $-5\cdot10^4$ and $-7\cdot10^4$ (last three data points) and is about 35°. If the surface can be regarded as consisting of a solid with a liquid, then the contact angle can be calculated using [15]

$$\cos\theta_{\text{water in cavity}} = 1 - \Phi_S + \Phi_S \cos\theta_Y \qquad (21)$$

with the fraction of solid on the top of the substrate $\Phi_S = 0.43$ (for $c = 0.8$). The contact angle according to this calculation (40°) is in agreement with the contact angle we find here. For these last droplets, high values of Δy are found. The contact line is in these cases pinned on the farther edge of a water-filled cavity (see Figure 8D).

Trends in the shape of advancing water fronts

In the remainder of this paper we will focus on advancing contact angles. Referring once again to the results of Figure 10B, we typically initiated calculations with the drop near the lower boundary on the y-axis in such a way that the resulting drop shape assumes properties of an advancing one. Then, as in Figure 10B ten subsequent increases of the amount of the liquid component were implemented. The average contact angle θ (along the x-direction and at $z = h + 3$) were again averaged over these ten droplets to obtain $\langle\theta\rangle$. Typically one or more de-pinning events were accepted in this averaging. Recall, that in the advancing branch the contact angle in a de-pinning event changes only slightly. The standard deviations were averaged similarly.

Effect of cavity size *d*

The size of the inverse opals in the calculations, which is linked to experimental sizes by the width of the interface, invariably is much smaller than the size of inverse opals used in experiments. To study the effect of size of the structures on the (double) averaged advancing contact angle $\langle\theta\rangle$, droplets on inverse opals with cavity diameters ranging from 9 to 52 have been recorded. The trend observed for this series of sizes, can be extrapolated to even bigger sizes without the need to calculate those. In these calculations the spacing between the cavities was set to $d - 1$, that is, the cavities were slightly overlapping so that a small hole connects the cavities. The cut-off fraction is kept at $c = 0.8$.

As shown in Figure 11, the $\langle\theta\rangle$ is an increasing function of the cavity diameter d. For $d > 40$ $\langle\theta\rangle$ reaches a plateau. The levelling off hence implies that it is not necessary to increase the cavity sizes even more to reach the experimental limits.

The fact that $\langle\theta\rangle$ can increase above θ_Y is attributed to the pinning of the contact line around the cavities. For very small cavities we observed that the average angle can be smaller than θ_Y (grey horizontal line in Figure 11). Small cavity sizes are similar to the small confinements D used in the one-gradient slits of Figure 5. From these slit calculations we know that small values of D need only a small oversaturation to fill the slit with the liquid. Similarly, very small cavities can easily be

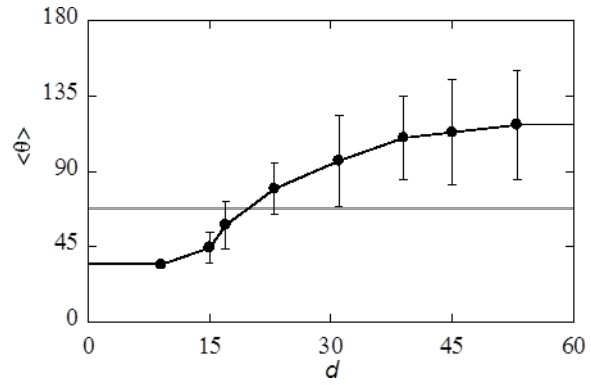

Figure 11: Advancing averaged contact angle $\langle\theta\rangle$ and standard deviation as a function of the cavity diameter d (in lattice units) for a hexagonally ordered inverse opal with cut-off fraction c = 0.8, distance between cavities $s = d - 1$ and slightly hydrophilic surface properties $\chi_S = -0.3$. The grey line is contact angle θ_Y on a smooth surface.

filled with the liquid. We refer to this situation as the impregnated wetting state (Figure 1). Indeed the inverse opal with $d < 10$ are in the impregnated state and it is natural to expect that for this case $\langle\theta\rangle < \theta_Y$: the effective top surface in front of the water front consists of the solid with patches of liquid, just as is the case for a receding droplet. The advancing contact angle $\langle\theta\rangle$ found for these structures (see Figure 11) corresponds to the receding contact angles presented in Figure 10B.

For the structure with d = 15 the situation is rather complex. It appears that some, but not all, cavities in front of the droplet are filled with liquid. In the process of advancing the liquid front, we add more and more of the liquid. As soon as an additional cavity is filled, the volume for the droplet decreases and this reduces the curvature and the corresponding oversaturation in the vapour phase. This decrease in oversaturation after filling subsequent cavities prevents other cavities to fill up. The number of cavities filled in front of the water front, depends on the size of the droplets on top of the inverse opal: the smaller the droplet, the higher the curvature, thus the more oversaturation. The more cavities are filled, the lower is the advancing contact angle $\langle\theta\rangle$ as the surface becomes effectively hydrophilic. The droplet size dependence will imply small changes in the dependence of $\langle\theta\rangle$ as a function of d in Figure 11. For the drop sizes used to compute Figure 11 $\langle\theta\rangle = \theta_Y$ occurs approximately at d = 20.

For the inverse opals with $d \geq 20$ only cavities directly under the droplet are filled (Wenzel wetting state). The water front encounters the same fraction of flat solid top surface, Φ_S for all cavity sizes, but the increase in $\langle\theta\rangle$ with d depends on the strength of the pinning effects and this allows $\langle\theta\rangle$ to increase with d above θ_Y.

Effect of the S/L interaction parameter χ_S

Let us next focus on the interaction of the liquid with the substrate via the S/L interaction parameter χ_S. The more negative this parameter the more hydrophilic (solvophilic) the surface is. When the χ_S is positive we may refer to the surface as hydrophobic (solvophobic). We select for this study hexagonally ordered inverse opals with a cavity size d = 39. As shown in Figure 11 such cavity sizes give wetting features in the plateau region where the size dependence was essentially lost. We consider here the case that the cut-off fraction is c = 0.9. This c-value is chosen to mimic the inverse opal in [10]. The distance between the cavities was set to $s = d - 1$ (cavities are connected to each other by small openings).

In Figure 12 the grey curve represents the contact angle θ_Y on the smooth surface as a function of χ_S and this result is reproduced from Figure 5 for ease of comparison. The average advancing contact angle $\langle\theta\rangle$ increases with decreasing hydrophilicity (solvophilicity) of the substrate. However, for $\chi_S > -0.6$ the advancing contact angle is systematically above θ_Y, whereas it is systematically below θ_Y when $\chi_S < -0.6$.

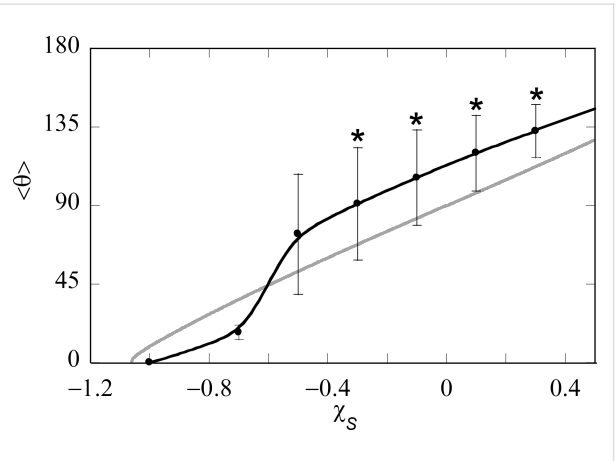

Figure 12: Advancing contact angle $\langle\theta\rangle$ and the corresponding fluctuations (measured along the x-direction) indicated as error bars, as a function of the affinity of the solvent for the substrate phase χ_S for a hexagonal inverse opal with cavity sizes d = 39, cut-off fraction c = 0.9 and spacing between the cavities $s = d - 1 = 38$. The contact angle on a smooth surface is shown with a grey line (copied from Figure 4). Stars indicate that the cavities under the water front remain empty (Cassie–Baxter wetting state).

The wetting transition, which is the point for which θ becomes 0, occurs at a value of χ_S which is slightly less hydrophilic for the inverse opal as for the smooth surface. In the low contact angle cases all cavities under the droplets are filled (impregnating wetting state). The filled cavities render the surface slightly more hydrophilic than the smooth surface (see Equation 1) and this caused the early wetting transition for the inverse opal as compared to the smooth surface.

The inverse opal remains in the impregnating wetting state for small but finite contact angles $\chi_S = -0.7$. In these cases the advancing contact angle is lower than the corresponding θ_Y. The wetting switches to the Wenzel state by increasing the hydrophilicity further to $\chi_S = -0.5$. Now the advancing contact angle is larger than θ_Y. Eventually, the wetting switches to a Cassie–Baxter wetting state for higher values of χ_S. These cases are labelled by the asterisk in Figure 12. Again the advancing contact angle is larger than θ_Y, and the difference $\langle\theta\rangle - \theta_Y$ is roughly constant, that is, it does not depend whether there is the Wenzel or the Cassie–Baxter state. This result suggests that for the advancing angle, it does not matter whether air is entrapped underneath (observed for $\chi_S \geq -0.3$) the droplet or not (observed for $\chi_S \geq -0.5$). This implies that the increase in observed $\langle\theta\rangle$ compared to θ_Y cannot be explained in terms of wetting state. Rather, pinning of the contact line and the de-pinning transition should be considered. The immobilization of the contact line on the kinks in the surface (as explained in Figure 2) on this hexagonally packed inverse opal induces the contact line to curve and extend ($\Delta y > 0$), which is energetically unfavourable. The contact line is even further extended after a de-pinning transition (increase in Δy), indicating that in the stress perpendicular to the surface has increased. However, $\langle\theta\rangle$ decreased locally to values close to θ on a smooth surface, showing that stress in the vertical direction is released after the transition. The average $\langle\theta\rangle$ is still higher than θ_Y directly after the de-pinning transition. This is caused by the build-up of stress at the other cavity (we consider two rows of cavities).

The interplay between curvature perpendicular to the surface (here discussed in terms of $\langle\theta\rangle$) and parallel to the surface (here discussed in terms of Δy of the contact line) results in an overall high $\langle\theta\rangle$. Whether the cavity under the moving water front fills with liquid or remains filled with air depends on χ_S: Air is entrapped for more hydrophobic materials, but the cavities fill for a more hydrophilic material. The pinned water front on a surface with higher χ_S can withstand higher $\langle\theta\rangle$ before stress starts to build up and the de-pinning transition occurs.

Effect of cut-off height *c* at constant spacing *s*

Experimentally one can control the inverse opal structure by the cut-off height *h*, or equivalently to the cut-off fraction *c*. It is of interest to consider the effect of the cut-off height from a computation point of view. We can study this for a fixed spacing *s* between the cavities (in this section) or with a fixed fraction of solid in the top of the substrate Φ_S (next section). In both cases we choose slightly hydrophilic substrates with $\chi_S = -0.3$. This value of χ_S gives $\theta_Y = 68°$. Similarly as in the previous paragraph we fix $d = 39$ and $s = d - 1$. Obviously the limits $c = 0$ and $c = 1$ are the same as the smooth surface. In between these two limits the surface structure is characterised by a top surface layer with a fraction of Φ_S of the sites being the solid. The top layers are given in two-gradient contour plots in Figure 13C. When $c = 0.5$ the amount of S (dark blue colour) is minimal: both in the limits $c = 0$ and $c = 1$ the cross-sections are completely blue (not shown).

Correspondingly, the contact line fluctuations, as monitored by Δy, are averaged over ten "snapshots" while increasing the drop volume. The result is given by $\langle\Delta y\rangle$. In both limits $c = 0$ and $c = 1$ the surface is ideally smooth and the three-phase contact line will not fluctuate in the *x*-direction. In between these limits $\langle\Delta y\rangle > 0$ because the contact line becomes pinned.

The advancing contact angle $\langle\theta\rangle$ together with the standard deviation of this angle (measured in the *x*-direction) is presented in Figure 13A as a function of the parameter $c = h/d$. The corresponding fluctuations of the three-phase contact line $\langle\Delta y\rangle$ (measured in the *x*-direction at a height $z = h + 3$) are given in Figure 13B.

Inspection of Figure 13A shows that by far the most interesting region is for $0.5 < c < 1$. For $c < 0.5$ the average advancing contact $\langle\theta\rangle$ hardly differs from θ_Y. However, for small values of the cut-off fraction the contact line is already significantly curved (Figure 13B) and the surface structure alters $\theta(x)$ locally to hydrophobic values $\theta > 90°$. The average $\langle\theta\rangle$ for $0.51 < c < 0.95$ is higher than θ_Y on a smooth surface, though locally, $\theta(x)$ may be smaller. The variation of θ along the *x*-direction (depicted as vertical line) extends to values $\theta < 68°$ for most values of *c*. A maximum in $\langle\theta\rangle$ is found at $c \approx 0.80$, with $\langle\theta\rangle = 110 \pm 30°$. A local minimum in Δy at this value of *c* is found, which likely is coupled to the need to keep the overall curvature in the drop constant.

Two parameters of the surface structure that are important for contact line pinning are changed when *c* is varied: the fraction flat solid top surface Φ_S, which is the fraction of flat solid at the top of the surface (dark blue in Figure 13C) and the angle of the kink, θ_{kink} (see section S2 of Supporting Information File 1 for calculation of θ_{kink} and section S3 of Supporting Information File 1 and Equation 16 for the calculation of Φ_S). Both, $\Phi_S \cdot 100$ and θ_{kink} are plotted in Figure 13A. The value of $\Phi_S \cdot 100$ equals 100 in both limits of *c* and has a minimum at $c = 0.5$. θ_{kink} is 180° at $c = 0$, and decreases to 0 at $c = 1$. The latter parameter is considered important for hydrophilic materials to obtain hydrophobic contact angles. It has been suggested that only for $\theta_Y < \theta_{kink}$ pinning can occur, and a barrier for the water front to enter the cavities is obtained, resulting in air entrapment and the possibility of obtaining higher contact angles θ. However, in our case, θ_{kink} is smaller than θ_Y for most values of *c*, and no jump in $\langle\theta\rangle$ is observed between $c = 0.51$ ($\theta_{kink} > \theta_Y$) and

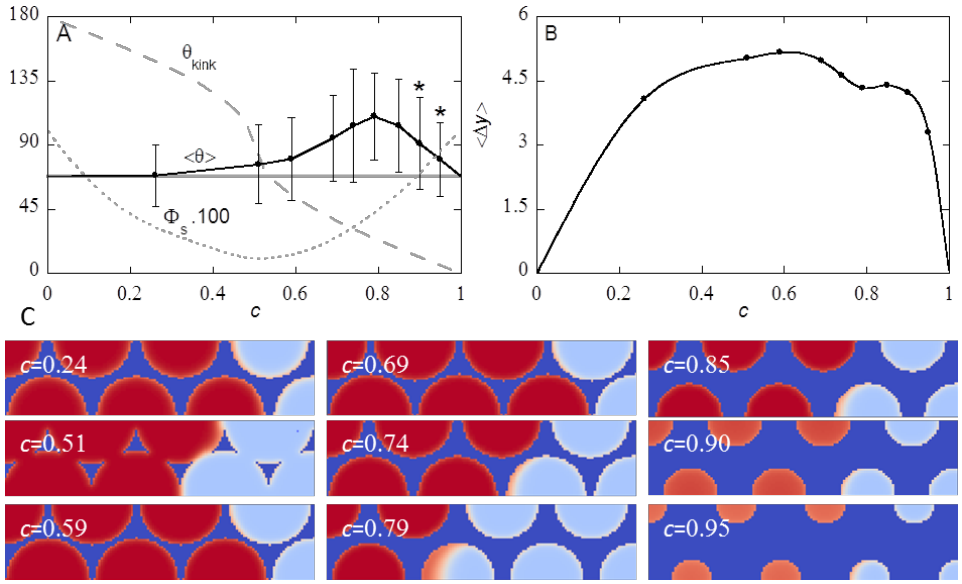

Figure 13: A) Advancing contact angle $\langle\theta\rangle$ and the corresponding standard deviation as measure of variation in the *x*-direction as function of the cut-off fraction *c*. The horizontal grey line is the contact angle θ_Y on a smooth surface, the grey dashed line is the angle of the kink θ_{kink} at different values of *c* and the grey dotted line is $\Phi_S \cdot 100$. Stars indicate that the cavities under the water front are filled with vapour (Cassie–Baxter wetting state). B) Corresponding average variation in *y*-position $\langle\Delta y\rangle$ at $z = h + 3$ as function of the cut-off fraction *c*. The hexagonally ordered inverse opal has cavity diameter $d = 39$, spacing between the cavities $s = d - 1 = 38$, and $\chi_S = -0.3$. C) The distribution of solid S at the top layer of the substrate, that is $\varphi_S(x, y, h)$. The dark blue colour implies density of the solid is unity. The red colour indicates that the opening of the cavity is filled by the solvent. The light blue colour means that the cavity opening is filled with vapour. Orange colour implies that the solvent density is in between the liquid and the vapour. The value of *c* is indicated.

$c = 0.59$ ($\theta_{kink} < \theta_Y$), and no air entrapment is found for $0.59 < c < 0.85$.

For $c = 0.26$, θ_{kink} is too large for pinning to occur according to the argument presented Figure 2. However, an advancing water front is immobilized at the front of a cavity, and moves in one step to a position in front of the next cavity. Hence, despite of the small θ_{kink} in our calculations a true de-pinning transition is found.

In our case the pinning of the contact line is due to the complex 3D-structure of the surface: the cavities are placed close to each other, and the contact line thus encounters multiple cavities on a short distance. If the water front was not pinned at the front of a cavity, but rather partly filled the cavity, this would result in a larger L–S interface and a longer contact line. This is apparently energetically more unfavourable than pinning the contact line in front of a cavity. Hence, the contact line pinning is governed by the 3D-structure, and not by the simple 1D-argument presented in Figure 2.

When looking at the top surface (Figure 13C) for $c = 0.26$, we see that some cavities on the left are filled (red), while the last 1.5 cavities are not filled (light blue). The last upper cavity is just in front of the contact line. Some liquid (red colour) is present at this value of *z*. Moreover, the situation for $c = 0.74$, which has a similar top surface but a different θ_{kink}, is comparable.

For *c* close to 0.5, the substrate is not a continuous structure, but consists of discrete triangular "pillars" (see Figure 13C). Contact line pinning also occurs for discrete shapes [19,46]. Assuming that pinning is mainly found on the top surface in line with observations for $c = 0.26$, the length over which pinning can take place is limited. However, also in this case a de-pinning transition is observed for an advancing water front. Hence the pinning is not limited to the flat part of the top surface (the dark blue surfaces in Figure 13C) for all values of *c*, but pinning occurs over the 3D structure.

Decreasing or increasing *c* from $c = 0.5$ results in a continuous top layer. The contact line can hereby be pinned at the front of every cavity. For higher values of Φ_S, the contact line is expected to be exclusively located on the top surface (and thus at constant *z*). Higher values of Φ_S (thus smaller cavities) also result in a surface that is more similar to a smooth surface.

In Figure 13C, the liquid-filled cavities are shown in red, whereas vapour-filled cavities are light blue. This is observed for all *c* up to $c = 0.85$. However, for $c = 0.90$ and $c = 0.95$, we observe a colour in between red and light blue for cavities under the droplet (left hand side). This suggests that at that height,

neither a liquid, nor a vapour phase is present, and thus that the interface is located at that value of z.

Effect of cut-off height c at constant Φ_S

One may argue that the true effect of the cut-off height is seen for cases where h (or equivalently c) is varied at a fixed amount of S in the top layer of the substrate, that is for fixed value of Φ_S. To do so, one has to vary the inter-cavity spacing s simultaneously when the cut-off height is changed. Note that the true limits $c = 0$ and $c = 1$ are hard to reach with fixed Φ_S as it requires odd distances between the cavities.

The behaviour of the advancing contact angle as well as the contact line fluctuations are recorded for this scenario in Figure 14. Here we have chosen $\Phi_S = 0.43$, which corresponds to $c = 0.79$ (near the maximum) of Figure 13. Note that all the top surfaces used in Figure 14 are similar to the result shown in Figure 13C for $c = 0.79$.

It is natural to compare results between Figure 13 and Figure 14. For values of $c < 0.79$, the average contact angles differ very little. In Figure 14 the average angle appears slightly larger. There is one dramatic difference between Figure 13 and Figure 14. Compare, for example, the top surface for $c = 0.51$. While in the case of fixed distance between the cavities s there are individual posts with $\Phi_S \approx 0.1$ (Figure 13C), there is a continuous solid phase in Figure 14 as $\Phi_S = 0.43$. Nevertheless, the average contact angles were hardly affected.

At $c > 0.79$, $\langle\theta\rangle$ at constant Φ_S (Figure 14) keeps growing with the increase in c, while at fixed s the contact angles decrease again. The decrease in $\langle\theta\rangle$ for $c > 0.79$ in the case of constant s (Figure 13) can thus be attributed to the top surface: Higher c result in smaller cavities and thus in a surface that is more similar to a smooth surface. The increase in $\langle\theta\rangle$ found for increasing c at constant Φ_S implies that, assuming a constant line tension, a higher θ_{kink} for a hexagonally packed surface structure gives rise to a higher barrier for a de-pinning transition to occur and thus higher average contact angles can be maintained. The higher average contact angles are produced with lower and lower fluctuations of the shape of the contact line. Eventually, at the limit of $c = 1$ the fluctuations must vanish by definition.

Interestingly, it is found that the cavities under the water front remain empty for $c = 0.85$ (and up) at $\Phi_S = 0.43$, whereas the cavities were filled for $c = 0.85$ at $s = 38$ ($\Phi_S = 0.55$). Bringing the openings of the cavities closer to each other thus prevents water from entering the cavity.

Summary and Outlook

We have implemented a regular solution lattice model to study the wetting on a structurally complex surface. The interaction between vacancies and liquid is parameterised in a regular solution model by the Flory–Huggins parameter χ. This parameter controls the width of the interface between liquid and vapour. The model allows for a detailed description of the solid phase and the liquid–solid interaction parameter χ_S is the only parameter to control the hydrophilic/hydrophobic (solphophilic/solvophobic) character of the substrate. We find very complex and interesting wetting states when this model is applied to hexagonally ordered cavities in an inverse opal. It is found that the three-phase contact line is curved and becomes pinned at the cavity openings. Under the droplet the cavities can either be filled with water (impregnated; Wenzel) or filled with the vapour (Cassie–Baxter). No discontinuity in the contact angle θ is observed for water fronts that are either in the Wenzel state or Cassie–Baxter state, implying that the water front shape is not influenced by air entrapment under the water front, but is rather determined by the surface encountered by the contact line. The pinning of the contact line cannot solely be discussed in terms of the kink that a surface structure makes with respect to the top surface, θ_{kink}. Also, for $\theta_{kink} > \theta_Y$, de-pinning transitions are

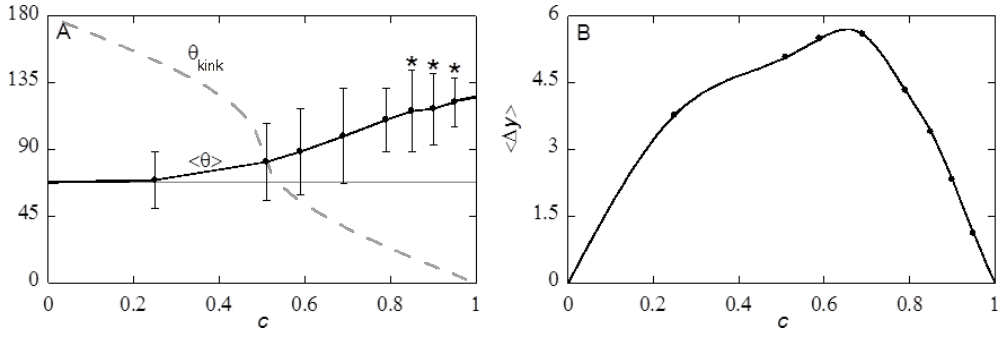

Figure 14: A) The advancing contact angle $\langle\theta\rangle$ and standard deviation as function of cut-off fraction c for fixed value of the solid fraction in the top-layer of the substrate $\Phi_S = 0.43$. The grey line is θ_Y on a smooth surface and the grey dashed line is the angle of the kink at different c. Stars indicate that the cavity under the liquid front are vapour-filled (Cassie–Baxter wetting state). B) Variation in y-position $\langle\Delta y\rangle$ as function of cut-off fraction c for $d = 39$ and $\chi_S = -0.3$.

found, and the spacing between the cavities influence whether a cavity under a water front is solvent-filled or vapour-filled. Hence, the full 3D-structure, rather than one parameter (θ_{kink}) should be taken into account. We found a large difference between advancing and receding contact angles, which are also attributed to pinning of the three-phase contact line. More specifically, it was found that while the smooth surface has a contact angle much lower than 90° the advancing contact angles in the inverse opal can be much larger than 90°. That is, slightly hydrophilic substrates can give hydrophobic contact angles.

Our method can readily be extended to mimic experimental conditions more closely. An interesting case is the wetting of an inverse opal of polypyrrole [10]. The inverse opal of polypyrrole does not have a smooth top surface. Rather, the top surface showed a positive slope radiating from the position of the sacrificial particle. This more complex surface structure can be implemented easily by a more elaborated way to represent the substrate. Furthermore, polypyrrole is a hydrophilic material. The angle θ_Y on a polypyrrole surface was measured to be about 20°. However, the inverse opal was made using sacrificial polystyrene particles. The particles were removed by dissolving them. This removal was expected to be incomplete, and the contact angle θ changed to about 80° for the polypyrrole surface. Polystyrene chains thus must have remained, e.g., in an adsorbed state onto the polypyrrole surface. These adsorbed polymers have a different hydrophilicity, but also changes the local roughness of the surface structures, resulting in both chemical and structural heterogeneities. These heterogeneities on molecular scale can be studied using the approach presented in this paper when the Scheutjens–Fleer machinery is more fully implemented. For example, we can easily consider polymer chains pinned at random locations along the surface of the inverse opal. It is even possible to consider polymer brushes on such substrates which may, e.g., preferentially change wetting characteristics of the top surface or the insides of the cavities [47]. Such decorated substrates may feature dramatic hysteresis effects in the contact angle, because the polymers can stabilize the three-phase contact line while the shape of the cavities induces pinning of the contact line. Hence polymers may introduce a second length scale in inverse opal surface structures.

In the current work we have solved the regular solution model using the self-consistent field (SCF) machinery. Only low memory costs were required to find SCF solutions that are linearly proportional to the volume, that is, the number of lattice sites in the system (M_x, M_y, M_z). Also the CPU time scales only linearly with the volume. Here we focused on very small systems and used a desktop PC to find accurate results in a few minutes CPU time. Alternatively, the complete set of equations can be solved on a GPU and using CUDA technology the results may be generated 10 to 100 times faster [48]. As a result systems which are 10 times larger in each direction should still be feasible, while keeping the wall-time for the computations at less than an hour. In this case the regular solution model captures the macroscopically relevant sizes and we do not need to rely on extrapolations.

Conclusion

Regular solution theory is used to study the wetting behaviour of a simplistic molecular model on a complex inverse opal surface topology. The model features molecular input parameters and gives interfacial energies, contact angles and three-phase contact line shapes. As a result, advancing as well as receding wetting front scenarios were considered. It was found that there is a large contact angle hysteresis in these systems, which was attributed to contact line pinning. We have seen that the cavities can be filled by the liquid or remain dry, i.e., filled by vapour. Cavities in front of the droplet may be filled by a capillary condensation effect, while receding contact angles typically do not empty the liquid filled cavities. Interestingly, when the substrate is slightly hydrophilic it is possible that advancing contact angles have contact angles larger than 90°.

Supporting Information

Supporting Information File 1

Detailed mathematical calculations.
[http://www.beilstein-journals.org/bjnano/content/supplementary/2190-4286-7-129-S1.pdf]

Acknowledgements

S. A. and M. K. acknowledge The Netherlands Organization for Scientific Research (NWO) for financial support.

References

1. Cheng, Y.-T.; Rodak, D. E. *Appl. Phys. Lett.* **2005,** *86,* 144101. doi:10.1063/1.1895487
2. Guo, C.; Feng, L.; Zhai, J.; Wang, G.; Song, Y.; Jiang, L.; Zhu, D. *ChemPhysChem* **2004,** *5,* 750–753. doi:10.1002/cphc.200400013
3. Abdelsalam, M. E.; Bartlett, P. N.; Kelf, T.; Baumberg, J. *Langmuir* **2005,** *21,* 1753–1757. doi:10.1021/la047468q
4. Zhu, M.; Zuo, W.; Yu, H.; Yang, W.; Chen, Y. *J. Mater. Sci.* **2006,** *41,* 3793–3797. doi:10.1007/s10853-005-5910-z
5. Cao, L.; Hu, H.-H.; Gao, D. *Langmuir* **2007,** *23,* 4310–4314. doi:10.1021/la063572r
6. Ma, Y.; Cao, X.; Feng, X.; Ma, Y.; Zou, H. *Polymer* **2007,** *48,* 7455–7460. doi:10.1016/j.polymer.2007.10.038
7. Feng, L.; Song, Y.; Zhai, J.; Liu, B.; Xu, J.; Jiang, L.; Zhu, D. *Angew. Chem.* **2003,** *115,* 824–826. doi:10.1002/ange.200390181
8. Hosono, E.; Fujihara, S.; Honma, I.; Zhou, H. *J. Am. Chem. Soc.* **2005,** *127,* 13458–13459. doi:10.1021/ja053745j

9. Karlsson, M.; Forsberg, P.; Nikolajeff, F. *Langmuir* **2010,** *26,* 889–893. doi:10.1021/la902361c
10. Akerboom, S.; Pujari, S. P.; Turak, A.; Kamperman, M. *ACS Appl. Mater. Interfaces* **2015,** *7,* 16507–16517. doi:10.1021/acsami.5b03903
11. Wenzel, R. N. *Ind. Eng. Chem.* **1936,** *28,* 988–994. doi:10.1021/ie50320a024
12. Liu, J.-L.; Feng, X.-Q.; Wang, G.; Yu, S.-W. *J. Phys.: Condens. Matter* **2007,** *19,* 356002. doi:10.1088/0953-8984/19/35/356002
13. Marmur, A. *Langmuir* **2008,** *24,* 7573–7579. doi:10.1021/la800304r
14. Choi, H.-J.; Choo, S.; Shin, J.-H.; Kim, K.-I.; Lee, H. *J. Phys. Chem. C* **2013,** *117,* 24354–24359. doi:10.1021/jp4070399
15. Bormashenko, E.; Bormashenko, Y.; Whyman, G.; Pogreb, R.; Stanevsky, O. *J. Colloid Interface Sci.* **2006,** *302,* 308–311. doi:10.1016/j.jcis.2006.06.016
16. Cassie, A. B. D.; Baxter, S. *Trans. Faraday Soc.* **1944,** *40,* 546–551. doi:10.1039/tf9444000546
17. Herminghaus, S.; Brinkmann, M.; Seemann, R. *Annu. Rev. Mater. Res.* **2008,** *38,* 101–121. doi:10.1146/annurev.matsci.38.060407.130335
18. Papadopoulos, P.; Deng, X.; Mammen, L.; Drotlef, D.-M.; Battagliarin, G.; Li, C.; Müllen, K.; Landfester, K.; del Campo, A.; Butt, H.-J. *Langmuir* **2012,** *28,* 8392–8398. doi:10.1021/la300379u
19. Forsberg, P. S. H.; Priest, C.; Brinkmann, M.; Sedev, R.; Ralston, J. *Langmuir* **2010,** *26,* 860–865. doi:10.1021/la902296d
20. Bormashenko, E.; Musin, A.; Whyman, G.; Zinigrad, M. *Langmuir* **2012,** *28,* 3460–3464. doi:10.1021/la204424n
21. Tuteja, A.; Choi, W.; Ma, M.; Mabry, J. M.; Mazzella, S. A.; Rutledge, G. C.; McKinley, G. H. *Science* **2007,** *318,* 1618–1622. doi:10.1126/science.1148326
22. Hensel, R.; Helbig, R.; Aland, S.; Braun, H.-G.; Voigt, A.; Neinhuis, C.; Werner, C. *Langmuir* **2013,** *29,* 1100–1112. doi:10.1021/la304179b
23. Savoy, E. S.; Escobedo, F. A. *Langmuir* **2012,** *28,* 16080–16090. doi:10.1021/la303407r
24. Mugele, F.; Becker, T.; Nikopoulos, R.; Kohonen, M.; Herminghaus, S. *J. Adhes. Sci. Technol.* **2002,** *16,* 951–964. doi:10.1163/156856102760136490
25. Wu, J.; Zhang, M.; Wang, X.; Li, S.; Wen, W. *Langmuir* **2011,** *27,* 5705–5708. doi:10.1021/la200697k
26. de Gennes, P. G. *Rev. Mod. Phys.* **1985,** *57,* 827–863. doi:10.1103/RevModPhys.57.827
27. Chamakos, N. T.; Kavousanakis, M. E.; Papathanasiou, A. G. *Soft Matter* **2013,** *9,* 9624–9632. doi:10.1039/c3sm51377g
28. Patankar, N. A. *J. Adhes. Sci. Technol.* **2009,** *23,* 413–433. doi:10.1163/156856108X370073
29. Pashos, G.; Kokkoris, G.; Boudouvis, A. G. *J. Comput. Phys.* **2015,** *283,* 258–270. doi:10.1016/j.jcp.2014.11.045
30. Park, J.-Y.; Ha, M.-Y.; Choi, H.-J.; Hong, S.-D.; Yoon, H.-S. *J. Mech. Sci. Technol.* **2011,** *25,* 323–332. doi:10.1007/s12206-010-1218-2
31. Kumar, V.; Sridhar, S.; Errington, J. R. *J. Chem. Phys.* **2011,** *135,* 184702. doi:10.1063/1.3655817
32. Zhang, Z.; Kim, H.; Ha, M. Y.; Jang, J. *Phys. Chem. Chem. Phys.* **2014,** *16,* 5613–5621. doi:10.1039/c3cp54976c
33. Dupuis, A.; Yeomans, J. M. *Langmuir* **2005,** *21,* 2624–2629. doi:10.1021/la047348i
34. Pooley, C. M.; Kusumaatmaja, H.; Yeomans, J. M. *Phys. Rev. E* **2008,** *78,* 056709. doi:10.1103/PhysRevE.78.056709
35. Vrancken, R. J.; Kusumaatmaja, H.; Hermans, K.; Prenen, A. M.; Pierre-Louis, O.; Bastiaansen, C. W. M.; Broer, D. J. *Langmuir* **2010,** *26,* 3335–3341. doi:10.1021/la903091s
36. Kavousanakis, M. E.; Colosqui, C. E.; Kevrekidis, I. G.; Papathanasiou, A. G. *Soft Matter* **2012,** *8,* 7928–7936. doi:10.1039/c2sm25377a
37. Blow, M. L.; Kusumaatmaja, H.; Yeomans, J. M. *J. Phys.: Condens. Matter* **2009,** *21,* 464125. doi:10.1088/0953-8984/21/46/464125
38. De Coninck, J.; Blake, T. D. *Annu. Rev. Mater. Res.* **2008,** *38,* 1–22. doi:10.1146/annurev.matsci.38.060407.130339
39. van der Waals, J. D. *Over de Continuiteit van den Gas-en Vloeistoftoestand;* AW Sijthoff: Netherlands, 1973.
40. Safran, S. A. *Statistical thermodynamics of surfaces, interfaces, and membranes;* Addison-Wesley: Boston, MA, U.S.A., 1994.
41. Stiopkin, I. V.; Weeraman, C.; Pieniazek, P. A.; Shalhout, F. Y.; Skinner, J. L.; Benderskii, A. V. *Nature* **2011,** *474,* 192–195. doi:10.1038/nature10173
42. Lee, Y.-J.; Braun, P. V. *Adv. Mater.* **2003,** *15,* 563–566. doi:10.1002/adma.200304588
43. Li, H.; Vienneau, G.; Jones, M.; Subramanian, B.; Robichaud, J.; Djaoued, Y. *J. Mater. Chem. C* **2014,** *2,* 7804–7810. doi:10.1039/C4TC01401D
44. Couturier, J.-P.; Sütterlin, M.; Laschewsky, A.; Hettrich, C.; Wischerhoff, E. *Angew. Chem., Int. Ed.* **2015,** *54,* 6641–6644. doi:10.1002/anie.201500674
45. Bormashenko, E. *Colloids Surf., A* **2008,** *324,* 47–50. doi:10.1016/j.colsurfa.2008.03.025
46. Gao, L.; McCarthy, T. J. *Langmuir* **2006,** *22,* 2966–2967. doi:10.1021/la0532149
47. de Vos, W. M.; Leermakers, F. A. M. *Polymer* **2009,** *50,* 305–316. doi:10.1016/j.polymer.2008.10.025
48. Harish, P.; Narayanan, P. J. Accelerating Large Graph Algorithms on the GPU Using CUDA. In *High performance computing – HiPC 2007,* 14th International Conference, Goa, India, Dec 18–21, 2007; Aluru, S.; Parashar, M.; Badrinath, R.; Prasanna, V. K., Eds.; Springer: Berlin, Germany, 2007; pp 197–208. doi:10.1007/978-3-540-77220-0_21

License and Terms

The definitive version of this article is the electronic one which can be found at: doi:10.3762/bjnano.7.129

BEILSTEIN JOURNAL OF NANOTECHNOLOGY

Surface roughness rather than surface chemistry essentially affects insect adhesion

Matt W. England[1], Tomoya Sato[1], Makoto Yagihashi[2], Atsushi Hozumi[*1], Stanislav N. Gorb[3] and Elena V. Gorb[*3]

Full Research Paper

Open Access

Address:
[1]National Institute of Advanced Industrial Science and Technology (AIST), 2266-98, Anagahora, Shimoshidami, Moriyama, Nagoya 463-8560, Japan, [2]Nagoya Municipal Industrial Research Institute, 4-41, Rokuban, Atsuta, Nagoya 456-0058, Japan and [3]Zoological Institute: Functional Morphology and Biomechanics, Kiel University, Am Botanischen Garten 9, D - 24118 Kiel, Germany

Email:
Atsushi Hozumi[*] - a.hozumi@aist.go.jp; Elena V. Gorb[*] - egorb@zoologie.uni-kiel.de

* Corresponding author

Keywords:
insect attachment; superhydrophilicity; superhydrophobicity; superoleophobicity; surface structures

Beilstein J. Nanotechnol. **2016,** *7,* 1471–1479.
doi:10.3762/bjnano.7.139

Received: 24 June 2016
Accepted: 20 September 2016
Published: 18 October 2016

This article is part of the Thematic Series "Biological and biomimetic materials and surfaces".

Associate Editor: K. Koch

Abstract

The attachment ability of ladybird beetles *Coccinella septempunctata* was systematically investigated on eight types of surface, each with different chemical and topographical properties. The results of traction force tests clearly demonstrated that chemical surface properties, such as static/dynamic de-wettability of water and oil caused by specific chemical compositions, had no significant effect on the attachment of the beetles. Surface roughness was found to be the dominant factor, strongly affecting the attachment ability of the beetles.

Introduction

The development of functional coatings that artificially mimic the properties of surfaces found in nature [1-4] to produce exceptional wetting/dewetting properties, such as superhydrophobicity, superhydrophilicity, and superoleophobicity (more commonly known as superamniphobicity or superomniphobicity), has been a major topic for research over the past decade [5-15].

There are countless examples of functional surfaces inspired by plants, such as lotus leaves [5,13] and the pitchers of carnivorous plants [9,14] that can be used to tune the wetting/dewetting properties of surfaces on various substrates. Certain of these natural surfaces can effectively prevent wetting by water, while simultaneously protecting against attachment by insects by taking advantage of the same or very similar surface fea-

tures [16-23]. Unfortunately, these natural anti-attachment properties have received relatively little attention from researchers working on surface science and engineering [24,25]. Another possible reason might be that the properties of unwettable biological surfaces, other than surface wetting/de-wetting, have not been tested. The question of whether surface chemistry or surface roughness is primarily responsible for natural anti-attachment properties has also not been fully resolved. Therefore, a comparative study of the attachment behavior of insects on artificially designed (low/high surface energy) surfaces of varying surface roughness, has been postulated as an effective strategy to identify the most important parameters influencing insect attachment.

Many insects, including beetles, can attach to inverted surfaces using specific hairy adhesive pads, covered with tenent setae, which secrete an adhesive fluid which typically consists of a mixture of alcohols, fatty acids, and hydrocarbons [26-32]. Several hypotheses exist on how plant surfaces prevent insect attachment. These are typically based on (1) the reduction of the contact area between the substrate and the insect adhesive pad through surface micro-roughness, (2) a decrease in substrate surface energy that enhances de-wetting of the insect attachment fluid, (3) fluid absorption by textured substrates, (4) contamination of the insect pads by easily erodible particles of the substrate, and (5) the reduction of wetting by pad fluid due to coverage of the substrate by another fluid (or solid which can be dissolved by the pad fluid) [22]. These mechanisms are to some extent conventional strategies utilized in functional surface design that gives us a unique chance to develop artificial surfaces with such properties, and test their anti-adhesive effects on insects [5-8,10-13,15]. However, recent studies on insect attachment have yielded contradicting results. For example, a previous experimental study on attachment of the beetle *Gastrophysa viridula* to the leaf surface of its host plant *Rumex obtusifolius*, and artificial micro-roughened and smooth (hydrophobic and hydrophilic) surfaces, has shown a stronger insect performance on smooth surfaces when compared to those with micro-roughness [33]. It was also found that surface hydrophobicity alone resulted in some decrease in the attachment force of the beetles, but when combined with surface micro-roughness it caused an even more pronounced reduction. Prüm et al. [17] measured the traction force of the beetle *Leptinotarsa decemlineata* on different plant surfaces and their artificial replicas, and reported that surface roughness exerted a strong influence on attachment, whereas surface chemistry was found to have no significant influence, despite both of these affecting the magnitude of water contact angles (CAs). Additionally, the attachment of the leaf beetle *Gastrophysa viridula* did not strongly depend on the free energy of the surface of the substrate [34]. More recently, the attachment strength of the beetle *Galerucella nymphaeae* on surfaces with different surface energies, showing CAs in the range from 6° to 109°, was examined [35]. These beetles, both at their larval and adult stages, showed the highest forces on surfaces with water CAs close to 83° (similar to those of their host plant), while hydrophilic (CAs of 6 and 26°) and hydrophobic (CA of 109°) surfaces caused a reduction of their adhesive ability.

A strong dependence of adhesive ability on the chemistry of the substrates during locomotion underwater was recently found for the beetle *Gastrophysa viridula* [34]. Using air bubbles trapped between their adhesive setae, these beetles are able to walk on flooded substrates, including those under water. Their attachment to hydrophilic surfaces was reduced when under water, compared to their attachment in air; whereas the attachment to hydrophobic surfaces under water was considerably stronger, and comparable to that observed in air. The oil-covered hairy pads on the feet of the beetle show a pinning effect, which retains air bubbles, and capillary attachment is produced by bubbles in contact with the hydrophobic substrate. Additionally, the liquid bridges of the pad between the foot and the substrate also produce capillary forces. Inspired by this idea, artificial silicone polymer structures with underwater adhesive properties were fabricated [34].

Thus, the relationship between surface structures and the attachment of insects, in combination with their particular chemical/physical properties, has not yet been fully resolved. Therefore, in order to obtain a deeper understanding of this bio-attachment phenomenon, it is crucial to systematically investigate the influence of both the surface chemistry and surface morphology on insect attachment properties using a greater range of surfaces with different surface wettabilities, in combination with both smooth and rough surface textures. Specifically, we focused our attention on both the static CAs of water and oil (*n*-hexadecane), and their dynamic (advancing (θ_A) and receding (θ_R)) CAs, especially CA hysteresis ($\Delta\theta$, the difference between the values of θ_A and θ_R), which is a mass-independent measure of the resistance to macroscopic liquid drop movement on inclined surfaces.

In this study, we investigated eight different surfaces. Three of these were smooth with different surface wettabilities, including two types of hydrophobic monolayers, with alkyl- and perfluoroalkyl-terminated functional groups. The third smooth surface was a hydrophobic/oleophilic alkylsilane-derived hybrid film, showing low CA hysteresis for water and *n*-hexadecane. In addition, we also studied three rough surfaces with different wettabilities. For these, we used a commercially available superhydrophobic coating system, which was also used to prepare a rough superhydrophilic surface, by subjecting it to

vacuum UV (VUV) light treatment. A superomniphobic surface (defined here as a surface exhibiting both superhydrophobicity and superoleophobicity) was created using candle soot as templates for SiO_2 nanoparticles, which were modified with a perfluoroalkylsilane monolayer. All surfaces were prepared on Si substrates. We measured traction forces of adult seven-spotted ladybird beetles *Coccinella septempunctata*, both males and females, on these six sample surfaces and two reference surfaces, i.e., smooth, hydrophilic silicon wafers (Si) and glass surfaces. Our sample surfaces displayed a wide range of surface chemical and topographical properties, and while both of these had a significant effect on the magnitude of CAs for probe liquids, the attachment abilities of the ladybird beetles were found to be predominantly influenced by the surface topography.

Experimental

Materials

Ethanol, 0.01 M HCl, and *n*-hexadecane were purchased from Wako Pure Chemical Industries Ltd. (Osaka, Japan). Tetramethoxysilane (TMOS, $Si(OCH_3)_4$) and *n*-octadecyltrimethoxysilane (ODS, $CH_3(CH_2)_{17}Si(OCH_3)_3$) were purchased from Tokyo Chemical Industry Co., Ltd. (Tokyo, Japan). (Heptadecafluoro-1,1,2,2-tetrahydrodecyl)trimethoxysilane (FAS17, $CF_3(CF_2)_7CH_2CH_2Si(OCH_3)_3$), (heptadecafluoro-1,1,2,2-tetrahydrodecyl)trichlorosilane (FAS17-Cl, $CF_3(CF_2)_7CH_2CH_2SiCl_3$), and decyltriethoxysilane (C_{10}, $CH_3(CH_2)_9Si(OC_2H_5)_3$) were purchased from Gelest Inc. (Morrisville, PA, USA). Never Wet™ (superhydrophobic coatings) was purchased from Rust-Oleum Corporation (Vernon Hills, IL, USA). All chemicals were used as received without further purification.

Preparation of flat and rough sample surfaces

Two smooth, hydrophobic monolayer-covered surfaces, terminated with octadecylsilyl ($CH_3(CH_2)_{17}$-) or perfluoroalkyl ($CF_3(CF_2)_7CH_2CH_2$-) groups, were prepared using chemical vapor deposition (CVD) of ODS or FAS17 [36], respectively. UV–ozone treated Si substrates (2 × 2 cm^2 and 5 × 5 cm^2) were placed on a heat-resistant glass plate (18 × 18 × 0.4 cm^3) with a small aluminum-made vessel, or alternately placed in a Teflon container with a glass vessel, containing 0.2 mL of organosilane (ODS or FAS17), in a dry N_2 atmosphere at less than 5 % relative humidity. Another heat-resistant glass plate was then placed on top of it using an O-ring (approximately 150 mm diameter and 8 mm thickness) as a spacer, and the four corners of the glass plates were secured using four clamps. Alternately, the Teflon container was sealed with an airtight screw-on Teflon cap. The reaction container was then heated for three days in an oven maintained at 180 °C for ODS and 150 °C for FAS17. Finally, the treated samples were rinsed with *n*-hexane, then water, and finally blown dry with a stream of N_2. Besides these two flat monolayer-covered surfaces, we also prepared a smooth alkylsilane (C_{10})-derived hybrid film using conventional co-hydrolysis and co-condensation [10]. Briefly, precursor solutions were prepared by mixing C_{10} and TMOS in an ethanol/hydrochloric acid solution for 24 h at room temperature (25 ± 2 °C). The typical molar ratio of the precursor solution was 0.73 C_{10}:2.92 TMOS:32 EtOH:14 H_2O:7.7 × 10^{-3} HCl. The precursor solution was then spin-coated (500 rpm for 5 s and 1000 rpm for 10 s) onto UV–ozone-cleaned Si substrates (5 × 5 cm^2) at room temperature, under a relative humidity of (40 ± 5)%. All samples were dried in air at room temperature for more than 24 h. Details of our preparation methods for the monolayers and hybrid film have been described elsewhere [10,12]. Three rough surfaces, each showing different wetting properties (superhydrophobicity, superhydrophilicity, and superomnipobicity) and morphologies were prepared as follows. The commercially available Never Wet coating system was used to prepare two rough superhydrophobic surfaces. Base coats were first deposited onto UV-cleaned Si substrates (2 × 2 cm^2 and 5 × 5 cm^2), then dried in air at room temperature (25 ± 2 °C) for more than 30 min. Next, topcoats were deposited onto the surfaces and cured at 100 °C for 24 h, hereafter referred to as Never Wet. Superhydrophilic surfaces were prepared by exposing superhydrophobic Never Wet surfaces to VUV light generated from an excimer lamp (Ushio Inc., UER20-172 V; λ = 172 nm and 10 mW/cm^2) at 10^3 Pa for 2 min, hereafter referred to as VUV-Never Wet. Superomniphobic surfaces were prepared according to a method modified from a report previously published by Deng et al [37]. The candle-soot-covered Si substrates (2 × 2 cm^2 and 5 × 5 cm^2) were exposed to VUV light at 10^3 Pa for 30 min. The samples were then exposed to TMOS vapor for 4 h at 80 °C using the CVD method described previously. Next, the samples underwent thermal calcination in air for 3 h at 600 °C in order to remove any organic components, and thus obtain SiO_2 nanostructures. After VUV irradiation at 10^3 Pa for 30 min, the samples were finally exposed to a FAS17-Cl vapor at room temperature (25 ± 2 °C) for more than 3 h under reduced pressure, hereafter referred to as Soot-TMOS-FAS17Cl.

Characterization of sample surfaces

The thicknesses of the ODS and FAS17 monolayers were measured using ellipsometry (Philips, PZ2000). The thicknesses of the superhydrophobic (Never Wet), superhydrophilic (VUV-Never Wet), and superomniphobic films (Soot-TMOS-FAS17Cl) were estimated from cross-sectional images acquired by a scanning electron microscope (SEM, Phenom Pro Scanning Electron Microscope, Phenom World). The surface morphologies of the samples were either observed using the same SEM system or by atomic force microscope in a tapping mode

(AFM, XE-100, Park Systems), with a Si probe (910M-NCHR; spring constant of 42 N/m and response frequency of 330 kHz, Park Systems). The surface roughness (root-mean square roughness, R_{rms}) were estimated using two separate techniques due to the huge disparity in the size of surface textures on smooth and rough samples. Our five smooth samples (glass, Si, ODS, FAS17, and C_{10}-hybrid) were estimated by AFM, while those of the three rough samples (Never Wet, VUV-Never Wet, and Soot-TMOS-FAS17Cl) were measured using a stylus profilometer (Surftest SJ-301, Mitutoyo Corp.).

Static and dynamic CA data (θ_S and θ_A/θ_R values) for water and oil (*n*-hexadecane) were recorded using CA goniometers (model CA-V150, Kyowa Interface Science). The CA data reported here were determined by averaging values measured at 5–10 different points on each surface of the sample. All values for each sample were in a range of ±2°.

Surface chemical properties of the surfaces of the samples were studied by applying X-ray photoelectron spectroscopy (XPS). Spectra were obtained using a Physical Electronics Quantum 2000 spectrometer with 200 μm spot size and monochromatic Al Kα radiation (1486.68 eV). The X-ray source was operated at 50 W and 15 kV with the pass energy of the analyzer at 29.35 eV. The pressure in the analysis chamber was around 6×10^{-9} Pa during all measurements. Core-level signals were obtained at a photoelectron takeoff angle of 15° (surface-sensitive mode) with respect to the sample surface. The binding energy (BE) scales were referenced to 284.6 eV, as determined by the locations of the peak maxima of the C 1s spectra of a hydrocarbon (CH_x). Surface compositions were determined by the corresponding core-level spectral area ratios, calculated using the relative sensitivity factor method. The relative error for all XPS data used to determine surface composition was estimated to be ±2%.

Insect force tests

Insect attachment ability was studied in traction experiments with tethered adult seven-spotted ladybird beetles *Coccinella septempunctata* (Coleoptera, Coccinellidae) by using a load cell force transducer (10 g capacity, Biopac Systems Ltd., Santa Barbara, CA, USA) as described by Gorb et al [23]. Insects were collected near Stohl (surroundings of Kiel, Germany). Forces generated by both males and females walking horizontally on six different surfaces (five smooth and three rough, each with different surface chemical and physical properties, (see above)) were measured. Obtained force–time curves were used to estimate the maximal traction force. Experiments were performed at 23 °C temperature and 26–29% relative humidity. We tested 10 male and 10 females and carried out 160 traction tests in total.

The experimental design included eight successive force tests with each insect individual: first on smooth, hydrophilic glass to check insect fitness, then on the other seven samples (Si, ODS, FAS 17, C_{10}-hybrid, Never Wet, VUV-Never Wet, and Soot-TMOS-FAS17Cl) in a random order. In order to regain their superhydrophilic properties, Si and VUV-Never Wet samples, prior to the force tests, were plasma treated for 8 min with compressed air (pressure = 2.0 mbar) by applying a low pressure plasma system (Zepto, Diener electronic, Ebhausen, Germany), working at 100 W and 40 kHz regime. The samples were used in traction force experiments during maximum of 60 min after the plasma treatment.

Statistical analyses of the force values were carried out with SigmaStat 3.5 (Systat Software Inc., Point Richmond, CA, USA). For one-way ANOVA (Kruskal–Wallis one-way ANOVA on ranks), data obtained with males and females were pooled together. The effects of the sex of insect individuals and the surface type on the traction force values were examined using two-way ANOVA. Pairwise comparisons of sexes and surfaces were performed with the Tukey test. Force values are given as the mean ± standard deviation (SD).

Results and Discussion

As shown in Figure 1, all sample surfaces observed by AFM appeared to be smooth over the entire scanning areas (3×3 μm^2). The average R_{rms} values of ODS- and FAS17-monolayer-covered Si surfaces were very low (Table 1), indicating that the Si substrates could be modified uniformly (their thicknesses were between 1 and 2 nm) without any marked change in morphology (compared with the R_{rms} of an Si surface). Although the film thickness and R_{rms} of the C_{10}-hybrid film itself was up to 700 times thicker (700 nm) and approximately 10 times higher (1.24 nm), respectively, than those of ODS and FAS17 monolayers, its surface was also fairly smooth. In contrast, SEM images shown in Figure 2 confirmed that films of the three rough surfaces, Never Wet, VUV-Never Wet, and Soot-TMOS-FAS17Cl, were substantially thicker (estimated by cross-sectional SEM images) than the monolayers and hybrid film, and also highly textured (Table 1). Due to these particulate film formation on these surfaces, their R_{rms} values were extremely high, around three to four orders of magnitude higher than those of the four smooth surfaces, as estimated by a stylus profilometer.

Surface dewetting properties were investigated by measuring static/dynamic CAs (θ_S, θ_A, and θ_R) of water and *n*-hexadecane droplets. As shown in Table 1, they were found to be strongly dependent on both surface chemical and topographical properties. Water CA measurements confirmed that the glass, Si and VUV-Never Wet surfaces were superhydrophilic with θ_S close

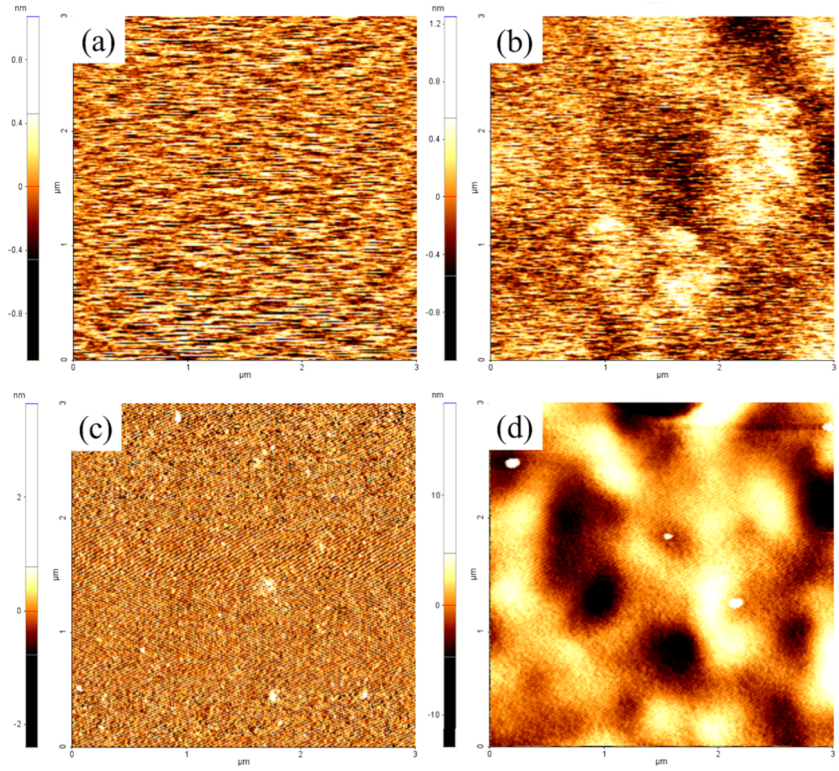

Figure 1: Typical AFM images of Si substrates before (a) and after (b) ODS-monolayer formation, (c) FAS17-monolayer formation, and (d) C_{10}-hybrid film formation (scan areas are 3 × 3 μm^2).

Table 1: Surface properties of the samples.

sample	θ_S water	θ_A/θ_R water	θ_S *n*-hexadecane	θ_A/θ_R *n*-hexadecane	thickness	R_{rms}[a]
Si	—	—	—	—	—	0.16 nm
ODS	103°	106°/96°	10°	12°/5°	1.9 nm	0.23 nm
FAS17	113°	121°/108°	70°	73°/60°	1.1 nm	0.27 nm
C_{10}-hybrid	111°	114°/106°	35°	36°/35°	700 nm	1.24 nm
Never Wet	155°	160°/158°	dissolved	—	≈35 μm	5.2 μm
VUV-Never Wet	—	—	dissolved	—	≈35 μm	6.3 μm
Soot-TMOS-FAS17Cl	163°	165°/160°	155°	161°/153°	<1.6 μm	0.2 μm

[a]R_{rms} values of Si with and without an ODS-monolayer, FAS17-monolayer, and C_{10}-hybrid film were estimated using AFM images (3 × 3 μm^2) shown in Figure 2; those of Never Wet, VUV-Never Wet and Soot-TMOS-FAS17Cl were estimated by a stylus profilometer.

to zero, while the other five surfaces exhibited either hydrophobic (ODS, FAS17 and C_{10}-hybrid surfaces; water CAs greater than 100°) or superhydrophobic (Never Wet and Soot-TMOS-FAS17Cl surfaces; water CAs larger than 150°) properties. Water droplets on the latter surfaces moved very easily and would roll off at very low tilt angles of the substrate because of their extremely large CAs and low CA hysteresis (Δθ = 2–5°). On the other hand, while the static/dynamic CAs of smooth C_{10}-hybrid surfaces were considerably lower than those of the superhydrophobic surfaces, the CA hysteresis of water on the hybrid film was also low (Δθ = 8°, the lowest of the smooth surfaces). Thus, contrasting with the smooth ODS and FAS17 monolayer surfaces, water droplets similarly slid off the C_{10}-hybrid surfaces at low tilt angles, regardless of the magnitude of their static/dynamic CAs [10,36].

The CAs of *n*-hexadecane showed significantly greater variation. Monolayers of ODS and FAS17, and C_{10}-hybrid film surfaces were all oleophilic with θ_S of 10°, 70°, and 35°, respectively. Among them, the C_{10}-hybrid film surface in particular exhibited negligible CA hysteresis (Δθ = 1°), and excellent dynamic dewettability [10]. Unfortunately, the Never Wet sur-

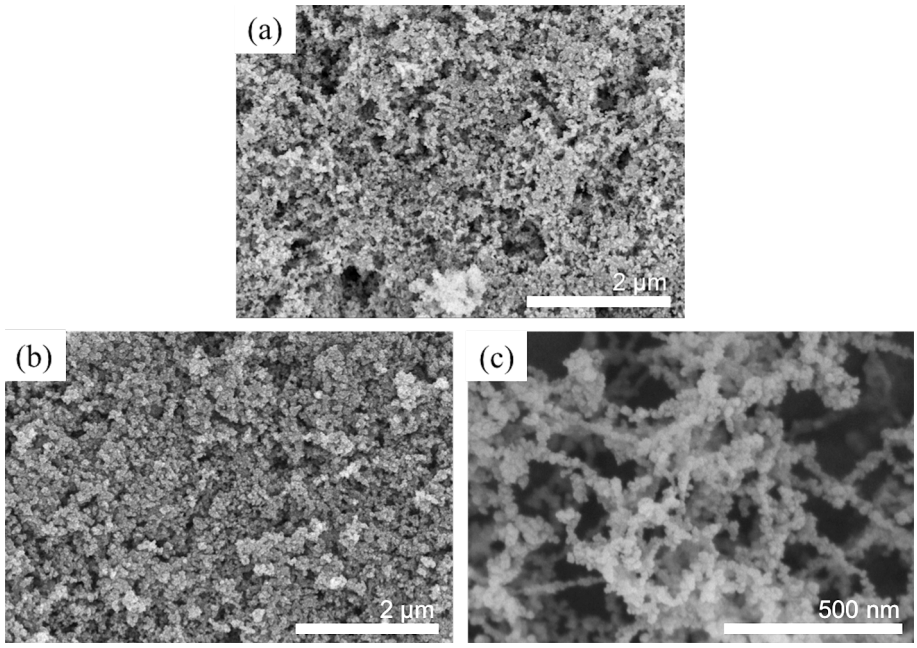

Figure 2: Typical top-down-view SEM images of sample surfaces: (a) Never Wet, (b) VUV-Never Wet, and (c) Soot-TMOS-FAS17Cl.

faces, both before and after VUV irradiation, were dissolved by the *n*-hexadecane. However, the Soot-TMOS-FAS17Cl surface exhibited very high θ_S (155°) and low CA hysteresis ($\Delta\theta$ = 8°) for *n*-hexadecane, and thus *n*-hexadecane droplets on this surface could move, without pinning, more smoothly than they could on a smooth FAS17 surface ($\Delta\theta$ = 13°).

The relationships between surface wettability and chemical composition of our sample surfaces were established using XPS. The surface chemical compositions of each sample are summarized in Table 2. All non-perfluorinated sample surfaces were primarily composed of three elements (Si, oxygen (O), and carbon (C)). As expected, the Never Wet surface showed a decrease in C concentration (ca. 4 atom %) and an increase in the surface O concentration (ca. 6 atom %) following only 2 min VUV irradiation, in agreement with its marked increase in hydrophilicity (superhydrophilicity). Interestingly, the XPS analysis also revealed that the Never Wet surface had the lowest concentration of C (ca. 24 atom %) of any non-perfluorinated sample surface and showed excellent static/dynamic dewetting behavior. In addition, in spite of both perfluorinated sample surfaces (FAS17 and Soot-TMOS-FAS17Cl) showing very high surface fluorine concentrations (above 40 atom %), the former surface displayed inferior static/dynamic dewettability compared to that of the latter one. This clearly indicated that surface roughness, rather than C and F concentrations, had the strongest influence upon surface wettability.

Based on the surface chemical and physical properties of our samples shown above, we next examined the attachment ability of *Coccinella septempunctata* beetles by measuring their traction forces on these surfaces. The average traction force produced by the insects on test surfaces ranged from 0.56 to 9.82 mN (Figure 3). All insects performed well on reference smooth, hydrophilic glass surfaces, showing force values either higher than (compared to C_{10}-hybrid, Never Wet, VUV-Never

Table 2: Sample surface compositions as estimated by XPS.

sample	Si (atom %)	O (atom %)	C (atom %)	F (atom %)
Si	60.1	39.9	—	—
ODS	27.7	41.5	30.8	—
FAS17	12.7	13.3	33.1	40.9
C_{10}-hybrid	18.2	29.1	52.7	—
Never Wet	27.7	46.1	24.2	—
VUV-Never Wet	27.6	52.0	20.4	—
Soot-TMOS-FAS17Cl	9.6	15.6	26.7	46.2

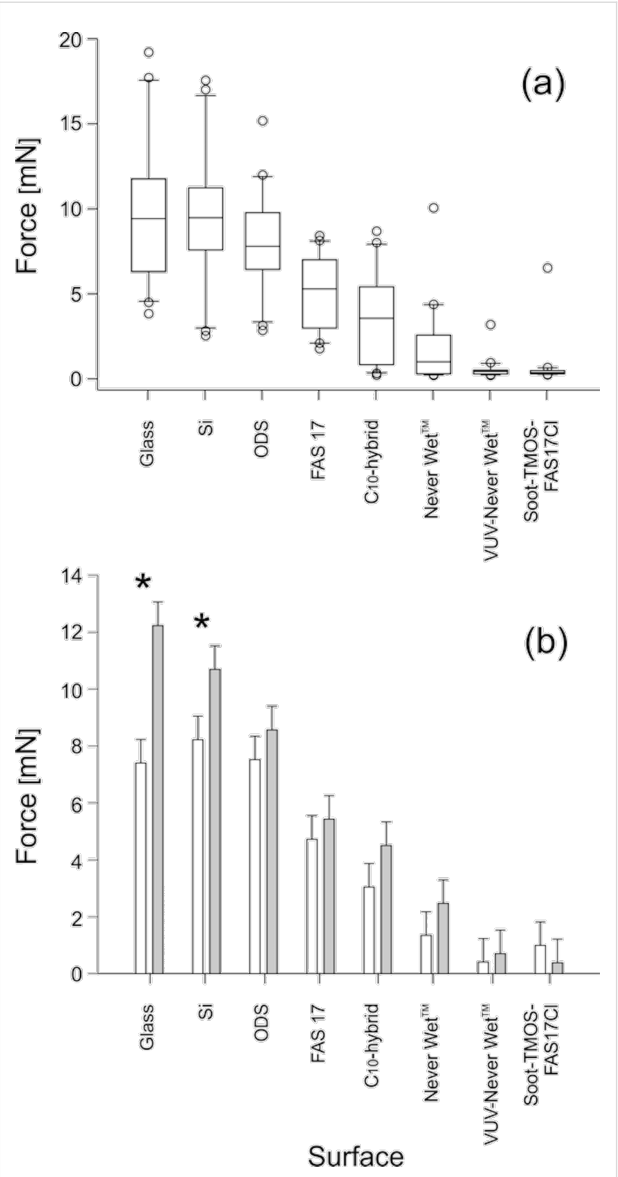

Figure 3: Traction forces of *Coccinella septempunctata* beetles measured on different sample surfaces: (a) data on males and females pooled together; (b) males (grey bars) and females (white bars). Asterisks in (b) indicate statistically significant differences between forces generated by males vs females (Tukey test, $P < 0.05$).

Wet^{TM}, and Soot-TMOS-FAS17Cl; Tukey test, $P < 0.05$) or similar to (compared to Si, ODS, and FAS17; Tukey test, $P > 0.05$) those obtained on other samples (Figure 3a). Among our samples (Kruskal–Wallis one-way ANOVA on ranks: $H_{6,139} = 123.062$, $P < 0.001$), two distinct groups can be clearly distinguished: smooth surfaces showing successful insect attachment (Si, ODS, and FAS17) and rough ones reducing the attachment (Never Wet, VUV-Never Wet, and Soot-TMOS-FAS17Cl). Interestingly, no statistical differences were detected between surfaces within each group (Tukey test, $P > 0.05$) indicating no significant effect of the surface dewetting properties on insect attachment. Only smooth C_{10}-hybrid samples showed intermediate results, differing ($P < 0.05$) from smooth Si and similar surfaces ($P > 0.05$) to rough Never Wet (both Tukey test). Both the sex of the insect individuals (Figure 3b) and the surface type affected force values (two-way ANOVA: $F_{1,139} = 4.992$, $P = 0.027$ and $F_{6,139} = 40.878$, $P < 0.001$, respectively). However, there was no statistically significant interaction between these two factors (two-way ANOVA: $F_{6,139} = 0.763$, $P = 0.601$).

Our results show that the chemistry of smooth surfaces plays some role in the beetle attachment. The general trend is that hydrophobic and oleophobic substrates tend to reduce the attachment forces of beetles toward such surfaces. In addition, the results of previous studies on this matter have been fairly heterogeneous. In a recent publication, data from the literature dealing with force measurements of different insects on surfaces with different surface energies were carefully compared [35]. No significant dependence of insect attachment forces on water CAs was shown in the five experiments recorded in the four studies compared. However, seven experimental set-ups from six different studies revealed dependence of attachment forces on water CAs. Generally in the latter studies, at surfaces with water CAs above 100°, attachment forces were lower than those on surfaces with water CAs below 40°. It is important to note that in all of these studies different species, developmental stages, sexes and experimental designs were used. In some of these studies, insect species that are strongly specialized to host plants whose leaf surfaces have very specific surface energies (water CA about 80°), such as the beetle *Galerucella nympheae* which lives on the leaf surface of the water lily, the maximum attachment force was detected at the intermediate range of water CAs, approximately corresponding to those of the plant leaves [35].

Careful analysis of our data shows that there is no direct dependence of the attachment force of the beetle *Coccinella septempunctata* on the surface energies of the smooth substrates, as measured by the magnitude of CAs. It also seems that other factors, in addition to the surface energy, influence beetle attachment. These factors are presumably related to the different characters of chemical substances, which may mediate physical and chemical interactions in contact to different extents. In contrast, the fact that insect attachment is very sensitive to the substrate roughness is well-known, due to numerous previous studies on the subject [16,19-21,23,29,33,38]. Particularly strong reductions have been observed on textured substrates with R_{rms} in the range of 0.1 to 3 µm [16,23,29,33,38]. These results were also confirmed by the present study. However, in spite of our surfaces having completely different physical/chemical properties, there seem to be no differences in the

attachment forces of beetles on rough substrates with different surface energies. We suspect this unusual attachment behavior is probably related to different physical parameters, particularly in the case of superhydrophilic/superoleophilic and superhydrophobic/superoleophobic surfaces. For the former types of surface, it is probably due to overly strong fluid absorption from the pads (Figure 4a,b). In the latter case, it is presumably due to wetting reduction by the pad fluid (Figure 4c,d). Additionally, at the sites of solid–solid contact between insect pads and substrates, the true contact area and contribution of van der Waals forces are believed to be effectively reduced for both types of textured substrate, despite them having different wettabilities (Figure 4b,d). In our present case, Never Wet and VUV-Never Wet samples would correspond to Figure 4b, while the Soot-TMOS-FAS17Cl surfaces are comparable to Figure 4d.

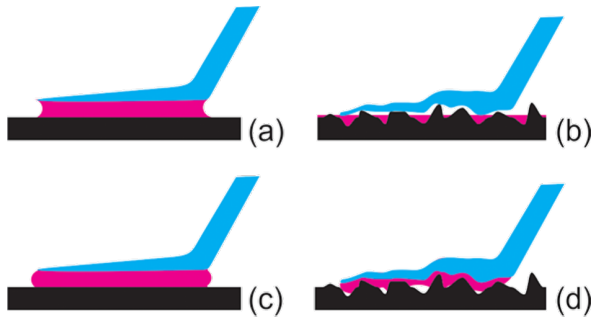

Figure 4: Hypothetical wetting behavior of the pad fluid (purple) in the contact region between the tenent setal tip (blue) and different sample surfaces (black): (a,c) flat surfaces, (b,d) textured surfaces; (a,b) fluids that readily wet the surfaces, (c,d) and fluids that poorly wet the surfaces.

These effects were previously modeled to explain how the fluid flows on textured substrates with different roughness parameters and surface energies [39]. These numerical studies demonstrated that a higher density of geometrical surface structures of the rigid substrate results in a greater loss of fluid from the pad. The draining rate of the pad fluid is more rapid on fine roughness. A decreased affinity of the substrate to the pad fluid leads to significant reduction of the fluid loss. However, the substrate will not be wetted and will likely become slippery for the pad [39]. Our data demonstrated here provide clear experimental evidence for previous numerical predictions.

Attachment of male *C. septempunctata* was significantly stronger on the smooth hydrophilic surfaces. This effect was less pronounced or even vanished on our textured surfaces, which has been previously explained by the differences in the contact shape of the tenent setae [23,38].

In summary, we have clearly shown that the insect anti-adhesive effect is due to both surface chemistry and texture, but it is primarily driven by the substrate roughness, and less by surface chemistry. It seems to be a universal effect for both dry [40,41] and wet (but not glue-mediated) [23,29,38,42] adhesive systems.

Acknowledgements

The authors thank Charlotte Bellmann and Ingo Grawe (both Kiel University) for their assistance with the force measurements and Emre Kizilkan (Kiel University) for the introduction into the plasma treatment device. This work was partially supported by CARTRIB Project of The Leverhulme Trust (S. N. Gorb and E. V. Gorb) and JSPS KAKENHI Grant Number JP24120005 (A. Hozumi) in Scientific Research on Innovative Areas“Innovative Materials Engineering Based on Biological Diversity”.

References

1. Bhushan, B. *Philos. Trans. R. Soc. London, Ser. A* **2009,** *367,* 1445–1486. doi:10.1098/rsta.2009.0011
2. Koch, K.; Barthlott, W. *Philos. Trans. R. Soc. London, Ser. A* **2009,** *367,* 1487–1509. doi:10.1098/rsta.2009.0022
3. Tuteja, A.; Choi, W.; McKinley, G. H.; Cohen, R. E.; Rubner, M. F. *MRS Bull.* **2008,** *33,* 752–758. doi:10.1557/mrs2008.161
4. Wong, T.-S.; Sun, T.; Feng, L.; Aizenberg, J. *MRS Bull.* **2013,** *38,* 366–371. doi:10.1557/mrs.2013.99
5. Patankar, N. A. *Langmuir* **2004,** *20,* 8209–8213. doi:10.1021/la048629t
6. Tuteja, A.; Choi, W.; Ma, M. L.; Mabry, J. M.; Mazzella, S. A.; Rutledge, G. C.; McKinley, G. H.; Cohen, R. E. *Science* **2007,** *318,* 1618–1622. doi:10.1126/science.1148326
7. Tuteja, A.; Choi, W.; Mabry, J. M.; McKinley, G. H.; Cohen, R. E. *Proc. Natl. Acad. Sci. U. S. A.* **2008,** *105,* 18200–18205. doi:10.1073/pnas.0804872105
8. Hozumi, A.; McCarthy, T. J. *Langmuir* **2010,** *26,* 2567–2573. doi:10.1021/la9028518
9. Wong, T.-S.; Kang, S. H.; Tang, S. K. Y.; Smythe, E. J.; Hatton, B. D.; Grinthal, A.; Aizenberg, J. *Nature* **2011,** *477,* 443–447. doi:10.1038/nature10447
10. Urata, C.; Cheng, D. F.; Masheder, B.; Hozumi, A. *RSC Adv.* **2012,** *2,* 9805–9808. doi:10.1039/c2ra21360e
11. Urata, C.; Masheder, B.; Cheng, D. F.; Hozumi, A. *Langmuir* **2013,** *29,* 12472–12482. doi:10.1021/la402714s
12. Urata, C.; Masheder, B.; Cheng, D. F.; Miranda, D. F.; Dunderdale, G. J.; Miyamae, T.; Hozumi, A. *Langmuir* **2014,** *30,* 4049–4055. doi:10.1021/la500548v
13. Latthe, S. S.; Terashima, C.; Nakata, K.; Fujishima, A. *Molecules* **2014,** *19,* 4256–4283. doi:10.3390/molecules19044256
14. Miranda, D. F.; Urata, C.; Masheder, B.; Dunderdale, G. J.; Yagihashi, M.; Hozumi, A. *APL Mater.* **2014,** *2,* No. 056108. doi:10.1063/1.4876636
15. Simpson, J. T.; Hunter, S. R.; Aytug, T. *Rep. Prog. Phys.* **2015,** *78,* No. 086501. doi:10.1088/0034-4885/78/8/086501
16. Prüm, B.; Seidel, R.; Bohn, H. F.; Speck, T. *J. R. Soc., Interface* **2012,** *9,* 127–135. doi:10.1098/rsif.2011.0202

17. Prüm, B.; Bohn, H. F.; Seidel, R.; Rubach, S.; Speck, T. *Acta Biomater.* **2013,** *9,* 6360–6368. doi:10.1016/j.actbio.2013.01.030
18. Gorb, E.; Haas, K.; Henrich, A.; Enders, S.; Barbakadze, N.; Gorb, S. *J. Exp. Biol.* **2005,** *208,* 4651–4662. doi:10.1242/jeb.01939
19. Stork, N. E. *Entomol. Exp. Appl.* **1980,** *28,* 100–107. doi:10.1111/j.1570-7458.1980.tb02992.x
20. Eigenbrode, S. D.; White, C.; Rohde, M.; Simon, C. J. *Environ. Entomol.* **1998,** *27,* 902–909. doi:10.1093/ee/27.4.902
21. Eigenbrode, S. D.; Kabalo, N. N. *Entomol. Exp. Appl.* **1999,** *91,* 125–130. doi:10.1046/j.1570-7458.1999.00474.x
22. Gorb, E. V.; Gorb, S. N. *Entomol. Exp. Appl.* **2002,** *105,* 13–28. doi:10.1046/j.1570-7458.2002.01028.x
23. Gorb, E. V.; Hosoda, N.; Miksch, C.; Gorb, S. N. *J. R. Soc., Interface* **2010,** *7,* 1571–1579. doi:10.1098/rsif.2010.0081
24. Peisker, H.; Gorb, S. N. *J. Exp. Biol.* **2010,** *213,* 3457–3462. doi:10.1242/jeb.043661
25. Purtov, J.; Gorb, E. V.; Steinhart, M.; Gorb, S. N. *Appl. Phys. A* **2013,** *111,* 183–189. doi:10.1007/s00339-012-7520-3
26. Gorb, S. N.; Beutel, R. G.; Gorb, E. V.; Jiao, Y.; Kastner, V.; Niederegger, S.; Popov, V. L.; Scherge, M.; Schwarz, U.; Vötsch, W. *Integr. Comp. Biol.* **2002,** *42,* 1127–1139. doi:10.1093/icb/42.6.1127
27. Ishii, S. *Appl. Entomol. Zool.* **1987,** *22,* 222–228.
28. Eisner, T.; Aneshansley, D. J. *Proc. Natl. Acad. Sci. U. S. A.* **2000,** *97,* 6568–6573. doi:10.1073/pnas.97.12.6568
29. Gorb, S. N. *Attachment Devices of Insect Cuticle;* Kluwer Academic Publishers: Dordrecht, Netherlands, 2001.
30. Federle, W.; Riehle, M.; Curtis, A. S. G.; Full, R. J. *Integr. Comp. Biol.* **2002,** *42,* 1100–1106. doi:10.1093/icb/42.6.1100
31. Vötsch, W.; Nicholson, G.; Müller, R.; Stierhof, Y.-D.; Gorb, S.; Schwarz, U. *Insect Biochem. Mol. Biol.* **2002,** *32,* 1605–1613. doi:10.1016/S0965-1748(02)00098-X
32. Geiselhardt, S. F.; Federle, W.; Prüm, B.; Geiselhardt, S.; Lamm, S.; Peschke, K. *J. Insect Physiol.* **2010,** *56,* 398–404. doi:10.1016/j.jinsphys.2009.11.016
33. Gorb, E.; Gorb, S. *Entomol. Exp. Appl.* **2009,** *130,* 222–228. doi:10.1111/j.1570-7458.2008.00806.x
34. Hosoda, N.; Gorb, S. N. *Proc. R. Soc. London, Ser. B* **2012,** *279,* 4236–4242. doi:10.1098/rspb.2012.1297
35. Grohmann, C.; Blankenstein, A.; Koops, S.; Gorb, S. N. *J. Exp. Biol.* **2014,** *217,* 4213–4220. doi:10.1242/jeb.108902
36. Hozumi, A.; Ushiyama, K.; Sugimura, H.; Takai, O. *Langmuir* **1999,** *15,* 7600–7604. doi:10.1021/la9809067
37. Deng, X.; Mammen, L.; Butt, H.-J.; Vollmer, D. *Science* **2012,** *335,* 67–70. doi:10.1126/science.1207115
38. Voigt, D.; Schuppert, J. M.; Dattinger, S.; Gorb, S. N. *J. Insect Physiol.* **2008,** *54,* 765–776. doi:10.1016/j.jinsphys.2008.02.006
39. Kovalev, A. E.; Filippov, A. E.; Gorb, S. N. *J. R. Soc., Interface* **2013,** *10,* 20120639. doi:10.1098/rsif.2012.0639
40. Huber, G.; Gorb, S. N.; Hosoda, N.; Spolenak, R.; Arzt, E. *Acta Biomater.* **2007,** *3,* 607–610. doi:10.1016/j.actbio.2007.01.007
41. Wolff, J. O.; Gorb, S. N. *J. Exp. Biol.* **2012,** *215,* 179–184. doi:10.1242/jeb.061507
42. Peressadko, A.; Gorb, S. N. Surface Profile and Friction Force Generated by Insects. In *First International Industrial Conference Bionik 2004,* Hannover, Germany, April 22–23, 2004; Boblan, I.; Bannasch, R., Eds.; Fortschr.-Ber. VDI Reihe: Düsseldorf, Germany, 2004; pp 257–261.

License and Terms

The definitive version of this article is the electronic one which can be found at:
doi:10.3762/bjnano.7.139

BEILSTEIN JOURNAL OF NANOTECHNOLOGY

Biomechanics of selected arborescent and shrubby monocotyledons

Tom Masselter*, Tobias Haushahn, Samuel Fink and Thomas Speck

Full Research Paper

Open Access

Address:
Plant Biomechanics Group, Botanic Garden, Faculty of Biology, University of Freiburg, Schänzlestraße 1, D-79104 Freiburg im Breisgau, Germany

Email:
Tom Masselter* - tom.masselter@biologie.uni-freiburg.de

* Corresponding author

Keywords:
arborescent monocotyledons; biomechanics; biomimetics; *Dracaena*; functional morphology

Beilstein J. Nanotechnol. **2016,** *7,* 1602–1619.
doi:10.3762/bjnano.7.154

Received: 01 June 2016
Accepted: 01 October 2016
Published: 07 November 2016

This article is part of the Thematic Series "Biological and biomimetic materials and surfaces".

Guest Editor: S. N. Gorb

Abstract

Main aims of the study are a deepened understanding of the mechanically relevant (ultra-)structures and the mechanical behaviour of various arborescent and shrubby monocotyledons and obtaining the structure–function relationships of different structurally conspicuous parts in *Dracaena marginata* stems. The stems of five different "woody" monocotyledon species were dissected and the mechanical properties of the most noticeable tissues in the five monocotyledons and, additionally, of individual vascular bundles in *D. marginata*, were tested under tensile stress. Results for Young's moduli and density of these tissues were assessed as well as the area, critical strain, Young's modulus and tensile strength of the vascular bundles in *Dracaena marginata*. These analyses allowed for generating a model for the mechanical interaction of tissues and vascular bundles of the stem in *D. marginata* as well as filling major "white spots" in property charts for biological materials. Additionally we shortly discuss the potential significance of such studies for the development of branched and unbranched bio-inspired fibre-reinforced materials and structures with enhanced properties.

Introduction

For many centuries, botanists and non-biologists alike have expressed their fascination about the conspicuous growth form of arborescent monocotyledons. Nevertheless, only in the middle of the 20th century first attempts were made to understand the form–structure–function relationships of these plants. To date, while the variation of physical properties from top to base and centre to periphery, as well as the underlying structural features, are well known in many dicotyledonous trees [1], these property shifts are still hardly studied in tree-like monocotyledons. This knowledge deficit is largely caused by a lack of interest for empirical data for monocotyledon stems and is a result of their insignificance as constructional material in many (industrialized) countries with the major exception of bamboo culms [2]. Results for physical properties of dicot plants cannot

be transferred to monocots as the organization of dicotyledonous stems is significantly different from that of monocotyledonous stems (Figure 1). The present study allows for closing some of these knowledge gaps and filling major "white spots" in natural material property charts. To this aim, analyses of the mechanical properties concentrate on two hierarchical levels: On a first level, the radial and axial Young's moduli of stem tissues in the five "woody" monocotyledon species are analysed (Figure 2A). In addition, in stems of *Dracaena marginata*, which was chosen as a representative model plant for "woody" monocotyledons (see below), the variations of the axial Young's modulus and the tissue densities at different radial and axial positions are assessed (Figure 2B). On a second hierarchical level, the Young's moduli and the tensile strengths of individual fibrous vascular bundles of *D. marginata* are investigated (Figure 2C). This enables a direct assessment of the contribution of the fibrous bundles to the mechanical properties of the underlying tissue by applying the rule of mixture. This procedure promises a considerable improvement to most studies that take a reverse indirect approach and extrapolate fibre properties by using the fibre volume fraction in the tissue [3-5]. Finally, the results for the mechanical properties of both tissues and fibrous vascular bundles are compared to available data from dicotyledonous and monocotyledonous stems.

The obtained data provide the basis for follow-up investigations on the branching mechanics of "woody" monocots. In addition, these data can be incorporated in finite element models at cell and tissue level that mirror the anisotropy and the stress–strain behaviour of the investigated plants at stem level [6,7]. This allows for a deepened understanding of the structural and mechanical requirements of *Dracaena marginata*, which was chosen as a representative model organism for arborescent monocotyledonous plants with lignified vascular bundles and anomalous secondary growth.

Morphology and anatomy of monocotyledons

The model plant *Dracaena marginata* was chosen for a generalized anatomical description (Figure 1A–C,E) as the morphology and anatomy of the other four monocotyledons analysed – *D. fragrans* (Figure 1D), *D. reflexa* (Figure 1G), *D. surculosa* (Figure 1H) and *Pandanus pygmaeus* (Figure 1F) – are very similar while differing in detail. Monocotyledon shoots are organized in an atactostele (Figure 1A), which means that individual vascular bundles with sclerenchymatous caps are dispersed irregularly within the ground tissue matrix (parenchyma) of the stem. The central cylinder is a multigradient structure in terms of size of vascular bundles (decrease towards periphery), number of vascular bundles (increase towards periphery) and cell size of the parenchymatous ground tissue (decrease towards periphery). These gradients are well visible in a cross-section of *D. marginata* (Figure 1A). Limited to a small group of monocotyledons, amongst these *D. marginata*, secondary vessels (Figure 1C) are formed at the border between the central cylinder and the surrounding cortex.

Results

1 Young's modulus of five different monocotyledons

Results for the Young's modulus from experimental setup one (see paragraph 1 in section 'Experimental') after measurements in axial direction are given in Figure 3A and in Supporting Information File 1 – Raw data. The box–whisker plots indicating median, interquartile range and extreme values show the range of values of the Young's modulus found for the different monocot species tested. The min–max ranges are 0.2017 GPa for *Dracaena fragrans* (median of axial Young's modulus: 0.1799 GPa), 0.2711 GPa for *D. marginata* (median of axial Young's modulus: 0.1235 GPa), 0.5445 GPa (median of axial Young's modulus: 1.2090 GPa) for *D. reflexa*, 1.6386 GPa for *D. surculosa* (median of axial Young's modulus: 2.5217 GPa) and 0.2697 GPa for *Pandanus pygmaeus* (median of axial Young's modulus: 0.1790 GPa). The normality assumption is not rejected on the basis of a Lilliefors test and the data are therefore additionally presented by mean and standard error of the mean for each plant respectively (see Supporting Information File 1 – Descriptive statistics). An ANOVA with post-hoc multiple comparison (with Bonferroni correction) on means shows no significant differences for the tree-like monocot species *D. marginata*, *D. fragrans* and *P. pygmaeus*. On the other hand, *D. surculosa* (shrub-like) and *D. reflexa* (tree-like) differ significantly (on the 5% level) from each other and also from the three other tree-like species (ANOVA; $F_{4,88} = 427.33$, P less than 0.001, see Supporting Information File 1 – Inferential statistics). The significances are shown in Figure 3 by letter grouping, where the same letter indicates no statistically significant difference. Notable is the significantly higher axial Young's modulus found in the shrub-like *D. surculosa*.

Measurements of the Young's modulus in radial direction (Figure 3B, see Supporting Information File 1 – Raw data) show in two tested species (*D. fragrans* and *D. marginata*) a wide range of values (min–max range of 0.0159 GPa for *D. fragrans* (median of radial Young's modulus: 0.0054 GPa), 0.0060 GPa for *D. marginata* (median of radial Young's modulus: 0.0029 GPa), and 0.0005 GPa for *Pandanus pygmaeus* (median of radial Young's modulus: 0.0010 GPa), which are visualized by a box–whisker plot of the data. As the assumption for normality (Lilliefors test) was rejected for *D. fragrans*, here the radial Young's moduli are additionally described with mean ranks and respective errors of the

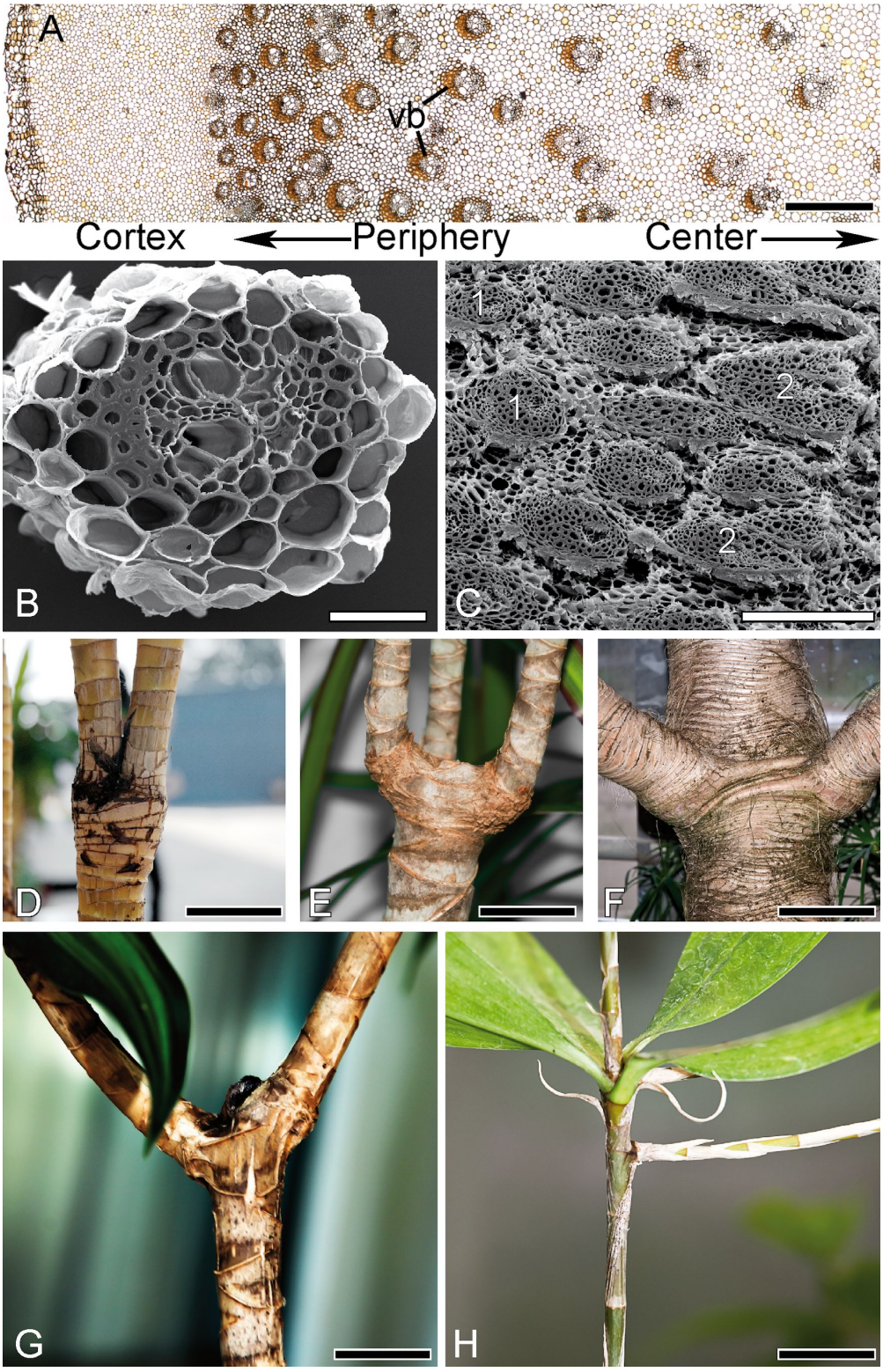

Figure 1: Morphology and anatomy of various monocotyledons. (A) Cross-section of *Dracaena marginata*, showing the dispersed vascular bundles (vb) in the parenchymatous matrix. (B) Cross-section of primary vascular bundle. (C) Cross-section of primary vascular bundles (1) and secondary (amphivasal) vascular bundles (2). (D) Branching morphology in *D. fragrans*. (E) Branching morphology in *D. marginata*. (F) Branching morphology in *Pandanus pygmaeus*. (G) Branching morphology in *D. reflexa*. (H) Branching morphology in *D. surculosa*. Scale bars: (A) 1 mm, (B) 0.1 mm, (C) 0.5 mm, (D) 50 mm, (E) 40 mm, (F) 150 mm, (G) 20 mm, (H) 20 mm.

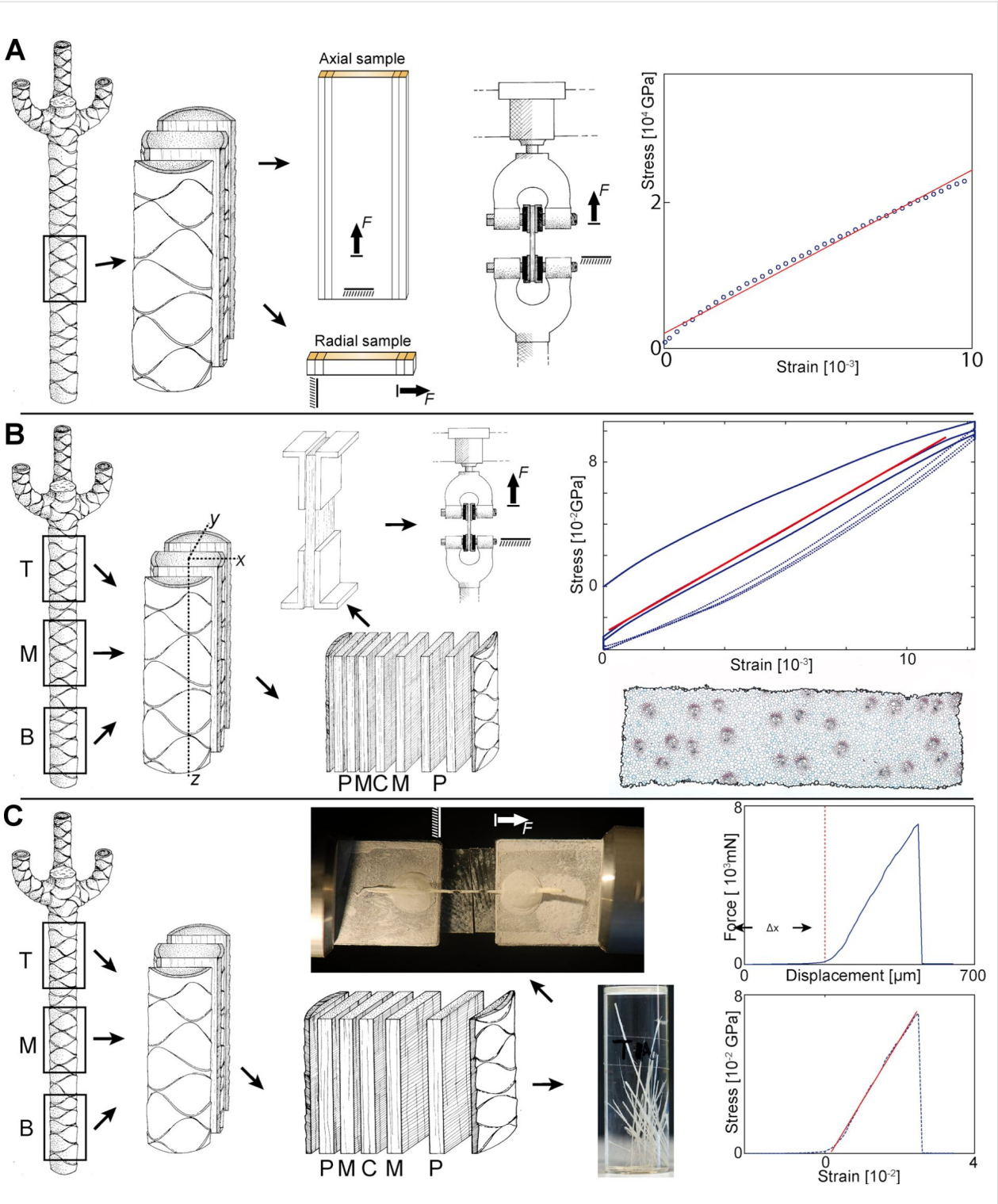

Figure 2: Experimental setups. (A) Setup for measurements of stem samples at various axial positions within the plant. Tensile Young's moduli were evaluated in radial and axial direction by the OLS (ordinary least squares) slope (red line) of the stress–strain diagram of respective datasets for all five tested monocots. (B) *D. marginata* was investigated in more detail. Samples with radial widths of *x* and *y* as well as an axial length of *z* were taken in this species from previously defined vertical (B, M and T) and radial zones (C, M, P) within the stem. Before testing, samples were fixed with glue to L-shaped aluminium brackets so that the samples could be tested under tensile stress. The evaluation of the Young's moduli was based on the OLS slope of the second load cycle (red line). Subsequently the cross-section of each sample was determined by analysing images of microtome slides. (C) Vascular bundles from *D. marginata* were extracted from the same defined zones as in (B), and tested until failure. *F* is the force acting on the samples, Δ*x* is the distance until a significant increase in force occurred.

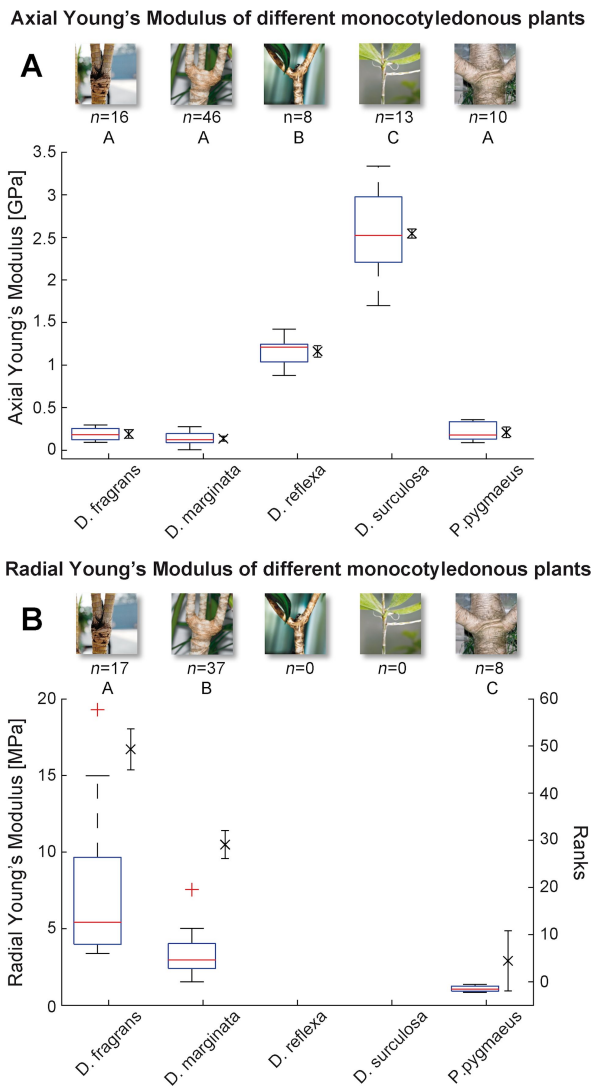

Figure 3: Axial (A) and radial (B) Young's moduli for *Dracaena fragrans*, *D. marginata*, *D. reflexa*, *D. surculosa* and *Pandanus pygmaeus*. Significances on the 5% level (group means (A), mean ranks (B)) are displayed in letter grouping, where identical letters group data with no significant difference. The number of tested samples is indicated by *n*. In both A and B, the full range of data is visualized by a boxplot of medians, quartiles (box), extreme values (whiskers) and potential outliers (+). In addition, the mean (×) and standard error (whiskers) are plotted as error-bar plot in A, whereas in B the mean ranks (×) and standard error (whiskers) are plotted as error-bar plot.

mean ranks. A Kruskall–Wallis test with post hoc multiple comparison shows significant differences (at 5% level) (chi-squared = 35.12, 2, *P* less than 0.001) between all measured plants, indicated in Figure 3B with letter grouping as described above (see Supporting Information File 1 – Inferential statistics). No results were obtained for *D. reflexa* and *D. surculosa* due to small radial dimensions of the stems that prohibited measurements. Values of axial and radial Young's moduli differ in all tested species by a factor between 7.46 and 171.

2 Young's modulus and density of stem samples in relation to the radial and axial position in *Dracaena marginata*

In Figure 4, density and axial Young's modulus are displayed for the different axial zones (basal (B), middle (M) and top (T)) and radial zones (periphery (B), middle (M) and centre (C)) of the tested plants, for the stems below branchings (plants 1–4) and a first order branch (plant 5). Plants 1 to 4, in which all samples consisted only of primary tissue, show a distinct U-shaped pattern for values of density and Young's modulus over the stem diameter for all three axial zones. It can be observed that the lowest value for density and Young's modulus (MoE) always occur in the radial centre of the stem and the values increase towards the periphery. In addition, the samples for these four tested plants show a similar trend in axial direction. The highest values, for density as well as for Young's modulus, occur at the stem base and decrease apically towards the top of the stem. This results in a twofold gradient within the plant stem (Figure 4). For plant 5, which holds a high amount of secondary tissue, the data for density and Young's modulus of primary and secondary tissues show a broad scatter across the diameter with no distinct tendency. Additionally, plant 5 shows a higher density and MoE as plants 1–4. Overall, the density lies in a range from 0.025 to 0.487 g/cm^3 with a mean value of 0.171 ± 0.11 g/cm^3, and the axial Young's modulus lies in a range between 0.03 and 1.62 GPa with a mean value of 0.52 ± 0.39 GPa.

Figure 5 shows the relationship between density and axial Young's modulus of the tested tissue samples of *D. marginata* on a log–log scale in a materials property chart in relation to other plant species and materials. A statistically significant exponential correlation exists between density and axial Young's modulus as well for primary as for secondary tissue (linear model (OLS): $F_{4,148}$, *P* less than 0.001, see Supporting Information File 3). It can also be seen that *D. marginata* covers a wide range of values for density and Young's modulus, a pattern that was also found for palms [8].

3 Tests of the vascular bundles of *Dracaena marginata*

Figure 6A–D shows cross-sectional area, critical strain, Young's moduli and tensile strength of individual vascular bundles of *D. marginata* for relative vertical (B,M,T) and relative radial positions (C,M,P) (see Supporting Information File 4 – Raw data and Descriptive statistics). The box–whisker plots show the range of measured values. In case of the cross-sectional area (Figure 6A) of the vascular bundles not all groups showed normal distribution, therefore the statistics were computed by Kruskal–Wallis test on mean ranks and only three groups differed significantly (chi-squared = 25.00, 7, *P* less than

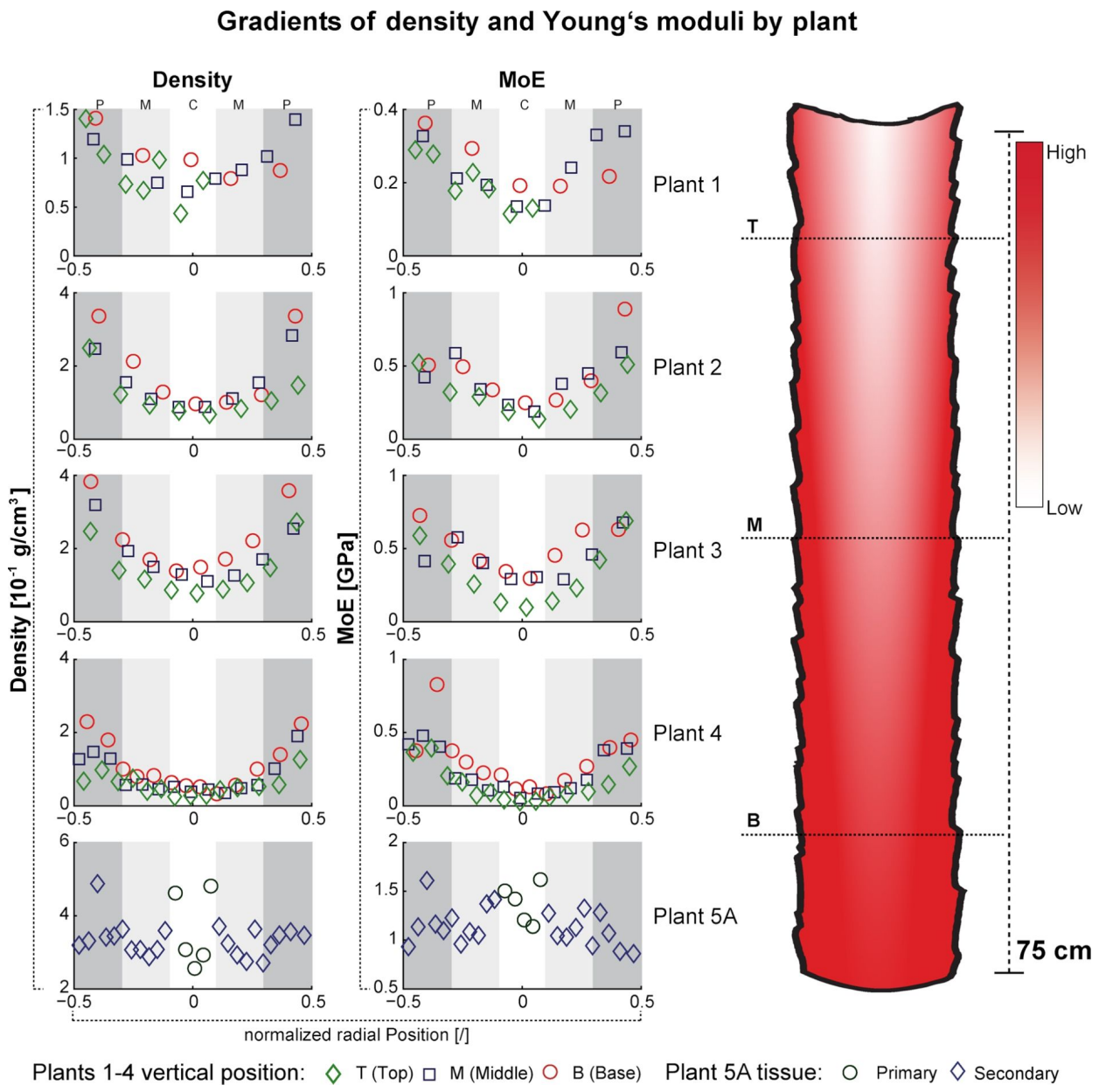

Figure 4: Dry density and Young's modulus (MoE) in five stem samples of *Dracaena marginata*. In radial positions from stem centre (C, white area) over middle position (M, light grey area) to stem periphery (P, dark grey area) shown by normalized radial position and categorized by vertical position, i.e., base (B), middle (M) and top (T) level of the respective stems. Plants 1–4 possess only primary tissue. In plant 5 set A, data are shown for primary and secondary tissues. Note the U-shaped data distribution of dry density and MoE for plants 1–4 and for the primary tissues of plant 5A. Also note the broad scatter in density and MoE across the diameter for the secondary tissue in plant 5A.

0.001; see Supporting Information File 4 - Inferential statistics). No significant differences in group means were obtained for critical strain (Figure 6B) of the vascular bundles, where normal distribution was not rejected and the multiple comparisons was based on an ANOVA on means (ANOVA; $F_{7,66} = 1.36$, $P = 2.3$) and a post hoc test with Bonferroni adjustment. The normality assumption was again not rejected for the measurements of Young's modulus (MoE) (ANOVA; $F_{7,66} = 32.20$, P less than 0.001) and tensile strength (ANOVA; $F_{7,66} = 22.35$, P less than 0.001) (Figure 6C,D respectively) and significant differences were observed between some groups for both strength and MoE. (We refer to Supporting Information File 4 – Inferential statistics, because the differences are too complex to show in Figure 6). Both strength and Young's modulus show a similar pattern as previously described for bulk tissue axial Young's moduli and density. For both mechanical properties a

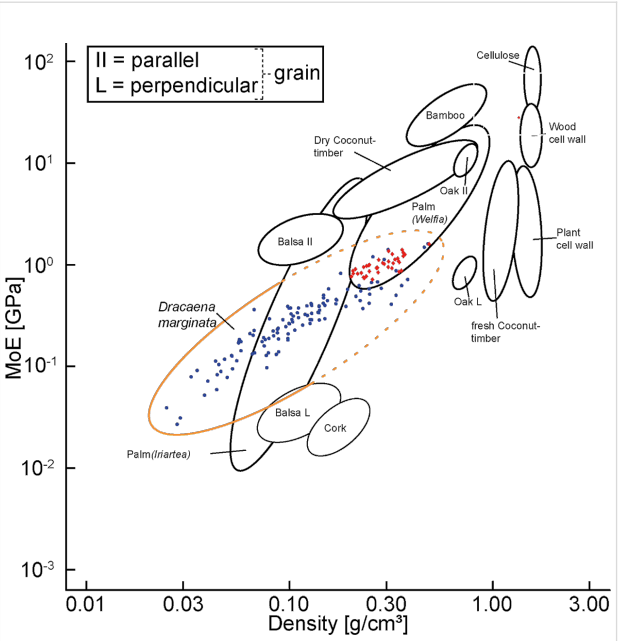

Figure 5: Materials property chart with measured values for stem samples of *Dracaena marginata*. Blue: primary tissues, red: secondary tissues in the log–log scale of Young's modulus (MoE) vs density. Samples tested parallel to the grain/vascular bundles (adapted from [9]).

marked increase can be observed in radial direction from centre to periphery and a decrease in vertical direction from base to top. No measurements were available for the top-centre position, as the preparation of the samples failed to yield fibres suitable for measurement. The Young's modulus (MoE) of all tested vascular bundles has a mean value of 2.77 ± 0.69 GPa.

4 Comparison of measured and calculated axial Young's moduli in *Dracaena marginata* using the Voigt Model

Figure 7 shows the axial Young's modulus calculated by the Voigt model compared to the measured values for bulk tissues (see also Figure 4) for plants 2–4 (see Supporting Information File 5 – Calculated data and Descriptive statistics). The calculated values for every sample are plotted as mean and standard deviation, whereas experimental measurements of the samples are plotted as diamonds. In the peripheral regions of the stem the values calculated via the Voigt model sometimes differ markedly from experimental measurements, but within central to middle regions the calculated values are in very good accordance with the bulk tissue measurements.

Discussion

Due to the lack of sufficient literature data for the comparison of mechanical properties of *Dracaena* to other massive monocotyledon stems, we also compared our measured data with data

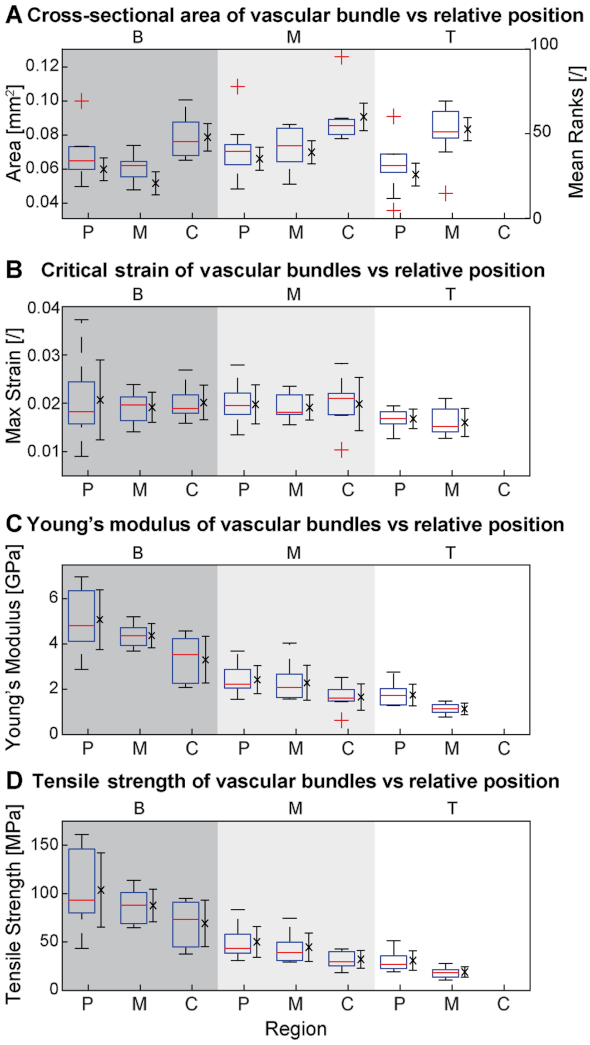

Figure 6: Morphometric data and material properties of vascular bundles of *Dracaena marginata*. (A) Cross-sectional area, (B) critical strain, (C) Young's modulus and (D) tensile strength of vascular bundles vs relative radial position (periphery (P), middle (M) and centre (C)) and axial position (basal (B, dark grey area), middle (M, light grey area) and top (T, white area)) within the stem. In A to D, the full range of data is visualized by a boxplot of medians, quartiles (box), extreme values (whiskers) and potential outliers (+). In addition, in A the mean ranks (×) and standard error (whiskers) are plotted as error-bar plot; whereas in B to D the mean (×) and standard error (whiskers) are plotted as error-bar plot.

from hollow culms of bamboo, horsetails and grasses as well as with massive herbaceous plants such as tobacco and with data from the wood of dicotyledons in order to present our data in a broad context.

1 Young's modulus of five different monocotyledons

The significantly higher values of Young's modulus of monocotyledons with rather small but potentially tree-like habit (*D. reflexa*), and a shrub-like habit (*Dracaena surculosa*) com-

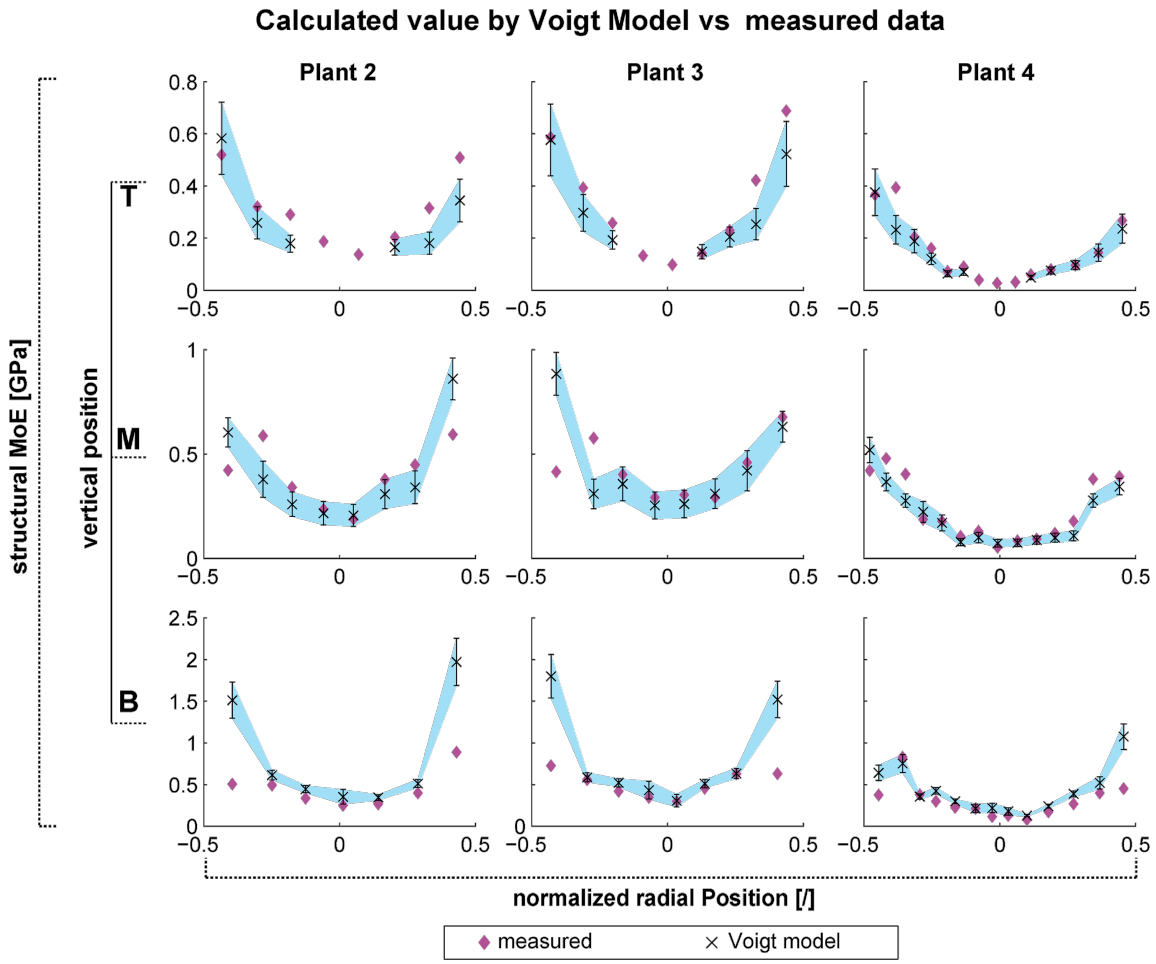

Figure 7: Measured vs calculated values (Voigt model) of the Young's modulus of *Dracaena marginata*. Measured values are indicated by diamonds. Values calculated by using the Voigt model are depicted by mean values (×) and their standard deviation (indicated by the whiskers). The range of calculated values is furthermore visualized by the blue area, which represents a linear interpolation between mean values and their standard deviation.

pared to the other three species with pronounced tree-like habit can be explained by two rationales. First, the stems of the tested specimen of *D. reflexa* and *D. surculosa* were very long and slender. These plants showed a much higher length-to-diameter (L/D) ratio (personal observation) than the investigated (other) tree-like monocots. At high L/D, the risk for Euler buckling increases and is met by the plants with an increased flexural stiffness via higher axial Young's moduli.

A second important reason might be the advantage of a rather stiff stem for the ability to branch at wide angles, which is typically observed in *D. surculosa* and *D. reflexa*. Their wide-angled branchings appear often rather T-shaped (in *D. surculosa* more pronounced than in *D. reflexa*; compare Figure 1H with Figure 1G) while the narrow-angled branchings in *D. fragrans* and *D. marginata* appear rather Y-shaped (Figure 1D,E). It could be shown in [10] that the stress at rupture of the stem–branch connection and the "compactness" of the stem (i.e., many vascular bundles in the stem and a very distinct boundary between stem and branch) is higher in *Freycinetia insignis*, a plant with a branching morphology very similar to *D. surculosa,* than the stress at rupture and the "compactness" in *D. reflexa*. This might be mirrored in an axial Young's modulus significantly higher in *D. surculosa* (similar to *Freycinetia insignis*) than in *D. reflexa*. It can also be hypothesized that the lack of such a "compactness" in the stem of *D. marginata* (see Figure 1A) and in *D. fragrans* [11,12] can be correlated to a lower Young's modulus of the stems, and that this entails markedly smaller branching angles.

We also hypothesize that the high values of the axial Young's modulus of *Dracaena surculosa* in rather young ontogenetic

stages (median of axial Young's modulus: 2.5217 GPa) are similar to the comparatively high stiffness in young palms that are mechanically "overbuilt" as documented in [8] as they cannot increase their flexural stiffness by secondary growth. This is also supported by the higher stress necessary for rupturing young branches of *F. insignis* [10], which lacks secondary growth as well. We assume that other monocots such as *Dracaena fragrans*, *D. marginata* or *D. reflexa* exhibit comparatively low Young's moduli in young ontogenetic stages (median of axial Young's modulus: 0.1799 GPa, 0.1235 GPa and 1.2090 GPa, respectively) due to their ability of secondary thickening. It allows for an increase in girth and formation of additional vascular bundles, which both contribute to a considerable increase in stiffness: The Young's moduli in old stages of *Dracaena manii* of 4.9GP [13] surpass the other values of arborescent young *Dracaena* species with secondary growth by 5 to 10 times, while they are only approximately twice as high as that of (the assumably "overbuilt") *D. surculosa*.

The comparatively low values of axial Young's modulus measured for a rather old specimen of *Pandanus pygmaeus* can be explained by the fact that many Pandanaceae lack "compact" and thereby stiff stems and tend to produce aerial roots which support the stem and especially outgoing branches [14,15].

The two orders of magnitude difference between the axial and radial Young's modulus indicate that the mechanical behaviour under axial tension is dominated by the vascular bundles [16] with a measured mean value of of 2.77 GPa in *D. marginata*. In contrast, the mechanical behaviour under radial tension is dominated by the parenchymatous tissue (Reuss model as described in [16] with a Young's modulus of 0.003 GPa in *D. marginata*, (values for the Young's modulus of parenchyma typically range between 0.001 and 0.003 GPa [17]). This assumption is further investigated via testing of individual vascular bundles and application of the Voigt model (see below).

2 Young's modulus and density of stem samples in relation to radial and axial position in *Dracaena marginata*

The results of the spatial investigation of *D. marginata* indicate a strong dependence of the Young's moduli on vertical and radial position (Figure 4) as well as on the density of the underlying tissue (Figure 5), which similarly has been demonstrated for palms [8,18] and more recently for Moso bamboo [2]. A multiple gradient in axial and radial direction has been shown here for density and Young's modulus (Figure 4) with both parameters increasing towards stem base and periphery as in *Flagellaria indica*, a monocot climber, which stiffens towards the base and the periphery [19]. A similar gradient in radial direction has also been demonstrated for the tensile strength of tissues at various radial positions within the stem of Moso bamboo [20] and for the axial Young's modulus of tissue strips in the culm of *Arundo donax* [21] as well as for the density in the oil palm *Elaeis guineensis* [22].

In *D. marginata*, an almost linear correlation of axial Young's modulus and density was found. However, these observations are only valid for the measured ranges of density, an extrapolation beyond these ranges would yield great uncertainties due to the relative young age of the tested plants. Though many authors postulate a correlation between tissue density and Young's modulus of a plant [23], in [24] it is argued that density alone is not sufficient for the evaluation of the Young's moduli. For *D. marginata*, we hypothesize that an increase in tissue density may correlate (amongst others) with (1) the number of vascular bundles, (2) the area fraction of the vascular bundles, (3) the type of vascular bundles, (4) the cell wall composition [25], and (5) the number of cell-wall layers in vascular bundles or parenchyma and thereby also lignification and stiffness.

The values for density and Young's modulus (Figure 5, mean value of 0.52 ± 0.39 GPa) are relatively low compared to other plants. The Young's modulus in *D. marginata* increases linearly with density for both primary and secondary tissues. This general trend is also known for bamboo [2,26] and wood [27], though a linearity of the correlation – as found in *D. marginata* – was only found in older stems of the black locust (*Robinia pseudoacacia*) [28]. In palms similar values of longitudinal Young's moduli are reported in fibre strips of thick-walled caps of vascular bundles tested under axial tension. These values ranged from 0.2 to 1 GPa in *Washingtonia robusta* [29], depending on the level of lignification. While we did not measure the degree of lignification in *D. marginata*, we assume that the density is a good indicator for the relative amount of lignification. As the density varies radially and longitudinally, a broad range of values in Youngs' moduli from unlignified (0.03 GPa) to well-lignified (1.62 GPa) values was to be expected. This indicates that despite the very different growth strategies in palms (primary thickening) and *D. marginata* (secondary thickening), very similar mechanical properties can be achieved by lignification, which is also considered as a key factor in adjusting stiffness [29]. This postulated correlation of density, Young`s modulus and lignification is also substantiated by the similarity of value ranges for both density and Young's modulus of *D. marginata* of 0.171 g·cm^{-3} and of *Iriartea* palms, another well-lignified palm [8] (Figure 5).

Similar values were measured also for the longitudinal Young's modulus of tissue strips from internodes in *Equisetum gigan-*

teum [30] and from internodes of *Equisetum hyemale* [31,32] as well as for the bending Young's modulus measured in axes of herbaceous dicotyledon plants such as tobacco [33].

These values of approx. 1 GPa for horsetails and 0.8 GPa for tobacco are well within the range of values found in *D. marginata*. The similarity cannot be explained by a similar degree of lignification as extant horsetails as well as herbaceous dicotyledon plants are not or very poorly lignified and rely on the turgor of their parenchymatous tissues (additionally to strengthening tissues such as collenchyma or sclerenchyma) for providing stiffness. While a high turgescence of parenchyma surely also adds to the stiffness in *D. marginata* (as the parenchyma acts as a spacer tissue that keeps the stiff vascular bundles in place), the amount of relative contribution of turgor to stiffness cannot be quantified by the methods used in this study and necessitates further analyses.

The axial Young's modulus of *D. marginata* with a mean value of 0.52 ± 0.39 GPa is markedly lower than that of the Moso bamboo with an MoE of 10.56 GPa [2]. It is also lower than the longitudinal Young's modulus in culms of *Arundo donax* with values of 9–10 GPa measured with bending tests [34], and within the lowest range of 1 to 11 GPa found in tensile tests of tissue strips of *Arundo donax* [21].

This is to be expected as the density (about 0.630 g·cm^{-3} for an unspecified bamboo [9] (see Figure 5)) and the degree of lignification of bamboo is much higher than that of *Dracaena* species. This also applies to woody plants such as conifers and broad-leafed trees such as the eastern white pine with a density of 0.350 g·cm^{-3} and a Young's modulus of 8.50 GPa as well as the Douglas fir, the white spruce and the northern oak with densities ranging from 0.360 to 0.630 g·cm^{-3} and Young's moduli ranging from 9.6 to 13.4 GPa [35]. However, the age of these trees was much higher than that of *D. marginata*. It can be assumed that *Dracaenaceae* can also attain higher values in older plants.

3 Tests of the vascular bundles of *Dracaena marginata*

The presence of a high number of rather small (Figure 6A) vascular bundles in the periphery and a comparatively lower number of larger vascular bundles in the centre can be well discerned in cross-sections of *Dracaena marginata* (Figure 1A). It can be also observed in many other monocotyledon plants such as palms [29], Moso bamboo [2] and the giant reed *Arundo donax* [34]. It was suggested in other studies that this increases the second moment of area of mechanically relevant tissues and thereby increases the flexural stiffness of the stems [21,29,34,36,37]. We also propose a similar increase of flexural stiffness of the stems of *D. marginata*. Though we did not measure the flexural stiffness of these plants in our study, the twofold increase of number of vascular bundles and their tensile Young's moduli towards the periphery both increase the second moment of area and the stiffness of mechanically important tissues so that the flexural stiffness of axes of *D. marginata* is also increased.

The lack of significant differences in the critical strain found for vascular bundles across the periphery and towards top or base (Figure 6B) can be explained by the similar structure of all vascular bundles so that no large differences in critical strain might be expected. This does not hold true, however, for the stress and the stress–strain ratios. These are very different in peripheral and radial positions and lead to very different Young's moduli (Figure 6C) and tensile strength of the vascular bundles (Figure 6D).

The Young's modulus of the vascular bundles with values ranging from mean values of 5.08 ± 1.33 in peripheral bundles at the stem base down to 1.74 GPa ± 0.48 GPa is largely overlapping the range of approx. 4.3 to 0.5 GPa reported for strips of the hypodermal sterome in *Equisetum hymale* [32]. This indicates that despite the fundamentally different developmental growth and systematic position of *D. marginata* and *E. hyemale*, the two plants respond to similar mechanical constraints imposed by the self-supporting growth habit by developing strengthening tissues with similar mechanical properties at the outermost periphery of their axes.

The Young's moduli of the vascular bundles in *D. marginata* are noticeably higher than that of fibre caps in the palm *Washingtonia robusta* measured for which values were approx. 0.4 to 0.5 GPa for fibre strips close to the phloem [38]. We assume that this is due to the very low level of lignification of these fibre strips in *W. robusta*. The values found for fresh bundles in palms and dragon trees are markedly lower than the value of 36 GPa measured for the Young's modulus in air-dry fibres of Moso bamboo [39], which represents one of the few values reported for other monocot bundles. We propose the same rationale as given for the tissues and attribute the higher values found in Moso bamboo to a higher level of lignification in bamboo as compared to *D. marginata*.

The increase of tensile Young's modulus (stiffness) of the vascular bundles is well correlated with the increase of the Young's modulus of the tissues. The twofold gradients, i.e., stiffer towards the outside and toward the base is also observed for the Young's moduli of the respective vascular bundles. This holds also true for the tensile strength of the vascular bundles. A single (radial) gradient for the tensile Young's modulus and

tensile strength of vascular bundles was also found across the culm wall in Moso bamboo [39].

Finally, the comparably high tensile strength of the vascular bundles at the periphery of the trunks is of high importance for stabilizing the stem–branch attachments as these are mainly supported by (the fibrous parts of) vascular bundles under tensile stress [40]. The absolute values with a mean of 55 ± 17 MPa are well below the values reported for bamboo which range from 810 MPa [4] for fresh samples to 550 MPa [39] for dry samples as well as 610 MPa [3,41] for samples of which the moisture content remains unclear. It can be stipulated that values for vascular bundles in the region of stem–branch attachments in *D. marginata* (which we did not measure) can also assume higher values as a mechanical response to higher load stresses imposed by lateral branches.

4 Comparison of measured and calculated longitudinal Young's moduli of tissues in *Dracaena marginata* using the Voigt model

The calculated values for the Young's modulus of the tissue using the Voigt model match the data for the measured values in *Dracaena marginata* very well except for the outermost peripheral positions in the stem (Figure 7). There, the data are sometimes markedly overestimated (basal position of plants) or slightly underestimated (top positions of plants) or both, i.e., slightly over- or underestimated (middle positions of the plants). The Voigt model depends upon three factors: (1) the Young's modulus of the ground tissue, (2) the Young's modulus of the vascular bundles, and (3) the volume fractions of ground tissue and vascular bundles. As we attributed a constant value to the Young's modulus of the ground tissue, the calculated values of our Voigt model can only change due to variation of the last two factors. The marked overestimation of the Young's modulus cannot be explained by the peripheral increase of the Young's modulus of the vascular bundles, which increases from centre to periphery approximately by a factor 1.5 (see Figure 6C), an augmentation which is in good accordance with the increase of the measured values for the Young's modulus of the tissues. Possible causes for the overestimation are drying and stiffening of the vascular bundles during testing or/and an overestimation of the volume fraction of the vascular bundles. Another possibility is the assumption (for the Voigt model) that the vascular bundles are perfectly arranged in parallel to the axis of the stem, which they are not. In fact, it was shown by Tomlinson and others that the intertwining course of the vascular bundles in *Dracaena* [11,12] and other monocotyledon stems [42-46] is highly complex and characterized by many anastomoses. The deviation of the vascular bundles from an idealised axial arrangement would also lead to an overestimation of the values calculated by the Voigt model.

Conclusion

The comparably high values of axial Young's modulus in tissues of the young shrub-like plants *Draceana surculosa* and *D. reflexa* are interpreted as a response to the increased "need" for higher bending stiffness of (1) their slender stems and (2) in the regions of stem branch–attachment. This is because *Draceana surculosa* and *D. reflexa* branch at higher branching angles than young tree-like *D. marginata* and *D. fragrans*, which have a thicker stem and branch with rather narrow angles. Moreover, the lack of secondary growth is hypothesized to lead to a mechanical "overbuilding" of young axes as present in palms [8]. It would have been worthwhile to analyse whether a consequent "underbuilding" of old axes as in palms [8] is present in *D. surculosa* and *F. insignis*. This is however prohibited by the absence of sufficiently old ontogenetic phases in *D. surculosa* and F. *insignis* as the entire shoot is replaced after inflorescence.

Results prove an axial and radial gradient of mechanically relevant properties in the stems of *D. marginata*. It could be shown that towards the base and the periphery of the stems there is an increase of density (as described for palms [8]) and of the axial Young's modulus of tissues as described in the radial direction for Moso bamboo [2].

While the values for density can reach the values of other monocotyledons such as bamboo, the axial Young's modulus is generally one order of magnitude lower [2]. This is interpreted as a consequence of the higher lignification of bamboo stems. The abundance of wood is also interpreted as one of the causes of the higher values for the axial Young's modulus in conifers and dicotyledonous trees such as Douglas fir, white spruce and northern oak [35] as compared to stems of *D. marginata*. Another reason is the less dense arrangement of the fibrous bundles in an atactostele in *D. marginata* and the dense arrangement of stiff tissues in conifers and dicotyledons. Relationships between density and the axial Young's modulus are visualized in a material property chart (Figure 5) and thereby fill major "white spots" for biological material properties.

The two-dimensional gradient as present for the axial Young's modulus of the tissues in *D. marginata* is also mirrored by a gradual increase of the Young's modulus and the tensile strength of the vascular bundles towards the base and the periphery. The Young's modulus of the vascular bundles is approx. five times higher than the Young's modulus of the bulk tissue, so that the measured values for the longitudinal Young's modulus of the tissues (first hierarchical level) can be assumed to be dominated by the values of the longitudinal Young's modulus of the vascular bundles (second hierarchical level). This assumption is verified by the good accordance of the

calculated values of the axial Young's modulus via the Voigt model.

The higher strength of fibrous bundles in the periphery is also vital for the support of (peripherally developing) branches in *D. marginata*.

Biomimetic approaches and outlook

The values for the Young' s modulus for the five tree- or shrub-like monocotyledons, the density–stiffness gradients along the axis of *D. marginata* and the values for the tensile strength and Young's modulus of the vascular bundles add to the knowledge and help to understand the functional anatomy and the biomechanics of arborescent monocotyledons. They also confirm the status of these plants as interesting concept generators for the development of branched and unbranched fibre-reinforced materials and structures with enhanced properties [6,47-49]. The axes of these plants consist of materials that combine low density with sufficient mechanical stiffness, which result in lightweight structures with optimized structural density–stiffness gradients. Additionally, the differentiation of the stem in ground tissue and vascular bundles is very similar to technical fibre-reinforced materials consisting of stiff fibres embedded in a more flexible matrix. Finally, the technical implementation of the functional principles of such plants can be aided by finite element modelling [7]. Further studies using in vivo magnetic resonance imaging allow for revealing the internal stress–strain relationships in mechanically loaded stems of monocotyledons [50] and shall be extended to other plants.

Experimental

Materials

Mechanical testing was performed on five different tree- or shrub-like monocotyledon species. Of the Dracaenaceae, three tree-like species with the potential for secondary growth, *Dracaena marginata*, *Dracaena fragrans* and *Dracaena reflexa*, as well as a shrub-like species, *Dracaena surculosa*, were tested. In addition, another tree-like monocotyledon without secondary growth, *Pandanus pygmaeus* (Pandanaceae), was also tested. All tree-like Dracaenaceae were purchased from commercial nurseries and cultivated in the Botanic Garden of the University of Freiburg. *D. surculosa* was also cultivated in the Botanic Garden Freiburg, whereas *P. pygmaeus* was cultivated at the Botanic Garden of the Technical University Dresden.

Methods

For measuring of the material properties three sets of experiments were performed: (1) Tensile tests on the stem tissue of all five species (Figure 2A), (2) a detailed tensile analysis of *D. marginata* tissues with respect to relative radial (Equation 7) and axial position (top, middle, base) within the plant stem (Figure 2B), and (3) a detailed tensile analysis of the vascular bundles of *D. marginata* also with respect to relative radial and axial position within the plant stem (Figure 2C). In (1) only the Young's moduli of the plants were assessed. In (2) material density, Young's moduli, water-content and area-fraction of vascular bundles of the samples were determined in a similar way as the methods described in [2]. In (3) the Young's moduli, the tensile strength and the critical strains were calculated.

Young's modulus of five different monocotyledons (1)

Testing procedure and determination of Young's moduli and strains

The axial (along the stem axis) as well as the radial Young's moduli of the five tree- or shrub-like monocots were measured under tensile stress by using two universal testing devices. An Instron® 4466 device (Instron, Norwood, Massachusetts, USA; retrofitted by Hegewald & Peschke, Nossen, Germany) was used for (1) *D. fragrans* (16/17 samples (axial/radial) from 5 plants), (2) *D. marginata* (46/37 samples from 10/9 plants), (3) *D. reflexa* (8/— samples from one plant) and (4) *D. surculosa* (13/— samples from one plant), and a Zwick-Roell Z250 (Zwick-Roell AG, Ulm, Germany) was used for (5) *P. pygmaeus* (10/8 samples from one plant (see Supporting Information File 1 – Raw data). Due to the low radial dimension of *D. reflexa* and *D. surculosa*, a test in radial direction was not feasible. Samples of varying size were cut from the stems and fixed in the clamps of the testing device (Figure 2A). The compressive force of the clamping jaws was carefully adjusted to prevent radial crushing of the sample but at the same time to prevent any axial slip during testing. Details on the individual testing procedures per plant are provided in Supporting Information File 2.

For the determination of the Young's modulus (MoE) an ordinary least squares fit (OLS) was performed with the Matlab (2014a, The Mathworks Inc., Natick, Massachusetts, USA) routine 'LinearModelFit' on the linear section (selected manually) of the stress–strain curve of each individual measurement (Figure 2A). The slope of the OLS corresponds to the Young's modulus of the sample. The tensile stresses (σ_Z) were calculated by dividing the measured force (F) by the cross-sectional area (A_{cross}) of the sample:

$$\sigma_z\,[\text{Pa}] = \frac{F}{A_{\text{cross}}}. \qquad (1)$$

The strains were calculated by dividing the measured displacements (Δl) by the free length of the sample (l_{free}):

$$\varepsilon[/] = \frac{\Delta l}{l_{\text{free}}}. \quad (2)$$

Descriptive and inferential statistics

For each plant species the descriptive statistics for the MoE, including mean, standard error of the mean (SE), standard deviation (STD), median, quartiles, interquartile range (IQR) and a Lilliefors test for normal distribution (H0: normal distribution), were computed in axial and radial direction (see Supporting Information File 1 – Descriptive statistics). An inter-species comparison was calculated in axial direction by one-way-ANOVA (H0: equality of means at α = 0.05) and a post hoc multiple comparison on means (Bonferroni adjustment, see Supporting Information File 1 – Inferential statistics). The results for the axial Young's modulus were plotted as a combination of a box–whisker plot indicating medians, quartiles, interquartile range and extreme values and an error-bar plot of means and standard error for each of the five tested plants (Figure 3A). As the Young's moduli in radial direction were not normally distributed (Lilliefors test) for all plants, an inter-species comparison was performed by a Kruskal–Wallis ANOVA on mean ranks (H0: equality of mean ranks at α = 0.05) with a post hoc multiple comparison on mean ranks (Tukey–Kramer, see Supporting Information File 1 – Inferential statistics). The results for the radial Young's moduli were plotted as a combination of a box–whisker plot and an error-bar plot of the mean ranks for each plant species except for *Dracaena reflexa* and *D. surculosa* for which no mechanical measurements could be performed (Figure 3B). Significances on the 5% level are displayed in letter grouping, whereby identical letters group data with no significant difference.

Young's modulus and density of stem samples in relation to relative radial and relative vertical position in *Dracaena marginata* (2)

Sample preparation and testing procedure

For a more detailed investigation of the Young's moduli within the selected representative species, five specimens of *D. marginata* were used. A total amount of 152 samples were collected in five different axes. 109 samples originate from four stems below branchings (termed plants 1–4), and 43 samples from a first-order branching (termed plant 5). The stems were divided into three axial zones in order to compare the Young's modulus in different tissue regions of the specimens. Out of each axial zone one cylindrical sample was taken (Figure 2B). Samples from the lower third of the sample were termed B (for basal zone), those in the intermediate part were termed M for (middle zone) and those in the upper third were termed T (for top zone). This axial subdivision could not be performed in the first order branch.

Subsequently, out of each cylindrical sample for B, M and T a long median rectangular section with the following dimensions was cut (Figure 2B): a (transverse) thickness x equal to the radial width of the stem in one direction, a depth y between 5 and 7 mm in the perpendicular direction, and a length z (between 7 and 10 mm) for the basal, middle or top part of the stem. As a result, three such median sections (B, M and T) originated from each of the four stems. In the first-order branch, one median rectangular section (termed 5A) was cut from the cylindrical sample of the branch as described above (Figure 2B) but an additional second tangential rectangular section (adjacent to the median section and termed 5B) was produced in order to gain more data on secondary vascular tissue. The data of the median section (5A) were used for the assessment of the regional dependency of the tissue density and Young's modulus (MoE) in Figure 4. The combined data of both sections (5A and 5B) were used for regression analysis of the density dependence of the MoE and in the materials property chart (see below for details).

To determine the radial variation of the material properties for each zone and plant, the original rectangular samples were then cut into smaller rectangular samples along the length and perpendicular to the width of the original sample (Figure 2B). Each sample now represents a radial position (P, M or C) within a defined axial zone (B, M, T) and plant. Despite the great care laid on producing regular rectangular samples with a defined radial width, a variation of the radial width (w) of the different cut samples between 1.13 and 2.90 mm (mean of 1.86 ± 0.39 mm) was inevitable because of deflections of the cutting knife due to the inhomogeneity of the stem tissue.

Each sample was then measured in tension with a universal testing device Instron® 4466 (Instron®, Norwood, Massachusetts, USA; retrofitted by Hegewald & Peschke, Nossen, Germany). To prevent slipping of the samples, they were fixed with all-purpose glue (Blitzschnelle Pipette, UHU GmbH & Co KG, Bühl, Germany) in four L-shaped aluminium brackets which then were clamped to the jaws of the testing device (Figure 2B). The free length (l_{free}) for each sample, which ranges from 14.6 to 26.3 mm, is important for the later calculation of strains and is documented in Supporting Information File 3 – Raw data. More details about the testing procedure (e.g., load capacity of the force transducer and boundary conditions of the test) are provided in Supporting Information File 2.

In order to obtain dry density, water content and cross-sectional area as well as the number and area of vascular bundles for each

of the mechanically tested samples, the samples were subsequently cut in one large and one small subsample. The small sample was embedded in PEG 2000 and thin sections of 25 µm thickness were produced with a microtome. Microscope images (Olympus BX61 microscope, Olympus Corp., Tokyo, Japan) of the cross-sections were then evaluated for cross-sectional area (A_{cross}) of the sample, number of vascular bundles ($\#_{vb}$) and total area of vascular bundles within the sample. Based on these images, it was also possible to determine visually if primary or secondary vascular tissue was predominant. The larger subsample was measured in length (l_{sub}, to calculate the fresh volume (V_{fresh})) and weighted on an electronic microscale (Mettler UMT2, Mettler-Toledo Ltd., Leicester, United Kingdom) to obtain the fresh mass (M_{fresh}). Subsequently, the sample was oven-dried at 60 °C for four days and the oven-dried mass (M_{dry}) was measured.

Data analysis and statistics

Young's Moduli and strains were computed from the slope of the second load cycle (Figure 2B) by the same methods described above for experiment (1) in Equation 1 and Equation 2.

The volume (V_{fresh}) of each fresh subsample was calculated by multiplying the subsamples length l_{sub} with the measured cross-sectional area (A_{cross}):

$$V_{fresh}\left[\mathrm{mm}^3\right] = l_{sub} \cdot A_{cross} \,. \tag{3}$$

The dry density (ρ_{dry}) was then calculated by dividing the oven-dried mass (M_{dry}) by the fresh volume (V_{fresh}) of the sample:

$$\rho_{dry}\left[\mathrm{g \cdot mm^{-3}}\right] = \frac{M_{dry}}{V_{fresh}} \,. \tag{4}$$

The water content (WC) is the difference between the fresh mass (M_{fresh}) and the oven-dried mass (M_{dry}) divided by the fresh mass (M_{fresh}):

$$WC[/] = \frac{M_{fresh} - M_{dry}}{M_{fresh}} \,. \tag{5}$$

The relative radial position of each sample was calculated (for all axial zones of all five plants) in order to be able to compare radial differences in axial Young's moduli and to assess if the Young's moduli in the centre of the stem (C, see Figure 4) differ from that in the periphery (P) or in the intermediate zone (M). The radial position of each sample, i.e., the radial distance from the centre of the stem, was calculated by using Equation 6 and Equation 7, where w_i is the radial width of each sample.

Diameter of stem section (D_{sect}):

$$D_{sect}\left[\mathrm{mm}\right] = \sum_{i=1}^{n} w_i \,. \tag{6}$$

Radial position of samples (P_{rad}):

$$P_{rad,j}\left[\mathrm{mm}\right] = \begin{cases} \frac{1}{2} w_j - \frac{1}{2} D_{sect} & \text{for } j = 1 \\ \sum_{i=1}^{j-1} w_i + \frac{1}{2} w_j - \frac{1}{2} D_{sect} & \text{for } j > 1 \end{cases} \,. \tag{7}$$

For the determination of the relative radial position (C, M and P), the data of the radial position is normalized by the diameter of the stem (Equation 8) and grouped according to Equations 9–11.

Normalized radial position of samples (P_{norm}):

$$P_{norm,j}\left[/\right] = \frac{P_{rad,j}}{D_{sect}} \,. \tag{8}$$

Relative radial position [grouping]:

$$\mathrm{C}[/] = \mathrm{abs}\left[P_{norm,j}\right] \in \left[0; \frac{1}{6}\right[\,, \tag{9}$$

$$\mathrm{M}[/] = \mathrm{abs}\left[P_{norm,j}\right] \in \left[\frac{1}{6}; \frac{1}{3}\right[\,, \tag{10}$$

$$\mathrm{P}[/] = \mathrm{abs}\left[P_{norm,j}\right] \in \left[\frac{1}{3}; \frac{1}{2}\right] \,. \tag{11}$$

In Figure 4 the dry density (ρ_{dry}) and the Young's modulus (MoE) are plotted versus the normalized radial position of each sample for all five plants. The ranges of the relative radial positions (C, M, P) are indicated by the intensity of the grayscales of the background in each graph.

For the evaluation of the relationship of MoE and ρ_{dry} an ordinary least squares fit (OLS) was performed with the Matlab

(2014a, The Mathworks Inc., Natick, Massachusetts, USA) routine 'LinearModelFit'. The data (MoE and ρ_{dry}) of all five plants (a total of 152 samples) was linearized by $\log_{10}$–$\log_{10}$ transformation (analogous to [8]) and grouped as primary and secondary tissues. As a linear regression model, the MoE was assessed with an interaction term of ρ_{dry} and tissue category ($\log_{10}(MoE) \approx 1 + \log_{10}\rho_{dry}$·tissue) returning a regression table with the statistics of the model (see Supporting Information File 3 - Linear regressions). An ANOVA was calculated to determine whether the slopes of primary and secondary tissues differed (see Supporting Information File 3 - ANOVA). The data for dry density and Young's modulus were integrated in a materials property chart (Figure 5).

Tests of the vascular bundles of *Dracaena marginata* (3)

Sample preparation and test procedure

The axial and radial positions of the rectangular samples were defined as for the stem tissues (see previous set of experiments). Across the diameter of the stem we obtained five rectangular samples (Figure 2C). These rectangular samples were then squeezed laterally to destroy parenchymatous cells and then submerged in H_2O_{dest} for the days in order to further macerate the parenchymatous tissue. We obtained a loose network of vascular bundles (Figure 2C). Individual bundles could then be separated by manual extraction (Figure 2C). By carefully pulling the bundles through two fingers, most residual parenchymatous tissue could be removed from the surface of the bundles. Each bundle was then fixed on two aluminium plates (Figure 2C) at a distance of roughly 10 mm with all-purpose glue (Blitzschnelle Pipette, UHU, GmbH & Co KG, Bühl, Germany). Samples were kept in a box with wet paper tissue until testing to prevent the samples from drying.

The tensile testing of the samples was performed at a constant speed of 5 µm/s until failure of the samples on a custom-made tension–compression testing device equipped with a load cell of 50 N maximal force. The free length of the samples was measured as the distance between the plates. Displacements until the first increase in force (distance Δx in Figure 2C) were subsequently added to the free length of the samples. The cross-sectional area of the vascular bundles was calculated using the diameter of the vascular bundles measured in images taken by a binocular (Olympus SZX 9, Olympus Corp., Tokyo, Japan) equipped with a digital camera. The images were taken from remaining ends of the vascular bundles after mechanical testing. The cross-sectional area was assumed as circular and constant over the length of the sample, an assumption that holds true in good approximation as proven by visual inspection of the undamaged vascular bundles. These test results allow for the determination of Young's modulus, critical strain (ε_{crit}) and tensile strength (σ_{max}) of the vascular bundles (see Supporting Information File 4 - Raw data).

Data analysis and statistics

For the determination of the Young's moduli an ordinary least squares fit (OLS) was performed as described above for the experiments in set (1). Critical strain is the strain at rupture at a critical force, and tensile strength is the stress at the critical force applied to the sample. The descriptive statistics for area, Young's modulus (MoE), critical strain and tensile strength were calculated as described above for experimental set (1) and are provided in Supporting Information File 4 – Descriptive statistics. As the results for the area were not normally distributed (Lilliefors test) for all groups, an inter-species comparison was performed by a Kruskal–Wallis ANOVA on mean ranks (H0: equality of mean ranks at $\alpha = 0.05$) with a post hoc multiple comparison on mean ranks (Tukey–Kramer, see Supporting Information File 4 – Inferential statistics). The results for the area were then plotted as a combination of a box–whisker plot indicating medians, quartiles, interquartile range and extreme values and an error-bar plot of mean ranks and standard error for each corresponding group/tissue zone (Figure 6A). Due to the normality of critical strain, MoE and tensile strength, a comparison between groups was calculated by one-way ANOVA (H0: equality of means at $\alpha = 0.05$) and a post hoc multiple comparison on means (Bonferroni adjustment, see Supporting Information File 4 – Inferential statistics). The results for critical strain, MoE and tensile strength were plotted as a combination of a box–whisker plot indicating medians, quartiles, interquartile range and extreme values and an error-bar plot of means and standard error for each of the corresponding group/tissue zone (Figure 6B–D).

Comparison of measured and calculated longitudinal Young's moduli of tissues in *Dracaena marginata* using the Voigt model (4)

In composite theory, an upper bound modulus for loading parallel to the fibres can be estimated by the rule of mixture, more precisely the Voigt Model [51]. It has been shown that this can also be applied to plant tissues [16] and to entire plant stems [49,52,53]. Hence, the plant bulk tissues (fibres and parenchyma) of *Dracaena marginata* are approximated to axially parallel, non-branching fibres embedded in a parenchymatous matrix. Here, the calculated Young's modulus of the bulk tissues MoE_t is the result of the Young's modulus of the vascular bundles (MoE_{vb}) and the Young's modulus of the ground tissue (MoE_{gt}) set in proportion to their volume fraction (Equation 12):

$$\mathrm{MoE_t}\left[\mathrm{N\cdot mm^{-2}}\right] = f\cdot \mathrm{MoE_{vb}} + \left(1-f\right)\cdot \mathrm{MoE_{gt}}\,, \quad (12)$$

where f is the volume fraction of the vascular bundles and is given by:

$$f\left[/\right] = \frac{V_{\mathrm{vb}}}{V_{\mathrm{t}}} = \frac{l\cdot\sum A_{\mathrm{vb},i}}{l\cdot A_{\mathrm{t}}} = \frac{A_{\mathrm{vb}}}{A_{\mathrm{t}}}\,, \quad (13)$$

with V_{vb} being the cumulative volume of all vascular bundles and V_{t} the volume of the bulk tissue. As the length l is a constant factor for both fibre and tissue, the volume fraction can be reduced to the area fraction of the cross-sections with A_{vb} being the cumulative cross-sectional area of all vascular bundles ($A_{\mathrm{vb},i}$) and A_{t} the cross-sectional area of the bulk tissue.

For every measured sample of plants 2–4, the bulk tissue $\mathrm{MoE_t}$ was calculated, therefore the data evaluated by the methods described for the experiment sets 1–3 are put together in the following manner: The mean value of the radial Young's modulus of *D. marginata* (0.0033 GPa, set 1) has been assigned to the ground tissue ($\mathrm{MoE_{gt}}$) because it can be assumed that these values are dominated by the ground tissue (Reuss model, see further elaborations in the Discussion section). Assignment/mapping of tissue data (see set 2) and fibre data (see set 3) has been made possible by the grouping of the tissue and fibre data in axial (B, M, T) and radial (P, M, C) zones. For every tissue sample measured (set 2), the cross-sectional area of the sample (A_{cross}) has been assigned to the cross-sectional area of the bulk tissue A_{t}. The cumulative cross-sectional area of the vascular bundles (A_{vb}) can be further described by the product of number of vascular bundles within a tissue cross-section ($\#_{\mathrm{vb}}$, result from methods in set 2) and the cross-sectional area of the vascular bundles ($A_{\mathrm{vb},i}$):

$$A_{\mathrm{vb}}\left[\mathrm{mm^2}\right] = \#_{\mathrm{vb}}\cdot A_{\mathrm{vb},i}\,. \quad (14)$$

Here, the simplification of a homogenous size of vascular bundles within each cross-sectional area has been made.

The number of calculations using the Voigt model (Figure 7) for each of the nine tissue zones –crosswise combinations of the tree axial zones, basal (B), middle (M) and top (T), with the three radial zones, periphery (P), middle (M) and centre (C) – correspond to the number of tissue samples in the tissue zones (Figure 4) multiplied by the number of measured vascular bundles in the assigned zone. In total 782 calculations have been made (see Supporting Information File 5 – Calculated data w. Voigt model).

For each zone, the calculations have been assessed by descriptive statistics (mean, STD, standard error of the mean, see Supporting Information File 5 – Descriptive statistics). The mean and standard deviation has been plotted versus the relative position for each plant individually in Figure 7. In addition, the measured value of each sample was added to the plot for comparison. If the values of the measured data are within the range of the standard deviation of the calculated data using the Voigt model, we consider the Voigt model as valid, i.e., able to adequately match the calculated with the measured Young's modulus of the tissue.

We use the Voigt model in the present study to test whether the measured values for the longitudinal Young's model of the tissues (first hierarchical level) are dominated by the values of the longitudinal Young's modulus of the vascular bundles (second hierarchical level).

Supporting Information

Supporting Information File 1

Raw data of measurements and statistics for stem segments of various monocotyledons.
[http://www.beilstein-journals.org/bjnano/content/supplementary/2190-4286-7-154-S1.xlsx]

Supporting Information File 2

Details on testing procedures of stem segments for various monocotyledons.
[http://www.beilstein-journals.org/bjnano/content/supplementary/2190-4286-7-154-S2.xlsx]

Supporting Information File 3

Raw data of measurements and statistics for stem segments of *Dracaena marginata.*
[http://www.beilstein-journals.org/bjnano/content/supplementary/2190-4286-7-154-S3.xlsx]

Supporting Information File 4

Raw data of measurements as well as statistics for individual vascular bundles of *Dracaena marginata*.
[http://www.beilstein-journals.org/bjnano/content/supplementary/2190-4286-7-154-S4.xlsx]

Supporting Information File 5

Data and statistics using Voigt's model for assessing the structural Young's modulus of *Dracaena marginata*.
[http://www.beilstein-journals.org/bjnano/content/supplementary/2190-4286-7-154-S5.xlsx]

Acknowledgements

The authors thank the German Research Foundation (DFG) for funding the study within the Priority Programme SPP 1420 'Biomimetic Materials Research: Functionality by Hierarchical Structuring of Materials'. We also gratefully acknowledge Sandra Eckert from the Plant Biomechanics Group in Freiburg for carrying out parts of the anatomical preparations, biomechanical testing, microscopic analyses and manuscript formatting as well as Prof. Dr. Siegfried Fink and his staff from the Forest-Botany Department in Freiburg for anatomical preparations. We also acknowledge Prof. Dr. Christoph Neinhuis and his staff from the Botanic Garden in Dresden for providing plant materials and helpful discussion on the data, as well as Prof. Dr. Maik Gude and his staff from the Institute of Lightweight Engineering and Polymer Technology in Dresden for the opportunity to use their testing devices and also for valuable discussions on the experiments and data. We would like to thank the three reviewers for critical examination of our study and for providing very helpful comments.

The authors dedicate this work to Prof. Dr. Wilhelm Barthlott for his merits in organismic botany.

References

1. Speck, T.; Burgert, I. *Annu. Rev. Mater. Res.* **2011,** *41,* 169–193. doi:10.1146/annurev-matsci-062910-100425
2. Dixon, P. G.; Gibson, L. J. *J. R. Soc., Interface* **2014,** *11,* 20140321. doi:10.1098/rsif.2014.0321
3. Amada, S.; Ichikawa, T.; Munekata, T.; Nagase, Y.; Shimizu, H. *Composites, Part B* **1997,** *28,* 13–20. doi:10.1016/S1359-8368(96)00020-0
4. Nogata, F.; Takahashi, H. *Compos. Eng.* **1995,** *5,* 743–751. doi:10.1016/0961-9526(95)00037-N
5. Shao, Z.-P.; Fang, C.-H.; Huang, S.-X.; Tian, G.-L. *Wood Sci. Technol.* **2010,** *44,* 655–666. doi:10.1007/s00226-009-0290-1
6. Schwager, H.; Haushahn, T.; Neinhuis, C.; Speck, T.; Masselter, T. *Adv. Eng. Mater.* **2010,** *12,* B695–B698. doi:10.1002/adem.201080057
7. Schwager, H.; Masselter, T.; Speck, T.; Neinhuis, C. *Proc. R. Soc. London, Ser. B* **2013,** *280,* 20132244. doi:10.1098/rspb.2013.2244
8. Rich, P. M. *Bot. Gaz. (Chicago)* **1987,** *148,* 42–50. doi:10.1086/337626
9. Gibson, L. J. *J. R. Soc., Interface* **2012,** *9,* 2749–2766. doi:10.1098/rsif.2012.0341
10. Masselter, T.; Eckert, S.; Speck, T. *Beilstein J. Nanotechnol.* **2011,** *2,* 173–185. doi:10.3762/bjnano.2.21
11. Zimmermann, M. H.; Tomlinson, P. B. *J. Arnold Arbor., Harv. Univ.* **1969,** *50,* 370–383.
12. Zimmermann, M. H.; Tomlinson, P. B. *J. Arnold Arbor., Harv. Univ.* **1970,** *51,* 478–492.
13. Torelli, N.; Trajković, J. *Holz Roh- Werkst. (1937-2008)* **2003,** *61,* 477–478.
14. Schoute, J. C. *Ann. Jard. Bot. Buitenzorg* **1906,** *20,* 53–87.
15. Zimmermann, M. H.; Tomlinson, P. B.; LeClaire, J. *Bot. J. Linn. Soc.* **1974,** *68,* 21–41. doi:10.1111/j.1095-8339.1974.tb01745.x
16. Niklas, K. J. *Plant biomechanics: an engineering approach to plant form and function;* University of Chicago Press: Illinois, USA, 1992.
17. Speck, T.; Schmitt, M. Tabellen. In *Biologie im Überblick, Lexikon der Biologie;* Schmitt, M., Ed.; Herder Verlag: Freiburg, Germany, 1992; Vol. 10, pp 187–328.
18. Kuo-Huang, L.-L.; Huang, Y.-S.; Chen, S.-S.; Huang, Y.-R. *IAWA J.* **2004,** *25,* 297–310. doi:10.1163/22941932-90000367
19. Hesse, L.; Wagner, S. T.; Neinhuis, C. *AoB Plants* **2016,** *8,* No. plw005. doi:10.1093/aobpla/plw005
20. Tan, T.; Rahbar, N.; Allameh, S. M.; Kwofie, S.; Dissmore, D.; Ghavami, K.; Soboyejo, W. O. *Acta Biomater.* **2011,** *7,* 3796–3803. doi:10.1016/j.actbio.2011.06.008
21. Rüggeberg, M.; Burgert, I.; Speck, T. *J. R. Soc., Interface* **2010,** *7,* 499–506. doi:10.1098/rsif.2009.0273
22. Najmie, M.; Khalid, K.; Sidek, A.; Jusoh, M. *Meas. Sci. Rev.* **2011,** *11,* 160–164. doi:10.2478/v10048-011-0026-x
23. Anten, N. P. R.; Schieving, F. *Am. Nat.* **2010,** *175,* 250–260. doi:10.1086/649581
24. Fournier, M.; Dlouha, J.; Jaouen, G.; Almeras, T. *J. Exp. Bot.* **2013,** *64,* 4793–4815. doi:10.1093/jxb/ert279
25. Reiterer, A.; Lichtenegger, H.; Tschegg, S.; Fratzl, P. *Philos. Mag. A* **1999,** *79,* 2173–2184. doi:10.1080/01418619908210415
26. Li, X. Physical, chemical, and mechanical properties of bamboo and its utilization potential for fiberboard manufacturing. M. SC. Thesis, Louisiana State University, USA, 2004.
27. Gibson, L. J.; Ashby, M. F. *Cellular solids: structure and properties,* 2nd ed.; Cambridge University Press: Cambridge, U.K., 1997. doi:10.1017/CBO9781139878326
28. Niklas, K. J. *Ann. Bot. (Oxford, U. K.)* **1997,** *79,* 265–272. doi:10.1006/anbo.1996.0340
29. Rüggeberg, M.; Speck, T.; Burgert, I. *New Phytol.* **2009,** *182,* 443–450. doi:10.1111/j.1469-8137.2008.02759.x
30. Spatz, H.-C.; Köhler, L.; Speck, T. *Am. J. Bot.* **1998,** *85,* 305–314. doi:10.2307/2446321
31. Niklas, K. J. *Am. J. Bot.* **1989,** *76,* 521–531. doi:10.2307/2444346
32. Speck, T.; Speck, O.; Emanns, A.; Spatz, H.-C. *Bot. Acta* **1998,** *111,* 366–376. doi:10.1111/j.1438-8677.1998.tb00721.x
33. Anten, N. P. R.; Casado-Garcia, R.; Nagashima, H. *Am. Nat.* **2005,** *166,* 650–660. doi:10.1086/497442
34. Spatz, H.-C.; Beismann, H.; Brückert, F.; Emanns, A.; Speck, T. *Philos. Trans. R. Soc. London, Ser. B* **1997,** *352,* 1–10. doi:10.1098/rstb.1997.0001
35. Kretschmann, D. Mechanical properties of wood. In *Forest Products Service 2010. Wood Handbook;* Ross, R. J., Ed.; Forest Products Laboratory USDA: Madison, WI, U.S.A., 2010; pp 100–145.
36. Spatz, H. C.; Speck, T.; Vogellehner, D. *Bot. Acta* **1990,** *103,* 123–130. doi:10.1111/j.1438-8677.1990.tb00137.x
37. Spatz, H. C.; Beismann, H.; Emanns, A.; Speck, T. *Biomimetics* **1995,** *3,* 141–155.
38. Rüggeberg, M.; Speck, T.; Paris, O.; Lapierre, C.; Pollet, B.; Koch, G.; Burgert, I. *Proc. R. Soc. London, Ser. B* **2008,** *275,* 2221–2229. doi:10.1098/rspb.2008.0531
39. Li, H.; Shen, S. *J. Mater. Res.* **2011,** *26,* 2749–2756. doi:10.1557/jmr.2011.314
40. Haushahn, T.; Speck, T.; Masselter, T. *Am. J. Bot.* **2014,** *101,* 754–763. doi:10.3732/ajb.1300448
41. Amada, S.; Untao, S. *Composites, Part B* **2001,** *32,* 451–459. doi:10.1016/S1359-8368(01)00022-1
42. Zimmermann, M. H.; Tomlinson, P. B. *J. Arnold Arbor., Harv. Univ.* **1965,** *46,* 160–180.

43. Zimmermann, M. H.; Tomlinson, P. B. *J. Arnold Arbor., Harv. Univ.* **1967,** *48,* 122–142.
44. Zimmermann, M. H.; Tomlinson, P. B. *Am. J. Bot.* **1968,** *55,* 1100–1109. doi:10.2307/2440478
45. Zimmermann, M. H.; Tomlinson, P. B. *Bot. Gaz. (Chicago)* **1972,** *133,* 141–155. doi:10.1086/336628
46. Tomlinson, P. B. In *Advances in botanical research;* Preston, R. D., Ed.; Academic Press: London, U.K., 1970; Vol. 3, pp 207–292.
47. Haushahn, T.; Schwager, H.; Neinhuis, C.; Speck, T.; Masselter, T. *Bioinspired, Biomimetic Nanobiomater.* **2012,** *1,* 77–81. doi:10.1680/bbn.11.00011
48. Müller, L.; Milwich, M.; Gruhl, A.; Böhm, H.; Gude, M.; Haushahn, T.; Masselter, T. *Tech. Text.* **2013,** *56,* 231–235.
49. Speck, T.; Rowe, N. P.; Brüchert, F.; Haberer, W.; Gallenmüller, F.; Spatz, H. C. How plants adjust the “material properties” of their stems according to differing mechanical constraints during growth - an example of smart design in nature. In *Proceedings of the 1996 Engineering Systems Design and Analysis Conference,* Engin, A. E., Ed.; The American Society of Mechanical Engineers: New York, NY, USA, 1996; pp 233–241.
50. Hesse, L.; Masselter, T.; Leupold, J.; Spengler, N.; Speck, T.; Korvink, J. *Sci. Rep.* **2016,** *6,* No. 32685. doi:10.1038/srep32685
51. Voigt, W. *Ann. Phys.* **1889,** *274,* 573–587. doi:10.1002/andp.18892741206
52. Rowe, N. P.; Speck, T. *Rev. Palaeobot. Palynol.* **1998,** *102,* 43–62. doi:10.1016/S0034-6667(98)00013-X
53. Speck, T.; Rowe, N. P. A quantitative approach for analytically defining size, form and habit in living and fossil plants. In *The evolution of plant architecture;* Kurmann, M. H.; Hemsley, A. R., Eds.; Royal Botanic Gardens, Kew: Kew, U.K., 1999, 1999; pp 447–479.

License and Terms

BEILSTEIN JOURNAL OF NANOTECHNOLOGY

3D printing of mineral–polymer bone substitutes based on sodium alginate and calcium phosphate

Aleksey A. Egorov[1], Alexander Yu. Fedotov[1], Anton V. Mironov[2], Vladimir S. Komlev[*2], Vladimir K. Popov[2] and Yury V. Zobkov[1]

Letter

Open Access

Address:
[1]A. A. Baikov Institute of Metallurgy and Materials Science, Russian Academy of Sciences, Leninsky prospect 49, 119334, Moscow, Russia and [2]Institute of Photonic Technologies, Federal Scientific Research Centre "Crystallography and Photonics", Russian Academy of Sciences, 2 Pionerskaya St., 142092 Troitsk, Moscow, Russia

Email:
Vladimir S. Komlev[*] - komlev@mail.ru

* Corresponding author

Keywords:
3D printing; bone graft; calcium phosphate; composite materials; sodium alginate; tissue engineering

Beilstein J. Nanotechnol. **2016,** *7,* 1794–1799.
doi:10.3762/bjnano.7.172

Received: 24 March 2016
Accepted: 03 November 2016
Published: 21 November 2016

This article is part of the Thematic Series "Biological and biomimetic materials and surfaces".

Guest Editor: S. N. Gorb

Abstract

We demonstrate a relatively simple route for three-dimensional (3D) printing of complex-shaped biocompatible structures based on sodium alginate and calcium phosphate (CP) for bone tissue engineering. The fabrication of 3D composite structures was performed through the synthesis of inorganic particles within a biopolymer macromolecular network during 3D printing process. The formation of a new CP phase was studied through X-ray diffraction, Fourier transform infrared spectroscopy and scanning electron microscopy. Both the phase composition and the diameter of the CP particles depend on the concentration of a liquid component (i.e., the "ink"). The 3D printed structures were fabricated and found to have large interconnected porous systems (mean diameter ≈800 μm) and were found to possess compressive strengths from 0.45 to 1.0 MPa. This new approach can be effectively applied for fabrication of biocompatible scaffolds for bone tissue engineering constructions.

Introduction

3D printing is one promising methodology for tissue engineering constructions with specific architectonics and properties. It has the attractive advantages of both accurate and reproducible layer-by-layer fabrication of complex-shaped structures [1-4]. A number of biocompatible materials, such as polymers of different nature (both natural and synthetic), as well as a variety of calcium phosphates (CPs) are used for this purpose [2]. In this respect, the alginate-based materials are of particular interest. Alginate (extracellular polysaccharide) is a popular biomaterial because of a number of key advantages: convenient precursors, nontoxic, excellent biocompatibility and appropriate biodegradability [5-7]. Additionally, CPs are widely used

for bone graft substitution due to their chemical affinity to the bone mineral content [8]. One of the strategies to improve the bioactivity of the polymer-based materials is to incorporate some inorganic phase, such as CP particles, into their structure [9-11]. The 3D printing of these materials is usually achieved by simple ink jet processing of a mechanical mixture of starting ingredients (mineral/polymer components), producing desirable structures directly through layer-by-layer manufacture of the desired product [10]. Therefore, the final 3D product consists of a mechanical mixture of the polymer slurry with more-or-less homogeneously distributed CP particles.

In this work we propose a new biomimetic approach in which 3D printing of composite structures involves a chemical interaction of the polymer slurry with a liquid "ink", leading to in situ formation of a CP phase in the final product. It is well known that alginate allows precipitation of inorganic phases within its macromolecular network [7] and this process provides inorganic phases with different crystals sizes and morphologies [7,12]. For all these reasons, 3D printing of bioinspired structures has gained considerable interest since its inception, primarily because it can lead to artificial bone grafts that are close to native bone. In our experiments the formation of a new inorganic phase during the 3D printing process was monitored by X-ray diffraction (XRD), Fourier transform infrared (FTIR) spectroscopy and scanning electron microscopy (SEM), enabling us to find optimal parameters for the developed route.

Results and Discussion

3D printing is a powerful tool for the production of custom-designed and complex bone substitutes [2,3]. In our work, the fabrication of 3D composite structures was performed using a binary system based on aqueous solutions of sodium alginate containing PO_4^{3-} groups. A calcium chloride aqueous solution, as a second component, was used as a source of Ca^{2+} ions. The 3D composite structures were fabricated in a cubic shape ($8 \times 8 \times 5$ mm^3), comprising 30 interconnected longitudinal channels with dimensions of ≈800 × 800 μm^2 running through the samples (Figure 1). This structure resulted in optimal pores sizes and good interconnectivity, which are of great importance for the design of 3D bone substitutes for biomedical applications.

The CP phase was formed upon mixing of the polymer slurry containing ammonium hydrogen phosphate with a calcium chloride aqueous solution during the printing process according to the following reaction:

$$(NH_4)_2HPO_4 + Ca^{2+} + 2H_2O \rightarrow CaHPO_4 \cdot 2H_2O + 2NH_4$$

In fact, the mixture of the phosphate source with alginate gives rise to a homogeneous gel, suggesting an interaction between the biopolymer and the HPO_4^{2-}. The stability and homogeneity of this gel can be explained by possible interactions between the HPO_4^{2-} moiety and the carboxylate group of alginate. This physical bonding translates to mixtures that are rich in electronic pairs leading to a higher reactivity and mineralization potential that can be transformed into composite materials [13]. According to X-ray diffraction data, synthesis in the presence of glutamic acids in the reaction medium maintained at pH 4.5 ± 0.5 yields the formation of dicalcium phosphate dihydrate (DCPD) in the printed samples (Figure 2). When precipitation is performed at a higher pH, as reported in [7,14], the difference of electrical charges in alginate is greater. As a consequence, a more compact complex without compositional water is obtained. The formation of anhydrous dicalcium phosphate (monetite) would be then kinetically favored. The estimated average mineral contents are 90, 70 and 54% of DCPD for alginate concentrations of 0.25, 1.0 and 2.0 wt %, respectively.

Figure 3 shows SEM images of 3D printed samples, where inorganic matrix DCPD crystal is prepared with a 1 M solution of ammonium hydrogen phosphate and alginate concentration of 0.25 wt %. The morphology of the crystals show plate- and

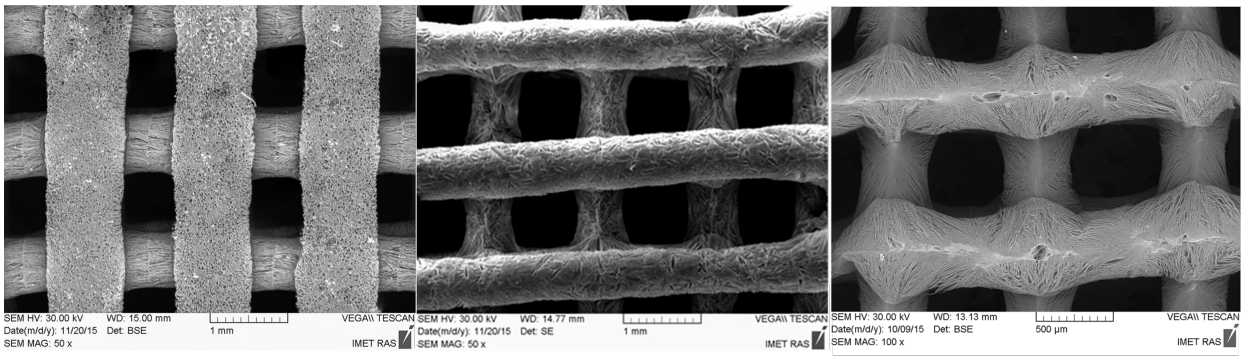

Figure 1: SEM micrographs of 3D printed samples.

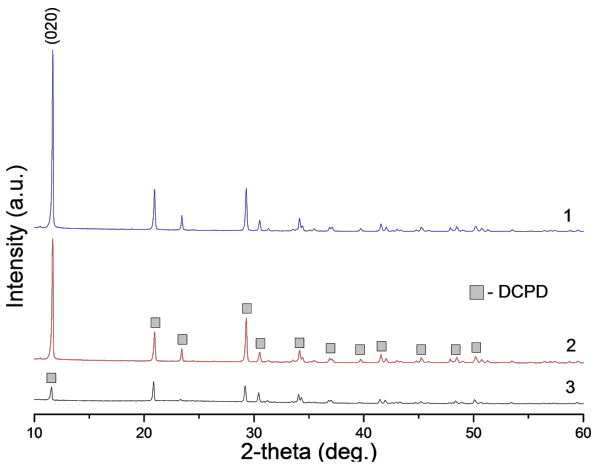

Figure 2: XRD spectra of 3D printed samples on the basis alginate with concentration (1) 0.25 wt %, (2) 1.0 wt % and (3) 2.0 wt %.

needle-like structures with different sizes. The formation of DCPD crystals is observed on the surface and internal regions of the 3D printed samples (Figure 3). Moreover, the SEM images demonstrate a decrease of plate-shaped DCPD particle for sizes from ≈40 to 1 μm with increasing alginate concentration from 0.25 wt % up to 2.0 wt % (Figure 4). This effect may be caused by an increase in concentration of heterogeneous nucleation centers of a calcium phosphate phase on the carboxyl groups of the amino acids. X-ray diffraction data lend support to this tendency: the height of the strongest peak (020) of DCPD decreases by a factor of 7 as the alginate and, correspondently, amino acid concentration increases from 0.25 to 2.0 wt % (Figure 2).

The FTIR spectra of DCPD exhibits principal characteristic bands known to be associated with PO_4 (ν_4) at 575 and 1125 cm^{-1}, (ν_1) at 981 cm^{-1}, (ν_3) at 870 cm^{-1} and 1056 cm^{-1}; as well as H_2O at 650 cm^{-1}, 790 cm^{-1} [15]. In our FTIR spec-

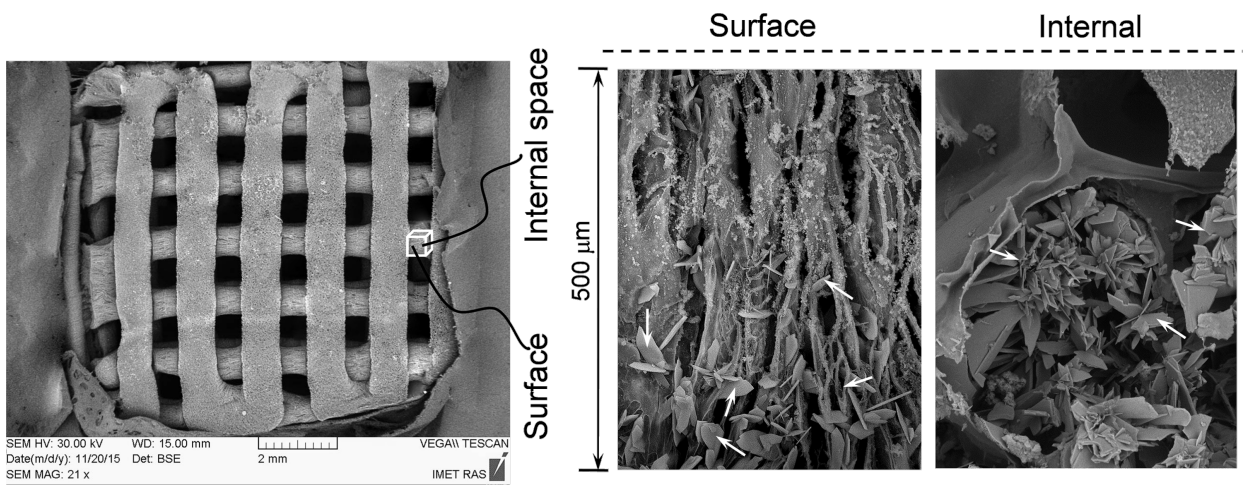

Figure 3: SEM images showing a general sample overview and details of the surface and internal region of a 3D printed sample (white arrows indicate DCPD crystals).

Figure 4: SEM micrographs of the microstructure of 3D printed samples on the basis of alginate with concentration of (a) 0.25, (b) 1.0 and (c) 2.0 wt %.

tra of 3D printed DCPD–alginate samples, the bands are shifted from 1125 cm^{-1} for DCPD to 1114 cm^{-1} and from 1056 to 1064 cm^{-1}. The bands at 981 cm^{-1}, 870 cm^{-1}, 575 cm^{-1} and 520 cm^{-1} shifted insignificantly (Figure 5). The H_2O bands were observed to shift from 650 to 636 cm^{-1}. Apparently, calcium phosphate reacts with alginate through the carboxyl groups of amino acids and calcium in calcium phosphate, because the frequency changes are observed for groups located near calcium ions in the phosphate structures [13].

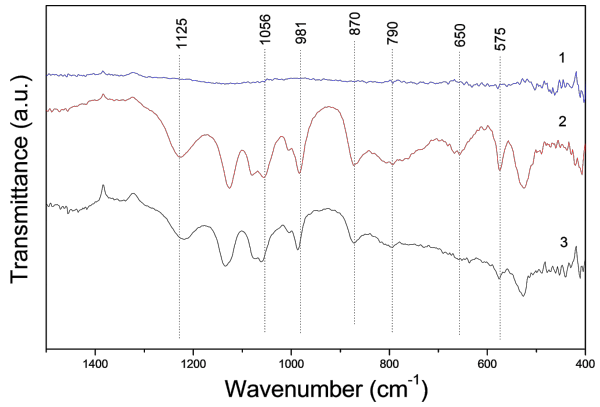

Figure 5: FTIR spectra of (1) sodium alginate, (2) DCPD, and (3) the 3D printed product.

The compressive strength of 3D printed samples is shown in Figure 6. The mechanical properties of 3D printed samples are relatively low due to the weak bonding between different printed layers. However, the compressive strength of composite materials increased with alginate concentration from 0.45 MPa up to about 1.0 MPa at $p \leq 0.005$. The increase in the compressive strength can be explained by an increase in alginate content within the 3D printed samples. Similar to our result it has been reported in the literature [16] that in situ precipitated calcium phosphate in polymeric composites tend to have lower mechanical strength.

The chemical and phase composition of the developed 3D printed samples can be adjusted further by chemical post-treatment. For instance, the hydrolysis of DCPD might lead to the development of an octacalcium phosphate phase and an adhesive effect between particles could take place [17].

Conclusion

We propose a new "biomimetic + 3D printing" approach for fabrication of complex-structured composite bone substitutes using appropriate raw materials and a new "ink". Depending on the processing parameters and conditions, it is possible to achieve materials with adjustable mechanical properties, specified composition, morphology and CP crystal size. Our results may provide a new approach for synthesis of highly osteogenic composite materials and for the effective fabrication of custom-designed implants and tissue engineering constructs via 3D printing on the commercial scale.

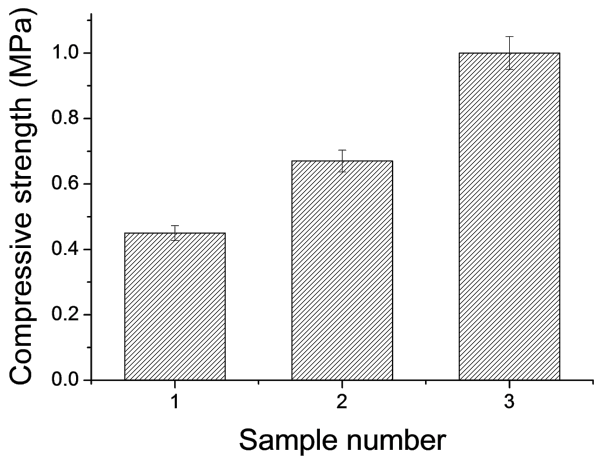

Figure 6: Compressive strength of 3D printed samples on the basis of alginate with concentration of (1) 0.25, (2) 1.0 and (3) 2.0 wt %.

Experimental

Materials

The fabrication of 3D composite structures was performed using a binary system based on aqueous solutions of sodium alginate. The polymer slurry of sodium alginate (CAS number 9005-38-3) with concentrations of 0.25, 1.0 and 2.0 wt % was prepared in distilled water in presence of glutamic acid ($C_5H_9NO_4$) (CAS number 56-86-0) with concentrations of 0.25, 1.0 and 2.0 wt %. Glutamic acid was used to maintain a low pH value. Then, a solution of ammonium hydrogen phosphate (CAS number 7783-28-0) with concentration of 5 wt % was added as the source of phosphorus in the system. The second "ink" was calcium chloride (CAS number 10043-52-4) water solution with a concentration of 10 wt %, being the source of calcium. All reagents were purchased from Sigma-Aldrich.

3D printing

A custom-designed 3D printer was used for our experiments, as shown in Figure 7. The initial reactant solutions were placed in two separate cartridges of 3D printer. Thereafter, they were injected through a nozzle (or needle, depending on the initial viscosity of the solutions) of disposable syringe on a cooled (−5 to −30 °C) flat glass substrate. The pH of the reaction medium was measured by an Econix-Expert 001 pH meter (Econix-Expert Ltd., Moscow, Russia) and maintained at pH 4.5 ± 0.5. The printed samples were deep-frozen at −50 °C and then freeze-dried at 6×10^{-5} atm for 10–12 h. Finally, the fabricated

3D structure was washed in distilled water and incubated at 37 °C for one day.

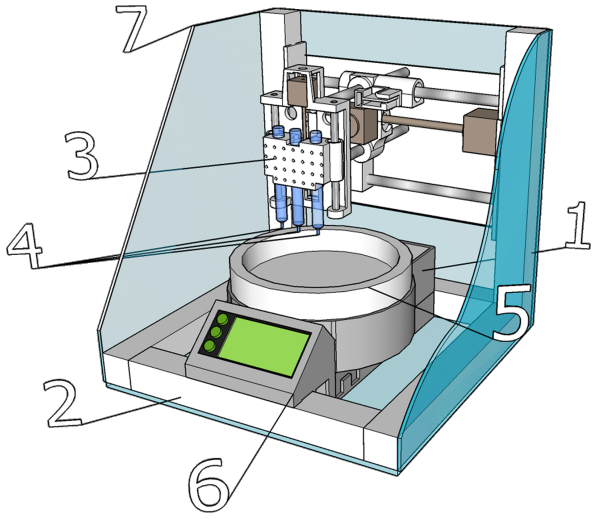

Figure 7: Custom-designed 3D printer. 1 - power supply; 2 - metal frame; 3 - printing head with a reservoir and heaters; 4 - nozzles; 5 - thermostatically controlled worktable; 6 - microcontroller unit and power electronic modules; 7 - sealed enclosure.

Characterization

As described in [17], the phase composition of the samples was analyzed by conventional X-ray diffraction (XRD) technique (Shimadzu XRD-6000, Japan, Ni-filtered Cu $K\alpha_1$ target, $\lambda = 1.54183$ Å). The samples were scanned at a 2θ angle from 10–60° with a 0.02° step and a preset time of 5 s. A scanning electron microscopy apparatus (Tescan Vega II, Czech Republic), operated in secondary and backscattered electron modes, was used for 3D microstructure analysis. The samples were sputter-coated with a 25 nm thick gold layer prior to imaging, imparting electrical conductivity to the surfaces. FTIR spectroscopy (Nicolet Avatar 330, England) was performed after mixing 1 mg of the grinded sample with 300 mg of KBr powder followed by compacting into a thin pellet in a stainless steel die with a 1 cm inner diameter. FTIR data were recorded over the range of 4000–400 cm^{-1} with 128 scans.

As described in [17] the compressive strength of the samples was evaluated in accordance with the ISO standard 83.100: Cellular materials. Five samples for each point were used. Compression testing was carried out using an Instron 5581 (Bucks, UK) testing machine operating at a crosshead speed of 1 mm/min. Statistical analysis was performed using SPSS software, version 17.0 (Statistical Package for Social Sciences, SPSS Inc., USA). The mean and standard deviation of compressive strength were calculated.

Acknowledgments

This work was supported by the Russian Science Foundation (project No. 15-13-00108).

References

1. Kim, S. S.; Utsunomiya, H.; Koski, J. A.; Wu, B. M.; Cima, M. J.; Sohn, J.; Mukai, K.; Griffith, L. G.; Vacanti, J. P. *Ann. Surg.* **1998,** *228,* 8–13.
2. Bose, S.; Vahabzadeh, S.; Bandyopadhyay, A. *Mater. Today* **2013,** *16,* 496–504. doi:10.1016/j.mattod.2013.11.017
3. Chia, H. N.; Wu, B. M. *J. Biol. Eng.* **2015,** *9,* 1–14.
4. Wang, X.; Schröder, H. C.; Müller, W. E. G. *Beilstein J. Nanotechnol.* **2014,** *5,* 610–621. doi:10.3762/bjnano.5.72
5. Rees, D. A. *Pure Appl. Chem.* **1981,** *53,* 1–14. doi:10.1351/pac198153010001
6. Li, Y.; Liu, Y.; Li, S.; Liang, G.; Jiang, C.; Hu, Q. *J. Biosci. Bioeng.* **2016,** *121,* 111–116. doi:10.1016/j.jbiosc.2015.04.020
7. Oliveira de Lima, D.; Aimoli, C. G.; Beppu, M. M. *Mat. Sci. Eng. C* **2009,** *29,* 1109–1113. doi:10.1016/j.msec.2008.09.019
8. Dorozhkin, S. V.; Epple, M. *Angew. Chem., Int. Ed.* **2002,** *41,* 3130–3146. doi:10.1002/1521-3773(20020902)41:17<3130::AID-ANIE3130>3.0.CO;2-1
9. Shor, L.; Güçeri, S.; Wen, X.; Gandhi, M.; Sun, W. *Biomaterials* **2007,** *28,* 5291–5297. doi:10.1016/j.biomaterials.2007.08.018
10. Serra, T.; Planell, J. A.; Navarro, M. *Acta Biomater.* **2013,** *9,* 5521–5530. doi:10.1016/j.actbio.2012.10.041
11. Inzana, J. A.; Olvera, D.; Fuller, S. M.; Kelly, J. P.; Graeve, O. A.; Schwarz, E. M.; Kates, S. L.; Awad, H. A. *Biomaterials* **2014,** *35,* 4026–4034. doi:10.1016/j.biomaterials.2014.01.064
12. Calvert, P.; Rieke, P. *Chem. Mater.* **1996,** *8,* 1715–1727. doi:10.1021/cm960126o
13. Amer, W.; Abdelouahdi, K.; Ramananarivo, H. R.; Fihri, A.; El Achaby, M.; Zahouily, M.; Barakat, A.; Djessas, K.; Clark, J.; Solhy, A. *Mat. Sci. Eng. C* **2014,** *35,* 341–346. doi:10.1016/j.msec.2013.11.012
14. Davis, T. A.; Volesky, B.; Mucci, A. *Water Res.* **2003,** *37,* 4311–4330. doi:10.1016/S0043-1354(03)00293-8
15. Xu, J.; Butler, I. S.; Gilson, D. F. R. *Spectrochim. Acta, Part A* **1999,** *55,* 2801–2809. doi:10.1016/S1386-1425(99)00090-6
16. Jin, H.-H.; Lee, C.-H.; Lee, W.-K.; Lee, J.-K.; Park, H.-C.; Yoon, S.-Y. *Mater. Lett.* **2008,** *62,* 1630–1633. doi:10.1016/j.matlet.2007.09.043
17. Komlev, V. S.; Popov, V. K.; Mironov, A. V.; Fedotov, A. Yu.; Teterina, A. Yu.; Smirnov, I. V.; Bozo, I. Y.; Rybko, V. A.; Deev, R. V. *Front. Bioeng. Biotechnol.* **2015,** *3,* No. 81. doi:10.3389/fbioe.2015.00081

BEILSTEIN JOURNAL OF NANOTECHNOLOGY

"Sticky invasion" – the physical properties of *Plantago lanceolata* L. seed mucilage

Agnieszka Kreitschitz*[1,2], Alexander Kovalev[2] and Stanislav N. Gorb[2]

Full Research Paper

Open Access

Address:
[1]Department of Plant Developmental Biology, Institute of Experimental Biology, University of Wrocław, ul. Kanonia 6/8, 50-328 Wrocław, Poland and [2]Department of Functional Morphology and Biomechanics, University of Kiel, Am Botanischen Garten 9, D-24118 Kiel, Germany

Email:
Agnieszka Kreitschitz* - agnieszka.kreitschitz@uwr.edu.pl

* Corresponding author

Keywords:
adhesion; cellulose mucilage; desiccation; friction; *Plantago lanceolata*

Beilstein J. Nanotechnol. **2016,** *7,* 1918–1927.
doi:10.3762/bjnano.7.183

Received: 14 August 2016
Accepted: 16 November 2016
Published: 05 December 2016

This article is part of the Thematic Series "Biological and biomimetic materials and surfaces".

Associate Editor: B. Bhushan

Abstract

The mucilage envelope of seeds has various functions including the provision of different ways for the dispersal of diaspores. Chemical composition and water content of the mucilage yield particular adhesive and frictional properties in the envelope that also influence the dispersal of seeds. To determine the physical properties of *Plantago lanceolata* seed mucilage we studied (1) composition, (2) desiccation, (3) adhesion, and (4) friction properties of the mucilage under different hydration conditions. We revealed the presence of cellulose fibrils in the mucilage, which are responsible for a continuous and even distribution of the mucilaginous layer on the seed surface. The measured values of adhesive and frictional properties differed significantly in comparison to the previously studied pectic mucilage of *Linum usitatissimum*. Also, the water loss from the cellulose mucilage was more rapid. The obtained different values can result from the presence of cellulose fibrils and their interaction with pectins in the mucilage. Because of this feature the mucilage of *P. lanceolata* may represent a more regularly ordered and stabile system than the pectic mucilage of flax, which lacks cellulose. In spite of the fact that *P. lanceolata* mucilage revealed different adhesive and frictional properties than the pectic mucilage, it still demonstrates an effective system promoting zoochoric seed dispersal. Cellulose may additionally prevent the mucilage against loss from the seed surface.

Introduction

The ability of seeds and fruits (diaspores) to form mucilage after hydration is known as myxospermy [1,2]. The mucilaginous diaspores are particularly characteristic of plants that grow in dry or disturbed habitats [1,3]. The presence of mucilage results in different benefits for the plant including (1) fixation of diaspores to the ground, (2) water supply essential for germinating an embryo or (3) egzo- and endozoochoric dispersal by animals [1-3].

Plantago lanceolata L. (narrow-leaf plantain) is a perennial herb known as a common weed, widely distributed in grasslands and roadsides of temperate regions of the world. It grows on a wide range of soils and is resistant to drought [4-6]. *P. lanceolata* is spread throughout the whole world excluding subarctic and low-lying tropical areas [5,7]. Species of the genus *Plantago* are used as a source of mucilage produced by vegetative parts [6] as well as by seeds [1].

Plantago seeds are dispersed by animals [8,9]. They can be eaten by sparrows and then spread by their droppings (endozoochory). Also, they can stick to the feet of the animals, the fur or the bird plumage enabling further dispersal (epizoochory) [8]. *P. lanceolata* seed mucilage was identified as an acid polysaccharide complex containing, in addition to pectins, different sugars, e.g., pentose, galactose, xylose [10,11]. The mucilage composed mainly of pectins is described as pectic type ("true slime") and is typical of, e.g., *Linaceae, Plantaginaceae* and *Poaceae* seeds [1,12]. Often mucilage possesses an additional cellulose skeleton and is then classified as cellulose mucilage, characteristic of taxa from many diverse families like Asteraceae, Brassicaceae, Lamiaceae [12-15].

Mucilage is produced by a special type of cells, namely mucilage-secreting cells (MSCs), which are an integral part of the seed/fruit coat. The cell wall of these particular cells undergoes modification during seed development, particularly resulting in an increased content of pectins [16]. Apart from pectins, hemicellulose (e.g., arabinoxylan) was also detected in *Plantago* mucilage [16]. Chemical analyses and diverse experimental techniques revealed that the mucilage comprised of a complex composition and structure that can be considered as a specialized pectin-rich secondary cell wall [17].

In the typical cell wall, two coexisting systems are present, one composed of cellulose–hemicellulose and one composed of pectins. They can interact with each other to form the network structure of the cell wall [18-20]. The spatial structure of the cell wall is also maintained through diverse bonds such as covalent bonds and ionic or hydrogen interactions [21]. Consequently, the interaction between individual components of the cell wall can influence its physical characteristics such as its mechanical properties [22].

The physical properties of the cell wall depend on its chemical composition. For example, the addition of certain matrix substances decreases the cell-wall stiffness [23], and lignification causes a higher mechanical strength [24]. Such changes of mechanical properties can also be seen in the case of mucilaginous cell wall. This wall that is rich in pectins form elastic, gel-like mucilage envelope after hydration [14,17]. Other components of the mucilage envelope such as cellulose fibrils also influence its properties and consequently its function.

Seed mucilage possesses a clearly defined nanostructure. Cellulose is a linear homopolymer of 1,4-ß-D-glucan units [25]. Cellulose chains are linked together to form elementary fibril, the size of which can vary depending on the cell-wall type (primary, secondary) and the presence of other components (hemicelluloses) coating the surface. The size of microfibrils, estimated for the primary cell wall, was in a range from 8 to 15 nm up to 30 nm [19,26,27]. Also, the fibrillary material of seed mucilage can vary in its size from thin cellulose fibrils of quince with about 5 nm [28] to fibrillary material of chia (*Salvia hispanica*) ranging between 15 to 45 nm [29]. Cellulose constitutes a kind of scaffold for other mucilage components, namely pectins and hemicelluloses, spread between the fibrils. They represent linear and/or branched polymers with size about 7 nm [27]. Considering the composition and the size of the individual components, mucilage can be treated as a specific kind of nanobiomaterial.

Cellulose is well known as natural and renewable plant polymer. Nano-cellulose is used in biomedicine, cosmetics and food industry [30]. Mucilage, which contains diverse polysaccharides, among them cellulose, exhibits a high cohesive and adhesive properties. Due to this features mucilage finds diverse applications in pharmacy as, e.g., tablet binders, disintegrants, emulsifiers, and suspending or thickening agent. Mucilage as polymer was also studied for the application in pharmaceutical dosage as, e.g., film coating agents, buccal films or nanoparticles [31].

In the study presented here, we examined adhesive and frictional properties of the mucilage of *Plantago lanceolata* and compared them to those previously studied for *Linum usitatissimum* [32]. Cellulose mucilage represents a much more developed and organized system in comparison to the simple pectic mucilage of *Linum usitatissimum* [1]. In addition to the characterization of mucilage, three types of experiments were performed in this study with *P. lanceolata* mucilaginous seeds: (1) measurement of the desiccation dynamics of the hydrated seeds; (2) pull-off force estimation and (3) characterisation of frictional properties. The latter two experiments were performed using different hydration conditions of the mucilage envelope. We used in our experiments the same devices, methods and conditions as in the previous work [32].

The following questions were asked: (1) Is there difference in the dynamics of water loss in different types of the mucilage? (2) How strong is the adhesion of the cellulose-containing mucilage at different stage of its desiccation on the smooth stiff

surface? (3) How does the desiccation change frictional properties of the cellulose-containing mucilage? (4) How do these properties differ between the cellulose mucilage type (*Plantago lanceolata*) and previously studied pectic mucilage (*Linum usitatissimum*) [32]? (5) How can the studied physical properties of *P. lanceolata* mucilage influence its seed dispersal?

Experimental

Composition of *Plantago lanceolata* mucilage

Mature seeds were collected along a dirt road in the wilderness near Wrocław, Poland. To examine the mucilage composition, staining reactions with 0.1% aqueous solution of ruthenium red (pectin staining), with 0.01% aqueous solution of methylene blue (cellulose staining) and with 0.1% aqueous solution of Direct Red 23 (specific for cellulose) were performed [15,33-35]. Crystalline cellulose in the mucilage envelope was analysed on the hydrated seeds using a polarized-light microscope Leica connected to camera Leica DFC 450 C and Las X software (Leica DM 6000B, Leica Microsystems GmbH, Germany). The images were taken using an Olympus BX-50 light microscope connected to a DP71 camera with Cell B imaging software (Olympus BX50, Olympus Optical Co, Poland) and Zeiss CLSM microscope (LSM 700 AXIO ZEISS, Germany; excitation 555, emission >560 nm)

For further experiments, seeds were hydrated in distilled water for 30 min to obtain the mucilage envelope. In each experiment, new seed samples were used.

For the next three experiments the whole experimental details and procedures have been carried out following the previous studies for *Linum usitatissimum* mucilaginous seeds [33].

Desiccation dynamics of the mucilage

The seeds of *P. lanceolata* were taken to perform experiments of desiccation dynamics. Five individual seeds were used and for each seed an individual measurement was carried out. After determination of the dry seed mass the seed was hydrated for 30 min to obtain mucilage envelope. Then the dynamic of water loss from the hydrated seed was continuously measured until the initial dry mass was reached. To control the weight measurements an Ultra Microbalance UMX2 and software Balance Link (Mettler-Toledo GmbH, Greifensee, Switzerland) were used.

During the experiments, room temperature and relative air humidity were continuously recorded using a Tinytag TGP-4500 (Gemini Data Loggers Ltd, United Kingdom). The measured temperature was 22–23 °C, the relative humidity was 30–37%.

Pull-off force measurements of the mucilage

For the pull-off force measurements five sets of measurements were made on five individual seeds. For the measurements a setup [32] consisting of force transducer, motorized micromanipulator (FORT100, World Precision Instruments, Sarasota, FL, USA), data acquisition system and software AcqKnowledge 3.7.0 (Biopac Systems Inc., Goleta, CA, USA), binocular microscope Leica MZ 12-5 (Germany) and video camera KODAK Motion Corder Analyzer Series SR (Eastman Kodak Co., San Diego, CA, USA) was used. The measurements were done on hydrated seeds (with developed mucilage envelope) and were performed until the adhesion force was no longer detectable. Images of the mucilage contact area were taken during the measurements, using a binocular microscope equipped with a video camera (KODAK) with coaxial illumination.

Friction measurements of the mucilage

A series of five measurements, each based on an individual seed set consisting of five seeds, was made. Five seeds were attached to the tilting platform [32]. After 30 min of seed hydration the measurements were started and continued until the mucilage completely dried out. For the measurements four different loads were used: (1) 15.7 mN, (2) 32 mN, (3) 47.1 mN and (4) 63.8 mN. These loads were applied repeatedly in ascending order (load 1, load 2, load 3, load 4, load 1 and so on). The seeds were fixed to a tiltable platform by adhesive tape and the load was applied in the form of a glass block with corresponding mass lying on the seeds. Then, the platform was tilted until the glass block began to move relative to the seeds. The tilt angle was determined from the built-in alidade and then used for calculating the static friction coefficient. The friction coefficient and adhesion force were both calculated from the measured results as described in [32]. Shortly, the critical angle, φ_c, at which the glass block started sliding corresponds to the following equation:

$$\varphi_c = \arctan\mu + \arcsin\frac{\mu F_{ad}}{\sqrt{1+\mu^2}F_{gb}}, \qquad (1)$$

where μ is the friction coefficient, F_{ad} is the adhesion force, $F_{gb} = m_{gb}\cdot g$, m_{gb} is the mass of the glass block, and $g = 9.813$ m/s^2 is the gravitational acceleration. At the same time, a special normalization procedure was carried out within each measurement set to obtain a smooth time dependence of the friction coefficient and adhesion force. The penalty function to the least square fit (according to Equation 2) was introduced, which is a second derivative of the estimated parameters with respect to time [36]. The friction coefficients and adhesion forces were found for each time using the following equation:

$$(\mu, F_{ad}) : \min\left\{\sum_t (\varphi_c - \varphi_m)^2 + \lambda^2 \sum_t \left|D^2(\mu + cF_{ad})\right|^2\right\}, \quad (2)$$

where the first sum minimizes the deviation of the estimated slip angle from the measured slip angle and the second sum is a regulatory term smoothing the curves of μ and F_{ad}. D^2 is an operator of the second derivative of time, λ is a regulatory parameter, c is a weighing factor between friction coefficient and adhesion force contributions. The regulatory parameter was selected to dispose of high amplitude peaks in the time dependence of the friction coefficient and to reproduce the shape of the time dependence of the adhesion force. Calculations were performed in Matlab 7.10 (The MathWorks, Natick, NA, USA).

Statistical analysis

Statistical analyses were performed with OriginPro 8 (OriginLab Corporation, Northampton, MA, USA). Comparison of means was performed with a two-sample t-test. Normal distribution and constant variance of data were verified before statistical analysis, and the P-value was set to $P < 0.001$ if one of both conditions was not achieved.

Results

Mucilage composition

The mucilage of *Plantago lanceolata* contained both pectin and cellulose components, which are characteristic of cellulose mucilage. Positive staining with ruthenium red (Figure 1A) revealed the presence of pectins in the mucilage. Staining with methylene blue (Figure 1B) and Direct Red 23 (Figure 1C) revealed the presence of cellulose. The cellulose fibrils kept the mass of pectins in place. The thickness of the mucilage envelope ranged from 350 to 450 μm. Cellulose fibrils were very delicate and embedded in the voluminous pectin mass. Crystalline cellulose in the mucilage was also visualized using a polarized light microscope (Figure 1 D). After hydration, the fibrils build a regular, radial "skeleton" (Figure 1 D) and, together with pectins, form a mucilage envelope surrounding the seed. Characteristic feature of *P. lanceolata* seed was that the mucilage envelope formed a continuous and evenly distributed layer on the seed surface.

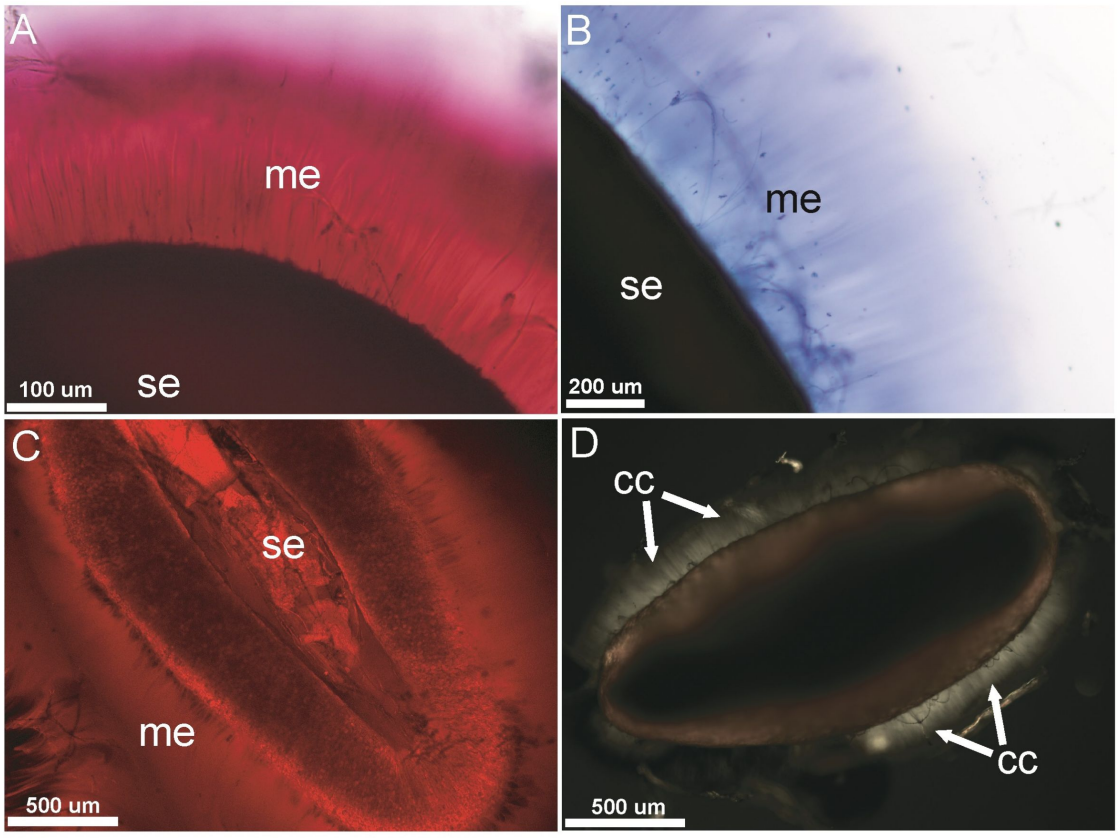

Figure 1: Mucilage composition. Bright field and fluorescence microscopy images of different staining reactions: A – pectin staining with ruthenium red; B – cellulose staining with methylene blue; C – cellulose staining with Direct Red 23, fluorescence image; D – detection of crystalline cellulose in polarized light. Characteristic signal of the cellulose fibrils (arrows); Cellulose fibrils are imbedded in the mass of pectins (cc – crystalline cellulose, me - mucilage envelope, se - seed).

Desiccation dynamics

The dry seed mass varied slightly between individual seeds (Table 1). After hydration, the maximum mass increased approximately fourfold, but differed slightly between the seeds (Table 1). The mass of absorbed water differed from 2.5 mg to 4.3 mg. The drying time (elapsed time until the fully hydrated seed achieved its dry mass) ranged from 90 to 180 min (Figure 2). The desiccation dynamics of the seeds clearly show three distinguishable phases: 30 min after hydration, 45 min after hydration and the latest linear phase. At a time of 30 min after hydration, the seeds lost 87.3 ± 1.7 % (mean ± SE) of the absorbed water, similar to the evaporation behavior of a water droplet (Figure 2). The nonlinear desiccation dynamics is easy to see in Figure 2. The deviation from linear dynamics may be related to the decreasing area from which water evaporates and a change in physicochemical properties of the mucilage depending on the water concentration. In two seeds the first phase was shortened to 15 min with followed by two sudden drops in the evaporation rate (Figure 2). These drops should correspond to jumps in the evaporation area. The second desiccation phase starts around 40 min after hydration. It is characterized by exponential desiccation and lasts for between 20 to 100 min. Such dynamics are typical for a physicochemical equilibrium and may be related to the evaporation of water bound to pectin molecules. The final desiccation phase is again linear and could be related to the slow evaporation of the rest of the water without change in the evaporation area. The rate of water loss during the first 35–40 min is comparable to the evaporation rate of a water drop.

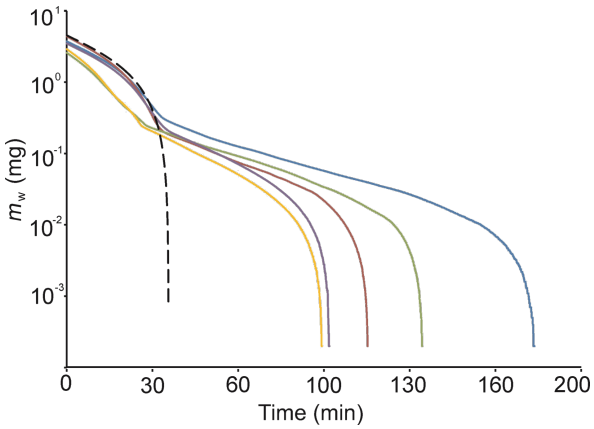

Figure 2: Desiccation dynamics of five individual plantain seeds (solid lines) and a water droplet (dashed line). m_w is mass of absorbed water or a water droplet mass. The first 30 min of desiccation of the water droplet and mucilage are comparable. After about 35–40 min the mucilage lost about 91% of the water while the water droplet completely evaporated.

Adhesive forces and contact area

The pull-off force of individual *P. lanceolata* mucilaginous seeds varied up to two orders of magnitude, 0.3–32 mN (Figure 3). Immediately after hydration, the pull-off force was low whereas the contact area between the mucilage and substrate was the largest. The pull-off force increased and reached a maximum when the mucilage envelope lost about 45–50% of water. The maximal pull-off force of individual seeds ranged between 14 and 32 mN (mean value 24 ± 3 mN). The contact area of fully hydrated seeds varied from 1.8 to 5 mm^2 and was below 0.01 mm^2 when the entire amount of absorbed water had been evaporated. At the same time, the adhesion stress, F_{ad}/A_0, continuously increased with time (Figure 4). The maximum adhesion stress reached 480 kPa. The seeds demonstrated detectable adhesion until between 11 and 29 minutes after hydration (Figure 3), presumably because of a different mucilage amount and water content in the envelope. The average time for reaching the maximum force was 16 ± 3 min. Very important and interesting was that the shape of the time-dependent pull-off force curves of individual seeds are very similar (Figure 3). After reaching a maximum value, they decreased rapidly and no adhesion was further detected.

Friction properties

The mean values of the friction coefficient, obtained for dry seeds of *P. lanceolata*, ranged from 0.4 to 0.5 (mean value 0.4 ± 0.01). Freshly hydrated seeds had an extremely low friction coefficient of about 0.05–0.08 (mean value 0.06 ± 0.01).

Table 1: The mass of *Plantago lanceolata* seeds before and after hydration.

seed	seed dry mass (mg)	seed mass after hydration (mg)	mass of absorbed water (mg)	seed mass increase after hydration (%)
1	1.3	5.7	4.3	410
2	1.5	4.1	2.5	260
3	1.7	5.2	3.4	290
4	1.3	4.2	2.9	310
5	1.3	5.0	3.7	380
average ± SD	1.4 ± 0.1	4.8 ± 0.6	3.4 ± 0.6	330 ± 62.8

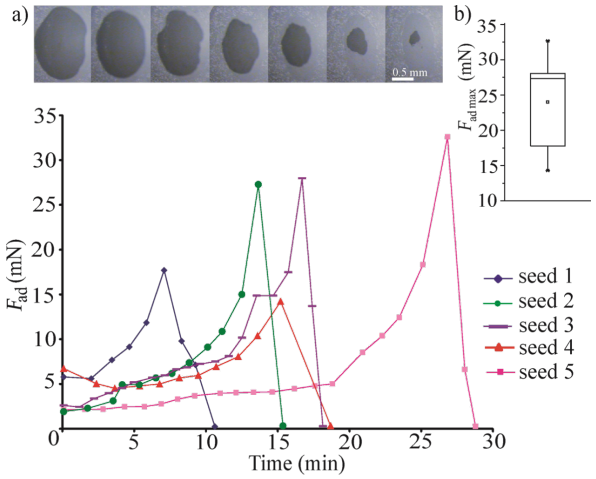

Figure 3: Adhesion force (F_{ad}) of mucilaginous seeds measured at different degrees of desiccation after full hydration. (a) Dynamics of the adhesion force is shown for five individual seeds. The top inset of microscopic images illustrates the decreasing contact area of one individual seed with the glass block under load during pull-off measurements. Interestingly, the adhesion–time curves of the individual seeds are comparable; (b) Box-and-whisker diagram of the mean maximum adhesion force of measured seeds, where the bottom and top of the box are the 25th and 75th percentiles, the band inside the box is the median; the ends of the whiskers are the 10th and 90th percentiles.

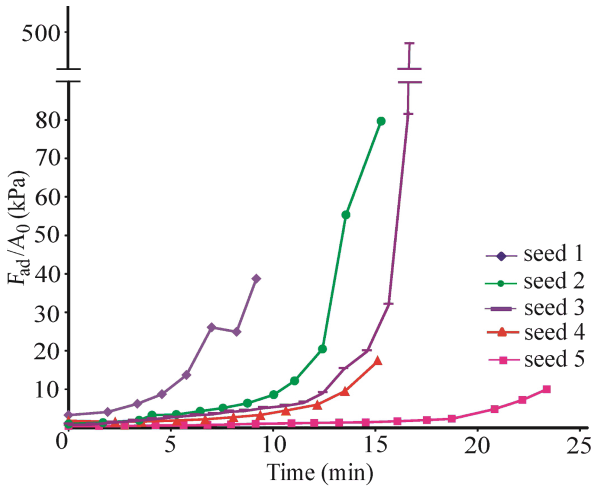

Figure 4: The ratio of pull-off force (F_{ad}) to contact area (A_0) (adhesion stress) for five individual seeds as a function of time. The smallest adhesion stress was observed for the seed demonstrated the highest contact area and pull-off force.

Subsequently, it rapidly increased during desiccation and, after 30 min of desiccation time, reached values of around 0.5–0.8 (mean value 0.74 ± 0.06) (Figure 5). At the same time, the mucilage envelope lost almost the entire amount of absorbed water. The highest measured value of the friction coefficient was 0.8. Because of the strong adhesion this friction coefficient was observed at a platform declination of 73°. After the maximum was reached, the friction coefficient slowly decreased (Figure 5). When the seeds had completely dried out (after about one hour after the hydration procedure), the values of the friction coefficient were comparable to those of the dry seeds. Interestingly, the maximal adhesion was reached earlier (at average desiccation times of about 16 min, see above).

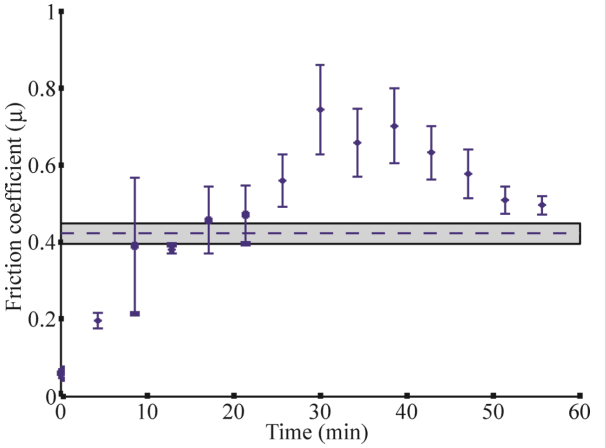

Figure 5: Dynamics of the friction coefficient, μ. The friction coefficient was calculated according to Equation 2 with λ = 7.75 and c = 0.012. The mean value of the friction coefficient for dry seeds is shown by the dotted line inside the gray box (standard deviation). Mean values of the friction coefficient for hydrated seeds are shown by stars, and error bars indicate standard deviation.

Discussion

We demonstrated that the seed mucilage of *Plantago lanceolata* represents a type of cellulose mucilage, which differs clearly in the physical properties from the pectic mucilage of previously studied *Linum usitatissimum* [32]. Because of the presence of cellulose, the mucilage of *P. lanceolata* represents a more ordered and stable system in comparison to the pectic type. This correlates with a weaker adhesion of this type of mucilage.

Cellulose fibrils are important for the distribution and retaining of the mucilage on the seed surface

The *P. lanceolata* mucilage was classified as “true slime”, consisting of pectins as the main component [12]. However, our study revealed, for the first time for this taxon, the presence of an additional, important component of the mucilaginous envelope, namely the cellulose fibrils. Specific staining reactions visualized delicate cellulose fibrils stretching out from the seed surface into the pectin mass and forming a regular, radially arranged skeleton. This kind of mucilage with cellulose fibrils is characteristic of many taxa from such families, as Asteraceae, Brassicaceae, Lamiaceae [1,13,15,16,34]. Also, in other *Plantago* species (*P. media, P. ovata*), we detected the presence of cellulose fibrils [14,37].

Water loss from the mucilage envelope

The maximum mass gain of *Plantago lanceolata* mucilaginous seeds after hydration was fourfold (4 mg) (Table 1) whereas in *Linum usitatissimum,* having a pectic envelope and lacking a cellulose "skeleton", it was a maximum of threefold (15 mg) [32], (t-test, $p = 0.04$). However, the water loss in the mucilage of *P. lanceolata* was much more rapid. After about 35 min., *P. lanceolata* mucilage lost, on average, 92% of absorbed water (Table 2), whereas flax seed mucilage at the same time lost, on average, only about 56% of absorbed water (t-test, $p = 0.003$).

The explanation of the differences in water absorption and desiccation between pectic and cellulose mucilage can be the chemical factors that influence the pectins structure and properties. For example a higher degree of methylation increases the capacity to form gels, whereas gelling is inhibited by increasing acetylation [38,39]. The presence of calcium ions slows down water transfer to cellulose and pectins and thus increases the cell-wall stiffness [19,40,41]. Also the presence of boron in the pectic network causes the reduction of the amount of water and contributes the cell-wall strength [19,40]. We can surmise that the existence of such interactions within the pectin–cellulose network can cause changes in the spatial structure of the mucilage and affects the hydration and dehydration processes.

The cellulose mucilage composition and structure can be also a reason for observed two main evaporation phases. The mucilaginous envelope shows two regions, an outer region composed mostly of unbranched pectins without cellulose and an inner region with cellulose fibrils and branched pectins [42,43]. The presence of branches is responsible for the formation of bonds with other molecules [19]. The components could form a mesh-filled network entrapping water for longer time [44]. This could be the reason of faster water evaporation from the outer layer (first phase) and slower (second phase) from the inner part of the envelope.

Mucilage adhesive properties

The mucilage adhesion increases with increasing water loss from the mucilage envelope [32]. In case of cellulose mucilage of *P. lanceolata,* the maximum adhesion was reached earlier in comparison to the pectic mucilage of *L. usitatissimum*. The possible reason for this behavior can be a higher desiccation rate of *P. lanceolata* mucilage and a special mucilage structure (mentioned above). This can also cause a faster fixation of *P. lanceolata* seed to the surface of, e.g., the body of an animal.

The *P. lanceolata* mucilage had a statistically significant smaller maximum pull-off force than the pectic mucilage of flax [32] (Figure 6a, t-test, $p = 0.002$). Our measurements of maximum adhesive forces demonstrated 2.5 times lower values for *P. lanceolata* cellulose mucilage in comparison to the pectic type [32] (t-test, $p = 0.008$). The maximal value for plantain seeds was just 33 mN whereas for flax it was 91 mN (Figure 6a, Table 3). The time for reaching maximum adhesion was half as long as for plantain (16 min) than for flax (30 min) (Table 3). Furthermore, the adhesion stress values at pull-off (F_{ad}/A_0) were 4.5 times smaller for plantain in comparison to flax (Figure 6b) (t-test, $p = 0.04$).

Adhesive properties of the cellulose mucilage

We infer that both chemical composition and structure of the mucilage plays an important role in adhesion. In the cell wall of MSCs, cellulose, hemicelluloses and pectins can be linked covalently in a form of network structure. Such an association

Table 2: Comparison of desiccation data for *Plantago lanceolata* (cellulose mucilage) and *Linum usitatissimum* (pectic mucilage).

measured feature	*Plantago lanceolata* mean ± SD (min–max)	*Linum usitatissimum* mean ± SD (min–max) [32]
mean water loss after 35 min, %	92 ± 0.8 (90–94)	57 ± 8 (37–78)
mass of absorbed water, mg	3 ± 0.3 (3–4)	10 ± 2 (6–15)
desiccation time, min	128 ± 15 (99–182)	229 ± 9 (206–252)

Table 3: Comparison of adhesion force data for *Plantago lanceolata* (cellulose mucilage) and *Linum usitatissimum* (pectic mucilage).

measured feature	*Plantago lanceolata* mean ± SD (min–max)	*Linum usitatissimum* mean ± SE (min–max) [32]
maximum adhesion force F_a, mN	24 ± 3 (14–33)	60 ± 8 (45–92)
contact area at F_a (A_0), mm^2	0.6 ± 0.1 (0.3–1)	1.2 ± 0.6 (0.2–3.5)
mean time for reaching F_a, min	16 ± 3 (7–27)	29 ± 5 (15–45)

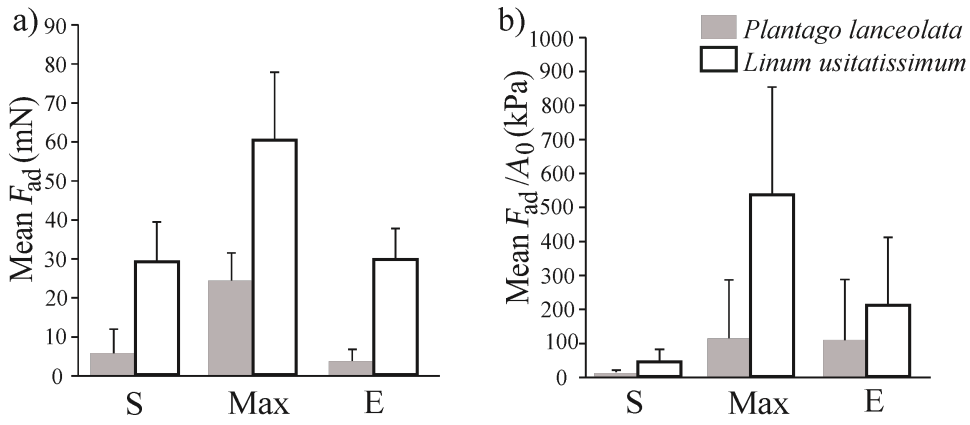

Figure 6: The comparison of the mean values of F_{ad} (adhesion force) and F_{ad}/A_0 (adhesion stress) at different desiccation conditions for *Plantago lanceolata* and *Linum usitatissimum*. S – at the beginning of the experiment, when the mucilage envelope contains water, Max – maximal value (when the mucilage envelope probably lost the most amount of water), E – at the end of the measurements (when the mucilage almost dried out).

between these polysaccharides has been described for typical cell wall, as well as for the wall of MSCs [17,41]. In *P. lanceolata,* pectins could be attached to the cellulose fibrils leading to a decrease in adhesive force as, most likely, not all pectin side chains can be involved in the adhesion processes on the surface. The cellulose microfibrils also provide mechanical stability for the cell wall [45]. This fact can explain the regular and comparable shapes of the adhesion–time curves obtained for individual *P. lanceolata* seeds. They looked very similar in their character. In the case of *L. usitatissimum*, mucilage viscosity strongly depends on the mixture of RG I (rhamnogalacturonan I) and arabinoxylan [42]. In *L. usitatissimum,* the adhesion–time curves of individual seeds differed strongly [32]. It can confirm that the presence of the cellulose in the mucilage of *P. lanceolata* acts as a stabilizing factor.

Mucilage adhesive properties in epizoochoric seed dispersal

Adhesion, by the mucilage, to feet, feathers or fur of animals, is a very effective dispersal method. Many different seeds are transported in this way between remote islands, including seeds of some *Plantago* species [8,46]. The ability of the seeds to adhere appeared shortly after hydration and became stronger with desiccation resulting in a strong sticking to an animal as dispersal agent. At this stage, the seeds can strongly adhere to, e.g., the plumage of birds. After drying, they can be actively or passively removed again.

In the case of flax mucilage, the adhesion ability intensified and degraded gradually whereas in plantain the adhesion ability, after reaching a maximum, degraded rapidly. The enhanced adhesion stress and quicker development of the maximal adhesion should allow the seed with cellulose mucilage (*P. lanceolata*) to attach more quickly to the surface. Also, the dynamics of water evaporation can be important for mucilaginous seed fixation to the ground or to the bodies of animals. The adhesion to bird plumage of diverse *Plantago* taxa mucilaginous seeds was also observed, providing an example of epizoochory for this species [8]. *P. lanceolata* counts to the wide spread species over the whole North America and to one of the world's 12 successful, non-cultivated colonizing species occurring almost throughout the whole world, what demonstrates a great potential of mucilaginous diaspores as dispersal units [5,7].

Frictional properties of mucilage and their role in endozoochoric seed dispersal

For freshly-hydrated plantain seeds, we observed low values of friction coefficient (0.06 ± 0.007; 0.05–0.08). It was slightly higher than those previously observed for hydrated flax seeds (0.05 ± 0.01; 0.04–0.05) [25] (Table 4, t-test, $p < 0.001$). The mucilage of plantain represents a heterogenous system composed of pectins and cellulose fibrils. Therefore, the mucilage of *P. lanceolata* exhibited a higher friction than the pectic mucilage of *L. usitatissimum*. However, the friction of *P. lanceolata* mucilaginous seeds should be sufficient for endozoochoric dispersal. *P. lanceolata* seeds can be eaten by birds, and because of the mucilage, which provides lubrication, the seeds can pass easier through the digestive system of the birds to be spread via this means. Viable seeds of plantain were found in pigeons, sparrows, bullfinch, greenfinch and cattle droppings [5,8]. It was also observed that seeds of plantain, which usually have 56% germination, yielded 100% germination after passing through a bird's digestive system [5]. Such examples of dispersal of mucilaginous seeds were observed in nature, e.g., for *Cecropia* [3].

Table 4: Comparison of friction data for *Plantago lanceolata* (cellulose mucilage) and *Linum usitatissimum* (pectic mucilage).

measured features	*Plantago lanceolata* mean ± SD (min–max)	*Linum usitatissimum* mean ± SD (min–max) [32]
friction coefficient, μ, of dry seeds	0.4 ± 0.01 (0.4–0.4)	0.2–0.3
friction coefficient, μ, of freshly hydrated seeds	0.06 ± 0.007 (0.05–0.08)	0.045 ± 0.01 (0.04–0.05)
Max sliding angle	73°	180°

Conclusion

In this study, we demonstrated structural and physical properties of mucilaginous seeds of *Plantago lanceolata*. The seed mucilage of *P. lanceolata* is characterized by the presence of cellulose fibrils. The loss of water from the mucilage envelope is a very dynamic process, affecting both the adhesive and frictional properties of the mucilage. Maximal adhesion was measured for mucilage after some degree of water loss. The lowest friction was measured in fully hydrated seeds. The presence of cellulose fibrils in the mucilage envelope can be responsible for the faster desiccation and weaker adhesion of plantain seed mucilage compared to flax. Since the cellulose mucilage *P. lanceolata* represents a more regularly ordered system than the pectic mucilage of *L. usitatissimum*, the course of adhesion force over desiccation time was more regular in plantain seeds when compared to flax. The presence of cellulose also results in the decrease of seed friction in its fully hydrated condition. Cellulose mucilage demonstrated weaker adhesive and frictional properties than the pectic type but it still indicates an effective system promoting zoochoric dispersal and/or attachment to the substratum (soil). As the *P. lanceolata* seed mucilage represents a special type of the cell wall rich in pectins, which is loosely organized and easy accessible, this type of mucilage could also be considered as a model for further mechanical studies of such modified type of the cell wall.

Acknowledgements

Many thanks to Joachim Oesert for his technical help during the experiments. The study was supported by the German Academic Exchange Office (DAAD - Deutscher Akademischer Austauschdienst) to A. Kreitschitz [grant No. 323/A/10/02617]. Victoria Kastner kindly provided linguistic corrections of the article.

References

1. Grubert, M. *Acta Biol. Venez.* **1974,** *8,* 315–551.
2. Ryding, O. *Syst. Geogr. Plants* **2001,** *71,* 503–514. doi:10.2307/3668696
3. Yang, X.; Baskin, J. M.; Baskin, C. C.; Huang, Z. *Perspect. Plant Ecol. Evol. Syst.* **2012,** *14,* 434–442. doi:10.1016/j.ppees.2012.09.002
4. Sagar, G. R.; Harper, J. L. *J. Ecol.* **1964,** *52,* 189–221. doi:10.2307/2257792
5. Cavers, P. B.; Bassett, I. J.; Crompton, C. W. *Can. J. Plant Sci.* **1980,** *60,* 1269–1282. doi:10.4141/cjps80-180
6. Stewart, A. V. *Proc. N. Z. Grassl. Assoc.* **1996,** *58,* 77–86.
7. Hegi, G. In *Illustrierte Flora von Mitteleuropa;* Hegi, G., Ed., Carl Hanser Verlag: München, Germany, 1965; Band VI, Teil 1, pp 559–604.
8. Ridley, H. N. *The dispersal of plants throughout the world;* 1930. Reprint Bishen Singh Mahendra Pal Singh, Dehra Dun: India, 1990.
9. Bruun, H. H.; Poschold, P. *Oikos* **2006,** *113,* 402–411. doi:10.1111/j.2006.0030-1299.14114.x
10. Mullan, J.; Percival, E. G. V. *J. Chem. Soc.* **1940,** 1501–1506. doi:10.1039/jr9400001501
11. Percival, E. G. V.; Willox, I. C. *J. Chem. Soc.* **1949,** 1608–1612. doi:10.1039/jr9490001608
12. Mühlethaler, K. *Exp. Cell Res.* **1950,** *1,* 341–350. doi:10.1016/0014-4827(50)90043-7
13. Wojciechowska, B. *Monogr. Bot.* **1966,** *21,* 3–243.
14. Kreitschitz, A. Biological Properties of Fruit and Seed Slime Envelope: How to Live, Fly, and Not Die. In *Functional surfaces in biology;* Gorb, S. N., Ed.; Springer: Berlin, Germany, 2009; Vol. 1, pp 11–30. doi:10.1007/978-1-4020-6697-9_2
15. Kreitschitz, A. *Seed Sci. Res.* **2012,** *22,* 177–189. doi:10.1017/S0960258512000098
16. Western, T. L. *Seed Sci. Res.* **2012,** *22,* 1–25. doi:10.1017/S0960258511000249
17. Haughn, G. W.; Western, T. L. *Front. Plant Sci.* **2012,** *3,* 64. doi:10.3389/fpls.2012.00064
18. Zykwinska, A.; Thibault, J.-F.; Ralet, M.-C. *J. Exp. Bot.* **2007,** *58,* 1795–1802. doi:10.1093/jxb/erm037
19. Caffal, K. H.; Mohnen, D. *Carbohydr. Res.* **2009,** *344,* 1879–1900. doi:10.1016/j.carres.2009.05.021
20. Scheller, H. V.; Ulskov, P. *Annu. Rev. Plant Biol.* **2010,** *61,* 263–289. doi:10.1146/annurev-arplant-042809-112315
21. Carpita, N. C.; Gibeaut, D. M. *Plant J.* **1993,** *3,* 1–30. doi:10.1111/j.1365-313X.1993.tb00007.x
22. Jarvis, M. C. *Plant, Cell Environ.* **1984,** *7,* 153–164. doi:10.1111/1365-3040.ep11614586
23. Burgert, I. *Am. J. Bot.* **2006,** *93,* 1391–1401. doi:10.3732/ajb.93.10.1391
24. Köhler, L.; Spatz, H.-C. *Planta* **2002,** *215,* 33–40. doi:10.1007/s00425-001-0718-9
25. Donaldson, L. *Wood Sci. Technol.* **2007,** *41,* 443–460. doi:10.1007/s00226-006-0121-6
26. McCann, M. C.; Wells, B.; Roberts, K. *J. Cell Sci.* **1990,** *96,* 323–334.
27. Fujino, T.; Sone, Y.; Mitsuishi, Y.; Itoh, T. *Plant Cell Physiol.* **2000,** *41,* 486–492. doi:10.1093/pcp/41.4.486
28. Ha, M.-A.; Apperley, D. C.; Evans, B. W.; Huxham, I. M.; Jardine, W. G.; Viëtor, R. J.; Reis, D.; Vian, B.; Jarvis, M. C. *Plant J.* **1998,** *16,* 183–190. doi:10.1046/j.1365-313x.1998.00291.x

29. de la Paz Saldago-Cruz, M.; Calderón-Domíniguez, G.; Chanona-Pérez, J.; Farrera-Rebollo, R. R.; Méndez-Méndez, J. V.; Díaz-Ramírez, M. *Ind. Crops Prod.* **2013,** *51,* 453–462. doi:10.1016/j.indcrop.2013.09.036
30. Joelovich, M. *BioResources* **2008,** *3,* 1403–1418.
31. Prajapati, D. V.; Jani, G. K.; Moradiya, N. G.; Randeria, N. P. *Carbohydr. Polym.* **2013,** *92,* 1685–1699. doi:10.1016/j.carbpol.2012.11.021
32. Kreitschitz, A.; Kovalev, A.; Gorb, S. N. *Acta Biomater.* **2015,** *17,* 152–159. doi:10.1016/j.actbio.2015.01.042
33. Braune, W.; Leman, A.; Taubert, H. *Praktikum z anatomii roślin;* PWN: Warszawa, Poland, 1975.
34. Kreitschitz, A.; Vallès, J. *Flora (Jena)* **2007,** *202,* 570–580. doi:10.1016/j.flora.2006.12.003
35. Liesche, J.; Ziomkiewicz, I.; Schulz, A. *BMC Plant Biol.* **2013,** *13,* 226. doi:10.1186/1471-2229-13-226
36. Monohan, J. F. *Numerical methods of statistics;* Cambridge University Press, 2001. doi:10.1017/CBO9780511812231
37. Kreitschitz, A. unpublished data.
38. Voragen, A. G. J.; Coenen, G.-J.; Verhoef, R. P.; Schols, H. A. *Struct. Chem.* **2009,** *20,* 263–275. doi:10.1007/s11224-009-9442-z
39. Melton, L. D.; Smith, B. G. Determining the Degree of Methylation and Acetylation of Pectin. In *Current Protocols in Food Analytical Chemistry;* Wrolstad, R. E., Ed.; John Wiley & Sons, 2001; E:E3:E3.4. doi:10.1002/0471142913.fae0304s00
40. Wang, T.; Tohge, T.; Ivakov, A.; Mueller-Roeber, B.; Fernie, A. R.; Mutwil, M.; Schippers, J. H. M.; Persson, S. *Plant Physiol.* **2015,** *169,* 1027–1041. doi:10.1104/pp.15.00962
41. Cosgrove, D. J. *J. Exp. Bot.* **2016,** *67,* 463–476. doi:10.1093/jxb/erv511
42. Naran, R.; Chen, G.; Carpita, N. C. *Plant Physiol.* **2008,** *148,* 132–141. doi:10.1104/pp.108.123513
43. Macquet, A.; Ralet, M.-C.; Kronenberger, J.; Marion-Poll, A.; North, H. M. *Plant Cell Physiol.* **2007,** *48,* 984–999. doi:10.1093/pcp/pcm068
44. Belton, P. S. *Int. J. Biol. Macromol.* **1997,** *21,* 81–88. doi:10.1016/S0141-8130(97)00045-7
45. Burgert, I.; Keplinger, T. *J. Exp. Bot.* **2013,** *64,* 4635–4649. doi:10.1093/jxb/ert255
46. De Lange, P. J.; Heenan, P. B.; Townsend, A. J. *N. Z. J. Bot.* **2009,** *47,* 133–137. doi:10.1080/00288250909509800

License and Terms

BEILSTEIN JOURNAL OF NANOTECHNOLOGY

The cleaner, the greener? Product sustainability assessment of the biomimetic façade paint Lotusan® in comparison to the conventional façade paint Jumbosil®

Florian Antony[1,2,3], Rainer Grießhammer[2], Thomas Speck[1,3,4] and Olga Speck[*1,3,5]

Full Research Paper

Open Access

Address:
[1]Plant Biomechanics Group, Botanic Garden, Faculty of Biology, University of Freiburg, 79104 Freiburg, Germany, [2]Öko-Institut e.V., Institute for Applied Ecology, 79017 Freiburg, Germany, [3]Competence Network Biomimetics, Germany, [4]Freiburg Materials Research Center (FMF), 79104 Freiburg, Germany and [5]Freiburg Centre for Interactive Materials and Bioinspired Technologies (FIT), 79110 Freiburg, Germany

Email:
Olga Speck* - olga.speck@biologie.uni-freiburg.de

* Corresponding author

Keywords:
biomimetic promise; life-cycle assessment (LCA); Lotus-Effect® technology; Lotusan®; product sustainability assessment (PROSA)

Beilstein J. Nanotechnol. **2016,** *7,* 2100–2115.
doi:10.3762/bjnano.7.200

Received: 29 July 2016
Accepted: 04 December 2016
Published: 29 December 2016

This article is part of the Thematic Series "Biological and biomimetic materials and surfaces".

Guest Editor: S. N. Gorb

Abstract

Background: The debate on the question whether biomimetics has a specific potential to contribute to sustainability is discussed among scientists, business leaders, politicians and those responsible for project funding. The objective of this paper is to contribute to this controversial debate by presenting the sustainability assessment of one of the most well-known and most successful biomimetic products: the façade paint Lotusan®.

Results: As a first step it has been examined and verified that the façade paint Lotusan® is correctly defined as a biomimetic product. Secondly, Lotusan® has been assessed and compared to a conventional façade paint within the course of a detailed product sustainability assessment (PROSA). For purposes of comparison, the façade paint Jumbosil® was chosen as reference for a conventional paint available on the market. The benefit analysis showed that both paints fulfil equally well the requirements of functional utility. With respect to the symbolic utility, Lotusan® has a particular added aesthetic value by the preservation of the optical quality over the life cycle. Within the social analysis no substantial differences between the two paints could be found regarding the handling and disposal of the final products. Regarding the life-cycle cost, Lotusan® is the more expensive product. However, the higher investment cost for a Lotusan®-based façade painting are more than compensated by the longer life time, resulting in both reduced overall material demand and lower labour cost. In terms of the life-cycle impact assessment, it can be ascertained that substantial differences between the paints arise from the respective service life, which are presented in terms of four scenario analyses.

Conclusion: In summary, the biomimetic façade paint Lotusan® has been identified as a cost-effective and at the same time resource-saving product. Based on the underlying data and assumptions it could be demonstrated that Lotusan®-based façade paintings have a comparatively low overall impact on the environment. Summarizing our results, it can be emphasized that Lotusan® is the more favourable product compared to Jumbosil® according to sustainability aspects.

Introduction

In-depth analyses of functions found in biology and the systematic transfer of the respective operating principles into technical applications is the essential aim of biomimetics [1,2]. Bringing together the competencies of experts from different scientific disciplines, biomimetics has been successfully established as an independent scientific discipline of continuously increasing visibility [3,4]. Especially in the context of architecture and building technologies a lot of innovative developments were derived from biological examples over the last years [5-7]. The analysis of plant surfaces as contribution to the systematics of plants lead to the discovery of the operating principle of the self-cleaning effect of plant surfaces. This was brought into the construction market as biomimetic self-cleaning façade paint [8]. The study of morphology and anatomy, mechanics and functional principles in biology has the potential to stimulate architects and engineers to new building solutions in architectural design and technical implementation such as the adaptive façade shading system flectofin® [6,9] or the bone-like ceiling of a lecture hall at the University of Freiburg [10,11].

The increasingly systematic research approach of biomimetics, aiming to find the most promising examples from biology for the development of technical innovations, has been accompanied by a debate about the specific potential of biomimetic solutions to contribute to sustainability [12-18]. Gebeshuber et al. also argue in this direction by envisaging possible scenarios of future development by mimicking biology and by promising to overcome some of the major global challenges as indicated by the so-called Millennium Project [19]. More recently and from the perspective of a higher abstraction level of learning from nature, the opportunities of mimicking ecosystem services for regenerative urban design have been analysed [20].

In principle, there are different interpretations of sustainability, but none of those is based on an absolute concept, but on comparisons and process orientation. From the point of view of the authors, sustainability has to be understood as a normative term and refers to a form of economic activity and lifestyle that is based on moral commitments to future generations.

Biomimetic products are often attributed to have an intrinsic potential to contribute to a more sustainable technology, with reference made to the inspiratory flow from living nature [16]. By introducing the term of the so-called “biomimetic promise” Arnim von Gleich characterised the discussion on sustainability in biomimetics. In addition, von Gleich also referred to requirements on the validity and limitations of the biomimetic promise [12]. Also J.F. Vincent expressed his conviction that biomimetics has the potential to contribute to a more sustainable future, while at the same time he warned that it is not sufficient to translate the lessons of nature into the present technology in any event [21]. As von Gleich stated before, the implementation of the biomimetic promise can only be regarded on a case-by-case basis [12,22,23].

From the perspective of scientific theory it might be a normative claim rather than a descriptive one that biomimetic innovations ought to deliver sustainable solutions [16-18]. This leads to the question as to whether bio-inspired innovations also have a specific quality in terms of sustainability [18]. Figuratively speaking, this means that sustainability may be a by-product of knowledge transfer from biology to technology. A much safer approach is the definition of sustainability as an initial objective and its explicit knowledge transfer in the course of the development of bio-inspired and biomimetic innovations [17,18].

However, Raibeck et al. point out that statements touting the benefits of biologically inspired sustainable engineering appear in the literature but also that limited scientific data exist in order to substantiate such statements [24]. Within their article they present a life-cycle inventory case study that quantifies the potential environmental benefits and burdens associated with “self-cleaning” surfaces, finally concluding that conventional approaches can be superior with respect to environmental impacts, when compared to self-cleaning surfaces [24]. However, it must be considered, that they compare the life-cycle of a self-cleaning surface based on a chemical coating cleaned only once to conventionally cleaned surfaces. Even though, this might be a realistic assumption for the assessed case study, it has to be noted, that a surface with a one-time “self-cleaning” functionality has to be seen as a rather poor example. This underpins the importance of a clear documentation of the basis of comparisons using life-cycle thinking tools. Therefore, great attention has been put on the documentation of the basis for the comparison in the study at hand.

A possible approach to assess the implementation of the biomimetic promise has been suggested by Antony et al., based on a

case study comparing a lightweight biomimetic ceiling structure from the late 1960s with two conventional up-to-date alternatives [16]. In a three-step process it is necessary to check first whether the product concerned is in fact a biomimetic innovation, and afterwards to analyse the sustainability of the product in terms of social, economic and environmental performance. Finally, it has to be decided whether the biomimetic promise is kept or not (Figure 1) [16].

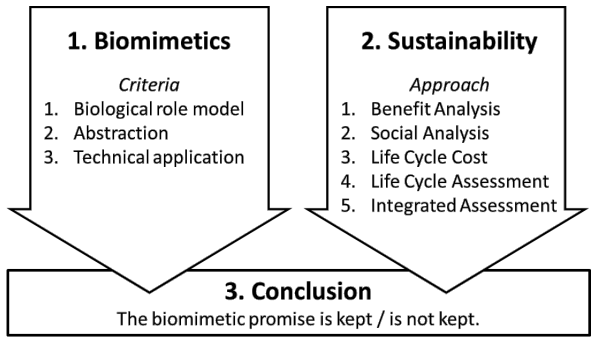

Figure 1: Three-stage validation procedure as to whether the biomimetic promise of an innovative biomimetic product is kept or not.

Regarding the check whether the product is biomimetic, the approach refers to the criteria defined in the VDI Guideline 6220 Biomimetics – Conception and Strategy [13]. Regarding the assessment process as to whether a product contributes to sustainability or not, the product sustainability assessment (PROSA) approach, proposed by Grießhammer et al., has been applied [25] (see also http://www.prosa.org).

In this context, it is important to note, that sustainability can be measured in various ways according to the underlying concept of sustainability. However, some international standards are provided by ISO also being part of the PROSA. To guarantee comparability of the analyses and the results generated it is essential to use the same methodology.

In recent years, a number of research programs, starting with BIONA by the German Federal Ministry of Education and Research (BMBF) and the scholarship program "Bionics" by the German Federal Environmental Foundation (DBU) have been set up to promote further projects eventually resulting in biomimetic, more sustainable and innovative improved products.

Especially in the field of biomimetics in architecture sustainability aspects have been discussed [26]. The currently running Collaborative Research Center TRR 141 "Biological Design and Integrative Structures – Analysis, Simulation and Implementation in Architecture", funded by the German Research Foundation (DFG), focuses on design and construction principles in biology and on their transfer to architecture and building construction. One of the topics addresses the investigation and validation of "the biomimetic promise: natural solutions as concept generators for sustainable technology development in the construction sector" (see http://www.trr141.de/).

Besides the expected results from the above Collaborative Research Center, and in order to reach defensible and sensible conclusions on the potential of biomimetic products to contribute to a more sustainable future, there is a need for further specific case studies based on sustainability assessments. A first approach to compare a biomimetic product with conventional alternatives using the PROSA approach has been performed by Antony et al. [16].

As a contribution to the discussion on sustainability in biomimetics, the present paper contains the second systematic product sustainability assessment of a biomimetic product. The product under investigation is one of the most widely known biomimetic products already available on the market, Lotusan®, a façade paint with self-cleaning properties.

Results and Discussion

Test of the criterion: Biomimetic product yes or no

As suggested by Antony et al. [16], clarifying whether the superhydrophobic properties of double-structured rough plant surfaces like the one of the sacred lotus (*Nelumbo nucifera*) have been abstracted from the biological model, and successfully applied to the façade paint Lotusan® is the first step. This clarification serves as basis for deciding whether Lotusan® has been defined correctly as biomimetic exterior paint. In the VDI guideline, the façade paint Lotusan® has been explicitly examined by an interdisciplinary expert team and has been evaluated as fulfilling the preconditions in order to be called biomimetic [27].

Existence of a biological example

The first criterion requires that a biological model or precedent was found and studied by researchers and developers [13]. Based on results in basic biological research, the initial description of self-cleaning properties was done by the German biologist Wilhelm Barthlott in the late 1970s. This became the starting point for the development of Lotusan® [28,29], a perfect example of a bottom-up process in biomimetics [1].

Understanding of the functional principle and abstraction

Within an abstraction phase the underlying functional principles of the biological model have to be translated into technolo-

gy-compatible language [13,27]. In the present case the functional principle of the self-cleaning property of the lotus leaf can be considered as a precisely matched combination of a micro-rough plant surface, including hydrophobic waxes as part of the structuring and therefore is particularly suited to interact with water and causing the water to repel.

Existence of a technical realization

The existence of a technical realization, at least as a prototype, is the third and final criterion [13]. The result, the technical application of self-cleaning properties is what became well known as the lotus effect. The patent application was submitted on 25th July 1995 and granted by the German Patent and Trademark Office on February 4th in 1999 [8]. Sto SE & Co. KGaA (79780 Stühlingen, Germany) acquired the patent rights in 2009 and holds the trademark „Lotus-Effect®“. The fact that the façade paint Lotusan® is available on the market since the late 1990s might be seen as a sufficient argument for the existence of a technical realization. The production of Lotusan® is realized in a large-scale industrial process not significantly different from other paint production processes. This offers the desirable and at the same time rare opportunity to compare a biomimetic product with a conventional product on the same level of technology.

In summary, Lotusan® fulfils all three criteria of a biomimetic product. However, the qualification by von Gleich with respect to the biomimetic promise needs a thorough case study. Therefore, we compared Lotusan® with a conventional façade paint. Since self-cleaning properties can be realized in quite different ways, for a variety of applications and by using different materials, evaluations regarding sustainability have to be repeated for each individual case.

Product sustainability assessment (PROSA)

PROSA is an extensive sustainability assessment tool, which spans complete product life cycles and value chains. It assesses and evaluates the environmental, economic and social opportunities and risks of future development trajectories [25]. In the course of the present study, a comprehensive set of analysing techniques has been applied by using benefit analysis, social analysis, life-cycle cost assessment, life-cycle assessment, and life-cycle scenario analysis. According to the PROSA methodology, the results of the individual analyses are finally brought together within the framework of an integrated sustainability assessment [25].

With regard to the basic meaning of assessing the ecological performance as part of a product sustainability assessment, within the present study special emphasis has been put on assessing the ecological performance of the biomimetic façade paint Lotusan® within the course of a life-cycle assessment (LCA). But also economic effects regarding the life-cycle cost were considered to be of importance, and therefore have been analysed in depth. For PROSA, the consideration of possible social effects associated with the assessed products throughout the product life cycle is of great importance. Accordingly, the social effects regarding raw material provision have also been assessed within the framework of an orientative analysis, which is in line with the PROSA methodology.

The assessment of the sustainability of products or processes in absolute terms is not possible and not desirable either. Therefore, the sustainability of Lotusan® has been assessed in comparison with the conventional façade paint Jumbosil®.

Basis for the comparison

In order to carry out the sustainability assessment of the façade paint Lotusan® as part of a comparison, it is of great importance to accurately determine with reliable quality, which other façade paints might be considered as potential alternatives. In a first step, this means to identify the essential functions of façade paints. These are mainly to cover the building as an exterior layer, including all the various functions such as, for example, protection of underlying building layers against environmental effects like weather or radiation. In this connection, the water vapour permeability of the paint is a very important physical property.

The façade paints available on the market can essentially be divided into two main categories: First, those that focus on maximum gas exchange, which might positively influence the climatization of the building. However, in this case moisture may penetrate quicker and deeper into the construction, eventually resulting in serious damage to the building structure, especially in regions with higher amounts of precipitation. Secondly, those paints focusing on hydrophobicity or water-repellency to build up a secure barrier against the penetration of moisture into deeper layers of the building. In this case sufficient gas permeability needs to be secured. Lotusan® was compared to a paint showing the same functional principle, providing a solid basis for the comparison of products.

Because a large number of façade paints is available on the market, Kougoulis et al. refer to about 20,000 products [30], the decision whether Lotusan® should be compared to a generic paint formulation, typical for a hydrophobic façade paint available on the market, or to a real product, as a reference for typical façade paints available on the market had to be made. Suggestions made by Kougoulis et al. [30], may serve as a basis for a generic formulation, but the scoping phase revealed that considerations on an unknown formulation allow only rough

approximations resulting in a serious increase of uncertainties having a negative influence on the informative validity of the study. Therefore, Lotusan® was compared to Jumbosil®, a conventional paint from the same manufacturer. This turned out to be advantageous in many respects. Both paints are produced in the same production plant by the same staff using the same auxiliary and operating materials and the same production facilities. Furthermore, a good and consistent data basis was available for both paints, meeting the requirement of symmetry for comparison. Lotusan® is available on the market for more than 10 years, facilitating the sustainability assessment of biomimetic products, which is challenged, for example, by the problem of defining a suitable reference product for comparison. Regarding the foresaid, a comparison between Lotusan® and Jumbosil® is largely unaffected by adverse effects. In addition, Jumbosil® most probably is a suitable proxy for typical paints on the market.

A typical detached single-family house with a ceiling height of 2.4 m, has a façade surface of 250 m^2 from which areas for windows and doors have to be deducted. Finally, for both options compared, a surface of 200 m^2 requiring painting, were set as reference.

With regard to the use phase, the material safety data sheets for both paints were checked for differences during application of the paints and the utilization phase, for example, regarding special precautions because of toxicological reasons as well as information concerning the end-of-life treatment. In both cases no special precautions are required as both colours do not contain any hazardous or other substances to concern about with respect to use or exposition.

Based on information contained in the technical data sheets, and verified by the manufacturers both paints can simply be painted over. In both scenarios of our approach no damaged areas emerge throughout the façade paintings service life time, which would require further actions of conservation.

Since empty buckets and lids result from each painting, waste treatment of packaging materials had been taken into account. They have been recorded together with the efforts of the end-of-life treatment of the paint on the building at the end of the life cycle of the building. The end-of-life treatment has been assumed as a treatment with currently conventional disposal techniques, including the demolition of the building, the sorting of different material fractions, transport and final disposal in an inert landfill.

Lotusan® (option 1): Lotusan® is a water-based silicone resin façade paint. In accordance with the reporting guideline on the ingredients of decorative paints published by the association of the German paint and printing ink manufacturers (VdL), Lotusan® consists of an emulsion of polyoxysiloxane, polymer dispersion, titanium dioxide, silicon dioxide, water and additives [31]. According to the technical bulletin [32], Lotusan® is characterized by a density of 1.4–1.6 g/mL, and is highly permeable to carbon dioxide and water vapour. Furthermore, it also provides a high degree of natural protection against algae and fungal attack. Lotusan® is extremely hydrophobic and shows no swelling. Contaminations like airborne dirt particles are washed away with the next rainfall.

Jumbosil® (option 2): Jumbosil® is a filled, silicone-annealed, dispersion-based façade paint. In accordance with the reporting guideline [31], Jumbosil® consists of polymer dispersion, titanium dioxide, calcium carbonate, silicate fillers, talcum, water, glycol ether, aliphatic compounds, additives and preserving agents [33]. Jumbosil® is characterized by a density of 1.5–1.6 g/mL and is, according to the technical data sheet, suitable for slightly filling, opaque exterior paintings on organic and mineral substrates. Jumbosil® is water-repellent and permeable to carbon dioxide and water vapour.

Comparing the material input for the formulation of Lotusan® and Jumbosil®: Primary data on the formulation of Lotusan® and Jumbosil® have been provided by the R&D-Section of Sto SE & Co. KGaA. A comparison of the formulation components is given in Table S1 (Supporting Information File 1).

Information on the physical composition of both façade paints, given as mass fractions, has been used for the modelling of the façade paint production. Where necessary, simplifications were employed and components reassigned. A first modelling setup has been checked in cooperation with chemical experts from Sto SE & Co. KGaA. In parallel, the case study by Kougoulis et al. [30] has been analysed to provide further evidence that the assumptions on the modelling of the formulation of the two paints are justified. Related to their mass, the most relevant formulation components of both paints are water, pigment, fillers and polymer dispersion.

The mass of TiO_2 is about 2 times higher in Lotusan® than in Jumbosil®. Similarly this applies to the 1.5 times higher water content of Lotusan® compared to Jumbosil®´s water content. On the other hand, the content of polymer dispersion in Jumbosil® is twice as high as the one in Lotusan®. The mass portion of fillers is 44% for Jumbosil® and 34% for Lotusan®, while the mass portion of additives is comparable. Additionally, 4% of silicone resin and 1% of silicone-based hydrophobizing agent is part of the formulation of Lotusan®.

Benefit analysis

In the framework of benefit analysis, Lotusan® und Jumbosil® are compared to each other with regard to the benefit derived from their use as façade paintings. Façade paint has to meet a broad variety of aspects of utility. Aspects of utility can be of various kinds, such as functional, emotional or even societal in nature. A sole analysis of the functional utility would involve the danger of being blind for other aspects of utility that play a decisive role regarding the choice and use of products or product services. From the point of view of a consumer, a product always has a variety of additional, not functional-related aspects of utility, which arise from symbolic and maybe societal considerations. In this respect, the consumer choice on a the utility of a product might be seen as a multi-dimensional decision matrix, and it cannot be assumed that consumers only decide on the basis of sole considerations about the functional utility. Therefore, in the framework of a product sustainability assessment, aspects of utility are being analysed more intensively than this would be possible by carrying out an LCA study alone, where the benefit of a product is recorded slightly above the functional utility [16,25].

The functional utility of products can be usually clearly defined. Because essential elements of practical utility are measurable, these aspects can be well compared in comparative product tests [25]. The diligent determination of the functional utility as well as the thorough documentation of the determination process is applied in the course of classical LCA studies. The functional utility, in this context called functional unit, serves as a quantifiable reference quantity. With regard to the comparison of Lotusan® and Jumbosil®, the functional utility can be defined as the provision of the outer layer of the building envelope and therefore also the protection of the building envelope against environmental influences. Both paints keep the deeper layers of the building envelope free from moisture, and can therefore contribute to maintaining the structural integrity of the building envelope. At the same time, both paints also have to allow for a sufficient level of permeability to gases such as carbon dioxide and oxygen.

Against the background of the above given description of functional utility, it can be stated that both paints are highly comparable. This also applies to the overall lifetime of the paints. According to information provided by the German Federal Ministry for the Environment, Nature Conservation, Building and Nuclear Safety, the expected product service life time of a silicone-based exterior painting is 15 years [34].

Regarding the super-hydrophobic properties of Lotusan®, together with its even higher permeability to carbon dioxide and oxygen compared to Jumbosil®, it can be assumed that Lotusan® might reach a longer service life. First insights from assessments provided by the manufacturer suggest this [35-37]. According to [34], a service life of 20 years can be assumed for dispersion-silicate façade paintings. Therefore, in the study at hand, different periods of service life have been assessed: 20 years for Lotusan® and 15 years for Jumbosil®. Because this might be a starting point for critics, it has been decided, in line with common practice of comparative product sustainability assessments, to also consider a shorter service life of only 15 years for a Lotusan®-based façade painting. Overall, it can be stated that both paints fulfil the practical utility in a similar way, albeit for different periods of time.

As mentioned before, the functional utility does not cover all utility dimensions that might be taken into account when choosing between different products. This applies even more in cases where there is a large degree of congruence in the practical utility. In such cases the symbolic utility and the societal utility gain importance for the decision-making process [16]. In addition to the functional properties, a façade paint obviously contributes significantly to the outward appearance of a building. Therefore, the façade painting can be seen as a representative and fundamental characteristic of a building. The façade's purity, or even more its technical cleanliness, is of great importance for the façade's perception of high optical quality. The optical quality of the paint is best at the time of façade painting. Throughout the paintings service life, impurities, for instance through rain and wind or even fouling caused by bacteria or fungal infestation lead to a progressive loss of optical quality of conventional façade paintings. In this respect, a major difference exists between the two compared façade paints. Because of Lotusan®'s pronounced hydrophobic characteristic, impurities and contaminations are washed away with the next rainfall. While the optical quality of conventional façade paintings decreases over the service life time, Lotusan® has the potential to constantly maintain the original optical properties for a longer time-span or even over the entire product life cycle, providing an added value in terms of a constantly high level of optical quality compared to the optical quality of conventional façade paints decreasing over time.

It should be stressed in conclusion that both façade paintings satisfy the requirements of practical utility equally well, but maybe for different periods of time. With regard to the symbolic utility, an additional benefit has to be attributed to the Lotusan® paint, since the self-cleaning effect enables it to constantly maintain the original optical quality over the entire service life span. The self-cleaning effect of a façade painted with Lotusan® can therefore be seen as an added value immanent to the product and might be regarded as an added symbolic utility.

In order to be able to finally assess which product, over the entire observation period and with regard to all relevant aspects of utility, performs as the better product, a systematic and integrated evaluation is required. A robust quantification of the functional utility of the two compared products is at the same time the starting point and an indispensable basis for the implementation of both LCA and life-cycle cost assessment (LCC) as the relevant life-cycle thinking tools used throughout the study.

In addition to this and on the basis of the results of LCA and LCC, the effectiveness of possible measures likely to be able to make up the loss in optical quality of a Jumbosil®-based façade painting has been analysed. The implementation of such measures could result in a more or less functional equivalence of symbolic utility of the both compared façade paints. An in-depth analysis has been performed for two possible measures throughout this study. The potential influence of customer choices has been analysed as part of a comparative scenario analysis. On the one hand, an additional painting after 12.5 years has been considered. From a technical point of view this would be an early replacement or, in other terms, an arbitrary shortening of the service life time. On the other hand the efforts of a façade cleaning after 7.5 years have been analysed. This allows a quantification of the aspects of utility, depending on customer behaviour, even though this means quantifying "value choices".

It should be noted that the results of the benefit analysis alone are insufficient to allow an accurate prioritization in favour of one of the façade paintings, at least until an added environmental or economic value of one of the two compared façade paints has been clearly shown during the course of the scenario analysis.

Social analysis

With regard to the production phase, the use phase and the final disposal at the end of the life cycle, no significant differences between the two façade paints could be identified. Regarding the provision of raw materials required for the two paints differences cannot be ruled out a priori. As there might be differences between the two paints, the bills of materials of the diverse formulation inputs have been checked.

The paint producer communicated on request that only such raw materials were used in the formulation of the paints investigated in the scope of this study that come from Germany or Europe. Concerning the provision of raw materials from Germany or Europe, it may be assumed that the relevant requirements for safety and health of workers and staff are met in this respect. While, against this background, the possibility that there is still potential for further improvement of safety at work cannot be strictly ruled out, it may be assumed that major differences relating to social effects between the two colours can be ruled out. Furthermore, it has been decided to also evaluate the ecotoxicity potential and the human toxicity potential related to the two product systems as part of the LCA. Using the respective indicators of the USEtox impact assessment model (see also Table S2, Supporting Information File 1) results are discussed within the framework of the discussion of LCA results.

In summary, significant social or societal differences or such relating to the health of customers were identified between the two façade paints, neither for production, nor for the processing at the site of the building or the disposal phase. The paints use very similar materials in their formulation. The above mentioned insights led to the conclusion that there no detailed analysis of social effects was needed within the framework of this case study.

Life-cycle cost assessment

A key part of a systematic and comprehensive product sustainability assessment is addressing the economic dimension of sustainability, as it can be assumed that the product-related cost is of great importance when customers have to decide between different products. The comparison of product-related cost takes into account the customer-related life-cycle cost. In this context, life-cycle cost is the cost that occurs throughout entire life cycle of the paints, also including the labour cost of painting the façade. Also of importance are operating expenditures, as for example expenditures for the heating of the building, and the cost arising from final demolition and disposal of the paints. Consequently, the comparison of the expected life-cycle cost covers the economical dimension as part of a product sustainability assessment.

In the scope of this study, both operating expenses and cost arising from final demolition and disposal are likely not to differ from each other with respect to the two paints. Both façade paints can be applied using the same technical equipment, and, as can be stated on the basis of information given by the product safety datasheet, the same occupational safety requirements can be applied to both of them [38,39]. The same applies to the end-of-life treatment.

The calculation of life-cycle cost is based on retail prices that are freely available in the internet. First of all, the average price per m^2 in the field of professional façade painting was being sought. For reasons of transparency, many painting companies disclose their retail price calculation on the company website. On the basis of these publications and of further similar calculations, a retail price of about 20.00 € per m^2 (including material

cost) could be retrieved as suitable approximation regarding the German market and including delivery and installation of the scaffold, possible pre-treatments such as façade cleaning, the required amount of paint and also the dismantling and return of the scaffold. All labour cost, overhead cost and the profit margin are also included therein. Table 1 shows the calculation of life-cycle cost for both paints.

Table 1: Results for the calculation of cost based on retail prices.

type of cost[a]	unit	Lotusan®	Jumbosil®
materials cost/l	(€)	11.91	5.95
materials cost/m²	(€)	4.29	2.38
material cost/façade	(€)	858.00	476.00
material cost/functional unit	(€)	3,432.00	2,380.00
total cost/m² (work + materials)	(€)	21.91	20.00
total cost/façade (work + material)	(€)	4,382.00	4,000.00
total cost/functional unit[b]	(€)	17,528.00	20,000.00
work (total)	(€)	14,096.00	17,620.00
	(%)	80.4	88.1
materials (total)	(€)	3,432.00	2,380.00
	(%)	19.6	11.9

[a]Materials cost is the cost for the paints, while total cost represents the sum of materials cost and labour cost of a professional painter.
[b]Because of three required repaint coatings with Lotusan® instead of four repaint coatings required when using Jumbosil® the total cost per functional unit for Lotusan® is lower than for Jumbosil®.

As both paints can be applied using the same techniques, it can be assumed that there are no differences regarding labour cost, overhead and the profit margin of the painter. Consequently, the retail price of 20.00 € per m^2 is made up of a fixed cost element for the execution of work, and the cost element of the façade paint itself. As Jumbosil® stands as reference for a typical product on the market, a price of 20.00 € per m^2 has been chosen as the retail price of Jumbosil®. For Jumbosil®, a retail price of 89.33 € per 15 litre bucket could be determined [40]. Assuming a consumption rate of 0.2 litres per m^2, and a two-layer coating given in the product data sheet [33] the materials cost was calculated. Compared to Jumbosil®, Lotusan® is the more costly product. For Lotusan®, the materials cost was calculated considering a retail price of 148.90 € per 12.5 litre bucket [40], assuming a consumption rate of 0.18 litres per m^2 and a two-layer coating given in the product data sheet [32]. With regard to the entire façade surface of 200 m^2, the Lotusan®-based façade painting is ca. 9% more expensive. Regarding the entire life cycle of 75 years, four repaint coatings have to be assumed for a Jumbosil®-based façade painting, while a Lotusan®-based façade painting only requires three repaint coatings. Consequently, the higher materials cost for a Lotusan®-based façade painting is more than compensated by the longer service life time, resulting in reduced overall materials consumption and lower labour cost. Cost savings over the entire building life cycle of 75 years sum up to 2,472 €.

It is important to note here, that some aspects have been neglected in the cost calculation given above. No discount, for example, has been taken into account for cost arising from repaint coatings to be carried out in the future. From the perspective of Lotusan®, this might be seen as a conservative assumption, as the Lotusan®-based façade painting has to be repainted one time fewer. Moreover, possible changes in materials and labour cost have also been neglected.

Life-cycle analysis

For the purpose of this study, a comparative LCA has been carried out based on the standards DIN EN ISO 14040: 2006 [41] and DIN EN ISO 14044: 2006 [42]. In concrete terms, this means a comparison between the possible environmental impacts associated with painting a façade with Lotusan® and Jumbosil®. The LCA was prepared "from cradle to grave" (Figure 2).

Goal- and scope definition and modelling of the two alternative façade paintings: The goal- and scope definition phase includes the determination of a functional unit (FU). In the present case the functional unit is equivalent to the functional utility, the provision of a structurally sound building through the provision of the outer layer of the building envelope. From this point of view, the two exterior paints can be considered as being equivalent in terms of equal functional utility and are directly comparable.

Throughout the 75 years life of the building, both a Lotusan®-based façade painting (three repainting coatings) and a Jumbosil®-based façade painting (four repaint coatings) have to be repainted. For this purpose, the production of the paints, their distribution to the building and the effort for assembling and dismantling the paint scaffold have to be taken into account. The software umberto (umberto NXT Universal © ifu hamburg 2013) has been used to prepare the LCA.

Life-cycle impact assessment: In the course of the life-cycle impact assessment (LCIA), potential environmental impacts of the two compared façade paints are determined by linking the LCI results, namely materials flow and energy flow, to specific environmental impact categories.

According to the requirements of [41], the selection of impact categories has to be done according to the goals of the study. In the framework of this study, a broad set of impact categories has been evaluated. The aim was to ensure that all relevant

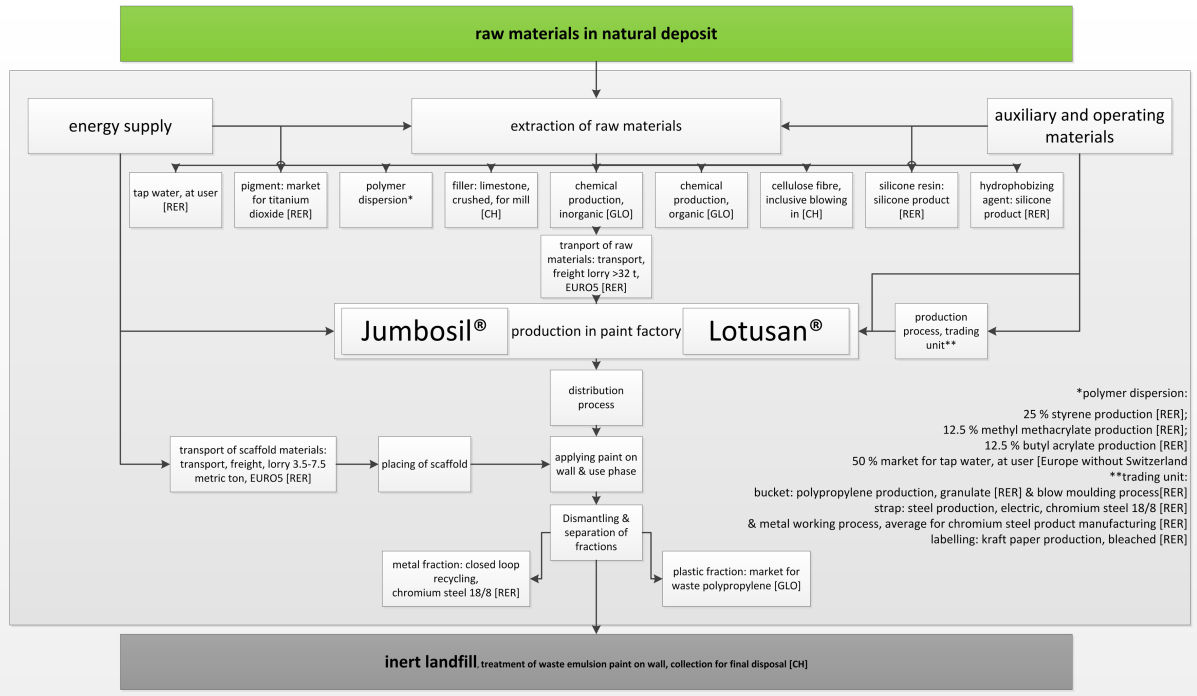

Figure 2: Schematic drawing of the system boundary with production and life-cycle steps for the two compared façade paints Lotusan® and Jumbosil® from cradle to grave.

environmental issues are covered by the selection of impact categories. Likewise, a special emphasis has been put on selecting such impact categories providing maximum transparency and representing the scientific state of the art.

Result monitoring was carried out by using a combination of four environmental impact assessment models, including the cumulative energy demand (CED_{fossil}, $CED_{nuclear}$, $CED_{non\text{-}renewable}$ as sum of the aforementioned), the ReCiPe environmental impact assessment model in the version of 2008, the IPCC method regarding the global warming potential (GWP) and the USEtox model for dealing with toxicology aspects related to the production and use of the two paints. A short description of the investigated categories is given in Table S2 (Supporting Information File 1). For an elaborate discussion of the different impact categories, we also refer to [43,44].

Results of the Life Cycle Impact Assessment: Table 2 shows the overall results for the two compared products both as absolute values as well as in terms of their share with respect to Lotusan®. All values are related to the functional unit of the provision of a façade painting of 200 m^2 over 75 years.

Results of the life-cycle impact assessment show that both paintings differ with regard to their potential environmental impact. Regarding the cumulative energy demand from non-renewable energy sources, the biomimetic product Lotusan® has a lower indicator value. Jumbosil® as the reference product has a 1.54-fold higher demand on non-renewable primary energy, which is mainly due to the higher share of polymer dispersion within the product formulation. A comparable situation is given with regard to the global warming potential (GWP). Jumbosil® has a GWP that is about a factor of 1.39-fold higher than that of Lotusan®. The higher share of polymer dispersion within the product formulation of Jumbosil® is the main reason also for the higher product related terrestrial acidification potential (TAP), the marine eutrophication potential (MEP) and the particulate matter formation potential (PMFP). However, freshwater depletion potential (WDP) and $USEtox_{ecotox}$ are considered, Jumbosil® achieves the lower values. This is mainly because of Lotusan®'s higher content of titanium dioxide (TiO_2). Regarding the remaining impact indicators both façade paints are equal within the calculation inaccuracy.

Contributions by life-cycle stages: The key issue of the contribution analysis is a clarification of the composition of the overall results and the identification of the processes that have the greatest influence on the overall results. A first analysis investigates the contributions by life-cycle stages along the entire service life cycle of the two products (Table S3, Supporting Information File 1). For both façade paints, the contributions by

Table 2: Overall results of the life-cycle impact assessment shown for each impact category.

impact indicator	abbreviation[a]	unit	Lotusan®	Jumbosil®	Jumbosil®/Lotusan®
cumulative non-renewable energy demand	$CED_{non\text{-}renewable}$	[GJ]	9.3	14.3	1.54
global warming potential	GWP_{100a}	[kg CO_2-e]	645	893	1.39
water depletion potential	WDP	[m^3]	4.82	3.78	0.78
terrestrial acidification	TAP_{100a}	[kg SO_2-e]	2.90	4.07	1.40
freshwater eutrophication	FEP	[kg P-e]	0.17	0.18	1.05
marine eutrophication	MEP	[kg N-e]	0.17	0.21	1.24
photochemical ozone formation potential	POFP	[kg NMVOC]	2.48	3.20	1.29
agricultural land occupation potential	ALOP	[m^2a]	32.42	30.54	0.94
human toxicity, total	$USEtox_{humantox}$	CTU	$7.52 \cdot 10^{-5}$	$7.65 \cdot 10^{-5}$	1.02
ecotoxicity, total	$USEtox_{ecotox}$	CTU	1448	1205	0.83
particulate matter formation potential	PMFP	[PM10-e]	1.28	1.43	1.12

[a]A description of the impact indicators used in this study is found in Table S2 (Supporting Information File 1).

the provision of the required raw materials are most important. This life-cycle stage contributes from 56% regarding CED up to 91% regarding $USEtox_{ecotox}$ to the overall indicator results of Lotusan®. Regarding Jumbosil®, contributions reach from 59% (GWP, NMVOC) up to 85% of the overall $USEtox_{ecotox}$ indicator result. An exception was found for Jumbosil® with regard to the ALOP. Here, the provision of raw materials contributes only about 40% to the overall indicator result. With regard to the ALOP, the production and provision of packaging materials are more important (Lotusan® 27%, Jumbosil® 41%) than for other impact categories.

Besides the provision of raw materials, the contributions by the use phase are also worth mentioning. With the exception of WDP (Lotusan® 4%; Jumbosil® 6%), the contribution to all impact categories are at a level of at least around 10% or even higher. Regarding CED and GWP, the use phase contributes from 21% (CED, Jumbosil®) to 26% (GWP, Lotusan®) to the overall indicator results.

Due to the large contribution from the provision of raw materials, an in-depth analysis on the shares of the different raw materials has been carried out (Table S4, Supporting Information File 1). For both paints, the main contributions arise from the provision of TiO_2 as white pigment. As already shown in Supporting Information Table S1, Lotusan® has a higher TiO_2 content (20%, compared to only 10% for Jumbosil®). Remarkable in this context are the results for the two USEtox indicators. They show that over 97% of the ecotoxicity potential related to the provision of raw materials required for Lotusan® trace back to the provision of TiO_2. The overall indicator result for $USEtox_{ecotox}$ is dominated by the TiO_2 provision, contributing more than 88% of the overall result for Lotusan®. The manufacturing phase and, in particular, the use phase are of only limited importance for this result.

Besides TiO_2, the provision of the polymer dispersion is likewise of some importance. This applies even more to Jumbosil®, due to the higher content of polymer dispersion. Regarding CED und GWP, the provision of polymer dispersion contributes about 55% to the overall indicator result of Jumbosil®. With regard to Lotusan®, the contribution by the silicone resin is also not negligible, making up 7–10% of the indicator results. Regarding ALOP, silicone resin contributes even about 20%.

Scenario analysis

The three scenario analyses described in the following have been calculated on the basis of considerations resulting from the benefit analysis. Within the base-case scenario, a service life of 20 years has been assumed for a Lotusan®-based façade painting, taking into account the additional properties of Lotusan® and its capacity to maintain the initial optical quality over the entire service life cycle. The assumption on the possible service life time is relevant for the results. Hence, both a reduced and an expanded service life time for a Lotusan®-based façade painting have been assessed.

With regard to the Jumbosil®-based façade paintings, two measures are described below that might at least temporarily be suitable in order to reach or regain equivalent optical quality. The scenarios do not aim at suggesting what customers should decide for, but it is the aim to show the implicit effects of a possible choice of customer. Results for all scenario analyses are given in Table 3.

Service life: (S1 Lotusan®) – Service life reduction using Lotusan® painting for 15 years instead of 20 years: Within the base-case scenario, a service life of 20 years has been assumed for Lotusan®-based façade paintings. As this assumption is result-relevant and may feed criticism, a service life time of

Table 3: Overall results of the scenario analyses[a,b].

impact category	Lotusan® service life: 20 years	Jumbosil® service life: 15 years	S1: Lotusan® service life: 15 years	S2: Lotusan® service life: 25 years	S3: Jumbosil® service life: 12.5 years	S4: Jumbosil® service life: 15 years plus additional façade cleaning after 7.5 years
$CED_{non\text{-}renewable}$	100%	154%	125%	75%	184%	190%
GWP_{100a}	100%	139%	125%	75%	166%	172%
WDP	100%	78%	125%	75%	94%	192%
TAP_{100a}	100%	140%	125%	75%	168%	162%
FEP	100%	105%	125%	75%	126%	128%
MEP	100%	124%	125%	75%	149%	144%
POFP	100%	129%	125%	75%	155%	164%
ALOP	100%	94%	125%	75%	113%	106%
$USEtox_{humantox}$	100%	102%	125%	75%	122%	128%
$USEtox_{ecotox}$	100%	83%	125%	75%	100%	92%
PMFP	100%	112%	125%	75%	135%	138%
Overall cost	100%	114%	125%	75%	137%	—[c]

[a]A description of the scenario analyses and of the parameters varied in S1 to S4 is given in the main text.
[b]Percentage values are normalized with respect to Lotusan® (set as 100%); higher values as 100% mean higher overall environmental impacts or higher cost.
[c]Because of lacking data on the typical cost for professional façade cleaning, no overall cost have been calculated for scenario S4.

15 years has been evaluated in analogy to the base-case assumption for Jumbosil®-based façade paintings. In this case, for the Lotusan®-based façade paintings as well four repainting coatings have to be taken into account. This results in a higher materials demand and in additional efforts in the course of the painting itself.

(S2 Lotusan®) – Service life expansion using Lotusan® paint for 25 years instead of 20 years: Both in terms of structural and functional properties as well as for providing sufficient optical quality, a possible 5 year service life expansion of Lotusan®, thus reaching an overall service life time of 25 years, has been evaluated.

(S3 Jumbosil®) – The effect of repainting the Jumbosil®-based façade paint after 12.5 years due to a loss of optical quality: In this scenario, the effect of a repainting of Jumbosil® after 12.5 years due to a loss of optic quality has been calculated. In technical terms, this can be seen as a customer-chosen reduction of service life time by 2.5 years (16%). Such customer behaviour is well known for example within the field of information and communications technology equipment, and has been recently described as "psychological obsolescence" [45]. A reduced product service life time of 12.5 years results in one additional painting over the 75 year life time of the building. Therefore, the environmental burden of one additional painting of the façade with Jumbosil® has been evaluated.

(S4 Jumbosil®) – Consideration of a professional façade cleaning of the Jumbosil®-based façade paint after 7.5 years: A professional façade cleaning might be able to temporarily stop and reduce the continuing loss of optical quality. Although this is not the same as the ability of constantly maintaining the optical quality at a high level by self-drying façade paint, customers might consider it satisfactory. In contrast to scenario S3 given above, a cleaning of the façade could lead customers to take advantage of the complete service life of 15 years. In general, a façade cleaning can be performed either using a mobile platform, or alternatively by putting up a scaffold. In both cases it is assumed that a lorry transport is needed to put either the elevating platform or the scaffold to the building. In particular, a transport distance of 20 km has been taken into account. Regarding the façade cleaning process itself, the demand of energy and freshwater for running a high-pressure cleaner have been taken into account, assuming a power consumption of 1.5 kW, a water demand of 350 litres per hour, and an assumed time requirement of 3 h per 200 m^2 façade. It is furthermore assumed that the façade cleaning can be done solely with clear water without detergents or other cleaning agents.

Integrated assessment and discussion

So far, all relevant dimensions of sustainability have been investigated within the course of the comparative product sustainability assessment independently of one another. However, dependencies exist between the individual PROSA tools applied in this comparison that need to be taken into consideration when discussing and interpreting the results [25]. This is especially true considering the challenge of bringing together the several findings of the individual analyses carried out within the prod-

uct sustainability assessment (Table 4). It has been decided to do the integrated assessment at a qualitative level as this yields maximum transparency of the results. While single numerical score values are better comparable, they do not offer a corresponding transparency. For a discussion of advantages and disadvantages of doing the integrated assessment at a quantitative or a qualitative level, we refer to the discussion in [16].

As has been found within the course of the benefit analysis, both paints fulfil the requirements of functional utility equally well, albeit for different periods of time (Lotusan® 20 years, Jumbosil® 15 years). Furthermore, Lotusan® has a particular added value with respect to the symbolic utility. The maintaining of the initial optical quality at a constantly high level over the entire product life cycle is something a Jumbosil®-based façade paint does not yield. From the perspective of the benefit analysis an additional benefit can be established for the Lotusan®-based façade painting.

The comparison has also been done regarding possible social effects. Thereby, both the bill of materials and the product safety data sheets of the final products have been checked for possible differences, with the result that no substantial differences exist with regard to the handling and disposal of the final

Table 4: Overview of the results for the individual analyses carried out within the product sustainability assessment.

analysis tool		Lotusan®	Jumbosil®
check on biomimetic product		biomimetic	—
benefit analyses	functional utility	Both paints fulfil the functional utility in a similar way, albeit for different periods of time. For Lotusan®-based façade paintings a 20 year service life is assumed, due to higher product qualities in terms of wettability and gas exchange.	Both paints fulfil the functional utility in a similar way, albeit over varying periods of time. For Jumbosil®-based façade paintings a 15 year service life is assumed.
	symbolic utility	Preservation of optical quality over the life cycle is an additional aesthetic value.	—
social life-cycle assessment	orienting analysis	No fundamental differences are expected (consequently no in-depth analysis was carried out).	
life-cycle cost assessment	operating expenses	No fundamental differences are assumed.	
	cost for demolition and final disposal	No fundamental differences are assumed.	
	overall materials cost	A Lotusan®-based façade painting is more expensive by 1.91 €/m^2. A service life of 20 years was taken into account.	
	labour cost	No fundamental differences are expected due to information given in the TDS; labour causes 81% of overall cost.	No fundamental differences are expected due to information given in the TDS; labour causes 88% of overall cost.
	overall cost	In absolute terms, the cost of a Lotusan®-based 200 m^2 façade painting are 4,382 € and therefore by 382 € more expensive than a Jumbosil®-based façade painting of the same dimensions. Cost are more than compensated by the longer service life time, resulting reduced overall materials demand and lower labour cost (only 3 instead of 4 repaintings). Cost savings over the entire building life cycle of 75 years sum up to 2,472 €.	The provision of a Jumbosil®-based façade painting is about 91% of the cost compared to the provision of a Lotusan®-based façade painting. The overall cost is strongly related to the assumed product service life times (see also results of scenario analyses below).
life-cycle assessment	CED, GWP, TAP, MEP, POFP, PMFP	Considering a life time of 75 years of the building, a Lotusan®-based façade painting might be advantageous compared to a Jumbosil®-based façade painting.	Considering a life time of 75 years of the building, the values for a Jumbosil®-based façade painting are about 10–54% higher than for a Lotusan®-based façade painting.
	FEP, ALOP, $USEtox_{humantox}$	Both façade paints lie within a similar range.	
	WDP, $USEtox_{humantox}$	Values for a Lotusan®-based façade painting are about 20–28% higher than for a Jumbosil®-based façade painting.	A Jumbosil®-based façade painting might be advantageous compared to a Lotusan®-based façade painting

Table 4: Overview of the results for the individual analyses carried out within the product sustainability assessment. (continued)

scenario analyses	S1: Service-life reduction of Lotusan®	25% increase of overall LCA and cost results. Lotusan® is a little more advantageous compared to Jumbosil® regarding CED, GWP and TAP. Regarding MEP and POFP both paints compare are at a comparable level. Regarding FEP, ALOP, USEtox and PMFP, indicator values for a Lotusan®-based façade painting are about 20–25% higher than for a Jumbosil®-based façade painting. Regarding WDP values are about 60% higher.	—
	S2: service-life expansion of Lotusan®	25 % reduction of overall LCA and cost results. Lotusan® is more advantageous compared to Jumbosil® in nearly all LCIA indicators and cost. Regarding WDP and $USEtox_{ecotox}$ both paints perform at a comparable level.	—
	S3: service-life reduction of Jumbosil®	—	Regarding CED, GWP, TAP, MEP, POFP, PMFP and also overall cost the existing gap widens. Regarding FEP, ALOP and $USEtox_{humantox}$ the result for Jumbosil® is now negative. Regarding WDP and $USEtox_{ecotox}$ the advantage of Jumbosil® is lost.
	S4: Additional façade cleaning of the Jumbosil®-based façade painting	—	Regarding CED, GWP and TAP, MEP, POFP and PMFP the existing gap widens. Regarding ALOP and $USEtox_{ecotox}$ the advantage of Jumbosil® is lost. Regarding WDP, FEP and $USEtox_{humantox}$ the result for Jumbosil® is now negative.

products. Concerning the provision of raw materials it has been decided to additionally evaluate the products regarding toxicology aspects within the LCA. In the course of conducting the LCA, the demand for titanium dioxide in both paints could be identified as main driver of toxicity potential indicator results. Regarding the base-case scenario, Lotusan® shows about 20% higher $USEtox_{humantox}$ indicator results, arising from the higher content of titanium dioxide. With regard to the $USEtox_{ecotox}$ indicator result, it can be established that the longer product service life of a Lotusan®-based façade painting counterbalances the additional demand for titanium dioxide. It should be noted that, taking into account the same service life time for both façade paintings (as analysed in scenario S1), indicator values for a Lotusan®-based façade painting are about 20–25% higher than for a Jumbosil®-based façade painting. Due to the fact that, according to the manufacturer, in both paints only raw materials from Europe were used in the product, it could have been ruled out that major differences exist in terms of social effects between the two paints compared within this study. As regards the safety of the final products, based on the information given in the product safety datasheets, it can be clearly stated that both paints do not contain any hazardous substances or substances the use of which and the exposition to which would cause concerns. From the point of view of the customers, they can therefore be seen as equally safe alternatives.

Regarding the life-cycle cost, Lotusan® is the more expensive product, but at the same time the higher investment cost for a Lotusan®-based façade painting are more than compensated by the longer service life time, resulting in reduced overall materials demand and lower labour cost (only three instead of four repaint coatings). Cost savings over the entire building life cycle of 75 years sum up to 2,472 € (ca. 10%). The cost saving is clearly related to the estimated longer service life of a Lotusan®-based façade painting. Taking into account the service life reduction of Lotusan® (scenario S1), the overall cost of a Lotusan®-based façade painting are correspondingly slightly higher (ca. 10%).

In terms of the life-cycle impact assessment, results differ for the two façade paints. While Lotusan® performs better regarding the majority of impact indicators (CED, GWP TAP, MEP, POFP, and PMFP), Jumbosil® performs better regarding WDP, $USEtox_{humantox}$. Regarding FEP, ALOP and $USEtox_{ecotox}$, both façade paints more or less lie within the same range.

In total, it can be ascertained that there are differences between the two paints compared. However, these differences are relatively minor in terms of the provision of raw materials and the production of the paints. The substantial differences between the paints arise from the service life of the façade paintings. This can be shown, for example, with regard to the findings of scenario S1 where the same number of repaint coatings for the entire life cycle of 75 years has been assessed for both Lotusan® and Jumbosil®. Results of scenario S1 show that Lotusan® is still a little more advantageous compared to Jumbosil® in terms of CED, GWP and TAP, while for FEP, ALOP, USEtox and PMFP the indicator values for a Lotusan®-based façade painting, are about 20–25% higher than for a Jumbosil®-based façade painting. For the majority of impact indicators it can be stated that the differences between the two façade paintings lie within the range of one additional repaint coating over the entire life time of the building of 75 years.

Conclusion

Within the course of the systematic product sustainability assessment at hand, the biomimetic façade paint Lotusan® has been compared to the conventional façade paint Jumbosil®. The Lotus-Effect® technology has been successfully put into practice in Lotusan® which is one of the best known and most widely used biomimetic products. Several aspects such as benefit analysis, LCC, LCA and scenario analysis have been addressed within the product sustainability assessment. Because of the outstanding functional utility of the product it can be seen as a useful measure of protecting a building against weathering. Furthered by the experimentally determined additional functionalities, a bigger service life time of 20 years has been ascribed to a Lotusan®-based façade painting. In conclusion, the biomimetic façade paint Lotusan® has been identified as a cost-effective and resource-saving product. Lotusan®-based façade paintings have a comparatively low overall impact on the environment. Furthermore, it could be reliably determined that the use of the product has no negative effect in terms of toxicology and social aspects.

Results of both LCC and LCA are highly dependent on the possible behaviour of customers. The differences in functional utility might justify a different behaviour of customers. In a few years, when some of the first reference objects will reach the estimated end of the first service life cycle, it will be interesting to see whether the estimated service life extension of five years of Lotusan®-based façade paintings constitutes an objectively justified presumption. Should it prove to be true, Lotusan® turns out as the favourable product, both in terms of economic performance and in terms of ecological relevance. It can therefore be asserted that with regard to Lotusan® the biomimetic promise is kept.

Supporting Information

Supporting Information File 1

Detailed data.
[http://www.beilstein-journals.org/bjnano/content/supplementary/2190-4286-7-200-S1.pdf]

Acknowledgements

This project was funded by the German Federal Ministry of Education and Research (FKZ 01RB0708B) in the framework of BIONA – Bionische Innovationen für nachhaltige Produkte und Technologien (FA, OS, TS). The current work on sustainability and biomimetics in architecture and building construction runs within the Collaborative research Centre (CRC) TRR 141 "Biological Design and Integrative Structures – Analysis, Simulation and Implementation in Architecture" (OS, TS) and is funded by the German Research Foundation (DFG). The authors thank Dr. Eike Messow, Dr. Andreas Weier, Alexander Färber and Reiner Schmid (Sto SE & Co. KGaA, Stühlingen, Germany) for providing us with the required data for performing the LCA. Carl-Otto Gensch (Öko-Institut e.V, Freiburg) is gratefully acknowledged for his helpful support and the fruitful discussions throughout the course of the study. We also thank Barbara Hochscheid for proof-reading the manuscript and for improving the English.

The authors dedicate this work to Prof. Dr. Wilhelm Barthlott for his merits in biomimetics and organismic botany.

References

1. Speck, T.; Speck, O. Process sequences in biomimetic research. In *Design and Nature IV;* Brebbia, C. A., Ed.; WIT Transactions on Ecology and the Environment, Vol. 114; WIT Press: Southampton, United Kingdom, 2008; pp 3–11. doi:10.2495/DN080011
2. Masselter, T.; Barthlott, W.; Bauer, G.; Bertling, J.; Ditsche-Kuru, P.; Gallenmüller, F.; Gude, M.; Hermann, M.; Immink, H.; Knippers, J.; Lienhard, J.; Luchsinger, R.; Lunz, K.; Mattheck, C.; Milwich, M.; Mölders, N.; Neinhuis, C.; Nellesen, A.; Rechberger, M.; Schleicher, S.; Schmitt, C.; Schwager, H.; Seidel, R.; Speck, O.; Stegmaier, T.; Tesari, I.; Thielen, M.; Speck, T. Biomimetic products. In *Biomimetics: Nature-based Innovation;* Bar-Cohen, Y., Ed.; CRC Press: Boca Raton, FL, U.S.A., 2011; pp 377–429.
3. Speck, T.; Neinhuis, C. *Naturwiss. Rundsch.* **2004,** *57,* 177–191.
4. Speck, T.; Speck, O. *Naturwiss. Rundsch.* **2015,** *68,* 510–522.
5. Gruber, P. Biomimetics in architecture. In *Biomimetics – Materials, Structures and Processes;* Gruber, P.; Bruckner, D.; Hellmich, C.; Schmiedmayer, H.-B.; Stachelberger, H.; Gebeshuber, I. C., Eds.; Biological and Medical Physics, Biomedical Engineering; Springer: Berlin, Germany, 2011; pp 127–148. doi:10.1007/978-3-642-11934-7_7
6. Knippers, J.; Speck, T. *Bioinspiration Biomimetics* **2012,** *7,* 015002. doi:10.1088/1748-3182/7/1/015002

7. *VDI 6226 Bionik: Architektur, Ingenieurbau, Industriedesign – Grundlagen; Biomimetics: Architecture, civil engineering, industrial design – Basic principles VDI 6226;* Beuth: Berlin, Germany, 2015.
8. Barthlott, W. Selbstreinigende Oberflächen von Gegenständen sowie Verfahren zur Herstellung derselben. EP 000000772514 B1, Dec 23, 1998.
9. Schleicher, S.; Lienhard, J.; Poppinga, S.; Speck, T.; Knippers, J. *Comput.-Aided Des.* **2015,** *60,* 105–117. doi:10.1016/j.cad.2014.01.005
10. Hecker, H.-D. Der Hörsaal des Zoologischen Instituts der Universität Freiburg. *Freiburger Universitätsblätter;* Rombach Verlag: Freiburg, Germany, 1969; Vol. 25, pp 49–52.
11. Hecker, H.-D.; Hecker, S. *Entwürfe und Bauten;* Herder Verlag: Freiburg, Germany, 2009.
12. von Gleich, A.; Pade, C.; Petschow, U.; Pissarskoi, E. *Bionik. Aktuelle Trends und künftige Potentiale. Endbericht des Forschungsprojekts "Potentiale und Trends der Bionik";* Federal Ministry of Education and Research (BMBF): Berlin, Germany, 2011.
13. *VDI 6220 Bionik: Konzeption und Strategie – Abgrenzung zwischen bionischen und konventionellen Verfahren/Produkten; Biomimetics: Conception and strategy – Differences between biomimetics and conventional methods/products VDI 6220;* Beuth: Berlin, Germany, 2012.
14. Antony, F.; Mai, F.; Speck, T.; Speck, O. *Naturwiss. Rundsch.* **2012,** *65,* 175–182.
15. Antony, F.; Grießhammer, R.; Speck, T.; Speck, O. Natur – (k)ein Vorbild für Nachhaltige Entwicklung. In *Bionik: Patente aus der Natur. 6. Bremer Bionik-Kongress – Tagungsbeiträge,* Kesel, A.; Zehren, D., Eds.; 2013; pp 164–170.
16. Antony, F.; Grießhammer, R.; Speck, T.; Speck, O. *Bioinspiration Biomimetics* **2014,** *9,* 016013. doi:10.1088/1748-3182/9/1/016013
17. Speck, O.; Speck, D.; Horn, R.; Gantner, J.; Sedlbauer, K.-P. *Bioinspiration Biomimetics* **2017,** in press.
18. Horn, R.; Gantner, J.; Widmer, L.; Sedlbauer, K.-P.; Speck, O. Bio-inspired Sustainability Assessment – A Conceptual Framework. In *Biomimetic Research for Architecture and Building Construction: Biological Design and Integrative Structures;* Knippers, J.; Nickel, K.; Speck, T., Eds.; Biologically-Inspired Systems, Vol. 9; Springer International Publishing: Switzerland, 2016; pp 361–377. doi:10.1007/978-3-319-46374-2_18
19. Gebeshuber, I. C.; Gruber, P.; Drack, M. *Proc. Inst. Mech. Eng., Part C* **2009,** *223,* 2899–2918. doi:10.1243/09544062JMES1563
20. Pedersen Zari, M. *Int. J. Sustainable Built Environ.* **2015,** *4,* 145–157. doi:10.1016/j.ijsbe.2015.02.004
21. Vincent, J. F. *Proc. Inst. Mech. Eng., Part H* **2009,** *223,* 919–939.
22. von Gleich, A. *Bionik: Ökologische Technik nach dem Vorbild der Natur;* Teubner: Stuttgart, Germany, 2001.
23. von Gleich, A. Berechtigung und Reichweite des "bionischen Versprechens". In *Bionik: Patente aus der Natur. 3. Bremer Bionik-Kongress – Tagungsbeiträge,* Bremen; Kesel, A.; Zehren, D., Eds.; 2006; pp 184–193.
24. Raibeck, L.; Reap, J.; Bras, B. *CIRP J. Manuf. Sci. Technol.* **2009,** *1,* 230–236. doi:10.1016/j.cirpj.2009.05.004
25. Griesshammer, R.; Buchert, M.; Gensch, C.-O.; Hochfeld, C.; Manhart, A.; Rüdenauer, I. PROSA – Product Sustainability Assessment. Beschreibung der Methode. Freiburg, Germany, 2007; http://www.prosa.org/fileadmin/user_upload/pdf/PROSA-gesamt_Finalversion_0407_red.pdf (accessed July 27, 2016).
26. John, G.; Clements-Croome, D.; Jeronimidis, G. *Build. Environ.* **2005,** *40,* 319–328. doi:10.1016/j.buildenv.2004.05.011
27. *VDI 6221 Bionik: Bionische Oberflächen; Biomimetics: Biomimetic surfaces VDI 6221;* Beuth: Berlin, Germany, 2013.
28. Barthlott, W.; Neinhuis, C. *Planta* **1997,** *202,* 1–8. doi:10.1007/s004250050096
29. Neinhuis, C.; Barthlott, W. *Ann. Bot. (Oxford, U. K.)* **1997,** *79,* 667–677. doi:10.1006/anbo.1997.0400
30. Kougoulis, J. S.; Kaps, R.; Wolf, O.; Walsh, B.; Bojczuk, K.; Derbyshire, P.; Crichton, T. Revision of EU European Ecolabel and Development of EU Green Public Procurement Criteria for Indoor and Outdoor Paints and Varnishes. *Green Public Procurement Background Report, European Commission, Joint Research Centre (JRC); Seville: Institute for Prospective Technological Studies (IPTS);* 2012. http://susproc.jrc.ec.europa.eu/paints/docs/Preliminary%20report.pdf
31. Verband der deutschen Lack- und Druckfarbenindustrie. VdL-RL 01 Richtlinie zur Deklaration von Inhaltsstoffen in Bautenlacken, Bautenfarben und verwandten Produkten, 4th revised November 2013. (accessed July 15, 2015). http://www.lackindustrie.de/Publikationen_/VdL-Richtlinien/Documents/VdL-Richtlinie%2001%20Bautenanstrichstoffe.pdf
32. Technical Bulletin Lotusan®: façade paint with Lotus effect® technology. http://www.sto.de (accessed July 15, 2015).
33. Technical Bulletin Jumbosil® QS. http://www.sto.de (accessed July 15, 2015).
34. Federal Institute for Research on Building, Urban Affairs and Spatial Development (BBSR). Nutzungsdauern von Bauteilen für Lebenszyklusanalysen nach Bewertungssystem Nachhaltiges Bauen (BNB). 2011; http://www.nachhaltigesbauen.de/fileadmin/pdf/baustoff_gebauededaten/BNB_Nutzungsdauern_von_Bauteilen__2011-11-03.pdf (accessed July 27, 2016).
35. Polymer Institut. Forschungsinstitut für polymere Baustoffe. Dr. R. Stenner GmbH 1999. Prüfbericht P1977-1. Prüfung des Verschmutzungsverhaltens verschiedener Fassadenfarben gemäß Methode „Lotus-Effekt“, unpublished data.
36. Fraunhofer Institute for Building Physics IBP 1999 Bestimmung der Oberflächenbenetzung und des Abtrockungsverhaltens von unterschiedlichen Fassadenbeschichtungen durch einen Kurzversuch, unpublished data.
37. Forschungsinstitut für Pigmente und Lacke e.V. (FPL), Prüfbericht Nr. AT 008/00, unpublished data.
38. Product Safety Data Sheet (SDS) Lotusan®: façade paint with Lotus-Effect® technology.. http://www.sto.de/webdocs/0000/SDB/M_03206-028_0101_DE_01_06.PDF (accessed July 28, 2016).
39. Product Safety Data Sheet (SDS) Jumbosil QS. http://www.sto.de/webdocs/0000/SDB/M_00223-001_0101_DE_02_05.PDF (accessed July 15, 2015).
40. http://www.farbenbote.de. (accessed July 16, 2015).
41. DIN EN ISO 14040: 2006-10 Environmental management – Life cycle assessment – Principles and framework, Beuth: Berlin, 2006.
42. DIN EN ISO 14044: 2006-10 Environmental management –Life cycle assessment – Requirements and guidelines, Beuth: Berlin, 2006.
43. Pant, R.; Bersani, R.; Pennington, D. W.; Brandao, M. ILCD Handbook - Analysis of existing environmental impact assessment methodologies for use in life cycle assessment-background document. 2010; http://eplca.jrc.ec.europa.eu/uploads/ILCD-Handbook-LCIA-Background-analysis-online-12March2010.pdf (accessed July 15, 2015).

44. Klöpffer, W.; Grahl, B. *Ökobilanz (LCA): ein Leitfaden für Ausbildung und Beruf;* John Wiley & Sons: Weinheim, Germany, 2009. doi:10.1002/9783527627158
45. Prakash, S.; Dehoust, G.; Gsell, M.; Schleicher, T.; Stamminger, R. Einfluss der Nutzungsdauer von Produkten auf ihre Umweltwirkung: Schaffung einer Informationsgrundlage und Entwicklung von Strategien gegen „Obsoleszenz". Zwischenbericht: Analyse der Entwicklung der Lebens-, Nutzungs- und Verweildauer von ausgewählten Produktgruppen. 2015; https://www.umweltbundesamt.de/sites/default/files/medien/378/publikationen/texte_10_2015_einfluss_der_nutzungsdauer_von_produkten_auf_ihre_umwelt_obsoleszenz_17.3.2015.pdf (accessed July 28, 2016).

BEILSTEIN JOURNAL OF NANOTECHNOLOGY

When the going gets rough – studying the effect of surface roughness on the adhesive abilities of tree frogs

Niall Crawford[1], Thomas Endlein[2], Jonathan T. Pham[3], Mathis Riehle[1] and W. Jon P. Barnes[*1]

Full Research Paper

Open Access

Address:
[1]Centre for Cell Engineering, Institute of Molecular Cell and Systems Biology, University of Glasgow, Glasgow, Scotland, UK, [2]Max Planck Institute for Intelligent Systems, Stuttgart, Germany and [3]Max Planck Institute for Polymer Research, Mainz, Germany

Email:
W. Jon P. Barnes[*] - Jon.Barnes@glasgow.ac.uk

* Corresponding author

Keywords:
adhesion; friction; *Litoria caerulea*; roughness; tree frog

Beilstein J. Nanotechnol. **2016,** *7,* 2116–2131.
doi:10.3762/bjnano.7.201

Received: 25 July 2016
Accepted: 30 November 2016
Published: 30 December 2016

This article is part of the Thematic Series "Biological and biomimetic materials and surfaces".

Guest Editor: S. N. Gorb

Abstract

Tree frogs need to adhere to surfaces of various roughnesses in their natural habitats; these include bark, leaves and rocks. Rough surfaces can alter the effectiveness of their toe pads, due to factors such as a change of real contact area and abrasion of the pad epithelium. Here, we tested the effect of surface roughness on the attachment abilities of the tree frog *Litoria caerulea*. This was done by testing shear and adhesive forces on artificial surfaces with controlled roughness, both on single toe pads and whole animal scales. It was shown that frogs can stick 2–3 times better on small scale roughnesses (3–6 µm asperities), producing higher adhesive and frictional forces, but relatively poorly on the larger scale roughnesses tested (58.5–562.5 µm asperities). Our experiments suggested that, on such surfaces, the pads secrete insufficient fluid to fill the space under the pad, leaving air pockets that would significantly reduce the Laplace pressure component of capillarity. Therefore, we measured how well the adhesive toe pad would conform to spherical asperities of known sizes using interference reflection microscopy. Based on experiments where the conformation of the pad to individual asperities was examined microscopically, our calculations indicate that the pad epithelium has a low elastic modulus, making it highly deformable.

Introduction

Tree frogs exhibit excellent climbing abilities which allow them to efficiently move through their typically arboreal habitat, doing so using specialised adhesive pads found distally on the ventral surface of each toe. The pads stick by means of 'wet adhesion', whereby a thin fluid layer is produced by the pad which creates capillary and viscosity forces between the pad and the surface [1-3]. The polygonal epithelial cells (approx. 10 µm in diameter) are covered with nanostructures, which are thought to create friction by direct contact with the surface [3]. The combination of the fluid filled adhesive area and the

specialised morphology allow the tree frogs to climb smooth vertical and overhanging surfaces.

The attachment ability of tree frogs is affected by both surface chemistry and surface roughness. Hydrophobic leaves (such as those on lotus leaves [4]), could affect the capillary forces produced by the pad (which require low fluid contact angles), and deprive the pads of adhesive ability. Indeed, many plant surfaces are hydrophobic, as this reduces water loss [5]. Turning to surface roughness, this affects the ability of the pad surface to form close contact with the surface. With fine-scale roughness, the volume of fluid produced by the toe pads may be sufficient to completely fill the gaps between the asperities (the 'flooded' regime described by Bhushan [6]), in which case adhesion will remain good. However, with larger asperities, this is no longer possible ('toe-dipping' and 'pill-box' regimes), and capillary forces will be reduced due to a decline in the Laplace pressure component of capillarity [7]. Bhushan's 'submerged' regime is that of a rock/torrent frog climbing water-covered rock, where the toe pads are completely submerged, thus abolishing any meniscus [8]. In such cases, capillary forces will be absent, and any adhesion will be likely due to rate-dependent viscous forces.

Roughness is a component of surface texture, a measure of the amplitude and frequency of deviations from a flat surface. Most natural surfaces are not smooth (unless polished by, for instance, the action of water), but will have a roughness that reflects the size of the component particles (e.g., sand grains in sandstone) [7]. They may also contain cracks, lumps and ridges which increase their roughness still further. Leaf surfaces may be relatively smooth, but their veins give high amplitude ridges that are distributed over their surfaces. Indeed, cuticular folds have been demonstrated to be slippery for beetles [9,10], and stomata also contribute to a leaf's roughness. Additionally, on some plants (e.g., the stems of *Macaranga* trees), one may find epicuticular wax crystals [11]. In *Macaranga*, the resulting slipperiness repels all insects except their specific ant partners [12]. Rough surfaces could also be abrasive and therefore potentially damaging to adhesive surfaces.

Despite extensive research on the adhesive abilities of tree frogs, most studies have involved testing their climbing capabilities on smooth surfaces [2,13,14]. On such surfaces, the toe pad fluid creates an ultra-thin layer, whilst the nanopillars that cover the surface of the pad epithelial cells come into very close (potentially direct) contact with the surface [3]. Thus the presence of surface asperities is likely to have a significant effect on adhesive ability. Early work by Barnes and co-workers [15] showed that tree frogs display minimum adhesive ability on an intermediate roughness which was larger than their cell morphology but smaller than the pad itself. Torrent frogs can stick well to wet and rough surfaces similar to their waterfall habitats, but both torrent frogs and tree frogs showed a decrease in performance as asperity size increased under dry conditions [8]. Other studies, including that of Emerson and Diehl [16], studied sticking on surfaces that varied in both roughness and chemistry, making precise conclusions difficult.

The pads of tree frogs are very soft and so should deform to mould around rough surfaces, as is seen in smooth padded insects [17]. The Young's modulus of the toe pads has been measured in several studies, an elastic modulus of 40–55 kPa based on AFM indentation being the most recent estimate [18]. Barnes et al. [19] carried out indentations at different depths and measured different degrees of stiffness at different depths, lower values for the elastic modulus resulting from larger indentations. This is probably due to the stiff outer keratinous surface of the pad. The toes also have extensive blood vessels beneath the pads which will contribute to the soft nature of the whole pad [19]. It is, however, unknown to what extent these soft pads can deform and adapt to different scales of roughness.

Here, the performance of tree frogs on rough surfaces was examined using a variety of techniques to test sticking ability, both at the toe pad level and in free climbing tree frogs, using different rough surfaces. In the main, polishing discs and sandpaper were used, since the range of roughnesses found in such materials was closest to the natural surfaces that a climbing tree frog would encounter. For the single toe pad force measurements, both translucent resin replicas of the sand and polishing papers and fabricated surfaces of known dimensions were used. The hypothesis tested was that, on rough surfaces with larger asperities (i.e., larger than the pad cell diameter of 10 μm), the increased cavity area between the pad and surfaces would be such that pad fluid secretion would be unable to fully fill the pad contact area, as proposed by Persson [20]. Such a situation would be reflected in a reduction in adhesive force. To gain further insight into this, interference reflection microscopy (IRM) was used to view the pad surface and observe how well it conformed to single asperities (glass beads) of different sizes by measuring the height profile of the pad conforming around particles, and observing at what asperity size air bubbles initially appeared.

Results

Attachment abilities of free climbing tree frogs

The frogs' climbing abilities were tested on different rough surfaces using the tilting board apparatus described in the Experimental section (n = 60 for all surfaces tested). At the beginning of the test, frogs usually exhibited a relaxed and crouched

posture with all legs tucked under the body. However, as the angle of the board increased, frogs would typically spread their limbs in order to help stay attached. This behaviour (which has been described in previous studies and is not unique to this experiment) helps in producing friction forces whilst keeping the peel angle of the pads low [21]. A 'smooth' glass surface was used as a control for the rough surface tests. Boxplots are shown below, comparing the performances of the frogs frictional (Figure 1A) and adhesive forces (Figure 1B). Mann–Whitney *U* tests were conducted on comparative sets of data ($n = 60$), with a Bonferroni correction implemented for multiple data usage.

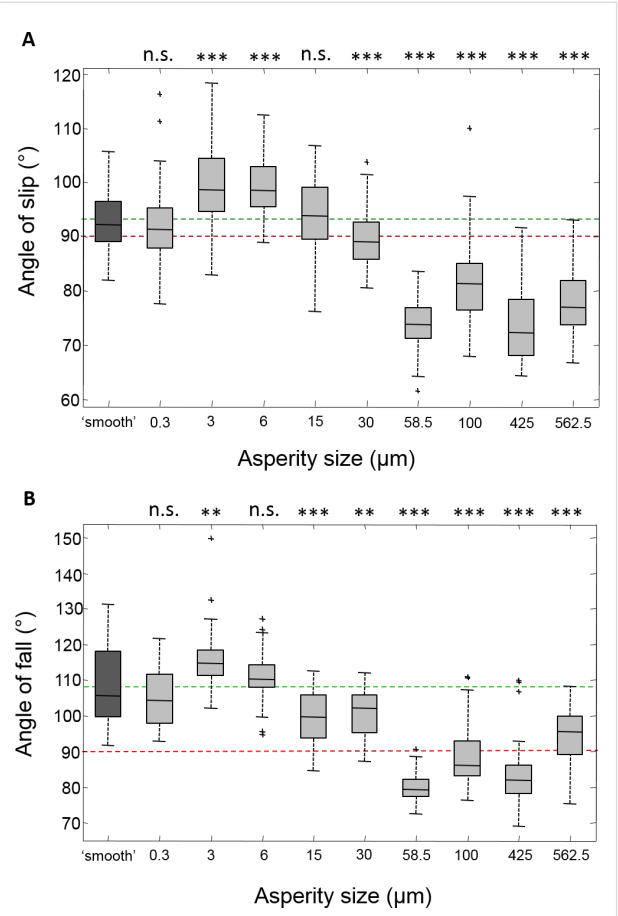

Figure 1: Box plots of slip (A) and fall (B) angles of free climbing tree frogs on different rough surfaces. Smooth glass is on the left, with increasing roughness (larger asperities) moving right across the *x*-axis. The red dashed line through 90° on the plot shows where friction forces are at a maximum, and where adhesive forces begin to play a role. The green dashed lines show mean values on the smooth surface to aid comparisons. Statistical tests which compare each surface with the smooth surface performance are shown above each box (due to the Bonferroni correction: 95% confidence interval $p = 0.0055$ (*), 99% $p = 0.0011$ (**), 99.9% $p = 0.00011$ (***), n.s. = not significant).

Slipping behaviour, an indication that frictional forces have reached their maximum, was generally not seen on the smooth surface until after 90° had been reached, and occurred at 92.89 ± 5.05°. All tests were compared to the smooth surface performance, which was the control surface. The frogs performed best on the smaller scale roughnesses, not slipping until a higher angle of 99.5 ± 7.44° on the 3 µm; this is significantly higher than the performance on the smooth ($z = -4.9915$, $p < 0.0001$). A similar result was seen on the 6 µm surface ($z = -5.7368$, $p < 0.0001$). As the roughness of the surfaces increased, this resulted in a decrease in the angle of slip. Slipping occurred before vertical (mean of 89.4°) on the 30 µm surface, significantly lower than on the smooth surface ($z = 3.6554$, $p < 0.0001$). On the largest roughnesses, frogs performed poorly, with the frogs failing to produce much friction and slipping at comparatively low angles.

The angles at which the frog fell off the surface are a measure of the maximum adhesive force produced by the frog (Figure 1B). As with friction, the frogs performed well on the smaller scale roughness, but poorly on the rougher surfaces. On the smooth surface, the frogs fell from the platform at 108.7 ± 10.9°, staying attached beyond vertical where the surface becomes an overhang. The best adhesion occurred on the 3 µm surface, the frogs staying attached until 115.2 ± 7.2° ($z = -3.388$, $p < 0.0007$). On the larger scale roughnesses (58.5 µm, 100 µm and 425 µm), the frogs usually failed to reach 90° and therefore seldom tested their adhesive ability. For the roughest surface (562.5 µm), there appeared to be some recovery, with frogs managing to stay attached until 94.9 ± 7.5° and showing some adhesive ability.

To summarise the tilting experiment, the tree frogs show significantly better performance on the smaller scale roughness (3–6 µm) compared to the smooth glass surface. However, on larger roughnesses (58.5–562.5 µm) the frogs performed worse, with frogs slipping and falling at significantly lower angles than on the glass.

Individual toe pad force measurements

In order to understand the performance of unrestrained frogs described above, the friction and adhesion of individual toe pads was measured under controlled conditions where contact area was recorded and defined surface geometries were used (see Experimental section). Single toe pads were tested on different rough surfaces ($n = 30$ for each surface tested), the extracted force per unit area measurements for adhesion and friction being plotted in Figure 2.

On smooth resin surfaces, the pads produced a mean maximum of 7.76 ± 12.9 kPa of frictional shear stress (Figure 2A). Forces initially increased with roughness, with the largest shear stresses being measured on the 6 µm surface (30.1 ± 13.8 kPa; $z = -5.1672$, $p < 0.00014$). Shear stress values on the 15 µm

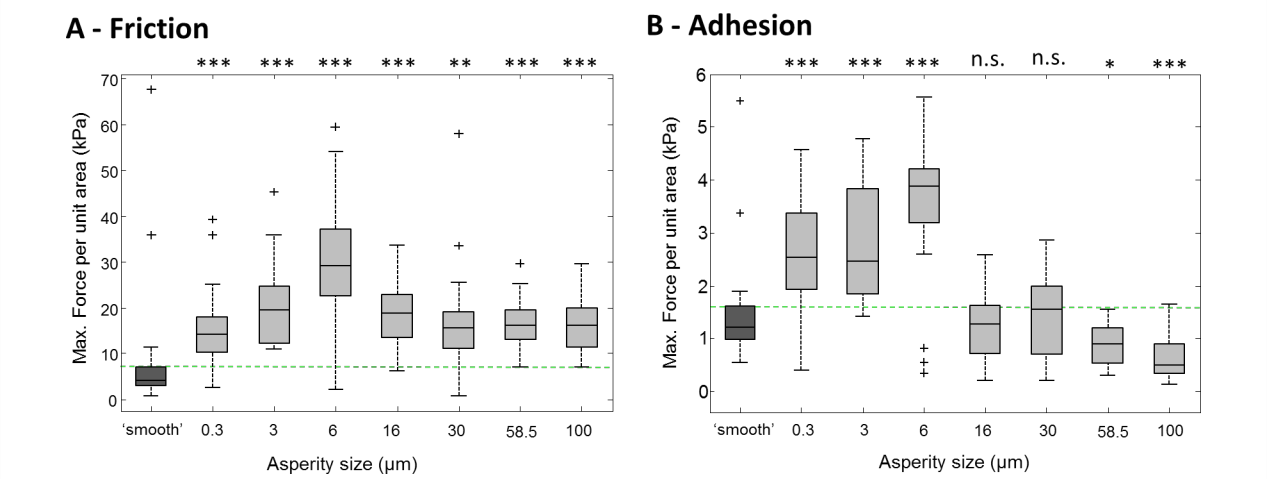

Figure 2: Single toe pad forces on rough surface replicates. Force per unit area has been calculated for friction (graph A) and for adhesion (graph B). Performances on surfaces of varying roughness (approximate asperity heights) are compared with 'smooth' surface performance (dark grey box, left). The green dashed lines show mean values on the smooth surface to aid comparisons. Statistical tests are denoted above each box (due to the Bonferroni correction: 95% confidence interval $p = 0.0071$ (*), 99% $p = 0.0014$ (**), 99.9% $p = 0.00014$ (***), and n.s. = not significant).

surfaces were 18.48 ± 6.1 kPa, higher than the smooth values ($z = -5.5663$, $p < 0.00014$), but lower than the forces on the 6 µm surface. The shear stress measured on the largest roughnesses tested were at a consistent level of ca. 16 kPa, still higher than those measured on the smooth surface (e.g., comparing smooth to 100 µm, $z = -5.5072$, $p < 0.00014$).

Adhesive forces (Figure 2B) measured were much lower than the friction forces. On the smooth surface they were measured as 1.74 ± 1.9 kPa, with peak adhesive forces occurring on the 6 µm surface (3.72 ± 1.5 kPa), significantly higher than on the smooth surface ($z = -4.4871$, $p < 0.00014$). On the two largest roughnesses tested on (58.5 and 100 µm), the adhesive forces were significantly lower than on the smooth surface, forces of 0.9 ± 0.8 kPa ($z = 3.0382$, $p = 0.0024$) and 0.66 ± 0.6 kPa ($z = 4.7828$, $p < 0.00014$) being measured for the 58.5 µm and 100 µm surfaces, respectively.

Using the same movements on the force plate, a different variation of rough surfaces made from PDMS were tested, where the only parameter changed between surfaces is the gap between the asperities on the surface. Force per unit area measurements on these rough surfaces were compared to forces measured on a smooth PDMS surface (Figure 3).

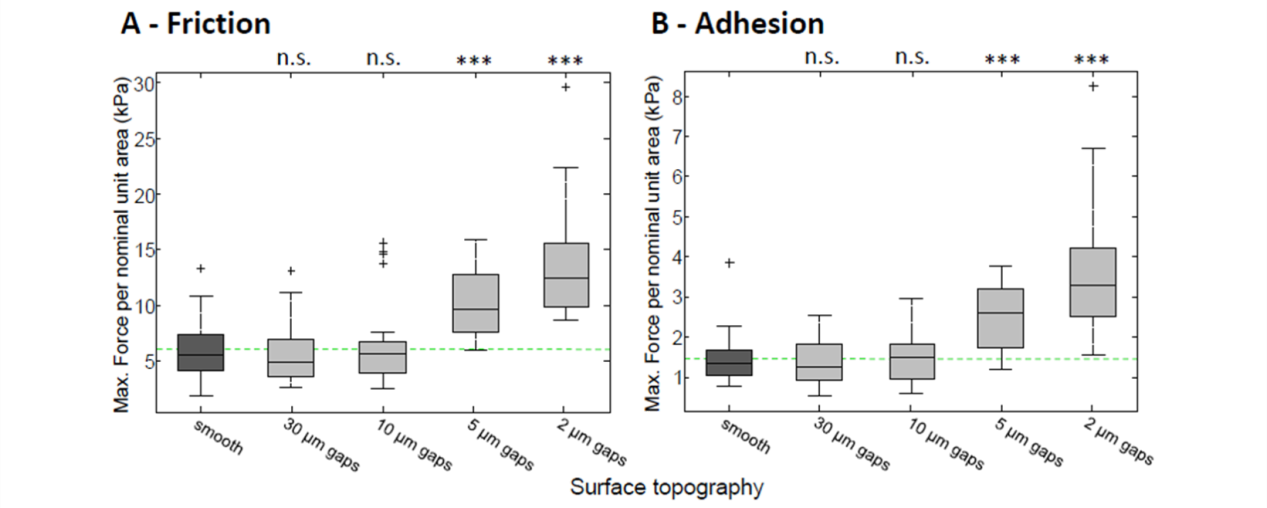

Figure 3: Force measurements of single toe pads on PDMS rough surfaces. The pads force per (nominal) unit area is shown for friction (A) and for adhesion (B), on rough surfaces (varying in the size of the gap between the asperities). They are compared to the forces produced on a smooth surface (dark grey). The green dashed lines show mean values on the smooth surface to aid comparisons. Statistical tests are denoted above each box (due to the Bonferroni correction: 95% confidence interval $p = 0.0125$ (*), 99% $p = 0.0025$ (**), 99.9% $p = 0.00025$ (***), and n.s. = not significant).

Shear stress values (n = 30) measured on a smooth PDMS surface (5.94 ± 2.6 kPa) were similar to those measured on the resin smooth surfaces. The highest friction forces were measured on the 2 µm gapped surface (13.7 ± 4.9 kPa), significantly higher than the smooth surface forces (t = −7.6879, p < 0.00025). An increase in the gap size resulted in shear stress gradually returning the levels seen on a smooth surface. Adhesive forces on the PDMS surfaces (n = 30) followed the same pattern as the shear stresses, with a peak of adhesive forces seen on the 2 µm gapped surface. Forces reached 3.49 ± 1.5 kPa, which was higher than the smooth values of 1.43 ± 0.6 kPa (p < 0.00025). An increase in the gap between pillars resulted in adhesive stress returning to smooth surface values.

To sum up the force measurements on individual toe pads, frictional forces are consistently higher than adhesive forces (>10 times so in some cases). The adhesive and frictional forces of the pads do, however, behave similarly on the rough surfaces. In particular, on the resin replicas, they both increase when roughness occurs on the small scale (i.e., on the 3 and 6 µm surfaces). At higher levels of roughness, shear stress, although lower, plateaus at a level above that seen on the smooth surface, while adhesive force declines to a lower level than on the smooth surface. Although the height of all pillars on the PDMS surfaces is the same, the gaps between them are varied. Surfaces where the pillars are close together are, in relation to the toe pads, rougher than when pillars are widely separated. Thus the highest forces are seen when the pillars are close together, the force values declining as the gaps between pillars are increased.

Using IRM to visualise pad contact

Using IRM (see Experimental section) allowed the pad/substrate contact to be visualised, where the polygonal cells of the pad can be seen to be in close contact with the surface, with channels between the cells to allow the flow of pad fluid throughout the contact area (Figure 4). This corresponds with toe pad studies previously conducted by Federle et al. [3], and allows pad/surface distances to be estimated at a cellular level. For this experiment, glass beads of different sizes were used as asperities on the surface, and the extent to which they disrupted the normal close contact of the pad to the surface recorded. The horizontal distances between the centre of each asperity and the nearest epithelial cell in close contact with the surface were measured and are plotted in Figure 5. The data has been labelled depending on whether fluid completely filled the gap between the pad, asperity and glass surface ('wet'), or whether an air pocket was present ('dry').

A general linear trend can be seen in the entire data, showing that, as bead size increases, the gap between the bead and the nearest point of pad close contact with the surface increases too (Spearman correlation test; Rho = 0.7307, n = 64, p < 0.001). For smaller bead sizes of up to 50–75 µm, the pad fluid completely fills this gap, but for larger beads, this is no longer the case and air bubbles are seen. This indicates that the size of the asperity affects whether fluid can fill the gap created by the asperity (comparison of gap distances from 'wet' and 'dry' gaps: Mann–Whitney U test, n = 48, z = 3.0466, p < 0.001). Interestingly, correlation tests on the separated data – fluid filled ('wet') or air bubbles present ('dry') show a significant linear correlation for the 'wet' measurements (Spearman correlation test; Rho = 0.7866, n = 48, p < 0.001), but not for the data points where fluid didn't fully fill the gaps (Spearman correlation test; Rho = 0.3947, n = 16, p = 0.1303). The fringes seen at the edge of the pads allow the initial slope of the pad (a linear fit through the first 4 data points, starting from the pad) as it leaves the surface to go over the bead to be measured. For all beads tested, a similar slope of the pad was seen (mean slope = 0.21 ± 0.09; n = 64), which indicates that the pad

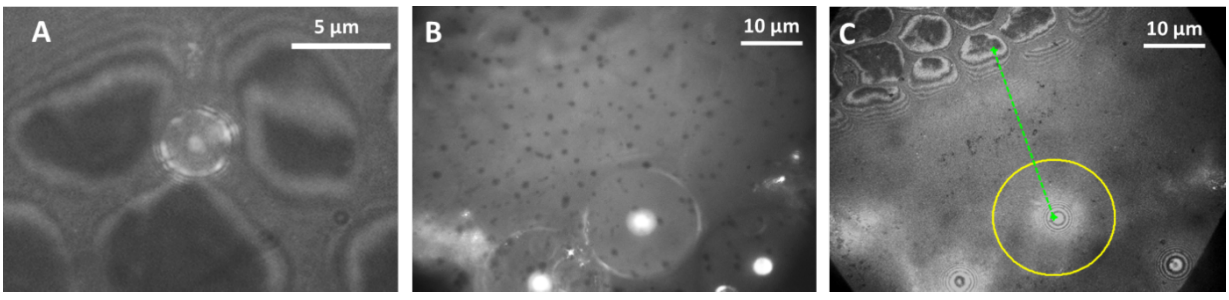

Figure 4: IRM images of the toe pad in contact around a glass bead. Interference fringes indicate the pad sloping away from the glass surface, due to the presence of a bead nearby. A) displays how smaller beads get trapped in the channels between the cells of the pad. B) and C) show two images taken at different focal planes; B) allows the circumference of the bead to be seen, which can then be recorded and superimposed on the second focal plane (C). The horizontal distance from the centre of the bead to the centre of the closest cell in close contact with the glass is marked by a green dashed line. The dark central part of each toe pad epithelial cell is the zero order dark fringe, representing a pad-glass distance of at most a few nanometres and is used as the starting point of the distance measurement, while the centre of the bead is the end point.

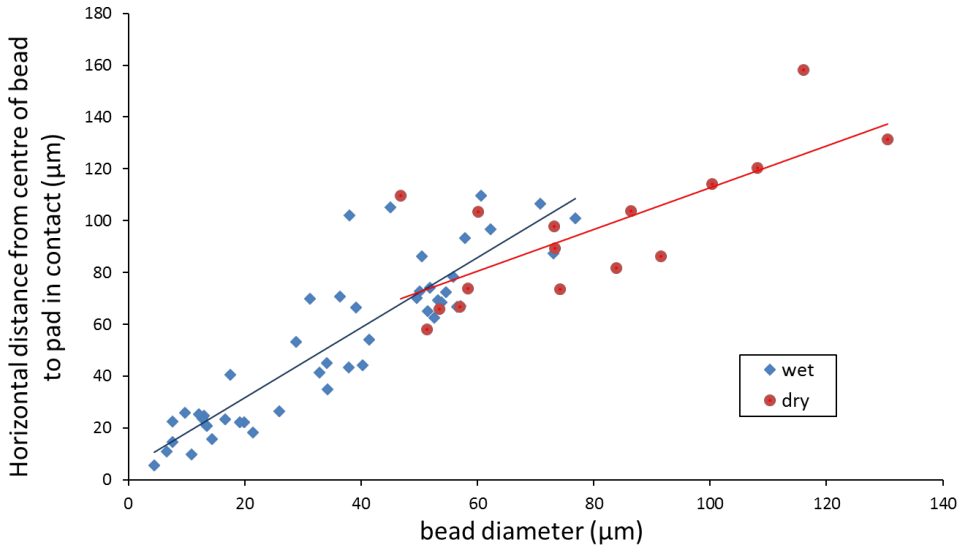

Figure 5: Scatterplot showing correlation between asperity size and pad contact (distance from bead centre to pad in contact with the surface). Data are differently coloured depending on whether fluid completely filled ('wet') or only partially filled ('dry') the gap created between the pad, bead and surface. In the latter case, the remaining space was filled by an air bubble.

is a highly soft material that can mould to the surface consistently. Indeed, the similarity of some of the measurements (Figure 6) to a sine wave indicates that bending occurs gradually (i.e., without any kinks). The degree of bending reflects the elastic modulus of the toe pad epithelium, an estimate of this appearing in the Discussion section.

Climbing on a rough and wet surface

Our experiments involving IRM indicated that frogs may be unable to produce sufficient pad fluid to fill gaps between asperities on the roughest surfaces. This would mean a loss of attachment ability as occurred on the rougher surfaces in the tilting experiment. Therefore, an additional test was done to see whether the addition of fluid to a rough surface increases the frictional and adhesive abilities of tree frogs (4 frogs used for experiments, n = 40). This was done using the tilting board apparatus, comparing the performances of frogs on a smooth glass surface and on a rough sandpaper surface under both dry and wet conditions. The 58.5 µm surface was used, as the frogs had performed poorly on this surface in the previous tilting experiment; it was also around this asperity size that air bubbles began to appear in the IRM experiments. For the wet conditions, water was sprayed onto the surface (using a water spraying mister) prior to each run of the test. As before, the angles at which the frogs slipped and fell were recorded, which relate to their frictional and adhesive abilities, respectively. Results for this experiment are shown in Figure 7.

The angles of slip and fall on the dry smooth surface (97.6 ± 6.2° for slip and 121.2 ± 6.1° for fall) were broadly similar to the results described previously (in the free climbing tree frog section). Likewise, the frogs also attached poorly to the dry rough surfaces (slip angle: 73.4 ± 4.98°, fall angle: 82.8 ± 3.7°). However, when water was introduced to the smooth surface, it caused a loss of friction in the frogs' pads. This lead to the frogs sliding at relatively low angles (66.1 ± 9.2°), which is worse than on the dry surface (z = 7.6739, p < 0.001). In contrast, when extra fluid was added to the rough surface, the frictional performance significantly improved from when the same surface was dry (Student's t-test: t = −18.3666, p < 0.001), so much so that the slip angle performance on the rough wet surface (95.6 ± 5.8°) did not significantly differ from the slip angles on a dry smooth surface (z = 1.5348, p = 0.1248).

For the angles of fall (representing maximum adhesive performance), the performance on a smooth, wet surface was lower than that on a smooth dry surface. However, even though the pads were continually slipping due to low friction, the frogs were able to stay attached until 111.9 ± 4.6°, demonstrating that they retain some adhesive ability. On the wetted rough surfaces, however, the frogs were able to adhere more strongly than when the same surface was dry. They stayed attached until 103.1 ± 7.1° when it was wet, compared to 82.8 ± 3.7° when the surface was dry (t = 16.198, p < 0.001).

These experiments show that the poor performance of frogs on the roughest surfaces can be significantly improved when the surface is wetted. However, on a smooth surface the presence of water leads to a drop in their climbing abilities, particularly frictional forces.

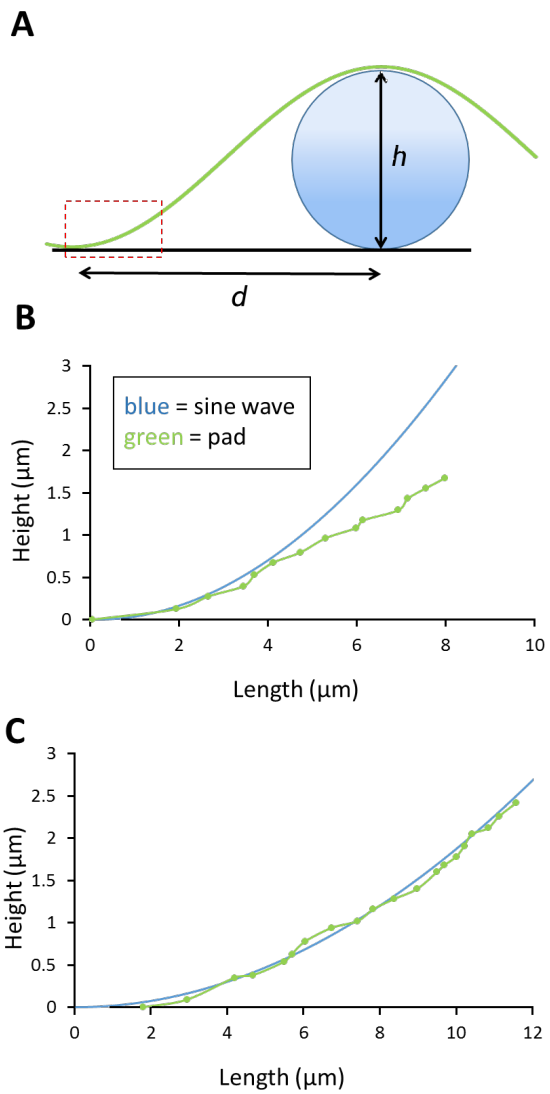

Figure 6: Modelling of the contact behaviour of the pad around a spherical asperity. A) Conceptual drawing showing the parameters used for the model. A sine wave with wavelength 2*d* was used to fit a spherical bead with diameter *h*. The initial contact of the pad separating quickly from the surface can be seen using IRM (indicated by the dashed box). B) for smaller bead sizes (here *h* = 32.79 µm) the data points only follow the sine wave initially (before showing a slope underneath the sine wave curve, indicating a soft material) whereas the fit is better for larger particle in example C (*h* = 57.92 µm).

Discussion

Tree frog adhesion

Most evidence supports the hypothesis that tree frogs adhere by capillary forces [2,13,22], but roles for other adhesive mechanisms (such as hydrodynamic forces) cannot be excluded. Indeed, it is very likely that viscosity-dependant hydrodynamic forces do play a role, as torrent/rock frogs that have toe pads like those of tree frogs [23] can adhere to rough surfaces with their toe pads completely covered in running water [8], a situation where capillary forces would be absent. Additionally, since toe pads make close contact to surfaces, a role for van der Waals forces cannot be excluded [3]. However, little evidence was found for such forces in a recent AFM study of the toe pads of *Litoria* [24]. Capillary forces are highest when the volume of fluid is at a minimum, particularly at the air–water interface around the edge of the pad, for it is the curvature of the meniscus that provides the adhesive force, either directly through tensile forces that depend on length (circumference of pad) or on pressure forces (Laplace pressure) that depend on the area under the pad [25].

Since tree frog adhesion depends upon a fluid joint and fluids tend to act as lubricants, it is surprising that tree frogs can generate high friction forces. Such forces are thought to be due to close contact between the tips of the nanopillars that cover the pad surface and the substrate. Indeed, friction forces are much larger than would be predicted by any system involving a continuous fluid layer under the pad [3].

Another important feature of toe pad fluid is its chemical composition. Although we have treated it as water in all these experiments, tree frogs appear to be able to adhere to hydrophobic surfaces just as easily as hydrophilic ones [26], which would not be the case if toe pad fluid were pure water. A preliminary biochemical analysis of the toe pad fluid [26] suggests the presence of carboxylic acids which could act as surfactants, lowering the contact angle, and thus allowing frogs to adhere to even strongly hydrophobic surfaces.

Our experiments

The whole animal tilting experiments provide direct data about the tree frog's capabilities on rough surfaces, as the slip and fall angles reflect friction and adhesive forces of the frogs [16]. With slip angles, an angle of 90° represents the maximum friction force that this technique can measure. One might therefore predict that, if a frog did not slip by 90° then it should not slip at all, but simply fall from the platform when the angle for maximum adhesion was reached. This occurred in some cases, but most of the frogs slipped before they fell. The most likely explanation of this is that, at these high angles when the frog's mass is pulling the animal away from the platform, there is a decrease in actual toe pad contact area. This means that, even if the shear stress continues to increase, the total force will eventually decline and the frog will slip. Adhesion measurements are also limited were the frog to be able to remain attached at 180° (upside-down). This often occurs with small frogs (mass: <5 g) [2], but not with the frogs used in this study.

The force measurements on single toe pads, on the other hand, provide data on the forces that can be generated by the toe pad epithelium and how they are affected by surface roughness.

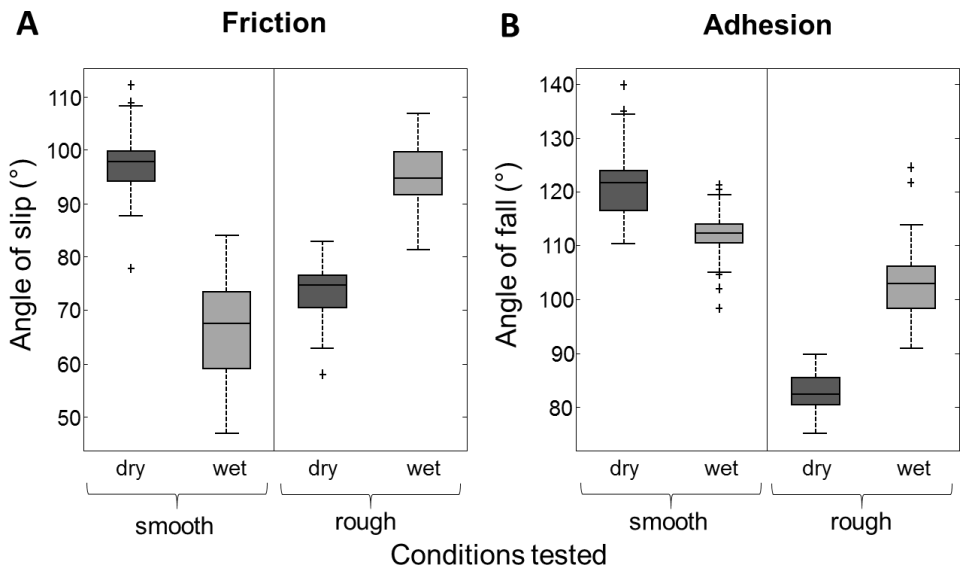

Figure 7: Boxplots displaying attachment performance of tree frogs in varying conditions. The angles of slip (A) and fall (B) of the frogs are shown for dry and wet surfaces, which could also be either rough or smooth.

Proximally-directed horizontal pulls provide information on the frictional capabilities of toe pads, while vertical pull-offs give information on adhesion. It is important to remember, however, that what is important to a climbing frog is the pull-off force, which has components of both adhesion and friction for all angles below 90° (and above 0°). The maximum adhesive capabilities of frogs can depend hugely on friction, for friction forces keep the pad/ground angle low, maximising the resultant (pull-off) force and preventing peeling of the pad from the surface [21]. Similar interactions occur in geckos [27]. This means that it is not possible to separate adhesion and friction unambiguously from whole animal tilting experiments, but the data remain useful in showing how surface roughness affects a tree frog's climbing performance.

As the frogs' sticking ability is reliant on wet adhesive forces, the fluid layer beneath the pad in contact with the surface is key to how effectively tree frogs can climb. Interference reflection microscopy (IRM), the third main technique utilised in this study, produces patterns of interference fringes between light reflected from the toe pad/fluid interface and light reflected from the coverslip/fluid interface. The fluid layer thickness can be calculated by comparing pairs of images of the same area of pad using two different wavelengths of monochromatic light [28]. This technique was first used on tree frogs to estimate the thickness of the fluid layer under the pad [3], and used here to study changes resulting from the presence of single asperities (glass spheres of various diameters). Small spheres can fit into the gaps between neighbouring epithelial cells, and air bubbles were present surrounding large spheres. Additionally, measurements of the thickness of the fluid layer immediately surrounding glass spheres of known diameter allowed for estimates of the reduced elastic modulus of the toe pad epithelium to be made (see below).

Rough surface effects on adhesion and friction

Friction: Both slip angles and friction forces on the surfaces increased as the roughness increased from very low values (a 'smooth' glass plate) (Figure 8A), reaching a peak for wavelengths in the range of 6–12 µm (spacing of asperities is approximately twice their height, as shown below in Table 1). This is in the range of the diameter of the toe pad epithelial cells (approx. 10 µm) and suggests that the large friction increase could have been due to interlocking of the tips of the asperities with the narrow channels that separate the epithelial cells (Figure 8B). Evidence for this comes from the IRM experiments, where the smallest beads used (<3 µm diameter) were

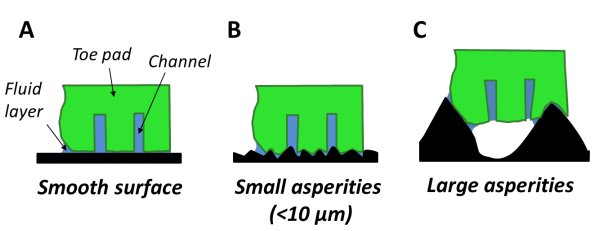

Figure 8: Simplified diagram predicting toe pad contact on different rough surfaces. Contact on a smooth surface (A) is shown, along with the pads conformity to rough surfaces with small (B) and large asperities (C).

often seen within the channels which separate the cells (Figure 4A). On the PDMS surfaces where the only variable is the spacing of the pillars, the increase in friction force was related to the density of asperities, and thus could have been caused by interlocking of the 2 μm diameter asperities with the 1–2 μm channels between the toe pad epithelial cells. An alternative explanation for this increase in friction relates to the fact that the toe pad epithelium can be thought of as a viscoelastic material and, as such, will dissipate energy when it is deformed [29]. Such energy would contribute to the friction force on rough surfaces. Indeed, such viscoelastic deformations can also enhance adhesion [30]. For larger roughnesses on the polishing disc surfaces (particle size ≥ 30 μm), slip angles are well below the values obtained on the 'smooth' surface, while single toe pad friction forces on the replicas remained higher than 'smooth' surface forces. Since friction in tree frogs has been shown experimentally to scale with area [31], and real contact area is increased on a rough surface, the increase in the friction force in relation to the glass surface would be predicted. But why did it not occur in whole animal experiments? A clue to the answer comes from the whole animal experiments where wet and dry surfaces were compared (Figure 7). Wetting the surface significantly increased slip angles on rough surfaces, presumably because the added water reduced the occurrence of air bubbles, such as those seen around large asperities in the IRM experiments. In the presence of such air bubbles, contact between pad and surface would be reduced rather than increased (Figure 8C). However, this explanation poses the question as to why air bubbles appear in whole animal experiments but not in the single pad force experiments. It could be explained by tree frogs toe pads not producing much fluid, and leaving some behind after every step. It is likely that a frog trying to hang on to a rotating platform will have a significantly thinner layer of fluid than in the force plate experiments, where only single measurements were made from any one toe pad (see Experimental section).

The tilting experiments of Endlein et al. [8] revealed a similar result, with the increase in roughness leading to lower fall angles under dry conditions. The addition of water led to an improved adhesive performance, but slipping occurred more frequently. Often, these slips were transient, the frogs reattaching after a slide of at most a few centimetres [8]. During such slides, fluid is removed from under the pad, the reattachment potentially occurring when the fluid thickness is sufficiently reduced for close contact to re-occur. As discussed by Hutt and Persson [32], any tendency for the pads to detach will be resisted by the reduction in pressure that develops in the thin film under the pad, which presses the pad to the substrate and therefore acts as a strong hydrodynamic adhesive (viscous adhesion). There must therefore be a fine balance for frogs with respect to the volume of pad fluid that they produce for effective climbing on a wide variety of surfaces. It is unclear how the fluid production is controlled in frogs, but as fluid is often left behind in steps [33], it must be replenished frequently.

Adhesion: For both fall angles and single pad adhesive forces, the pattern shows many similarities with slip angle/single pad friction force values. Fall angles were significantly higher on the 3 μm surface compared to the smooth surface, while single pad adhesive stresses were significantly increased for the 0.3, 3 and 6 μm resin surfaces. Such increases replicate the effects of fine rough surfaces on friction, and probably have a similar explanation. As adhesion has been experimentally shown to scale with pad area [13], and real contact area is increased on a rough surface, such fine rough surfaces could explain an increase in adhesive force. The increase in adhesion on the PDMS surfaces with higher densities of asperities probably has a similar explanation. On the surfaces with larger particle sizes, both fall angles and the adhesive stresses of single pads are reduced. These reductions may be due to loss of close contact and the presence of gaps in the fluid layer (seen with larger beads in the IRM experiments). There are two possible explanations for the presence of air bubbles under the pad in this situation, which are not mutually exclusive. First, the frogs may not be able to produce enough fluid to fill the increased space around the asperities. Second, the increased roughness may increase the drainage of fluid from the pad. Whatever the explanation, wetting the rough surface resulted in a significant increase in adhesion (Figure 7) as it would have reduced the numbers of air bubbles trapped below the pad. Reductions in the fall angles may also be caused by reductions in the friction forces. As described above, this would lead to sliding, which would cause an increase in the pad/surface angle with a concomitant reduction in the pull-off force (peeling theory of Kendall [34]). Interestingly, on the largest asperities tested, (the 562.5 μm beads surface), the frogs began to show an increase in adhesive ability (also noted by Barnes et al. [15]). This could be due to the beads' diameter being close to that of the frog's toe pads (area ca 4 mm^2); therefore close contact could be made by a significant proportion of the pad on the bead. This effect has also been seen in geckos, where adhesive forces on larger roughnesses were high, due to a restoration of spatula contact on each asperity [35].

Estimation of the elastic modulus of the toe pad

As described above, friction (and to a lesser extent adhesion) can be enhanced on rough surfaces by interlocking when the size and distribution of asperities matches the pattern of micro- or nanostructures on the surface of the toe pads. Since the toe pad epithelium is made of a relatively soft material, there is the

additional possibility that it will conform around asperities, further increasing friction and adhesion. Here we have made direct measurements of the conformation of the toe pad surface to asperities of known size, which can lead to estimates of the Young's modulus of tree frog toe pads. A similar analysis was used by Lorenz et al. [35], who studied the influence of contamination particles on the adhesion of viscoelastic materials.

Using interference reflection microscopy, which allows one to estimate fluid depth under the pad, it was possible to measure *d,* the distance between the centre of the glass bead and the nearest point of close contact of the pad with the glass surface. This is shown diagrammatically in Figure 6, which also shows some data points that are calculations of the fluid depth from interference minima seen under the microscope. Although the pad would not be expected to exactly follow a sine wave (as drawn on the figure), the data points indicate that the shape of the pad surface approximates to such a curve. The distance *d* is plotted against bead diameter in Figure 5. For small beads, the space surrounding the pad was entirely fluid-filled (plotted in blue). For larger beads, there were frequently air pockets as well (plotted in red).

To estimate the modulus, first consider the flat toe pad in contact with a flat underlying surface. The introduction of an asperity (e.g., a spherical bead) underneath the tree frog's foot will lead to an elastic energy penalty associated with the deformation of the toe pad as well as a change in surface energy associated with the interface opening. Assuming the bead and the underlying surface are infinitely stiff compared to the toe pad, only the soft toe pad will deform to accommodate the asperity. The total energy (U) of the system is then given by the elastic energy of the toe pad deformation and the surface energy of the opening by $U_{total} = U_{elastic} + U_{surface}$. We approximate the elastic energy according to Hertz theory with an indentation depth of h (i.e., bead diameter) and bead radius R, leading to $U_{elastic} = 4/3E^*R^{1/2}h^{5/2}$. Since the glass bead is taken to be infinitely stiff, here $1/E^* = (1 - \nu^2)/E$ where ν is Poisson's ratio of the toe pad (taken to be 0.5), the surface term is given by the circular opening that is produced by the asperity as $U_{surface} = \pi d^2 W$, where d is the distance from the bead to the pad in contact (i.e., the circular opening radius) and W is the work of adhesion. As the bead size increases, the opening size also increases as suggested by profiles presented in Figure 6. We thus make the assumption that $R \sim d/2$. This allows for the minimization of the energy dU_{total}/dd, leading to an approximated relationship between the bead size and opening size of $d^{3/2} \cong 4Eh^{5/2} / 9\sqrt{2}\pi W$. An elastic modulus can be estimated by plotting $d^{3/2}$ vs $h^{5/2}$ (Figure 9) with the slope scaling with the inverse of the so-called elastocapillary or elastoadhesive length scale, E/W.

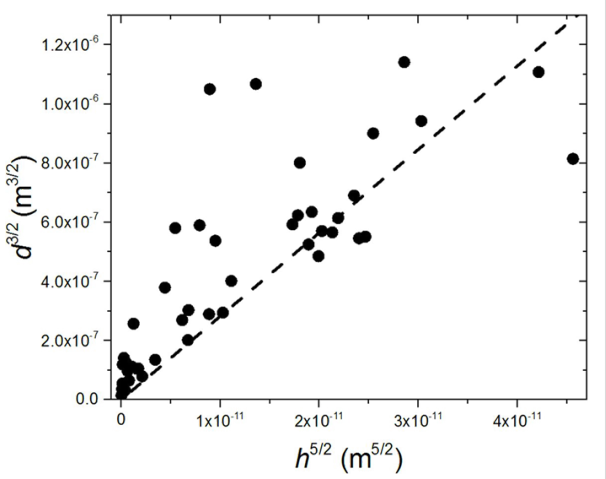

Figure 9: Graph of $d^{3/2}$ against $h^{5/2}$, where d is the distance from the nearest area of close contact to the bead centre and h is the diameter of the bead (see Figure 6A). The slope of the line of best fit enables the Young's Modulus of the pad to be estimated.

Using a value for the work of adhesion of 70 mN·m^{-1}, estimated for tree frog toe pads by Barnes et al. [19], and the slope of the best fit line of the $d^{3/2}$ vs $h^{5/2}$ plot in Figure 9, the elastic modulus is calculated to be $E \sim 20$ kPa. Indeed, the estimate here is comparable to the results of indentation experiments carried out on tree frogs by Barnes et al. [19] and Barnes et al. [18] which showed equivalently low toe pad elastic modulus values (in the 5–40 kPa range).

Although our results are consistent with prior reports, we note that there are a few points regarding our current analysis that should be taken with precaution. Our assumption of $2R \sim d$ excludes additional pre-factors and neglects the interface between the top of the bead and the toe pad that may also influence the calculated modulus. However, by observation of the relationship between R and d presented in Figure 5, we believe that our assumption is reasonable within a factor of 2. Additionally, the assumed work of adhesion may also be an overestimation since the fluid underneath the toe pad likely changes the interfacial energy. Such values, however, would also be within a factor of about 2. For example, a commonly used value for the work of adhesion of living tissue is 30 mN·m^{-1}. If such a value were substituted for the 70 mN·m^{-1} value used above, the resulting modulus would be closer to $E \sim 10$ kPa. Therefore, the elastic modulus found here is within the range of reported values in the literature [18,19,24].

Comparing performance with other climbing organisms

Several previous studies have examined the effect of surface roughness on the climbing capabilities of other adhesive pad bearing organisms. These include animals with hairy rather than

smooth adhesive pads, as well as animals which possess claws as well as adhesive pads. Additionally, there are studies of plant surfaces that have evolved to be anti-adhesive as far as insects are concerned.

The effects of surface roughness on animals with hairy pads (geckos, spiders, insects such as beetles) are reasonably predictable. When the particle size is big enough for the tip of the hair (often a spatula) to make full contact, adhesion and friction forces are similar to those on smooth surfaces. Only when the spatula size is larger than the particle size do the forces decline. For instance, the setal hairs of geckos are built so that they can adapt (acting like a soft material) and conform to rough surfaces of different length scales [36]. Their setae work least effectively on surfaces where the contact area of individual spatulae is split between several asperities (100 to 300 nm root mean squared roughness) [36]. Traction experiments in spiders yielded a similar result, with their adhesive hairs performing poorly when asperity sizes were between 300 nm and 1 μm [37].

The attachment of smooth adhesive pads is more complex. From our data, there is evidence of enhanced adhesion and friction when the wavelength of the surface is similar to that of the pad epithelial cells. Under such conditions, interlocking can occur, as has also been recorded in the euplantulae of stick insects, which consist of frictional ridges [38]. Larger scale roughnesses, on the other hand, appear to result in lower forces. In part this is due to insufficient fluid to fill the gaps between asperities. Kovalev et al. [39] found a similar result in flies (which have hairy pads), where fluid loss was related to the density of asperities. Attachment is also affected by the pad's stiffness, a low elastic modulus leading to improved moulding of the pad to asperities. The most relevant study in this regard is that of Zhou et al. [17], who tested both the smooth insect pads of cockroaches and the hairy adhesive pads of beetles on nanofabricated surfaces with controlled roughness parameters (the height and spacing of asperities), and found that both parameters affected whether the pads made full or only partial contact with the surface. Such a result indicates that the stiffness of the adhesive pad is another critical parameter in adhesion to rough surfaces, whether the pads are smooth or hairy. This analysis enabled the pad's effective elastic modulus to be estimated, by a rather more precise methodology than used here. The low values obtained in this study, which are similar to those of other studies [18,19,24], indicate that moulding of the pad surface to asperities will also occur in tree frogs, and will be a major factor in their ability to adhere to rough surfaces. Where insufficient bending occurs (see Figure 8C), air bubbles are likely to be formed, with a consequent reduction in adhesion.

Many climbing organisms utilise claws to climb on rough surfaces, which can interlock with asperities on vertical surfaces – this is seen in geckos [40], spiders [41] and many insects [42,43]. However the effectiveness of a claw is usually dependent on the asperity size being larger than the claw tip diameter [44]. When the claws fail to interlock on the surface, staying attached relies on the adhesive pads of the organism [45]. On the basis of tests with an artificial insect leg, Song et al. [46] claim that, in situations where both claws and pads are both operating, the total force may even exceed the sum of the forces that either system, acting on its own, would have produced.

A number of plants have evolved structures that deter insects (e.g., *Macaranga* trees [12]) or attempt to capture them (e.g., pitcher plants [47]). In both cases, the surfaces will be slippery or otherwise non-adhesive. In many cases, the slipperiness is produced by surfaces covered by epicuticular wax crystals, which break off, contaminating the insect's adhesive pads [48]. The fine cuticular folds on many surfaces of carnivorous plants may serve a similar function [9].

Conclusion

In this study, it was shown that tree frog adhesion and friction are significantly affected by surface roughness. Small scale roughness may increase adhesion/friction due to interlocking of asperities with the channels that separate the toe pad epithelial cells. However, in spite of the pad's low elastic modulus, large scale roughness usually has the opposite effect due to the pad's inability to mould to the asperities, leading to air bubbles appearing beneath the pad surface. Despite these limitations, tree frogs are still able to generate large forces when landing on a horizontal wooden rod with just one or two toe pads following a jump [49]. They can also climb the narrow twigs and branches of their natural environment by combining adhesion/friction with the ability to grasp even very small twigs [50]. We are thus building up a good understanding of both the underlying mechanisms and the ecology of tree frog adhesive mechanisms. But this study goes further: comparable to the drag reduction mechanisms of snake skin [51], the superhydrophobicity and self-cleaning mechanisms of lotus leaves [52], and the adhesive setae of geckos [53] the toe pads of tree frogs exhibit significant biomimetic potential to advance the technology of surface engineering. This is because they combine high friction under wet conditions [3] with self-cleaning [33]. Their main applications will likely be in the medical field, as Chen et al. already demonstrated their potential for use as surgical graspers [54].

Experimental

Experimental animals

Tree frogs *Litoria caerulea* (n = 8), were used in these investigations. Their mass was 16.7 ± 6.5 g (mean ± standard devia-

tion) and snout-vent length 57.6 ± 5.5 mm. The frogs were kept in vivaria (30 × 45 × 76 cm high) containing plants and dishes of chlorine-free fresh water at a temperature of approx. 28 °C. They were fed live crickets three times a week, dusted with a multi-vitamin supplement (Nutrobal, purchased from Peregrine Live Foods, Ongar, Essex, England). Before experimentation, the frogs were rinsed in chlorine-free water to remove any dirt or loose dead skin, and carefully blotted dry to prevent the excess water from affecting the frogs' performance.

Rough surfaces

Two different kinds of rough surfaces were used in this study, which displayed different topographic features (random asperities and regular patterns).

For whole animal tilting experiments, the rough surfaces (35 × 21 cm) used consisted of eight different grades of polishing discs and sandpaper (made from Aluminium oxide) from multiple sources (3M, USA; Norton abrasives, France; Ultratec, USA), a surface made from a monolayer of 1125 µm glass beads (Ballotini beads, Jencons, VWR International, Leicestershire, UK) and a control surface consisting of a glass plate. Thus, whilst the middle eight of these surfaces had identical surface energies (untested here), the roughest surface differed in both chemistry and the nature of the roughness, since glass beads are spherical, whilst the particles on sandpaper are, by their very nature, much more angular with sharper peaks formed by the particulate asperities on them.

For individual toe pad force measurements, replicas were made of the original surfaces using a low viscosity resin (TAAB laboratories equipment Ltd, UK). The use of resin provided a hard, transparent material that mimicked the sandpapers' structure by accurately conforming before setting. Their transparency allowed us to measure pad contact area optically. R_a values for both the originals and the replicas were measured using a Dektak stylus surface profiler (Veeco Dektak 6M Height Profiler, USA. Vertical resolution 0.1 nm) and shown in Table 1.

Fabricated rough surfaces with regular patterns of asperities were used exclusively for single toe pad force measurements, due to the fact that the surfaces could only be reproduced as small surfaces (ca 20 × 20 mm). These surfaces, made of polydimethylsiloxane (PDMS) were designed to provide transparent surfaces that would allow contact area to be visible through them as well as to provide standardised topographies whose specific dimensions were under experimenter control. The PDMS surfaces were fabricated using moulds kindly made by Dirk Drotlef at the Max Planck Institute for Polymer Research in Mainz. Moulds were created from thin silicon wafers, with micro-patterns etched onto the surface using microlithographic processing. This involves laying down a layer of SU-8 photoresist, then applying a mask to remove specific areas of resistance, and then etching the exposed areas to give the desired patterns. The moulds were negatives of the PDMS patterned surfaces, which produced surfaces consisting of round dimples having fixed measurements for both height (3 µm) and diameter (2 µm) for all surfaces used. Variation between surfaces came in the gap between each asperity. Gap sizes tested were 2, 5, 10 and 30 µm apart, with a smooth PDMS surface acting as a control. SEM imaging confirmed that the surfaces were successfully made (Figure 10D,E). Gap width was selected as the experimental variable, as this was considered the simplest single parameter to change to view the effects on real contact area and thus adhesive force.

PDMS is hydrophobic by nature, and so to cancel out any possible effect that surface energy may have on adhesive forces, the surfaces were plasma treated to make them uniformly

Table 1: List of average roughness values (R_a, in µm) for surfaces used in experiments (polishing discs/sandpaper and their resin copies). The wavelength (width of the asperities) was measured by viewing the surfaces under a microscope.

Surface (approx. asperity height)	Original surface R_a (µm)	Resin surface R_a (µm)	Wavelength (µm)
glass cover slip	0.01	0.02	–
0.3 µm	0.21	0.33	1.2
3 µm	1.4	1.6	8.3
6 µm	3.7	2.9	16
16 µm	4.6	5.4	29
30 µm	6.8	6.6	57
58.5 µm	15.5	14.1	100
100 µm	21.5	22	250
425 µm	33.3	–	833.3
562.5 µm (beaded surface)	127[a]	–	1125

[a]The R_a value of the 562.5 µm (beaded surface) was calculated using the formula in Supporting Information File 1.

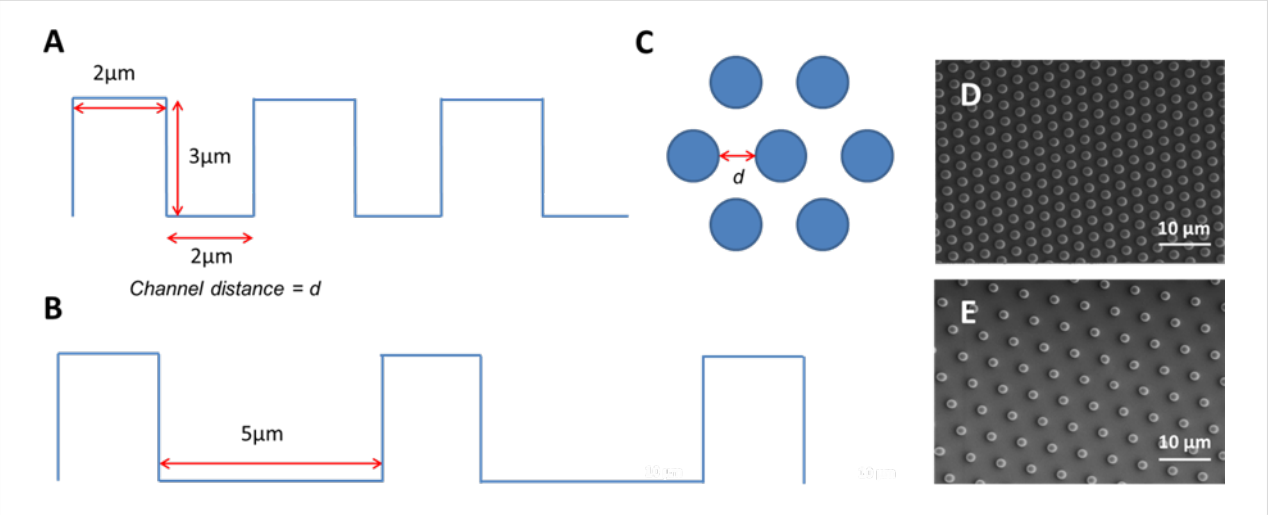

Figure 10: Diagram illustrating the topography of the PDMS structured surfaces. Each pillar on the surface has the same height and diameter, but varies in the gap between each pillar (d). Images A and B display gaps of 2 and 5 µm respectively, while image C shows the layout of pillars from above. Images D and E (gaps of 2 and 5 µm respectively) are SEM images of examples of the PDMS structured surfaces.

hydrophilic before being used each time. Although the precise pad fluid composition is unknown, the capillary forces they use rely on low contact angles with the surface, and so a hydrophobic surface has the potential to be detrimental to adhesion if the fluid is water based, which is still being investigated (as mentioned in the discussion). Plasma treatment involves placing the PDMS sample into a plasma cleaner (Harrick Plasma Inc., NY, USA). Tests were carried out within an hour of plasma treatment.

Tilting platform apparatus

To test the climbing performance of tree frogs on varying rough surfaces, attachment ability was measured using a tilting platform as used in several previous studies [8,13,16,31]. In this study, the frogs were placed on the rotating platform in a head up posture, and were tilted from a horizontal position (0°) to upside down (180°), to see at what angles the frogs would slip and fall from the board. Rotation was controlled by a Stuart SB3 rotator (Bibby Scientific Ltd, UK), which kept a constant rotation speed of approximately $4 \pm 1°\ s^{-1}$. The platform itself consisted of a wooden board (21 × 35 cm), to which the different rough surfaces could be attached using binder clips. A smooth glass surface acted as a control. The slip and fall angles for frogs on all of the surfaces were then compared to the control performance. Surface testing was continuously randomised to reduce any potential effect that fatigue could have on results.

The frog was encouraged to stick to the platform to the best of its abilities – a hand being waved around the frog to discourage it from jumping off the board. Whilst the frog was rotated, two angles were measured: when the frog began to slip (indicating maximum friction angle) and when the frog detached from the surface (indicating maximum adhesive angle). The angles were measured using a potentiometer attached to the back of the axial rod of the rotating board, and recorded using a custom LabView interface (LabVIEW Inc., National Instruments, USA). Angles can be converted to forces, so long as the mass of the frog is known, by simple equations (see [13]). These simple experiments have limitations, for the maximum friction force occurs at 90°, and the maximum adhesive force at 180°. Thus maximum friction force for any frog can only be calculated if slipping occurred before 90° and maximum adhesive force if falling occurred before 180°.

Measuring forces of single pads

Using a similar setup to Crawford et al. [33] the maximum friction and adhesive forces for individual toe pads were measured. A custom built force transducer, composed of strain gauges connected to a bending beam, was used to measure lateral (friction) and normal (adhesive) forces of the toe pad. The plate attached to the bending beam was interchangeable, allowing surfaces of differing roughness to be attached. The resin surfaces could be glued directly onto the bending beam, whilst the PDMS surfaces were attached to a ≈ 1 mm thick piece of flat polyethylene (15 × 15 mm), which had a small opening where the PDMS was situated to avoid impeding the visualisation of contact area. Since the PDMS surface was relatively thick and the hole in the polyethylene small, bending of the PDMS material whilst measuring forces was negligible.

The frog was restrained in a petri dish by a foam cushion which surrounded the body, with one leg extending out from the dish. Light suction on the dorsal side of the toe allowed alignment of

the pad with the force plate surface. The frog was then positioned so that the pad rested on the force plate which could be moved relative to it by a pair of computer-controlled precision manipulating stages (model PD-126M, Physik Instrumente, Karlsruhe, Germany). A force feedback system implemented in LabView was programmed to maintain a constant preload (2 mN) for measurements of friction forces. Simple LabView programs (similar to those used in Crawford et al. [33]) were used to move the pad over the force plate so that maximum frictional and adhesive forces could be measured. This involved a proximal lateral drag (5 mm drag at 1 mm s^{-1}), followed by a vertical pull off.

Above the setup, a camera (Basler, A602F 100 fps; Ahrensburg, Germany), attached to a stereo microscope (Wild Heerbrugg, Switzerland), allowed the pad area to be visualised during each measurement using coaxial illumination (light travelling through the optical path). This resulted in the pad showing darkly against a bright background. For some samples (particularly the resin surfaces) an additional external source of illumination was required to see the pad contact area with more clarity. Contact area was extracted in conjunction with the force measurements using a customised MATLAB script (Mathworks, Natick, USA) to give force per unit area (stress).

Once a successful trial had been conducted, the frog was either repositioned so that another toe pad was measured, or replaced with another frog. In this way, no pad was tested more than once, avoiding the possibility of reducing the available pad fluid with consequential effects on the force measurements. 30 trials were recorded on each surface.

Visualising pad contact

In order to gain further understanding of pad contact on rough surfaces, the contact area of the pad around individual asperities was visualised using interference reflection microscopy (IRM). Used on frogs previously by Federle et al. [3], IRM allows one to measure the thickness of the fluid layer beneath the pad and, in our experiments, the extent to which the pad epithelium moulds itself around asperities. The dark (minimum) and light (maximum) interference fringes represent interference between light reflected from the top surface of the coverslip on which the toe pad is resting and from the surface of the toe pad. By comparing images of the same group of cells using two different illuminating wavelengths, 436 nm (blue light) and 546 nm (green light) are most commonly used, it has been shown that the dark centres of each toe pad epithelial cell (Figure 4) are zero order dark fringes, representing distances of at most a few nanometers [3]. The distance between fringes depends on the refractive index of the coverslip and the wavelength of the monochromatic light (λ). The distance (d) between individual fringes can be calculated as (adapted from [45]):

$$d = \frac{\lambda}{4\eta\text{fluid}\left(1-\sin\left(\frac{\alpha}{2}\right)^2\right)}$$

where λ is the wavelength of the light and ηfluid is the refractive index of the toe pad fluid (1.335 according to measurements by [3]), and α = arcsin(INA/ηfluid) with INA being the illuminating numerical aperture.

Using this technique, it was possible to measure the degree of conformation of the soft pad surface to spheres of different sizes, which provided important insights into effects of different roughness scales on adhesion and friction. It also enabled us to estimate the Young's Modulus of Elasticity for the toe pad epithelium.

Individual frogs were restrained as in the single toe pad force measuring setup in such a way that a single toe pad made contact with a large coverslip (20 × 40 mm). The microscope, a Zeiss Axiovert 200M inverted microscope (Zeiss, Oberkochen, Germany) was set up for IRM, with bandpass filters within the illumination path to provide monochromatic light (546 nm, green light) and a custom built pinhole slider which defined the illumination numerical aperture (measured as 1.001) and reduces stray light. A high power objective lens (×63) was used so that individual cells could be visualised. A camera attached to the microscope (Evolution EX1, Princeton instruments, New Jersey, USA. Image dimensions: 1390 × 1040 pixels) recorded images of pad contact at the cellular level, allowing pad conformity around an asperity to be calculated as described above.

For the experiments, the glass surface was randomly covered with glass beads (Ballotini beads, Jencons, VWR International, UK) of various sizes, ranging from 4.48 μm to 130.51 μm in diameter. The pad was then brought into contact with the surface and the beads to see how well it could conform to the beads present. Using Matlab scripts written specifically for this technique, the distance between the point where the pad is in close contact (seen as the dark patch in the centre of each cell) and the centre of the bead could be measured (Figure 4). This allowed the effect of bead size on the gap size to be investigated. The spacing of the interference fringes from the point of closest contact allows the angle of the pad to the glass coverslip to be calculated, providing more detailed information on the effect of asperities on pad/substrate contact. With large beads, there was insufficient fluid underneath the pad to completely fill the gap, and air bubbles could be seen. Such bubbles would be expected

to reduce the adhesive forces that the pads could produce on such surfaces.

Statistical analysis

Statistical analyses for all the experiments were done using the statistic toolbox in Matlab r2011a. A Lilliefors test was used to determine the normality of each set. Depending on normality of the data, either a student *t*-test or a Wilcoxon rank sum test (also known as a Mann–Whitney U test), was used to compare pairs of data sets, both for the whole animal and single toe pad experiments. For the IRM experiments, linear rank correlation tests were conducted. Data used for multiple tests are corrected using a Bonferroni correction. Ranges of values are indicated by mean ± standard deviation. Boxes in the boxplot figures denote 25th and 75th percentiles, the whiskers display 99% of the data, the middle line shows the median, while outliers are shown as plusses (+).

Supporting Information

Supporting information explains the calculations of the average roughness (R_a) of a uniform monolayer of beads on a surface.

Supporting Information File 1

Calculating the R_a of a uniform bead monolayer surface.
[http://www.beilstein-journals.org/bjnano/content/supplementary/2190-4286-7-201-S1.pdf]

Acknowledgements

We wish to thank Dirk Drotlef (MPI for Polymer Research, Mainz, Germany) for creating the moulds used to make the PDMS surfaces in the force measurement experiments, Michael Kappl (Max Planck Institute for Polymer Research, Mainz) for useful discussions, and Ian MacLaren (University of Glasgow) for help and advice on calculating average roughness on a beaded monolayer surface. This research was supported by the German Research Foundation (Deutsche Forschungsgemeinschaft, DFG), Priority Programme SPP1420, "Biomimetic Materials Research: Functionality by Hierarchical Structuring of Materials". J.T.P. was supported by a fellowship from the Alexander von Humboldt Foundation."

References

1. Crawford, N. A. The biomechanics of tree frog adhesion under challenging conditions. Ph.D. Thesis, University of Glasgow, United Kingdom, 2016.
2. Hanna, G.; Barnes, W. J. P. *J. Exp. Biol.* **1991,** *155,* 103–125.
3. Federle, W.; Barnes, W. J. P.; Baumgartner, W.; Drechsler, P.; Smith, J. M. *J. R. Soc., Interface* **2006,** *3,* 689–697. doi:10.1098/rsif.2006.0135
4. Barthlott, W.; Neinhuis, C. *Planta* **1997,** *202,* 1–8. doi:10.1007/s004250050096
5. Koch, K.; Bhushan, B.; Barthlott, W. *Soft Matter* **2008,** *4,* 1943–1963. doi:10.1039/b804854a
6. Bhushan, B. *Introduction to Tribology;* Jon Wiley & Sons, Inc.: New York, NY, U.S.A., 2002.
7. Scherge, M.; Gorb, S. N. *Biological Micro- and nanotribology: Nature's Solutions;* Springer: Berlin, Germany, 2001. doi:10.1007/978-3-662-04431-5
8. Endlein, T.; Barnes, W. J. P.; Samuel, D. S.; Crawford, N. A.; Biaw, A. B.; Grafe, U. *PLoS One* **2013,** *8,* e73810. doi:10.1371/journal.pone.0073810
9. Prüm, B.; Seidel, R.; Bohn, H. F.; Speck, T. *J. R. Soc., Interface* **2012,** *9,* 127–135. doi:10.1098/rsif.2011.0202
10. Prüm, B.; Bohn, H. F.; Seidel, R.; Rubach, S.; Speck, T. *Acta Biomater.* **2013,** *9,* 6360–6368. doi:10.1016/j.actbio.2013.01.030
11. Barthlott, W. Scanning electron microscopy of the epidermal surface in plants. In *Scanning electron microscopy in taxonomy and functional morphology;* Claughter, D., Ed.; The University of California: Clarendon for the Systematics Association: CA, U.S.A., 1990.
12. Federle, W.; Maschwitz, U.; Fiala, B.; Riederer, M.; Hölldobler, B. *Oecologia* **1997,** *112,* 217–224. doi:10.1007/s004420050303
13. Barnes, W. J. P.; Oines, C.; Smith, J. M. *J. Comp. Physiol., A* **2006,** *192,* 1179–1191. doi:10.1007/s00359-006-0146-1
14. Smith, J. M.; Barnes, W. J. P.; Downie, J. R.; Ruxton, G. D. *J. Zool.* **2006,** *270,* 372–383. doi:10.1111/j.1469-7998.2006.00145.x
15. Barnes, W. J. P.; Smith, J. M.; Oines, C.; Mundl, M. *Tire Tech. Int.* **2002,** 56–60.
16. Emerson, S. B.; Diehl, D. *Biol. J. Linn. Soc.* **1980,** *13,* 199–216. doi:10.1111/j.1095-8312.1980.tb00082.x
17. Zhou, Y.; Robinson, A.; Steiner, U.; Federle, W. *J. R. Soc., Interface* **2014,** *11,* 20140499. doi:10.1098/rsif.2014.0499
18. Barnes, W. J. P.; Baum, M.; Peisker, H.; Gorb, S. N. *J. Morphol.* **2013,** *274,* 1384–1396. doi:10.1002/jmor.20186
19. Barnes, W. J. P.; Goodwyn, P. J. P.; Nokhbatolfoghahai, M.; Gorb, S. N. *J. Comp. Physiol., A* **2011,** *197,* 969–978. doi:10.1007/s00359-011-0658-1
20. Persson, B. N. J. *J. Phys.: Condens. Matter* **2007,** *19,* 376110. doi:10.1088/0953-8984/19/37/376110
21. Endlein, T.; Ji, A.; Samuel, D. A.; Yao, N.; Wang, Z.; Barnes, W. J. P.; Federle, W.; Kappl, M.; Zhengdong, D. *J. R. Soc., Interface* **2013,** *10,* 20120838. doi:10.1098/rsif.2012.0838
22. Endlein, T.; Barnes, W. J. P. Wet adhesion in tree and torrent frogs. In *Encyclopedia of nanotechnology, Part 2;* Bhushan, B., Ed.; Springer: Berlin, Germany, 2015; pp 1–20. doi:10.1007/978-94-007-6178-0_257-2
23. Drotlef, D. M.; Appel, E.; Peisker, H.; Dening, K.; del Campo, A.; Gorb, S. N.; Barnes, W. J. P. *Interface Focus* **2015,** *5,* 20140036. doi:10.1098/rsfs.2014.0036
24. Kappl, M.; Kaveh, F.; Barnes, W. J. P. *Bioinspiration Biomimetics* **2016,** *11,* 035003. doi:10.1088/1748-3190/11/3/035003
25. Zhu, L.-Y. *IEEE Trans. Magn.* **1999,** *35,* 2415–2417. doi:10.1109/20.800843
26. Barnes, W. J. P.; Khannoon, E.; Crawford, N.; Endlein, T. *American Adhesion Society Annual Meeting*, **2016**, Abstract 69.
27. Autumn, K.; Dittmore, A.; Santos, D.; Spenko, M.; Cutkosky, M. *J. Exp. Biol.* **2006,** *209,* 3569–3579. doi:10.1242/jeb.02486
28. Gingell, D.; Todd, I. *Biophys. J.* **1979,** *26,* 507–526. doi:10.1016/S0006-3495(79)85268-6

29. Kendall, K. *Molecular adhesion and its applications: the sticky universe;* Kluwer Academic Publishers: New York, NY, U.S.A., 2001; pp 428 ff.
30. Persson, B. N. J.; Brener, E. A. *Phys. Rev. E* **2005,** *71,* 036123. doi:10.1103/PhysRevE.71.036123
31. Matz, D.; Wuttke, S.; Barnes, W. J. P. *Comp. Biochem. Physiol., Part A: Mol. Integr. Physiol.* **2008,** *150,* S90. doi:10.1016/j.cbpa.2008.04.169
32. Hutt, W.; Persson, B. N. J. *J. Chem. Phys.* **2016,** *144,* 124903. doi:10.1063/1.4944384
33. Crawford, N.; Endlein, T.; Barnes, W. J. P. *J. Exp. Biol.* **2012,** *215,* 3965–3972. doi:10.1242/jeb.073809
34. Kendall, K. *J. Phys. D: Appl. Phys.* **1975,** *8,* 1449–1452. doi:10.1088/0022-3727/8/13/005
35. Lorenz, B.; Krick, B. A.; Mulakaluri, N.; Smolyakova, M.; Dieluweit, S.; Sawyer, W. G.; Persson, B. N. J. *J. Phys.: Condens. Matter* **2013,** *25,* 225004. doi:10.1088/0953-8984/25/22/225004
36. Huber, G.; Gorb, S. N.; Hosoda, N.; Spolenak, R.; Arzt, E. *Acta Biomater.* **2007,** *3,* 607–610. doi:10.1016/j.actbio.2007.01.007
37. Wolff, J. O.; Gorb, S. N. *J. Exp. Biol.* **2012,** *215,* 179–184. doi:10.1242/jeb.061507
38. Clemente, C. J.; Dirks, J.-H.; Barbero, D.; Steiner, U.; Federle, W. *J. Comp. Physiol., A* **2009,** *195,* 805–814. doi:10.1007/s00359-009-0457-0
39. Kovalev, A. E.; Filippov, A. E.; Gorb, S. N. *J. R. Soc., Interface* **2013,** *10,* 20120639. doi:10.1098/rsif.2012.0639
40. Zani, P. A. *J. Evol. Biol.* **2000,** *13,* 316–325. doi:10.1046/j.1420-9101.2000.00166.x
41. Kesel, A. B.; Martin, A.; Seidl, T. *J. Exp. Biol.* **2003,** *206,* 2733–2738. doi:10.1242/jeb.00478
42. Dai, Z.; Gorb, S. N.; Schwarz, U. *J. Exp. Biol.* **2002,** *205,* 2479–2488.
43. Bullock, J. M. R.; Federle, W. *Insect Sci.* **2011,** *18,* 298–304. doi:10.1111/j.1744-7917.2010.01369.x
44. Labonte, D.; Federle, W. *Philos. Trans. R. Soc., B* **2015,** *370,* 20140027. doi:10.1098/rstb.2014.0027
45. Endlein, T.; Federle, W. *J. Comp. Physiol., A* **2008,** *194,* 49–60. doi:10.1007/s00359-007-0287-x
46. Song, Y.; Dai, Z.; Wang, Z.; Ji, A.; Gorb, S. N. *Sci. Rep.* **2016,** *6,* 26219. doi:10.1038/srep26219
47. Bauer, U.; Scharmann, M.; Skepper, J.; Federle, W. *Proc. R. Soc. London, Ser. B* **2013,** *280,* 20122569. doi:10.1098/rspb.2012.2569
48. Gaume, L.; Perret, P.; Gorb, E.; Gorb, S.; Labat, J.-J.; Rowe, N. *Arthropod Struct. Dev.* **2004,** *33,* 103–111. doi:10.1016/j.asd.2003.11.005
49. Bijma, N. N.; Gorb, S. N.; Kleinteich, T. *J. Comp. Physiol., A* **2016,** *202,* 267–276. doi:10.1007/s00359-016-1069-0
50. Herrel, A.; Perrenoud, M.; Decamps, T.; Abdala, V.; Manzano, A.; Pouydebat, E. *J. Exp. Biol.* **2013,** *216,* 3599–3605. doi:10.1242/jeb.090027
51. Lang, A.; Habegger, M. L.; Motta, P. Shark Skin Drag Reduction. In *Encyclopedia of Nanotechnology;* Bhushan, B., Ed.; Springer: Berlin, Germany, 2015; pp 1–8. doi:10.1007/978-94-007-6178-0_266-2
52. Neinhuis, C.; Barthlott, W. *Ann. Bot. (Oxford, U. K.)* **1997,** *79,* 667–677. doi:10.1006/anbo.1997.0400
53. Kroner, E.; Arzt, E. Gecko adhesion. In *Encyclopedia of Nanotechnology,* 2nd ed.; Bhushan, B., Ed.; Springer: Berlin, Germany, 2015; pp 1–12.
54. Chen, H.; Zhang, L.; Zhang, D.; Zhang, P.; Han, Z. *ACS Appl. Mater. Interfaces* **2015,** *7,* 13987–13995. doi:10.1021/acsami.5b03039

License and Terms

BEILSTEIN JOURNAL OF NANOTECHNOLOGY

Structural and tribometric characterization of biomimetically inspired synthetic "insect adhesives"

Matthias W. Speidel[1], Malte Kleemeier[2], Andreas Hartwig[2,3], Klaus Rischka[2], Angelika Ellermann[4], Rolf Daniels[4] and Oliver Betz[*1]

Full Research Paper

Open Access

Address:
[1]Institut für Evolution und Ökologie, Universität Tübingen, Auf der Morgenstelle 28, D-72076 Tübingen, Germany, [2]Fraunhofer-Institut für Fertigungstechnik und Angewandte Materialforschung, Wiener Str. 12, D-28359 Bremen, Germany, [3]Universität Bremen, Fachbereich 2 Biologie/Chemie, Leobener Str., 28359 Bremen, Germany and [4]Pharmazeutisches Institut, Universität Tübingen, Pharmazeutische Technologie und Biopharmazie, Auf der Morgenstelle 8, D-72076 Tübingen, Germany

Email:
Oliver Betz[*] - oliver.betz@uni-tuebingen.de

* Corresponding author

Keywords:
adhesion; bionics; emulsion; friction; insects

Beilstein J. Nanotechnol. **2017,** *8,* 45–63.
doi:10.3762/bjnano.8.6

Received: 31 May 2016
Accepted: 14 December 2016
Published: 06 January 2017

This article is part of the Thematic Series "Biological and biomimetic materials and surfaces".

Guest Editor: S. N. Gorb

Abstract

Background: Based on previous chemical analyses of insect tarsal adhesives, we prepared 12 heterogeneous synthetic emulsions mimicking the polar/non-polar principle, analysed their microscopical structure and tested their adhesive, frictional, and rheological properties.

Results: The prepared emulsions varied in their consistency from solid rubber-like, over soft elastic, to fluid (watery or oily). With droplet sizes >100 nm, all the emulsions belonged to the common type of macroemulsions. The emulsions of the first generation generally showed broader droplet-size ranges compared with the second generation, especially when less defined components such as petrolatum or waxes were present in the lipophilic fraction of the first generation of emulsions. Some of the prepared emulsions showed a yield point and were Bingham fluids. Tribometric adhesion was tested via probe tack tests. Compared with the "second generation" (containing less viscous components), the "first generation" emulsions were much more adhesive (31–93 mN), a finding attributable to their highly viscous components, i.e., wax, petrolatum, gelatin and poly(vinyl alcohol). In the second generation emulsions, we attained much lower adhesivenesses, ranging between 1–18 mN. The adhesive performance was drastically reduced in the emulsions that contained albumin as the protein component or that lacked protein. Tribometric shear tests were performed at moderate normal loads. Our measured friction forces (4–93 mN in the first and 0.1–5.8 mN in the second generation emulsions) were comparatively low. Differences in shear performance were related to the chemical composition and emulsion structure.

Conclusion: By varying their chemical composition, synthetic heterogeneous adhesive emulsions can be adjusted to have diverse consistencies and are able to mimic certain rheological and tribological properties of natural tarsal insect adhesives.

Introduction

During evolution, insects have developed the ability to move vertically and upside-down on various kinds of surface, a feat that has facilitated their successful exploration of a huge diversity of habitats. In this context, insects have evolved two distinctly different mechanisms to attach themselves to a variety of substrates, i.e., hairy surfaces and smooth flexible pads [1]. Usually, both types of adhesive devices involve supplementary adhesive fluids produced by glandular systems underlying the adhesive cuticular structures [2-4]. One major function of these liquid adhesives is to wet and maximize the contact area with the substrate by filling its surface irregularities [5,6]. In addition, viscous and capillary forces are conveyed by the adhesive secretion [7-12]. Recently, the suggestion has been made, that during friction regimes, insect adhesives induce rate-dependent viscosity changes caused by non-Newtonian shear strains [5,13,14].

Chemical analyses of adhesive insect secretions employed during locomotion have revealed that they form heterogeneous (emulsion-like) mixtures of aliphatic lipids, carbohydrates and proteins [4,15-19]. Adhesive secretions may form both oil-in-water (o/w) [20-22] or water-in-oil (w/o) emulsions [14,23]. Possible functional advantages lie in (i) their increased flexibility towards substrates of different surface energy and polarity, (ii) their possible non-Newtonian viscosity shifts implying adjustable viscosities [24,25] and (iii) the formation of lipoid shields that prevent the aqueous fraction of an adhesive from desiccation and its sticking to the walls of the outlet ductule [4,20,26]. Moreover, within the lipoid fraction itself, both the specific constitution and the mixing ratio of the various hydrocarbon molecules might also largely influence their adhesive performance possibly via viscosity and surface tension effects, molecular re-orientations and the intermolecular attraction of the hydrocarbon chains in the thin liquid films [27]. In hydrocarbon molecules, viscosity is positively correlated with chain length, whereas the degree of unsaturation and the number of double bonds and methyl branches have the opposite effect. The position of the double bonds and the methyl branches modify this behaviour [27]. Indeed, in the potato beetle *Leptinotarsa decemlineata*, the supplementation of unsaturated components (e.g., *cis*-alkenes) to the adhesive tarsal secretions results in a significant reduction of friction forces [28].

Recent chemical analyses of the tarsal adhesives of the locust *Schistocerca gregarina* [15] and the Madagascan hissing cockroach *Gromphadorrhina portentosa* [16,17] have confirmed that the lipoid phase of their adhesives consists of *n*-alkanes (in the range of C_{23}–C_{49} in *S. gregaria* and C_{27}–C_{34} in *G. portentosa*), internally branched monomethyl-, dimethyl- and trimethyl- (the latter substance in *S. gregaria* only) alkanes and long-chain fatty acids and aldehydes (in *S. gregaria* only). In the tarsal adhesives of the hairy adhesive systems of the frog beetle *Sagra femorata* and carrion beetles of the genus *Nicrophorus,* Gerhardt et al. [17] have established a hydrocarbon spectrum in the C-range between C_{18} and C_{39} including *n*-alkanes, mono-, di-, tri- and tetramethyl branched alkanes, alkenes, alkadienes and one aldehyde (the latter substance in *S. femortata* only).

The established long-chain *n*-alkanes suggest a semi-solid (grease-like) consistency of the adhesive emulsion with increased viscosity, in accordance with the properties of a Bingham fluid. Such a property would consolidate several functional principles and properties that are essential for effective locomotion: (1) improving slip resistance, (2) facilitating subsequent tarsal release from the substrate, (3) reducing the loss of tarsal fluid on the substrate, (4) keeping the adhesive compliable for perfect adaption to the surface micro-roughness and (5) protecting of the tarsal adhesive pads from contamination and abrasive damage [15]. In addition, our recently performed analyses [15,18] have confirmed the presence of polysaccharides, peptides and (glycosylated) proteins in the adhesive secretion of the desert locust *Schistocerca gregaria* and the Madagascan hissing cockroach *Gromphadorhina portentosa* and have thus confirmed previous assumptions of Vötsch et al. [21].

Although the analysis of the structure and the function of the emulsion-like adhesives of insects is still in its infancy, these adhesives combine interesting properties relevant for possible commercial applications and the development of biomimetically inspired lipid-based adhesives. We have used the available chemical data [4,15-18,21] concerning the heterogeneous composition of insect tarsal secretions to prepare synthetic adhesives based upon the biological "polar/non-polar" principle. We have investigated the way that both the adhesive and the frictional performance of the adhesive are influenced by the co-occurrence of highly polar and highly non-polar components in combination with amphiphilic substances, whereby our preparations have covered both liquid and semi-solid (grease-like) alternatives. Such heterogeneously assembled emulsions

have the potential of being optimized with respect to certain required properties.

For the preparation of synthetic "insect adhesives", we abstracted the chemical components revealed in the chemical analyses of the insect examples mentioned above by replacing their components by low-priced and simply producible natural or synthetic compounds of comparable structure and properties. We developed two consecutive generations (designated as "first" and "second" generation) of synthetic emulsions mimicking the lipid-based "polar/non-polar" insect example. In the first generation (containing highly viscous components), the non-polar phase was represented by microcrystalline wax or petrolatum (trademark Vaseline) consisting of hydrocarbons of various lengths (C_{30}–C_{70}) and branching positions. The aqueous polar phase was enriched by the water-soluble protein/peptide mixture gelatin or poly(vinyl alcohol), which is considered as a carbohydrate equivalent because of its numerous hydroxy groups. In our preparations, the gelatin was plasticized by the addition of glycerine.

Our second generation of synthetic "insect adhesives" (containing less viscous components) consisted of the *n*-alkane octacosane (C_{28}) and the hexamethyl-alkane squalane (C_{30}) representing hydrocarbons of defined structure and length within the range of C_{23}–C_{49} as established in the biological role models. Albumin and gelatin were substitutes for proteinogenic amino acids, with the surfactant Span 80 (Sorbitane monooleate**)** being used as a combined replacement for fatty acids and carbohydrates. The general composition of the emulsions and assignment to the used abbreviations is summarized in Table 1. Although emulsions are very common in technical applications and have extensively been examined, it is still not trivial to properly prepare and characterize them. The reason is that emulsions are not in a thermodynamic equilibrium, but rather represent a “frozen state”, which depends not only on their composition, but also strongly on their way of preparation [29-31]. This is especially the case for adjusting their non-Newtonian rheological behaviour and their droplet distribution. The purpose of our contribution is not to present completely new kinds of emulsion, but to use emulsions in a biomimetic context. Due to the small amounts of attainable natural tarsal secretions, it is hardly possible to determine their droplet sizes and other emulsion parameters. Therefore, the artificial emulsions prepared and used in the present contribution are used as rough models to indirectly deduce how the biological adhesives are probably structured and how they perform. This is the reason why we follow a typical process sequence of biomimetic research [32], i.e., we intend to mimick tribological properties of tarsal insect adhesives by preparing a second generation of technical emulsions on the basis of insights gained from a first (more imperfect) generation. Since natural tarsal adhesive emul-

Table 1: List of the prepared synthetic emulsions and their main composition.

generation	name of emulsion	hydrocarbon	emulsifier[a]	protein	carbohydrate equivalent	amphiphilic compound (fatty acid + carbohydrate)[b]	consistency at room temperature (22 °C)	emulsion character[c]
1	VG50	petrolatum	SDS	gelatin solution	—	—	solid	o/w
1	VP50	petrolatum	SDS	—	poly(vinyl alcohol) solution	—	soft	o/w
1	WG20	microcrystalline wax	SDS	gelatin solution	—	—	solid	o/w
1	WP20	microcrystalline wax	SDS	—	poly(vinyl alcohol) solution	—	solid	o/w
2	SA2	squalane	SDS	albumin	—	Span 80	liquid	o/w
2	SG2	squalane	SDS	gelatin	—	Span 80	solid	o/w
2	OA2	octacosane	SDS	albumin	—	Span 80	liquid	o/w
2	OG2	octacosane	SDS	gelatin	—	Span 80	solid	o/w
2	SW2	squalane	SDS	—	—	Span 80	liquid	o/w
2	OW2	octacosane	SDS	—	—	Span 80	liquid	o/w
2	SA4	squalane	AOT	albumin	—	Span 80	oily	w/o?
2	SG4	squalane	AOT	gelatin	—	Span 80	oily	w/o?

[a]SDS = sodium dodecyl sulfate, AOT = sodium bis(2-ethylhexyl) sulfosuccinate (Aerosol-OT).
[b]Span 80 = sorbitan monostearate.
[c]o/w = oil-in-water emulsion, w/o? = presumably water-in-oil emulsion.

sions of insects are hard to isolate and thus not well accessible to experimental approaches, our "biomimetic approach" will help to (i) understand possible structural and functional principles that make up such adhesives and (ii) develop technical protocols how to test and mimick them. On a long term perspective, such approaches will help to technically utilize insect tarsal adhesives principles.

In total, we prepared 12 synthetic "insect" emulsions that were structurally characterized by microscopic techniques such as bright field, fluorescence and cryo-scanning electron microscopy (cryo-SEM) and laser diffraction particle size analysis. Parameters of particular interest were their phase volume ratios and droplet-size distributions. Their adhesive and frictional performances were determined by nanotribometric measurements. We thus aimed at clarifying the influence of the various chemical compounds such as lipids, proteins and carbohydrates on the tribometric and rheological properties of the emulsions. Statistical correlation analyses aided the evaluation of the interrelationships between the structural, chemical and performance attributes of the emulsions.

Results

Structural characterization of synthetic emulsions

Table S1 (in Supporting Information File 1) summarizes the structural parameters of each emulsion as revealed by bright field/fluorescence microscopy and cryo-scanning electron microscopy (SEM). In general, the droplet sizes determined by the various methods, such as bright field/fluorescence microscopy and cryo-SEM, were in good correspondence, except for the larger size range of droplets as shown by the bright field/fluorescence microscopic images in comparison with those by cryo-SEM. The microscopic analyses revealed that the first generation provided a broader droplet size range with extremely large individual droplets leading to platykurtic kurtosis (Supporting Information File 1, Table S1). In contrast, most second generation emulsions showed narrower droplet size ranges, as indicated by their almost mesokurtic or leptokurtic distributions (Supporting Information File 1, Table S1). Both the emulsions within the second generation (SW2, OW2) without proteins possessed a narrower droplet size range compared with the emulsions having protein additions. Furthermore, all emulsion of both generations, except OA2 and OG2, had an almost symmetrical to positive skewness in common (Supporting Information File 1, Table S1). With regard to the rigidity of the emulsions at room temperature, the emulsions of the first generation were either solid or soft, whereas those of the second generation showed an aqueous or oily consistence (except for SG2 and OG2, which also exhibited a solid appearance) (Table 1; Supporting Information File 1, Table S1). In contrast to all other emulsions, those based on octacosane featured polyhedral droplets, which had a crystal-like appearance (Figure 1e,f; Supporting Information File 1, Figure S1a,b,f). In addition, in two out of three cases, the presence of octacosane led to unstable phases and to the formation of clumps within these emulsions (Supporting Information File 1, Table S1). Within emulsion SA2 (Supporting Information File 1, Table S1), the aqueous and the oily phase rapidly separated. The analysis of the emulsions of both generations by fluorescence microscopy revealed that all emulsions, except SA4 and SG4, displayed fluorescent droplets only thereby indicating the presence of oil-in-water (o/w) emulsions (Figure 1a,c; Supporting Information File 1, Table S1; Figure S2a,e,g). Vice versa, the two emulsions SA4 and SG4 possessed a fluorescent outer phase surrounding non-fluorescent droplets thus indicating the presence of water-in-oil (w/o) emulsions (Figure 1g; Supporting Information File 1, Table S1; Figure S1g). Against all expectations, the cyro-SEM images of SA4 and SG4 showed visible droplets within the outer lipid phase (Figure 1h; Supporting Information File 1, Figure S1h). These droplets possibly represented the remnants of water droplets that had not as yet fully evaporated. The dilution of both these emulsions with the assumed outer phase squalane was not possible and merely led to floating emulsion fragments within the squalane phase. Dilution with water was possible in SA4 only (Supporting Information File 1, Table S1).

Rheological characterization of selected emulsions

The rheological behaviour of selected emulsions was characterized by using the plate–plate geometry of the rheometer. In order to obtain information concerning the behaviour at different shear rates, they were increased from 0 up to 60 s^{-1}. For this analysis, we examined the emulsions consisting of squalane and the proteins gelatin and albumin, respectively. We propose that a yield point is required for a locomotion adhesive to prevent the sliding of a non-moving insect from a vertical smooth surface. Therefore, the rheological properties were measured only for formulations that showed pronounced non-Newtonian flow behaviour by qualitative observation, a prerequisite for a rheological yield point. This was the case for the emulsions based on squalane and proteins. As a further structural difference, depending on their chemical composition, these emulsions showed oil-in-water (SA2 and SG2) or water-in-oil (SA4 and SG4) morphologies. As SG2 has a solid character at room temperature, the chemically related pair SA2 and SG2 was measured at 40 °C, whereas the pair SA4 and SG4 was measured at 25 °C. As the general rheological behaviour of the emulsions was to be evaluated (and not the exact viscosities), this procedure was acceptable. The measurements are shown in Figure 2. The emulsions SG2, SA4 and SG4 behaved as Bingham fluids showing yield stresses of 0.04 Pa, 2.5 Pa and

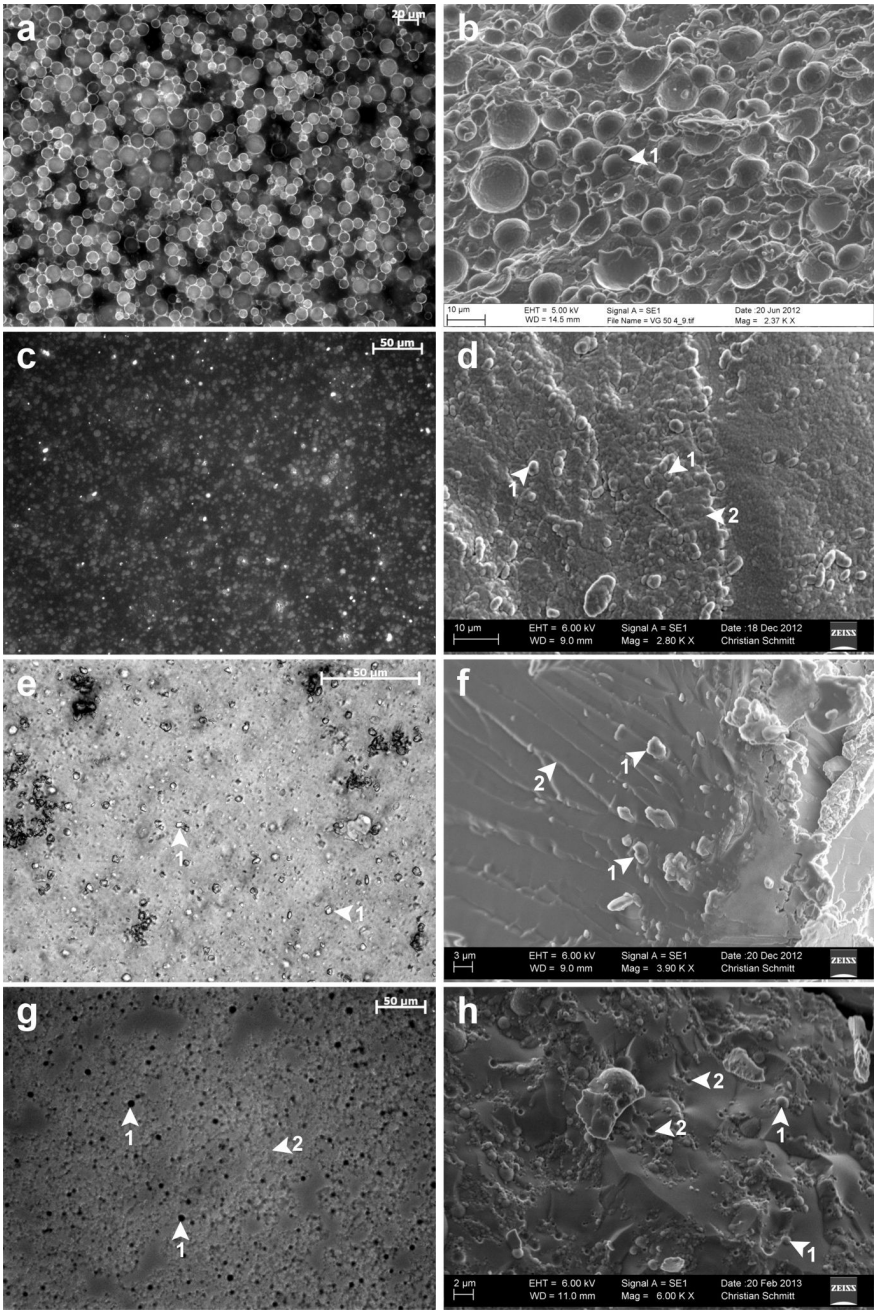

Figure 1: Droplet distribution of selected emulsions of the first and second generation. Left side: appearance of the emulsions under bright field light or fluorescence microscopy; right side: appearance of the emulsions under cryo-SEM. (a) Densely distributed fluorescent lipid droplets of emulsion VG50 (Sudan-III-stained emulsion was examined under light excitation of 300–400 nm). The fluorescent droplets are indicative of the o/w characteristic of this emulsion, because these fluorescent oily droplets form the inner phase. The outer hydrophilic phase is reduced because of evaporation. (b) Embedded, densely distributed droplets of emulsion VG50 surrounded by a slightly textured boundary layer (arrow 1). The emulsion has a droplet size range of about <1–50 µm, whereas most of the droplets lie between 5–15 µm. (c) Densely distributed fluorescent lipid droplets of the emulsion SG2 (Sudan-III-stained emulsion was examined under light excitation of 530–560 nm). The fluorescent droplets are indicative of the o/w characteristic of emulsion SG2, because these fluorescent oily droplets form the inner phase. (d) Distributed droplets (1) of emulsion SG2 embedded in an outer phase (2) with a rough appearance having a flaked structure. Main size range of round- to oval-shaped droplets is about <1–5 µm. (e) Loosely scattered and polyhedral droplets (1) of emulsion OA2 by light microscopy. The emulsion was examined under bright field after dilution with water. The lipid phase octacosane (1) consisted of solid polyhedral fragments causing aggregation. (f) Polyhedral fragments (1) of emulsion OA2 embedded in a lamellar-layered outer phase (2). Main size range of fragments is about <1–3 µm. (g) Non-fluorescent droplets (1) of emulsion SA4 embedded in a fluorescent outer phase (2) (the Sudan-III-stained emulsion was examined under light excitation of 530–560 nm). The non-fluorescent droplets in combination with the fluorescent outer phase are indicative of a w/o emulsion. (h) Smooth emulsion surface of SA4 consisting of both droplets (1) and cavities (2). The cavities (<1–2 µm) seem to represent the remains of evaporated water droplets following the sublimation step, whereas the unaffected droplets probably represent those that have not fully evaporated. Main size range of visible droplets is about 1–4 µm.

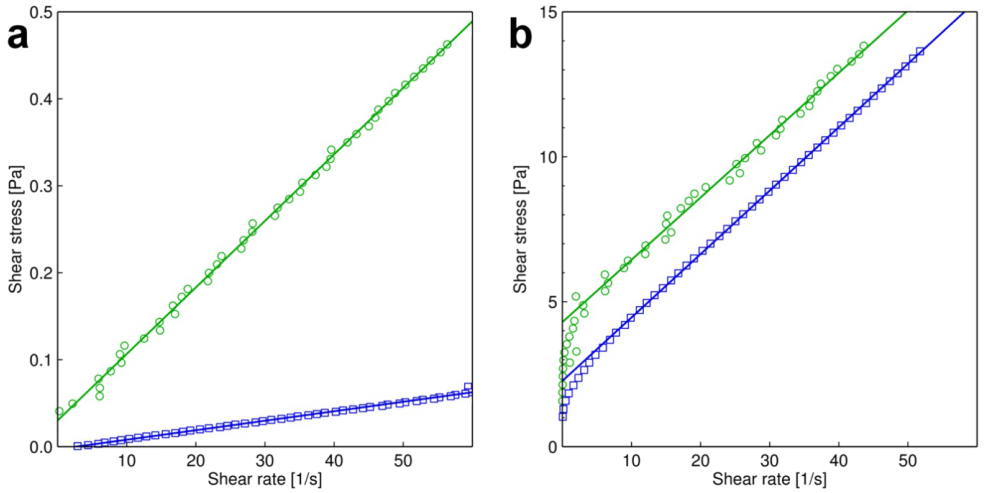

Figure 2: Rheological characterization of selected emulsions obtained by using plate-plate rheology within a shear rate range up to 60 s^{-1}. (a) Green circles: emulsion SG2, blue squares: emulsion SA2, both measured at 40 °C. (b) Green circles: emulsion SG4, blue squares: emulsion SA4, both measured at 25 °C.

4 Pa. In contrast, SA2 behaved as a normal Newtonian fluid. In principle, the viscosities of the emulsions could be predicted from available models using the viscosity, the volume fractions and the droplet sizes of their components [33,34]. However, as some of the applied components (e.g., proteins) have an amphiphilic character, the prepared emulsions show a rather complicated morphology. In addition, according to their non-Newtonian rheological behaviour, such a calculation would be complex and beyond the purpose of this article.

Tribological characterization of emulsions

Adhesion

The first generation of emulsions showed a significantly stronger adhesion than the second (Mann–Whitney-U test; $p < 0.001$; $N = 12$), i.e., more than twice as high an adhesion force (Figure 3; Supporting Information File 1, Table S2). Within the first generation, the adhesion of all emulsions, except VG50 and VP50, did not significantly differ from each other (Figure 3a; Supporting Information File 1, Table S3).

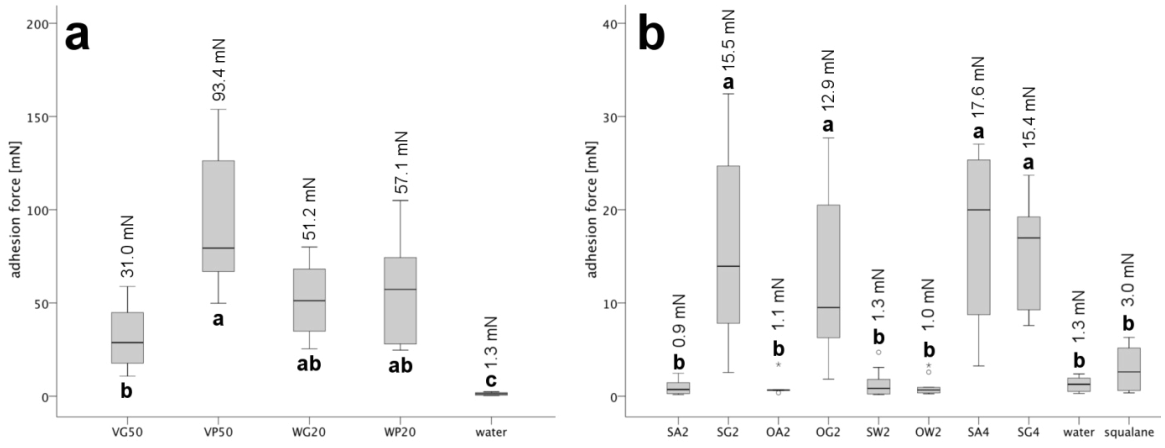

Figure 3: Box-plots of the adhesion forces of both generations of emulsions. The statistical comparison of the adhesion refers to the common logarithmized adhesion forces. Significant differences between the emulsion of logarithmized values (Supporting Information File 1, Tables S3 and S4) are indicated by different small letters (Kruskal–Wallis ANOVA followed by Kruskal–Wallis post hoc multiple comparisons). The measured values refer to a surface area of the silicium wafer of 6.45 mm^2 and a normal load of 3.3 mN. The value above each box depicts the arithmetic mean of its adhesion measurements as reported in Supporting Information File 1, Table S2. (a) Adhesion forces of the first generation (Supporting Information File 1, Table S2). All four emulsions show similar adhesion forces, whereby the combination of petrolatum and poly(vinyl alcohol) solution in VP50 generated the highest forces. (b) Adhesion forces of the second generation (Supporting Information File 1, Table S2). The addition of gelatin gives stronger adhesion forces in the emulsions SG2, OG2 and SG4. The asterisk and circles above and below the boxes categorize outliers (asterisk) and extreme values (circle). Outliers are defined as values showing a distance of 1.5–3 times of the box height from the box border (25% and 75% quantile), whereas the distance of extreme values is larger than 3 times the box height.

However, emulsion VP50 exhibited the clear tendency of having the highest adhesion force, whereas emulsion VG50 showed the lowest adhesion force (Supporting Information File 1, Table S2). Moreover, all four emulsions revealed significantly higher adhesion compared with the control water (Figure 3a; Supporting Information File 1, Tables S2 and S3). Among the second generation, the four emulsions SG2, OG2, SA4 and SG4 (with average adhesion values between 13 and 17 mN) showed significantly stronger adhesion than the other emulsions of the second generation (Figure 3b; Supporting Information File 1, Tables S2 and S4). The remaining emulsions SA2, OA2, SW2 and OW2 and the controls water and squalane revealed no significant differences between one another (Figure 3b; Supporting Information File 1, Table S4). The adhesion force of these emulsions and water was between 0.9 and 1.34 mN (Supporting Information File 1, Table S2). Compared with these emulsions, the hydrophobic control squalane had slightly stronger adhesive abilities (3 mN) (Supporting Information File 1, Table S2).

Friction

First generation of emulsions: For the slowest speed (50 µm s^{-1}), emulsion WG20 showed the highest friction force (39 mN), whereas at the higher velocities (200 and 500 µm s^{-1}), emulsion VG50 gave the highest friction performance (39 mN and 32 mN, respectively) (Figure 4a; Supporting Information File 1, Table S2). Whereas the friction force increased with increasing sliding speed in VG50, VP50 and WP20, the opposite was the case in WG20 (Figure 4a, Supporting Information File 1, Tables S2 and S11). In addition, the friction curves of emulsion VG50 showed a stick and slip pattern (not shown), especially at 50 µm s^{-1}; this was caused by the short-term sticking of the emulsion surface to the wafer alternating with a sudden tearing of the adhered surface once the maximum shear force was exceeded. For 50 and 200 µm s^{-1}, emulsions VP50 and WP20 showed the lowest friction forces (Figure 4a; Supporting Information File 1, Table S2). Based on the statistical analysis, the emulsions based on poly(vinyl alcohol), namely VP50 and WP20, did not significantly differ from each other for all three speeds (Supporting Information File 1, Tables S5, S6 and S7). The same holds true for the two emulsions based on gelatin, namely VG50 and WG20, for the speeds 50 and 200 µm s^{-1} (Supporting Information File 1, Tables S5 and S6). Compared with the two controls of glass and water, emulsions VG50, VP50, WG20 and WP20 always gave significantly higher friction values (Supporting Information File 1, Tables S5, S6 and S7).

Second generation of emulsion: Overall, the friction performance of these emulsions was significantly lower compared

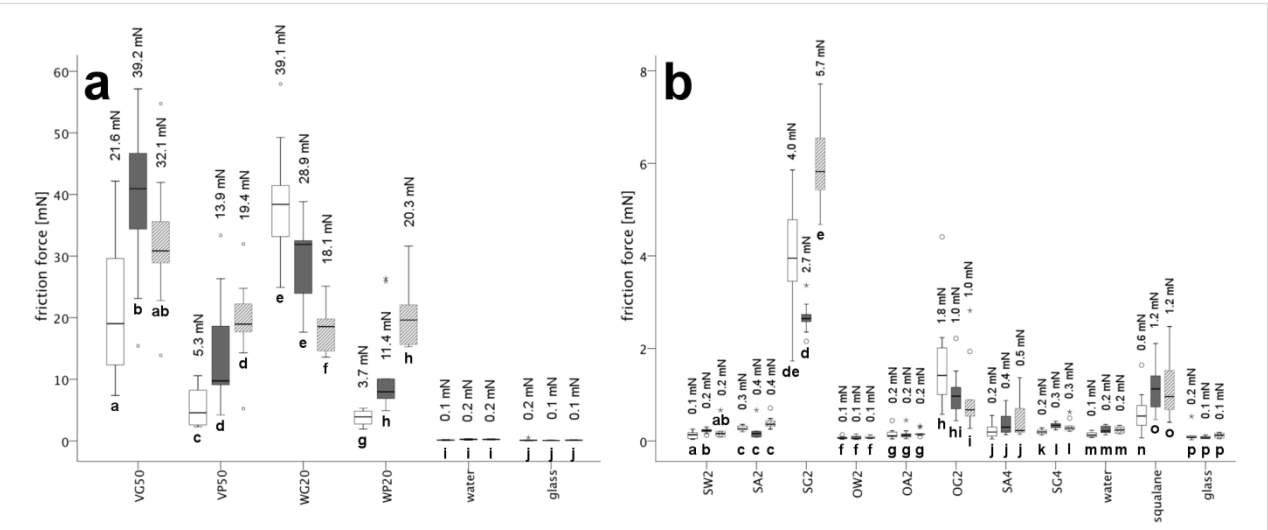

Figure 4: Box-plots of the friction forces of the emulsions of both emulsion generations at speeds of 50 (white), 200 (dark grey) and 500 (grey striped) µm s^{-1}. The asterisk and circles above and below the boxes categorize outliers (asterisk) and extreme values (circle). Outliers are defined as values showing a distance of 1.5–3 times the box height from the box border (25% and 75% quantile), whereas the distance of extreme values is larger than 3 times of the box height. Significant differences between the three different velocities within an emulsion of logarithmized values (Supporting Information File 1, Tables S11 and S12) are indicated by different small letters (Friedman test followed by Friedman post hoc multiple comparisons). The statistical comparison of the friction within each emulsion refers to common logarithmized friction forces. The measured values refer to a surface area of the silicium wafer of 6.45 mm^2 and a normal load of 0.6 mN. The value above each box depicts the arithmetic mean of its friction measurements as reported in Supporting Information File 1, Table S2. (a) Friction forces of the first generation (Supporting Information File 1, Table S2). The three emulsions VG50, VP50 and WP20 show an increase in the friction force with increasing speed, whereas the frictional performance of WG20 decreased with increasing speed. (b) Friction forces of the second generation (Supporting Information File 1, Table S2). The velocity only influences the emulsions SG2 and OG2 and the control group squalane, whereas the frictional performance of the remaining emulsions does not change with speeds.

with that of the first generation (Mann–Whitney-U test; $p < 0.001$; $N = 12$). For all the three speeds, the friction values of emulsions SA2, OA2, SW2, OW2, SA4 and SG4 were relatively low (similar to the controls water and glass) amounting from 0.1 to 0.5 mN (Supporting Information File 1, Table S2; the lowest values being attained in the protein-free emulsions SW2 and OW2). Among these emulsions, the friction forces of emulsions SA2, SA4 and SG4 were significantly higher than that of OW2 (for all velocities) and of OA2 and SW2 (for some velocities) (Figure 4b; Supporting Information File 1, Tables S2 and S8–S10), whereas the others showed no statistically confirmed differences among each other (Supporting Information File 1, Tables S8–S10). At 50 μm s^{-1}, emulsion OG2 showed a significantly higher friction ability (arithmetic mean: 1.8 mN) than the previously mentioned emulsions, namely SA2, OA2, SW2, OW2, SA4 and SG4. With increasing velocity, the difference among OG2 and the other emulsions decreased (Figure 4b; Supporting Information File 1, Tables S8–S10). The highest friction forces within the second generation were measured for SG2 in a range of 2.7–5.7 mN for all three speeds (Supporting Information File 1, Table S2). Because of the high friction values of emulsion SG2, its difference was significant in comparison with all second generation emulsions, water and glass, except for OG2 and the control squalane (Supporting Information File 1, Tables S8–10). The third control group squalane showed slightly, but significantly, higher friction values (arithmetic means: 0.6–1.2 mN) than emulsions OA2, SW2, OW2, SA4 and SG4 and the two controls water and glass (Figure 4b; Supporting Information File 1, Tables S2 and S8–S10).

Whereas emulsions SA2, OA2, OW2 and SA4 and the two controls water and glass showed no dependence on the sliding velocity, this was indeed the case for emulsions SG2, OG2 and the control group squalane (Figure 4b; Supporting Information File 1, Table S12). The friction values of SW2 and SG4 varied only slightly with increasing speed (Supporting Information File 1, Tables S2 and S12). Similar to squalane, the friction forces of SG2 increased with increasing speed, but initially the friction force dropped, although not significantly, over the course of 50 to 200 μm s^{-1} (Figure 4b; Supporting Information File 1, Tables S2 and S12). The friction behaviour of emulsion OG2 was similar to that of the first generation emulsion WG20 (Figure 4a), showing a significant decrease in friction force with increasing sliding speed (Figure 4b; Supporting Information File 1, Tables S2 and S12).

Statistical relationships between structural, chemical and tribological parameters

Relationship between chemical composition and structure of the emulsions (Supporting Information File 1, Table S13): Generally, all the structural parameters that were related to the droplet size of an emulsion (25–90% quantile, arithmetic mean, median, mode, standard deviation (Supporting Information File 1, Table S1)) showed a positive statistical correlation to the chemical compounds Vaseline, glycerine and SDS (sodium dodecyl sulfate), occurring mostly within the first generation of emulsions. The non-ionic surfactant Span 80 and the ionic surfactant AOT (sodium bis(2-ethylhexyl) sulfosuccinate) significantly influenced the droplet size of the 10% quantile and the phase volume. The excess kurtosis, representing the distribution of the droplet sizes, only correlated with the hydrophobic compound octacosane, which was used for the second generation emulsions OA2, OG2 and OW2.

Relationship between structure and adhesive/frictional performance of the emulsions (Supporting Information File 1, Table S14): The droplet size within the range of the 50–90% quantile and the droplet-size-dependent parameters (arithmetic mean, median, standard deviation) correlated positively with both the adhesive and the frictional performance, i.e., emulsions with higher droplet sizes showed higher adhesion and friction forces. The excess kurtosis correlated negatively to the friction ability and to the adhesion by trend, showing increased frictional and adhesive performances attributable to more balanced droplet-size distributions. From our correlations between the emulsion structure and its chemical composition (Supporting Information File 1, Table S13), we infer that the excess kurtosis is only influenced by the presence of the hydrophobic compound octacosane as used in emulsions OA2, OG2 and OW2. Moreover, the phase volume ratio showed no correlation related to the frictional performance.

Relationship between chemical composition and adhesive/frictional performance of the emulsion (Supporting Information File 1, Table S15): The compounds Vaseline, microcrystalline wax, poly(vinyl alcohol) (only at the highest sliding speed of 500 μm s^{-1}), glycerine, gelatin and sodium dodecyl sulphate (SDS) showed a positive significant relationship with friction. In addition, friction was also negatively affected by the non-ionic surfactant Span 80 at an almost significant level. In contrast, adhesive performance correlated positively with poly(vinyl alcohol) and the ionic surfactant SDS, whereas the chemical compounds Vaseline, microcrystalline wax and gelatin influenced adhesion only by trend.

Discussion

In contrast to bioinspired materials based on microstructured surfaces [35,36], the molecular biomimetics of the adhesive liquids (adhesives) involved in biological adhesive systems remains in its infancy [37,38]. Emulsion-based glues are widely spread in technology and are deployed not only in casein glues, but also in releasable contact adhesives such as tapes, patches

and labels. However, in all known technical systems, the emulsion coalesces rapidly after application, forming a more or less homogeneous organic bond line.

Insect adhesive emulsions combine polar and non-polar components, and this combination might be decisive for the achievement of functional properties that are of high technical relevance, such as (i) versatility towards polar and non-polar surfaces, (ii) reversibility of the adhesive contact and (iii) robustness towards contamination and exsiccation.

Basing our present contribution on previous chemical analyses of insect tarsal adhesives [4,15-18,21], we have prepared heterogeneous synthetic emulsions mimicking the polar/non-polar principle, analysed their microscopical structure, and tested their adhesive, frictional and rheological properties. In total, we have prepared and tested 12 different biomimetic "insect adhesives" and, depending on their composition, have been able to attain a broad spectrum of micromechanical properties (cf. Figures 2–4). This shows that synthetic heterogeneous adhesive emulsions can, in principle, be adjusted by varying their chemical composition in such a way that they are able to mimic certain rheological and tribological properties of the biological role model and by their having various consistencies (cf. Supporting Information File 1, Table S1). With regard to their chemical composition, other than of water and hydrocarbons, we have used amphiphilic compounds selected on the basis of their resemblance to such compounds in nature. Moreover, in addition to proteins, these are amphiphilic polymers (namely poly(vinyl alcohol)) and tensides (namely Span 80), both mimicking fatty acids and carbohydrate compounds in natural role models.

Structure

The prepared emulsions varied in their consistency from solid rubber-like, over soft elastic, to fluid (watery or oily). In general, the use of gelatin as the protein component (VG50, WG20, SG2, OG2) made the emulsions solid and rubber-like, because of the gel-like consistency of gelatin at room temperature. The only exception was the presumed water-in-oil (w/o) emulsion SG4. Despite its large amount of gelatin, the addition of squalane (fluid at room temperature) together with the ionic emulsifier AOT kept this emulsion in an oily state. Similar to gelatin, the addition of high-melting microcrystalline wax (WG20, WP20) led to a solid (rubber- to brittle-like) consistency, which, on the other hand, could be softened by the addition of poly(vinyl alcohol) (VP50). The remaining emulsions consistently showed a fluid consistence, which could be mostly ascribed to the use of squalane (if combined with albumin or gelatin at low concentration or if the protein component was omitted completely).

Most of our prepared synthetic emulsions represented oil-in-water (o/w) emulsions. Two emulsions (SA4 and SG4) that were stabilized with the hydrophilic emulsifier AOT were water-in-oil (w/o) emulsions, although the true nature, especially of SG4, remained ambiguous. With droplet sizes >100 nm, all the emulsions belonged to the common type of macroemulsions, although the emulsions can readily be classified according to differences with regard to their droplet-size distributions (Supporting Information File 1, Table S1). The emulsions of the first generation generally showed broader (more platykurtic) droplet size ranges with higher standard deviations compared with the second generation. This was certainly the result of the employment of less defined components such as petrolatum or waxes (consisting of hydrocarbons of various lengths and degrees of branching) in the lipophilic fraction of the first generation of emulsion. The use of clearly defined hydrocarbons (octacosane or squalane) together with the employment of the additional surfactant Span 80 in the second generation of emulsion in most cases resulted in narrower (almost mesokurtic or leptokurtic) distributions (showing lower standard deviations). Among the second generation emulsions, both the protein-free emulsions (SW2, OW2) clearly showed smaller droplet sizes compared with the protein-containing emulsions. This is probably caused by the presence of the much smaller amphiphilic Span 80 molecules, which are able to form common emulsion drops. In contrast, the large protein molecules (even in the presence of the smaller Span 80 emulsifier molecules) need a much larger area once they form the interphase between the aqueous and the oil phase. Most likely, because of their large molecular size, the proteins are even able to form bridges between smaller droplets previously emulsified by the Span 80 molecules. For insect adhesive emulsions, few data are available on the droplet sizes of the inner phase. They are in the range between 100 nanometers and several micrometers [14,20,21] and thus fit well in the range of almost all of our second generation emulsions (cf. Supporting Information File 1, Table S1).

Interestingly, in the (second generation) octacosane-based oil-in-water (o/w) emulsions, the octacosane forms solid crystal-like particles that are suspended in the outer matrix; this is certainly attributable to the high-melting temperature of octacosane (>60 °C). Such colloidal suspension-like behaviour corresponds well to the assumed nature of the outer lipid layer of the insect cuticle [4,28,39,40] and can also be assumed for insect tarsal adhesives being mere derivatives of the outer free lipid layer of the general body cuticle [41-43]. Such mixtures of high-melting straight *n*-alkanes with low-melting alkenes or methyl-branched alkanes keep the suspensions in a semi-solid condition over a broad range of temperatures. The in situ phase differentiation of alkanes and alkenes/methyl-branched alkanes

at ambient temperatures, forming a colloid suspension of solid wax crystals within a liquid matrix [28], might induce rate-dependent viscosity changes caused by non-Newtonian shear strains. Non-Newtonian viscosity shifts are also common properties of emulsions [24,25], which consist of an aqueous phase dispersed in an oily continuous phase or vice versa. Hence, we wished to test our synthetic "insect adhesives" for such shear thinning properties in shear tests and to compare their adhesive and frictional properties with a nanotribometer.

Rheology

Previously, in insect tarsal adhesive systems, any kind of liquid functioning as a reversible adhesive during movement was thought to exhibit a non-Newtonian Bingham-like rheological yield point for the production of sufficient static friction in order to prevent sliding on vertical substrates when the insect was at rest [14]. Such flow behaviour is actually considered a general characteristic of emulsions, whereupon the yield points are differently pronounced [29]. We subjected four of our 12 synthetic emulsions to plate-plate rheology. To different extents, emulsions SG2 (0.04 Pa), SA4 (2.5 Pa) and SG4 (4 Pa) show Bingham-like behavior, whereas the rheology of SA2 is consistent with a Newtonian fluid. The latter o/w emulsion has a watery consistence and shows a comparatively low phase volume ratio (0.06) with only small and widely scattered oil droplets, which suggests that in this case the continuous water phase outweighs any influence of the dispersed oil phase. The rheological comparison between the emulsions SG2 and SA2 suggests that albumin has a lower ability to form emulsions with yield points than does gelatin. This behaviour is also pronounced in both the water-in-oil (w/o) emulsions SA4 and SG4 (cf. Figure 2b). Gelatin is known to form gel-like structures, which is probably the reason for more pronounced yield points in the gelatin-based emulsions. In the w/o emulsions, the polymeric protein components probably form hydrophilic drops within the hydrophobic phase. To initiate flow, these drops must be deformed, probably leading to the observed yield point.

Adhesion

In terms of their adhesive performance, our prepared emulsions showed considerable differences, ranging from 1–93 mN. Compared with the second generation, the first generation emulsions were much more adhesive (31–93 mN); this is attributable to their highly viscous components, i.e., wax and petrolatum (with their long chain lengths), gelatin and poly(vinyl alcohol) (Supporting Information File 1, Table S1). Because of its slight tackiness, poly(vinyl alcohol) is actually employed as component of technical glues [44]. In the second generation emulsions, we attained much lower values of adhesiveness, ranging between 1–18 mN. Whereas the gelatin-containing emulsions of this generation still showed comparatively high stickiness (13–15 mN), the adhesive performance was drastically reduced in the emulsions that contained albumin as the protein component or that did not contain any protein at all (0.9–1.3 mN). In this respect, they resembled the controls of water and pure squalane (although the adhesiveness of pure squalane tended to be slightly higher). Although containing the protein component albumin instead of gelatin, the adhesiveness of the presumed water-in-oil (w/o) emulsion SA4 was as large as in the gelatin-containing emulsion SG4. This indicates that both proteins are mainly present in the aqueous phase of the emulsion surrounded by the same oil phase, the latter forming the contact with the substrate and thus determining the adhesive performance. The similar adhesive performance of both these emulsions further supports the view that both these emulsions are actually water-in-oil (w/o) emulsions. Both albumin and gelatin are proteins that have been used in artificial adhesives but they were applied mainly in the past.

Although, the adhesive structures of insects are deployed in a reversible manner, depending on the biological context (e.g., locomotion versus prey-capture), the required forces can vary considerably [4,45]. Such different demands are well reflected by the different values of adhesiveness of our synthetic emulsions. Because of their small quantities, only a few attempts have been undertaken, to date, to determine the adhesive stress of insect tarsal adhesives in isolation from their underlying cuticle [5,46]. Moreover, to our knowledge, no attempts have as yet been undertaken to quantify the portion that the adhesive secretion contributes to the total adhesive performance of an intact insect tarsus with respect to diverse surface regimes. For effective locomotion, the adhesive and/or cohesive forces must be held at a moderate level to enable the rapid and effortless re-release of the tarsal surface after contact formation. In the wet adhesive systems of insect tarsi, adhesive stresses (tenacities) measured without shear range between 1.1 and 7 kPa [47]. These values have been determined in intact tarsi and are the result of the combined properties of the viscoelastic tarsus cuticle together with the overlying adhesive secretion. Related to the surface area of the used measuring heads, the adhesive stresses of our prepared synthetic emulsions are in the range of 7.9–14.4 (first generation) and 0.2–2.8 kPa (second generation). From this perspective, the adhesive strength of our first generation of emulsions appears over-large in terms of the necessity to create reversible attachment structures mimicking insect attachment structures employed in locomotion (this holds true all the more, since we have tested the adhesive strength of the fluids between two rigid plates that show no distortion during their separation). During the detachment process, excessively sticky tarsal insect adhesives might actually transfer their viscous dissipation to the viscoelastic cuticle, largely hampering tarsal

release. Indeed, recent empirical and theoretical analyses in stick insects predict that the adhesive strength and viscosity of the tarsal secretion should be rather low, thereby decreasing viscous dissipation during tarsal retraction [48]. From this perspective, our four second generation emulsions SA2, OA2, SW2 and OW2 (all combining the hydrocarbons squalane or octacosane with the protein albumin or leaving out the protein component) might come closest to this demand. Their fluid consistency might also help to compensate for the roughness of microstructured surfaces to maximize contact. During the separation of the wafer from the glass surface, their failure was cohesive, i.e., the fluid thread broke somewhere in its middle. Many insect tarsal adhesives might behave similarly, with the tarsal adhesive possibly being cohesively adjusted in a way that minimizes material loss.

From a biomimetic perspective, four of the second generation emulsions that combine considerably increased (though still moderate) adhesive strength (about 2 kPa) with a semi-solid (rubber-like) (SG2, OG2) or oily (SA4, SG4) appearance might be of special interest. Indeed, the hydrocarbon pattern established by recent chemical analyses suggests a similar semi-solid (grease-like) consistency of insect adhesives [15-17] and such a property would consolidate several functions in the context of effective locomotion (and possibly technical applications) such as Bingham-like slip resistance, tarsal releasability, desiccation resistance, mechanical compliance and protection from abrasive damage. Tarsal releasability might be brought by since the tarsal adhesive secretion actually acting as a kind of "release-layer" (due to its reduced wetting ability according to its semi-solid consistence), minimizing the viscous dissipation of both the adhesive liquid and the viscoelastic pad material during detachment [48]. On the contrary, adhesive systems employed in prey-capture, such as the sticky labial pads (paraglossae) of *Stenus* species (Coleoptera, Staphylinidae), seem largely to depend on such energy-dissipating effects of both the viscous adhesive and the highly elastic (resilin-containing) pad material in order to attain sufficiently high adhesion ([49] and Figure 6 in [50]). Hence, a comparison of both the chemical composition of the glue and the viscoelastic behaviour of the pad cuticle involved in this system with those deployed in tarsal attachment would be of interest.

Friction

In dynamic attachment situations such as adhesive fluid-mediated insect locomotion, attachment forces are largely determined by the viscosity of the fluid, because of its influence on the shear stress generated during friction. High viscosity fluids should therefore be avoided during locomotion, because this would be counterproductive for the detachment process. In our experiments, in order to ensure that the shear stress of the bulk emulsions was assessed in a hydrostatic or hydrodynamic sliding regime (preventing solid–solid contact between the sliding surfaces or solidification processes that might occur in confined liquids), the load employed for measuring friction was set considerably lower than in the adhesion experiments, thereby maximizing film thickness. In accordance with theory that predicts lower friction with increasing film thickness [51,52], our measured shear stresses, i.e., the reported friction forces divided by the surface area of the used measuring heads, are comparatively low (0.6–7.3 kPa in the first and 0.009–0.9 kPa in the second generation emulsions). Being mainly determined by the viscosity of the emulsions, they are far from reaching the friction values measured in the isolated adhesive secretion of stick insects (lying in the range of about 100 kPa [5]) or intact insect tarsi (that can attain several hundred kPa [47,53,54]). Such differences are largely attributable to the different film thicknesses that have arisen during these experiments. Whereas, in thick fluid films, friction is largely determined by the viscosity of the liquid, in thin films, friction can be enhanced by processes such as (1) the formation of dry contacts by dewetting, (2) the solid-like behaviour of the liquid attributable to non-Newtonian properties, (3) the molecular ordering of the liquid at zones at which the film becomes thinner than a few monolayers and (4) the penetration of surface irregularities through the liquid film resulting in solid–solid contacts (cf. discussion in [55]). The influence of film thickness can also be seen in our experiments. Although we assume that in all of our experiments, we measured in the regimes of hydrostatic or hydrodynamic lubrication (cf. [56]), our nanotribometric experiments revealed much higher shear stresses than the plate-plate rheology. Whereas most experimental conditions were basically comparable in both these methods, they differed in the obtained layer film thickness (gap size). In the plate–plate-rheology, it amounted to 540 µm, which ensures the characterization of the emulsions as a bulk component. In contrast, in the nanotribometry experiments, the film thickness was 43 µm at maximum (probably lower according to the applied normal load), which ensured similar conditions as expected for insect tarsi during locomotion. Several mechanisms might influence the flow behaviour of liquids in confined spaces (e.g., [56,57]). In our nanotribometry experiments, at least the larger droplets of the emulsions are in the size range of the measurement gap applied, so that they might have become deformed or even finer dispersed under these conditions and this way changed the rheological behaviour of the emulsions compared to the properties of the bulk.

Friction was tested at three different sliding speeds to make the comparisons between the emulsions more reliable with respect to possible velocity dependencies of the friction performance. According to their (semi-)solid consistency (which is attribut-

able to the higher viscosity of their constituents), our first generation emulsions showed a considerably higher friction performance, ranging from 4–93 mN (depending on the sliding speed) compared with the emulsions of the second generation and the squalane and water controls. Because of to their often rubber-like appearance, our measurements of these emulsions probably did not take place in the fluid friction regime but represent rubber friction [56]. Moreover, in such a regime, one expects an increase of friction with increasing sliding velocity [58-60] as has been shown by most of our first generation emulsions. In emulsion WG20, we established the opposite behaviour, i.e., the friction force decreased with increasing sliding velocity (Figure 4a). In this case, at the slowest sliding speed, we observed a clear stick–slip behaviour, which is known to produce especially high friction at local asperities but to decrease at higher sliding speeds [56,61].

The emulsions of the second generation show considerably lower friction forces that, depending on sliding velocity, range from 0.1–5.8 mN. Most of these emulsions show friction values as low as that of water, being even lower than the pure squalane used as a control. In the oil-in-water (o/w) emulsions, the phase volume ratio amounted to <1, so that their flow characteristics were largely dominated by the continuous watery phase. In combination with the use of the ionic surfactant SDS (which lowers the surface tension even further), this probably explains the low friction values of these emulsions. By contrast, two of the oil-in-water (o/w) emulsions (SG2, OG2) showed increased friction values; this can be ascribed to their semi-solid (rubber-like) appearance (because of their gelatin content) that was previously mentioned as explaining their increased adhesiveness (see section Discussion/Adhesion). Both the presumed water-in-oil (w/o) emulsions (SA4, SG4) show friction performances that are slightly increased towards both the water control and the above-mentioned oil-in-water (o/w) emulsions showing water-like low friction values. In these emulsions, the oily proportion is largely increased with respect to the water fraction, so that the lipid component squalane is able to take effect in enhancing the friction.

The friction values measured under the mediation of an emulsion almost always showed higher values than the friction obtained under dry conditions (i.e., direct sliding of the smooth wafer onto the smooth glass surface), suggesting a friction-enhancing effect of the fluid, even if its friction performance is similarly low to that of water (Figure 4b, Supporting Information File 1, Table S2). Under the dynamic situation of sliding friction in a soft tribology regime with elastomer-like tarsal adhesion structures (cf. [29]), this can be attributed to the contribution of the viscous forces of these fluids to friction.

Conclusion

In the present contribution, we abstracted the polar/non-polar principle of emulsions to mimic the tarsal liquid that is secreted from insect feet in order to enhance tarsal attachment. One central property that we desired to achieve was the combination of reversible adhesion and easy release (peeling off) from the substrate. Whereas such a combination is difficult to attain with conventional adhesive systems, it is essential for insects for effective locomotion. Although many constructional adhesives (e.g., casein glues, adhesive tapes, medical patches and adhesive labels) are heterogeneous, their emulsions easily lose their structure after application resulting in a homogeneous bond line. The "polar/non-polar" principle involving lipid components has not as yet been accomplished in this context, although it might help to construct versatile adhesive systems that, for instance, make possible repeated and reversible contact and release without the degradation of the adhesive performance. Similar to the insect role model, such biofunctional adhesives might be combinable with microstructured adherents (e.g., technical polymer foams and sheets) in order to make use of possible synergisms between the structural component of the carrier (e.g., its viscoelasticity or the geometry of its surface) and the physico-chemical properties of the adhesive. The combination of emulsion-based adhesives and porous carrier materials should make possible the fine-tuning of bonding technological properties, especially in the range of low adhesive forces. Possible fields of application are initially non-sticky tapes whose adhesiveness can be activated by compressive stress, medical (with active pharmaceutical ingredients loadable and easily (free of pain) removable) patches, fluid-supplied medical patches for the treatment of burns and, with respect to their adhesiveness, controllable capillarity-based adhesion devices [62].

The adhesive strengths of our synthetic "insect emulsions" of the second generation lie well within the range of tenacities measured in intact insect tarsi. Considering their droplet sizes, they also seem to be structurally most similar to their biological role models. In our experiments, we measured the adhesive performance between two rigid (non-deformable) plates, whereas in tribological measurements of intact tarsi, one always measures the influence of the energy dissipation in the viscoelastic cuticle, which provides additional resistance towards separation. This suggests that natural insect tarsal adhesives actually show only low adhesive strengths that are in the range of a few kilopascal. Such properties have been produced especially in four of the emulsions of the second generation (SA2, OA2, SW2, OW2) by using the hydrocarbon components squalane (liquid at room temperature) or octacosane (solid at room temperature), the latter forming a colloidal lipid suspension. Whereas the adhesion and friction properties of these

emulsions are similar to those of water, they probably show, because of their hydrocarbon components, additional functional properties of technical relevance such as improved resistance towards desiccation and contamination, and beneficial wetting properties towards both hydrophilic and hydrophobic surfaces.

The low adhesive strengths of natural insect tarsal adhesives are in strong contrast to the extremely high shear stresses measured in intact insect tarsi; these stresses can exceed adhesive tenacities by one to two orders of magnitude. We must assume that such discrepancies are the result of thin film thickness and boundary lubrication effects [56] in combination with the viscoelastic properties of pliable tarsal cuticles. In our nanotribometric friction experiments involving low normal loads and high liquid film thicknesses, we did not determine shear stresses under the conditions of such very thin liquid films in confined geometries, but rather assessed the viscosity of the bulk emulsion. As expected, these experiments revealed especially low shear stresses in the four emulsions of the second generation (SA2, OA2, SW2, OW2) that had previously shown low adhesive strengths. In addition, despite of their relatively high adhesiveness, the two presumed water-in-oil (w/o) emulsions SA4 and SG4 of the second generation exhibited similarly low shear stresses. Such behaviour (low shear stress at relatively high adhesive strength) might make possible the easy detachment of adhesive bonds by applying shear forces to the connected surfaces. Both these emulsions might actually resemble our biological role models most closely, since previous studies on the emulsion structure of insect tarsal adhesives have provided evidence that they are water-in-oil emulsions [14,23]. From this perspective, our technical emulsions might provide a clue as to the way that tarsal insect adhesives reconcile easy detachment at moderately high adhesive strength. In both these emulsions, our rheological experiments have established Bingham fluid-like shear thinning behaviour that shows an initial minimum "yield stress" before the emulsion start to flow [14].

In addition to such oily water-in-oil (w/o) emulsions, many insects [16,17] seem to exhibit (semi-)solid-like tarsal adhesives as achieved in all of our preparations of the first generation and two emulsions (SG2, OG2) of the second generation. In particular, in natural insect adhesives, the complex composition with fluidity enhancers (represented by branched and unsaturated hydrocarbons) adds to a semi-solid-like base. In addition, a melting point depression attributable to mixtures of diverse hydrocarbons might support such behaviour. In particular, OG2 comes close to the demand of low shear stress at moderately high adhesive strength that should facilitate detachment.

Our research suggests that technical systems inspired by emulsion-like insect adhesives might benefit from the possibility of adjusting their adhesive connections to current demands. In such devices, undesired detachment can be combined with easy removability, whereby the required attachment and detachment forces can be fine-tuned via polar and non-polar components and amphiphilic emulsifiers, their respective mixing ratios and the specific conditions under which the emulsions are prepared.

Experimental

Preparation and composition of synthetic emulsions

Preparation of synthetic first generation emulsions (VG50, VP50, WG20 and WP20)

The following solutions were prepared to form the desired emulsions:

- A gelatin/glycerine solution (20 wt %) was prepared by mixing 64.5 g gelatin (Sigma-Aldrich, Munich, Germany), 35.5 g glycerine (Ph. Eur., Sigma-Aldrich), 0.10 g sodium azide (as biocide, Sigma-Aldrich) with 400 mL deionized water. The obtained mixture was stirred at 40 °C until the gelatin had been completely dissolved.
- A poly(vinyl alcohol) solution (20 wt %) was obtained by the addition of 100 g poly(vinyl alcohol) (Mowiol 10-98, Ter Hell & Co. GmbH, Hamburg, Germany) and 0.10 g sodium azide to 400 mL deionized water. The obtained mixture was stirred at 80 °C for 2.5 h until the poly(vinyl alcohol) had been completely dissolved.

In the case of stained emulsions, the hydrophobic components microcrystalline wax (Sasolwax® 1800, Sasol Germany GmbH, Hamburg, Germany) and Vaseline (Ph. Eur., Sigma-Aldrich) were mixed with 0.01 wt % Sudan III (Sigma-Aldrich) at 80 °C until complete dissolution of the dye.

The emulsions were created by mixing sodium dodecyl sulfate (SDS) (Sigma-Aldrich) with the poly(vinyl alcohol) or gelatin solution in a SpeedMixer™ cup. After addition of the wax or Vaseline, the samples were homogenized in a SpeedMixer™ (Hauschild & Co. KG, Hamm, Germany) for three times at 3500 rpm for 30 s. The compositions of the prepared emulsions are shown in Table 2.

Preparation of synthetic second generation emulsions (SA2, SG2, OA2, OG2, SW2, OW2, SA4 and SG4)

A sodium azide solution was obtained by dissolving 80 mg sodium azide in 400 mL deionized water. A sodium azide/SDS solution was prepared by dissolving 80 mg sodium azide and 96 mg SDS in 400 mL deionized water.

Table 2: Composition of first generation emulsions.

emulsion name	hydrophilic solution	hydrophobic component	amount SDS
VG50	30 g poly(vinyl alcohol) solution	30 g Vaseline	172 mg
VP50	30 g gelatin solution	30 g Vaseline	172 mg
WG20	48 g poly(vinyl alcohol) solution	12 g Sasol wax	69 mg
WP20	48 g gelatin solution	12 g Sasol wax	69 mg

In the case of stained emulsions, squalane (>95% technical grade, Sigma-Aldrich) and octacosane (99%, Sigma-Aldrich) were mixed with 1.5 ppm Sudan III until they had dissolved at room temperature and 80 °C, respectively.

The protein-containing emulsions were created by dissolving gelatin or albumin (Fraction V, >98%, Carl Roth GmbH & Co. KG, Karlsruhe, Germany) in 46 g of the prepared sodium azide/SDS solution. Albumin and gelatin were dissolved at room temperature and 40 °C, respectively. The hydrocarbon (squalane or octacosane) and the surfactant Span 80 (sorbitan monooleate, for synthesis, Carl Roth GmbH & Co. KG) were added to the solution. The mixture was homogenized by the impact of ultrasound (Bandelin Sonoplus, Bandelin electronic GmbH & Co. KG, Berlin, Germany) with the ultrasound transducer UW 2070, stepped standard horn SH 213G and sonotrode VS70T. During sonification with maximum ultrasound power, the temperature of the solution had to be controlled and kept between 60 and 65 °C. The sonification time did not exceed 1 min. The two protein-free emulsions SW2 and OW2 were prepared in the same way as the protein-containing emulsions, but without adding proteins. The compositions of the protein-containing and protein-free emulsions are shown in Table 3.

The inverse (w/o) emulsions were prepared by dissolving albumin and gelatin in a sodium azide solution at room temperature and 40 °C, respectively. A second solution was prepared with squalane, Span 80 and AOT (sodium di(ethylhexyl)sulfosuccinate, Sigma-Aldrich) by continuous stirring. Both solutions were combined and homogenized by ultrasound (see conditions above). The compositions of the inverse emulsions are shown in Table 4.

The general appearance of the prepared emulsions (cf. Supporting Information File 1, Table S1) of both the first and the second generation was evaluated by mechanically probing them with a spattle.

Descriptive analysis of emulsion structure

Light optical and fluorescence microscopy

Microscopic assessment of the emulsions was performed by using an optical light microscope Zeiss Imager.Z1 (Carl Zeiss Microscopy GmbH, Jena, Germany). Both types of emulsion, water-in-oil (w/o) emulsions and oil-in-water (o/w) emulsions, were diluted with the respective outer phase prior to microscopic assessment. In the case of solid emulsions, a piece of the emulsion was picked and transferred into a microcentrifuge tube containing the respective outer phase. The mixture was liquefied by briefly being heated on a hot plate (Heidolph MR 3001 K; Heidolph Instruments GmbH, Schwabach, Germany). Some droplets of the diluted emulsions were placed on a microscope slide and carefully covered with a coverslip avoiding the entrapment of air bubbles.

The phase distribution of the emulsions was assessed by fluorescence microscopy of the stained emulsions. Fluorescent emulsions were formulated by dissolving Sudan III in the oil phase at a concentration of 0.1 % (w/w). Images were obtained

Table 3: Composition of second generation emulsions with and without protein content.

emulsion name	squalane	octacosane	Span 80	sodium azide/SDS solution	albumin	gelatin
SA2	1.98 g	—	0.84 g	46 g	3.18 g	—
SG2	1.98 g	—	0.84 g	46 g	—	3.18 g
OA2	—	1.98 g	0.84 g	46 g	3.18 g	—
OG2	—	1.98 g	0.84 g	46 g	—	3.18 g
SW2	1.98 g	—	0.84 g	46 g	—	—
OW2	—	1.98 g	0.84 g	46 g	—	—

Table 4: Composition of second generation inverse emulsions.

emulsion name	squalane	AOT	Span 80	sodium azide solution	albumin	gelatin
SA4	25.6 g	0.11 g	10.8 g	14.6 g	1.0 g	—
SG4	25.6 g	0.11 g	10.8 g	14.6 g	—	1.0 g

with a fluorescence microscope (Zeiss Imager.Z1; Carl Zeiss Microscopy GmbH) by using an HBO 100 mercury lamp, the filter set 43 (excitation: 550/25, emission: 605/70) and the filter set 49 (excitation: 365, emission: 445/50). In both light and fluorescent microscopy, images were recorded with an AxiCam MRm camera (Carl Zeiss Microscopy GmbH) and Axiovison 4.7.1 software (Carl Zeiss Microscopy GmbH). For fluorescent microscopy, the oil phase was identified as the fluorescent phase, whereas the aqueous phase appeared dark.

Cryo scanning electron microscopy (cryo-SEM)

For this application, we mainly followed an already established protocol ("method 1" in [63]). In the case of solid emulsions, a small piece with dimensions 6.5 mm × 4.1 mm × 3.0 mm was cut out and glued into the hole of a copper carrier with Tissue-Tek® O.C.T.TM (Sakura Finetek Europe B. V., Alphen aan den Rijn, The Netherlands). In the case of liquid emulsions, the emulsion was homogenized by an ultrasonic transducer UP200S (Hielscher Ultrasonics, Teltow, Germany) at an intensity of 85% for two minutes. After homogenization, the liquid was added in a hole of a copper carrier until the formation of a bulge on the surface of the carrier. We used the transfer unit/preparation chamber Emitech K1250X (Quorum Technologies, Laughton, UK) (the sublimation time amounted to 3–4 min at −95 °C to −80 °C) and the SEM Evo LS10 (Carl Zeiss Microscopy GmbH, Jena, Germany).

The resulting cryo-SEM images were analyzed by single measurements of about 20 randomly distributed droplets by using the digital image processing software AxioVision (v. 4.6.3, Carl Zeiss Microscopy GmbH).

Determination of type of emulsion

The fluorescent microscopical images were used to evaluate the type of emulsion, i.e., oil-in-water (o/w) versus water-in-oil (w/o). Emulsions with fluorescent droplets against a dark background were classified as oil-in-water (o/w) emulsions, because only the stained lipid phase possessed fluorescent properties. Vice versa, fluorescence shown by the outer phase only in combination with dark (non-fluorescent) droplets was indicative of a water-in-oil (w/o) emulsion.

Droplet-size distribution

The analysis of the droplet-size distribution was based on both the microscopic fluorescent and bright field images. To this aim, in Adobe® Photoshop® CS4 11.0, clear visible droplets within a selection of 1–3 fluorescent and bright field images (Supporting Information File 1, Figure S3a) were painted with an intense colour, i.e., green or red (Supporting Information File 1, Figure S3b). In ImageJ (W. Rasband, v. 1.47n), all the coloured droplets were marked by the "colour threshold tool" to convert them into a black and white image with clear black droplets. The largest and the smallest diameter of each droplet was measured by the function "analyze particles". Based on the arithmetic means of the smallest and the largest diameter of a droplet, the main size range of droplets within the light/fluorescence microscopy was defined by the range of the 15% and the 85% quantiles. Afterwards, the volume V of the measured droplets was calculated by Equation 1.

$$V = \frac{1}{6}\pi d^3, \quad (1)$$

where d is the arithmetic mean of the smallest and largest diameter of a droplet. For a better overview, all the volumes were arranged in certain defined droplet-size groups. Therefore, a Microsoft EXCEL table with defined droplet-size ranges and equivalent volume ranges was created that served as a template to sort all the measured volumes. The percentage by volume (Equation 2) was calculated to illustrate the actual percentage of each group compared with the total volume of all the droplets together:

$$V\% = \frac{\text{volume size of group} \cdot \text{number of droplets}}{\text{total volume of all droplets}} \cdot 100 \quad (2)$$

Determination of droplet sizes by Laser diffraction

The droplet-size distribution of the emulsions was determined by laser diffraction by using a Beckmann Coulter LS (Brea, CA, USA) equipped with a micro liquid module as the measurement cell. The applied detection range was 0.04–2000 µm and the optical model used for calculation of droplet-size distribution was Fraunhofer plus PIDS. For the measurements, the samples were diluted with deionized water.

Calculation of phase volume ratios

The phase volumes of the dispersed and continuous fractions of the prepared emulsions used as model adhesives were estimated by the applied composition. The volumes of the dispersed and the continuous phases were determined based on their densities (Supporting Information File 1, Table S16). The amphiphilic compounds AOT and SDS were not considered as they could not be assigned to one of the phases. These compounds formed instead the interphase [64], which had an unknown thickness and also contained unknown amounts of the hydrophilic and hydrophobic compounds. However, for the non-ionic surfactant Span 80, three possible distributions were assumed: (1) Span 80 fully dissolved in the hydrophilic fraction, (2) Span 80 fully dissolved in the hydrophobic fraction or (3) the fatty acid section of Span 80 dissolved in the hydrophobic fraction, whereas the sorbitan section dissolved in the

hydrophilic fraction. The calculation of the phase volume of each emulsion was achieved by the division of the volume of the dispersed phase by the volume of the continuous phase. The standard deviation originated because of the unclear distribution of Span 80. However, we estimate the error of the determined phase volume to be lower than 10% relative.

Rheological characterization of selected emulsions

The major goal of these experiments was the confirmation of the existence of a yield point as is characteristic for Bingham fluids. The rheological behaviour of selected emulsions was determined with an AR 1000-N Rheometer (TA Instruments, New Castle, DE, USA) by using plate–plate geometry in shear stress controlled measurement mode. Plates with a diameter of 22 mm were applied and the gap size was 540 µm. The shear rate range was 1–60 s^{-1} and the measurement temperature was 25 °C for emulsions SA4 and SG4 and 40 °C for emulsions SA2 and SG2.

Tribological determination of adhesion and friction

The tribological measurements were performed with a nanotribometer NTR^2 (CSM© Instruments, Peseux, Switzerland) equipped with the dual beam cantilever STH-001. This cantilever features a highly sensitive dual beam spring, which is able to measure forces in the *x*- and *z*-direction with a resolution of 30 nN. Both adhesion and friction forces are detected by two independent high-resolution capacitive sensors, whereas a piezo actuator provides smooth and steady motion at a slow pace. The actual measuring head consists of an even and almost square-shaped SiO_2-coated silicon wafer plate (SilChem, Freiberg, Germany) of 6.45 mm^2 (4P02/50, orientation 100, bulk-doping with n/phosphorus). Its thickness amounted to 380 µm. Abrasive blast cleaning resulted in roughness values of 1.88 µm (Ra) and 2.40 µm (Rq), respectively. The surface energy of the pristine silicon wafer is 35 mN m^{-1} and 31 mN m^{-1} after abrasive blast cleaning, respectively. Before measurement, the solid emulsions were heated in a water bath to 35–40 °C yielding a spreadable consistency. The liquid emulsions were homogenized by the ultrasonic transducer UP200S at an intensity of 85% for two minutes. Afterwards, the emulsions were applied to a glass slide within an interspace (0.8 × 4.0 cm), confined by stripes of Sellotape™ or Scotch® Tape. The height of the tape was 43 µm leading to an emulsion film thickness of the highly viscous emulsions (WP20, WG20, VP50, VG50, SG2, OG2, SA4, SG4) of the same height. In the case of the aqueous, low viscous emulsions (SA2, OA2, SW2, OW2), 60 µL of one emulsion was applied onto the glass slide within the interspace and smoothed out with the tip of a pipette. Preliminary pretests showed that if we had used less than 60 µL, the liquid film within the interspace would have contracted (due to its high surface energy) from the outside towards the center, which would have prevented measurements on continuous and steady liquid films. The excess fluid was pressed out beyond the tape borders upon the displacement of the liquid due to the applied normal force. The measurements were performed at room temperature (≈22 °C).

Adhesion measurements

The adhesion force was determined by pressing a SiO_2-coated silicon wafer plate on the emulsion film followed by continuously pulling it away perpendicularly to the surface. Once the wafer touched the surface with a contact load of 0.3 mN, the measurement started. The pressure was then increased up until 3.3 mN with a loading rate of 0.1 mN s^{-1}. After being held at 3.3 mN for two seconds, the pressure decreased with an unloading rate of 0.1 mN s^{-1}. At a load of 0.3 mN, the wafer was retracted with a speed of 33.3 µm s^{-1}. The software Indentation 5.15 (CSM© Instruments, Peseux, Switzerland) was used for recording and analysing the adhesion measurements. After the baseline had been set at a value before any pressure was applied, the lowest value represented the adhesion force.

In the experiments, the silicon wafer was immersed into a smear of the emulsion to be tested, pressed to the surface of the microscope slide and eventually retracted at a constant speed normal to the contact surface (without shear or pulling forces). In such a setup, which involves a relatively high amount of fluid, one mainly measures the adhesion that corresponds to the viscosity of the fluid as is typical in viscous (Stefan) adhesion regimes [65]. Our experiment is comparable with a probe tack test as commonly carried out for pressure sensitive adhesives (PSA). Wetting takes place as soon as the probe comes into contact with the emulsion. In our experiments, in most of the emulsions, failure was cohesive, since after separation, parts of the emulsion were present on both formed surfaces. In this case, the energy required for separation depends mainly on the viscosity of the emulsion and, in addition, on the formation of fibrils during the separation of the surfaces. Only in the four gelatin-containing emulsions (VG50, WG20, SG2, OG2) with solid consistence at room temperature did the wafer seem to separate directly at the surface of the emulsion, since no remnants of it were left on its surface after separation. This is indicative of the high viscosity and cross-linking of the adhesive leading to high cohesive strengths. The required force in this case depends mainly on the surface energies of the probe and the adhesive and to a minor extent to the deformation of the adhesive.

Friction measurements

The friction force was determined by dragging the SiO_2-coated silicon wafer over the surface of the emulsion within the tape confined interspace with a load of 0.6 mN. The wafer was rubbed with an oscillating motion of 3–5 cycles over the sur-

face, whereby one cycle represents one full forward and backward motion. Every emulsion was sampled at three different dragging speeds and distances, i.e., 50 µm s^{-1} (distance of 500 µm), 200 µm s^{-1} (distance of 700 µm) and 500 µm s^{-1} (distance of 800 µm). The friction curves were recorded and analysed with the software TriboX 4.4.T (CSM© Instruments, Peseux, Switzerland). The last cycle was always ignored, because sometimes it was not completely finished. The friction force F_f was calculated via Equation 3:

$$F_f = \mu \cdot F_N \quad (3)$$

where µ is the friction coefficient and F_N is the normal load. For one measurement, the arithmetic mean of the sliding friction values of all performed cycles was calculated considering forward motion only.

Statistical analyses

In terms of the structural data, various descriptive statistics (e.g., mean value, median, excess kurtosis) were calculated from the combined frequency distributions of the droplet volumes measured by laser diffraction and by fluorescent and bright field images. Whereas volumes associated with droplet sizes >1.5 µm were taken from the microscopical analysis (Supporting Information File 1, Figure S3c), all volumes determined by fluorescent and bright field images belonging to droplets <1.5 µm were replaced by the results of the laser diffraction. As the limitation of the angular resolution of the microscope is approached, the reliability of droplet sizes <1.5 µm decreases, whereas the laser diffraction offers accurate resolution in the nanometer range.

With respect of the performance data (adhesion and friction), all the statistical analyses were performed on logarithmized values. Before logarithmization, the number one was added to all the values in order to avoid negative logarithms. Any statistical differences in adhesion and friction between the emulsions were tested by a nonparametric Kruskal–Wallis ANOVA followed by Kruskal–Wallis post hoc multiple comparisons. In addition, the grand means of the first and second generation of emulsions were compared with a Mann–Whitney U test. For a comparison of the influence of the various speeds in the friction experiments, a Friedman test followed Friedman post hoc multiple comparisons was performed.

Additionally, all descriptive, tribological and chemical parameters were correlated against each other to reveal any relationships between these categories. For this analysis, the structural parameters of the two controls water and squalane were defined by 0. Moreover, deviating from our descriptive statistics (Supporting Information File 1, Table S1), the phase volume ratio was calculated by dividing the hydrophobic (oily) phase by the hydrophilic (watery) phase. This was necessary to attain a consistent interpretation of the results with respect to o/w and w/o emulsions. All the statistical analyses were performed with IBM® SPSS® Statistics 22 on logarithmized values. Before logarithmization, the number one was added to all the values of the chemical and tribological parameters and the descriptive parameters were increased by 2.573 to avoid negative logarithms (the excess kurtosis −1.573 of the emulsion WG20 was the lowest value).

The levels of significance were classified into four groups symbolized by asterisks (*), i.e., * representing $p < 0.05$, ** representing $p < 0.01$ and * * * representing $p < 0.001$. One asterisk in brackets (*) represents an almost significant test result at the 10% significance level, indicating that there is at least a trend towards significance.

Supporting Information

Supporting Information features additional emulsion images of both the first and the second generation, structural characteristics of all the emulsions, values of the adhesion and friction experiments and the specific test statistics.

Supporting Information File 1

Additional figures and tables.
[http://www.beilstein-journals.org/bjnano/content/supplementary/2190-4286-8-6-S1.pdf]

Acknowledgements

This work was supported by a grant from the German Science Foundation DFG (no. PAK 478) to Oliver Betz and Andreas Hartwig. We thank Monika Meinert for technical assistance with the cryo-SEM and Antonina Krieger for preparing the adhesive formulations. Stefan Fischer provided the image of the insect tarsus in the graphical abstract. Theresa Jones corrected the English. Three anonymous reviewers provided helpful comments to improve our manuscript.

References

1. Beutel, R. G.; Gorb, S. N. *J. Zool. Syst. Evol. Res.* **2001,** *39,* 177–207. doi:10.1046/j.1439-0469.2001.00155.x
2. Edwards, J. S.; Tarkanian, M. *Proc. R. Entomol. Soc. London, Ser. A* **1970,** *45,* 1–5. doi:10.1111/j.1365-3032.1970.tb00691.x
3. Dixon, A. F. G.; Croghan, P. C.; Gowing, R. P. *J. Exp. Biol.* **1990,** *152,* 243–253.

4. Betz, O. Adhesive exocrine glands in insects: morphology, ultrastructure, and adhesive secretion. In *Biological adhesive systems - From nature to technical and medical application;* von Byern, J.; Grunwald, I., Eds.; Springer: Berlin, Germany, 2010; pp 111–152. doi:10.1007/978-3-7091-0286-2_8
5. Drechsler, P.; Federle, W. *J. Comp. Physiol., A* **2006,** *192,* 1213–1222. doi:10.1007/s00359-006-0150-5
6. Persson, B. N. J. *J. Adhes. Sci. Technol.* **2007,** *21,* 1145–1173. doi:10.1163/156856107782328335
7. Dewitz, H. *Pfluegers Arch. Gesamte Physiol. Menschen Tiere* **1884,** *33,* 440–481. doi:10.1007/bf01628473
8. Stork, N. E. *J. Exp. Biol.* **1980,** *88,* 91–107.
9. Walker, G.; Yule, A. B.; Ratcliffe, J. *J. Zool.* **1985,** *205,* 297–307. doi:10.1111/j.1469-7998.1985.tb03536.x
10. Walker, G. *Int. J. Adhes. Adhes.* **1993,** *13,* 3–7. doi:10.1016/0143-7496(93)90002-Q
11. Lees, A. D.; Hardie, J. *J. Exp. Biol.* **1988,** *136,* 209–228.
12. Langer, M. G.; Ruppersberg, J. P.; Gorb, S. *Proc. R. Soc. London, Ser. B* **2004,** *271,* 2209–2215. doi:10.1098/rspb.2004.2850
13. Drechsler, P. H. Mechanics of adhesion and friction in stick insects and tree frogs. Ph.D. Thesis, University of Würzburg, Germany, 2008.
14. Dirks, J.-H.; Clemente, C. J.; Federle, W. *J. R. Soc., Interface* **2010,** *7,* 587–593. doi:10.1098/rsif.2009.0308
15. Reitz, M.; Gerhardt, H.; Schmitt, C.; Betz, O.; Albert, K.; Lämmerhofer, M. *Anal. Chim. Acta* **2015,** *854,* 47–60. doi:10.1016/j.aca.2014.10.056
16. Gerhardt, H.; Schmitt, C.; Betz, O.; Albert, K.; Lämmerhofer, M. *J. Chromatogr. A* **2015,** *1388,* 24–35. doi:10.1016/j.chroma.2015.02.027
17. Gerhardt, H.; Betz, O.; Albert, K.; Lämmerhofer, M. *J. Chem. Ecol.* **2016,** *42,* 725–738. doi:10.1007/s10886-016-0718-7
18. Betz, O.; Verheyden, A. N.; Maurer, A.; Schmitt, C.; Braun, J.; Kowalik, T.; Grunwald, I.; Hartwig, A.; Neuenfeldt, M. *Insect Mol. Biol.* **2016,** *25,* 541–549. doi:10.1111/imb.12241
19. Geiselhardt, S. F.; Geiselhardt, S.; Peschke, K. *Chemoecology* **2009,** *19,* 185–193. doi:10.1007/s00049-009-0021-y
20. Kölsch, G. *Can. J. Zool.* **2000,** *78,* 465–475. doi:10.1139/z99-213
21. Vötsch, W.; Nicholson, G.; Müller, R.; Stierhof, Y.-D.; Gorb, S.; Schwarz, U. *Insect Biochem. Mol. Biol.* **2002,** *32,* 1605–1613. doi:10.1016/S0965-1748(02)00098-X
22. Gorb, S. N. *Philos. Trans. R. Soc. London, Ser. A* **2008,** *366,* 1557–1574. doi:10.1098/rsta.2007.2172
23. Federle, W.; Riehle, M.; Curtis, A. S. G.; Full, R. J. *Integr. Comp. Biol.* **2002,** *42,* 1100–1106. doi:10.1093/icb/42.6.1100
24. Barnes, H. A. *Colloids Surf., A* **1994,** *91,* 89–95. doi:10.1016/0927-7757(93)02719-U
25. Bibette, J.; Leal Calderon, F.; Poulin, P. *Rep. Prog. Phys.* **1999,** *62,* 969–1033. doi:10.1088/0034-4885/62/6/203
26. Peisker, H.; Gorb, S. N. *J. Exp. Biol.* **2012,** *215,* 1266–1271. doi:10.1242/jeb.065722
27. Geiselhardt, S. F. Chemical, morphological and biomechanical aspects of tarsal attachment in beetles. Ph.D. Thesis, University of Freiburg, Germany, 2009.
28. Geiselhardt, S. F.; Lamm, S.; Gack, C.; Peschke, K. *J. Comp. Physiol., A* **2010,** *196,* 369–378. doi:10.1007/s00359-010-0522-8
29. Douaire, M.; Stephenson, T.; Norton, I. T. *J. Food Eng.* **2014,** *139,* 24–30. doi:10.1016/j.jfoodeng.2014.04.007
30. Farah, M. A.; Oliveira, R. C.; Caldas, J. N.; Rajagopal, K. *J. Pet. Sci. Eng.* **2005,** *48,* 169–184. doi:10.1016/j.petrol.2005.06.014
31. Lee, H. M.; Lee, J. W.; Park, O. O. *J. Colloid Interface Sci.* **1997,** *185,* 297–305. doi:10.1006/jcis.1996.4592
32. Speck, T.; Speck, O. Process sequences in biomimetic research. In *Design and Nature IV;* Brebbia, C. A., Ed.; WIT Transactions on Ecology and the Environment, Vol. 114; WIT Press: Southampton, United Kingdom, 2008; pp 3–11. doi:10.2495/DN080011
33. Derkach, S. R. *Adv. Colloid Interface Sci.* **2009,** *151,* 1–23. doi:10.1016/j.cis.2009.07.001
34. Pal, R. *Curr. Opin. Colloid Interface Sci.* **2011,** *16,* 41–60. doi:10.1016/j.cocis.2010.10.001
35. Chan, E. P.; Greiner, C.; Arzt, E.; Crosby, A. J. *MRS Bull.* **2007,** *32,* 496–503. doi:10.1557/mrs2007.84
36. Gorb, S. N.; Sinha, M.; Peressadko, A.; Daltorio, K. A.; Quinn, R. D. *Bioinspiration Biomimetics* **2007,** *2,* 117–125. doi:10.1088/1748-3182/2/4/S01
37. Li, W.; Kong, X. H.; Ruan, M.; Ma, F. M.; Jiang, Y. F.; Liu, M. Z.; Chen, Y.; Zuo, X. H. *Philos. Trans. R. Soc. London, Ser. A* **2010,** *368,* 4869–4890. doi:10.1098/rsta.2010.0197
38. Flammang, P.; Santos, R. *Interface Focus* **2015,** *5,* 20140086. doi:10.1098/rsfs.2014.0086
39. Gibbs, A.; Pomonis, J. G. *Comp. Biochem. Physiol., Part B: Biochem. Mol. Biol.* **1995,** *112,* 243–249. doi:10.1016/0305-0491(95)00081-x
40. Gibbs, A. *J. Insect Physiol.* **2002,** *48,* 391–400. doi:10.1016/S0022-1910(02)00059-8
41. Attygalle, A. B.; Aneshansley, D. J.; Meinwald, J.; Eisner, T. *Zoology (Jena, Ger.)* **2000,** *103,* 1–6.
42. Hasenfuss, I. *Zoomorphologie* **1977,** *87,* 51–64. doi:10.1007/BF02568741
43. Hasenfuss, I. *Zoomorphology* **1999,** *119,* 143–162. doi:10.1007/s004350050088
44. Habenicht, G. *Kleben: Grundlagen, Technologien, Anwendungen;* Springer: Berlin, Germany, 2009.
45. Betz, O.; Kölsch, G. *Arthropod Struct. Dev.* **2004,** *33,* 3–30. doi:10.1016/j.asd.2003.10.002
46. Jiao, Y.; Gorb, S.; Scherge, M. *J. Exp. Biol.* **2000,** *203,* 1887–1895.
47. Labonte, D.; Federle, F. *Philos. Trans. R. Soc. London, Ser. B* **2015,** *370,* 20140027. doi:10.1098/rstb.2014.0027
48. Labonte, D.; Federle, W. *Soft Matter* **2015,** *11,* 8661–8673. doi:10.1039/C5SM01496D
49. Koerner, L.; Gorb, S. N.; Betz, O. *J. Insect Physiol.* **2012,** *58,* 155–163. doi:10.1016/j.jinsphys.2011.11.001
50. Koerner, L.; Gorb, S. N.; Betz, O. *Zoology* **2012,** *115,* 117–127. doi:10.1016/j.zool.2011.09.006
51. Israelachvili, J. N. *Intermolecular and Surface Forces,* 3rd ed.; Academic Press: New York, NY, U.S.A., 2011.
52. Bhushan, B. *J. Vac. Sci. Technol., B* **2003,** *21,* 2262–2296. doi:10.1116/1.1627336
53. Clemente, C. J.; Federle, W. *Proc. R. Soc. London, Ser. B* **2008,** *275,* 1329–1336. doi:10.1098/rspb.2007.1660
54. Bullock, J. M. R.; Drechsler, P.; Federle, W. *J. Exp. Biol.* **2008,** *211,* 3333–3343. doi:10.1242/jeb.020941
55. Federle, W.; Baumgartner, W.; Hölldobler, B. *J. Exp. Biol.* **2004,** *207,* 67–74. doi:10.1242/jeb.00716
56. Mate, C. M. *Tribology on the small scale - A bottom up approach to friction, lubrication, and wear;* Oxford University Press: New York, NY, U.S.A., 2008.

57. Yoshizawa, H.; Chen, Y. L.; Israelachvili, J. *J. Phys. Chem.* **1993,** *97,* 4128–4140. doi:10.1021/j100118a033
58. Ariano, R. *Rubber Chem. Technol.* **1930,** *3,* 286–292. doi:10.5254/1.3535485
59. Derieux, J. B. *Rubber Chem. Technol.* **1935,** *8,* 441–442. doi:10.5254/1.3539455
60. Schallamach, A. *Proc. Phys. Soc., London, Sect. B* **1953,** *66,* 386–392. doi:10.1088/0370-1301/66/5/306
61. Rieger, H. Experimentelle und theoretische Untersuchungen zur Gummireibung in einem großen Geschwindigkeits- und Temperaturbereich unter Berücksichtigung der Reibungswärme. Ph.D. Thesis, Fakultät für Maschinenwesen und Elektrotechnik der Technische Hochschule München, München, Germany, 1968.
62. Vogel, M. J.; Steen, P. H. *Proc. Natl. Acad. Sci. U. S. A.* **2010,** *107,* 3377–3381. doi:10.1073/pnas.0914720107
63. Gorb, S. N.; Voigt, D.; Gorb, E. V. Visualisation of small fluid droplets on biological and artifical surfaces using the cryo-SEM approach. In *Modern Research and Educational Topics in Microscopy;* Méndez-Vilas, A.; Diaz, J., Eds.; Formatex Badajoz: Spain, 2007; pp 812–819.
64. Hartwig, A.; Meissner, R.; Merten, C.; Schiffels, P.; Wand, P.; Grunwald, I. *J. Adhesion* **2013,** *89,* 77–95. doi:10.1080/00218464.2013.731363
65. Stefan, J. *Ann. Phys.* **1875,** *230,* 316–318. doi:10.1002/andp.18752300213

License and Terms

BEILSTEIN JOURNAL OF NANOTECHNOLOGY

Innovations from the “ivory tower”: Wilhelm Barthlott and the paradigm shift in surface science

Christoph Neinhuis

Commentary

Open Access

Address:
Institute for Botany, Technische Universität Dresden, 01062 Dresden, Germany

Email:
Christoph Neinhuis - christoph.neinhuis@tu-dresden.de

Keywords:
Wilhelm Barthlott; 70th birthday; self-cleaning surfaces; lotus-effect

Beilstein J. Nanotechnol. **2017,** *8,* 394–402.
doi:10.3762/bjnano.8.41

Received: 11 August 2016
Accepted: 20 January 2017
Published: 08 February 2017

This article is part of the Thematic Series "Biological and biomimetic materials and surfaces".

Guest Editor: S. N. Gorb

Abstract

This article is mainly about borders that have tremendous influence on our daily life, although many of them exist and act mostly unrecognized. In this article the first objective will be to address more generally the relation between university and society or industry, borders within universities, borders in thinking and the huge amount of misunderstandings and losses resulting from these obvious or hidden borders. In the second part and in more detail, the article will highlight the impact of the research conducted by Wilhelm Barthlott throughout his scientific career during which not only one border was removed, shifted or became more penetrable. Among the various fields of interest not mentioned here (e.g., systematics of Cactaceae, diversity and evolution of epiphytes, the unique natural history of isolated rocky outcrops called inselbergs, or the global distribution of biodiversity), plant surfaces and especially the tremendous diversity of minute structures on leaves, fruits, seeds and other parts of plants represent a common thread through 40 years of scientific career of Wilhelm Barthlott. Based on research that was regarded already old-fashioned in the 1970s and 1980s, systematic botany, results and knowledge were accumulated that, some 20 years later, initiated a fundamental turnover in how surfaces were recognized not only in biology, but even more evident in materials science.

Separation

Most obviously, borders are meant to separate two or more entities from another (Figure 1). It might be our atmosphere separating us from space, an ocean separating two continents, a door in a building separating two rooms, down to a layer of atoms between a bulk material and its environment. Borders are inevitably necessary as can be seen from the compartmentation of a cell by membranes, essential for the function of all living organisms from archaea to the majestic blue whale, and eventually the biosphere.

On the other hand, borders separate in a sense that two entities are not able to get in contact with each other. Be it for the

exchange of matter, energy or information, or to look at or touch something or someone, or to mix or merge two components for the good or the bad.

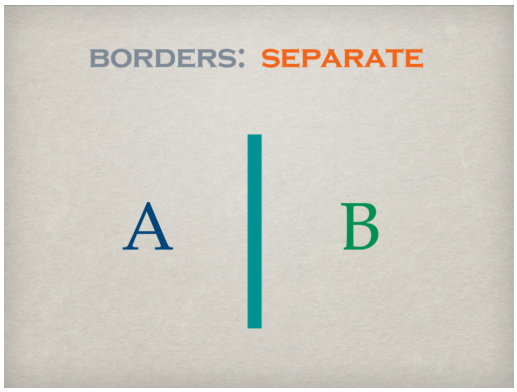

Figure 1: The bar separates A from B, one of the main functions of borders.

In addition, borders define space in which a given activity may take place or not, without affecting the neighbouring space (Figure 2). It may be a playground for children, a research lab, a space station, or a submarine. And in many cases, borders provide shelter or act as a protective cover, enabling individual development, or experimental approaches off the main stream that may or may not be successful, at least not at a given time.

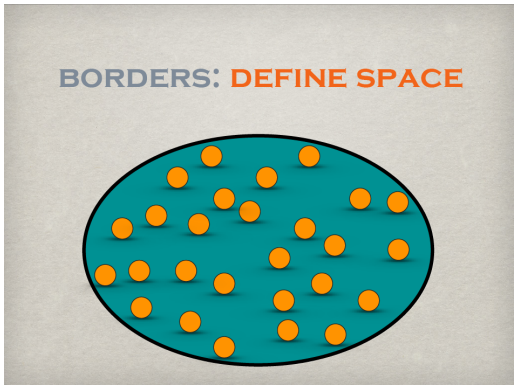

Figure 2: The circle encloses a defined space separated from the surrounding.

These entities, separated from a dominating larger environment, may serve as incubators fostering new approaches that on the one hand may never be applied or that on the other hand anticipate developments becoming relevant at a much later stage, often disconnected from the original work. We know a large number of inventions, drafts of machinery or theories that were commonly accepted, received attention, or became important only years or even centuries after their conception. In this regard, Leonardo da Vinci is one of the most frequently mentioned names, because he was obviously ahead of his time in many fields of natural history, medicine, and various aspects of engineering. Quite a number of such developments took place in a small space like the iconic “garage” serving as a nucleus for later industrial complexes or multinational companies, examples of which are well known. In addition the people initiating such a development or starting such businesses not rarely are very individualistic characters. Universities belong to those rare institutions providing space and resources in which unique characters, for which the term “nerd” has become popular, are able to unfold creativity and realize odd projects in a specific way of combining life and work.

Cultural differences

The knowledge transfer from universities (basic but, in part, also applied research, i.e., the “ivory tower”) to industry (i.e., in the meaning of earning money with applications) represents one of the repeatedly discussed borders. Within the scientific community a certain amount of disinterest exists with regard to the needs of industry or society. Confronted with these needs scientists like to claim the “freedom of research and teaching” for themselves. But it may also be the fear of control, to be under constraints or undue influence of industry, pressure on performance or more generally being exposed to critique eventually putting in question the relevance of someone’s activities.

Vice versa industry and/or society often show a considerable amount of ignorance with respect to the irritating thematic diversity and specific culture at universities, often referred to as “creative chaos” in a rather positive sense or, more negatively, inefficiency. If confronted with the nature of everyday scientific life (which may include lying on a sofa, pretending to think thoroughly or endless chatting without an agenda in contrast to sitting at an organised desk or attending a well-prepared and structured business meeting), people not familiar with this kind of working environment show a certain amount of helplessness, if not ignorance. In such situations statements are made that might contain phrases including those claiming that “these people are paid with public money” and that “their work should be of relevance to society or industry”, i.e., “return on investment” instead of “research in the ivory tower”. Such arguments are quickly and gratefully adopted by politicians as well, who prefer predictability over spontaneity and a manageable amount of topics over thematic variability and, finally and most important, control instead of free individualistic behaviour.

As a consequence universities or other research institutions may appear as a parallel world in contrast to industry although both aim at solving problems, however, with different aims and outcomes (Table 1):

Table 1: Differences in motivation to solve problems in industry and the scientific world.

industry	academia
economic success	satisfying personal curiosity
yields	third-party funding
shareholder value	impact points
market share	publications

These differences in aims and interests are inherently connected to different methods, internal procedures, control mechanisms, or parameters for success (Figure 3). When faced with a problem, companies offering a given technology usually try to improve this technology. They aim to find a better solution securing a given success on the market, but not necessarily the best solution for the problem; although these paths to improve the technology are potentially open. The improvement preferentially happens at highest speed and lowest costs to maximise economic success, an approach that is a priori biased usually neglecting other, probably more successful solutions on a longer time scale.

The first reaction of scientists to a given problem is similar, in the way that an appropriate experimental setup will be chosen to solve this problem. In this respect the process may be comparatively biased as well. The outcome, however, is not a better product that may remain unchanged for a considerable amount of time, but a new problem, resulting in a new experiment, hypothesis, theory, or method and therefore increased knowledge in an iterative process. Both approaches have their pros and cons and one is not necessarily better than the other. Many companies, especially those active in information technology, try to establish similar environments for individuality to foster creative solution finding.

Exploring different ways in parallel, although most of them may represent dead ends, is taken for granted in universities, and this is probably the most distinct difference between a company and a university lab. Nobody is surprised or will be blamed if an experimental setup fails or does not lead to the desired result (except the people who was running the experiment and needed the results). This is simply part of the job. Exploring all these possibilities, on the other hand, may result in unexpected and surprising results, eventually providing a technological, theoretical or methodological breakthrough. Not surprisingly, a considerable amount of such groundbreaking results derived from university research or institutions that are, at least partly, dedicated to basic research (Figure 4).

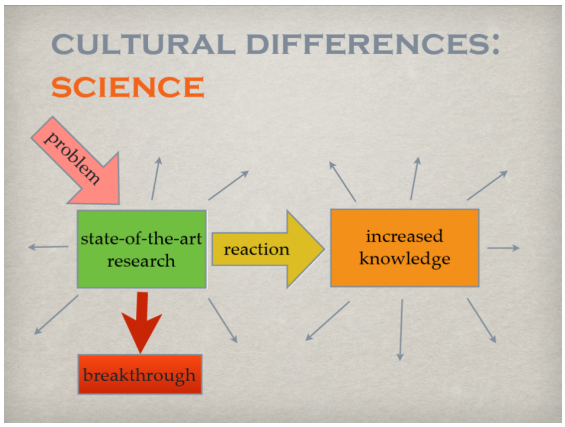

Figure 4: Achieving a breakthrough by following ideas off the mainstream.

As mentioned above, borders define space and may represent limits that, at least at a given time, might be impossible to overcome. Claiming freedom of research inherently includes the duty to use this freedom, or to fill the available space (Figure 5).

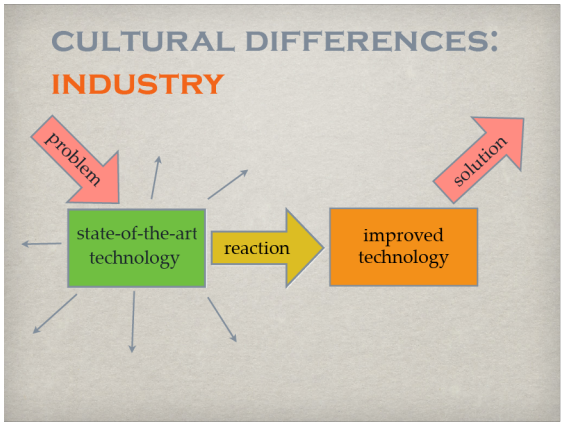

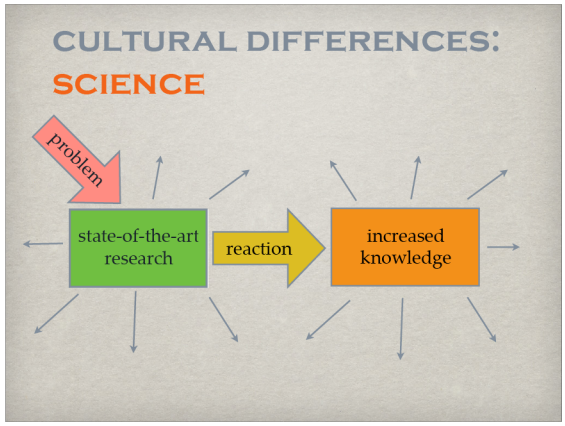

Figure 3: Some of the cultural differences between industry and science.

There might be temporary obstacles such as of technological nature as can be seen from computer industry in which computational power and storage capacity is increased on a regular basis by improved manufacturing processes. Others may be of ethical nature, such as the genetic engineering of microbes or the cloning of humans. A third obstacle may be intellectual property rights, hindering research and development. But all these obstacles are temporary. On the long run, everything that is possible will be realized, once an idea, a method, or a theory has become public and the technology is available. Not using the available space, however, allows for a niche existence without much attendance from the public or the scientific community. It allows for creating an "oasis of well-being" to avoid competition, to spend a nice time in a relaxed environment, a picture likely to be used by the public, politicians or business consultants invited to "optimise" structures and processes at universities.

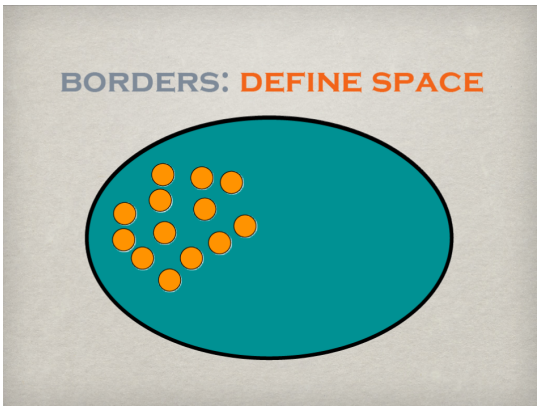

Figure 5: The available space for opportunities may be explored but does not necessarily need to be.

Selectivity

Selectivity is another important feature of borders (Figure 6). There are hardly any impenetrable borders as such. Therefore, a certain amount of exchange will always take place. Selectivity may be related to the exchange of matter, e.g., semipermeable membranes of cells and organelles, to the exchange of information regulated by confidentiality agreements, or to the loss of energy minimised by insulating material fixed to a façade. In the relation between university and industry and/or society, selectivity may be represented by the amount of results published or communicated by the scientific community ("I decide to publish only what I want"). On the other hand, the demand from industry and/or society is highly selective as well. Only results and information regarded as "relevant" under the constraints of applied filters will be extracted from the huge pool of accumulated knowledge irrespective of what is available and offered ("give me only the information that I want").

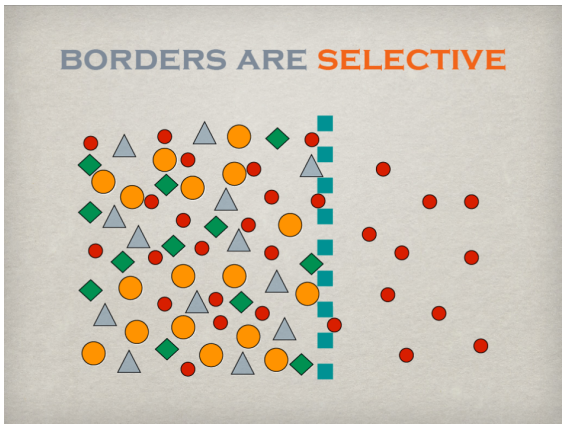

Figure 6: The selective permeability is another main function of borders.

These constraints are, in particular, scientific relevance and a framework that is based, among other things, on evaluations, performance criteria, impact factors and h-index, and the amount of third-party funding. This framework arises from political specifications such as quality pacts or target agreements. Thus, opportunistic behaviour is rewarded (you will be funded, if…; the idea is nice, but the reviewer suggests that…; you could get more staff after adding…) and research is shaped according to external criteria; proposals are formulated to fit into program descriptions, self-censorship is becoming the second nature of scientists.

Most importantly, the resilience of the scientific system/community to respond to future challenges will be severely threatened by reducing diversity and mainstreaming research. This is probably one of the most important lessons to be learned from nature: With increasing diversity ecosystems seem to be more resilient against external influences and disturbance [1,2].

Along with the processes mentioned above other developments are emerging with consequences hard to predict, such as the equalisation of universities and Fachhochschulen (universities of applied sciences) in Germany. The repeatedly demanded and rewarded "relevance", flanked by political measures, potentially allows industry to exploit universities. Even more, the expectations are that outstanding performance can be achieved without an appropriate investment into the institutions. Examples are the salaries of Ph.D. students and university staff, or the financial basis that governments are willing to provide for research and teaching at universities. The selective demand for results and information may result in a reduction of the diversity of research topics at universities on the one hand. On the other hand, the political framework suffocates creativity and will cause frustration by those not regarded as "relevant". It may even lead to the sell-out of scientists on the border of self-

abandonment. At the same time, exactly the same people claim that we need new ideas, innovative technologies and clever production tools to address the upcoming challenges for our societies, requiring out-of-the-box thinking, unconventional research approaches and sometimes weird stuff off the mainstream. One of these examples represents the early work of Wilhelm Barthlott.

Systematic botany, epicuticular waxes and a paradigm shift in interface science

In the 1970th, a new era began for the young Ph.D. student Wilhelm Barthlott at the Institute for Botany of the University of Heidelberg. He received one of the first scanning electron microscopes in German botany and started to intensively study the fascinating world of micro- and nanostructures of leaves, flowers, seeds or pollen grains.

Starting point was a distinct interest in systematics, i.e., the science of recording and arranging organisms according to their relation to each other as well as their natural history in connection with a botanic garden, which was keeping extensive collections, being at his disposal. During his approach to conduct broad surveys among various groups of plants, he soon recognized that certain structures were not distributed randomly but characteristic for distinct genera, families or higher-order groups. One of the first structures studied in detail were seeds [3-8]. Apart from the sole description of structures based on the surveys functional aspects of plants were always considered as well [3,6,9-11].

Soon, and even more intensively, Wilhelm Barthlott concentrated on those minute structures on leaves, shoots, or flowers, called epicuticular waxes [12-28]. During these extensive surveys thousands of species have been characterised by scanning electron microscopy compiling, to our knowledge, the largest dataset on plant epicuticular surface features. Epicuticular waxes are made up of various soluble lipids and, at least most of them, originate from self-assembly, again a topic studied in various different types of crystals accompanied by recrystallization experiments and modern microscopy techniques [29-38].

Examining plant surfaces, especially fine structures of micrometre size and smaller, through scanning electron microscopy needed careful preparation, including cleaning of the surfaces. After repeating these procedures again and again, Wilhelm Barthlott eventually realized that certain surfaces needed to be cleaned before examination while others did not. Surprisingly those surfaces that were already rather clean always turned out to be rough in certain dimensions and water-repellent, while those that were contaminated always were rather smooth or structured at a larger scale and readily wettable. He carried out simple experiments with *Tropaeolum majus* (Indian cress) by gluing small glass slides onto the surface of the leaves for a couple of weeks. A comparison of both surfaces, those of the leaves and those of the glass slides, revealed that the leaves were clean, while the glass slides were more or less densely covered by particles. Based on that observation, Wilhelm Barthlott formulated the hypothesis very early that “self-cleaning” might be one of the most important functions of rough water-repellent leaf surfaces [12] (Figure 7). This was elaborated in more detail later and the possibility of a technical application was already indicated [14].

Some years later, now appointed as professor for botany at the University of Bonn, Wilhelm Barthlott resumed this research. This was the time when I entered his group as student assistant. Based on numerous experiments revealing qualitative and quantitative data we were able to prove the astonishing self-cleaning properties of rough water-repellent surfaces by the end of the 1980s and realized that it was not published as a property of biological surfaces. Although this particular feature is easily observed and has nowadays become a standard experiment even in schools teaching bionics or biomimetics, it was virtually impos-

Figure 7: Fundamentals of self-cleaning in plants: a rough, hydrophobic surface (left) causes water to form spheres not adhering to the leaf (middle) removing particles while running off the leaf (right).

sible to publish the results. Apart from an internal report of the University of Bonn [39] several attempts to publish the results failed. Finally, with the help of the former editor Andreas Sievers, the paper appeared in "Planta" five years after the first submission [40] followed by a survey about the characterisation and distribution of self-cleaning surfaces among plants [41]. Regardless of the scepticism from the scientific community, self-cleaning surfaces nowadays are well known. The transfer and technical application have received several awards and the trademark "Lotus-Effect" has become a kind of synonym for functional water-repellent or even only hydrophobic surfaces. Follow-up investigations have been published in all major journals and the original paper, until now, is cited on average every second or third day. A total number of several thousand articles dealing with micro- and nanostructured, water-repellent surfaces emphasises the significance of the original findings. Although the number of economically successful products featuring self-cleaning properties is rather limited, self-cleaning based on rough hydrophobic surfaces initiated a new field of research and represents a paradigm shift in interface science.

So what happened and what can we derive?

Coming back to the picture of borders introduced above we may use self-cleaning surfaces as an example. First there is a field of research, systematic botany, often called "Orchideenfach" in German, i.e., an atypical academic discipline. Systematic botanists led a niche existence in their small academic world, were usually not very successful in raising third-party funding and published in journals with little or no impact at all and as such of limited public interest. This kind of existence, on the one hand, allows spending a whole scientific career, as mentioned above, in a kind of "oasis of well-being", escaping competition, never proving any relevance for the society. On the other hand, research is conducted in a protected environment, without much pressure from outside, dealing with topics off the mainstream (Figure 8). This happens most probably in a much more open-minded community, in which unconventional solutions for problems are more likely found than in an environment with a much more biased research focus.

In this particular example, one result of the research was the answer to the question of the systematic affinities of sacred lotus (*Nelumbo nucifera*). For the longest time scientist considered water lilies (*Nymphaea*) to be the closest relatives of lotus. However, epicuticular waxes, small tubules mainly composed of the secondary alcohol nonacosan-10-ol, as well as a specific group of alkaloids, implied that poppies (Papaveraceae) were more likely the sistergroup [42], results which were independently substantiated by molecular data [43].

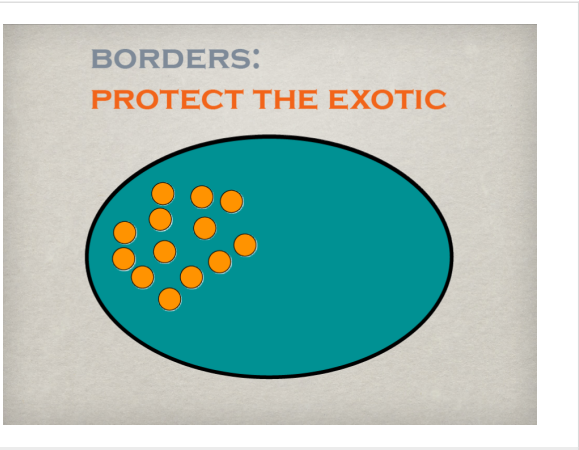

Figure 8: Borders separating a space from the surrounding may serve as a protective cover allowing for developments without external pressure or constraints.

Nice, but who cares? Typical results that nobody is really interested in, virtually useless, and without hardly any practical use for industry. This is what business consultants use to call irrelevant and what the general public usually ignores. However, during these investigations a tremendous amount of data and knowledge about plant surfaces was accumulated that turned out to be essential for the later research on functional aspects of surfaces.

Reluctance

After recognizing that self-cleaning in biological surfaces obviously was overlooked and realizing that a great potential for a transfer in technical surfaces existed, we contacted several companies introducing these fascinating properties to R&D departments. At that time we already cultivated quite a number of lotus plants for experiments and demonstrations allowing us to carry out simple experiments with leaves that were contaminated and cleaned by simply rinsing them with water.

Although everybody was electrified and instantaneously understood the principle and the potential, the outcome was frustrating. Again it was reluctance. The arguments were always the same: These are living organisms, much too complicated to understand and therefore it will be impossible to transfer the properties into a technical material. As a result, no cooperation could be established to move on and start a more practical project. Nobody was willing to invest in such a project and take the risk of failure.

The picture changed fundamentally after we decided to produce some simple technical surfaces that provided the basic requirements for self-cleaning, namely a hydrophobic material and a certain roughness. Several attempts to reproduce lotus surfaces by embossing and other more sophisticated methods failed

Figure 9: Is lotus related to water lilies (upper left) or poppies (lower left)? Epicuticular wax tubules (lower right) shared by ranunculids were one argument to place *Nelumbo* (upper right) close to the latter systematic group.

because of inappropriate technical skills and machinery. The first successful approach was rather simple: a commercially available polymer plate, which we covered with epoxy-resin glue fixing a layer of subsequently applied microscopic particles of PTFE. Although rather unstable with respect to mechanical influences, the plates exhibited the same properties as the lotus leaves. Figure 10 shows one of these early attempts. The plate has two sides, one smooth and one covered with PTFE particles. After contaminating both sides with toner from a photocopier and the red staining powder Sudan III, the plate was briefly rinsed with water. While the smooth side retained a considerable amount of particles, the structured one was completely cleaned. When we demonstrated this to several companies the reaction was completely different and the concept found acceptance.

Coming back to the picture that was introduced above, the following happened: Both the information demand from the industrial side as well as well as the information offer from the university side were filtered according to previous experience and knowledge . By realising these simple demonstrators the quality of information provided by the university changed and this in turn induced a different reception.

The filter changed

The pore size of the filter changed, the border became permeable for a different type and quality of information because it was not “complicated biology” anymore but the property of

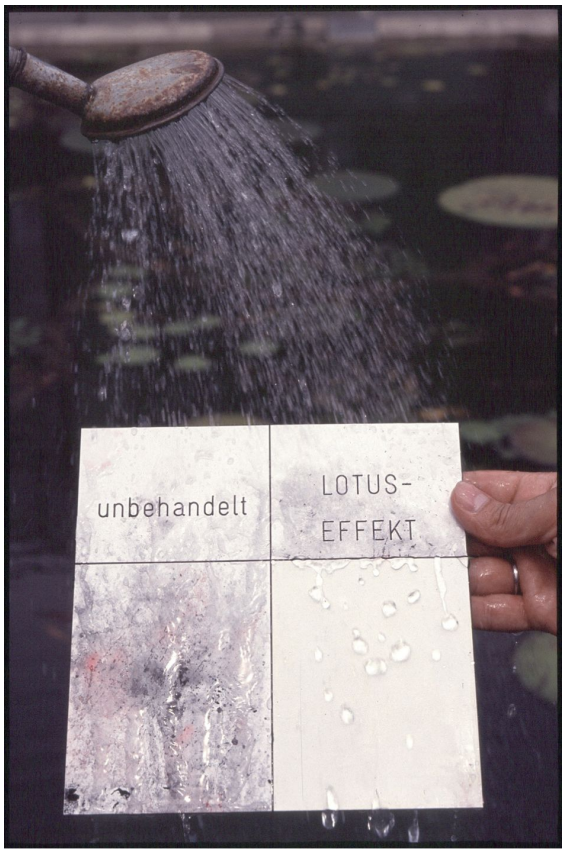

Figure 10: First demonstrator exhibiting the principle of self-cleaning derived from lotus leaves.

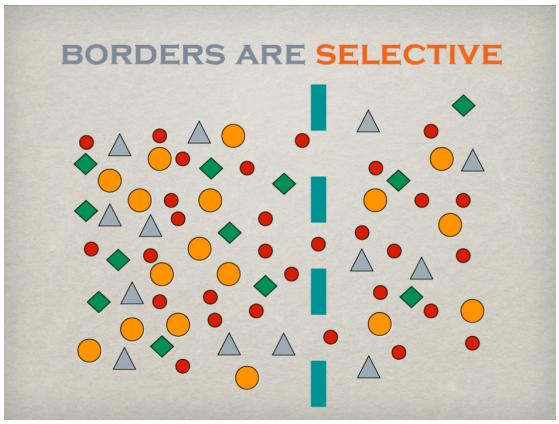

Figure 11: Depending on new developments, or changes in perception the selection criteria and, as a result, the permeability of the border may change .

self-cleaning was now demonstrated with a material that people in the industry were familiar with.

And now we received the attention we were looking for and much more because the whole effect could be easily demonstrated, transported strong pictures and everybody who saw a demonstration was sure to have understood the principle. After that, the interest of companies from all kinds of fields was tremendous and a new kind of research was initiated. Although functional surfaces have been a topic of great interest and importance before, the whole field received a boost that still holds on today.

And another result became apparent, although quite a while later: the acceptance of bioinspired technology. Although self-cleaning surfaces were not the first technically applied inspirations derived from biological models – well-known examples are evolutionary algorithms [44,45], “winglets” at the tips of airplane wings [46], “riblets” derived from shark skins [47], or form optimization of components based on tree growth [48] –, biomimetic approaches are still regarded as exceptional and not suitable to serve as examples for a general approach. Although at least some of them, such as Claus Mattheck´s computer-aided optimisation and other methods, have been widely applied in engineering.

Although the number of commercially available products exhibiting self-cleaning properties based on rough hydrophobic surfaces similar to those of lotus leaves is rather limited, the field was opened and there was a positive reception from the general public, politics and, most important, industry. Paving the way and initiating all these new developments is probably the biggest achievement of this irrelevant little research project, which started about 40 years ago. The niche has become mainstream, the orchid has become relevant.

Conclusion

Not everything that appears to be exotic and strange is irrelevant. Diversity, in all its various aspects should be maintained, even at high cost. Environments, be it biological, political, or economical change. This is their nature and we need to be prepared. We do not know the solutions for future challenges, we even do not know the challenges, but they will appear sooner or later and, who knows, may be some eccentric, spleeny young student is already puzzling about the solution.

This is a plea for the largest diversity possible under given circumstances in research and teaching. A reclusive existence in a niche at a university institute, a museum or even a lab off the beaten track in a company might imply snugness or laziness of the inhabitants. But it also means a little less conformity, a little bit more freedom, disorder, creativity and frankness for unconventional approaches. We need both worlds, both kinds of people, approaches and mentalities.

Wilhelm Barthlott represents one of these open-minded, unconventionally thinking people, off the beaten track who influenced the nature of many borders and paved new paths in the field of functional surfaces and other research areas. As mentioned above this was only one of his research topics among many that I did not mention. His contributions to the systematics of Cactaceae, the first comparative studies of rocky outcrops called “inselbergs” on a global scale, and finally the mapping of the global biodiversity including his long-lasting and continuing plea for the conservation of the whole of biological diversity will remain incentive and duty for future scientists.

References

1. Knoke, T.; Paul, C.; Hildebrandt, P.; Calvas, B.; Castro, L. M.; Härtl, F.; Döllerer, M.; Hamer, U.; Windhorst, D.; Wiersma, Y. F.; Curatola Fernández, G. F.; Obermeier, W. A.; Adams, J.; Breuer, L.; Mosandl, R.; Beck, E.; Weber, M.; Stimm, B.; Haber, W.; Furst, C.; Bendix, J. *Nat. Commun.* **2016,** *7,* No. 11877. doi:10.1038/ncomms11877
2. Newbold, T.; Hudson, L. N.; Arnell, A. P.; Contu, S.; De Palma, A.; Ferrier, S.; Hill, S. L. L.; Hoskins, A. J.; Lysenko, I.; Phillips, H. R. P.; Burton, V. J.; Chng, C. W. T.; Emerson, S.; Gao, D.; Pask-Hale, G.; Hutton, J.; Jung, M.; Sanchez-Ortiz, K.; Simmons, B. I.; Whitmee, S.; Zhang, H.; Scharlemann, J. P. W.; Purvis, A. *Science* **2016,** *353,* 288–291. doi:10.1126/science.aaf2201
3. Rauh, W.; Barthlott, W.; Ehler, N. *Bot. Jahrb. Syst. Pflanzengesch. Pflanzengeogr.* **1975,** *96,* 353–374.
4. Ehler, N.; Barthlott, W. *Bot. Jahrb. Syst. Pflanzengesch. Pflanzengeogr.* **1978,** *99,* 329–340.

5. Barthlott, W.; Voit, G. *Plant Syst. Evol.* **1979,** *132,* 205–229. doi:10.1007/BF00990466
6. Barthlott, W.; Ziegler, B. *Ber. Dtsch. Bot. Ges.* **1980,** *93,* 391–403.
7. Barthlott, W.; Ziegler, B. *Ber. Dtsch. Bot. Ges.* **1981,** *94,* 267–273.
8. Barthlott, W. In *Current Concepts in Plant Taxonomy;* Moore, V. H.; Moore, D. M., Eds.; Academic Press: London, United Kingdom, 1984.
9. Rauh, W.; Schill, R.; Ehler, N.; Barthlott, W. *J. Bromeliad Soc.* **1973,** *23,* 89–109.
10. Barthlott, W. In *8th World Orchid Conference,* German Orchid Society: Frankfurt, Germany, 1975; pp 438–443.
11. Barthlott, W.; Schultze-Motel, W. *Willdenowia* **1981,** *11,* 3–11.
12. Barthlott, W.; Ehler, N. *Trop. Subtrop. Pflanzenwelt* **1977,** *19,* 367–467.
13. Barthlott, W. *Nord. J. Bot.* **1981,** *3,* 345–355. doi:10.1111/j.1756-1051.1981.tb00704.x
14. Barthlott, W.; Wollenweber, E. *Trop. Subtrop. Pflanzenwelt* **1981,** *32,* 35–97.
15. Barthlott, W.; Frölich, D. *Plant Syst. Evol.* **1983,** *142,* 171–185. doi:10.1007/BF00985897
16. Behnke, H.-D.; Barthlott, W. *Nord. J. Bot.* **1983,** *3,* 43–66. doi:10.1111/j.1756-1051.1983.tb01444.x
17. Engel, T.; Barthlott, W. *Plant Syst. Evol.* **1988,** *161,* 71–85. doi:10.1007/BF00936014
18. Fehrenbach, S.; Barthlott, W. *Bot. Jahrb. Syst. Pflanzengesch. Pflanzengeogr.* **1988,** *109,* 407–428.
19. Frölich, D.; Barthlott, W. *Trop. Subtrop. Pflanzenwelt* **1988,** *63,* 279–409.
20. Barthlott, W. Evolution and Systematics of the Caryophyllales. Behnke, H. D.; Mabry, T. J., Eds.; Springer: Berlin, Germany, 1993; pp 75–86.
21. Ditsch, F.; Barthlott, W. *Trop. Subtrop. Pflanzenwelt* **1994,** *88,* 7–74.
22. Hennig, S.; Barthlott, W.; Meusel, I.; Theisen, I. *Trop. Subtrop. Pflanzenwelt* **1994,** *90,* 5–60.
23. Theisen, I.; Barthlott, W. *Trop. Subtrop. Pflanzenwelt* **1994,** *89,* 7–62.
24. Ditsch, F.; Patha, H.; Barthlott, W. *Beitr. Biol. Pflanz.* **1995,** *68,* 297–310.
25. Ditsch, F.; Barthlott, W. *Trop. Subtrop. Pflanzenwelt* **1997,** *97,* 1–248.
26. Wilhelmi, H.; Barthlott, W. *Trop. Subtrop. Pflanzenwelt* **1997,** *96,* 7–48.
27. Barthlott, W.; Neinhuis, C.; Cutler, D.; Ditsch, F.; Meusel, I.; Theisen, I.; Wilhelmi, H. *Bot. J. Linn. Soc.* **1998,** *126,* 237–260. doi:10.1111/j.1095-8339.1998.tb02529.x
28. Barthlott, W.; Theisen, I. In *The families and genera of vascular plants;* Kubitzki, K., Ed.; Springer: Berlin, Germany, 1998; Vol. III, pp 20–22.
29. Meusel, I.; Leistner, E.; Barthlott, W. *Plant Syst. Evol.* **1994,** *193,* 115–123. doi:10.1007/BF00983545
30. Meusel, I.; Neinhuis, C.; Markstädter, C.; Barthlott, W. *Can. J. Bot.* **1999,** *77,* 706–720. doi:10.1139/b98-229
31. Ensikat, H. J.; Neinhuis, C.; Barthlott, W. *Int. J. Plant Sci. (Chicago, IL, U. S.)* **2000,** *161,* 143–148.
32. Meusel, I.; Barthlott, W.; Kutzke, H.; Barbier, B. *Powder Diffr.* **2000,** *15,* 123–129. doi:10.1017/S0885715600010976
33. Meusel, I.; Neinhuis, C.; Markstädter, C.; Barthlott, W. *Plant Biol.* **2000,** *2,* 462–470. doi:10.1055/s-2000-5961
34. Koch, K.; Dommisse, A.; Neinhuis, C.; Barthlott, W. In *Scanning Tunneling Microscopy/Spectroscopy and Related Techniques;* Koenraad, P. M.; Kemerink, M., Eds.; American Institute of Physics: Melville, NY, U.S.A., 2003; pp 457–460.
35. Koch, K.; Barthlott, W.; Koch, S.; Hommes, A.; Wandelt, K.; Mamdouh, W.; De-Feyter, S.; Broekmann, P. *Planta* **2005,** *223,* 258–270. doi:10.1007/s00425-005-0081-3
36. Ensikat, H. J.; Boese, B.; Mader, W.; Barthlott, W.; Koch, K. *Chem. Phys. Lipids* **2006,** *144,* 45–59. doi:10.1016/j.chemphyslip.2006.06.016
37. Koch, K.; Domisse, A.; Barthlott, W. *Cryst. Growth Des.* **2006,** *6,* 2571–2578. doi:10.1021/cg060035w
38. Koch, K.; Dommisse, A.; Niemietz, A.; Barthlott, W.; Wandelt, K. *Surf. Sci.* **2009,** *603,* 1961–1968. doi:10.1016/j.susc.2009.03.019
39. Barthlott, W. Die Selbstreinigungsfähigkeit pflanzlicher Oberflächen durch Epicuticularwachse. *Klima- und Umweltforschung an der Universität Bonn;* Rheinische Friedrich-Wilhelms-Universität: Bonn, Germany, 1992; pp 117–120.
40. Barthlott, W.; Neinhuis, C. *Planta* **1997,** *202,* 1–7. doi:10.1007/s004250050096
41. Neinhuis, C.; Barthlott, W. *Ann. Bot. (Oxford, U. K.)* **1997,** *79,* 667–677. doi:10.1006/anbo.1997.0400
42. Barthlott, W.; Neinhuis, C.; Jetter, R.; Bourauel, T.; Riederer, M. *Flora (Jena)* **1996,** *191,* 169–174.
43. The Angiosperm Phylogeny Group. *Bot. J. Linn. Soc.* **2016,** *181,* 1–20. doi:10.1111/boj.12385
44. Rechenberg, I. *Evolutionsstrategie-Optimierung technischer Systeme nach Prinzipien der biologischen Evolution;* Frommann-Holzboog: Stuttgart, Germany, 1994.
45. Schwefel, H. P. *Evolution and optimum seeking;* John Wiley & Sons: New York, NY, U.S.A., 1995.
46. Ishimitsu, K. K.; Van Devender, N.; Dodson, R. O.; Brault, P. C.; Byers, B. A.; Johnson, R. P.; Syring, R. P.; Schaefer, M. P.; Endorf, D. R.; McGinnis, C.; Conley, N. E.; Grant, M. *Technical Report No. AFFDL-TR-76-6;* Boeing Commercial Airplane Company: Seattle, WA, U.S.A., 1976; p 191.
47. Bechert, D. W.; Bruse, M.; Hage, W. *Exp. Fluids* **2000,** *28,* 403–412. doi:10.1007/s003480050400
48. Mattheck, C. *Design in Nature;* Springer: Berlin, Germany, 2004.

License and Terms